Springer Environmental Science and Engineering

Ronald C. Surdam *Editor*

# Geological $CO_2$ Storage Characterization

## The Key to Deploying Clean Fossil Energy Technology

Springer

# Geological $CO_2$ Storage Characterization

# Springer Environmental Science and Engineering

For further volumes:
http://www.springer.com/series/10177

Ronald C. Surdam
Editor

# Geological $CO_2$ Storage Characterization

## The Key to Deploying Clean Fossil Energy Technology

Springer

*Editor*
Ronald C. Surdam
Carbon Management Institute
University of Wyoming
Laramie
USA

Additional material to this book can be downloaded from http://extra.springer.com

ISSN 2194-3214 ISSN 2194-3222 (electronic)
ISBN 978-1-4614-5787-9 ISBN 978-1-4614-5788-6 (eBook)
DOI 10.1007/978-1-4614-5788-6
Springer New York Heidelberg Dordrecht London

Library of Congress Control Number: 2013956748

© Springer Science+Business Media New York 2013
This work is subject to copyright. All rights are reserved by the Publisher, whether the whole or part of the material is concerned, specifically the rights of translation, reprinting, reuse of illustrations, recitation, broadcasting, reproduction on microfilms or in any other physical way, and transmission or information storage and retrieval, electronic adaptation, computer software, or by similar or dissimilar methodology now known or hereafter developed. Exempted from this legal reservation are brief excerpts in connection with reviews or scholarly analysis or material supplied specifically for the purpose of being entered and executed on a computer system, for exclusive use by the purchaser of the work. Duplication of this publication or parts thereof is permitted only under the provisions of the Copyright Law of the Publisher's location, in its current version, and permission for use must always be obtained from Springer. Permissions for use may be obtained through RightsLink at the Copyright Clearance Center. Violations are liable to prosecution under the respective Copyright Law.
The use of general descriptive names, registered names, trademarks, service marks, etc. in this publication does not imply, even in the absence of a specific statement, that such names are exempt from the relevant protective laws and regulations and therefore free for general use.
While the advice and information in this book are believed to be true and accurate at the date of publication, neither the authors nor the editors nor the publisher can accept any legal responsibility for any errors or omissions that may be made. The publisher makes no warranty, express or implied, with respect to the material contained herein.

Printed on acid-free paper

Springer is part of Springer Science+Business Media (www.springer.com)

*This book is dedicated to the earth scientists who provided the geological foundation for this study. Although there are many worthy of mention, there are a few that deserve special recognition: Donald Carlisle (problem recognition and solution strategies), Clarence Hall (value of field work), Franklyn Van Houten (the art of observation on the outcrop), John Harms (reconstructing depositional environments from stratification sequences), Hans Eugster (reading the chemistry of rocks), Ken Stanley (geological syntheses), Dick Sheppard and Dick Hay (the role of diagenesis), John Warme (value of core observations), Jim Boles (attention to petrographic detail), and Donald Boyd (importance of detailed observation). All of these scientists were truly exceptional in the volume of knowledge they were readily willing to share, but whom will probably never get the recognition they deserve.*

*Lastly, the dedication of this book would be remiss without mention of the huge amount of work that Shanna Dahl, Deputy Director of the University of Wyoming, Carbon Management Institute, has provided to the task of constructing this book.*

Ronald C. Surdam

# Preface

The primary purpose of this book is to assist future CCS, or CCUS investigations in characterizing potential geological $CO_2$ storage sites well enough so that all of the information required by regulators to permit commercial $CO_2$ storage facilities are provided. The Wyoming Carbon Underground Project (WY-CUSP) is part of the U.S. Department of Energy Geological $CO_2$ Storage Site Characterization Program. In 2010 DOE awarded funding to 10 $CO_2$ geological storage characterization projects. The WY-CUSP program under the direction of the University of Wyoming Carbon Management Institute (CMI) was one of the awardees (project DE-FE0002142: Site Characterization of the Highest-Priority Geologic Formations for $CO_2$ Storage in Wyoming; Principal Investigator, Ronald C. Surdam). The State of Wyoming through the U.W. School of Energy Resources generously provided matching funds for the WY-CUSP program. This book deals with most of the trials and tribulations required to achieve the ultimate goal of the WY-CUSP program: delivery of a certified commercial $CO_2$ storage site that could be used either as a surge tank for $CO_2$ utilization or for permanent sequestration of greenhouse gas (GHG) emissions, or for both.

The rationale for the WY-CUSP program is manifold: first is the effort to establish a mechanism that provides the potential to stabilize or reduce GHG emissions in order to reduce the rate of global warming; secondly to protect Wyoming's coal extraction and future coal-to-chemical industries by providing storage capacity for anthropogenic $CO_2$; thirdly to provide a source of anthropogenic $CO_2$ for enhanced oil recovery projects (at present rates of $CO_2$ production from gas processing plants it would take 150–200 years to recover Wyoming's stranded oil; fourthly to retrieve reservoir information essential for the expansion of natural gas storage in Wyoming; and lastly to establish more robust databases for two very important hydrocarbon reservoirs in Wyoming (substantially reduce uncertainty for all dynamic models of Tensleep/Weber Sandstone and Madison Limestone fluid-flow and rock/fluid systems).

To satisfy the WY-CUSP program rationale the following goals were set: to improve estimates of $CO_2$ reservoir storage capacity, to evaluate the long-term integrity and permanence of confining layers, and to manage injection pressures and brine production in order to optimize $CO_2$ storage efficiency for the most significant

storage reservoir (Tensleep/Weber and Madison Formations) at the Rock Springs Uplift (RSU), a premier $CO_2$ storage site in Wyoming.

To achieve this goal it was necessary to complete the following research objectives; (1) reduce uncertainty in estimates of $CO_2$ storage capacity of key storage reservoir intervals at the RSU; (2) evaluate and ensure $CO_2$ storage permanence at the RSU site by focusing on the sealing characteristics and 3-D interval heterogeneity of the Paleozoic and Mesozoic confining layers; (3) improve the efficiency of potential storage operations by designing an optimal coupled $CO_2$ injection/brine production strategy that ensures effective pressure management, and (4) improve the efficiency of brine treatment at the surface, including the effective use of the elevated temperature and pressure of the brines, recovery of potable water and extraction of metals.

Early efforts by the Wyoming State Geological Survey (WSGS) and the CMI determined that the Tensleep/Weber Sandstones and Madison Limestone were the highest priority $CO_2$ storage reservoirs in Wyoming. Regional studies also determined that the Rock Springs Uplift in southwestern Wyoming was a premier $CO_2$ storage structure/site in the state. The RSU is characterized by 4-way closure, with 10,000 ft of structural relief and extends from approximately 35 mi in an east-west direction, and 50 mi in a north-south direction. The WY-CUSP started with a large potential trap for storage of fluids, but with very little information regarding the nature of the reservoir intervals, distribution and continuity of confining layers or the rock/fluid properties of the reservoir and sealing lithologies. The original data available to CMI included 19 well reports that penetrated the Paleozoic stratigraphic interval in an area of approximately 2,000 $mi^2$, outcrops of key rock units 50–100 mi from the potential test area, well reports, regional maps and topical reports mainly housed in the Wyoming Oil and Gas Conservation Commission, WSGS, and the United States Geological Survey.

This book traces the steps taken by CMI and the WY-CUSP program to get from minimal regional data to a complete characterization of the Rock Springs Uplift as a certified commercial-level geological $CO_2$ storage site.

This trek will be described in 14 chapters covering the following subjects: (1) global warming and climate change: 45 million-year-old rocks in Wyoming support the concept (the context, need and role of CCUS in solving this global problem); (2) regional inventory and prioritization of potential $CO_2$ storage reservoirs in Wyoming: the origins of the WY-CUSP program—the search for the highest priority $CO_2$ geological storage site in the Rocky Mountain Region; (3) legal framework: carbon storage regulations, required permits and access to the study area; (4) the development of the WY-CUSP site characterization strategy—the role of 3-D seismic surveys and stratigraphic test wells; (5) storage site selection, with special emphasis on the proximity to sources of both anthropogenic and natural $CO_2$; (6) retrieval of crucial geologic data: the importance of a stratigraphic test well and 3-D seismic survey—key observations derived from core, well logs, borehole tests and seismic attribute acquisition; (7) utility of 3-D seismic attribute analysis and a VSP survey for assessing potential carbon sequestration targets (8) hydrologic data acquisition and observations—the importance of characterizing formation fluids; (9) predicting

spatial permeability in targeted storage reservoirs and seals on the RSU– a method that increases the accuracy of 3-D flow simulations of $CO_2$ storage applications; (10) advances in estimating the geological $CO_2$ storage capacity of the Madison Limestone and Weber Sandstone on the RSU by utilizing detailed 3-D reservoir characterization and geological uncertainty reduction (numerical simulations that include 3-D heterogeneity of reservoir petrophysical properties; displaced fluid/pressure management; (11) displaced fluid management—the key to commercial-scale geologic $CO_2$ storage; (12) illustration of the advantages of deploying innovative, multiple-resource development strategies designed to foster the sustainability of energy and environmental resources—strategies that greatly increase the value of $CO_2$ storage and utilization; (13) a feasibility study of the integration of geological $CO_2$ storage with enhanced oil recovery ($CO_2$ flooding) in the Ordos Basin, China and elsewhere; and (14) WY-CUSP integrated strategy for the detailed and accurate characterization of potential $CO_2$ storage reservoir and storage sites. Taken together these 14 chapters represent an effective and efficient process to improve estimates of $CO_2$ reservoir storage capacity, to evaluate the long-term integrity and permanence of confining layers, and the management of injection pressures and brine production and treatment in order to optimize $CO_2$ storage. Although the chapters in this book represent important steps to evaluating and optimizing $CO_2$ storage, each of the chapters is designed to stand alone.

Our aim in constructing the book was to positively affect and assist future global $CO_2$ storage and utilization projects. It is our firm belief that continued industrialization and global expansion of quality of life will require ever-increasing efforts to effectively store GHG emissions—without an exponential increase in the effort to store $CO_2$, neither further industrialization or global improvements in the quality of life and standard of living will be possible. Hopefully this book will expedite the global effort to retrieve energy, while sustaining environmental quality. Anyone interested in CCS, or CCUS should find this body of work helpful in executing their own projects to provide economic energy, while minimizing the development of undesireable environmental footprints. There is an old adage that, “a smart person learns from experience, but a wise person learns from the experience of others.” It is with that thought that we offer the WY-CUSP experience for the benefit of all others in their efforts to decrease or stabilize global GHG emissions by utilizing $CO_2$ geological storage.

# Acknowledgements

The Wyoming Carbon Underground Storage Project (WY-CUSP) site characterization project is funded in part by the U.S. Department of Energy's National Energy Technology Laboratory (Project DE-FE0002142), and the Carbon Management Institute (CMI) would like to thank D.O.E. and our D.O.E. Project Manager Bill Aljoe. Also CMI acknowledges the financial support from the State of Wyoming. We acknowledge the help of Terry Miller in set up of the finite volume grids; and Phil Stauffer and Hailing Deng for help with details of FEHM. In addition, thanks to Dynamic Graphics, Inc. for allowing us to use their EarthVision software and to Schlumberger for allowing us access to their Eclipse and Petrel software packages. Also, we acknowledge the support provided by the Wyoming Oil and Gas Conservation Commission and the Department of Environmental Quality. Very importantly, we thank Shanna Dahl, Shauna Bury, and Allory Deiss—all colleagues at CMI—for their outstanding support.

Also we acknowledge the contributions provided to the WY-CUSP program and construction of this book made by our colleagues at the University of Wyoming: Erin Campbell-Stone and Ranie Lynds, Jim Myers and Robert Kirkwood, John Kaszuba and Vladimir Alvarado, Subhashis Mallick, Carol Frost, and their students. For the chapter on the Ordos Basin the contributions of Yongzhen Chen, Tin Tin Luo, and Jiaping Gao from the Shaanxi Provincial Institute of Energy Resources and Chemical Engineering at Northwest University, Xian, and the Yanchang Petroleum Company are acknowledged.

The Laboratory contributions made by the following facilities are gratefully acknowledged: Intertek Laboratory, USGS Core Libraries, Wyoming Analytical Laboratories, UW Stable Isotope Facility, UW Materials Characterization Laboratory, Energy Laboratories, and Wagner Petrographics.

Lastly, we acknowledge the support provided to the WY-CUSP program by our partners: Baker Hughes, Inc., including Paul Williams, Sam Zettle, Dana Dale, and Danny Dorsey, and TRUE Drilling Co. of Casper, WY.

Other major contributors to the WY-CUSP include Los Alamos National Laboratory, Lawrence Livermore National Laboratory, PetroArc International, New England Research, Geokinetics, EMTek, and the Wyoming State Geological Survey.

Other significant supporters of the WY-CUSP program include UW Vice-President of Research Bill Gern, UW Provost Myron Allen, and Mark Northam, Director of the UW School of Energy Resources. Lastly, Lynne Boomgaarden was a truly invaluable member of our team by providing the legal expertise and ability to expedite a multitude of required county, state, and federal permits, and David Copeland, a key member of our team, particularly with respect to editing manuscripts and organizing figures. To both Lynne and David we gratefully acknowledge your support.

Thanks to all the above individuals, institutions, and corporations that played a role in the success of the WY-CUSP Program.

# Contents

# Contributors

**Ramsey D. Bentley** Carbon Management Institute Laramie, University of Wyoming, Laramie, USA

**Lynne Boomgaarden** Crowley Fleck PLLP, Cheyenne, WY, USA

**Shanna C. Dahl** Carbon Management Institute, Laramie, WY, USA

**Yuri Ganshin** Carbon Management Institute Laramie, University of Wyoming, Laramie, USA

**Mario Garcia-Gonzalez** Universidad Industrial de Santander, Bucaramanga, Colombia

**Zunsheng Jiao** Carbon Management Institute Laramie, University of Wyoming, Laramie, USA

**J. Fred McLaughlin** Carbon Management Institute, Laramie, WY, USA

**Scott A. Quillinan** Carbon Management Institute Laramie, University of Wyoming, Laramie, USA

**Ronald C. Surdam** Carbon Management Institute Laramie, University of Wyoming, Laramie, USA

**Yajun Wang** Shaanxi Provincial Institute of Energy Resources and Chemical Engineering Xian, Shaanxi, P. R. China

**Lifa Zhou** Shaanxi Provincial Institute of Energy Resources and Chemical Engineering Xian, Shaanxi, P. R. China

# Chapter 1
# Geological Observations Supporting Dynamic Climatic Changes

**Ronald C. Surdam**

**Abstract** The Eocene Green River Formation in Wyoming has long served as a standard for lacustrine depositional systems. This lacustrine formation, excluding the culminating phase, was deposited in a closed hydrographic basin. The position of the boundary between lake and mudflat margin was dictated by the inflow/evaporation ratio (inflow greater than evaporation = transgression; inflow less than evaporation = regression). All members of the Green River Formation are characterized by repetitive stratification sequences. In the Tipton and Laney members, the repetitive stratification sequences are laminated, kerogen-rich carbonates with fish fossils overlain by dolostone with numerous desiccation features. In contrast, in the middle member (Wilkins Peak), the typical stratification sequence is trona (evaporate) overlain by dolostone, overlain by kerogen-rich carbonate (oil shale). All these stratification sequences can be explained as products of dynamic climate change and a consequent imbalance between inflow and evaporation which probably resulted from the earth's processional variations. The evidence for global warming and climate change (prior to anthropogenic green house gas (GHG) emissions) is undeniable. The crucial question is, *are anthropogenic GHG emissions accelerating the rate of climate change?* The confluence of rising global temperature with substantial increases in GHG emissions since the beginning of the industrial revolution strongly suggests that the answer to this question is *yes*.

## 1.1 Climate Change and Global Warming

Over the past decade, the development of carbon capture and storage (CCS), and of clean coal technology in general, has been closely linked to climate change and global warming. As a result, some CCS detractors have discounted the importance of CCS because they simply do not believe in climate change and global warming. Much of the disagreement and resulting criticism of the importance of CCS in

R. C. Surdam (✉)
Carbon Management Institute Laramie, University of Wyoming, Laramie, USA
e-mail: rsurdam@uwyo.edu

R. C. Surdam (ed.), *Geological $CO_2$ Storage Characterization,*
Springer Environmental Science and Engineering, DOI 10.1007/978-1-4614-5788-6_1,
© Springer Science+Business Media New York 2013

near-future global energy/industrial development stems from some policymakers' misperceptions of the role of science in this controversy. In brief, science does not uncover truths: rather, science reduces uncertainties. When, over time, all observations, experiments, and measurements from diverse scientific disciplines—without serious contradiction—support a working scientific hypothesis, it becomes scientific doctrine. Examples of this process include Darwin's theory of evolution and Einstein's theory of relativity. A theory becomes doctrine when uncertainties related to the theory have been reduced as much as possible (typically, when all available observations support the stated theory). It is important to realize that scientific doctrine is not *truth*, for future new observations, experiments, and measurements may require modification or replacement of the doctrine. Thus, established scientific doctrine is constantly tested over time.

Ideologues, particularly with respect to religious and sociopolitical programs, often find themselves in contentious debate with scientific doctrine because their dogma is based in faith (firm belief in truths not subject to scientific testing). Such irresolvable debates between faith-based dogma and scientific doctrine are often marked by bitterness, divisiveness, and partisanship. No resolution of these debates seems possible because no common ground between static truth and dynamically evolving scientific doctrine exists.

Scientists debate, too, but resolution tends to follow from a mutual effort to reduce uncertainty. Initially, when the ideas of climate change and global warming—and particularly their relationship to greenhouse gas (GHG) emissions—were proposed, the scientific community was divided, and healthy debate ensued. Over time, scientific doubt concerning the relationship between GHG emissions and global warming has waned and almost disappeared, largely due to the convergence of affirmative results from multidisciplinary scientific research and testing. At present, a strong scientific consensus that anthropogenic GHG emissions are contributing to global warming exists.

To those of us familiar with the geology of the lacustrine Eocene Green River Formation in Wyoming, Colorado, and Utah, this consensus is not surprising. As discussed in the following section, scientists studying the stratigraphic framework of the Eocene Green River Formation have long considered global warming and climate change to be essential concepts that explain observations about the dynamics of ancient lakes Gosiute and Uinta (Green River Formation).

## 1.2 Ancient and Modern Analogs of Climate Change

The Green River Formation deposited in Eocene Lake Gosiute in southwestern Wyoming and northern Colorado is stratigraphically divided into three members, from bottom to top the Tipton, Wilkins Peak, and Laney members (Fig. 1.1). Both the Tipton and Laney members are characterized by numerous oil shale and dolostone layers (laminated kerogen-rich or kerogen-poor carbonates), and the Wilkins Peak Member is characterized by 42 or more trona beds and some oil shales

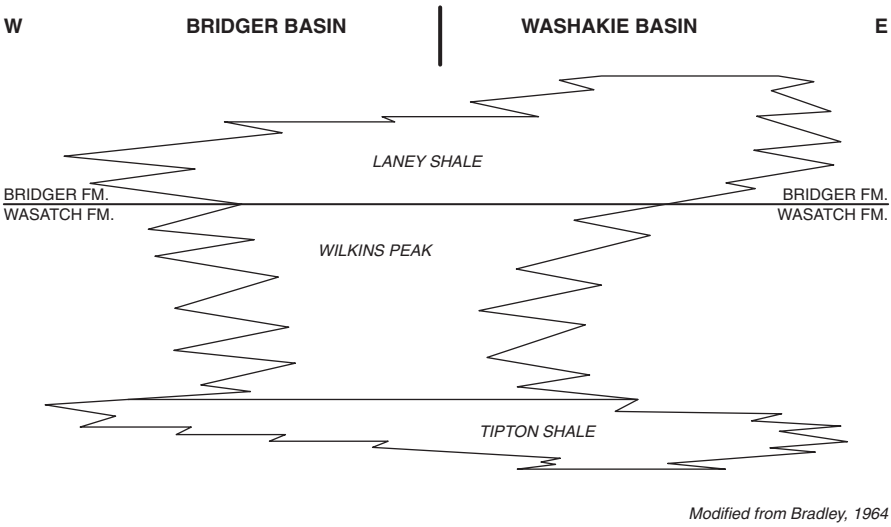


**Fig. 1.1** Generalized stratigraphic framework of the Eocene Green River Formation in southwestern Wyoming (Tipton, Wilkins Peak, and Laney members). (Modified from Bradley 1964)

(Culbertson 1971). Typically, these three members are interpreted, respectively, as high, low, and high stands of Lake Gosiute. The Tipton and Laney members, dominated by kerogen-rich carbonate deposition (oil shale), are generally considered to represent a humid climate with marked seasonality (similar to that of present-day central Florida; Bradley 1973). The Wilkins Peak Member, dominated by evaporites, represents a humid climate with substantial seasonal aridity (similar to the present-day bottom of the East African Rift Valley; Eugster and Surdam 1973).

The sedimentology and resultant stratigraphy and stratification sequences characterizing each of these members were produced in a highly complex depositional system best described as a "playa-lake complex" (Eugster and Surdam 1973; Bradley 1973; Surdam and Wolfbauer 1975; Eugster and Hardie 1975; Surdam and Stanley 1979). In all stages but its culminating phase, the lake occupied a closed hydrographic basin with a lacustrine environment transgressing or regressing across a fringing playa mudflat (across an extremely low topographic gradient of probably 1–2 feet per mile) as a result of an imbalance between inflow and evaporation (Fig. 1.2). On the basis of paleobotanical evidence, MacGinitie (1969) suggested that Lake Gosiute was approximately 1000 feet above sea level during the Eocene (approximately 45 m.y.b.p.). Lake Gosiute persisted for approximately 4 million years during the Eocene (Bradley 1964). The lake level fluctuated often, with oil shale and trona beds as alternating products. Consequently, the stratification sequence in each member represents a detailed record of this dynamic inflow/evaporation imbalance (climatic change) during the Eocene.

First, consider a typical stratification sequence in the Laney Member on the playa-lake fringe (Fig. 1.3a). The sequence starts with strandline deposition (algal rip-ups, algal stromatolites, pisolites/oolites, and/or ostracodal limestones) over-

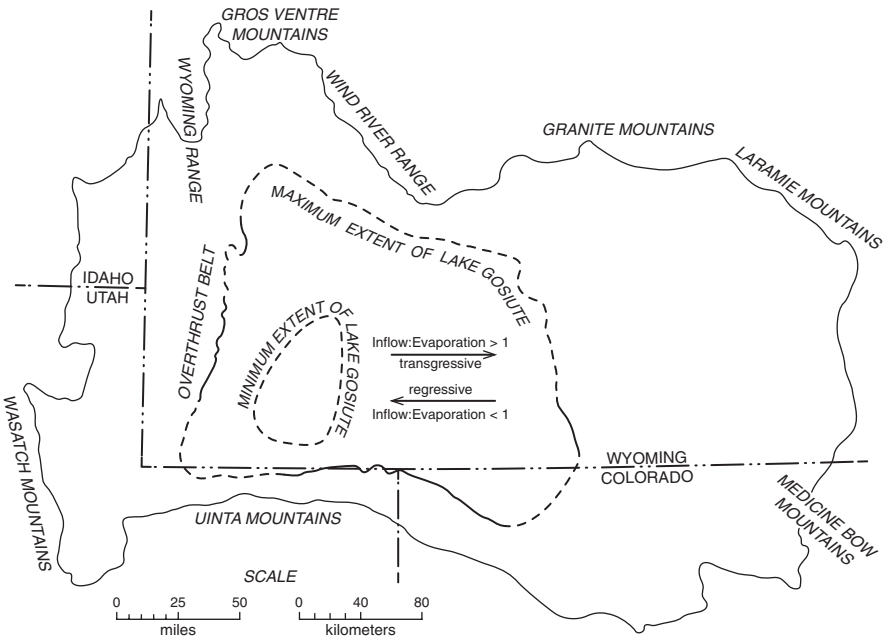


**Fig. 1.2** Closed hydrostratigraphic basin characterizing all but the culminating stages of ancient Lake Gosiute. Also shown are the maximum and minimum extents of Eocene Lake Gosiute. (Modified from Bradley 1964)

lain by kerogen-rich laminated carbonate (oil shale) commonly containing fossil fish. Finally, the lacustrine portion of the sequence is overlain by dolomitic mudflat deposition commonly including saline mineral casts and molds, mud-cracks, and Magadi-type chert. This stratification sequence, or some modification of the sequence, was repeated vertically as the lake transgressed and regressed across a particular geographic location (Fig. 1.3b). In positions near the geographic center of Lake Gosiute during the Laney stage, the repetitive stratification sequences consist of alternating kerogen-rich and kerogen-poor laminated carbonate (Fig. 1.3c). When the playa fringe was minimized (inflow: evaporation ratio >1), the laminated carbonate is kerogen-rich and calcitic, whereas when the playa fringe is more dominant (inflow: evaporation ratio <1), the laminated carbonate is kerogen-poor and dolomitic (Fig. 1.3d). The Laney stratification sequences shown in Fig. 1.3a–d are typical of the interaction of the lake and fringing playa mudflat as the climate changed: variable inflow-to-evaporation ratio in a closed hydrographic basin. The Laney stratification sequences shown in Fig. 1.3c,d are typical of the sedimentologic changes that took place at the lake center as a result of climatic changes in the closed hydrographic basin during a relatively high stand of the lake.

During a relatively low stand of Lake Gosiute (Wilkins Peak Member), the depositional system also was characterized by imbalances between inflow and evaporation strongly influenced by climatic changes (Fig. 1.4a). Typically, the stratification

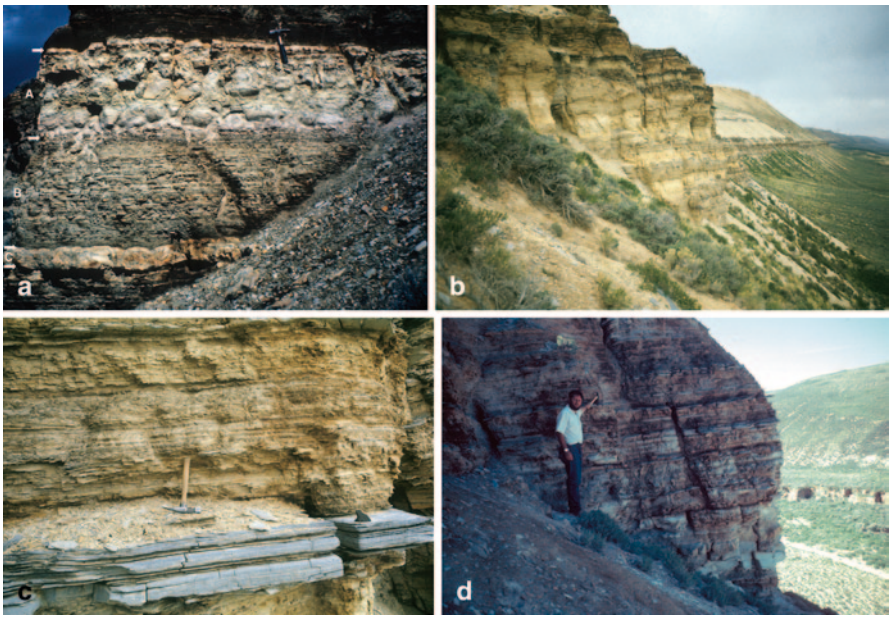


**Fig. 1.3** **(a)** Typical lacustrine depositional cycle in the Laney Member along the Kinney Rim. The strandline deposits [C] composed of stromatolites, pisolites/oolites and/or ostracodal limestones, overlain by kerogenous laminated carbonates (oil shale [B] commonly containing fossil fish), is overlain by dolomitic mudstone [A] including saline mineral casts/molds, mudcracks, and Magadi-type chert. This stratification sequence is interpreted as the result of the lake transgressing over the playa-mudflat fringe (inflow:evaporation > 1) and then regressing sharply due to an abrupt change in the regional inflow:evaporation ratio (> 1). Rock hammer for scale. **(b)** Repetition of stratigraphic sequence shown in (a). View is to the south along the Kinney Rim, demonstrating the repetitive nature of the transgressive/regressive stratification sequences (lake-mudflat-lake). Within both the lacustrine and mudflat portions of the sequence, many vertical variations best explained by climatic dynamics exist, but note the sharp contact between the dark lacustrine sequences and the light mudflat sequences (indicating an abrupt lake-level decline). In the background, the buff-colored sequence is a tuffaceous-evaporite lithofacies (dolomite/analceme-rich rock with nahcolite/trona molds) that separates the Laney Member into similar upper and lower portions. **(c)** Stratification sequence characterizing rocks deposited in the Laney Member in a lake-center position. Note that unlike the stratification sequence shown in Fig. 1.3a (a more marginal lake position), there are no strandline deposits, but instead layers of kerogen-rich laminated carbonates (high stand with reduced influence of the fringing playa mudflat) overlain by kerogen-poor laminated carbonate (significant influence from the fringing mudflat). Both lithofacies were deposited in a lacustrine environment. Rock hammer for scale. **(d)** Repetitive stratification sequences in laminated carbonate lithofacies near geographic center of Lake Gosiute during Laney stage. Sequences are alternating layers of kerogen-rich (dark) and kerogen-poor (light) laminated carbonate in the lower part of the Laney Member at Green's Canyon near Green River, Wyoming. Kerogen-rich layers consist of calcite (depositional system dominated by lacustrine processes), whereas the kerogen-poor layers consist of dolomite (depositional system dominated by playa mudflat processes)

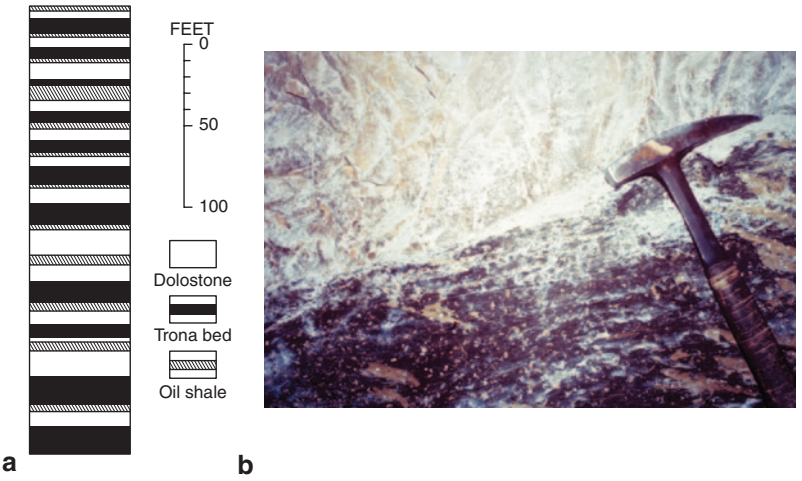


**Fig. 1.4** **(a)** Partial composite columnar section of Wilkins Peak Member (Green River Formation) in the trona area of Wyoming. (Modified from Culbertson 1971). **(b)** Sharp contact between oil shale (black) and trona (white) from underground at trona mine. This photo illustrates the relationship between oil shale and trona shown in the Wilkins Peak Member in Fig. 1.3a. The sharp boundary is best interpreted as indicating an extremely rapid climatic change (change in inflow:evaporation ratio) from high-stand conditions to low-stand conditions

sequence starts with an evaporite deposit (i.e., trona with or without halite deposited from a concentrated brine-rich alkaline fluid column–relatively organic-poor and highly evaporitic lake/pond within the minimum extent of the lake) (Fig. 1.2), overlain by a dolostone (lacustrine environment dominated by a wide fringing mudflat—transport of dolomitic mud from playa fringe to lacustrine environment), and in turn overlain by an oil shale (kerogen-rich carbonate deposited as the lacustrine environment was expanding) (Fig. 1.4a). There are approximately 42 individual trona beds within the Wilkins Peak Member, almost all of which are underlain by a bed of oil shale (Fig. 1.4b) (Culbertson 1971). The sharp contact between oil shale and trona deposition (Fig. 1.4a) could only have resulted from a drastic and abrupt change in inflow and evaporation as part of a highly dynamic climatic system.

In summary, all stratigraphic sequences in both the Laney Member (high stand) and Wilkins Peak Member (low stand) are the product of climatic factors (evaporation and inflow) that caused the lake to transgress (expand) and regress (contract) across a very low topographic gradient in a closed hydrographic basin. In a transgression, the lake expands and the playa fringe shrinks, whereas during a regression, the lake shrinks and the playa fringe expands (Fig. 1.2).

To understand the climatic variations characterizing ancient Lake Gosiute, it is useful to examine modern analogs of the two lithologic end members—oil shale and trona. After a comprehensive search for modern oil shale analogs, Bradley (1970) suggested that Mud Lake in central Florida has many comparable attributes. Mud Lake (Fig. 1.5a) is very shallow: in the driest seasons, it may be as shallow as 22 cm


**Fig. 1.5** **(a)** Mud Lake, in modern-day central Florida. On the basis of the work of Bradley (1970), this lake is commonly cited as a potential modern analog for oil shale deposition. (Tracy Enright, US Geologic Survey photo) **(b)** Modern Lake Magadi, Kenya. Huge amounts of trona have been deposited in this lake over the last 10,000 years

deep, and in the wettest seasons it may be 85 cm deep. The algal sediment makes up a layer about 1 m thick at the bottom of the lake (Bradley 1970).

The modern analog for trona is Lake Magadi, which lies at the lowest point in the East African Rift, Kenya (Fig. 1.5b). Except during the rainy season, which is relatively short but intense, inflow into the lake comes mainly from peripheral springs.

The observations with respect to the stratigraphic sequence described above relate only to the pre-culminating stages of basin evolution: that portion of the lake characterized as a closed hydrographic basin (Fig. 1.6). In the culminating phase of Eocene Lake Gosiute (Green River Formation), the lake evolved from a closed hydrographic regime (saline alkaline lake) to an open hydrographic regime (freshwater lake). This evolution marked a substantial enlargement of the hydrographic basin (increased inflow from the north), a rapid increase in the progradation of terrigenous material from north to south, and an outflow of lake water into the Piceance Creek basin to the south (Fig. 1.6) (Surdam and Stanley 1979, 1980).

Crucial in the analysis of climatic effects on the stratification sequences that characterize Lake Gosiute is determining the temporal aspects of the sequences in both high and low stands of the lake. In evaluating the stratigraphic sequence during a high stand of Lake Gosiute, a well-documented case from West Africa is pertinent to this discussion. Lake Bosumtwi in Ghana, West Africa is located in a meteorite impact crater in a rainforest. For at least 13,000 years, the crater has been a closed hydrographic basin (Talbot and Delibrias 1980). During this 13,000-year period, the high stands of the lake lasted for 2000–2500 years and were interrupted by short but intense regressions, or low stands (Fig. 1.7) (Talbot and Delibrias 1980; Talbot 1988; Talbot and Johannesson 1992). As shown in Fig. 1.7, the duration of lake level low stands ranged from 200 to 500 years, with very steep rates of lake level decline (inflow $\ll$ evaporation). In contrast, the high stands of the lake lasted longer and remained stable until punctuated by intense declines in lake level (Fig. 1.7).

Insight into the temporal aspects of stratigraphic sequences characterizing the Wilkins Peak Member can be gained by observing a trona-depositing modern analog: Lake Magadi in Kenya (Baker 1958, 1963; Eugster 1969, 1970). The

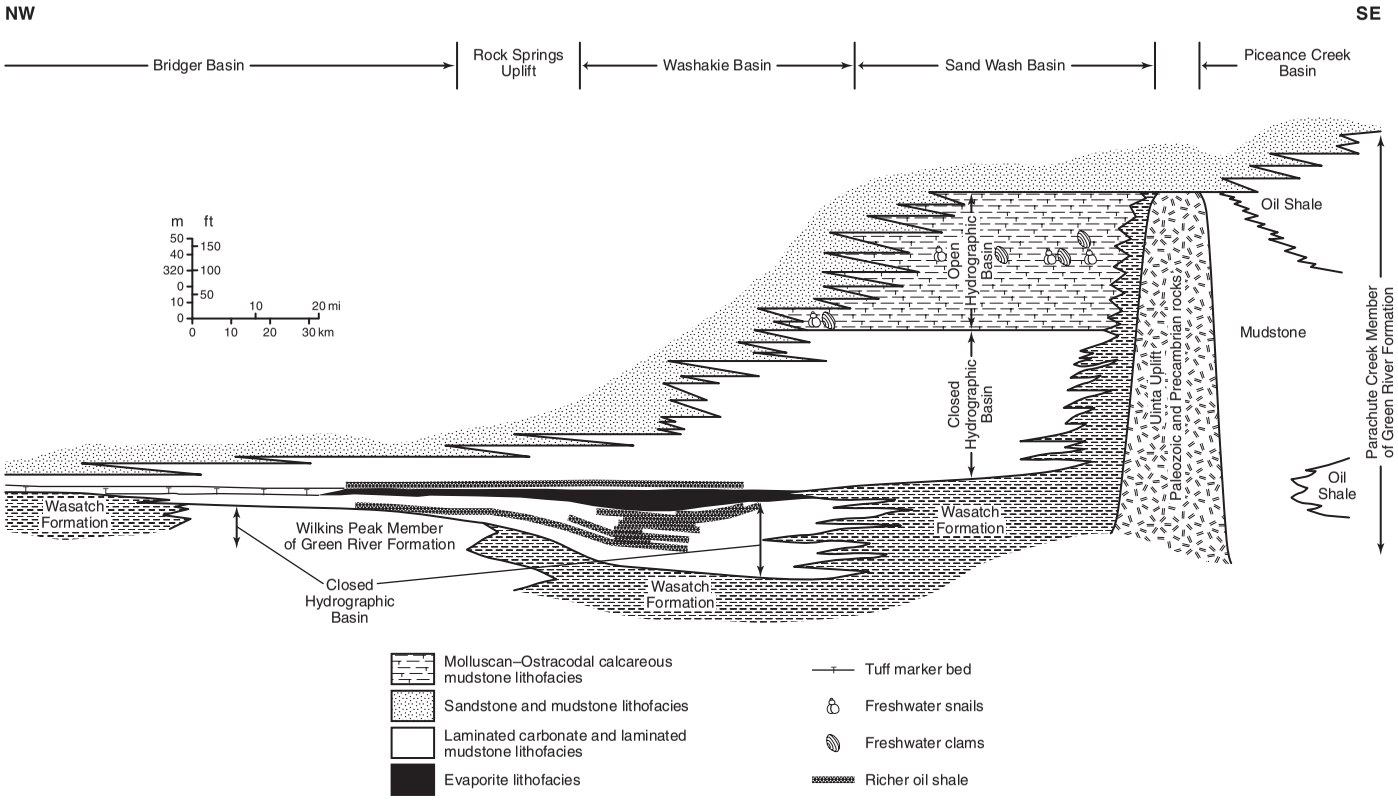


**Fig. 1.6** Lithofacies and marker beds from northwest to southeast in the Laney Member, Green River Formation, Wyoming and Colorado. This cross section demonstrates that during deposition of the Laney Member, Lake Gosiute evolved from a playa lake with oil shale deposition, to a playa with evaporate deposition, to a playa lake with oil shale deposition, and finally to a fresh water lake. During all but the final stages of the lake, the hydrographic basin was closed, and deposition was controlled by the imbalance between inflow and evaporation. In the fresh-water stage, the hydrographic basin expanded and became open with additional inflow from the north and outflow to the south in the Piceance Basin. This chapter deals with Lake Gosiute only during the time period in which the hydrographic basin was closed. (Modified from Surdam and Stanley 1979)

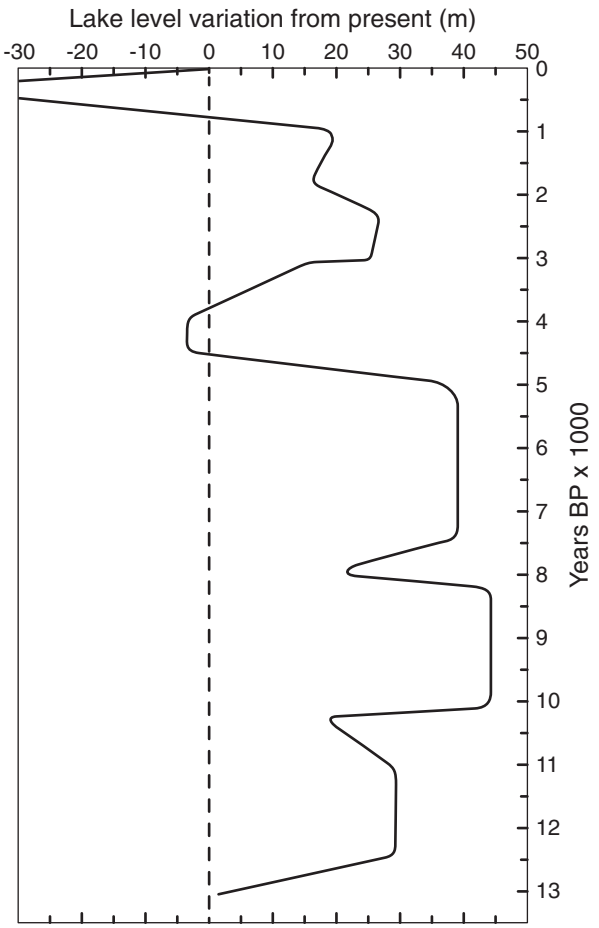


**Fig. 1.7** Water level curve for Lake Bosumtwi, Ghana, West Africa over the past 13,500 years. Lake Bosumtwi is a crater lake in a closed hydrographic basin, and has been for at least the past 13,000 years. (Modified from Talbot and Delibrias 1980)

present-day evaporite series at Lake Magadi is characterized by substantial trona deposition (Fig. 1.8a). The 9100-year-old, organic-rich High Magadi Beds along the basin margin clearly express an earlier high stand of Lake Magadi (Fig. 1.8b). These are organic-rich laminated beds with a mineralogic composition of detrital silicates, saline minerals, calcite, sodium silicates, quartz, and authigenic zeolites (Surdam and Eugster 1976) (Fig. 1.8c). So, in 9000–10,000 years, the Lake Magadi depositional system (closed hydrographic basin) has evolved from organic-rich laminated sediments to trona deposits (Fig. 1.13a,c) as a result of a marked decrease in the inflow: evaporation ratio.

In both modern analogs described (high and low stands of lakes Bosumtwi and Magadi), the formation of the most recent "modern" stratification sequence occurred over 2500–10,000 years. In both cases, the stratification sequences forming at lakes Bosumtwi and Magadi are the result of climatic change. Stratification sequences of 2500–10,000 years duration fit neatly with the number of observed


**Fig. 1.8** **(a)** Modern trona mining operation at Lake Magadi, Kenya. The dredge is extracting the trona beds; if the dredge shut down, it would become trona-locked because the brine is saturated with trona. The trona beds are masses of trona crystals filled with brine. As the trona is mined, the brine flows out of the trona to form the "lake" upon which the dredge is floating. **(b)** Present-day Magadi mudflats with trona efflorescent crust. The 10,000-year high-stand shoreline of Lake Magadi (High Magadi Beds) is in the background. **(c)** High Magadi Beds associated with the high-stand shoreline shown in (b). The sediments are organic-rich (black) with fish fossils. The white layers consist of magadiite, a hydrous sodium silicate that, with time, reacts to Magadi-type cherts. Carbon-14 dating suggests that these organic-rich sediments are approximately 10,000 years old. Therefore, over the past 10,000 years the lake evolved from a relatively fresh lake supporting a fish population to a saline, alkaline lake precipitating trona

stratification sequences in the Tipton, Wilkins Peak, and Laney members of the Green River Formation, and are compatible with the age dates for the Lake Gosiute temporal framework.

In summary, during the last 10,000 years in "modern" lacustrine environments, the same types of stratification sequences are observed as those repeatedly characterizing the high- and low-stand stratigraphic framework of ancient Lake Gosiute. Although the detailed climatic mechanisms driving the Eocene climate are not well understood, the best explanation for the Eocene stratification sequences is that they are the product of climatic changes resulting in substantial alterations in inflow: evaporation ratios in a closed hydrographic basin.

Fischer and Roberts (1991), studying the organic-rich laminated sediments in the Green River Formation, considered the coupled kerogen-rich and kerogen-poor layers as the result of varving (record of a year's deposition), as did Bradley (1929). Fischer and Roberts (1991) and Ripepe et al. (1991) interpreted the variations in

thickness, lithology, and color banding of the laminae couplets and series of couplets as the result of climatic change within the lacustrine environment. They suggested two strong bimodal periodicities, one following a six-year cycle resulting from an El Niño-type (ENSO) phenomenon of atmospheric dynamics, the other following an eleven-year pattern interpreted as the result of the sunspot cycle (Fischer and Roberts 1991; Ripepe et al. 1991). On a larger scale, they observed processional variations with a mean period of 20,000 years and a bundling of a set of five of these on the 100,000-year eccentricity cycle. The observations of small- and large-scale depositional aspects (cyclical variations) in the stratigraphic framework of ancient Eocene Lake Gosiute can be explained neatly by such climatic dynamics. According to Fischer and Roberts, the Surdam and Stanley (1979) interpretation of regressional shoreline cycles in the Green River Formation as processional cycles is well founded.

## 1.3 Global Warming—Trends and Projections

The geologic evidence for climatic change in present and ancient lacustrine environments in closed hydrographic basins is overwhelming. The vital question remaining is whether the huge increase in anthropogenic greenhouse gas emissions that began during the Industrial Revolution and continues today is accelerating the rate and intensity of climate change and global warming.

The scientific consensus is that the rapid increase in $CO_2$ emissions since 1900 is due to anthropogenic causes, particularly the burning of fossil fuels: from 1850–2000, annual anthropogenic $CO_2$ emissions increased exponentially from millions of tons to 4 billion tons (USEIA 2012). As a result, assessments by the Intergovernmental Panel on Climate Change (IPCC) (Meehl et al. 2007) suggest that the earth's climate has warmed by 1.1–1.6 °F over the past century, and that anthropogenic activity is "very likely" a dominant driving factor. Most importantly, according to the National Oceanic and Atmospheric Administration's National Climatic Data Center (2012), the warming of the globe has continued over the last decade.

In 2013 at the Hawaiian monitoring site atmospheric $CO_2$ was measured at 400 ppm. In 1958 the level of atmospheric $CO_2$ was 350 ppm, so $CO_2$ concentrations in the atmosphere have increased approximately 1 ppm/yr. Globally at this rate the atmospheric $CO_2$ concentration will reach 450 ppm in 50 years or less, and will be accompanied by a 2 °C increase in global temperature. A 2 °C in global temperature increase could result in forests in Greenland and sea level rises of 10–20 m (33–66 ft). The most alarming climate observation occurred from 1961 to 2008. The total heat content of the oceans has increased by approximately $225 \times 10^{21}$ joules. (Church et. al., 2011). Clearly the danger is that the rate of global climate change will outstrip the rate of human adaptation!

The National Research Council (2011) predicts that without stabilization of $CO_2$ emissions at near-present-day levels, the following global and North American changes will occur.

Key global projections:

- For every 2 °F of warming, models project about a 15 % decrease in the extent of annually averaged sea ice and a 25 % decrease in September Arctic sea ice.
- The coastal sections of the Greenland and Antarctic ice sheets are expected to continue to melt or slide into the ocean. If the rate of this ice melting increases in the 21st century, the melted ice sheets would add significantly to global sea level rise.

Key US projections:

- Northern hemisphere snow cover is expected to decrease by approximately 15 % by the year 2100.
- Models project that the snow season will continue to shorten, with snow accumulation beginning later and melting starting earlier. Snowpack is expected to decrease in many regions.
- Permafrost is expected to continue to thaw in northern latitudes. This would have large impacts in Alaska.

## 1.4 Global Warming—the Challenge and a Necessary and Viable Countermeasure

It is evident that in North America and elsewhere on the planet, these changes will result in increased average temperatures, more frequent and intense heat waves and drought, northern areas becoming wetter and southern areas becoming drier, more heavy precipitation events, precipitation falling as rain rather than snow, and more frequent and intense Atlantic hurricanes. With anthropogenic greenhouse gas (GHG) emissions continuing to increase at the present rate, the timing of "tipping points" for adaptation will accelerate while climatic effects intensify, with societal costs rising prohibitively. Obviously, such predicted changes—should they become reality—would devastate humankind.

The work presented in this book is vitally important because carbon capture and sequestration/storage is currently the only known way to stabilize anthropogenic greenhouse gas emissions in a world of unconstrained industrialization. During the 21st century, nations with expanding economies will not be able to continue to grow without ever-increasing GHG production: in this situation, the availability of technology capable of stabilizing or reducing atmospheric GHG emissions is absolutely essential. In the following pages we will offer a strategy for storing huge amounts of $CO_2$.

## References

Baker HP (1958) Geology of the Magadi area. Kenya Geologic Survey Report 42

Baker BH (1963) Geology of the area south of Magadi. Geologic Survey of Kenya Report 61

Bradley WH (1929) The varves and climate of the Green River Epoch. U.S. Geologic Survey Professional Paper 158E:87–110

Bradley WH (1964) Geology of the Green River Formation and associated Eocene rocks in southwestern Wyoming and adjacent parts of Colorado and Utah. U.S. Geologic Survey Professional Paper 496-A, p. A1–A86

Bradley WH (1970) Green River oil shale – concept of origin extended. Geol Soc Am Bull 81:990–993

Bradley WH (1973) Oil shale formed in desert environment: Green River Formation, Wyoming. Geol Soc Am Bull 84(4):1121–1124

Church JA, White NJ, Konikow LF, Domingues CM, Cogley JG, Rignot E, Gregory JM, Van Den Broeke MR, Monaghan AJ, Velicogna I (2011) Revisting the Earth's sea-level and energy budgets from 1961 to 2008. Geophysics Resource Letter: 38(L18601). 10.1029/2011GL048794 (http://dx.doi.org/10.1029/2011GLO48794)

Culbertson WC (1971) Stratigraphy of the trona deposits in the Green River Formation, southwest Wyoming. Univ Wyoming Contrib Geol 10:15–23

Eugster HP (1969) Inorganic bedded cherts from the Magadi area, Kenya. Contrib Mineral Petrol 22:1–31

Eugster HP (1970) Chemistry and origin of the brines of Lake Magadi, Kenya. Mineral Soc Am Special Publ 3:215–235

Eugster HP, Hardie LA (1975) Sedimentation in an ancient playa-lake complex: the Wilkins Peak Member of the Green River Formation of Wyoming. Geol Soc Am Bull 86(3):319–334

Eugster HP, Surdam RC (1973) Depositional environment of the Green River Formation of Wyoming: a preliminary report. Geol Soc Am Bull 84(4):1115–1120

Fischer AG, Roberts LT (1991) Cyclicity in the Green River Formation (lacustrine Eocene) of Wyoming. J Sediment Petrol 61(7):1146–1154

MacGinitie HD (1969) The Eocene Green River flora of northwestern Colorado and northeastern Utah. University of California Publications in the Geologic Sciences, vol 83

Meehl GA et al (2007) Chap. 10, Global climate projections. In: Solomon S et al (eds) Climate change 2007: the physical science basis. Cambridge U.P., Cambridge and New York, Box 10.2, Equilibrium climate sensitivity. [IPCC AR4 WGI: Contribution of Working Group I to Fourth Assessment Report of the International Panel on Climate Change]

National Oceanic and Atmospheric Administration (2012) http://www.ncdc.noaa.gov/oa/ncdc.html

National Research Council (2011) Climate stabilization targets: Emissions, concentrations, and impacts over decades to millennia. National Academies Press, Washington, D.C

Ripepe M, Roberts LT, Fischer AG (1991) ENSO and sunspot cycles in varved Eocene oil shales from image analysis. J Sediment Petrol 61(7):1155–1163

Surdam RC, Eugster HP (1976) Mineral reactions in the sedimentary deposits of the Lake Magadi region, Kenya. Geol Soc Am Bull 87:1739–1752

Surdam RC, Stanley KO (1979) Lacustrine sedimentation during the culminating phase of Eocene Lake Gosiute, Wyoming (Green River Formation). Geol Soc Am Bull 90(1):93–110

Surdam RC, Stanley KO (1980) Effects of changes in drainage-basin boundaries on sedimentation in Eocene lakes Gosiute and Uinta of Wyoming, Utah, and Colorado. Geology 8:135–139

Surdam RC, Wolfbauer CA (1975) Green River Formation, Wyoming: a playa-lake complex. Geol Soc Am Bull 86(3):335–345

Talbot MR (1988) The origins of lacustrine oil source rocks: evidence from the lakes of tropical Africa. Geol Soc Lond Special Publ 40:29–43

Talbot MR, Delibrias G (1980) A new late Pleistocene-Holocene water-level curve for Lake Bosumtwi, Ghana. Earth Planet Sci Lett 47:336–344

Talbot MR, Johannessen T (1992) A high resolution palaeoclimatic record for the last 27,500 years in tropical West Africa from the carbon and nitrogen isotopic composition of lacustrine organic matter. Earth Planet Sci Lett 110:23–37

U.S. Energy Information Administration (USEIA) (2012) Greenhouse gases' effect on the climate. http://www.eia.gov/energyexplained/index.cfm?page=environme nt_how_ghg_affect_climate

# Chapter 2
# The Story of the Wyoming Carbon Underground Storage Project (WY-CUSP), and the Regional Inventory and Prioritization of Potential $CO_2$ Storage Reservoirs in Wyoming

**Ramsey D. Bentley and Ronald C. Surdam**

**Abstract** The Wyoming Carbon Underground Storage Project (WY-CUSP) is a statewide effort to identify, inventory, prioritize, and characterize the most outstanding $CO_2$ storage reservoirs and the premier storage site in Wyoming. The WY-CUSP project is managed by the Carbon Management Institute (CMI) at the University of Wyoming with support from the US Department of Energy, State of Wyoming, and industrial partners. In its search for an optimum carbon dioxide storage reservoir in Wyoming, CMI first inventoried and examined the state's hydrocarbon reservoirs, for these are reservoirs with proven fluid storage capacity. The inventory and prioritization of storage reservoirs and storage sites was based on the following criteria: (1) thickness, areal extent, and petrophysical properties of the reservoir rocks, (2) presence of a fluid trap and adequate confining layers, (3) suitable temperature, pressure, and rock/fluid chemistry regimes, (4) salinity of the formation fluids in the storage reservoir rocks, and (5) volumetrics of the storage site. It became apparent that the Mississippian Madison Limestone and Pennsylvanian Weber/Tensleep Sandstone were the highest-priority potential $CO_2$ storage stratigraphic intervals, and that the Rock Springs Uplift (RSU) in southwestern Wyoming was the premier $CO_2$ storage site in the state. A drill site on the northeastern flank of the RSU was highly prospective in offering high-quality reservoir rock at a depth that provides sufficient temperature and pressure for carbon dioxide storage. A very-large-scale, large-capacity trap on the RSU has several competent sealing rock units, and available data show that the reservoir rocks contain very saline formation water. Abundant sources of carbon dioxide are nearby, notably the Jim Bridger Power Plant.

R. D. Bentley (✉) · R. C. Surdam
Carbon Management Institute Laramie, University of Wyoming, Laramie, USA
e-mail: RBentley@uwyo.edu

R. C. Surdam
e-mail: rsurdam@uwyo.edu

R. C. Surdam (ed.), *Geological $CO_2$ Storage Characterization,*
Springer Environmental Science and Engineering, DOI 10.1007/978-1-4614-5788-6_2,
© Springer Science+Business Media New York 2013

## 2.1 WY-CUSP and the RSU Model

The Wyoming Carbon Underground Storage Project (WY-CUSP) is a pioneering research initiative to investigate and characterize two potential carbon storage reservoirs, the Weber and Madison Formations, both deep saline aquifers on the Rock Springs Uplift (RSU) in southwestern Wyoming. WY-CUSP is managed by the Carbon Management Institute (CMI), a part of the University of Wyoming, School of Energy Resources. Scientists from the University of Wyoming, the Wyoming State Geologic Survey, and Los Alamos National Laboratory, and industry partners collaborated with CMI on the project. The WY-CUSP Program has resulted in a detailed characterization of the potential storage reservoirs and storage site.

Site characterization is the process of assessing the suitability of a reservoir for $CO_2$ storage. This process includes conducting geophysical surveys, drilling test wells, and using sophisticated computer models to predict where the injected $CO_2$ will migrate, how efficiently the storage volume will be filled, and how well the storage site will perform over time. The strategy, evolution, techniques, and results of our site characterization on the Rock Springs Uplift, described in subsequent chapters, compose the RSU Model for carbon sequestration, storage, and use.

## 2.2 Inventory and Evaluation of Potential Storage Reservoirs

To inform our choice among possible $CO_2$ storage reservoirs and storage sites in Wyoming, CMI first inventoried and examined the state's hydrocarbon reservoirs, for these are reservoirs with proven fluid storage capacity. Wyoming has an abundance of hydrocarbon reservoirs. To determine their suitability as target sites and formations for carbon storage and sequestration, these reservoirs were inventoried and examined statewide. Every major sedimentary basin in the state showed potential, and each contained the promising target formations described below, although in a variety of geologic settings (Fig. 2.1). Cretaceous reservoirs in the Powder River Basin were of particular interest, as were several older and deeper Paleozoic units in all the basins.

To identify an optimum $CO_2$ storage reservoir in Wyoming and a corresponding optimum WY-CUSP test well site, CMI prioritized reservoirs on the basis of the following characteristics (Surdam and Jiao 2007):

- Reservoir rock of sufficient area and thickness (capacity) and with sufficient porosity (unit capacity, percentage of voids) and permeability (deliverability) to accommodate substantial amounts of $CO_2$.
- A fluid trap, a geologic setting in which the reservoir-rock fluids are trapped by adjacent nearly impermeable rock units and sealing faults.
- Reservoir conditions of temperature, pressure, and rock/fluid chemistry that allow the reservoir to accept large amounts of $CO_2$ without incurring damage.

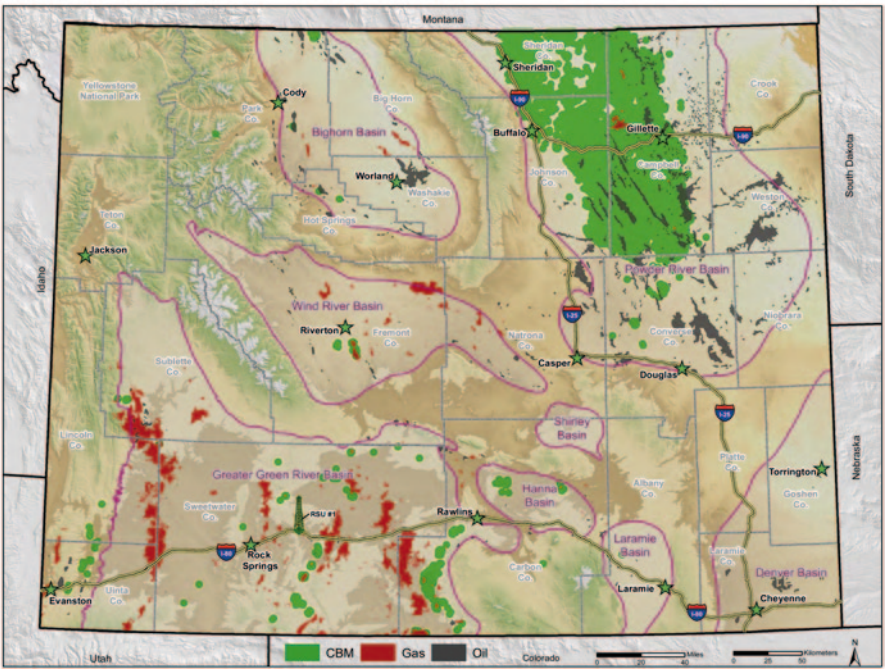


**Fig. 2.1** Major sedimentary basins and hydrocarbon reservoirs in Wyoming. Modified from Debruin, 2007, 2012

- Water quality in the reservoir of more than 10,000 ppm total dissolved solids, as prescribed by the Safe Drinking Water Act Underground Sources of Drinking Water (USDW) criterion that groundwater containing less than 10,000 ppm total dissolved solids may be suitable for development as drinking water and therefore must be protected.

Upper and Lower Cretaceous rocks in the Powder River Basin (PRB) were targeted primarily because many of them were oil and gas producers characterized as discrete compartmentalized sandstone units fully sealed and encased by shales. Because they were isolated as compartmentalized units, once they had been produced for hydrocarbons and essentially "emptied out" of fluids they could provide space for $CO_2$ storage; their impermeable enclosing seals would preclude refilling by meteoric or formation water from aquifers above or below the compartmentalized units. Included in this field category was the Muddy Sandstone in several fields, including Amos Draw. Other targets included the Dakota Sandstone (uppermost Cloverly Formation) at Buck Draw, and the Shannon Sandstone at Hartzog Draw and Sussex Sandstone at House Creek (both members of the Cody Shale).

Although these field areas were promising, they are relatively small. Large storage capacity is necessary for commercial-scale sequestration because the sources of the $CO_2$, power plants and other stationary fossil-fuel-burning sites, produce large amounts of $CO_2$. This size factor does not preclude these smaller sites as potential

small-scale storage sites, for example in integrated power generation/enhanced oil recovery (EOR) projects (see Chap. 12). Opportunities for EOR are many in the PRB, both in the Cretaceous reservoirs cited and in deeper Paleozoic oil reservoirs, such as the Minnelusa.

The Minnelusa Formation in the PRB is equivalent to the Weber/Tensleep Sandstone in other Wyoming basins. One of the most prolific oil and gas producing formations in the state, the Weber/Tensleep is a prime target for $CO_2$ sequestration and storage site selection.

Another Paleozoic unit, the Madison Limestone, is a well-developed reservoir unit throughout the state. The Madison showed promise as a sequestration target in the PRB but was deemed unsuitable due to its status as an underground source of drinking water (USDW) for the City of Gillette, among others. This factor became increasingly important in sequestration site selection, ruling out the Madison in the PRB and in much of the Bighorn Basin, where it is found in very favorable geologic structural situations but is shallow and connected to fresh-water recharge. The Tensleep and Madison at greater depth and toward the center of the Bighorn Basin were considered, but sparse drill-stem data and undetermined trapping made their prospects tenuous.

As the inventory and evaluation progressed, the Weber/Tensleep Sandstone and the Madison Limestone continued to stand out as particularly suitable for carbon storage and sequestration. Both were proven fluid storage units statewide, especially in southwest Wyoming (DeBruin 1993). As well, several large geologic structures containing the two formations presented opportunities for large-scale storage-reservoir development. These structures include the Moxa Arch and the Rock Springs Uplift; the latter chosen as the location of the WY-CUSP project. These structures hold the two formations in deep, isolated environments, with formation-water TDS well above 10,000 ppm and no hydrologic connection to outcrop (Surdam and Jiao 2007). Numerous oil and gas accumulations occur in both formations in the Greater Green River Basin (GGRB). The Madison is host to one of the largest accumulations of carbon dioxide, methane, and helium in the world on the Labarge Anticline (the northern part of the Moxa Arch), located approximately 90 mi northwest of the WY-CUSP well site (Stilwell 1989).

The Rock Springs Uplift is a large (50 × 35 mi, 80 × 55 km) doubly-plunging anticlinal structure, asymmetric with the steeper limb on the west side, and is host to 45 distinct oil and gas fields. Most production is from Upper Cretaceous Mesaverde Group reservoirs (Almond, Ericson, Rock Springs, and Blair Formations) (Surdam and Jiao 2007). Several oil and gas fields produce from the Pennsylvanian Weber and Mississippian Madison, and these fields lie within approximately 20 mi of the RSU #1 well site. The North Brady and South Brady fields lie about 20 mi southeast of the well site; both produce prolifically from the Weber (among other, shallower zones). About 20 mi east–southeast of the well site lies Table Rock field, where both the Weber and Madison are prolific hydrocarbon producers. Both the Brady North/South and Table Rock field areas are on faulted anticlines on the east and southeast flanks of the Rock Springs Uplift. These fields are separated from the main RSU by faults that appear to form up-dip seals. North Baxter Basin field is

located approximately 14 mi west of the RSU #1 well site on the crest of the RSU. Several deep wells drilled there during field development tested significant amounts of $CO_2$ from both the Weber and the Madison (Wyoming Oil and Gas Conservation Commission (2007–2013); Oil and Gas Fields Symposium Committee 1979). Although they are distant from the RSU #1 drill site, these fields, as well as others in the GGRB, were evidence that reservoir-quality rocks would be present at the site chosen for the RSU #1 well, and confirmed the proven storage potential of these two targeted formations. In fact, the Weber and Madison were already proven as $CO_2$ reservoirs on the basis of drill-stem tests at North Baxter field. With the great areal extent of the RSU, preliminary estimates of sequestration potential at the Rock Springs Uplift were huge, in the neighborhood of 26 billion tonnes of $CO_2$. This amount of saline storage reservoir capacity could accommodate 485 years of Wyoming's annual $CO_2$ emissions of approximately 54 million tonnes per year (2007 figures; Surdam and Jiao 2007).

Because the Weber and Madison were seen to be reservoir-quality formations, it followed that they had impermeable confining layers acting as seals to fluid movement or upward leakage. On the basis of reported fluid characteristics of each oil and gas field in the area, it was evident that each formation had a particular mix of formation fluids. These fluids varied from one oil and gas field to another depending on local structural setting, subsurface fluid flow, and stratigraphic facies changes. What was evident were differences in fluid composition between the Weber and the Madison and between the Weber and overlying Phosphoria. Not only did it appear that each formation has a competent seal of its own, the Amsden capping the Madison, the Phosphoria capping the Weber; it was also recognized that multiple thick seals exist up-section in Triassic rocks such as the Dinwoody Formation as well as much higher up in the thick section of Cretaceous shales. This combination of seals, actually stacked multiple seals, led to further confidence in the premise that injected $CO_2$ would remain within the Weber and the Madison on the RSU.

## 2.3 The Choice of Site and Reservoirs

With this combination of high-quality reservoir rock, stacked competent sealing units, a very large trapping structure, and highly saline formation water in the target zones (saline aquifers), the RSU became the area of choice as a substantial $CO_2$ sequestration/storage site. To test this choice, a suitable drill site was located on the northeastern flank of the RSU, within 2 mi of the Jim Bridger power plant, the largest coal-fired plant in Wyoming and largest single producer of $CO_2$.

In summary, the Rock Springs Uplift and the RSU #1 well site were chosen on the basis of these criteria:

- Good quality and quantity of reservoir rock, Madison Limestone and Weber Sandstone, coupled with adjacent highly effective sealing formations, including the Amsden, Phosphoria, and Dinwoody. Drillstem tests from the RSU and

producing wells on the LaBarge Platform have demonstrated that these confining layers are capable of trapping helium.
- Effective geologic structure: the Rock Springs Uplift, a very large anticlinal structure with four-way closure.
- Saline aquifers: both the Weber and Madison formation waters have TDS of well over 10,000 ppm, easily above USDW standards.
- $CO_2$ source proximity: Jim Bridger coal-fired power plant less than two miles away, largest $CO_2$ emitter in the state. Nearby trona plants.
- State land with state-owned mineral estate available; provided relative ease and timeliness of permitting.
- Site access: a Black Butte Coal Company haul road runs through the available state section. This haul road was suitable for mobilizing a drilling rig and heavy traffic. The Black Butte Coal Company was very cooperative in allowing use of their haul road for access, which reduced costs considerably by eliminating the need to build an expensive access road.
- Drilling-water source available nearby at Jim Bridger plant site.

## References

DeBruin R (1993) Overview of oil and gas geology of Wyoming. In: Snoke AW, Steidtmann JR, Roberts SM (eds) Geology of Wyoming. Wyoming State Geologic Survey Memoir No. 5, pp 836–873

DeBruin RH (2007, 2012) Oil and gas map of Wyoming. Wyoming State Geological Survey Map Series 55 (MS-55). Scale 1:500,000

Stilwell DP (1989) $CO_2$ resources of the Moxa Arch and the Madison reservoir. Wyoming Geologic Association Fortieth Field Conference Guidebook, pp 105–115

Surdam RC, Jiao J (2007) The Rock Springs Uplift – an outstanding geologic $CO_2$ sequestration site in southwest Wyoming. Wyoming State Geologic Survey Challenges in Geologic Resource Development No. 2

Oil and Gas Fields Symposium Committee (eds) (1979) Wyoming oil and gas fields symposium, Greater Green River Basin, Wyoming. Wyoming Geologic Association

Wyoming Oil and Gas Conservation Commission http://wogcc.state.wy.us/. Accessed 2007–2013

# Chapter 3
# Legal Framework: Carbon Storage Regulations and Access for the Wyoming Carbon Underground Storage Project (WY-CUSP)

**Lynne Boomgaarden and Shanna C. Dahl**

**Abstract** One of the most important and difficult tasks for any site characterization project is following all regulatory and permitting requirements. Much of the surface access in and around the Rock Springs Uplift #1 well (RSU #1 well) is checkerboarded with federal, state and private surface rights creating a difficult permitting situation. In addition, different phases of the project required permitting from more than one regulatory agency. CMI was required to acquire access permits, regulatory permits, and private letters granting access.

## 3.1 Introduction

Authorizations required to legally conduct surface and subsurface activities related to geologic site characterization and $CO_2$ storage in deep saline reservoirs are many and varied. Land and mineral owners covering the geographic area of a well site(s) and respective area(s) of review also may be numerous and may fall into federal, state, and private ownership categories (Fig. 3.1). While *each individual project must be carefully evaluated on its own facts to determine what permits and access authorizations are required at a particular site and within a particular jurisdiction*, this chapter will provide a basic checklist of permits and issues compiled based on experience in permitting the University of Wyoming Carbon Management Institute's stratigraphic test well, the RSU #1, drilled in conjunction with WY-CUSP Phase I research, DOE Project DE-FE0002142. This important research well was successfully drilled and completed to a depth of 12,810 ft on state-owned surface and subsurface in Section 16, Township 20 North, Range 101 West, Sweetwater County, Wyoming.

L. Boomgaarden (✉)
Crowley Fleck PLLP, Cheyenne, WY, USA
e-mail: lboomgaarden@crowleyfleck.com

S. C. Dahl
Carbon Management Institute, Laramie, WY, USA
e-mail: sdahl2@uwyo.edu

R. C. Surdam (ed.), *Geological $CO_2$ Storage Characterization,*
Springer Environmental Science and Engineering, DOI 10.1007/978-1-4614-5788-6_3,
© Springer Science+Business Media New York 2013

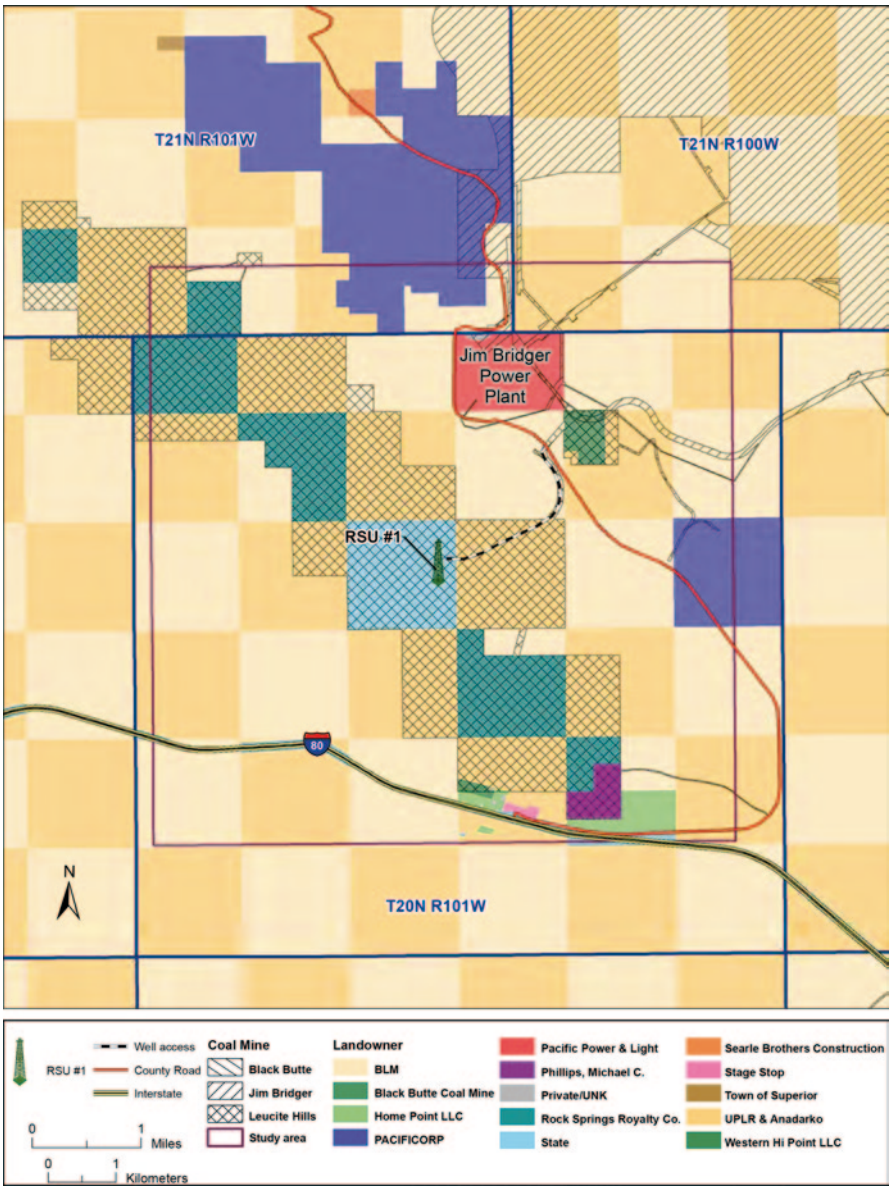


**Fig. 3.1** Land ownership and access, WY-CUSP study area on the Rock Springs Uplift, superimposed on a checkerboard pattern of land sections. The RSU #1 well is in Section 16, T20N, R101W

## 3.2 Regulation of Geologic Site Characterization Activities

### *3.2.1 Seismic Study*

The basic steps necessary at the beginning of the seismic study were to determine the nature of the study and distinguish it from conventional mineral exploration, as appropriate. The geographic area along with surface and subsurface ownership needed to be defined within the exterior boundaries of the study area. Once those parameters were clarified it was necessary to obtain all access and regulatory permits.

**Access** To secure appropriate access and to avoid trespass liability, it is necessary to obtain the permission of each affected surface and mineral owner prior to conducting any seismic operations on each owner's property. For WY-CUSP Phase I, industry partner Geokinetics obtained permits from each affected surface and mineral owner using a company-specific permit form.

State land access for seismic survey activity is governed by the Board of Land Commissioner Rules and Regulations. Rules and regulations are specific for each state and each circumstance, and it is important to review the requirements. The rules for state land access in Wyoming can be found in Chapter 16; http://soswy.state.wy.us/Rules/RULES/8204.pdf.

In addition to state land rules and requirements for access, requirements for conducting seismic survey activity on federal lands were also reviewed. Those rules and regulations are set forth in Bureau of Land Management (BLM) Handbook H-3150-1: Onshore Oil and Gas Geophysical Exploration Surface Management Requirements: http://www.blm.gov/pgdata/etc/medialib/blm/wo/Information_Resources_Management/policy/blm_handbook.Par.82968.File.dat/h3150-1.pdf.

**Regulation** Regulation requirements for the seismic survey are governed by the Wyoming Oil and Gas Conservation Commission (WOGCC). Industry Partner Geokinetics was responsible for obtaining permits and posting bonds as required by WOGCC Rules, Chapter 4, Section 6. It is important to note that new WOGCC Rules regarding seismic exploration bonding are forthcoming following the amendment of W.S. 30-5-104(d)(v)(A) by the 2013 Wyoming State Legislature.

### *3.2.2 Test Well Drilling*

The type and purpose of a test well determines which regulatory agency(ies) has jurisdiction and which statutes and rules apply. As with the seismic survey, the permitting process is multi-fold and requires numerous different types of permits.

**Access** In determining well site access and to avoid trespass liability, it is necessary to obtain the permission of each surface owner whose property must be crossed in order to access the well site and each owner on whose property the well site will

be located. The RSU #1 well required access approval and permitting from federal, state and private surface owners.

To meet federal access requirements, CMI applied for (Standard Form SF299) and obtained a BLM right-of-way permit, Serial No. WYW167769. The permit authorized use of an existing Black Butte Coal Company haul road across federal land. Pursuant to 43 CFR 2804.16 and 43 CFR 2806.14, CMI was exempt from payment of cost recovery or rental fees.

State permitting requirements required obtaining a Temporary Use Permit from the Wyoming Office of State Lands & Investments (OSLI) and State Board of Land Commissioners. The Temporary Use Permit (TUP) pursuant to Board of Land Commissioners Rules, Chapter 14, authorized CMI to locate, drill, and complete the test well on state trust land for the purpose of data gathering and monitoring. The initial term for the TUP was two years, allowing time for completion of the research activities. A new two year TUP was later approved and issued for the purpose of conducting injectivity testing and installing geophones for microseismic monitoring.

OSLI did not require CMI to post a bond to secure reclamation costs or fee payments as the RSU #1 was for research and monitoring purposes and was not going to be used for $CO_2$ storage. In order to avoid interference with the geologic site characterization research, the State Board of Land Commissioners, in conjunction with the approval of the TUP, temporarily withdrew the study area from oil and gas leasing.

Long-term micro-seismic monitoring may require approval of a Special Use Lease pursuant to Board of Land Commissioners Rules, Chapter 5. See https://lands.state.wy.us/ and http://soswy.state.wy.us/Rules/RULES/6566.pdf.

To meet the private land owner requirements, CMI obtained well site access via private road from Black Butte Coal and Anadarko in the form of individual letters of agreement. Access under these agreements was conditioned on CMI obtaining a BLM right-of-way to cross federal lands.

**Regulation** From a regulatory standpoint no federal approvals were required to drill, complete or test the RSU #1 well. At the state level CMI worked with two different agencies to obtain the appropriate regulatory permits, the WOGCC and the Office of the State Engineer (OSE). CMI submitted an Application for Permit to Drill (APD) the RSU #1 stratigraphic test/monitoring well to the WOGCC in accordance with WOGCC Rules, Chapter 3, Sect. 9. The APD was administratively approved; see http://wogcc.state.wy.us/.

Baker Hughes, a WY-CUSP industry partner, obtained a Temporary Appropriation of Surface Water Permit from the OSE to provide approximately 15,000 barrels (630,000 gallons) of water for drilling and washdown uses; see https://sites.google.com/a/wyo.gov/seo/. The water was appropriated from the Green River and pumped from a surge pond pursuant to a private agreement between Baker Hughes and PacifiCorp, the operator of the Jim Bridger Power Plant.

Working with local agencies in Sweetwater County, CMI obtained a Sweetwater County Oil and Gas Well Construction/Use Permit in accordance with county ordinance. Application for this permit required a description of the nature of sewage treatment at the wellsite, submission of a hazardous chemicals inventory, and

coordination with county emergency management personnel. Due to the location and duration of drilling and testing activities, no county road access and license and no conditional use permit for temporary housing or man camps were required. All activities were conducted within Sweetwater County; none of the activities were conducted within city or town limits, see http://www.sweet.wy.us/.

### *3.2.3 Injectivity Testing*

After the RSU #1 well was capped and temporarily abandoned, it became necessary to gain additional data from the well. Well re-entry and injectivity testing had additional permitting requirements. In order to determine which regulatory agency(ies) have jurisdiction and which statutes and rules apply, it was necessary to define the nature of the testing to be conducted and the type of injectate to be used.

CMI chose to utilize water as a surrogate for supercritical $CO_2$ in the injectivity testing. Accordingly, the Wyoming Department of Environmental Quality (WDEQ), Water Quality Division (WQD), issued a Class I Non-Hazardous Underground Injection Control (UIC) Program Permit, Permit No. 12-257, in accordance with WDEQ/WQD Rules and Regulations Chapter 13. This Class I UIC permit authorized short-term injection of non-contact process water from the Jim Bridger Power Plant surge pond under specified injection volumes and rates and other applicable permit conditions. Issuance of the Class I UIC permit required UW/CMI to post a security bond with WDEQ in the form of a letter of credit in the amount of $140,000.00; see http://deq.state.wy.us/wqd/.

In addition to the Class I UIC permit, a Temporary Appropriation of Surface Water Permit was obtained from and approved by the OSE. This permit was approved to provide approximately 84,000 gallons of water for injectivity testing. Water was appropriated from the Green River and was pumped by Baker Hughes from a surge pond pursuant to a private agreement with PacifiCorp.

### *3.2.4 Well Cataloging*

Another aspect of the WY-CUSP project that required permitting was the well Cataloging and Inspection. This aspect of the project required access to many different federal, state and private surface areas. To avoid trespass liability, CMI negotiated access agreements with respective federal, state and private land owners for the sole purpose of entering on and crossing specific properties to develop a well catalog and borehole risk assessment within the area of review. These agreements identified who would be performing the work, during what time period(s), and what equipment would be used. The agreements limited motorized vehicle use to established roads and mandated safety training for access to certain mining properties.

## 3.3 Regulation of $CO_2$ Injection and Storage

The next step for the RSU #1 well and project would be to move to a $CO_2$ storage site/surge tank scenario. Although no plans exist to make this conversion in the near future, we felt that it would be prudent to understand the appropriate permitting requirements.

In the future, if the RSU #1 well were utilized for $CO_2$ injection or a new well were drilled to inject $CO_2$, a UIC Program Class VI permit would be required. Geologic storage of $CO_2$ is governed by the US Environmental Protection Agency (EPA) pursuant to UIC Program Class VI Well Regulations, 75 Fed. Reg. 77230 (Dec. 10, 2010); 40 CFR 146.82–146.95. UIC Class VI program elements include: site characterization, area of review (AoR), well construction, well operation, site monitoring, post-injection site care (PISC), public participation, financial responsibility, and site closure. For access to guidance documents see http://water.epa.gov/type/groundwater/uic/wells_sequestration.cfm.

Permitting through the EPA will change once the WDEQ applies for and obtains primacy over UIC Program Class VI wells; all Class VI well applications will be submitted to and approved by WDEQ/WQD. WDEQ/WQD anticipates submitting its primacy application package to the EPA by June 30, 2014. See WDEQ/WQD Rules and Regulations, Chapter 24 (published November 2010, but subject to amendment and approval by EPA).

Beyond the federal and state requirements, many county officials have indicated that any well drilled for injection and storage of $CO_2$ will require a county well construction permit and likely will require a conditional use permit for long-term waste disposal, housing, and possible hazardous materials management.

# Chapter 4
# A Strategy for Designing an Optimal Characterization Study of the Premier Carbon Capture, Utilization and Storage Site in Wyoming

**Ronald C. Surdam**

**Abstract** The strategy adapted by the WY-CUSP team to accomplish their primary goal involved the following steps:

1. Inventory and prioritize the potential $CO_2$ storage reservoirs and storage sites in Wyoming, and select the storage reservoir(s) and site to be targeted.
2. Determine sources of available data for the targeted priority storage reservoir(s) and site.
3. Perform preliminary numerical simulations of a variety of $CO_2$ storage scenarios at the selected site, utilizing available data.
4. Design a new, robust data-acquisition program (3-D seismic survey and test well logging) that would provide the WY-CUSP team with the ability to attack the key barriers to accurate site characterization (pressure management and 3-D heterogeneity of petrophysical parameters of storage reservoirs and seals).
5. Develop a formation brine production and treatment program and facility that would result in required pressure management during commercial-scale CCUS on the selected site—a facility that functions as a profit center, not a punitive element, during commercial geologic $CO_2$ sequestration.
6. Simulate a variety of potential $CO_2$ storage scenarios on the selected site using realistic reservoir models that include, among other elements, the 3-D heterogeneity of petrophysical parameters, in order to provide significant uncertainty reduction in both performance assessment and risk analysis.
7. Accomplish the primary goal of the WY-CUSP program—to provide all essential information, data, interrelations, evaluations, and modeling results required by government regulations in order to permit construction of a commercial $CO_2$ storage facility on the RSU.

R. C. Surdam (✉)
Carbon Management Institute Laramie, University of Wyoming, Laramie, USA
e-mail: rsurdam@uwyo.edu

R. C. Surdam (ed.), *Geological $CO_2$ Storage Characterization,*
Springer Environmental Science and Engineering, DOI 10.1007/978-1-4614-5788-6_4,
© Springer Science+Business Media New York 2013

## 4.1 The Wyoming Carbon Underground Storage Project (WY-CUSP)

When the CMI team decided to delineate outstanding geologic $CO_2$ storage sites in Wyoming, they had several tasks to complete before the characterization work could be initiated. Essentially, these initial tasks were: (1) to inventory and prioritize the potential $CO_2$ storage reservoirs and sites in Wyoming; (2) to determine sources of available data for the highest-priority sites; and (3) once the storage intervals and site were selected, to choose a study site suitable for characterization.

Early in this preliminary work it was demonstrated that the Paleozoic Madison Limestone and Weber/Tensleep Sandstone were the leading candidate stratigraphic storage intervals. This conclusion was founded on the volume of pore space, given the porosity (typically 5–10%) and thicknesses (Madison Limestone, ~400 ft, 120 m; Weber Sandstone, ~700 ft, 210 m) of the potential storage intervals.

The Rock Springs Uplift and the Moxa Arch (La Barge Platform) were the two highest-priority storage sites. The Rock Springs Uplift was chosen because the reservoir intervals are closer to the surface (6000–12,000 ft (1800–3600 m) deep) on the uplift, whereas the reservoir interval on the Moxa Arch is ~18,000 ft deep (5500 m). Importantly, there is only a trace of hydrocarbons in the Paleozoic reservoir interval on the Rock Springs Uplift, whereas the Paleozoic rocks on the Moxa Arch contain substantial hydrocarbon accumulations and associated significant hydrocarbon production.

The Rock Springs Uplift is an elliptical structure, 50 mi (80 km) north–south and 35 mi (55 km) east–west, with four-way closure and ~10,000 ft (3000 m) of structural relief. In addition, the Rock Springs Uplift is a relatively recent structure; there is no topographic indication of its presence prior to 45 million years ago (Surdam and Jiao 2007).

This last aspect of the RSU is important because it explains why the formation fluids in both storage reservoirs are so saline (70,000–100,000 mg/L). The closest surface outcrops of these two Paleozoic stratigraphic units are 50–100 mi (80–160 km) away, so there has been no meteoric reflux into these units on the RSU. It bears repeating, because of the importance relative to the Paleozoic Madison and Weber formations as potential $CO_2$ storage reservoirs, that there is no chance that underground sources of drinking water (USDW, < 10,000 mg/L salinity) are within these formations on the RSU. The US Environmental Protection Agency will not allow $CO_2$ storage in rock/fluid storage systems containing USDW.

After surveying potential sites for a CCUS characterization study on the Rock Springs Uplift, the CMI team chose a state section on the east flank of the structure where the nearest Paleozoic hydrocarbon production, the Brady Unit, is 20 mi (30 km) away and separated from the RSU by a significant fault. The 2200-MW Jim Bridger Power Plant, the largest $CO_2$ emitter in the state (15 Mt/yr) is located about 2 mi (3 km) north of the study site. The Black Butte coal company has a network of well maintained haul roads in the area, so ready access to the study site is established. Finally, the topography in the area is relatively subdued, so acquisition of 3-D seismic information wouldn't be hampered by troublesome relief.

## 4.2 Sources of Available Databases

Our search for existing data relative to the RSU yielded three primary databases. The Wyoming Oil and Gas Conservation Commission in Casper, Wyoming, possesses the most thorough Wyoming digitized database in existence. The Wyoming State Geologic Survey also has a valuable database on southwestern Wyoming, mainly in the form of maps and topical reports. The USGS Core Library in Denver contains several high-quality Weber and Madison cores from southwestern Wyoming.

## 4.3 Preliminary Modeling

One of the first tasks addressed by CMI after DOE funding had been secured was to build preliminary numerical simulations utilizing regional data derived from the literature and the Wyoming Oil and Gas Conservation Commission database (Stauffer et al. 2009; Surdam et al. 2009, 2010). The performance assessment produced by these early numerical simulations was fraught with geologic uncertainty. However, these early attempts were invaluable because they pointed out two crucial points.

First, the most critical problem with commercial-scale geologic $CO_2$ sequestration is the management of displaced fluids. The early simulations suggested that formation brines would have to be removed with injection of $CO_2$ in a one-to-one ratio. Our simulations of a variety of $CO_2$ injection scenarios showed that without pressure management through removal of formation fluids, pressures would quickly exceed fracture pressures during injection. The CMI team concluded early in the study that any CCUS strategy on the RSU had to integrate fluid production and water treatment with injection and storage of $CO_2$.

Second, it also was apparent from the preliminary numerical simulations that the greatest uncertainty in the performance assessment and modeling of $CO_2$ sequestration processes is the characterization of geologic heterogeneity in three dimensions. The objective of much of our subsequent research has been to significantly reduce that uncertainty.

## 4.4 Essential New Data

From these preliminary observations it was apparent that a more robust database was essential to achieving the WY-CUSP objectives. First, because the closest existing well penetrations of the Madison Limestone and Weber Sandstone on the RSU are approximately 18 mi (29 km) up-dip from the study area at the crest of the structure, and the closest outcrops are 50–100 mi (80–160 km) away, it was essential to drill a stratigraphic test well at the chosen study site. Second, to be able to project observations made at the well out into a realistic storage domain, it was essential to acquire a 3-D seismic survey of the study area. Thus, an integral part of the CMI plan was to

reduce uncertainty in our RSU characterization project by integrating 3-D seismic techniques with stratigraphic test well observations. This approach has been absolutely crucial in reducing uncertainty in the RSU $CO_2$ injection/storage performance assessments. From the stratigraphic test well the project gained 900+ ft (270+ m) of high-quality core (rock samples) from the storage reservoirs and confining layers, a wide variety of well logs, fluid samples, DST's, injectivity measurements, VSPs, in situ temperature and pressure measurements, stress/strain properties, fracture gradients, and capillary properties, among other measures. This sample set, combined with a multitude of laboratory measurements, comprises a truly robust catalog of diverse databases. Combining these new robust databases with the seismic attribute volumes resulting from modern seismic analytical techniques has resulted in a new, powerful approach to evaluating 3-D spatial distributions of both reservoir and confining layer characteristic. The new data and this powerful evaluation approach to geologic $CO_2$ storage are described in detail in subsequent chapters.

## 4.5 Goals of WY-CUSP

The primary goal of the Wyoming Carbon Underground Storage Project (WY-CUSP) is to provide all essential information, data, interrelations, evaluations, and modeling results required by government regulations in order to permit construction of a commercial geologic $CO_2$ storage facility on the RSU. The modeling results should include injected $CO_2$ plume size and fluid-flow dynamics, area of review configuration (storage domain), performance assessments, and risk analyses for a spectrum of realistic $CO_2$ injection and storage configurations. With information provided by WY-CUSP, the potential operator of a commercial geologic $CO_2$ storage facility on the RSU should be able to proceed directly to the permitting phase of the project.

Secondary goals of the WY-CUSP program are to:

- Protect Wyoming's coal extraction and future coal-to-chemical industries (provide storage capacity for anthropogenic $CO_2$).
- Provide surge-tank storage of anthropogenic $CO_2$ for a 20–50 year state-wide enhanced oil recovery program. By way of comparison, using the $CO_2$ produced by the two gas processing plants in Wyoming, it would take 150–200 years to recover Wyoming's stranded oil. These comparisons were made by comparing the amount of $CO_2$ required to produce a barrel of oil with the amount of $CO_2$ produced by the two gas-processing plants.
- Retrieve reservoir information essential for expansion of natural gas storage in Wyoming.
- Establish a more robust database for two important hydrocarbon reservoirs in Wyoming, substantially reducing uncertainty for all dynamic models of Weber/Tensleep and Madison fluid-flow and rock/fluid systems.

## References

Stauffer PH, Surdam RC, Jiao ZS, Miller T (2009) Combing geologic data and numerical modeling to improve estimates of the $CO_2$ sequestration potential of the Rock Springs Uplift, Wyoming. In: Proceeding of the 9th Greenhouse Gas Technology Conference. Energy Procedia 1(1): 2714–2724. Elsevier

Surdam RC, Jiao Z (2007) The Rock Springs Uplift: an outstanding geologic $CO_2$ sequestration site in southwest Wyoming. Wyoming State Geologic Survey Challenges in Geologic Resources Development No. 2

Surdam RC, Jiao Z, Stauffer P, Miller T (2009) An integrated strategy for carbon management combining geologic $CO_2$ sequestration, displaced fluid production, and water treatment. Wyoming State Geologic Survey Challenges in Geologic Resource Development No. 8

Surdam RC, Jiao Z, DeBruin RH, Bently RD (2010) Shale gas potential of the Mowry Shale in Wyoming Laramide basins. Wyoming State Geologic Survey challenges in Resource Development No. 9

# Chapter 5
# Regional Geologic History, $CO_2$ Source Inventory, and Groundwater Risk Assessment of a Potential $CO_2$ Sequestration Site on the Rock Springs Uplift in Southwest Wyoming

**J. Fred McLaughlin, Ramsey D. Bentley and Scott A. Quillinan**

**Abstract** The location of a potential carbon capture and sequestration (CCS) project in southwest Wyoming is evaluated with emphasis on the site location, geologic history, location of potential drinking-water aquifers, and proximity to sources of both anthropogenic and natural $CO_2$. Natural and anthropogenic $CO_2$ sources were mapped in Wyoming to define their relation to enhanced oil recovery opportunities and prospective storage sites. Of the nearly 60 Mt of anthropogenic $CO_2$ emissions reported in Wyoming, half were located in the Greater Green River Basin (GGRB) in southwest Wyoming. The Rock Springs Uplift (RSU) $CO_2$ storage site is located in the GGRB, and is a promising structure for commercial $CO_2$ storage/surge tank development. Successful economic utilization of natural and anthropogenic $CO_2$ depends on near-by sources, infrastructure, areas of resource depletion suitable for enhanced recovery, and areas of potential storage.

The RSU is the GGRB's youngest Laramide uplift (45 m.y.b.p.). Strata on the RSU are largely offset by a blind thrust fault on the western border of the asymmetric anticline. The sedimentary section at the well site consists of more than 4100 m of Paleozoic and Mesozoic rocks and spans nearly 500 m.y. of geologic history. Investigations were conducted to characterize potential Paleozoic reservoirs and their associated seals. The Paleozoic reservoirs are located at depths over 3400 m; approximately 280 m of core was recovered from the Pennsylvanian Weber Sandstone and Mississippian Madison Limestone and associated seals for analysis of reservoir and sealing characteristics. Lithology and geologic history have resulted in a stratigraphic section on the RSU that has deep, thick reservoirs and multiple overlying seals.

A major concern in long-term CCS is the potential for leakage and the resulting risk of contamination of overlying groundwater aquifers. It is therefore important

J. Fred McLaughlin (✉) · R. D. Bentley · S. A. Quillinan
Carbon Management Institute, Laramie, WY, USA
e-mail: Derf1@uwyo.edu

R. D. Bentley
e-mail: RBentley@uwyo.edu

S. A. Quillinan
e-mail: scottyq@uwyo.edu

R. C. Surdam (ed.), *Geological $CO_2$ Storage Characterization,*
Springer Environmental Science and Engineering, DOI 10.1007/978-1-4614-5788-6_5,
© Springer Science+Business Media New York 2013

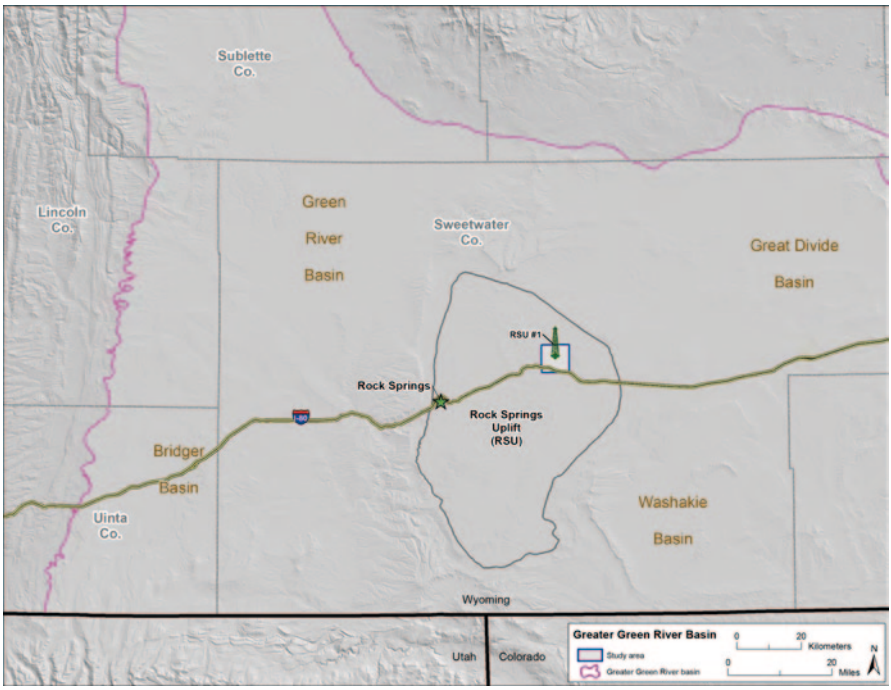


**Fig. 5.1** Map including Greater Green River Basin, subbasins, study area, and location of stratigraphic test well

to characterize the groundwater resources of associated aquifers and active groundwater wells at potential CCS sites. Groundwater use at and near the storage site is sparse: only four groundwater permits for drinking water wells were identified in the area. Two intervals of potential potable water were identified in the Cretaceous Ericson Sandstone during completion of the RSU #1 well. On the basis of an extensive literary search and petrophysical data from the RSU #1 well, sequestering $CO_2$ in the Weber and Madison aquifers at the study site poses no perceptible threat to current groundwater use or resources.

## 5.1 Location

The Greater Green River Basin (GGRB), located in southwestern Wyoming and parts of northeastern Utah and northwestern Colorado, occupies approximately 20,000 $mi^2$ (52,000 $km^2$) and encompasses several subbasins (Fig. 5.1). Among the geologic structures that partition the subbasins, the largest is the Rock Springs Uplift (RSU), a north–south trending, asymmetric, doubly-plunging anticline that divides the Green River Basin to the west from the Great Divide and Washakie

Basins to the east (Fig. 5.1). The RSU #1 test well site is located on the northeast flank of the RSU, near the center of the GGRB. The study area is a 25-$mi^2$ (65-$km^2$) area on the northeast flank of the uplift centered in Township 20N, Range 101W. At this center point of the study area a 12,810-ft-deep (3904 m) well, RSU #1, was drilled for rock and fluid sampling and injection testing (Fig. 5.1). At the well site the surface geology is Almond Formation, the uppermost unit of the Upper Cretaceous Mesaverde Group, and minor Quaternary alluvial deposits. Bedding in the study area strikes NW–SE and dips between 5° and 7° NE. The well is 34 mi (55 km) east of Rock Springs via I-80 and is less than 2 mi (3 km) from the Jim Bridger Power Plant.

## 5.2 Commercial Sources of $CO_2$ in Wyoming

Although the primary geographical focus of this study is southwestern Wyoming, available data allowed the construction of a statewide inventory of both anthropogenic carbon dioxide ($CO_2$) sources and naturally occurring $CO_2$ sources. A significant result of this statewide coverage was the realization that a large percentage of the commercial $CO_2$ sources are in the southwestern part of the state, near the CCS study site.

### *5.2.1 Anthropogenic Sources*

Although the focus of this section is to identify *commercial* sources of $CO_2$, the anthropogenic sources presented here would more appropriately be termed *potential* commercial sources, for at present $CO_2$ capture from these facilities may be impracticable from an economic or technical standpoint. Becoming viable commercial sources in the future depends on the development of carbon capture techniques more efficient than those currently practiced.

The US Environmental Protection Agency responded to the FY2008 Consolidated Appropriations Act (H.R. 2764; Public Law 110–161) with the Mandatory Reporting of Greenhouse Gases Rule (74 FR 56260), which requires reporting of greenhouse gas (GHG) emission data from large sources and suppliers in the United States. The requirement covers all facilities that emit 25,000 tonnes (25 kt) or more per year of GHGs, including non-biogenic $CO_2$, methane, nitrous oxide, several types of fluorocarbons, and biogenic $CO_2$. The data reported by these facilities became available online in January 2012 and comprises data for 2010, the first reporting year (EPA 2012). Figure 5.2 lists and locates the facilities in the USEPA database that constitute the primary anthropogenic commercial $CO_2$ source sites in Wyoming in 2010. Data for reporting year 2011, released in February 2013, shows an increase in reported emissions of nearly 4 Mt over the 2010 emissions (EPA 2013). This increase is mainly due to an increase in emissions at the Exxon Mobil

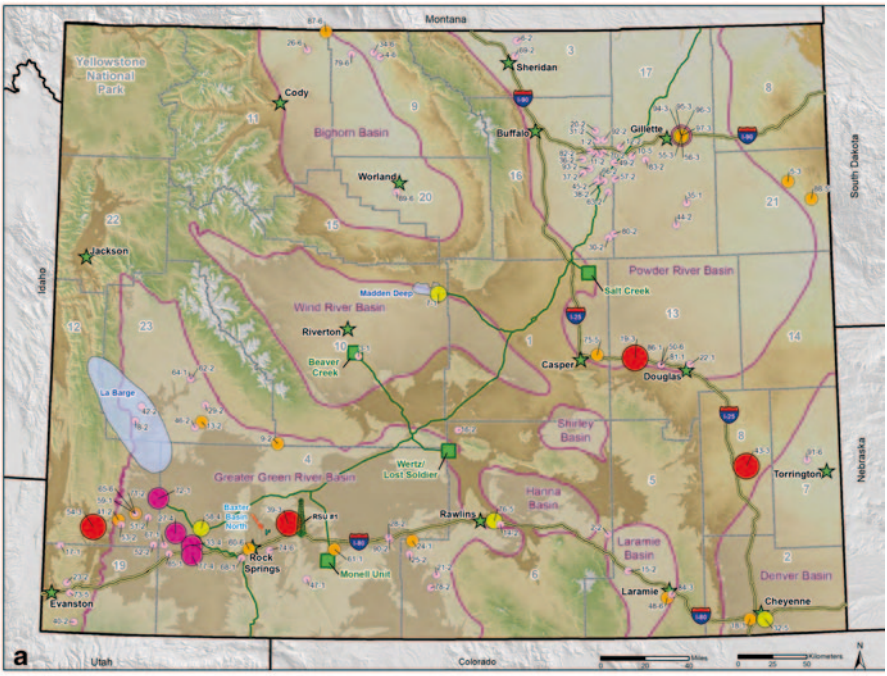


| No. | Co. | Facility | Facility code | $CO_2$ kt/yr |
|---|---|---|---|---|
| 1 | 18 | Amazon-Conga | CS | 41 |
| 2 | 6 | Arlington | CS | 41 |
| 3 | 10 | Beaver Creek | GP | 43 |
| 4 | 9 | Bentonite Performance Minerals | IP | 43 |
| 5 | 21 | Osage | PP | 220 |
| 6 | 3 | Bpe Prairie Dog Booster | PP | 27 |
| 7 | 10 | Burlington Resources Lost Cabin | GP | 784 |
| 8 | 23 | Big Piney | CS | 63 |
| 9 | 10 | Bird Canyon | CS | 119 |
| 10 | 17 | Bison Treating Facility | RF | 47 |
| 11 | 16 | Bolster | CS | 28 |
| 12 | 17 | Bombsite/Nichols | CS | 52 |
| 13 | 23 | Bridger | CS | 173 |
| 14 | 6 | CIG Station 5660 Rawlins | CS | 66 |
| 15 | 5 | CIG Station 5670 Laramie | CS | 44 |
| 16 | 6 | CIG Station 5690 Muddy Gap | CS | 26 |
| 17 | 19 | Carter Creek | GP | 59 |
| 18 | 2 | Cheyenne Plant | GP | 337 |
| 19 | 13 | Dave Johnston | PP | 5,436 |
| 20 | 16 | Deer Gulch-Falcon | CS | 31 |
| 21 | 6 | Doty Mountain | CS | 26 |
| 22 | 13 | Douglas | GP | 47 |
| 23 | 19 | East Painter Facility | CS | 59 |
| 24 | 6 | Echo Springs | GP | 290 |
| 25 | 6 | Eight Mile Lake | CS | 51 |
| 26 | 11 | Encore Energy Partners | IP | 74 |
| 27 | 4 | FMC Westvaco | TM | 1,609 |
| 28 | 4 | Frewen Lake | CS | 51 |
| 29 | 23 | Falcon | CS | 74 |
| 30 | 16 | Fletcher-Terhune | CS | 48 |
| 31 | 16 | Flying Creek/ Bridge Draw | CS | 63 |
| 32 | 2 | Frontier Refining | RF | 531 |
| 33 | 4 | General Chemical | TM | 1,631 |
| 34 | 9 | Georgia Pacific Corporation | TM | 32 |
| 35 | 17 | Hilight-Reno Junction | GP | 89 |
| 36 | 16 | Indian Creek-Crow | CS | 38 |
| 37 | 16 | Jameson-Kessler | CS | 31 |
| 38 | 16 | JAG | CS | 40 |
| 39 | 4 | Jim Bridger | PP | 14,768 |
| 40 | 19 | KRGT Co. - Coyote Creek | CS | 40 |
| 41 | 12 | KRGT Co. - Muddy Creek | CS | 232 |
| 42 | 23 | Labarge | CS | 53 |
| 43 | 8 | Laramie River Station | PP | 13,358 |
| 44 | 17 | Little Thunder-Stratus | CS | 26 |
| 45 | 16 | Luke-Gus | CS | 32 |
| 46 | 23 | Luman | CS | 44 |
| 47 | 4 | Merit Energy Co Brady | GP | 49 |
| 48 | 5 | Mountain Cement Co. | IP | 272 |
| 49 | 17 | Malibu-Surfer | CS | 29 |
| 50 | 13 | Medicine Bow Treatment Facility | IP | 59 |
| 51 | 12 | Moxa North | CS | 34 |
| 52 | 12 | Moxa South | CS | 34 |
| 53 | 12 | Northwest Pipeline - Muddy Creek | CS | 28 |
| 54 | 12 | Naughton | PP | 5,337 |
| 55 | 17 | Neil Simpson | PP | 306 |
| 56 | 17 | Neil Simpson II | PP | 816 |
| 57 | 17 | Newport-Laguna | CS | 32 |
| 58 | 4 | OCI Wyoming | TM | 763 |
| 59 | 12 | Opal | GP | 492 |
| 60 | 4 | P4 Production | IP | 203 |
| 61 | 4 | Patrick Draw | GP | 126 |
| 62 | 23 | Paradise | CS | 97 |
| 63 | 16 | Perla | CS | 35 |
| 64 | 23 | Pinedale Complex | GP | 80 |
| 65 | 12 | Pioneer Cryogenic Plant | IP | 35 |
| 66 | 16 | Pumpkin-Bruno | CS | 45 |
| 67 | 4 | QEP Field Services Blacks Fork | GP | 63 |
| 68 | 4 | Questar Rock Springs Complex | GP | 72 |
| 69 | 3 | Rucki 15 | CS | 37 |
| 70 | 16 | River-Nile | CS | 43 |
| 71 | 12 | Robertson | CS | 42 |
| 72 | 12 | Shute Creek Facility | GP | 1,169 |
| 73 | 19 | Silver Eagle Refining | RF | 30 |
| 74 | 4 | Simplot Phosphates | IP | 48 |
| 75 | 1 | Sinclair Casper Refining Co. | RF | 229 |
| 76 | 6 | Sinclair Oil Corporation | RF | 944 |
| 77 | 4 | Solvay Chemicals, Inc. | TM | 1,112 |
| 78 | 6 | Sun Dog | CS | 38 |
| 79 | 9 | The Western Sugar Cooperative | IP | 36 |
| 80 | 16 | Tex-Dallas | CS | 53 |
| 81 | 13 | Thunder Creek Gas Services Buckshot | GP | 48 |
| 82 | 16 | Thunder Creek | CS | 58 |
| 83 | 17 | Thunder Creek Gas Services Mtg. | CS | 98 |
| 84 | 5 | UW Central Energy Plant | PP | 50 |
| 85 | 4 | WGR Operating Granger | GP | 65 |
| 86 | 13 | WIC Station 7950 Douglas | GP | 85 |
| 87 | 11 | Wyoming Lime Producers | IP | 162 |
| 88 | 21 | Wyoming Refining Co. | RF | 120 |
| 89 | 20 | Wyoming Sugar Co. | IP | 26 |
| 90 | 4 | Wamsutter | CS | 93 |
| 91 | 7 | Western Sugar Cooperative | IP | 92 |
| 92 | 16 | Westwind-Astra | CS | 33 |
| 93 | 16 | Whiskey Draw-Jack Daniels | CS | 70 |
| 94 | 17 | Wygen I | PP | 744 |
| 95 | 17 | Wygen II | PP | 873 |
| 96 | 17 | Wygen III | PP | 568 |
| 97 | 17 | Wyodak | PP | 2,902 |
| | | | Total | 59,825 |

Facility

| Map code | Facility type | Facility code |
|---|---|---|
| -1 | Gas processing plant | GP |
| -2 | Compressor station | CS |
| -3 | Coal fired power plant | PP |
| -4 | Trona mine | TM |
| -5 | Refinery | RF |
| -6 | Industrial plant | IP |

Stationary $CO_2$ emissions by basin

| Basin | $CO_2$ kt/yr |
|---|---|
| Bighorn | 298 |
| Denver | 960 |
| Greater Green River | 23,829 |
| Hanna | <1 |
| Laramie | 365 |
| Powder River | 13,170 |
| Shirley | <1 |
| Wind River | 827 |
| subtotal | 39,449 |
| Extrabasinal | 20,376 |
| Total | 59,825 |

County codes

| Code | County | Code | County |
|---|---|---|---|
| 1 | Natrona | 12 | Lincoln |
| 2 | Laramie | 13 | Converse |
| 3 | Sheridan | 14 | Niobrara |
| 4 | Sweetwater | 15 | Hot Springs |
| 5 | Albany | 16 | Johnson |
| 6 | Carbon | 17 | Campbell |
| 7 | Goshen | 19 | Uinta |
| 8 | Crook | 20 | Washakie |
| 8 | Platte | 21 | Weston |
| 9 | Big Horn | 22 | Teton |
| 10 | Fremont | 23 | Sublette |
| 11 | Park | | |

$CO_2$ emmisions (kt/yr)

- 0 - 100
- 100 - 500
- 500 - 1,000
- 1,000 - 5,000
- 5,000 - 15,000

Explanation

- RSU #1
- 11-3 [map No.] - [Facility code]
- Facility
- City
- $CO_2$ pipeline
- EOR $CO_2$ flood field
- Energy basin*
- $CO_2$ producing field
- Prospective $CO_2$ producing field
- County boundary

*Basin outlines from De Bruin 2007

b

**Fig. 5.2** Major stationary anthropogenic sources of emitted $CO_2$ in Wyoming: facilities emitting more than 25 kt/yr of $CO_2$, as reported to the EPA Greenhouse Gas Reporting Program for 2010

Shute Creek facility and the startup of the Dry Fork Station coal-fired power plant in the Powder River Basin. Dry Fork Station, with a planned capacity of 385 MW, is not included in Fig. 5.2.

Figure 5.2 shows that of the nearly 60 Mt of emissions reported in the state, half are from the southwestern part of the state (the Greater Green River Basin). The Greater Green River Basin is host to the largest coal-fired power plant in the state (the Jim Bridger Power Plant), four trona mines and processing facilities, and a number of oil-and-gas-related pipeline compressor stations and gas plants. The RSU #1 test well is approximately 2 mi (3.2 km) from the Jim Bridger plant.

### *5.2.2 Natural Sources*

Figure 5.3 depicts an inventory of oil and gas wells statewide with $CO_2$ as a product constituent. These wells represent both viable commercial $CO_2$ source areas and potential source areas. The information depicted is based on data published by the US Bureau of Mines (Biggs and Espach 1960; Moore and Sigler 1987) and the Wyoming Oil and Gas Conservation Commission (WOGCC 2013). These data include a comprehensive list of gas analyses collected from oil and gas wells throughout Wyoming. Using a reported minimum of 4 % $CO_2$ in the gas tested resulted in a list of 66 wells in 32 field or wildcat areas. Several wells had multiple gas samples from different geological units, for a total of 95 samples reported (Fig. 5.3).

Paleozoic rocks are the source of the $CO_2$ tested in 50 of the 66 wells; Cenozoic and Mesozoic rocks are represented in the other 16 wells. Several of those 16 wells are located in the Madden Deep Field (Wind River Basin) and Brady Field (Washakie Basin).

By far the most wells with reported $CO_2$ are located in the Greater Green River Basin/Overthrust Belt area of southwestern Wyoming. The Riley Ridge/LaBarge Platform area shows the greatest number of wells with the highest concentrations of $CO_2$, followed by the Moxa Arch and the Rock Springs Uplift. $CO_2$ concentrations range from 60 % to 96 % of the total gas concentration at Riley Ridge/LaBarge, 15–92 % on the Moxa Arch, and 16–82 % on the Rock Springs Uplift.

Figure 5.3 shows two field areas where naturally occurring $CO_2$ is either being produced commercially or will be in the very near future. At present, Exxon Mobil Corporation sells approximately 6.4 Mt of naturally occurring $CO_2$ for use at five EOR projects in Colorado and Wyoming. The $CO_2$ is produced from the LaBarge field area, one of the largest naturally occurring $CO_2$ accumulations in the world. Denbury Resources is developing a 20-in (51-cm) $CO_2$ pipeline from this field area as well. The capacity of Denbury's pipeline will be on the order of 13–14 Mt/yr. This $CO_2$ is to be transported north through Wyoming and into Montana for use in EOR projects. Denbury has also purchased the rights to $CO_2$ produced at the Madden Deep Field, near the center of the state. That $CO_2$ will be shipped to Montana as well (De Bruin 2011).


| No. | Co. | CO2/% | Depth | Field | Unit |
|---|---|---|---|---|---|
| 1 | 12 | 95.0 | 16,460 | Raptor | Madison |
| 2 | 3 | 6.1 | 260 | Spence Dome | Tensleep |
| 3 | 17 | 12.7 | 7,900 | Kuehne SE | Minnelusa |
| 4 | 6 | 4.2 | 8,784 | Barrel Springs E | Mesaverde |
| 5 | 6 | 4.0 | 8,041 | Blue Gap | Mesaverde |
| 6 | 6 | 4.0 | 10,000 | Wamsutter | Mesaverde |
| 7 | 6 | 9.5 | 10,700 | Sugar Creek | Tensleep |
| 8 | 10 | 5.1 | 14,709 | Madden Deep | Mesaverde |
| 9 | 10 | 5.0 | 8,842 | Pony Creek | Fort Union |
| 10 | 10 | 4.7 | 8,842 | Pony Creek | Fort Union |
| 11 | 15 | 6.2 | 2,915 | Black Mountain | Embar *1 |
| 12 | 12 | 92.1 | 17,562 | Bruff Unit | Madison |
| 13 | 12 | 7.3 | 14,635 | Carter Creek | Mission Canyon *2 |
| 14 | 12 | 74.2 | 18,004 | Bruff Unit | Madison |
| 15 | 12 | 95.9 | 16,040 | Fontenelle | Bighorn |
| 16 | 12 | 80.4 | 16,549 | Wild Cat | Madison |
| 17 | 12 | 19.5 | 14,935 | Wild Cat | Phosphoria |
| 18 | 1 | 5.5 | 653 | Iron Creek | Dakota *3 |
| 19 | 14 | 14.3 | 6,180 | Buck Creek | Leo *4 |
| 20 | 14 | 4.7 | 6,694 | Ant Hills N | Leo *4 |
| 21 | 11 | 6.1 | 4,338 | Elk Basin | Tensleep |
| 22 | 11 | 13.9 | 4,711 | Elk Basin | Tensleep |
| 23 | 11 | 16.3 | 3,938 | Elk Basin | Tensleep |
| 24 | 11 | 4.2 | 5,800 | Elk Basin | Tensleep |

| No. | Co. | CO2/% | Depth | Field | Unit |
|---|---|---|---|---|---|
| 25 | 11 | 4.3 | 8,800 | Silver Tip | Embar + *5 |
| 26 | 11 | 4.8 | 9,037 | Silver Tip | Madison |
| 27 | 12 | 82.2 | 15,153 | Riley Ridge | Bighorn |
| 28 | 12 | 76.6 | 15,153 | Riley Ridge | Bighorn |
| 29 | 23 | 85.5 | 15,095 | Riley Ridge | Bighorn |
| 30 | 23 | 64.2 | 12,878 | Riley Ridge | Tensleep |
| 31 | 12 | 60.4 | 15,750 | Riley Ridge | Madison |
| 32 | 12 | 67.3 | 14,818 | Riley Ridge | Darby |
| 33 | 23 | 67.2 | 14,818 | Riley Ridge | Darby |
| 34 | 12 | 65.7 | 13,006 | Riley Ridge | Phosphoria |
| 35 | 23 | 63.5 | 12,842 | Riley Ridge | Phosphoria |
| 36 | 12 | 63.4 | 14,335 | Riley Ridge | Madison |
| 37 | 23 | 63.3 | 12,760 | Riley Ridge | CDZ *6 |
| 38 | 23 | 63.3 | 12,760 | Riley Ridge | CDZ *6 |
| 39 | 23 | 62.7 | 14,335 | Riley Ridge | Madison |
| 40 | 23 | 62.4 | 12,767 | Riley Ridge | Phosphoria |
| 41 | 12 | 62.2 | 13,084 | Riley Ridge | Tensleep |
| 42 | 12 | 62.2 | 13,084 | Riley Ridge | Tensleep |
| 43 | 12 | 62.1 | 13,006 | Riley Ridge | Phosphoria |
| 44 | 23 | 62.0 | 14,335 | Riley Ridge | Madison |
| 45 | 12 | 87.2 | 17,316 | Riley Ridge | Bighorn |
| 46 | 12 | 72.8 | 14,480 | Riley Ridge | Madison |
| 47 | 12 | 76.2 | 15,893 | Riley Ridge | Madison |
| 48 | 23 | 61.9 | 12,842 | Riley Ridge | Phosphoria |

| No. | Co. | CO2/% | Depth | Field | Unit |
|---|---|---|---|---|---|
| 49 | 23 | 61.6 | 12,774 | Riley Ridge | Phosphoria |
| 50 | 23 | 61.3 | 12,774 | Riley Ridge | Phosphoria |
| 51 | 23 | 60.2 | 13,904 | Riley Ridge | Madison |
| 52 | 23 | 59.2 | 13,904 | Riley Ridge | Madison |
| 53 | 12 | 68.4 | 14,437 | Riley Ridge | Madison |
| 54 | 12 | 59.4 | 14,437 | Riley Ridge | Madison |
| 55 | 12 | 69.7 | 14,627 | Riley Ridge | Madison |
| 56 | 4 | 82.0 | 7,507 | Baxter Basin N | Morgan *7 |
| 57 | 4 | 72.1 | 6,214 | Baxter Basin N | Weber |
| 58 | 4 | 26.4 | 14,400 | Brady Deep Unit | Weber |
| 59 | 4 | 74.2 | 12,600 | Brady Deep Unit | Nugget |
| 60 | 4 | 73.9 | 12,000 | Brady Deep Unit | Nugget |
| 61 | 4 | 24.8 | 14,400 | Brady Deep Unit | Weber |
| 62 | 4 | 27.6 | 14,400 | Brady Deep Unit | Weber |
| 63 | 4 | 24.7 | 14,400 | Brady Deep Unit | Weber |
| 64 | 4 | 69.6 | 12,600 | Brady Deep Unit | Nugget |
| 65 | 4 | 27.5 | 14,400 | Brady Deep Unit | Weber |
| 66 | 4 | 72.3 | 12,600 | Brady Deep Unit | Nugget |
| 67 | 4 | 25.8 | 14,400 | Brady Deep Unit | Weber |
| 68 | 4 | 5.7 | 12,750 | Bush Lake | Almond |
| 69 | 19 | 85.5 | 18,398 | Church Buttes | Madison |
| 70 | 4 | 8.1 | 301 | Lost Soldier | Frontier |
| 71 | 4 | 5.7 | 1,510 | Lost Soldier | Lakota *8 |
| 72 | 4 | 31.7 | 6,990 | Lost Soldier | Tensleep |

| No. | Co. | CO2/% | Depth | Field | Unit |
|---|---|---|---|---|---|
| 73 | 4 | 5.6 | 12,307 | Moxa | Almond |
| 74 | 4 | 28.2 | 6,910 | Pretty Water Creek | Phosphoria |
| 75 | 4 | 16.5 | 18,116 | Table Rock | Madison |
| 76 | 4 | 10.6 | 17,240 | Table Rock | Weber |
| 77 | 4 | 15.0 | 18,020 | Table Rock | Madison |
| 78 | 4 | 15.8 | 19,000 | Table Rock | Madison |
| 79 | 4 | 17.0 | 18,287 | Table Rock | Madison |
| 80 | 4 | 15.8 | 18,116 | Table Rock | Madison |
| 81 | 4 | 5.4 | 8,317 | Wild Cat | Mesaverde |
| 82 | 19 | 14.7 | 17,260 | BK5 *9 | Weber |
| 83 | 19 | 23.8 | 18,200 | BK5 *9 | Morgan *7 |
| 84 | 19 | 20.2 | 18,200 | BK5 *9 | Morgan *7 |
| 85 | 19 | 23.1 | 18,213 | BK5 *9 | Morgan *7 |
| 86 | 19 | 22.9 | 17,740 | Church Buttes | Morgan *7 |
| 87 | 19 | 20.4 | 18,060 | Church Buttes | Morgan *7 |
| 88 | 19 | 86.6 | 18,431 | Church Buttes | Madison |
| 89 | 19 | 29.3 | 18,086 | Church Buttes | Morgan *7 |
| 90 | 19 | 93.3 | 12,840 | WC-CC *10 | Mission Canyon *2 |
| 91 | 19 | 23.3 | 12,840 | WC-CC *10 | Mission Canyon *2 |
| 92 | 10 | 19.0 | 17,424 | Madden Deep | Madison |
| 93 | 6 | 52.0 | 5,700 | Wertz | Tensleep |
| 94 | 6 | 18.5 | 6,600 | Wertz | Madison |
| 95 | 6 | 40.5 | 6,100 | Wertz | Amsden |

*1. Phosphoria-Dinwoody(?) equivalent
*2. Limestone unit in the Madison Group
*3. Sandstone, uppermost unit in the Cloverly
*4. Sandstone unit in the Minnelusa
*5. Phosphoria, Dinwoody, and Tensleep
*6. Commingled deep zones
*7. Weber, lower part, equivalent
*8. Sandstone, lowermost unit in the Cloverly
*9. Butcher Knife Springs
*10. Whitney Canyon/Carter Creek

County codes

| Code | County | Code | County | Code | County | Code | County |
|---|---|---|---|---|---|---|---|
| 1 | Natrona | 7 | Goshen | 12 | Lincoln | 19 | Uinta |
| 2 | Laramie | 8 | Crook | 13 | Converse | 20 | Washakie |
| 3 | Sheridan | 8 | Platte | 14 | Niobrara | 21 | Weston |
| 4 | Sweetwater | 9 | Big Horn | 15 | Hot Springs | 22 | Teton |
| 5 | Albany | 10 | Fremont | 16 | Johnson | 23 | Sublette |
| 6 | Carbon | 11 | Park | 17 | Campbell | | |

RSU #1
11-3 [No.] - [CO2/%]
Facility
City

Explanation
Energy basin*
CO2 producing field
Prospective CO2 producing field
County boundary
*Basin outlines from De Bruin 2007

b

**Fig. 5.3** Natural sources of $CO_2$ in Wyoming: wells showing 4 % or greater $CO_2$ content in produced gas, as reported to the WOGCC

## 5.3 Geology

The present geologic landscape across much of Wyoming was sculpted by the Sevier and Laramide orogenies, which spanned nearly 95 million years from approximately 130–35 m.y.b.p. (Heller et al. 1986; Roehler 1992; Brown 1993; Royse 1993; DeCelles et al. 1995). Tectonism associated with these orogenies formed most of the local and regional geologic structures that now define the structural boundaries of the GGRB and its subbasins.

While there is current debate as to the connection between the two orogenies, the Sevier is generally defined as an older, thin-skinned deformation event that created the Fold and Thrust Belt (Royse 1993). Laramide deformation overlaps and follows the Sevier Orogeny and is characterized by thick-skinned deformation such as the basement-involved thrusts that uplifted the Wind River Range and the Rock Springs Uplift (Love 1961; Brown 1993). At approximately 140 m.y.b.p. the early stages of Sevier tectonism uplifted the Fold and Thrust Belt on the current basin's western border, creating the western margin of the early GGRB. Laramide tectonism, beginning 80 m.y.b.p., then uplifted ranges to the north, east, and south, effectively bracketing the basin on all sides. The surrounding uplifts were thrust toward the center of the basin, severing the continuity from peripheral outcrop to basin center of Paleozoic strata and decreasing lateral meteoric recharge from surface to depth.

The Rock Springs Uplift is the GGRB's youngest Laramide uplift; faulting was active through the late Eocene (Roehler 1992). Strata of the RSU are mostly offset along a blind thrust fault on the western border of the anticline (Fig. 5.4) (Love 1961). Movement along the thrust fault was westward, resulting in drag-fold-style asymmetry; formations dip steeply on the west side of the anticlinal crest and more shallowly east of the crest (Fig. 5.4). The oldest unit exposed on the surface of the uplift is the Baxter Shale, which crops out on the crest of the anticline. The Baxter Shale is less resistant to weathering than the clastic units that flank the anticline; a result is the Baxter Basin, the topographic low at the top of the uplift (Fig. 5.4).

Post-Laramide tectonism is notable in the GGRB, as there was an active period of regional extension in the Neogene (Mederos et al. 2005; Bader 2008, 2009). Bader (2008) correlates high-angle normal faults southeast of the study site to Neogene extension. Lange et al. (2000) suggest that this extension could be responsible for the formation/reactivation of the Farson Lineament and the Leucite Hills volcanism; both areas are proximal to the study site.

The sedimentary section at the well site consists of more than 13,500 ft (4100 m) of Paleozoic and Mesozoic rocks and spans over 500 m.y. of geologic history (Fig. 5.5). Laramide uplift followed by renewed denudation in the Pliocene removed several thousand feet of Tertiary sediment and obliterated the Cenozoic sedimentary section at the well site. The sedimentary section consists of terrestrial and marine deposits; marine sediments are predominant in both thickness and number (Love et al. 1993). The resulting sedimentary sequence at the well site is predominantly fine-grained shales, clay, and siltstone, more than 8500 ft (2600 m) of which

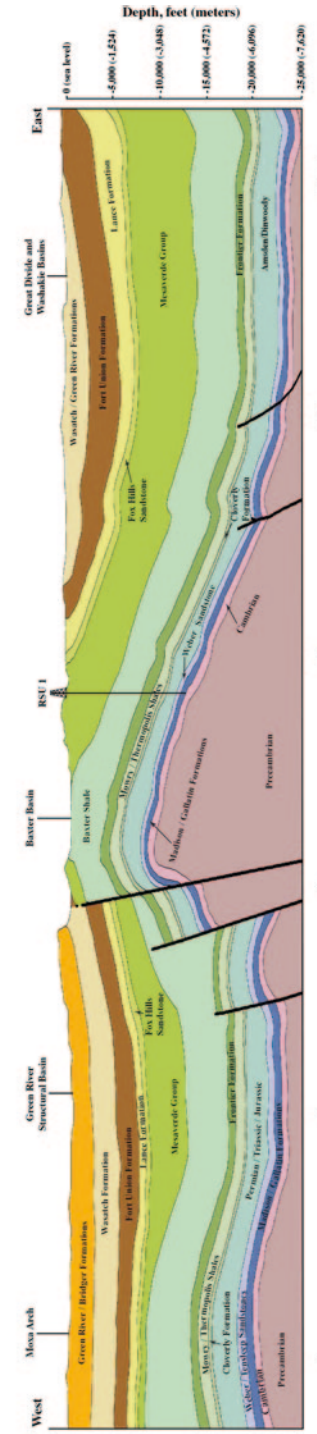


**Fig. 5.4** Stylized cross section across the RSU and adjacent subbasins showing the position of the RSU #1 well (modified from Clarey and Thompson 2010)

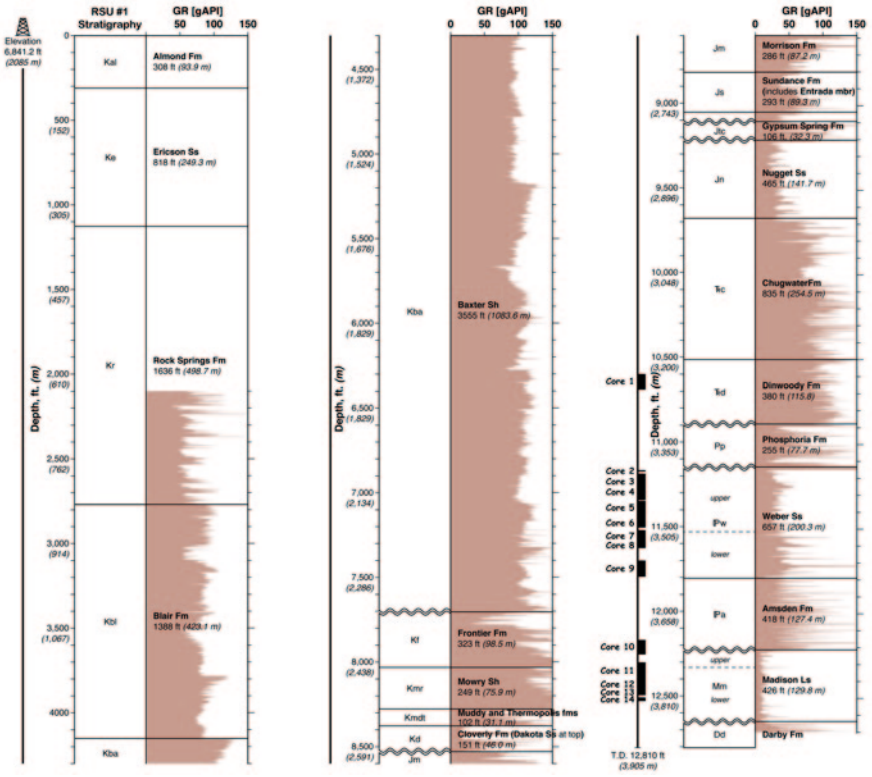


**Fig. 5.5** Stratigraphic column for the RSU #1 well including gamma log and cored intervals

are Cretaceous sediments. These Cretaceous sediments were deposited into, or on the margins of, the Cretaceous Western Interior Seaway (Steidtmann 1993). They are dominantly marine shales, though several formations were deposited during regressive periods and are clastic. The Cretaceous shales are important in this study as potential seals for $CO_2$ storage intervals. For instance, the Cretaceous Mowry Shale, a siliceous, laterally continuous organic marine shale, has proven an effective hydrocarbon seal on the crest of the RSU (Fig. 5.4 and 5.5) (WOGCC 2013). The Cretaceous Baxter Shale, a massive shale and siltstone unit more than 3500 ft (1066 m) thick, is prevalent across the GGRB; the Baxter Shale effectively traps hydrocarbons on the crest of the RSU (WOGCC 2013). Petrophysical data from the RSU #1 and data from nearby oil fields suggest that several Cretaceous clastic formations could also act as potential storage reservoirs; these include the Frontier, Muddy, and Dakota sands (WOGCC 2013).

While this study does not focus on the 1150 ft (350 m) of marine and terrestrial Jurassic sediments, several potential reservoirs within them are worth noting with respect to $CO_2$ sequestration (Fig. 5.4 and 5.5). The Nugget Sandstone (Triassic and Jurassic), a laterally continuous eolian sandstone, has proven an effective hydrocar-

bon reservoir in other parts of the GGRB, including the neighboring Brady Field, 18 mi (29 km) from the RSU #1 well site (WOGCC 2013). The Jurassic Entrada Sandstone is relatively thin at the well site, but regional petrophysical data suggests that it is porous and laterally continuous. Either of these formations could prove useful for future CCS projects on the RSU and could significantly increase the sequestration capacity of the study site area.

## 5.4 Regional Geologic and Depositional History of Targeted Formations

The bulk of the Carbon Management Institute's (CMI) work on the study site consisted in characterizing the Paleozoic reservoirs and associated seals. The Paleozoic reservoirs are approximately 1100 ft (335 m) thick at the well site, and are more than 11,100 ft (3400 m) below the land surface (Fig. 5.5). Approximately 827.5 ft (252.2 m) of core was recovered from the Pennsylvanian Weber Sandstone and Mississippian Madison Limestone for analysis of reservoir characteristics. Associated seals, specifically lower Triassic formations, consist of approximately 1215 ft (370.3 m) of shallow marine and terrestrial sediment. The Triassic sediments, a mix of redbeds, shales, clastics, and evaporates, are documented seals in southwest Wyoming (WOGCC 2013). Nearly 90 ft (27 m) of core was recovered from the lower Triassic section for sealing lithology characterization (Fig. 5.5).

The targeted reservoirs and seals were deposited over a period of nearly 150 m.y. (Love et al. 1993). The oldest reservoir, the Mississippian Madison Limestone, disconformably overlies Devonian deposits (Love et al. 1993). At the beginning of the Mississippian, warm, shallow inland seas covered most of Wyoming (Maughan 1963). The regional sea level and associated sediment deposition at the study site were controlled by the southwest–northeast-trending Transcontinental Arch to the east and south, the Antler Foredeep basin to the west, and the Central Montana Trough to the north (Elrick 1990; Reid and Dorobek 1993; Buoniconti 2008). As a result of the regional structural setting, the Madison was deposited as a northwestward-prograding carbonate ramp across most of Wyoming (Sando 1976; Gutshick and Sandberg 1983; Westphal et al. 2004). Madison deposition took place over a dynamic period of geologic history; active tectonism resulted in greenhouse and glacial periods, widespread volcanism, eustatic seas, and regional orogeny, all of which left imprints on the architecture, mineralogy, and geochemistry of the Madison Limestone (see Chap. 6). The immediate, pre-burial impact of active tectonism and fluctuating sea level on the Madison Limestone forced the dolomitization of the original carbonate across much of Wyoming (Katz 2008). This early diagenetic episode had a large impact on local and regional reservoir properties, and is the primary reason that the Madison is such an attractive storage reservoir (Westphal et al. 2004). A period of epeirogenic uplift, primarily focused in southeast Wyoming, led to subaerial exposure of the Madison, triggering erosion and a hiatus in the depositional record evidenced by the regional paleokarst topography at the top of the

formation (Harshman 1972; Sando et al. 1975). This uplift was the first of three episodes of regional tectonism beginning in the middle Mississippian and continuing through the Late Pennsylvanian; the response to these stress episodes elevated the Ancestral Rocky Mountains (Maughan 1963; Kluth 1986). Episodic tectonism and eustatic seas created a multitude of depositional environments and resulted in the sandstone, siltstone, shale, limestone, and dolomite of the Amsden Formation at the study site (Sando et al. 1975).

Conformably overlying the Amsden Formation is the Middle-Late Pennsylvanian Weber Sandstone, which is composed of eolian and marine deposits (Love et al. 1993). At the study site, the Weber Sandstone is divided into upper and lower facies that correspond to regional depositional environments (see Chap. 6). At the beginning of Weber deposition a shallow, warm epicontinental sea stretched across the Wyoming shelf, resulting in the subaqueous carbonate deposits and clastic and near-shore carbonate deposits of the lower facies (Maughan 1967; Mallory 1967, 1975). During a period of foreland deformation, paleo-depositional trends across the Wyoming shelf were altered as highlands formed to the north and west in what had been predominantly open seaways since the Devonian (Blackstone 1963; Kluth 1986). The epeiric sea receded, and massive, southward-marching dune fields spread across most of Wyoming, resulting in the cross-bedded eolian deposits of the upper facies (Opdyke and Runcorn 1960; Tonnsen 1986). These eolian rocks correspond to similar facies in the Tensleep, Minnelusa, and other equivalent formations elsewhere in Wyoming (Maughan 1967).

At the onset of the Permian, widespread erosion resulted in disconformity between the overlying Permian Phosphoria Formation and underlying Weber Sandstone (McKee et al. 1959). The Permian was marked by both compressional and extensional tectonism (Blackstone 1963; Tonnsen 1986). This tectonism coincided with the initial development of Wyoming's modern sedimentary basins (Tonnsen 1986). Evidence of certain proto-basins—the Greater Green, Bighorn, and Powder River basins—includes concentrations of Guadalupian (Upper Permian) evaporites and dolomites within the confines of these isolated lowlands (Tonnsen). At the study site, the base of the Phosphoria Formation is delineated by organic shale. Above the organic shale, the Phosphoria is a combination of shales, carbonates, and evaporates, indicative of marine deposition.

Disconformably overlying the Phosphoria Formation is the lower Triassic Dinwoody Formation. The Dinwoody consists of alternating light green shales and redbeds, siltstones, and thin layers of carbonates and evaporites (Love and Christiansen 1985; Rowley et al. 1985). The presence and distribution of abundant terrestrially-derived clastic material, oxidized clays, and evaporites indicate that the Triassic Dinwoody was deposited in shallow, dynamic seas that deepened westward (Picard 1993).

Though primary deposition and lithology left indelible imprints on the geologic character of the selected reservoir and seal lithologies, post-burial processes have also had a great impact on their holding and sealing capacities. CMI investigated the nature and timing of diagenesis, burial history, petrography, cementation, porosity types, geochemical evolution, fluid evolution and migration, and structural

deformation of the targeted formations in order to fully characterize the impact of injecting $CO_2$ into these deep, saline reservoirs (see Chap. 6 and 8).

## 5.5 Inventory of Current Groundwater Development and Summary of Hydrogeology

### *5.5.1 Introduction*

A major concern in long-term carbon capture and sequestration (CCS) is the potential for leakage, and the resulting risk of contamination of groundwater aquifers. It is therefore important to catalog and describe the baseline groundwater quality of associated aquifers and active groundwater wells at potential CCS sites. CMI took inventory of all groundwater wells within the 36 $mi^2$ (93 $km^2$) township, Township 20 North, Range 101 West (T20N, R101W), surrounding the study area in Section 16 (Sect. 16) and expanded it to include all the drinking water wells in the seven adjacent townships. In addition to the well inventory, a literature search was conducted to identify and characterize hydrogeologic units—aquifers and confining units—on the RSU. Finally, CMI identified and catalogued fresh water zones during drilling of the RSU #1 well. These measures can be used as an example of providing groundwater data to inform a $CO_2$ reservoir-site characterization.

### *5.5.2 Inventory of Groundwater Wells*

CMI cataloged the groundwater wells within T20N, R101W. Data was collected from the Wyoming State Engineers Office (WSEO), which issues water-well permits in Wyoming. Only one groundwater well, a monitoring well near the RSU #1 well, was identified in Sect. 16. The entire township contains 133 permitted groundwater wells. The purposes of these wells vary: four wells are designated for domestic use, five wells for industrial/railroad use, four wells for miscellaneous use, and most wells (120) for monitoring groundwater activities and quality. The monitoring-well network was created in response to many years of industrial activity in the area (particularly that of the railroad, surface and underground coal mines, landfill operations, and a coal-fired power plant); it provides solid historical baseline data and in-place monitoring infrastructure. In addition to the 133 wells located within this township, 5 drinking-water wells were identified in the seven adjacent townships. The high concentration of preexisting monitoring wells (120) coupled with a low concentration of domestic wells (9) made the RSU a good candidate for CCS, from a groundwater perspective.

All four domestic drinking water wells identified within the township are located in Sect. 27, approximately 3 mi (2.8 km) south–southwest of the RSU #1 well. The

completion depths of the wells are 90, 90, 305, and 340 ft (25, 25, 95, and 105 m) below the land surface. They are likely completed in clastic units of the Upper Cretaceous Mesaverde Group. The five domestic groundwater wells adjacent to the study site are located in T20N, R102W, Sect. 20. These wells are approximately 5 mi (8 km) west, and up-dip, of the study site. Their completion depths range between 240 and 300 ft (75 and 90 m); all are completed within the Ericson Sandstone of the Mesaverde Group (Fig. 5.2).

The nine wells cataloged as industrial/railroad and miscellaneous are water-supply wells for the Black Butte coal mine, the Jim Bridger power plant, the Wyoming Department of Transportation, and the Union Pacific Railroad. The completion depths of these wells range from 18 ft to 1451 ft (5–440 m).

Most of the groundwater well permits for wells surrounding our study site were issued for monitoring wells. These wells are used to monitor the elevation and quality of groundwater near selected sites at risk for contamination. The completion depths of the monitoring wells range from 10 ft to 344 ft (3–105 m). Some monitoring wells have associated petrophysical and baseline water-quality data.

### *5.5.3 Summary of Hydrogeologic Units*

Eight distinct designated hydrogeologic units (aquifers or confining units) overlie the potential CCS Paleozoic reservoirs at the study site (Bartos and Hallberg 2010): from top to bottom the Mesaverde aquifer, Baxter–Mowry confining unit, Cloverly aquifer, Morrison confining unit, Sundance aquifer, Gypsum Spring confining unit, Nugget aquifer, and Chugwater–Dinwoody confining unit (Fig. 5.2). Below these units are the Weber/Tensleep aquifer, Amsden confining unit, and Madison aquifer. The Madison and Weber, the potential CCS reservoirs, are discussed extensively throughout this report; this section focuses on the hydrogeologic units that overlie them. Fresh water was identified in only two intervals in the RSU #1 well within 2000 ft (610 m) of the surface (groundwater wells rarely exceed 1000 ft (304 m) in the GGRB). Nonetheless, it is important to fully investigate all potential USEPA Underground Sources of Drinking Water (USDW) aquifers.

#### 5.5.3.1 Mesozoic Hydrogeologic Units

Mesozoic rocks in the study area on the Rock Springs Uplift run from the land surface to a depth of 10,895 ft (3321 m) (Fig. 5.2). RSU #1 well logs indicate that 23 % of that thickness is composed of sandy lithologies that could be water bearing. This is slightly lower than the estimate of Freethey and Cordy (1991) that 25–50 % of the Mesozoic section in the RSU could be water bearing.

Recharge to the Mesozoic sediments is primarily through direct infiltration from outcrop (Bartos and Hallberg 2010). However, there is also evidence for vertical groundwater flow between Mesozoic aquifers. Freethey and Cordy (1991) suggests

there is a hydraulic gradient favorable for vertical flow on the western flank of the RSU. These authors also identified an area on the southern side of the RSU that may favor downward movement of groundwater from Cenozoic aquifers to Mesozoic aquifers of 20 acre-ft to 50 acre-ft (25,000–60,000 $m^3$) per year. No vertical groundwater movement has been identified at the study area.

Freethey and Cordy (1991) defined the Mesozoic section of the RSU as good to moderate for water yielding potential, on the basis of more than 1000 ft (304 m) of saturated thickness and good-to-moderate recharge potential. However, these authors also identified the RSU as having marginal-to-poor transmissivities, less than 100 ft to 500 ft per day (ft/d) (30–150 m/d) with water quality extremely variable with depth. Near recharge areas the water can be relatively fresh but with increasing depth may record salinities three times that of sea water (Bartos et al. 2010). Bartos and Hallberg (2010) suggested that outside the outcrop areas the "hydraulic properties, great depth and minimal precipitation and recharge, and the generally poor water quality prevent widespread development of aquifers in Mesozoic rocks." From the groundwater well inventory conducted for this study we learned that groundwater development in the Mesozoic aquifers adjacent to the WY-CUSP study area has been limited.

**Mesaverde Aquifer** The Mesaverde aquifer includes the Almond Formation, Ericson Sandstone, Rock Springs Formation, and Blair Formation. These geologic units crop out around the flanks of the RSU. The Mesaverde Group was deposited during transgressive and regressive cycles in swamp, fluvial, delta, lagoonal, shoreline, shallow marine, and near-shore marine environments. Thus there are alternating sequences of shale, sand, and (in places) coal. The sandstones are identified as aquifers, and interbedded shales act as local confining units.

Freethey and Cordy (1991) estimated that the Mesaverde aquifer on the flanks of the RSU has less than 500 ft (152 m) of saturated thickness and a total dissolved solids concentration of less than 1000 mg/L. Bartos et al. (2010) later refined TDS estimates to range from 342 mg/L to 7860 mg/L.

At the RSU #1 well the Mesaverde aquifer extends from the land surface to 4150 ft (1265 m) below the land surface. Fresh water was encountered in the Ericson Sandstone at depth intervals of 330–358 ft (101–109 m) and 840–886 ft (256–270 m). Available regional data (n=3) of the Ericson suggests TDS ranges from 441 mg/L to 1031 mg/L. In a statistical summary of the NWIS database, Bartos et al. (2010) reported that most samples were suitable for domestic use, but that concentrations of alpha radioactivity (all samples) and radium-226 plus radium-228 (67% of samples) exceeded health-based standards, and that aesthetic standards for domestic use were also breeched for iron (100%), manganese (100%), sulfate (25%), TDS (25%) and pH (20% less than lower limit, 6.50).[1] The Ericson is the only formation in the Mesaverde Group in which fresh water was encountered in the RSU #1 well.

[1] See Bartos et al. (2010) for water-quality summaries of other hydrogeologic units on the RSU and in contiguous areas of the Green River Basin.

**Baxter–Mowry Confining Unit** The Baxter–Mowry confining unit is composed of the Upper Cretaceous Aspen, Baxter, Mowry, Steele, Cody, Thermopolis, and Hilliard Shales, the Muddy Sandstone; and the Frontier, Niobrara, and Blind Bull formations (Freethey and Cordy 1991). It is a laterally extensive confining unit and ranges in thickness from 5000 ft to 14,000 ft (1524–4267 m) (Freethey and Cordy). It serves as a hydrogeologic divide between the overlying Mesaverde aquifer system and underlying Mesozoic hydrogeologic units. Bartos and Hallberg (2010) reported that the Frontier Formation and the Muddy Sandstone may contain local aquifers, but suggests that these waters likely would be associated with high salinities.

At the RSU #1 well the Baxter–Mowry confining unit is 4229 ft (1289 m) thick, extending from 4150 ft to 8379 ft (1265–2554 m) below the land surface. The only water-bearing zones in the Baxter–Mowry confining unit may be two 20 ft (6 m) sand intervals in the Frontier Formation and 15 ft (5 m) and 5 ft (2 m) sand intervals in the Muddy Sandstone. The resistivity measured within these intervals suggests that the fluid is saline (TDS > 10,000 mg/L). As reported in previous works and confirmed in this study, the lateral continuity and thickness of this low-permeability material define a major hydrologic divide between the aquifers above and below the Baxter–Mowry confining unit, (Ahern et al. 1981; Collentine et al. 1981; Freethey and Cordy 1991; Bartos and Hallberg 2010).

**Cloverly Aquifer** The Cloverly aquifer is present throughout the GGRB; it is composed primarily of the Cloverly Formation (or Dakota Sandstone) and includes the Bear River Formation and the Gannet Group in the northern and western GGRB (Freethey and Cordy 1991; Bartos and Hallberg 2010). The aquifer is composed of sandstone beds and is confined above by the Baxter–Mowry confining unit and below by the Morrison Formation (Bartos and Hallberg 2010; Love and Christiansen 1993). Freethey and Cordy estimated that the Cloverly aquifer on the RSU has an approximate saturated thickness between 100 ft and 500 ft (30 m and 152 m).

At the RSU #1 well the Cloverly aquifer extends in depth from 8379 ft to 8530 ft (2554–2600 m) below the land surface, spanning 140 ft (42 m). The Cloverly aquifer contains three sandstone beds, each 30 ft (9 m) thick, separated by 10–20 ft (3–6 m) of shale.

**Morrison Confining Unit** The Morrison confining unit has been poorly defined within the GGRB and commonly is undifferentiated from the overlying Cloverly Formation or underlying Sundance Formation (e.g., Love and Christiansen 1985). Freethey and Cordy (1991) noted that the fine-grained lithologies of the Morrison Formation are unlikely to host an extensive aquifer. Bartos and Hallberg (2010) noted that the Morrison Formation can contain sandy lithologies that might act as local aquifers. Sixteen samples from the RSU have been catalogued in the USGS Produced Waters Database. The TDS concentration in these samples ranges from 2163 mg/L to 40,803 mg/L. A statistical summary of these samples from Bartos et al. (2010) found that all produced water samples from the Morrison Formation have characteristics and constituent concentrations that exceed standards for domestic use.

At the RSU #1 well the Morison Formation is 8530 ft to 8816 ft (2600 m to 2687 m) below the land surface. The lithology is predominantly shale with one sandy/shaley 25 ft (7.6 m) interval about 8600 ft (2620 m) below the land surface.

**Sundance Aquifer** The interbedded sandstone, siltstone, and shale that compose the Sundance aquifer were deposited in marginal marine and continental environments. The Sundance aquifer is reported as 50–75 % sandstone with an estimated saturated thickness of less than 100 ft (30 m) (Freethey and Cordy 1991). Freethey et al. (1988) and Freethey and Cordy (1991) reported that TDS concentrations in the combined Sundance and Nugget aquifers on the RSU may range from 3000 mg/L to 35,000 mg/L. The USGS Produced Waters Database has 10 records from the Sundance aquifer on the RSU, which show TDS concentrations of 9469 mg/L to 37,378 mg/L.

The Sundance aquifer in the RSU #1 well contains the Entrada Sandstone, the basal unit of the Sundance. The Entrada Sandstone is a cross-bedded eolian sandstone (Tweto 1976; Rowley et al. 1985). The combined thickness of the Sundance is 293 ft (89 m), 8816 ft–9109 ft (2687–2776 m) below the land surface. The general lithology consists of an upper sandstone (approximately 74 ft, 23 m), a middle section of fine-grained material (approximately 165 ft, 50 m), and the basal Entrada Sandstone (approximately 54 ft, 16 m).

**Gypsum Spring Confining Unit** The Gypsum Spring confining unit separates the Sundance aquifer from the underlying Nugget aquifer in some areas of the GGRB. Love et al. (1993) show that on parts of the RSU the Gypsum Spring confining unit is missing: this could allow hydrogeologic connection between the Nugget aquifer and the Sundance aquifer. The Gypsum Spring confining unit was deposited in a marginal marine setting with abundant transgressive and regressive sequences of the Jurassic sea (Freethey and Cordy 1991). The Gypsum Spring confining unit at the RSU #1 well occurs over a 106-ft (32-m) depth interval—9109 ft to 9215 ft (2776–2809 m) below the land surface.

**Nugget Aquifer** The Nugget aquifer is composed of eolian, gray to dull-red, cross-bedded sandstone (Freethey and Cordy 1991; Love and Christiansen 1985). Freethey and Cordy reported that in the vicinity of the RSU the saturated thickness of the Nugget aquifer is estimated to range from 500 ft to 1000 ft (152–305 m). The USGS Produced Waters Database provides records of 21 produced water samples from the Nugget on the RSU. These samples, mostly from the western flank of the uplift, range in TDS concentrations from 4998 mg/L to 95,670 mg/L. The lowest salinities were measured in samples from the Baxter Basin North field. All the produced water samples exceed aesthetic standards for domestic use in chloride and TDS concentrations and many exceed sulfate standards (53 %) (Bartos et al. 2010).

The Nugget in the RSU #1 well has a thickness of 465 ft (142 m) and extends from 9215 ft to 9680 ft (2809–2950 m) below the land surface. The lithology determined from the gamma log is a relatively uniform sandstone. Measured log porosity within the Nugget ranges from 3 % to higher than 30 %, with an average porosity of 13 %. Formation fluids within the Nugget have low resistivity, which suggests high

salinity. High measured porosity, combined with thick lateral confining units make the Nugget an intriguing additional target for $CO_2$ storage.

**Chugwater–Dinwoody Confining Unit** The Chugwater–Dinwoody confining unit consists of the Chugwater and Dinwoody formations. The rocks composing this hydrogeologic unit are mainly shale and siltstone with lesser interbedded sandstone and limestone. The Chugwater–Dinwoody confining unit is laterally extensive and typically deeply buried across the GGRB. Freethey and Cordy (1991) suggest that this confining unit hydraulically separates the Mesozoic hydrogeologic units from the underlying Paleozoic hydrogeologic units. One water-quality sample reported in the USGS Produced Waters Database, taken through a drill-stem test at Baxter Basin South on the southwestern flank of the RSU, showed a TDS of 5600 mg/L.

The Chugwater–Dinwoody confining unit at the RSU #1 well has a thickness of 1215 ft (370 m), extending from 9680 ft to 10,895 ft (2950–3321 m) below the land surface. Density porosity measured from the log suite suggests little to no porosity, with the exception of one 30 ft (9 m) sandy shale interval near the top of the formation. On the basis of high shale content, formation thickness, and low porosity it is likely that the Chugwater–Dinwoody confining unit within the study area is a hydrologic divide between the Mesozoic and Paleozoic aquifers. This conclusion is consistent with the findings of Freethey and Cordy (1991) and is supported by the FIV (fluid inclusion volatiles) work described by Campbell-Stone et al. (2010), which documented that the Dinwoody Formation is an effective seal.

#### 5.5.3.2 Paleozoic Hydrogeologic Units

The Paleozoic hydrogeologic units in the RSU #1 well extend from 10,895 ft (3321 m) below the land surface to the top of the Precambrian basement at about 13,500 ft (4115 m) below the land surface. Regionally, the Paleozoic aquifers in the GGRB are not used as a source of groundwater except sparsely in outcrop areas, because these units are deeply buried and contain highly mineralized water. Due to the sparsity of groundwater development, Paleozoic hydrogeologic units are generally grouped and described as zones.[2] The zones described by Bartos and Hallberg (2010) are Upper Paleozoic aquifers, Upper Paleozoic confining units, and Lower–Middle Paleozoic aquifer system. Within these zones are the Paleozoic hydrogeologic units of interest in this study, the Weber/Tensleep aquifer, Amsden confining unit, and Madison aquifer (Fig. 5.2).

**Weber/Tensleep Aquifer** The Weber/Tensleep aquifer is isolated above by the Chugwater–Dinwoody confining unit and below by the Amsden confining unit.

[2] For previous zonings of Paleozoic strata cf. Ahern et al. (1981), Collentine et al. (1981), Taylor et al. (1986), Linder-Lunsford et al. (1989), and Bartos and Hallberg (2010); summarized in Bartos and Hallberg (2010), Fig. 5.4.

The thickness of this hydrogeologic unit is measured at 912 ft (278 m) at the RSU #1 well. Geldon (2003b) documented that groundwater flow in our study area is to the northeast. The TDS concentration in the Weber/Tensleep measured in three oil and gas fields on the western side of the RSU (Pretty Water Creek, Baxter North, and Baxter Middle) approaches 72,000 mg/L (USGS Produced Waters Database; WOGCC). In the RSU #1 well TDS was measured at 89,800 mg/L. As the Weber Sandstone is a target formation, its recorded fluid chemistry is described in detail in Chap. 8.

**Amsden Confining Unit** Little is known about the groundwater potential of the Amsden confining unit. Several previous studies are in agreement that due to low permeability and great depth, the groundwater potential is poor (Berry 1960; McGreevy 1969); the unit is generally considered an "aquitard" (Collentine et al. 1981). One water quality record is cataloged in the Produced Waters Database: a drill stem test conducted in the Baxter Basin North field measured a TDS concentration in the Amsden of 88,893 mg/L. In the RSU #1 well the Amsden formation is roughly 418 ft (127 m) thick and is composed of red to gray shale, with thin layers of limestone and dolomite.

**Madison Aquifer** The Madison aquifer is confined above by the Amsden confining unit and below by the Darby confining unit. Geldon (2003a, b), who mapped and estimated the lithologies of the Madison aquifer throughout the GGRB, describes the Madison aquifer in the GGRB as consisting mostly of dolostone with subordinate limestone. The porosity and permeability of the Madison aquifer are chiefly secondary (Berry 1960; Collentine et al. 1981; Johnson and Huntoon 1994), as evidenced in thin section by hypersaline dolomitization and solution cavities (see Chap. 6).

At the RSU #1 well the Madison Limestone is roughly 426 ft (130 m) thick and consists of a tight upper zone of limestone (115 ft, 35 m) and a lower dolomitized zone (311 ft, 95 m). The water quality measured in the Madison Limestone in the RSU #1 well has a TDS concentration of 86,500 mg/L.

### *5.5.4 Conclusion*

The RSU #1 stratigraphic test well is located near the largest point-source emissions of anthropogenic $CO_2$ in the State of Wyoming, as well as the primary enhanced oil recovery supply pipeline corridor in the State. The well is located on the northeast flank of the RSU, a large asymmetric anticline that formed at the end of the Laramide Orogeny. Several geologic formations were identified as having reservoir characteristics favorable for $CO_2$ injection, specifically the Weber Sandstone and Madison Limestone.

The results of this investigation find that groundwater use in the study area is sparse. Only four groundwater permits for drinking water wells were identified in the study area. These were located more than three miles from the proposed site of $CO_2$ injection. 120 permits were identified for monitoring wells within the study

area. Many of the monitoring well permits have geological and water quality data associated with their records, some of which predates portions of the industrial activity that they were to monitor, thus creating a robust baseline for water quality in the study area.

Two intervals of fresh water were identified in the Ericson Sandstone during the completion of the RSU #1 well. On the basis of an extensive literary search and petrophysical data from the RSU #1 well, we conclude that no other stratigraphic intervals are favorable for future groundwater development. It is important to note that several confining units were identified within the stratigraphic column of the study area. Among these are the Baxter–Mowry confining unit and the Chugwater–Dinwoody confining unit. The presence of these hydrogeologic divides implies that there is little, if any, groundwater communication between aquifers within the RSU.

From this investigation we conclude that sequestering $CO_2$ in the Tensleep-Weber and Madison aquifers on the RSU poses no perceptible threat to current groundwater use and resources.

## References

Ahern J, Collentine M, Cooke S (1981) Occurrence and characteristics of ground water in the Green River Basin and Overthrust Belt, Wyoming. Report to U.S. Environmental Protection Agency by Water Resource Research Institute, University of Wyoming, Laramie, vols V-A and V-B (pl.)

Bader JW (2008) Structural and tectonic evolution of the Cherokee Ridge arch, south-central Wyoming: implications for recurring strike-slip along the Cheyenne Belt suture zone. Rocky Mount Geol 43(1):23–40

Bader JW (2009) Structural and tectonic evolution of the Douglas Creek arch, the Douglas Creek fault zone, and environs, northwestern Colorado and northeastern Utah: implications for petroleum accumulation in the Piceance and Uinta basins. Rocky Mount Geol 44(2):121–145

Bartos TT, Hallberg L (2010) Chapter 5, Groundwater and hydrogeologic units. In: Copeland D, Ewald E (eds) Available groundwater determination technical memorandum, Green River Basin Water Plan II. Report to the Wyoming Water Development Commission by the Wyoming State Geological Survey et al., pp 5-1–5–94

Bartos TT, Hallberg L, Clark M (2010) Chapter 6, Groundwater quality. In: Copeland D, Ewald E (eds) Available groundwater determination technical memorandum, Green River Basin Water Plan II. Report to the Wyoming Water Development Commission by the Wyoming State Geological Survey et al., pp 6-1–6–94

Berry DW (1960) Geology and ground-water resources of the Rawlins area, Carbon County, Wyoming. U.S. Geological Survey Water Supply Paper 1458, pl. scale 1:63,360

Biggs P, Espach RH (1960) Petroleum and natural gas fields in Wyoming. U.S. Bureau of Mines Bulletin 582

Blackstone DL (1963) Development of geologic structure in Central Rocky Mountains. American Association of Petroleum Geologists Memoir 2, pp 160 -179

Brown WG (1993) Structural style of Laramide basement-cored uplifts and associated folds. In: Snoke AW, Steidtmann JR, Roberts SM (eds) Geology of Wyoming. Geological Survey of Wyoming Memoir No. 5, pp 312–371

Buoniconti MR (2008) The evolution of the carbonate shelf margins and fill of the Antler Foreland Basin by prograding Mississipian carbonates, northern U.S. Rockies. Dissertation, University of Miami

Campbell-Stone E, Lynds R, Frost C, Becker TP, Diem B (2010) The Wyoming carbon underground storage project: geologic characterization of the Moxa Arch and Rock Springs Uplift. Energy Procedia 4, pp 4656–4663

Clarey K, Thompson M (2010) Chapter 2, Study Area. In: Copeland D, Ewald E (eds) Available groundwater determination technical memorandum, Green River Basin Water Plan II. Report to the Wyoming Water Development Commission by the Wyoming State Geological Survey et al., pp 2-1–2–36.

Collentine M, Libra R, Feathers KR, Hamden L (1981) Occurrence and characteristics of ground water in the Great Divide and Washakie Basins. Water Resources Institute, University of Wyoming, Laramie, vols VI-A and VI-B (pl.)

De Bruin RH (2011) Carbon dioxide ($CO_2$) map of Wyoming. Wyoming State Geological Survey Map Series 90, scale 1:500,000

DeCelles PG, Lawton TF, Gautam M (1995) Thrust timing, growth of structural culminations, and synorogenic sedimentation in the type Sevier orogenic belt, Western United States. Geology 23(8):699–702

Dobbin CE, Hoots HW, Dane CH, Hancock ET (1929) Geology of the Rock Creek oil field and adjacent areas, Carbon and Albany counties, Wyoming. U.S. Geol Survey Bull 806-D:131–153

Elrick M (1990) Development of cyclic ramp-to-basin carbonate deposits, Lower Mississippian, Wyoming and Montana. Dissertation, Virginia Polytechnic Institute and State University

EPA (2012) U.S. Environmental Protection Agency. http://epa.gov/climatechange/emissions/ghgdata/2010data.html. Accessed January 2012

EPA (2013) U.S. Environment Protection Agency. http://epa.gov/climatechange/emissions/ghgdata/2011data.html. Accessed February 2013

Freethey GW, Cordy GE (1991) Geohydrology of Mesozoic rocks in the Upper Colorado River Basin, in Arizona, Colorado, New Mexico, Utah and Wyoming, excluding the San Juan Basin, Regional aquifer-system analysis – Upper Colorado River Basin. U.S. Geological Survey Professional Paper 1411–C

Freethey GW, Kimball BA, Wilberg DE, Hood JW (1988) General hydrology of the aquifers of Mesozoic age, Upper Colorado River Basin, excluding the San Juan Basin – Colorado, Utah, Wyoming, and Arizona. U.S. Geological Survey Hydrologic Investigations Atlas HA-698, 15 maps on 2 sheets, scales 1:2,500, 000 and 1:500,000

Geldon AL (2003a) Geohydrology of Paleozoic rocks in the Upper Colorado River Basin in Arizona, Colorado, New Mexico, Utah and Wyoming, excluding the San Juan Basin, Regional aquifer-system analysis – Upper Colorado River Basin. U.S. Geological Survey Professional Paper 1411–A

Geldon AL (2003b) Hydrologic properties and ground-water flow systems of the Paleozoic rocks in the Upper Colorado River Basin, Arizona, Colorado, New Mexico, Utah and Wyoming, excluding the San Juan Basin, Regional aquifer-system analysis – Upper Colorado River Basin. U.S. Geological Survey Professional Paper 1411–B

Glover KC, Naftz DL, Martin LJ (1998) Geohydrology of Tertiary rocks in the Upper Colorado River Basin in Colorado, Utah and Wyoming, excluding the San Juan Basin, Regional aquifer-system analysis [RASA]. U.S. Geological Survey Water Resources Investigations Report 96–4105

Gutshick RC, Sandberg CA (1983) Mississippian continental margins of the conterminous United States. In: Stanley DJ, Moore GT (eds) The shelf: critical interface on the continental margins. Society of Economic Paleontologists and Mineralogists Special Publication No. 33, pp 79–96

Harshman EN (1972) Geology and uranium deposits, Shirley Basin area, Wyoming. U.S. Geological Survey Professional Paper 745

Heller PL, Bowler SS, Chambers HP, Coogan JC, Hagen ES, Shuster MW, Winslow NS, Lawton TF (1986) Time of initial thrusting in the Sevier orogenic belt, Idaho, Wyoming and Utah. Geology 14:388–391

Johnson SA, Huntoon PW (1994) Permeability architecture and groundwater circulation along a fault-severed margin, northern Hanna Basin, Carbon County, Wyoming. Report for the University of Wyoming Water Resources Center, Laramie

Katz DA (2008) Early and late diagenetic processes of Mississippian carbonates, Northern U.S. Rockies. Dissertation, University of Miami

Kluth CF (1986) Plate tectonics of the ancestral Rocky Mountains. In: Peterson JA (ed) Paleotectonics and sedimentation of the Rocky Mountains, United States. American Association of Petroleum Geologists Memoir 41, pp 353–369

Lange RA, Carmichael ISE, Hall CM (2000) $^{40}Ar/^{39}Ar$ chronology of the Leucite Hills, Wyoming: eruption rates, erosion rates and an evolving temperature structure of the underlying mantle. Earth Planet Sci Lett 174:329–340

Linder-Lunsford JB, Kimball BA, Chafin DT, Bryant CG (1989) Hydrogeology of the aquifers of Paleozoic age, Upper Colorado River Basin, excluding the San Juan Basin, in Colorado, Utah, Wyoming and Arizona. U.S. Geological Survey Hydrologic Investigations Atlas HA-702, 2 sheets, scales 1:2,500,000 and 1:500,000

Love JD (1961) Definition of the Green River, Great Divide, and Washakie Basins, southwestern Wyoming. Am Assoc Petrol Geol Bull 45(10):1749–1755

Love JD, Christiansen AC (compilers) (1985) Geologic map of Wyoming. U.S. Geological Survey, scale 1: 500,000

Love JD, Christiansen AC, Ver Ploeg` AJ (compilers) (1993) Stratigraphic chart showing Phanerozoic nomenclature for the state of Wyoming. Wyoming State Geological Survey Map Series 41 (MS–41)

Mallory WW (1967) Pennsylvanian and associated rocks in Wyoming. U.S. Geological Professional Paper 554-G, pp G1–G31

Mallory WW (1975) Middle and southern Rocky Mountains, northern Colorado Plateau, and eastern Great Basin region. In: McKee ED, Crosby EJ (coordinators) Paleotectonic investigations of the Pennsylvanian System in the United States, Part I. Introduction and regional analysis of the Pennsylvanian system. U.S. Geological Survey Professional Paper 853-N, pp 265–278

Mankiewicz D, Steidtmann JR (1979) Depositional environments and diagenesis of the Tensleep Sanstone, eastern Big Horn Basin, Wyoming. Society of Economic Paleontologists and Mineralogists Special Publication No. 26, pp 319–336

Martin LJ (1996) Geohydrology of Tertiary rocks in the Green River structural basin in Wyoming, Utah and Colorado. U.S. Geological Survey Water-Resources Investigations Report 92–4164

Maughan EK (1963) Mississippian rocks in the Laramie Range, Wyoming, and adjacent areas. In: Geological Survey Research 1963. U.S. Geological Survey Professional Paper 475-C, pp C23–C27

Maughan EK (1967) Eastern Wyoming, eastern Montana and the Dakotas. In: McKee ED, Oriel SS (eds) Paleotectonic investigations of the Permian system in the United States: U.S. Geological Survey Professional Paper 515, pp 125–152

McGreevy LJ, Hodson WG, Rucker SJ, IV, (1969) Ground-water resources of the Wind River Indian Reservation, Wyoming: U.S. Geological Survey Water-Supply Paper 1576-I, pp 145

McKee ED, Oriel SS, Ketner KB, MacLachlan ME, Goldsmith JW, MacLachlan JC, Mudge MR (1959) Paleotectonic maps of the Triassic System. U.S. Geological Survey Miscellaneous Geologic Investigations Map I-300, 9 pl.

Mederos S, Tikoff B, Bankey V (2005) Geometry, timing, and continuity of the Rock Springs uplift, Wyoming, and Douglas Creek arch, Colorado: Implications for uplift mechanisms in the Rocky Mountain foreland, U.S.A. Rocky Mount Geol 40:167–191.

Moore B, Sigler S (1987) Analyses of natural gases 1917–85. U.S. Bureau of Mines Information Circular 9129

Opdyke ND, Runcorn SK (1960) Wind direction in the western United States in the late Paleozoic. Geol Soc Am Bull 71:959–971

Picard MD (1993) The early Mesozoic history in Wyoming. In: Snoke AW, Steidtmann JR, Roberts SM (eds) Geology of Wyoming. Geological Survey of Wyoming Memoir No. 5, pp 210–248

Reid SK, Dorobek SL (1993) Sequence stratigraphy and evolution of a progradational, foreland carbonate ramp, Lower Mississipian Mission Canyon Formation and stratigraphic equivalents, Montana and Idaho. In: Loucks RG, Sarg JF (eds) Recent developments and applications. American Association of Petroleum Geologists Memoir 57, pp 327–352

Roehler HW (1992) Description and correlation of Eocene rocks in stratigraphic reference sections for the Green River and Washakie basins, southwest Wyoming. U.S. Geological Survey Professional Paper 1506–D

Rowley PD, Hansen WR, Tweto O, Carara PE (1985) Geologic map of the Vernal quadrangle, Colorado, Utah and Wyoming: US Geological Survey Miscellaneous Investigations Series Map I-1526, scale 1:250,000

Royse F Jr (1993) An overview of the geologic structure of the thrust belt in Wyoming, northern Utah, and eastern Idaho. In: Snoke AW, Steidtmann JR, Roberts SM (eds) Geology of Wyoming. Geological Survey of Wyoming Memoir No. 5, pp 272–311

Sando WJ (1976) Madison Limestone (Devonian and Mississipian), east flank of the Bighorn Mountains, Wyoming. In: Laudon RB, Curry WH III, Runge JS (eds) Geology and energy resources of the Powder River [Basin]. Wyoming Geological Association 28th Annual Field Conference Guidebook, pp 45–52

Sando WJ, Gordon M Jr, Dutro JT Jr (1975) Stratigraphy and geologic history of the Amsden Formation (Mississippian and Pennsylvanian) of Wyoming. U.S. Geological Survey Professional Paper 848–A

Steidtmann JR (1993) The Cretaceous foreland basin and its sedimentary record. In: Snoke AW, Steidtmann JR, Roberts SM (eds) Geology of Wyoming. Geological Survey of Wyoming Memoir No. 5, pp 250–271

Taylor OJ, Freethey G, Glover KC (1986) Upper Colorado River Basin regional aquifer-system study. In: Sun RJ (ed) Regional aquifer system analysis [RASA] program of the U.S. Geological Survey, summary of projects, 1978–1984, Active Phase I, Regional aquifer system projects. U.S. Geological Survey Circular 1002, pp 223–233

Tonnsen JJ (1986) Influence of tectonic terranes adjacent to the Precambrian Wyoming Province on Phanerozoic stratigraphy in the Rocky Mountain region. In: Peterson JA (ed) Paleotectonics and sedimentation in the Rocky Mountain Region, United States. American Association of Petroleum Geologists Memoir 41, pp 41–53

Tweto O (compiler) (1976) Geologic map of the Craig 1° × 2° quadrangle, northwestern Colorado: U.S. Geological Survey Miscellaneous Investigations Series Map I-972, scale 1:250,000

Westphal H, Eberli GP, Smith LB, Grammer GM, Kislak J (2004) Reservoir characterization of the Mississippian Madison Formation, Wind River Basin, Wyoming. Am Assoc Petrol Geol Bull 88:405–432

WOGCC (2013) Wyoming Oil and Gas Conservation Commission, Casper. http://wogcc.state.wy.us/. Accessed continually 2009–2013 (Sect. 5.2) and Feb. 2013 (Sect. 5.3, 5.4)

# Chapter 6
# Detailed Geologic Characterization of Core and Well Data from the Weber and Madison Formations and Associated Seals at a Potential $CO_2$ Sequestration Site in Southwest Wyoming: Definining the Lithologic, Geochemical, Diagenetic, and Burial Histories Relative to Successful $CO_2$ Storage

**J. Fred McLaughlin and Mario Garcia-Gonzalez**

**Abstract** The Paleozoic strata of the Rocks Springs Uplift (RSU), southwestern Wyoming, have been identified as potential $CO_2$ storage reservoirs. The lithologic, diagenetic, geochemical, and burial histories of RSU strata were investigated to aid in the geologic characterization of the study site. Log data and core samples were collected from a 12,810 ft (3904 m) stratigraphic test well on the northeast flank of the RSU. The Weber and Madison Formations were found to have porous zones in distinct lithofacies: Weber eolianites have porosity and permeability values that average 6.3 % and 2.7 mD, and Madison dolostones have porosity and permeability values that average 13.1 % and 22.7 mD.

Dolomitization, cementation, pressure solution, dissolution, sulfate reduction, and other diagenetic reactions were largely responsible for the creation or destruction of porosity in these formations. Geologic characterization indicates that both formations are heterogeneous but contain suitable reservoir zones for injection and sequestration. Overall, the Madison Limestone has superior reservoir qualities.

Analysis of primary sealing lithologies at the study site suggests that the lower Triassic section, Amsden Formation, and upper part of the Madison Limestone can confine injected $CO_2$. Analyses of the sealing formations established that porosity is lower than 4.6 % and micropores are dominant, permeability is below 0.005 mD, and displacement pressures exceed 900 psi (6205 kPa).

Local and regional burial history reconstruction models were completed to augment the reservoir sequestration pressure management plan. A 1-D burial history reconstruction of the study site shows the sedimentary column reaching a maximum

J. Fred McLaughlin (✉)
Carbon Management Institute, Laramie, WY, USA
e-mail: derf1@uwyo.edu

M. Garcia-Gonzalez
Universidad Industrial de Santander, Bucaramanga, Colombia
e-mail: mgarciag@uis.edu.co

R. C. Surdam (ed.), *Geological $CO_2$ Storage Characterization,*
Springer Environmental Science and Engineering, DOI 10.1007/978-1-4614-5788-6_6,
© Springer Science+Business Media New York 2013

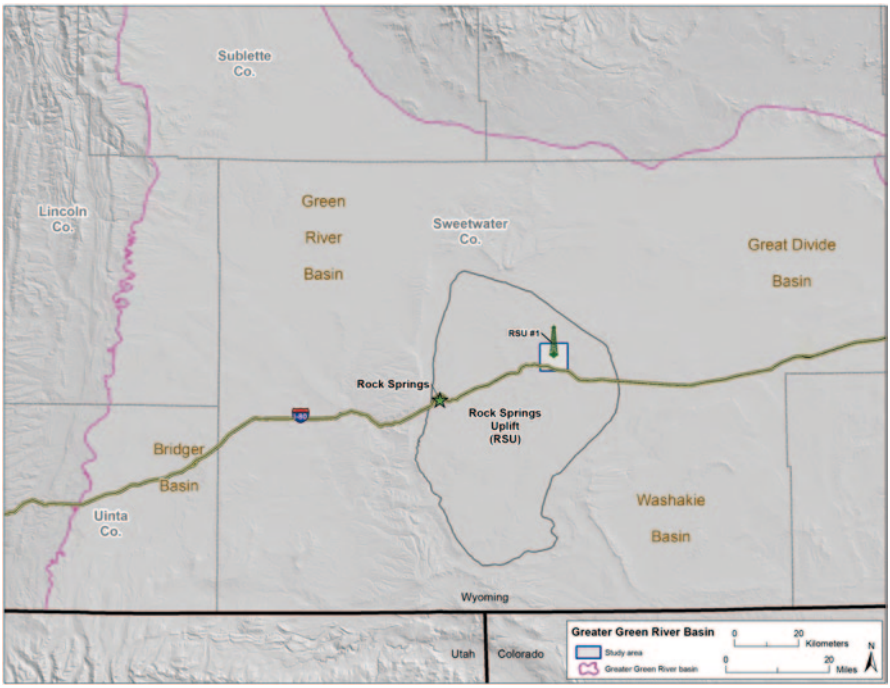


**Fig. 6.1** The Greater Green River Basin in southwest Wyoming and adjacent states, select subbasins, Rock Springs Uplift, study site, and RSU #1 well site

depth greater than 8400 m (27,600 ft), maximum temperatures greater than 150 °C (302 °F), and maximum pressures approaching 255 MPa (2.5 kbars). Regional 2-D burial and geochemical history models show that several source rocks have re-entered the hydrocarbon window.

Robust geologic characterization of reservoirs and seals from the study site and interpretation of their diagenetic, geochemical, and burial histories suggest that the Rock Springs Uplift has geologic conditions suitable for the injection and storage of $CO_2$.

## 6.1 Introduction

Preliminary geologic studies identified the Rock Springs Uplift (RSU) in Wyoming's Greater Green River Basin (GGRB) as a promising structure for long-term $CO_2$ storage (Surdam and Jiao 2007) (Fig. 6.1). In addition to its large size, the RSU contains a thick sedimentary section of potential reservoirs and seals; the geologic structure and lithology meet the screening criteria for sequestration of $CO_2$ in

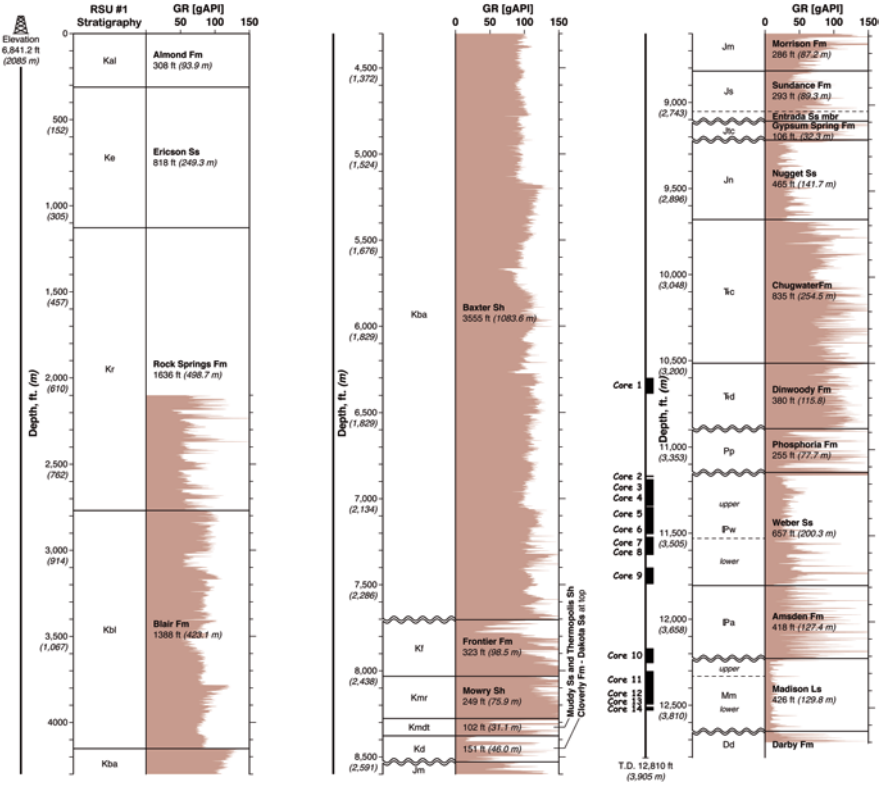


**Fig. 6.2** Stratigraphic column for the RSU #1 well site relative to the gamma log and cored intervals

sedimentary units compiled by Bachu (2002, 2008) and Bachu and Stewart (2002) (Fig. 6.2).

Though preliminary assessments suggested that this structure is suitable for $CO_2$ storage, a geologic characterization of potential seal and reservoir rocks was necessary for a comprehensive evaluation. To complete this task, a 12,810-ft (3904-m) stratigraphic test well (RSU #1) was drilled on the northeast flank of the RSU for the purpose of obtaining core samples and petrophysical data. Approximately 914 ft (278 m) of core was recovered from potential Paleozoic reservoirs (Weber Sandstone and Madison Limestone) and associated Mesozoic and Paleozoic seals (Table 6.1 and Fig. 6.2). The core was characterized for its lithology, mineralogy, reservoir properties, sealing potential, geochemistry, and petrography. In addition, the core and petrophysical data were used to interpret the depositional, burial, geochemical, and diagenetic histories of the targeted formations. These data were used to define geologic heterogeneity of strata at the study site, and populate numerical and geochemical simulations to create robust and accurate injection models.

**Table 6.1** Core inventory and depths, RSU #1 well

| Core No. | Formation | Depth, ft (m) | Depth, ft (m) | Core length, ft (m) |
|---|---|---|---|---|
| #1 | lower Triassic section | 10,600 (3231) | 10,689 (3258) | 89.0 (27) |
| Total | lower Triassic section | | | 89.0 (27) |
| #2 | Weber | 11,169 (3404) | 11,169.5 (3404.2) | 0.5 (0.2) |
| #3 | Weber | 11,185 (3409) | 11,276 (3437) | 91.0 (28) |
| #4 | Weber | 11,276 (3437) | 11,344.2 (3458) | 69.2 (21) |
| #5 | Weber | 11,348 (3459) | 11,471 (3496) | 123.0 (37) |
| #6 | Weber | 11,471 (3496) | 11,507.5 (3507) | 36.5 (11) |
| #7 | Weber | 11,520 (3511) | 11,597 (3511) | 77 (24) |
| #8 | Weber | 11,597 (3535) | 11,625 (3543) | 28.0 (8.5) |
| #9 | Weber | 11,701 (3566) | 11,792 (3594) | 91.0 (28) |
| Total | Weber | | | 519.5 (158) |
| #10 | Amsden/Madison | 12,169 (3709) | 12,257.2 (3736) | 88.2 (27) |
| Total | Amsden | | | 56.0 (17) |
| #11 | Madison | 12,301 (3749) | 12,393 (3777) | 92.0 (28) |
| #12 | Madison | 12,393 (3777) | 12,477.7 (3803) | 84.7 (26) |
| #13 | Madison | 12,477.7 (3803) | 12,494 (3808) | 17.0 (5) |
| #14 | Madison | 12,511 (3813) | 12,530.5 (3819) | 19.5 (6) |
| #15 | Madison | 12,532 (3820) | 12,536 (3821) | 4.0 (1.2) |
| Total | Madison | | | 249.5 (76) |
| Total | core | | | 914.0 (278.5) |

## 6.2 Methods

CMI recovered 916 ft (278 m) of core from the lower Triassic section, Weber, Amsden, and Madison formations (Table 6.1 and Fig. 6.2). Core samples were described macroscopically using visual inspection, a Zeiss V8 stereoscope, and high-resolution photographs provided by Petro Arc International. Sedimentological and textural features described from macroscopic analysis include lithofacies, stratification, lamination, bioturbation, fractures, cross-bedding, ripples, grain characteristics, cementation, matrix characteristics, and mineral composition. Porosity and oil stains were also recorded.

Select end trims and plugs were sent to Wagner Petrographic, Lindon, Utah, for thin section preparation. Most of the thin sections were stained for calcite and ferroan carbonates and impregnated with epoxy for porosity evaluation. Petrographic analysis of the thin sections was done on a Carl Zeiss Stereo Discovery V8 microscope with an AxioCam MRc camera attachment and Axiovision 4.8.2 imaging software. Thin sections were analyzed to characterize microfacies, grain relations and mineralogy, deformation characteristics, porosity, primary and authigenic minerals, and diagenetic alteration.

Facies were defined using the classifications of Folk (1959), Embry and Klovan (1971), and James (1984). The depositional environment of lithologic sequences was interpreted using the facies associations indicated by Reading (1984).

Stable isotopes were analyzed from whole-rock powders at the University of Wyoming's Stable Isotope Facility on a ThermoFinnigan Delta Plus GasBench.

Porosity, permeability, and displacement pressure were measured on core plugs at Intertek Laboratories, Houston, Texas. Wellbore and petrophysical data was collected by Baker Hughes, Houston. Coring was performed by True Oil Company, Casper, Wyoming.

Methodology and model parameters for the 1-D and 2-D burial history models, geochemical models, and vitrinite reflectance are detailed in Sect. 6.6. CMI would like to thank Schlumberger for the academic use of their Petromod® software at the Universidad Industrial de Santander, which was crucial for the creation of these models.

## 6.3 Lithology, Diagenesis, and Petrography of the Weber Sandstone

### *6.3.1 General Lithology*

At the RSU #1 well site, the Weber Sandstone lies between 11,150 ft and 11,807 ft (3399 m and 3599 m) below the land surface. Approximately 520 ft (159 m) of core was recovered from the Weber Sandstone (Table 6.1 and Fig. 6.2). The Weber comprises an upper, eolian unit and a basal, marine unit. Macroscopic analysis of the core, along with observations from petrophysical data identified five macroscopic lithofacies within these units (Fig. 6.3).

**Eolian Sandstone Facies** Laminated, cross-bedded quartz sandstone with inclination angles of 5–24°. Grain size varies from lower-fine to upper-fine (150–250 μm); dominantly quartz (95%) with minor feldspars, clay, cements, and heavy accessory minerals. Most grains are subangular. This facies is concentrated in the upper unit of the Weber Sandstone.

**Bioturbated Sandstone Facies** Extensive bioturbation resulted in disrupted laminations and cross-bedding planes; ripple marks are also common. Cross-bedding is still present in some intervals. The grain size is generally lower-fine (125–177 μm). The mineral composition is typically quartz (>90%), cement (5%), feldspar (<5%), clay matrix (<2%), and trace heavy accessory minerals. Pyrite nodules are commonly associated with organic matter, and are likely byproducts of sulfate reduction. This facies is found throughout the formation. Figure 6.3 illustrates the relation of well-log and macroscopic characteristics of this facies and differences from the eolian sandstone facies. Both facies are dominant in the upper unit of the Weber, and show distinct differences in density, porosity, and conductivity. The eolian sandstone facies has lower density values, and higher porosity and conductivity values than the bioturbated sandstone facies.

**Clastic Carbonate Facies** Fine-grained clastic carbonate composed of limestone or dolostone, fossil fragments, and detrital clastic grains in a micritic matrix. This facies occurs in both units.

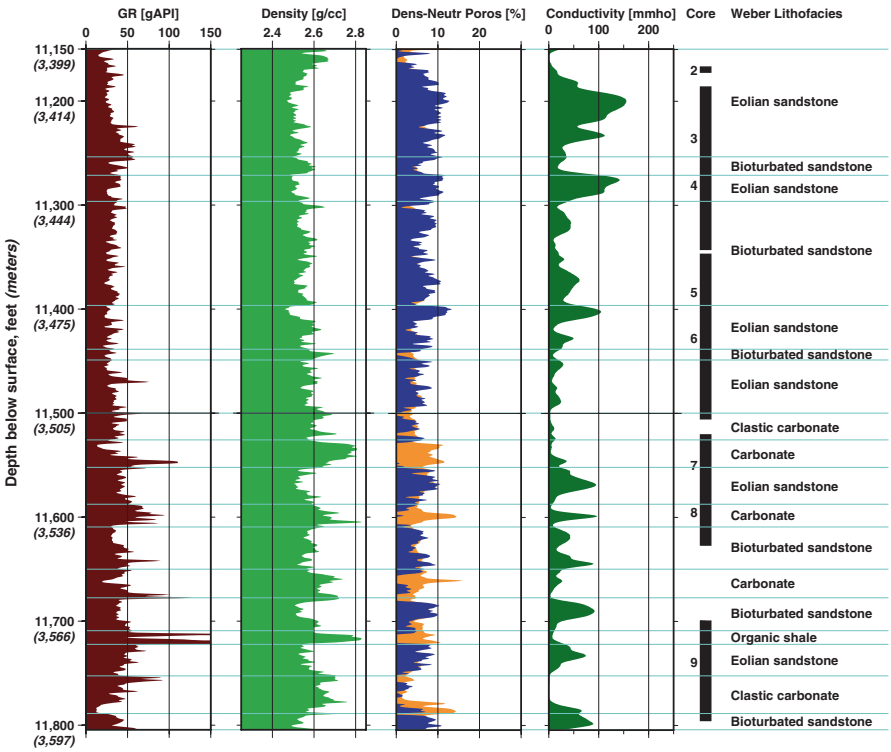


**Fig. 6.3** Lithofacies interpretation of the Weber Sandstone from macroscopic core analysis and petrophysical data showing relation of lithofacies to petrophysical data. Cored intervals are also included

**Carbonate Facies** Limestone and dolostone beds in the basal unit of the Weber which contain multiple sub-facies including sucrosic and burial dolostones, biomicrites, micrites, and laminated carbonates.

**Organic Shale Facies** Greenish-gray to black, laminated claystone with organic and detrital clasts and abundant pyrite framboids. This unit is found only in the basal unit of the Weber Sandstone.

The variable lithology of the Weber Sandstone is related to a dynamic depositional environment. The basal unit of the Weber was deposited in subaqueous and supratidal marine environments, as well as near-shore sabkhas, resulting in interbedded limestone, dolostone, organic shale, clastic carbonate, evaporite, and cross-bedded, eolianite sand (Mankiewicz and Steidtmann 1979; Fryberger et al. 1983; Edman and Surdam 1984; Moore 1984; Bowker and Jackson 1989; Krystinik 1990a, b; Robinson 1992; Cole and Mullen 1992). At the study site, the basal unit of the Weber is between 11,530 ft and 11,807 ft (3514 m and 3599 m) below the land surface. The basal unit is separated from the upper unit by a dolostone bed that is the topmost marine carbonate of substantial thickness in the formation

(though it is worth mentioning that the clastic carbonate sandstone facies, which sits atop the dolostone, has mixed marine and eolian depositional attributes) (Fig. 6.3). Multiple low-porosity carbonate and argillaceous beds, and nearly complete cementation within clastic beds, diminish its overall $CO_2$ storage capacity. The basal unit contains several thin, stacked, impermeable shale layers and has generally low measured permeability (< 0.09 mD average; 30 samples), though several thin, semi-permeable layers were identified (> 0.3 mD) (Table 6.3).

At the study site, the upper unit of the Weber Sandstone is between 11,150 ft and 11,530 ft (3399 m and 3514 m) below the land surface (Fig. 6.2). The upper unit was mostly deposited in a massive, prograding eolian dune field that stretched across portions of Wyoming, Utah, Colorado, and Montana (Mankiewicz and Steidtmann 1979; Moore 1984; Bowker and Jackson 1989; Krystinik 1990a, b; Robinson 1992; Cole and Mullen 1992). It is dominantly composed of clastic material, and has higher overall porosity and permeability than the basal marine unit, making it a better target for $CO_2$ storage (Table 6.2). The enhanced reservoir characteristics of the upper eolian unit are related to its deposition, source, lithology, burial, and diagenetic history.

Eolian deposition resulted in bimodal grain sorting; layers of larger, detrital grains are interlayered with smaller grains and fine material (Fig. 6.4a). Grain sorting was repeated as dunes built and migrated, resulting in pin-stripe laminae and the characteristic cross-beds of the Weber Sandstone (Fryberger and Schenk 1988; Mankiewicz and Steidtmann 1979; Fryberger et al. 1983) (Fig. 6.4a). Along with the bimodal grain-size distribution and cross-bedded laminae, multiple pre-burial depositional features are preserved within the upper unit of the Weber, including scoured surfaces, interdunal deposits, and bioturbated zones.

### *6.3.2 Detrital Clasts*

Analyses of the clastic detrital material indicate that the Weber Sandstone at the study site is a quartz arenite, sometimes felspathic, containing various concentrations of accessory minerals (Dott 1964). The composition of the primary clasts, notably the high percentage of quartz with sparse reactive minerals, suggests that the source sediment was mature (Boggs 2000). Quartz grains are commonly undulatory; some grains contain exsolved rutile needles and record evidence of grain boundary migration and deformation lamellae; many contain pre-depositional fluid inclusions (Fig. 6.4b,c). Most of the high-pressure deformation features are relicts from the source provenances, some of which are metamorphic (Boggs 2000; Passchier and Trouw 2005). However, post-depositional burial-related deformation textures are prevalent, especially pressure solution and sutured grains, compaction-related brittle deformation, and grains enclosed by secondary overgrowths (commonly polygonal with 120° triple points) with the same optical orientation as the detrital grain (Fig. 6.4c). On the basis of these diagenetic textures, portions of the Weber at the study site could be classified as an orthoquartzite (Krynine 1948).

**Table 6.2** Measured permeability and porosity of Weber core samples

| Sample Depth | | Permeability | | | | Porosity | | Density |
|---|---|---|---|---|---|---|---|---|
| | | 800 psi NCS | | Reservoir NCS | | 800 NCS | Res. NCS | |
| | | to Air | Klinken-berg | to Air | Klinken-berg | Porosity | Porosity | |
| (ft) | (m) | (mD) | | (mD) | | (percent) | | (g/cm$^3$) |
| 11,194.1 | 3412.0 | 0.616 | 0.514 | 0.504 | 0.415 | 6.238 | 6.067 | 2.65 |
| 11,197.7 | 3413.1 | 5.569 | 5.061 | 5.082 | 4.601 | 8.455 | 7.880 | 2.61 |
| 11,200.1 | 3413.8 | 6.940 | 6.360 | 6.280 | 5.730 | 7.649 | 6.814 | 2.64 |
| 11,209.9 | 3416.8 | 15.800 | 14.900 | 13.800 | 12.900 | 8.140 | 8.184 | 2.64 |
| 11,221.0 | 3420.2 | 1.115 | 0.938 | 0.966 | 0.837 | 7.407 | 6.774 | 2.60 |
| 11,227.1 | 3422.0 | 1.310 | 1.150 | 1.120 | 0.969 | 7.648 | 7.413 | 2.63 |
| 11,240.0 | 3426.0 | 4.362 | 3.924 | 3.951 | 3.538 | 8.701 | 7.852 | 2.60 |
| 11,251.2 | 3429.4 | 0.108 | 0.077 | 0.079 | 0.053 | 5.827 | 5.189 | 2.61 |
| 11,262.0 | 3432.7 | 1.056 | 0.883 | 0.933 | 0.777 | 8.046 | 7.322 | 2.60 |
| 11,268.0 | 3434.5 | 1.067 | 0.930 | 0.925 | 0.802 | 6.314 | 5.708 | 2.61 |
| 11,276.6 | 3437.1 | 5.370 | 4.874 | 4.986 | 4.512 | 9.330 | 8.683 | 2.59 |
| 11,280.3 | 3438.2 | 5.368 | 4.872 | 5.080 | 4.600 | 8.030 | 7.381 | 2.61 |
| 11,285.0 | 3439.7 | 6.370 | 5.821 | 5.775 | 5.257 | 7.534 | 7.187 | 2.62 |
| 11,286.6 | 3440.1 | 2.235 | 1.943 | 2.053 | 1.777 | 6.821 | 6.097 | 2.60 |
| 11,295.0 | 3442.7 | 3.175 | 2.813 | 2.941 | 2.596 | 7.489 | 6.938 | 2.61 |
| 11,305.5 | 3445.9 | 0.063 | 0.040 | 0.036 | 0.021 | 5.065 | 4.874 | 2.64 |
| 11,319.5 | 3450.2 | 0.431 | 0.348 | 0.280 | 0.350 | 6.244 | 5.443 | 2.61 |
| 11,325.1 | 3451.9 | 1.259 | 1.108 | 1.089 | 0.951 | 6.930 | 6.335 | 2.61 |
| 11,333.5 | 3454.5 | 0.076 | 0.049 | 0.038 | 0.022 | 5.423 | 4.003 | 2.60 |
| 11,350.0 | 3459.5 | 0.036 | 0.020 | 0.017 | 0.008 | 4.053 | 3.051 | 2.62 |
| 11,361.0 | 3462.8 | 2.327 | 2.024 | 2.175 | 1.886 | 7.183 | 6.800 | 2.61 |
| 11,374.0 | 3466.8 | 5.249 | 4.754 | 4.940 | 4.463 | 7.389 | 7.144 | 2.62 |
| 11,380.7 | 3468.8 | 8.255 | 7.610 | 7.720 | 7.100 | 9.073 | 8.473 | 2.60 |
| 11,400.0 | 3474.7 | 0.462 | 0.568 | 0.405 | 0.502 | 6.494 | 5.820 | 2.63 |
| 11,405.3 | 3476.3 | 0.006 | 0.002 | 0.001 | 0.000 | 2.334 | 1.679 | 2.64 |
| 11,410.0 | 3477.8 | 9.763 | 9.055 | 9.190 | 8.802 | 9.183 | 8.844 | 2.61 |
| 11,420.0 | 3480.8 | 0.074 | 0.048 | 0.051 | 0.032 | 4.725 | 4.128 | 2.61 |
| 11,425.4 | 3482.5 | 0.026 | 0.044 | 0.012 | 0.022 | 4.695 | 3.613 | 2.62 |
| 11,434.9 | 3485.4 | 0.454 | 0.545 | 0.344 | 0.421 | 7.381 | 5.966 | 2.60 |
| 11,437.2 | 3486.0 | 1.458 | 1.635 | 1.159 | 1.313 | 6.885 | 6.178 | 2.62 |
| 11,445.2 | 3488.5 | 0.377 | 0.458 | 0.300 | 0.370 | 6.018 | 4.873 | 2.60 |
| 11,464.5 | 3494.4 | 0.070 | 0.102 | 0.033 | 0.052 | 2.987 | 2.204 | 2.71 |
| 11,473.6 | 3497.1 | 0.150 | 0.202 | 0.083 | 0.118 | 5.849 | 5.412 | 2.64 |
| 11,481.2 | 3499.5 | 0.014 | 0.006 | 0.001 | 0.000 | 3.524 | 2.396 | 2.65 |
| 11,485.4 | 3500.7 | 0.386 | 0.474 | 0.280 | 0.351 | 6.702 | 6.018 | 2.61 |
| 11,495.0 | 3503.7 | 0.091 | 0.131 | 0.036 | 0.057 | 5.743 | 5.122 | 2.63 |
| 11,500.0 | 3505.2 | 0.328 | 0.266 | 0.206 | 0.266 | 7.042 | 6.222 | 2.63 |
| 11,508.0 | 3507.6 | 0.025 | 0.010 | 0.001 | 0.000 | 2.744 | 2.039 | 2.67 |
| 11,510.0 | 3508.2 | 0.001 | 0.003 | 0.001 | 0.003 | 2.147 | 0.468 | 2.62 |
| 11,521.0 | 3511.6 | 0.059 | 0.093 | 0.022 | 0.040 | 5.069 | 4.452 | 2.64 |
| 11,526.7 | 3513.3 | 0.026 | 0.014 | 0.005 | 0.002 | 2.026 | 1.578 | 2.74 |
| 11,537.0 | 3516.5 | 1.258 | 1.056 | 0.502 | 0.406 | 8.737 | 7.789 | 2.81 |
| 11,549.9 | 3520.4 | 0.116 | 0.080 | 0.042 | 0.025 | 4.671 | 3.888 | 2.77 |

**Table 6.2** (continued)

| Sample Depth | | Permeability | | | | Porosity | | Density |
|---|---|---|---|---|---|---|---|---|
| | | 800 psi NCS | | Reservoir NCS | | 800 NCS | Res. NCS | |
| | | to Air | Klinken-berg | to Air | Klinken-berg | Porosity | Porosity | |
| (ft) | (m) | (mD) | | (mD) | | (percent) | | (g/cm$^3$) |
| 11,560.0 | 3523.5 | 0.042 | 0.024 | 0.011 | 0.005 | 5.345 | 4.708 | 2.63 |
| 11,569.9 | 3526.5 | 0.532 | 0.436 | 0.393 | 0.316 | 8.094 | 7.397 | 2.64 |
| 11,580.0 | 3529.6 | 0.380 | 0.302 | 0.251 | 0.195 | 8.125 | 7.123 | 2.62 |
| 11,588.5 | 3532.2 | 0.083 | 0.050 | 0.014 | 0.007 | 5.169 | 4.361 | 2.63 |
| 11,602.3 | 3536.4 | 0.069 | 0.043 | 0.011 | 0.005 | 2.815 | 2.035 | 2.79 |
| 11,610.5 | 3538.9 | 0.067 | 0.043 | 0.013 | 0.006 | 1.930 | 1.158 | 2.79 |
| 11,622.8 | 3542.6 | 0.087 | 0.056 | 0.020 | 0.020 | 5.557 | 4.821 | 2.63 |
| 11,705.0 | 3567.7 | 0.031 | 0.017 | 0.013 | 0.006 | 4.253 | 3.614 | 2.63 |
| 11,715.1 | 3570.8 | 0.040 | 0.022 | 0.012 | 0.005 | 6.359 | 4.923 | 2.65 |
| 11,725.0 | 3573.8 | 0.007 | 0.002 | 0.002 | 0.001 | 1.198 | 0.402 | 2.72 |
| 11,745.0 | 3579.9 | 0.058 | 0.033 | 0.009 | 0.004 | 4.878 | 4.011 | 2.65 |
| 11,764.2 | 3585.7 | 0.009 | 0.004 | 0.002 | 0.001 | 0.798 | 0.075 | 2.69 |
| 11,766.8 | 3586.5 | 0.016 | 0.006 | 0.004 | 0.001 | 1.289 | 0.689 | 2.65 |
| 11,775.0 | 3589.0 | 0.004 | 0.001 | 0.003 | 0.001 | 1.375 | 0.278 | 2.66 |
| 11,785.0 | 3592.1 | 0.019 | 0.009 | 0.005 | 0.002 | 3.887 | 3.574 | 2.76 |
| 11,786.0 | 3592.4 | 0.062 | 0.039 | 0.012 | 0.006 | 5.107 | 4.222 | 2.78 |
| 11,790.0 | 3593.6 | 0.738 | 0.618 | 0.371 | 0.296 | 10.823 | 9.790 | 2.73 |

**Table 6.3** Isotopic analyses of Weber carbonates

| Stable Isotopic Values for carbonates in the Weber Sandstone | | |
|---|---|---|
| Depth | Carbon | Oxygen |
| 11,169.2 | −3.5 | −11.6 |
| 11,209.1 | −1.9 | 3.6 |
| 11,570.0 | −1.4 | 2.7 |
| 11,620.0 | 0.0 | −2.5 |
| 11,720.0 | −1.7 | 3.8 |
| 11,726.4 | −3.2 | −7.0 |
| 11,763.3 | −2.3 | −4.6 |
| 11,788.1 | −0.7 | −2.8 |

Detrital quartz grains are commonly sorted by size, typical of eolian quartz arenites, which can affect porosity, permeability, and diagenetic responses within the unit (Fryberger et al. 1983; Krystinik 1990a, b).

At the study site, feldspar grains include both plagioclase and alkali feldspars, and vary in size and shape. The feldspars are frequent, though concentrations vary. They are typically subrounded to rounded, and plagioclase commonly retains a distinct lath-shape (Fig. 6.4d). Most feldspar grains have been diagenetically altered or degraded to some degree and exhibit rims, pits, dissolution pores, and authigenic minerals (Fig. 6.4e). In some grains, porosity has increased as a result of intragranular dissolution (Fig. 6.4e). Feldspar grains commonly have deformation twins and bent lamellae, evidence of a high-pressure provenance (Fig. 6.4d). Besides detrital

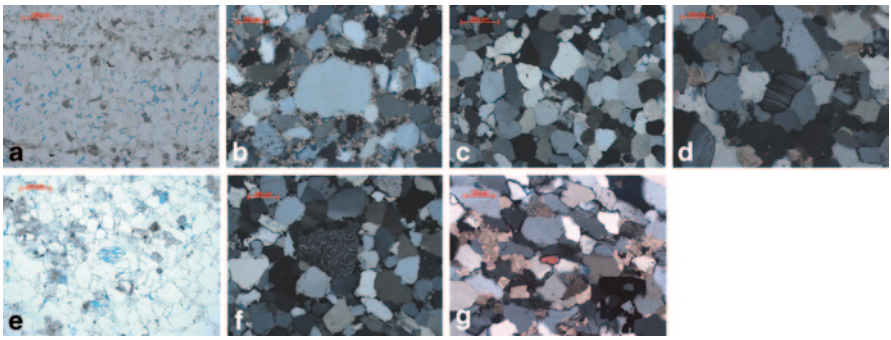


**Fig. 6.4** (**a**) 11,227 ft (3422 m) characteristic Weber Sandstone eolianite displaying grain bimodality, dolomitized pinstripes, porosity (blue epoxy), and pressure solution and overgrowths. Note the scarcity of cement and reactive grains, such as feldspars. (**b**) 11,209.9 ft (3417 m) rutilated quartz grain indicative of a granulite-grade source provenance surrounding by micro-dolomite crystals. Rutilated grain and adjacent quartz grains contain abundant fluid inclusions. Porosity is largely destroyed by pressure solution. (**c**) 11,194.1 ft (3412 m) Polyphase quartz grain in the center of the slide. This slide highlights alteration of quartz grains by pressure solution, polygonal quartz overgrowth, 120° (or approximate) triple junction grain boundaries, the original grain boundaries and dust rims, undulosity, and fluid inclusions. (**d**) 11,305.5 ft (3446 m) Bent and deformed twins in a lath-shaped plagioclase grain. This slide contains an orthoclase grain with trace amounts of dissolution in the bottom left corner. This slide includes dolomite crystals and clusters. Note the lack of pressure solution in the feldspar grains relative to quartz grains. (**e**) 11,305.5 ft (3446 m) Dissolution along the twin planes of a plagioclase crystal (center) resulting in enhanced intragranular porosity. (**f**) 11,169.2 ft (3404 m) Lithic chert fragment in Weber sandstone. (**g**) 11,420 ft (3481 m) Detrital zircon crystal surrounding by quartz grains, dolomite clusters, and a pyrite grain (bottom right corner, enveloping quartz grains and likely replacing anhydrite; pyrite crystallized prior to pressure solution)

quartz and feldspar, these rocks include lithic chert fragments, rare biotite flakes, and heavy accessory minerals including zircon, apatite, sphene (titanite), ilmenite, pyrite, and tourmaline (Fig. 6.4f, g). In addition to primary detrital clasts, the Weber contains an abundance of authigenic minerals.

### *6.3.3 Authigenic minerals*

Authigenic minerals are present throughout eolianites of the Weber, primarily as cement between clastic grains. Common cements include calcite, dolomite, anhydrite, and quartz. Diagenetic calcite and dolomite are found in both the eolian and marine units of the Weber. Most calcite within the formation is found as cement, which is characteristic of quartz arenites (Boggs 2000). The calcite cement is poikilotopic, can be twinned, and is typically found in areas with larger detrital clasts (Fig. 6.5a). The volume of the calcite cement between grains varies from absent to total fill, and affects the overall porosity (Fig. 6.5b). In Weber carbonates, calcite cement is associated with anhydrite, chert, and burial dolomites. Calcite cement can preserve

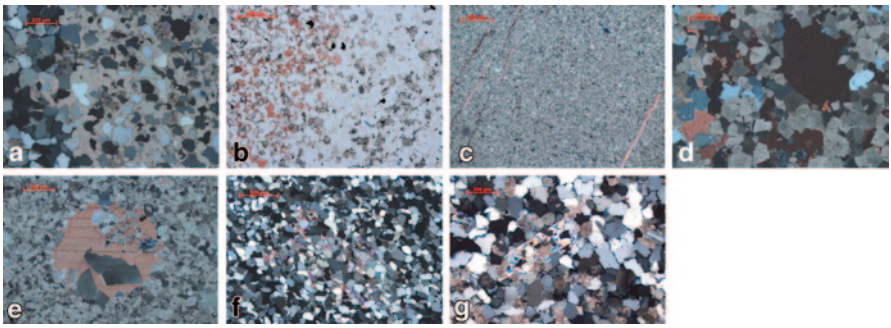


**Fig. 6.5** (**a**) 11,417.2 ft (3480 m) Poikilotopic calcite cement enveloping dolomite and detrital grains. Grains within the cement maintain spacing and lack evidence of pressure solution (as compared with grains in the western corner of the slide). (**b**) 11,400 ft (3475 m) Calcite cement, stained red, maintaining grain spacing in Weber eolianite. Porosity outside of cemented regions has largely collapsed due to pressure solution and overgrowths. Dolomite, pyrite and anhydrite are present. (**c**) 11,725 ft (3574 m) Sucrosic dolostone cut by subvertical calcite veins. (**d**) 11,549.9 ft (3520 m) Clastic dolostone in the Weber featuring undulosic burial dolomites, euhedral quartz, chert, and poikilotopic, twinned, vug-filling calcite. (**e**) 11,543 ft (3518 m) Carbonate-filled vug in Weber dolostone. Vug includes twinned calcite, undulosic saddle dolomites, and chert. (**f**) 11,240 ft (3426 m) Poikilotopic anhydrite being replaced by calcite in Weber eolianite. (**g**) 11,417.2 ft (3480 m) Anhydrite lath in the Weber sandstone. This crystal precipitated prior to most secondary quartz precipitation

primary pore spaces between clasts (Fig. 6.5b). In addition to poikilotopic calcite cement, blocky, twinned calcite crystals fill veins and fractures (Fig. 6.5c).

There were several episodes of dolomitization in the Weber. The basal, marine unit has beds of both limestone and dolomite, suggesting that dolomitization was selective relative to alternating sea level and hypersaline waters or to variable freshwater influx throughout deposition. Dolostone beds are commonly sucrosic, with subhedral to euhedral crystals (Fig. 6.5c). There are also dolostone beds with massive, euhedral, undulose dolomite crystals (Fig. 6.5d). Non-bedded dolomite crystals are common in clastic beds. Dolomite crystals in the eolian sections are concentrated in thin bands, or clusters, within the finest-grained laminae (Fig. 6.4a). In hand sample and thin section they are readily identifiable, as they form darker bands that define cross-beds (though these dark bands can also be pyritic). These dolomites are fine-grained, subhedral to euhedral crystals that contain abundant inclusions and commonly form radiating clusters (Fig. 6.4a, g). Dolomitizes within argillaceous sands, typically deeper in the formation, display different petrographic characteristics: these dolomite crystals are commonly randomly dispersed, as opposed to concentrated within fine-grained laminae (Fig. 6.4b). Some of the crystals have numerous inclusions, similar to eolian dolomite, but there are also clean crystals that tend to have a greater degree of luminescence. They also precipitate in clusters of subhedral to euhedral crystals, or as individual crystals that are euhedral and less cloudy. Large, undulose saddle dolomites commonly fill pore space in Weber carbonates (Fig. 6.5e).

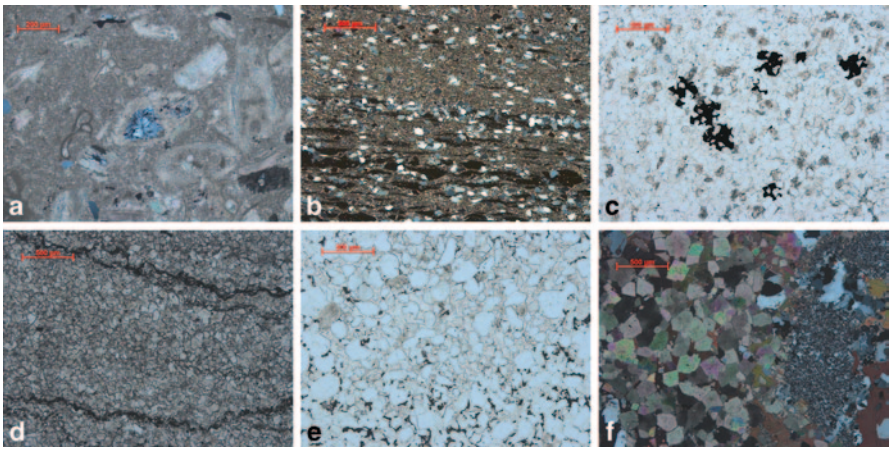


**Fig. 6.6** (**a**) 11,763.3 ft (3585 m) Chert and pyrite filling molds in a Weber limestone bed. (**b**) 11,720 ft (3572 m) Deformed chert (dark blebs) in shale at the base of the Weber along with clastic, detrital grains and authigenic pyrite. (**c**) 11,319.5 (3450 m) Pyrite replacing anhydrite laths in Weber eolianite. (**d**) 11,766.8 (3586 m) Sub horizontal stylolites in a Weber dolostone bed. (**e**) 11,169.2 ft (3404 m) Residual, solidified hydrocarbons coating detrital grains. Twinned, poikilotopic calcite cement in the center of the slide preserves pore space (note less hydrocarbon in residual cement zone). (**f**) 11,602 ft (3536 m) Euhedral burial dolomites, chert, sutured quartz grains, and poikilotopic calcite cement

High concentrations of sulfate minerals such as gypsum and anhydrite are typically associated with coastal dunes and sabkhas (Fryberger and Schenk 1988). In the Weber, anhydrite is prevalent as bladed (lath) crystals, poikilotopic and blocky cements, and late-stage hydrothermal anhydrite. Anhydrite cement is commonly concentrated in zones with larger clasts, similarly to calcite cement (Fig. 6.5f). Anhydrite cement is more common than laths and is found in both the eolian and marine sediments. Anhydrite crystals within blocky cement are typically euhedral. Anhydrite cement in the eolianites is frequently altered to calcite (Fig. 6.5f). In the marine sediments, anhydrite cement is found replacing carbonates. Anhydrite laths are typically found in porous zones within clastic units, commonly as single crystals (Fig. 6.5g).

Silica cement—chert, megaquartz, and quartz overgrowths—crystallized throughout the burial history of the Weber. Chert and megaquartz commonly fill molds in limestone and dolostone of the basal unit (Fig. 6.6a). Bands of silica cement, mostly chert, are found in the shale in the basal unit (Fig. 6.6b). They can be texturally deformed, indicating deformational flow (Fig. 6b). Some secondary chert is associated with carbonate and anhydrite cement (Fig. 6.5d). Overgrowths on quartz grains within the Weber are ubiquitous (Fig. 6.4a, c, d, f, 6.5a, b). Quartz overgrowths share the optical orientation of the grains they envelope. Original grain shapes are easily identified by pronounced dust rims (Fig. 6.4c). Overgrowths are commonly polygonal, with straight-edge grain boundaries and interfacial angles

that range from acute to 120° (Fig. 6.4c). Quartz overgrowths negatively impact porosity in the eolianites. In sediment where cements have dissolved, subsequent silica cementation and overgrowths commonly destroy all porosity (Fig. 5a, b).

Authigenic pyrite is common throughout the Weber and found in several forms: euhedral pyrites that are either random or grouped in horizontal bands, pyritic nodules composed of numerous euhedral grains, replacive pyrites, and massive bladed pyrite (Fig. 6.4g, 6.5b, 6.6b, c). Petrographic analyses suggest that there were multiple generations of pyrite associated with different types of diagenetic alteration.

### *6.3.4 Diagenetic History*

Dolomitization in the Weber likely began before the formation was completely buried. Near-shore basal limestones were subject to fluctuating and chemically diverse waters, resulting in the dolomitization of carbonate muds (Fig. 6.4a). Stable isotope analysis showed enrichment in oxygen composition, up to 3.8‰ $\delta^{18}O$, which indicates the dolomite crystallized at low temperatures in evaporitic, hypersaline waters (Land 1980; Scholle and Scholle 2003) (Table 6.3). During and directly after eolianite deposition, these hypersaline waters infiltrated the formation, initiating feldspar degradation, evaporite deposition, and dolomitization of finer-grained material. Most Weber dolomites are typical of a near-surface or wet sand or sabkha environment; the carbonate muds, clays, silts, and organic matter that define laminae acted as nucleation sites for dolomite crystallization as fluids repeatedly inundated the sands. This interpretation of the Weber depositional environment has been noted by previous workers (Mankiewicz and Steidtmann 1979; Fryberger et al. 1983; Edman and Surdam 1984; Krystinik 1990a, b). Early diagenetic alteration of fine-grain material to dolomite has affected reservoir properties of the Weber Sandstone at the study site: vertical permeability is low relative to horizontal permeability, as dolomitization along the fine-grained, second-order surfaces impedes vertical fluid flow (Fryberger and Schenk 1988). Generally, the earliest diagenetic alterations resulted in an overall loss of porosity.

As the formation was buried, carbonate solubility in the pore water decreased, resulting in precipitation of poikilotopic carbonate cements (Krystinik 1990b) (Fig. 6.5a, b). It is possible that early-burial bacterial sulfate reduction, evidenced by framboidal pyrites, increased carbonate alkalinity and the precipitation rate of calcite cement (Machel 1998). Feldspars continued to decompose and dissolve, forming authigenic clays and intragranular porosity (Fig. 6.4e). As the burial temperatures increased, gypsum cements dehydrated, forming anhydrite (Murray 1964). Early-burial diagenetic alteration of the Weber resulted in widespread geochemical alteration of the pore fluids and decreased net porosity.

Increasing burial pressure resulted in the compaction and brittle deformation of quartz grains, particularly in areas lacking cement or at contact points between grains. As the pressure and temperature continued increasing, brittle deformation

ceased and was replaced by widespread pressure solution of quartz grains (Fig. 6.4g, 6.5b, 6.6b, c). Quartz grains were sutured and dissolved at contact points or where cements were absent (Fig. 6.4g, 6.5b, 6.6b, c). Dissolved silica recrystallized as euhedral quartz overgrowths in areas of low differential stress, such as cement-free pores (Passchier and Trouw 2005) (Fig. 6.4g, 6.5b, 6.6b, c). Pressure solution was also responsible for formation of stylolites in the carbonate facies (Fig. 6.6d). As a result of silica dissolution and precipitation, net porosity continually decreased. Pressure solution, migration, and recrystallization of silica proceeded episodically throughout the burial history.

Prior to maximum burial, hydrocarbons infiltrated and migrated through the formation, leaving stains and residual organics that have since solidified (Fig. 6.6e). The measured total organic carbon (TOC) in Weber core samples was less than 0.09 weight percent Type III Kerogen, the hydrogen index ranged between 88 and 104, and the production index ranged between 0.67 and 0.93 (Table 6.4). These data show that concentrations of residual organic matter are mostly minor and overmature, similar to a stained carrier bed, which suggests migration prior to maximum burial and thermal exposure (Peters 1986). Higher concentrations of residual organic matter are found near a small zone at the top of the Weber where hydrocarbons migrated along the contact with the Phosphoria Formation. The USGS considers peak oil generation and expulsion from the Phosphoria, the primary Paleozoic source rock in the Greater Green River Basin (GGRB), to have occurred between 85 and 68 m.y.b.p., well before maximum burial of the Rock Springs Uplift (Roberts et al. 2005). This interpretation concurs with multiple reservoir studies from surrounding Weber/Tensleep oil fields (Mankiewicz and Steidtmann 1979; Edman and Surdam 1984; Moore 1984; Bowker and Jackson 1989; Robinson 1992; Cole and Mullen 1992). There is evidence for lighter oil in portions of the eolian Weber specifically, fluorescence of core material, which could be the result of geologically-recent hydrocarbon migration, or of saturation of the core with the diesel constituent in the drilling mud (Fig. 6.7).

Episodic migration of reducing fluids left a significant imprint on the diagenetic history of the Weber, and the petrographic and geochemical evidence for carbonate dissolution and thermal chemical sulfate reduction is especially robust. The organic fluids and reactive gases forced dissolution of carbonate cement, reopening some pore space (Fig. 6.5b). Similar hydrocarbon-related porosity enhancements are observed in adjacent Weber fields (Robinson 1992). The presence of hydrocarbons may have impeded quartz cementation, at least partially, helping to retain porosity (Kupecz et al. 1997; Teinturier and Pironon 2004). Methane and hydrogen sulfide gases altered cements, carbonates, reactive detrital grains, shale, and muds by *thermochemical sulfate reduction* (TSR). Anhydrite cement was reduced and replaced by calcite and chert (Siebert 1985; Machel 1998) (Fig. 6.5f). Anhydrite blades subjected to reducing fluids were pyritized (Fig. 6.6c). Residual clays, muds, and organics reacted with hydrogen sulfide, precipitating late-stage pyrite. Undulose, saddle-shaped burial dolomites precipitated by TSR. Burial dolomite crystals grew in open pore space across much of the Weber (Fig. 6.5e). Dolostone beds in the basal Weber contain large, undulose saddle dolomites, poikilotopic calcite ce-

**Table 6.4** Organic analyses of core samples

| Formation | Depth ft (m) | Leco TOC (wt% HC) | Rock-Eval S1 (mg HC/g) | Rock-Eval S2 (mg HC/g) | Rock-Eval S3 (mg $CO_2$/g) | Hydrogen Index (S2 × 100/TOC) | Oxygen Index (S3 × 100/TOC) | Production Index (S1/(S1 + S2) |
|---|---|---|---|---|---|---|---|---|
| Weber | 11340.05 (3456.4) | 0.07 | 0.12 | 0.06 | 0.02 | 88 | 29 | 0.67 |
| Weber | 11597.05 (3534.8) | 0.09 | 1.29 | 0.09 | 0.14 | 99 | 155 | 0.93 |
| Weber | 11782.05 (3591.2) | 0.05 | 0.13 | 0.05 | 0.04 | 104 | 83 | 0.72 |
| Amsden | 12203 (3719.5 | 0.1 | 0.68 | 0.07 | 0.19 | 70 | 190 | 0.91 |
| Madison | 12309.1 (3751.8) | 0.06 | | | | | | |
| Madison | 12324 (3756.4) | 0.04 | | | | | | |
| Madison | 12335.25 (3759.8) | 0.04 | 0.2 | 0.05 | 0.03 | 137 | 82 | 0.8 |
| Madison | 12339.1 (3761.0) | 0.11 | | | | | | |
| Madison | 12345.7 (3763.) | 0.48 | | | | | | |
| Madison | 12350.2 (3764.3) | 0.08 | | | | | | |
| Madison | 12379.85 (3773.4) | 0.09 | | | | | | |
| Madison | 12411.52 (3783.0) | 0.28 | | | | | | |
| Madison | 12495.3 (3808.6) | 0.09 | | | | | | |
| | | | (amount of HC @ 300 °C) | (amount of HC @ 550 °C) | $CO_2$ from organics | | | |

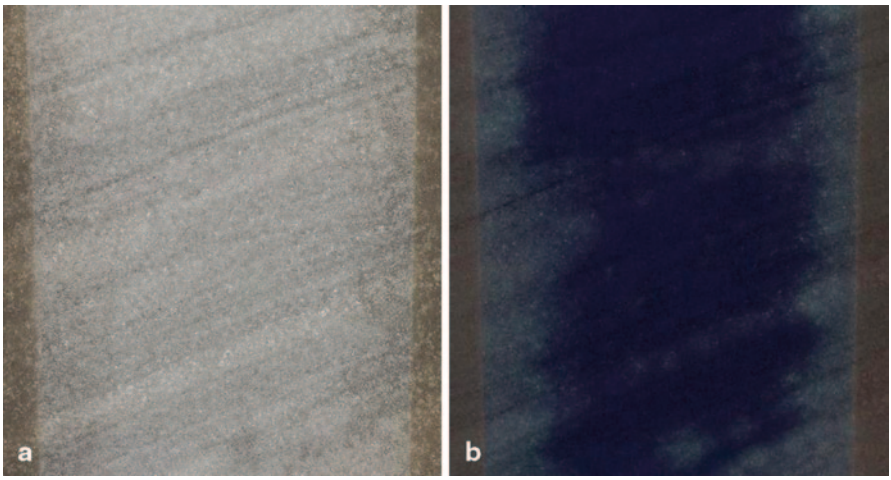


**Fig. 6.7** Core samples from the Weber Sandstone at 11,481.4 ft (3500 m) deep. (**a**) Eolian sandstone showing pinstriped cross-bedding under white light illumination. (**b**) Ultraviolet image of a, showing fluorescence due to the presence of hydrocarbon (natural or introduced during core extraction). Width of the field is 5 cm

ment, and chert, indicative of TSR reactions (Searl 1989; Scholle and Scholle 2003) (Fig. 6.6f).

Diagenesis continued as the Weber reached maximum burial depth. Quartz cementation resumed, decreasing the net porosity. It is possible that euhedral quartz crystals and overgrowths have continued to precipitate until recently; we base this on silica saturation in formation fluids and petrographic evidence for late crystallization. A burial model of the Weber reached a depth of more than 26,000 ft (8000 m) and temperatures near 300 °F (150 °C), which is approaching the conditions of zeolite facies metamorphism.

As the Rock Springs anticline was folded and uplifted by Laramide compressional forces, regional stresses were relieved in faults and fractures. Image log analysis of fractures indicates that both natural and drilling-induced fractures are near-vertical and oriented northeast–southwest, close to the present-day maximum horizontal stress. Weber fractures are frequently mineralized, and record a period of fluctuating reservoir pressure and fluid migration (Fig. 6.5c).

Though the stratigraphic section has been uplifted and unroofed, the Weber is currently deep enough to experience diagenesis. Analysis of formation fluids suggests that quartz is saturated and could precipitate if current reservoir conditions were to change. Formation fluids are undersaturated with respect to anyhdrite, indicating the possibility of anhydrite dissolution, and that anhydrite cement and laths formed under fluid conditions different from present conditions (for formation fluid analysis see Chap. 8). Twinned calcite cement and layers of burial dolomite suggests periods of dynamic reservoir conditions late in the diagenetic history, which could be the result of extraneous fluids or fluctuating reservoir pressure, tempera-

ture, and fluid excursions. Depending on location and regional geologic history, there is potential for fluid incursion alteration from two extraneous, geologically-recent sources: the migration of organic fluids from the Washakie Basin or from fluids associated with nearby volcanic intrusives (Fig. 6.1). A USGS analysis of source rocks in the adjacent Washakie Basin indicates that they are currently at temperatures conducive to hydrocarbon generation (Roberts et al. 2005). The nearby Leucite Hills, Quaternary ultrapotassic intrusives, had the potential to briefly increase local temperatures and vent volcanic gases, specifically $CO_2$ and nitrogen (Sobolev et al. 1971; Spera 1981; Wyllie and Huang 1976; Holloway 1981; Papale et al. 1998). It is possible that volcanic venting resulted in varying gas concentrations and fluid compositions.

### *6.3.5 Porosity and Permeability Variances in the Weber Sandstone*

The highest permeability in the Weber is measured in a 240-ft (73-m) interval in the upper, eolian unit (Table 6.2). The measured permeability through this section ranges from 0.001 mD to 13.8 mD and averages 2.7 mD (30 samples). The porosity ranges from 1.7 to 8.8% and averages 6.3% (30 samples). Pore size within the Weber is mostly uniform, though dissolution of reactive minerals has resulted in some anomalously large pores (>400 μm). Porosity is strongly correlative to measured permeability; this allowed CMI researchers to create permeability models from seismic porosity data (see Chap. 9).

The measured permeability in the basal, marine unit of the Weber ranges from 0.001 mD to 0.5 mD and averages 0.09 mD (30 samples) (Table 6.2). The porosity ranges from 0.1 to 9.8% and averages 3.9% (30 samples) (Table 6.2). Porosity is not strongly correlative to permeability; this suggests that the existing pore space could be isolated.

The porosity in the high-permeability interval in the upper unit is largely a function of two processes; depositional environment and later diagenetic alteration. In eolianites, porosity distribution is commonly related to grain size, as the largest pore spaces are typically located among the largest grains. Deposition has resulted in anisotropic permeability in the eolian Weber: permeability is generally higher along flow paths that are parallel or sub-parallel to cross-bedding and laminae, and lower vertically (Bowker and Jackson 1989; Robinson 1992). Reservoir parameters characterized during a mini-drill-stem test indicated that vertical permeability is an order of magnitude lower than horizontal permeability (Table 6.5). The anisotropy of the Weber reservoir will likely influence $CO_2$ plume migration at the study site. Fortuitously, image log analyses and regional paleo-flow studies show modeled $CO_2$ flow paths that are parallel or sub-parallel to most of the highly-permeable cross-bedding planes. In massive sands porosity is not grain-size selective, and permeability generally lacks preferred directionality.

**Table 6.5** In situ reservoir tests performed by Baker Hughes

| Formation | Test | Depths ft (m) | $k_{xy}$ (mD) | $k_z$ (mD) | $k_z/k_{xy}$ (mD) | Pressure (psia) |
|---|---|---|---|---|---|---|
| Weber | Mini-DST | 11,383.5–11,413.5 (3469.8–3469.7) | 1.73 | 0.41 | 0.24 | 4860.35 |
| Madison | VIT | 12,331.6–12,391.6 (3758.7–3776.9) | 4.16 | 0.48 | 0.12 | 5312.47 |

Though they are sometimes depositionally distinct, highly permeable eolian and massive sand lithologies share common diagenetic features. Both have largely avoided the intense mechanical compaction, pressure solution, quartz overgrowths, and silica cementation seen in similar lithologies with lower porosity; they thus retain a higher percentage of pre-burial pore space. In addition, these zones tend to contain lesser amounts of calcite and anhydrite cements. The lower permeability in the rest of the Weber Sandstone is attributed to mechanical compaction, pressure solution, quartz overgrowths, cements of calcite, anhydrite and silica, or discontinuous or isolated pore space.

## 6.4 Lithology, Diagenesis, and Petrography of the Madison Limestone

### *6.4.1 General Lithology*

The Madison Limestone can generally be divided into two main lithologic facies; a basal dolostone unit and an upper limestone unit. Macroscopic analyses of the core coupled with petrophysical data identify five macroscopic litholofacies within the two units (Fig. 6.8):

**Limestone Facies Biomicrites** biosparites, and biolithites; primary depositional and organic structures are mostly unaltered.

**Brecciated Limestone Facies** Brecciated limestone clasts and claystone cemented with calcite and chert; formed during evaporite dissolution and collapse.

**Fractured Dolostone Facies** Fractured and dissolved dolostone. Fractures are partially cemented and are commonly subvertical.

**Dolostone Facies** Predominantly yellowish, dolomite spar. Most of the primary structures were destroyed by dolomitization.

**Porous Dolostone Facies** Distinguished by extensive partial dissolution resulting in vugs and molds in a dolostone matrix (secondary porosity).

Though primarily composed of carbonates, the Madison also includes minor argillaceous zones and multi-mineralic collapse breccias and karst (identified as

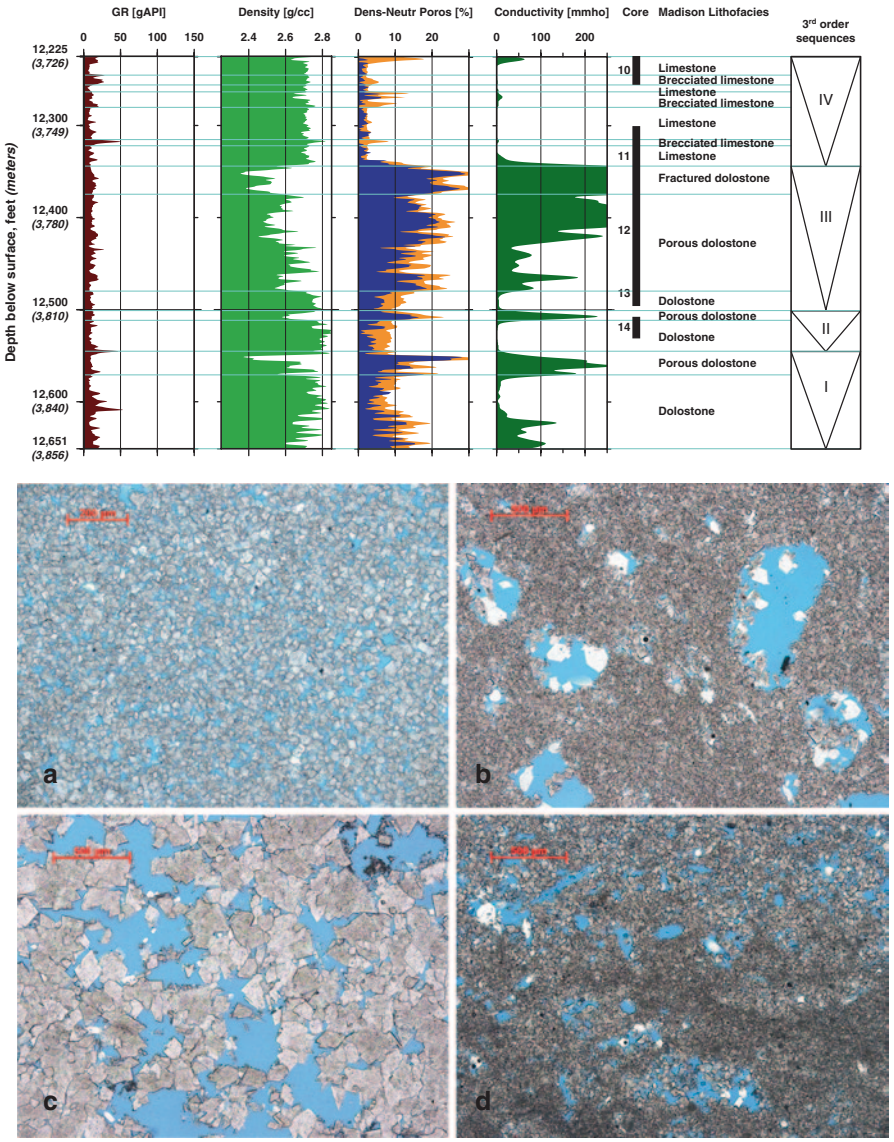


**Fig. 6.8** Lithofacies interpretation of the Madison Limestone from macroscopic core analysis and petrophysical data showing relation of lithofacies and 3rd-order sequences to petrophysical data. Cored interval is also included. (**a**) 12,343 ft (3762 m) Dolostone displaying typical intergranular porosity; bimodal grain distribution, laminations, minor cements and secondary quartz. (**b**) 12,399.8 ft (3779 m) Dolostone displaying typical moldic porosity. Large molds are randomly distributed in a finer-grained dolostone matrix (which is mostly devoid of pore space). Molds are full of secondary, authigenic minerals such as quartz, halite, and dolostone. (**c**) 12,476.6 ft (3803 m) Dolostone displaying typical vuggy porosity; large-grained sub- to euhedral dolostone with irregularly shaped pores. (**d**) 12,512.0 ft (3814 m) Dolostone displaying typical mixed porosity; top portion of the slide has intergranular porosity, and the bottom portion of the slide includes moldic and vuggy porosity. (**e**) 12,353.2 ft (3765.2) Poikilotopic anhydrite in intergranular-porosity dolostone. (**f**) 12,399.8 ft (3779 m) Blocky, tabular anhydrite, and anhydrite laths filling a mold in Madison dolostone. Anhydrite crystals have brittle fractures. (**g**) 12,399.8 ft (3779 m) Mold-filling anhydrite (bladed, tabular, and poikilotopic) and replacive dolomite in a chert nodule

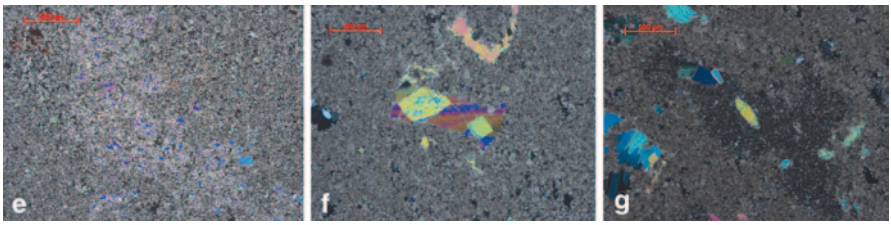


**Fig 6.8** (continued)

brecciated limestone facies, though originally evaporite beds). These non-carbonate lithofacies are characteristic of the Madison Limestone. Karst, and karst topography at the top of the formation, is documented across most of the state; collapse breccias are regionally extensive and have been correlated with evaporite beds as far north as the Williston Basin in Montana and the Dakotas; and argillaceous zones at the base of the Madison are related to changes in the regional depositional environment (Middleton 1961; Sando 1977; Sonnenfeld 1996).

Sequence-stratigraphic studies of the Madison across Wyoming describe it as composed of as many as six correlative 3rd-order sequences (Sonnenfeld 1996; Smith et al. 2004; Westphal et al. 2004; Katz 2008). This indicates that as the Madison was deposited, eustatic fluctuations and depositional environments were regional in scale, as was diagenesis at or near the surface. Data from this study identified a total of four 3rd-order sequences, three within the dolostone and one within the limestone; 3rd-order sequences contain multiple, smaller-scale, higher-frequency cycles (Fig. 6.8). The sequences correlate with those defined by Westphal et al. (2004) in central Wyoming. This is important to this study, because near-surface dolomitization created most of the porosity and permeability of the Madison reservoir, and these diagenetic responses are likely regional (Smith et al. 2004; Ehrenberg 2006; Katz 2008).

### *6.4.2 Petrographic Analysis of Madison Core Samples*

**Upper Limestone Unit** At the study site the upper limestone unit lies between 12,225 ft and 12,343 ft (3726 m and 3762 m) below the land surface, with one 8-in. (20-cm) remnant at 12,360 ft (3767 m) (Fig. 6.2, 6.28). Microfacies within the limestone unit comprise micrites, biomicrites (ranging from fossiliferous to packed), laminated biolithites, biosparites, and pelmicrites (Folk 1962). Detrital clastic grains are nearly nonexistent, but there are minor mudstones and clastic carbonates near the top of the formation. Post-depositional textures and minerals such as bioturbation, silica cements, stylolites, pyrite, mineralized veins, neomorphic calcite, burial dolomites, and collapse breccias are common. Microfacies within the limestone are commonly sequential, and the unit as a whole represents deposition along a prograding shallow-marine carbonate (also noted by Sonnenfeld 1996;

Smith et al. 2004; Westphal et al. 2004; Katz 2008). Minor porosity is sometimes exhibited in molds and collapse breccias, though the limestone facies generally has low porosity and permeability (Table 6.6). Displacement pressure analyses suggest that the impermeable limestone facies could safely contain a gas column of injected $CO_2$ without infiltration (see Sect. 6.5.3).

**Basal Dolostone Unit** At the study site, the dolostone unit lies between 12,343 ft and 12,651 ft (3762 m and 3856 m) below the land surface (Fig. 6.2, 6.8). Though dolomitization was generally fabric-destructive, several remnant microfacies are distinguishable, including biolithites and biomicrites. Dolostone fabrics range from planar-A to planar-S, xenotopic to idiotopic, and are mostly equigranular. Multiple studies, and stable isotopic compositions of the RSU #1 core, indicate that dolomitization took place in low-temperature, hypersaline conditions at or near the surface (Table 6.7) (Sonnenfeld 1996; Smith et al. 2004; Westphal et al. 2004; Katz 2008). Dolomitization of the limestone and subsequent dissolution created porosity, and the Madison exhibits four types: intergranular, moldic, vuggy, and mixed.

**Dolostone Porosity** *Intergranular porosity* occurs between individual dolomite crystals and is a function of grain size, shape, and spacing (Fig. 6.8a). Intergranular porosity zones are mostly found near the top of the dolostone, and the dolomites within the section are commonly bimodal (Fig. 6.8a). This suggests dolomitization of biolithites or laminated mudstones (Westpahl et al. 2004). Depending on sizes of the grains, these zones could have anisotropic permeability similar to that of the Weber eolianites. The measured porosity of intragranular zones ranges from 0.3 to 22.4 % with an average of 11.7 % (12 samples; Table 6.6).

*Moldic porosity* occurs in zones within the molds of anhydrite crystals, shells, bones, and other biologic remnants that are scattered in a dolomitized matrix of various grain size (Fig. 6.8a). These zones were fossiliferous and packed biomicrites.

*Vuggy porosity* is indicated by vugs within a dolomitized matrix of mixed grain sizes (Fig. 6.8c). Vugs formed by secondary dissolution in biomicrites and pelmicrites.

*Mixed porosity* combines intergrannular, moldic, and vuggy porosity (Fig. 6.8d). Mixed moldic and vuggy zones are common. The porosity of mixed moldic and vuggy zones ranges from 0.3 to 22.2 % and averages 13.3 % (42 samples; Table 6.6). Mixed intergranular porosity and moldic or vuggy porosity are not nearly as common; they could represent facies contacts or unusual alteration of the matrix.

**Additional Mineralogy** In addition to dolomite, the lower Madison contains minor clays; cements of anhydrite, silica, and calcite; pyrite; late-stage carbonates (calcite and dolomite); halite; aluminosilicates; residual hydrocarbons; and authigenic quartz.

*Anhydrite* displays three textures: poikilotopic cement; blocky, tabular crystals; and bladed laths. Poikilotopic anhydrite cement is typically found in intergranular porosity zones, and is often prominent (Fig. 6.8e). Anhydrite laths fill molds and vugs (Fig. 6.8f, g). Some laths are replaced by tabular anhydrite, indicating two generations (Fig. 8f). Laths are also found within fossiliferous silica cement and

**Table 6.6** Measured permeability and porosity of Madison core samples. Porosity type corresponds to the descriptions in Sect. 6.4.2; V = Vuggy, IG = Intergranular, M = Moldic, Limestone generally lacks porosity

| Sample Depth | | Permeability | | | | Porosity | | Density | Porosity Type |
|---|---|---|---|---|---|---|---|---|---|
| | | 800 psi NCS | | Reservoir NCS | | 800 NCS | Res. NCS | | |
| | | to Air | Klinkenberg | to Air | Klinkenberg | Porosity | Porosity | | |
| (ft) | (m) | (mD) | | (mD) | | (percent) | | (g/cm$^3$) | |
| 12,250.0 | 3733.8 | 0.001 | 0.000 | 0.000 | 0.000 | 1.33 | 0.31 | 2.70 | Limestone |
| 12,333.0 | 3759.1 | 0.001 | 0.000 | 0.000 | 0.000 | 0.90 | 0.26 | 2.70 | Limestone |
| 12,240.0 | 3730.8 | 0.043 | 0.026 | 0.003 | 0.001 | 2.90 | 1.81 | 2.69 | Limestone |
| 12,255.9 | 3735.6 | 0.013 | 0.006 | 0.001 | 0.000 | 1.03 | 0.26 | 2.69 | Limestone |
| 12,309.3 | 3751.9 | 0.008 | 0.003 | 0.001 | 0.000 | 1.30 | 0.29 | 2.68 | Limestone |
| 12,318.0 | 3754.5 | 0.012 | 0.005 | 0.001 | 0.000 | 1.28 | 0.32 | 2.68 | Limestone |
| 12,323.8 | 3756.3 | 0.003 | 0.001 | 0.001 | 0.000 | 0.48 | 0.30 | 2.68 | Limestone |
| 12,339.9 | 3761.2 | 0.871 | 0.753 | 0.183 | 0.139 | 5.62 | 3.79 | 2.81 | V |
| 12,349.9 | 3764.2 | 63.398 | 61.351 | 61.449 | 59.438 | 22.85 | 22.42 | 2.81 | IG |
| 12,355.9 | 3766.1 | 23.745 | 22.572 | 22.576 | 21.440 | 18.48 | 17.95 | 2.80 | IG |
| 12,365.5 | 3769.0 | 21.513 | 20.407 | 20.639 | 19.551 | 22.15 | 21.42 | 2.81 | V |
| 12,370.4 | 3770.5 | 17.582 | 16.603 | 16.544 | 15.595 | 20.15 | 19.15 | 2.80 | IG |
| 12,375.0 | 3771.9 | 11.256 | 10.491 | 10.524 | 9.796 | 16.17 | 15.52 | 2.81 | IG |
| 12,381.9 | 3774.0 | 2.903 | 2.563 | 2.666 | 2.343 | 12.11 | 11.31 | 2.83 | IG |
| 12,384.6 | 3774.8 | 2.235 | 1.944 | 2.030 | 1.756 | 12.54 | 11.69 | 2.83 | IG |
| 12,393.5 | 3777.5 | 4.503 | 4.057 | 4.076 | 3.655 | 15.32 | 14.48 | 2.84 | IG |
| 12,400.0 | 3779.5 | 3.058 | 2.705 | 2.141 | 1.858 | 14.16 | 12.99 | 2.79 | IG |
| 12,403.0 | 3780.4 | 15.680 | 14.752 | 5.822 | 5.299 | 14.04 | 12.96 | 2.83 | IG |
| 12,406.4 | 3781.5 | 20.722 | 19.633 | 18.711 | 17.683 | 19.67 | 17.95 | 2.82 | IG |
| 12,407.8 | 3781.9 | 1.491 | 1.263 | 1.242 | 1.044 | 14.82 | 13.94 | 2.81 | M |
| 12,410.6 | 3782.7 | 27.847 | 26.545 | 23.946 | 22.754 | 16.17 | 15.04 | 2.80 | IG |
| 12,414.4 | 3783.9 | 21.060 | 21.060 | 15.990 | 15.990 | 18.70 | 17.45 | 2.79 | M |
| 12,421.7 | 3786.1 | 105.955 | 103.216 | 96.296 | 93.674 | 20.81 | 19.82 | 2.81 | V |
| 12,428.9 | 3788.3 | 18.635 | 17.611 | 16.847 | 15.880 | 20.11 | 19.09 | 2.81 | IG |
| 12,432.8 | 3789.5 | 0.421 | 0.340 | 0.291 | 0.228 | 9.42 | 8.60 | 2.85 | V |
| 12,436.4 | 3790.6 | 9.193 | 8.503 | 8.377 | 7.728 | 19.33 | 18.75 | 2.82 | M |
| 12,437.7 | 3791.0 | 5.534 | 5.025 | 1.470 | 1.244 | 8.58 | 7.70 | 2.82 | M |
| 12,444.6 | 3793.1 | 2.389 | 2.134 | 1.763 | 1.559 | 13.97 | 13.17 | 2.81 | V |
| 12,448.1 | 3794.2 | 1.996 | 1.780 | 1.535 | 1.359 | 13.90 | 12.98 | 2.81 | M |
| 12,453.0 | 3795.7 | 4.102 | 3.677 | 3.414 | 3.033 | 16.12 | 15.01 | 2.83 | V |
| 12,460.0 | 3797.8 | 37.713 | 36.177 | 35.290 | 33.806 | 14.63 | 13.29 | 2.80 | M |
| 12,463.7 | 3798.9 | 57.243 | 55.299 | 53.123 | 51.263 | 15.73 | 14.42 | 2.79 | M |
| 12,469.5 | 3800.7 | 15.331 | 14.411 | 14.255 | 13.369 | 10.58 | 9.42 | 2.80 | V |
| 12,476.5 | 3802.8 | 149.503 | 146.216 | 142.933 | 139.740 | 19.75 | 18.88 | 2.77 | V |
| 12,482.2 | 3804.6 | 15.350 | 14.410 | 14.470 | 13.559 | 11.05 | 9.98 | 2.79 | V |
| 12,489.8 | 3806.9 | 4.982 | 4.509 | 4.194 | 3.766 | 6.16 | 5.88 | 2.81 | M |
| 12,491.7 | 3807.5 | 1.387 | 1.087 | 0.546 | 0.419 | 12.27 | 10.61 | 2.80 | V |
| 12,498.9 | 3809.6 | 1.608 | 1.370 | 1.175 | 0.980 | 6.03 | 4.90 | 2.80 | V |
| 12,511.5 | 3813.5 | 77.224 | 74.898 | 73.122 | 70.883 | 20.72 | 19.67 | 2.80 | V |
| 12,513.5 | 3814.1 | 13.413 | 12.566 | 10.137 | 9.416 | 12.83 | 11.92 | 2.81 | M |
| 12,341.8 | 3761.8 | 12.300 | 11.500 | 10.900 | 10.200 | 10.68 | 8.18 | 2.83 | M |
| 12,348.9 | 3763.9 | 33.100 | 31.700 | 16.900 | 15.900 | 18.05 | 9.03 | 2.84 | V |
| 12,353.2 | 3765.2 | 87.100 | 84.600 | 82.600 | 80.100 | 27.42 | 15.24 | 2.82 | V |

**Table 6.6** (continued)

| Sample Depth | | Permeability | | | | Porosity | | Density | Porosity Type |
|---|---|---|---|---|---|---|---|---|---|
| | | 800 psi NCS | | Reservoir NCS | | 800 NCS | Res. NCS | | |
| | | to Air | Klinkenberg | to Air | Klinkenberg | Porosity | Porosity | | |
| (ft) | (m) | (mD) | | (mD) | | (percent) | | (g/cm$^3$) | |
| 12,354.7 | 3765.7 | 42.300 | 40.700 | 40.400 | 38.800 | 23.47 | 19.15 | 2.82 | V |
| 12,358.5 | 3766.9 | 0.255 | 0.194 | 0.183 | 0.135 | 9.63 | 7.55 | 2.84 | V |
| 12,362.8 | 3768.2 | 2.620 | 2.360 | 2.250 | 2.010 | 16.92 | 15.39 | 2.83 | V |
| 12,372.7 | 3771.2 | 18.700 | 17.700 | 17.800 | 16.800 | 19.04 | 14.15 | 2.83 | V |
| 12,382.7 | 3774.3 | 0.504 | 0.408 | 0.309 | 0.241 | 9.14 | 9.68 | 2.79 | V |
| 12,399.0 | 3779.2 | 0.666 | 0.552 | 0.372 | 0.292 | 11.62 | 11.73 | 2.83 | V |
| 12,406.2 | 3781.4 | 3.750 | 3.420 | 2.870 | 2.590 | 14.94 | 14.51 | 2.83 | V |
| 12,414.5 | 3783.9 | 11.800 | 11.000 | 11.700 | 9.940 | 17.72 | 14.82 | 2.83 | V |
| 12,415.1 | 3784.1 | 7.490 | 6.880 | 6.630 | 6.060 | 18.48 | 15.74 | 2.85 | V |
| 12,421.5 | 3786.1 | 183.000 | 178.000 | 176.000 | 173.000 | 20.09 | 18.66 | 2.84 | V |
| 12,461.0 | 3798.1 | 1.560 | 1.360 | 1.350 | 1.680 | 13.62 | 13.52 | 2.84 | V |
| 12,480.5 | 3804.1 | 6.360 | 5.820 | 5.840 | 5.340 | 11.80 | 10.12 | 2.87 | V |
| 12,511.6 | 3813.5 | 24.600 | 23.400 | 22.600 | 21.400 | 16.41 | 15.93 | 2.83 | V |

filling fractures and veins (Fig. 6.8g, 6.9a). Tabular anhydrite is found filling molds, vugs, fractures, and veins (Fig. 6.8f, g, 6.9a). Anhydrite is associated with calcite and silica and is commonly replaced by both (Fig. 9a, b). Tabular and bladed anhydrite commonly contains non-propagating, brittle fractures which could be due to compaction-related brittle deformation—or to core recovery (Fig. 6.8f, g).

*Calcite*, primarily as poikilotopic cement, is typically found in dolostones with intergranular porosity (Fig. 6.9c). It is commonly associated with cements of anhydrite and silica. Tabular calcite fills veins, fractures, and inclusions and is frequently twinned (Fig. 6.9d). Brittle and plastic deformation of tabular calcite is evident as cracks within crystals and bent twins, respectively (Fig. 6.9d).

*Burial dolomites* formed as crystals and poikilotopic cement. Burial dolomite crystals are mostly euhedral and sometimes saddle-shaped (Fig. 6.9d). They can be distinguished by undulosity, distinct internal cleavage, saddle-shape, lack of inclusions, location within developed pore space, and variance in crystal size and shape relative to matrix dolomites (Fig. 6.9d, e). Some late-stage, burial dolomite crystals are comparable to authigenic quartz crystals: both are euhedral and have crystalized in developed pore space. Poikilotopic dolomites are not as prevalent. They can be massive, single lens-shaped crystals or tabular crystals grouped in zones (Fig. 6.9f). They can be poikilotopic, enveloping smaller, euhedral dolomite crystals and blebs of chert (Fig. 6.9f).

*Siliceous minerals* are common throughout the dolostone. Siliceous cements include chert, chalcedony, and megaquartz. Siliceous cements are deposited in layers and lenses, and also fill molds and vugs (Fig. 6.8g, 6.9b). Lenses of siliceous ce-

**Table 6.7** Isotopic analysis of Madison carbonates

| Stable isotopic values for Madison formation carbonates | | |
|---|---|---|
| Depth | Carbon | Oxygen |
| 12,227.9 | 0.7 | −1.3 |
| 12,233.0 | 0.4 | −0.2 |
| 12,241.4 | −2.5 | −5.3 |
| 12,243.7 | −2.2 | −5.3 |
| 12,249.8 | −2.0 | −5.6 |
| 12,304.7 | −1.6 | −4.8 |
| 12, 307.8 | −2.2 | −10.6 |
| 12,314.8 | −1.9 | −4.5 |
| 12,323.8 | −1.4 | −5.4 |
| 12,329.2 | −1.9 | −5.9 |
| 12,333.0 | −3.1 | −5.3 |
| 12,336.8 | −4.9 | −5.5 |
| 12,343.0 | −1.2 | 2.4 |
| 12,343.6 | −0.9 | 0.8 |
| 12,350.0 | −0.7 | −2.3 |
| 12,354.9 | −1.1 | −11.1 |
| 12,355.7 | −3.0 | −13.0 |
| 12,356.7 | 0.0 | −1.9 |
| 12,360.7 | −1.4 | −4.7 |
| 12,365.6 | 0.8 | −0.7 |
| 12,371.1 | 0.4 | 0.1 |
| 12,374.5 | −0.2 | 1.4 |
| 12,377.7 | 0.0 | −1.3 |
| 12,383.5 | −0.9 | −7.9 |
| 12,385.1 | 0.5 | 0.7 |
| 12,393.3 | 0.7 | −0.6 |
| 12,398.5 | 0.4 | 1.1 |
| 12,403.4 | 0.0 | 1.5 |
| 12,406.4 | 0.4 | 1.9 |
| 12,414.6 | −1.2 | 2.4 |
| 12,421.1 | −0.4 | 2.3 |
| 12,429.0 | 0.5 | 3.2 |
| 12,432.8 | 0.7 | 1.5 |
| 12,438.0 | 0.0 | −1.1 |
| 12,446.0 | 0.9 | 2.4 |
| 12,453.0 | 0.9 | 1.6 |
| 12,457.4 | 0.5 | 2.5 |
| 12,463.9 | 0.6 | 2.2 |
| 12,468.8 | 0.0 | −0.7 |
| 12,476.6 | 1.4 | −0.4 |
| 12,482.2 | 0.3 | 2.5 |
| 12,489.0 | 0.3 | 1.1 |
| 12,491.8 | 0.4 | 0.5 |
| 12,499.2 | 0.2 | 0.1 |
| 12,511.4 | 1.9 | −1.1 |
| 12,511.7 | 0.1 | −11.0 |
| 12,513.5 | 1.6 | −0.5 |
| 12,519.5 | 0.8 | 0.1 |
| 12,535.0 | 0.0 | 1.2 |

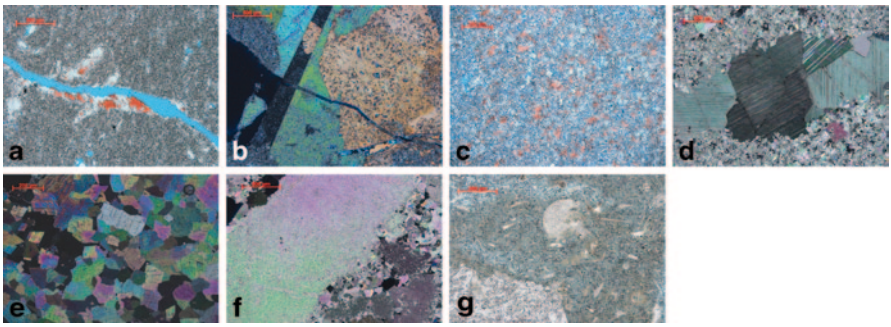


**Fig. 6.9** (**a**) 12,399.8 ft (3779 m) Calcite (stained red) replacing anhydrite in a partially-filled fracture. (**b**) 12,353.6 ft (3765 m) Anhydrite replaced by calcite, itself replaced by chert. An excellent example of mineral associations and reactions related to thermochemical sulfate reduction. (**c**) 12,356.7 ft (3766 m) Poikilotopic calcite cement in intergranular-porosity dolostone. (**d**) 12,335.2 ft (3760 m) Fracture-filling calcite. The tabular, twinned textures indicate precipitation under relatively high-temperature and pressure. (**e**) 12,480.5 ft (3804 m) Massive burial dolomites with pronounced internal cleavages and undulosity. (**f**) 12,489.7 ft (3807 m) Massive dolomite (light green) enveloping chert and smaller dolomite crystals. (**g**) 12,372.7 ft (3771 m) Mold-filling chert and chert cement in dolostone enveloping dolomite crystals

ment commonly preserve molds (Fig. 6.9g). Siliceous cement regularly contains anhydrite and calcite in molds and or vugs (Fig. 6.8g). Siliceous cement envelopes dispersed grains of euhedral dolomite and pyrite as well as preserving fossil molds (Fig. 6.8, 6.9g). In addition to siliceous cement, authigenic quartz crystals are prevalent in moldic and vuggy porosity zones (Fig. 6.8b, d, g, 6.9a). Quartz crystals are typically euhedral and contain fluid inclusions (Fig. 6.8b, d, g, 6.9a). Some authigenic quartz crystals appear undulatory (Fig. 6.10a). This could be due to deformation by high fluid pressure, though it is more likely the result of generational overgrowths or polycrystallinity (amalgamations of multiple smaller grains). Minor amounts of aluminosilicates (clays) are present in the Madison. The silica concentrations in the dolostone lie between 1.5 % and 13.3 %, and higher concentrations of silica typically correspond to lower porosity.

*Halite* is mostly restricted to pore-space in moldic and vuggy porosity zones (Fig. 6.8d, 6.10a). Pore-filling halite is commonly associated with anhydrite, which is typical of sabkha deposits (Krystinik 1990b). It is also possible that halite precipitated from residual brines trapped in the core during extraction.

*Pyrite* is abundant in the dolostones. It is subhedral to anhedral and is found as individual grains or bunched along stylolites (Fig. 6.10b). All pyrite is authigenic, crystallizing during sulfate reduction.

*Residual hydrocarbons* are present in the dolostone in low concentration. They are found in pores as small, rounded blebs or as stains or coatings on grain surfaces.

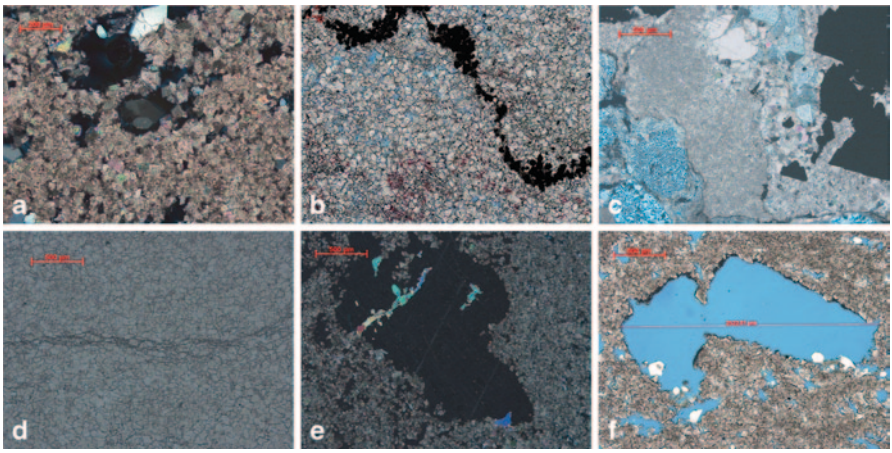


**Fig. 6.10** (**a**) 12,385.1 ft (3775 m) Authigenic euhedral quartz with apparent undulosity as a result of the amalgamation of multiple crystals. (**b**) 12,343 ft (3762 m) Pyritized stylolite and calcite (stained red) in dolostone. Mineralization of the stylolite suggests pressure solution preceded thermal chemical sulfate reduction. (**c**) 12,329 ft (3758 m) Collapse breccia showing burial alteration; neomorphic calcite, massive pyrites, ferroan saddle dolomites, chalcedony nodules and dissolution seams. Mineralogy and crystal textures indicate precipitation by thermal chemical sulfate precipitation at depth: alteration of evaporate bed was mesogenetic. (**d**) 12,256 ft (3735 m) Neomorphic calcite with subhorizontal proto-stylolite, pyrite, and minor quartz. (**e**) 12,375 ft (3772 m) Massive, replacive, poikilotopic calcite in dolostone. Note the leftover anhydrite (high birefringence) in the calcite, indicative of replacement by thermal chemical sulfate reduction. (**f**) 12,415.1 ft (3784.1) Massive dissolution pore in dolostone

### *6.4.3 Diagenetic History*

Diagenesis of the Madison Limestone began pre-burial as sea level fluctuated (Sonnenfeld 1996; Smith et al. 2004; Westphal et al. 2004; Ehrenberg et al. 2006; Katz 2008). Episodic dolomitization occurred in near-surface, evaporitic, hypersaline waters as evidenced by enriched oxygen isotopes in most dolostones (dolostone $\delta^{18}O$ values greater than 0.0‰, compared with −4.5 to −5.9‰ for primary limestones) both regionally and at the study site (Land 1980; Faure and Mensing 2005) (Table 6.7). A fluctuating sea level is also evidenced by regional collapse breccias, which initially were deposited as evaporite beds (Middleton 1961) (Fig. 6.10c). Prior to complete burial, marine regression partially or completely exposed the upper limestones of the Madison, creating karstic surfaces (Sonnenfeld 1996; Smith et al. 2004; Katz 2008). Also pre-burial or early post-burial evaporites precipitated in porous regions in the dolostone.

As the formation was progressively buried, carbonate solubility in the pore water decreased, resulting in precipitation of carbonate cements within intragranular dolostones (Fig. 6.9c). It is possible that early-burial bacterial sulfate reduction, evidenced by framboidal pyrites, increased carbonate alkalinity, which abetted precipitation of calcite cement (Machel 1998).

At increasing burial depths, temperature increased and gypsum dehydrated to form anhydrite (Murray 1964). Increased burial pressure led to carbonate pressure solution, dissolution, and stylolite formation (Passchier and Trouw 2005) (Fig. 6.10b, d).

Hydrocarbons migrated through parts of the dolostone prior to complete burial, as evidenced by widespread thermochemical sulfate reduction and residual solidified hydrocarbon. The timing of the hydrocarbon migration most likely coincides with the migration history described for the Weber (Sect. 6.3.4). The initial front of organic acids and associated gases lowered the pH of the brines, forcing carbonate dissolution (Mazzullo and Harris 1992). Volatile fluids reduced the residual minerals and clays dispersed throughout the formation or accumulated in stylolites, precipitating pyrite and pyritized stylolites (Fig. 6.10b, c). Hydrogen sulfide reduced sulfate anions in anhydrite, replacing the anhydrite with calcite and chert (Machel 1998) (Fig. 6.10e). Additional, non-replacive calcite precipitated as episodic hydrocarbon migrations altered the $CO_2$ partial pressure and pH in the reservoir fluids (Mazzullo and Harris 1992). Neomorphic calcite with abundant pyrite, chert, and ferroan saddle dolomites formed in collapse breccia (Fig. 6.10c). During thermal chemical sulfate reduction, burial dolomites crystallized in pore spaces or precipitated as poikilotopic cements (Machel 1998).

As the Rock Springs anticline was uplifted, compressional stresses formed brittle fractures and veins. These fractures were filled with tabular calcite and anhydrite, and record a period of fluctuating reservoir pressure and fluid migration. Late-stage, vein-filling carbonates are highly twinned and have depleted oxygen isotopes (less than −10.0‰ $\delta^{18}O$), both indicative of high-temperature burial crystallization (Land 1980; Faure and Mensing 2005).

Authigenic, euhedral quartz episodically crystallized in developed pore space. Multiple periods of crystallization are indicated by quartz overgrowths as well as by single euhedral crystals that amalgamated from multiple smaller crystals. Petrographic evidence of numerous quartz growth phases is further indication of a dynamic fluid environment. Laramide faulting and fracturing briefly altered reservoir pressures and impacted fluid compositions, possibly increasing quartz saturation and inducing precipitation. Episodic hydrocarbon migrations could also have influenced quartz precipitation (Teinturier and Pironon 2004). Fluids associated with Neogene deformation, discussed in the following paragraph, could have further impacted authigenic quartz formation. Analysis of the formation fluids indicates that the brine is saturated with respect to quartz, and that quartz has the potential to precipitate if forced (see Chap. 8).

In addition to alteration by Mesozoic organic fluids, there is evidence for late-stage extraneous fluid alteration, either from migrating organic fluids from the Washakie Basin or fluids associated with nearby volcanic intrusives. A USGS analysis of potential source rocks in the Washakie Basin indicates that some formations are currently at temperatures conducive to hydrocarbon production (Roberts et al. 2005). Post-Laramide diagenesis by reducing fluids is evident in anhydrite veins that have been altered to calcite by thermochemical sulfate reduction (Machel 1998). The Leucite Hills, Quaternary ultrapotassic intrusives, had the potential to

briefly increase local temperatures and vent volatile volcanic gases, specifically $CO_2$ and nitrogen (Sobolev et al. 1971; Spera 1981; Wyllie and Huang 1976; Holloway 1981; Papale et al. 1998).

Carbonate inclusions in authigenic quartz crystals indicate the possibility of emplacement during a period of elevated temperature and $CO_2$ partial pressure such as might be associated with Neogene volcanism. The secondary anhydrites that surround and cannibalize preexisting crystals could have been deposited in the presence of increased concentrations of $CO_2$. Furthermore, a commercial-size $CO_2$ field has been identified on the crest of the Rock Springs Uplift (WOGCC 2013). The source of these gases has not been determined; however, Neogene gas fields of similar character and composition from established volcanic sources have been reported in Utah, Colorado, and New Mexico (Gilfillan et al. 2008). It is possible that volcanic venting briefly altered the reservoir gas and fluid compositions, driving diagenesis in Paleozoic reservoirs across the northern RSU. Most importantly at the study site, migrations of Neogene $CO_2$ gas would have contributed to the dissolution of carbonates, increasing the porosity of the Madison reservoir rocks (see Chap. 8).

### *6.4.4 Porosity and Permeability Variance*

The most permeable zones in the Madison were measured in the dolostone lithofacies (Table 6.6). Within the dolostones, porosity type impacts permeability. Dolostone with intergranular porosity has permeability that ranges from 0.001 mD to 82.6 mD (12 samples) (Table 6.6). Total porosity in intergranular zones ranges from 0.3 to 22.4% (12 samples) (Table 6.6). Though the sample size is small, porosity appears to be correlative with permeability which allowed CMI to create permeability models from seismic porosity data.

The measured permeability in the moldic and vuggy dolostones ranges from 0.001 mD to 2245 mD and averages 75.7 mD (42 samples) (Table 6.6). The maximum value, 2245 mD, is likely an outlier: removing that datum results in a range from 0.001 mD to 176.0 mD and an average of 22.7 mD (41 samples) (Table 6.6). Porosity in the moldic and vuggy dolostone ranges from 0.3 to 19.8% and averages 13.1% (41 samples) (Table 6.6). Pore size within vuggy and moldic zones is variable, and pores as large as 3000 μm have been measured (Fig. 6.10f).

Most porosity in the Madison is primarily associated with early diagenetic alteration of carbonate lithologies. Dolomitization of biolithites created zones of intergranular porosity, and dolomitization and subsequent secondary dissolution of biomicrites created zones of moldic and vuggy porosity. Permeability in the intergranular zones is correlative with porosity, which is primarily regulated by grain size and distribution and the amount and distribution of cement. They are similar to Weber eolianites with regard to vertical anisotropy; reservoir parameters in intergranular zones characterized during a vertical interference test indicated that vertical permeability is an order of magnitude lower than horizontal permeability

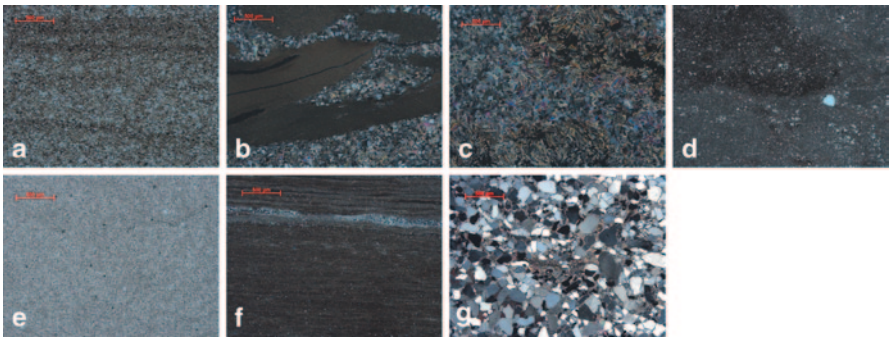


**Fig. 6.11** (**a**) 10,601.9 ft (3231 m) Typical cross-bedded Triassic siltstone. (**b**) 10,640.1 ft (3243 m) Intraclasts of shale in Triassic siltstone. Intraclasts of mudstone, shale, and carbonates are common. The matrix of the siltstone is predominantly anhydrite. (**c**) 10,633.8 ft (3241 m) Chicken-wire anhydrite nodules with halite in Triassic siltstone suggest precipitation in hypersaline, evaporative conditions. (**d**) 12,224 ft (3726 m) Clastic shale with hematitic mudstone intraclast in the Amsden Formation. (**e**) 12,199 ft (3718 m) Dolostone; sub- to euhedral dolomite crystals with detrital quartz and authigenic pyrite. Amsden carbonates, such as this dolostone, typically lack porosity. (**f**) 12,225 ft (3726 m) Hematitic, laminated shale at the base of the Amsden formation. Note the dolomitized layer near the top of the slide. (**g**) 12,215.6 ft (3723 m) Clastic siltstone in the Amsden Formation with carbonate and anhydrite cement. Aside from contact points, detrital grains are mostly free of pressure solution deformation

(Table 6.5). Porosity and permeability in the moldic and vuggy zones are highly variable and are constrained by the quantity of vugs and molds, the openness of the pore space relative to cements and authigenic minerals, and the interconnectivity of the pore space.

## 6.5 Analysis of Cored Sealing Lithologies

Core was extracted from three potential sealing lithologies; the lower Triassic section, the Pennsylvanian/Mississippian Amsden Formation, and the limestone lithofacies of the Mississippian Madison Limestone (Table 6.1 and Fig. 6.2). These units were evaluated for potential sealing capacity, pore character, lithology, and regional lithologic continuity.

### *6.5.1 The lower Triassic section*

The lower Triassic section lies at depths greater than 10,400 ft (3170 m) below the land surface at the well site. Approximately 90 ft (27 m) of core was recovered from the middle of the formation (Table 6.1 and Fig. 6.2). The core is primarily hematite-stained siltstone (Fig. 6.11a). It also contains shale, mudstone, evaporites,

**Table 6.8** Porosity and permeability measurements of core samples from sealing lithologies

| Sample No. | Sample Depth | | Permeability | | | | Porosity | | Density |
|---|---|---|---|---|---|---|---|---|---|
| | | | 800 psi NCS | | Reservoir NCS | | 800 NCS | Res. NCS | |
| | | | Air | Klinkenberg | Air | Klinkenberg | Porosity | Porosity | |
| | (ft) | (m) | (mD) | | (mD) | | (percent) | | (g/cm$^3$) |
| lower Triassic section | | | | | | | | | |
| 1 | 10,601.9 | 3231.5 | 0.005 | 0.002 | 0.001 | 0.000 | 1.64 | 1.00 | 2.71 |
| 120 | 10636.3 | 3241.9 | 0.11 | 0.075 | 0.001 | 0.000 | 1.79 | 0.62 | 2.73 |
| 125 | 10671.8 | 3252.8 | 0.01 | 0.005 | 0.001 | 0.000 | 2.54 | 1.43 | 2.67 |
| 18 | 10,682.1 | 3255.9 | 0.003 | 0.001 | 0.001 | 0.000 | 1.24 | 0.79 | 2.69 |
| Amsden Formation | | | | | | | | | |
| 186 | 12170.3 | 3709.5 | 0.016 | 0.008 | <0.001 | <0.001 | 2.05 | 0.59 | 2.68 |
| 190 | 12198.95 | 3718.2 | 0.159 | 0.21 | 0.028 | 0.045 | 3.62 | 2.04 | 2.80 |
| 195 | 12215.6 | 3723.3 | 0.183 | 0.129 | <0.001 | <0.001 | 2.90 | 1.27 | 2.64 |
| 199 | 12224.6 | 3726.1 | 0.002 | <0.001 | <0.001 | <0.001 | 4.98 | 2.58 | 2.83 |

clastic grains of quartz and feldspar, heavy accessory minerals, ooids, glauconite, intraclasts of mudstone and limestone, replacive dolomite, and abundant calcite and anhydrite cement (Fig. 6.11a, b). Petrographic analyses of core suggest that it was mostly deposited in a shallow, evaporative, oxidizing marine environment (Fig. 6.11c). Many of the clays composing the siltstones, shales, and cements, have been diagenetically altered; burial-related potassic clays and secondary cements of anhydrite and calcite are prevalent. Multiple zones within the core are pale green to white, indicating burial-related reduction of hematite.

Core was analyzed for porosity, permeability, and mercury capillary displacement pressure. Porosity ranges from 0.62 to 1.4%, and permeability is less than 0.001 mD (reservoir conditions) (Tables 6.8, 6.9). Pore throat radii are <2 μm, ranging between 0.001 μm and 1.6 μm (Table 6.9). Displacement pressures, calculated from mercury capillary injection tests, range between 939 psi and 2718 psi (6474 kPa and 18,740 kPa) (Table 6.9). These tests indicate that the Triassic sediment can effectively seal $CO_2$ within the underlying Weber reservoir.

Low measured porosity, permeability, and pore throat radii are ideal properties of seals (Downey 1994). These confining properties are attributable to both deposition and diagenetic alteration. Primary depositional features that would augment sealing characteristics of the siltstone include fine-grained impermeable shale, mudstone, intraclasts of mudstone and carbonate, and anhydrite (Ingram et al. 1997; Krushin 1997). Post-burial diagenetic alteration of fluids and minerals also enhanced the holding capacity of the siltstone through the precipitation of pore-filling calcite and anhydrite cements and oriented potassic phyllosilicates (Krushin 1997). The ductility of the formation also makes it less likely to fracture, further enhancing its sealing efficiency (Ingram et al. 1997, Downey 1994).

**Table 6.9** Mercury injection capillary pressure analysis and pore throat distribution of sealing lithologies

| Sample ID | Interval Depth (ft) | Helium Porosity (%) | Formation ID | Sample Type | Grain Density g/cc | Mercury/Air Displacement Pressure (psi) | Pore Throat Distribution | | | Swanson | |
|---|---|---|---|---|---|---|---|---|---|---|---|
| | | | | | | | Micropores <0.1 µm (%PV) | Intermediate 0.1–3 µm (%PV) | Macropores >3 µm (%PV) | Brine Permeability (mD) | Air Permeability (mD) |
| 1 | 10601.9 | 1.01 | lower Triassic section | Core Plug | 2.71 | 939.71 | 90.15 | 9.84 | 0.000 | 0.000 | 0.000 |
| 4 | 10605.8 | ND | lower Triassic section | Core Plug | ND | 1140.44 | 82.09 | 17.90 | 0.000 | 0.000 | 0.000 |
| 16 | 10656.4 | ND | lower Triassic section | Core Plug | ND | 2718.73 | 54.80 | 45.19 | 0.000 | 0.000 | 0.000 |
| 18 | 10682.1 | 0.99 | lower Triassic section | Core Plug | 2.69 | 1521.42 | 86.79 | 13.20 | 0.000 | 0.000 | 0.000 |
| 53 | 12197.4 | 4.95 | Amsden | Core Plug | 2.64 | 1381.10 | 83.32 | 16.67 | 0.000 | 0.001 | 0.005 |
| 187 | 12178.1 | ND | Amsden 1 | Core Plug | 2.91 | No Injection | 0.000 | 0.000 | 0.000 | 0.000 | 0.000 |
| 200 | 12227.3 | ND | Amsden 2 | Core Plug | 2.85 | No Injection | 0.000 | 0.000 | 0.000 | 0.000 | 0.000 |
| 59 | 12250.0 | 0.42 | Madison | Core Plug | 2.63 | 1253.69 | 100.00 | 0.000 | 0.000 | 0.000 | 0.000 |
| 206 | 12301.1 | ND | Madison 1 | Core Plug | 2.74 | No Injection | 0.000 | 0.000 | 0.000 | 0.000 | 0.000 |
| 214 | 12333.9 | ND | Madison 2 | Core Plug | 2.83 | 3630.11 | 100.00 | 0.000 | 0.000 | 0.000 | 0.000 |

### 6.5.2 The Amsden Formation

The Amsden Formation lies 11,807–12,225 ft (3600–3726 m) below the land surface at the well site, and approximately 56 ft (17 m) of core was recovered from the base of the formation (Table 6.1 and Fig. 6.2). Core recovered from the study site is composed primarily of shaly carbonates and clastic beds (Fig. 6.11d). It also contains collapse breccia, dolomite, limestone, mudstone, shale, clastic carbonate, evaporites, minor bimodal sands with glauconite, and intraclasts of mudstone, sandstone and carbonates (Fig. 6.11e, f, g). Petrographic analyses of Amsden core suggest that it was deposited in a fluctuating marine environment, with episodes of subaerial exposure (Fig. 6.11d, e, f, g). Diagenesis was pervasive; aside from remnant beds of fossiliferous limestone, much of the formation has been diagenetically altered or recrystallized.

Core was analyzed for porosity, permeability, and mercury capillary displacement pressure. The measured porosity ranges from 0.59 to 4.6%, and permeability ranges from <0.001 mD to 0.005 mD (reservoir conditions) (Tables 6.8, 6.9). Pore throat radii were <3 μm, ranging between 0.008 μm and 2.5 μm (Table 6.9). Displacement pressures, calculated from mercury capillary injection tests, range between 1381 psi to greater than 20,000 psi (9521 kPa and 137,895 kPa) (Table 6.9). These tests indicate that the Amsden can effectively seal injected $CO_2$ within the underlying Madison reservoir.

The low measured porosity, permeability, and pore throat radii of the Amsden are ideal properties for seals (Downey 1994). These confining properties can be attributed to diagenetic alteration. Unlike the Madison carbonates, the Amsden diagenetic carbonates are largely devoid of pore space (Fig. 6.11e). There is evidence of pre-existent moldic, vuggy, channel, and vein porosity, but most pore-space was subsequently filled with calcite, silica, and ferroan dolomite cements. Clastic lithofacies in the Amsden are cemented with diagenetic clay, silica, or carbonate, and have low porosity (Fig. 6.11d, g).

### 6.5.3 The Upper Limestone Unit of the Madison Limestone

The upper limestone unit of the Madison Limestone lies approximately 12,225–12,343 ft (3726–3762 m) below the land surface, and approximately 74 ft (23 m) of core was recovered from the unit (Table 6.1 and Fig. 6.2). The upper limestone unit includes limestone, minor mudstone and clastic carbonate, and collapse breccias. Core recovered from the well site is composed primarily of biomicrites and biosparites. It also contains post-depositional textures and minerals such as bioturbation, silica cement, stylolite, pyrite, and mineralized veins. Petrographic analyses of Madison core suggest that it was deposited in a prograding, shallow marine environment with periods of subaerial exposure. Most of the textures observed in the limestone facies are primary, as diagenesis was limited to vug-, mold-, and vein-filling cement, sulfate reduction, and pressure solution.

Core was analyzed for porosity, permeability, and mercury capillary displacement pressure. The measured porosity ranges from 0.2 to 0.42%, and permeability

is < 0.001 mD (reservoir conditions) (Tables 6.6, 6.9). Pore throat radii are < 0.3 µm, ranging between 0.05 µm and 0.25 µm (Table 6.9). Displacement pressures, measured in mercury capillary injection tests, range between 1253 psi and greater than 20,000 psi (8639 kPa and 137,895 kPa) (Table 6.9). Analyzed displacement pressures indicate that the upper limestone can seal injected $CO_2$ within the Madison dolostone unit without leaking.

The low measured porosity, permeability, and pore throat radii of the upper limestone unit are ideal properties of seals (Downey 1994). These confining properties are attributable to deposition and minor diagenetic cementation. Fine-grained depositional micrites, primary carbonate textures that compose most of the core, generally lack porosity. The molds and vugs in biomicrites are filled with diagenetic cements of silica and calcite, as are veins and fractures.

### *6.5.4 Regional Seal Evaluation*

Well logs from oil and gas fields across the RSU were investigated to characterize the lateral extent and lithologic heterogeneity of potential seals. Resistivity, porosity, and sonic well logs from the North Baxter Basin Field (approximately 14 mi (22.5 km) west of the study site), the Table Rock Field (approximately 20 mi (32 km) east), and the Brady Field (approximately 20 mi (32 km) southeast) indicate that the investigated seals are lithologically comparable and laterally continuous across the RSU. The confining properties of these units are evident in producing fields, where they effectively trap hydrocarbons and $CO_2$. Field data also identifies the upper limestone unit of the Madison as an effective seal (WOGCC 2013). In addition, recent work on the nearby Moxa Arch has identified the lower Triassic Dinwoody and Permian Amsden formations as effective seals in a natural $CO_2$ field (Becker and Lynds, 2012).

For additional information pertaining to other confining units and sealing formations present regionally and in the study area, see Chap. 5. It is important to note that additional Mesozoic formations (not cored for this study) are proven hydrocarbon seals at the Deadman Wash Field (approximately 1 mi (1.6 km) northeast), as well as at nearly forty other oil and gas producing fields across the RSU (WOGCC 2013). Additional seals would help increase the probability of long-term storage at the study area by providing alternative fluid seals in the event of a breach in one or more of the three primary seals discussed in Sects. 6.5.1, 6.5.2, 6.5.3.

## 6.6 Burial and Geochemical History of the Study Site

The burial history of the study site was reconstructed using stratigraphic and lithologic data from the study site and the regional geologic history as summarized by Love et al. (1993). The stratigraphy of the RSU has resulted from multiple depositional environments and orogenic events (see Chap. 5). The most recent orogenic activity resulted in the complete erosional removal of Tertiary strata at the study

site (Fig. 6.1, 6.2). As a consequence, the Upper Cretaceous Almond Formation is the youngest formation presently exposed at the land surface on the study site (Fig. 6.1, 6.2).

The burial history reconstruction of the RSU #1 well site shows burial at a fairly constant rate of approximately five meters per million years (5 m/m.y.) from the Late Cambrian to the Late Cretaceous period, interspersed with minor erosional events (Fig. 6.12a). From the Late Cretaceous to the Eocene the burial rate increased to approximately 65 m/m.y. Uplift-related denudation in the late Eocene was followed by deposition that lasted through the middle Neogene. Beginning in the late Neogene, renewed uplift and erosion elevated the strata to their current elevation (Fig. 6.12a).

The burial history reconstruction was used to generate 1-D profile models that define the thermal history, the timing of hydrocarbon generation and maturation, and calibrated time-temperature profiles at the study site (Fig. 6.12b, c,d). The models were calculated using a constant heat-flow of 25 mW/m$^2$ from 500 m.y.b.p., to 25 m.y.b.p. after which the heat flow was increased to 55 mW/m$^2$ and the kinetic parameters of Sweeney and Burnham (1990). These parameters agree with observations by Decker et al. (1980) and Heasler (1985) on geothermal regime in southern Wyoming. The results were calibrated with vitrinite reflectance values ($R_o$) measured on cuttings and core samples from the Phosphoria Formation (Table 6.10). Vitrinite particles from these formations have measured values ranging from 1.0 to 1.8 %, with an average value of 1.25 %, these values are comparable to calculated $R_o$ values illustrated on Fig. 6.12d. The measured temperature in the Madison Limestone from the RSU #1 well (95.5 °C at 3768 m) was used to calibrate the geochemical model, which calculated a temperature of 96 °C at 3720 m (Fig. 12b, c). The time-temperature calibration model shows Cambrian strata reaching depths near 8400 m (27,600 ft), maximum temperatures greater than 150 °C (302 °F), and pressures close to 255 MPa (2.5 kbars) (Fig. 12a, b–d). The calibrated 1-D geochemical model indicates that formations at the study site have re-entered the hydrocarbon window due to recent uplift and erosion.

The 2-D geochemical models were created to help determine the current potential for regional hydrocarbon generation, accumulation, and likely migration pathways. As hydrocarbons are less dense than formation brines, they could serve as a stand-in for modeling long-term $CO_2$ migration. In addition, the appearance of hydrocarbons in potential storage reservoirs could result in modifications to CMI's injection and water treatment scenarios. Investigating the potential for regional hydrocarbon production and migration is therefore important for any carbon capture and sequestration characterization.

The 2-D temperature model was calibrated using measured temperatures from the RSU #1 well and vitrinite reflectance analysis (Fig. 6.13a). The thickness and depositional data for regional Tertiary strata used in the 2-D modeling came from petrophysical data (WOGCC 2013). Again, the reconstructed temperature profile was obtained using a constant heat-flow of 25 mW/m$^2$ from 500 m.y.b.p. to 25 m.y.b.p, after which the heat flow was increased to 55 mW/m$^2$. The temperature distribution with depth resulted in calculated temperatures that closely match mea-

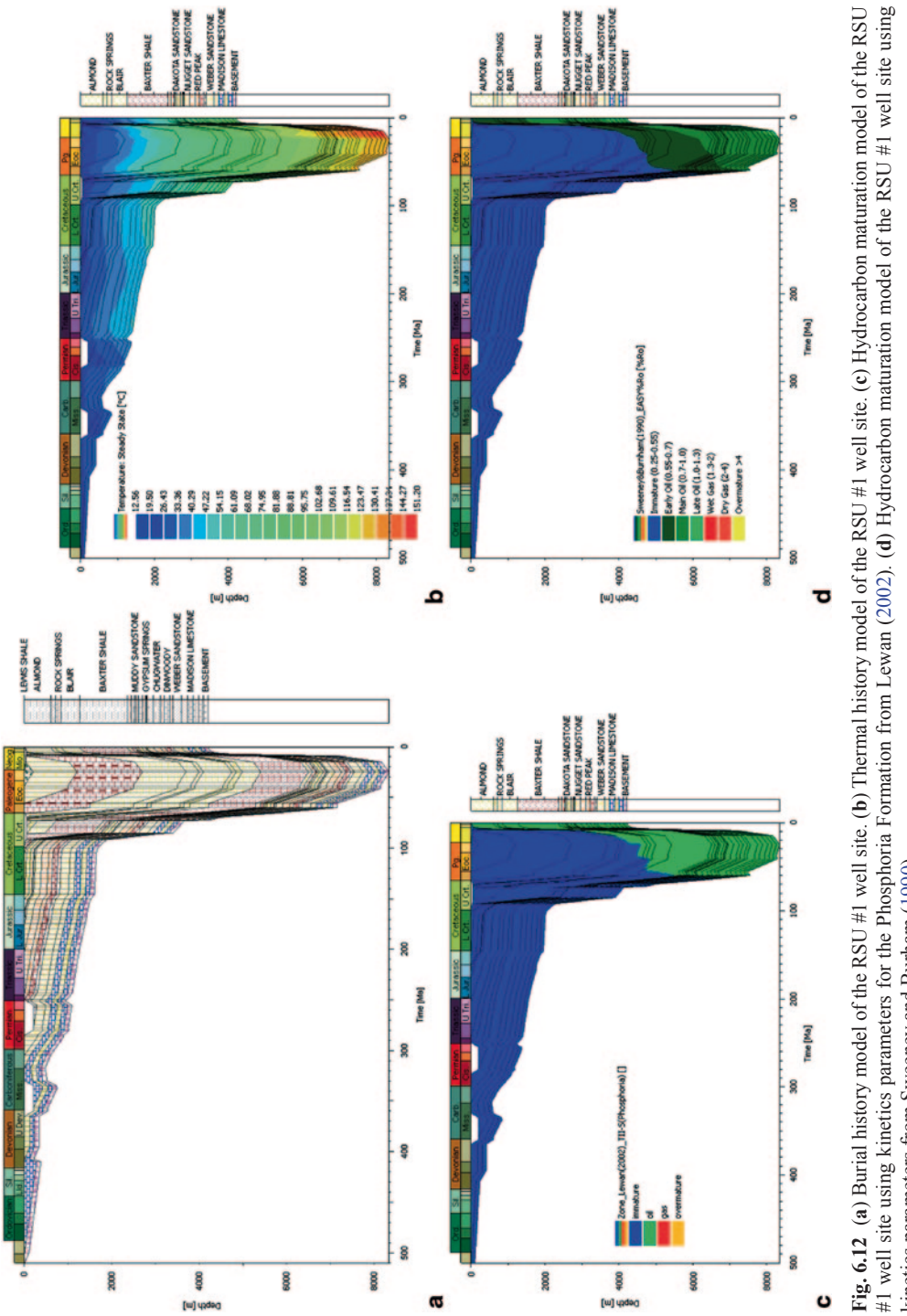


**Fig. 6.12** (**a**) Burial history model of the RSU #1 well site. (**b**) Thermal history model of the RSU #1 well site. (**c**) Hydrocarbon maturation model of the RSU #1 well site using kinetics parameters for the Phosphoria Formation from Lewan (2002). (**d**) Hydrocarbon maturation model of the RSU #1 well site using kinetics parameters from Sweeney and Burham (1990)

**Table 6.10** Vitrinite reflectance data ($R_o$) from Phosphoria cuttings

| $R_o$ (%) | Frequency |
|---|---|
| 0.2 | 0 |
| 0.4 | 0 |
| 0.6 | 0 |
| 0.8 | 0 |
| 1 | 2 |
| 1.2 | 4 |
| 1.4 | 1 |
| 1.6 | 0 |
| 1.8 | 1 |
| 2 | 0 |
| 2.2 | 0 |
| 2.4 | 0 |

sured temperatures from the RSU #1 well for the Weber and Madison formations (Fig. 6.13a).

The calculated $R_o$ and measured $R_o$ from Phosphoria samples are generally comparable. However, vitrinite macerals were relatively scarce, and the dataset is not as robust as anticipated. $R_o$ values for the model were calculated using the methods of Sweeney and Burnham (1990). The measured $R_o$ values from RSU #1 samples range between 1.0% and 1.8%, and the calculated $R_o$ values range between 0.7% and 1.3% (Table 6.10). Modeled results show a match between present-day temperatures and calculated temperatures (Fig. 6.13b). However, measured $R_o$ values are higher than calculated values; this could be due to the paucity of vitrinite particles or changes in the paleo-geothermal gradient.

The 2-D geochemical modeling followed the methodology of Welte et al. (1997), which includes: burial reconstruction and decompaction (back stripping analysis), reconstruction of time-temperature profiles, and hydrocarbon generation and maturation profiles. The geologic framework follows a cross section from Clarey and Thompson (2010, Fig. 2–5). Kinetic values for hydrocarbon maturation are from Lewan (1985) for the Phosphoria Formation, and the IES Tertiary coal kinetics are from the Petromod® software database. The Petromod 12 version was used to identify and delineate stratigraphic horizons, assign age and facies characteristics (lithology, compaction constant, porosity reduction during burial), and define the petroleum system. Modeled results suggest that potential source rocks, such as the Mesaverde Group, have re-entered the hydrocarbon window (Fig. 6.13b).

Migratory pathways for oil and gas were modeled across the RSU(Fig. 6.13c, d). These models suggest that hydrocarbons generated from source rocks generally migrate up-dip across the RSU, and if hydrocarbons were generated from the Phosphoria they could migrate along the contact with the Weber Sandstone (Fig. 6.13c, d). These models also suggest that hydrocarbons generated in adjacent basins could migrate into the RSU, as suggested by USGS petroleum systems analyses (Roberts et al. 2005) (Fig. 6.13c, d).

The burial model and 1-D profile of the RSU #1 study site suggest that the targeted reservoirs reached temperatures and pressures approaching zeolite facies metamorphism at maximum burial depths. The 1-D geochemical models show that

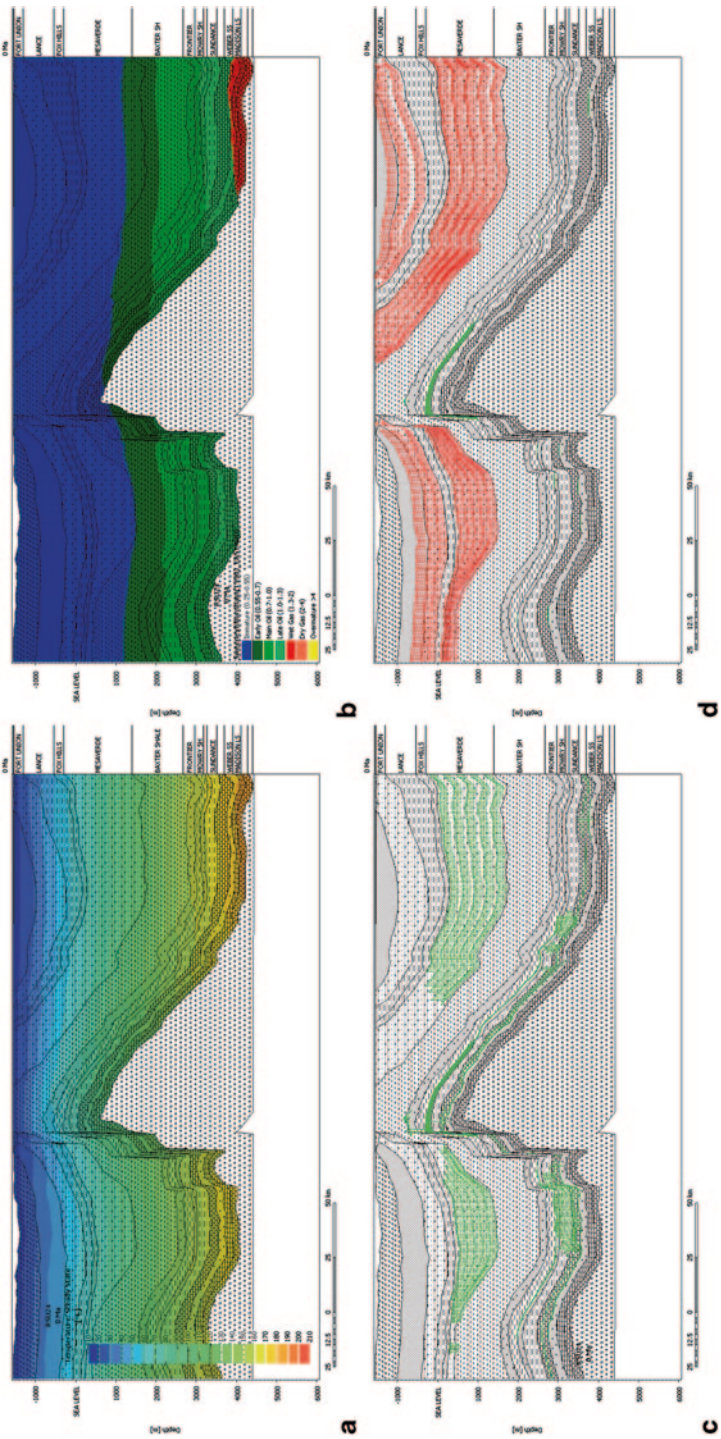


**Fig. 6.13** (**a**) Regional 2-D thermal model across the RSU and adjacent basins. Profile is west to east. (**b**) Regional 2-D hydrocarbon generation model displaying vitrinite correlations across the RSU and adjacent basins. Profile is west to east. (**c**) Oil generation and migration model across the RSU and adjacent basins. Profile is west to east. (**d**) Gas generation and migration model across the RSU and adjacent basins. Profile is west to east

recent denudation and late-stage uplift has lifted much of the RSU #1 stratigraphic column back into the hydrocarbon window.

Regional 2-D geochemical models indicate that source formations currently have the potential to generate hydrocarbons both locally and regionally, and that hydrocarbon migration pathways are generally up-dip. Though seismic and petrophysical data do not indicate that the study site is currently storing hydrocarbons, the influence and presence of hydrocarbons should be evaluated with regard to water treatment strategies.

## 6.7 Conclusions

The interpretation of data from the RSU #1 well indicates that intervals within the Paleozoic Weber Sandstone and Madison Limestone at the study site have porosity and permeability favorable for $CO_2$ injection. The porosity in both formations is largely a by-product of diagenetic alteration, specifically dolomitization, mineral cementation and dissolution, and thermal chemical sulfate reduction. There were multiple episodes of diagenesis throughout the burial history of both formations, and dissolution of calcite and mineralization of anhydrite are identified as potential analogs for geochemical reactions associated with $CO_2$ injection. Both reservoirs have prime porosity and permeability zones focused near the top of distinct lithofacies: the upper section of Weber eolianites and the upper section of Madison dolostones. Of the two potential reservoirs, the Madison has greater porosity and permeability.

Measured displacement pressures, pore magnitudes, mineralogy, and porosity and permeability analysis indicate that the lower Triassic section, Amsden Formation, and upper limestone lithofacies of the Madison can seal injected $CO_2$ within underlying reservoirs. In addition, regional data from producing oil and gas fields suggests that these seals are laterally continuous and are overlain by additional Cretaceous and Jurassic seals.

Profile modeling of the burial history of the RSU indicates that maximum burial took place during the Tertiary and was followed by rapid denudation. This modeling also shows that the denudation placed potential source rocks within the hydrocarbon generation window. Further 2-D temperature and geochemical modeling of the RSU and adjacent basins indicates that several potential source formations have re-entered the hydrocarbon window, and that produced hydrocarbons could migrate upward into the RSU. This should be a consideration in the future selection of $CO_2$ injection zones and water treatment scenarios.

Detailed analysis of core from targeted reservoirs and seals has allowed CMI researchers to fully characterize the lithology, mineralogy, depositional history, porosity, geologic heterogeneity, digenetic episodes and analogs, displacement pressures, and the burial and geochemical history of the RSU #1 study site. These data indicate that the Madison and Weber formations can store $CO_2$, and associated sealing units can effectively trap injected fluids. Data from this chapter was used to populate numerical $CO_2$ injection simulations at the study site.

## 6.8 Continuing Work

Work on the study site has been a collaborative effort among university, private, state, and industrial partners and researchers. Some of the on-going geologic characterization work, specifically graduate research overseen by professors in the University of Wyoming Geology and Geophysics Department, is pertinent to the geologic assessment of any sequestration study. Dr. Erin Campbell-Stone is working to characterize structural deformation, stress vectors, faults and fractures, and mechanical properties of reservoirs and seals, and to fully characterize sealing lithology. Upon completion, these studies will be integral to engineering and injection scenarios, and to defining the mechanical integrity of reservoirs and seals. Dr. James Myers is working on the completion of a storage-related risk assessment of the study site that will be used to characterize the potential for manmade leakage pathways. Dr. John Kaszuba is working on benchtop testing of geochemical reactions between reservoir rocks, seal rocks, brine, and $CO_2$ to further define potential water/rock reactions. He is also working to analyze surface and soil gases to provide baseline data for future sequestration monitoring. CMI researchers also continue to expand on the work presented here, and are currently focusing on the regional geologic characterization of the reservoirs and seals in southwest Wyoming.

## References

Akram M, Bakar ZA (2007) Correlation between uniaxial compressive strength and point load index for salt-range rocks. Pak J Eng Appl Sci 1:1–8

Boggs JR (2000) Principles of sedimentology and stratigraphy, 3rd ed. Merril, Toronto

Bachu S (2002) Sequestration of $CO_2$ in geological media in response to climate change: road map for site selection using the transform of the geological space into $CO_2$ space. Energ Convers Manage 43:87–102

Bachu S (2008) $CO_2$ storage in geological media: role, means, status and barriers to deployment. Prog Energ and Combust Sci 34:254–273

Bachu S, Stewart S (2002) Geological sequestration of anthropogenic carbon dioxide in the Western Canada sedimentary basin: suitability analysis. J Can Petrol Technol 41(2):32–40

Becker TP, Lynds R (2012) A geologic deconstruction of one of the world's largest natural accumulations of $CO_2$, Moxa arch, southwestern Wyoming. AAPG Bull 96(9):1643–1664

Bowker KA, Jackson WD (1989) The Weber Sandstone at Rangeley Field, Colorado. In: Sandstone Reservoirs. Rocky Mountain Association of Geologists, pp 65–80, 310–311

Clarey K, Thompson M (2010) Chapter 2, Study area. In: Copeland D, Ewald M (eds) Available groundwater determination [Greater Green River Basin]. Technical memorandum prepared for the Wyoming Water Development Commission by the Wyoming State Geological Survey et al. Wyoming State Geological Survey, Laramie, pp 2-1–2–36

Cole RD, Mullen CE (1992) Sedimentologic reservoir characterization of Tensleep Sandstone, South Casper Creek Field, Wyoming. In: Rediscover the Rockies. Wyoming Geological Association 43rd Annual Field Conference Guidebook, pp 121–137

Decker DE, Barker KR, Bucher GJ, Heasler HP (1980) Preliminary Heat Flow and Radioactivity Studies in Wyoming. J Geophys Res Solid Earth V 85:311–321

Dott RH (1964) Wacke, graywacke and matrix; what approach to immature sandstone classification? SEPM J Sediment Res 34(3):625–632

Downey MW (1994) Hydrocarbon seal rocks, Pt II, Essential elements. In: The petroleum system – from source to trap. American Association of Petroleum Geologists Memoir 60, pp 159–164
Edman JD, Surdam RC (1984) Diagenetic history of the Phosphoria, Tensleep and Madison Formations, Tip Top Field, Wyoming. In: Surdam RC, McDonald DA (eds) Clastic diagenesis American Association of Petroleum Geologists Memoir 37, pp 317–345
Ehrenberg SN, Eberli GP, Keramati M, Moallemi SA (2006) Porosity-permeability relationships in interlayered limestone-dolostone reservoirs. AAPG Bull 90(1):91–114
Embry AF, Klovan JE (1971) A late Devonian reef tract on Northeastern Banks Island, NWT. Canadian Petroleum Geology Bulletin 19:730–781
Faure GF, Mensing TM (2005) Isotopes: principles and applications, 3rd edn. Wiley, Hoboken, New Jersey
Folk RL (1959) Practical petrographic classification of limestone. AAPG Bull 43(1):1–38
Folk RL (1962) Spectral subdivision of limestone types. In: Ham WE (ed) Classification of carbonate rocks – a symposium. American Association of Petroleum Geologists Memoir 1, pp 62–84
Folk RL (1965) Petrology of sedimentary rocks (reprint). The Walter Geology Library, University of Texas. http://www.lib.utexas.edu/geo/folkready/entirefolkpdf.pdf
Fryberger SG (1990) Role of water in eolian deposition. In: Fryberger SG et al (eds) Modern and ancient eolian deposits: petroleum exploration and production. Rocky Mountain Section, Society of Economic Paleontologists and Mineralogists, pp 5-1–5–11
Fryberger SG, Schenk CJ (1988) Pin stripe lamination: a distinctive feature of modern and ancient eolian sediments. Sediment Geol 55(1):1–15
Fryberger SG, Abdulkader MA-S, Clisham TJ (1983) Eolian dune, interdune, sand sheet, and siliciclastic sabkha sediments of an offshore-prograding sand sea, Dhahran area, Saudi Arabia. AAPG Bull 67(2):280–312
Gilfillan S, Ballentine CJ, Holland G, Blagburn D, Lollar BS, Stevens S, Schoell M, Cassidy M (2008) The noble gas geochemistry of natural $CO_2$ gas reservoirs from the Colorado Plateau and Rocky Mountain provinces, USA. Geochim Cosmochim Acta 72(4):1174–1198
Heasler HP (1985) Geothermal resources of Wyoming. Department of Geology and Geophysics, University of Wyoming, Laramie. Map, scale 1:500.000
Ingram GM, Urai JL, Naylor MA (1997) Sealing processes and top seal assessment. Norw Petrol Soc Special Publ 7:165–174
James NP (1984) Swallowing-upward sequences in carbonates. In: Walker RG (ed) Facies models. Geological Association of Canada, Geoscience Canada reprint series1, p. 213–228
Katz DA (2008) Early and late diagenetic processes of Mississippian carbonates, northern US Rockies. PhD Dissertation, University of Miami
Kupecz J, Gluyas J, Block S (1997) Reservoir quality prediction in sandstones and carbonates: an overview. In: Kupecz J, Gluyas J, Block S (eds) Reservoir quality prediction in sandstones and carbonates. AAPG Memoir 69:vii–xxiv
Krushin JT (1997) Chap. 3, Seals, traps, and the petroleum system. AAPG Memoir 67:31–47
Krynine PD (1948) The megascopic study and field classification of sedimentary rocks. J Geol 56(2):130–165
Krystinik LF (1990a) Early diagenesis in continental eolian deposits. In: Fryberger SG et al (eds) Modern and ancient eolian deposits: petroleum exploration and production. Rocky Mountain Section, Society of Econonmic Paleontologists and Mineralologists, pp 8-1–8–11
Krystinik LF (1990b) Diagenesis in ancient eolian sandstone. In: Fryberger SG et al (eds) Modern and ancient eolian deposits: Petroleum exploration and production. Rocky Mountain Section, Society of Economic Paleontologists and Mineralogists, pp 14-1–14–14
Land LS (1980) The isotopic and trace element geochemistry of dolomite: the state of the art. In: Zenger DH et al (eds) Concepts and models of dolomitization. Society of Economic Paleontologists and Mineralogists Special Publication 28, pp 87–110
Lewan MD (1985) Evaluation of petroleum generation by hydrous pyrolysis experiments. Phil Trans R Soc 315:123–134
Lewan, M.D., Ruble T.E. , (2002) Comparison of Petroleum generation kinetics by isothermal hydrous and non-isothermal open-system pyrolysis. Organic Geochemistry, v. 33, 1457-1475

Love JD, Christiansen AC, Ver Ploeg A J (1993) Stratigraphic chart showing Phanerozoic nomenclature for the state of Wyoming. Wyoming State Geological Survey Map Series 41 (MS–41)
Machel HG (1998) Bacterial and thermochemical sulfate reduction in diagenetic settings; old and new insights. Sediment Geol 140(1–2):143–175
Mankiewicz D, Steidtmann JR (1979) Depositional environments and diagenesis of the Tensleep Sandstone, eastern Big Horn Basin, Wyoming. SEPM Special Publ 26:319–336
Mazzullo SJ, Harris PM (1992) Mesogenetic dissolution: its role in porosity development in carbonate reservoirs (1). AAPG Bull 76(5):607–620
Middleton GV (1961) Evaporite solution breccias from the Mississippian of southwest Montana. J Sediment Res 31(2):189–195
Moore DA (1984) The Tensleep Formation of the southeastern Big Horn Basin, Wyoming. In: The Permian and Pennsylvanian geology of Wyoming. Wyoming Geological Association 35th Annual Field Conference Guidebook, pp 273–279
Murray RC (1964) Origin and diagenesis of gypsum and anhydrite. J Sediment Res 34(3):512–523
Papale P, Neri A, Macedonio G (1998) The role of magma composition and water content in explosive eruptions – 1. Conduit ascent dynamics. J Volcanol Geoth Res 87:75–93
Passchier CW, Trouw RAJ (2005) Microtectonics, 2nd edn. Springer Verlag, Amsterdam and New York
Peters KE (1986) Guidelines for evaluating petroleum source rock using programmed pyrolysis. AAPG Bull 70(3):318–329
Reading HG, Levell BK (1996) Controls on the sedimentary rock record. In: Reading HG (ed) Sedimentary environments: processes, facies and stratigraphy. Blackwell Science: 5–36
Roberts LN, Lewan MD, Finn TM (2005) Burial history, thermal maturity, and oil and gas generation history of petroleum systems in the southwestern Wyoming province, Wyoming, Colorado and Utah. In: U.S. Geological Survey Southwest Wyoming Province Assessment Team: Petroleum systems and geologic assessment of oil and gas in the southwestern Wyoming province, Wyoming, Colorado, and Utah. U.S. Geological Survey Digital Data Series DDS-69–D
Robinson L (1992) Brady North; Brady South. In: Wyoming oil and gas fields symposium, Greater Green River Basin and Overthrust Belt. Wyoming Geological Association, Casper, pp 56–62
Sando WJ (1974) Ancient solution phenomena in the Madison Limestone (Mississippian) of north central Wyoming. U.S. Geol Surv J Res 2:133–141
Sando WJ (1977) Stratigraphy of the Madison Group (Mississippian) in the northern part of the Wyoming-Idaho overthrust belt and adjacent areas. In: Heisey EL et al (eds) Rocky Mountain thrust belt geology and resources. Wyoming Geological Association 29th Annual Field Conference Guidebook, pp 173–177
Scholle PA, Ulmer-Scholle DS (2003) A color guide to the petrography of carbonate rocks: grains, textures, porosity, diagenesis. AAPG Memoir 77
Searl A (1989) Saddle dolomite: a new view of its nature and origin. Mineral Mag 53(pt 5):547–555
Siebert RM (1985) The origin of hydrogen sulfide, elemental sulfur, carbon dioxide, and nitrogen in reservoirs. Timing of siliciclastic diagenesis: relationship to hydrocarbon migration. Sixth Annual Research Conference, Gulf Coast Section, Society of Economic Paleontologists and Mineralogists Foundation Program and Abstracts, pp 30–31
Smith LB Jr, Eberli GP, Sonnenfeld M (2004) Sequence stratigraphic and paleogeographic distribution of reservoir-quality dolomite, Madison Formation, Wyoming and Montana. In: Grammer GM et al (eds) Integration of modern and outcrop analogs in reservoir modeling. American Association of Petroleum Geologists Memoir 80, pp 67–92
Sonnenfeld MD (1996) Sequence evolution and hierarchy within the lower Mississipppian Madison Limestone of Wyoming. In: Longman MW, Sonnenfeld MD (eds), Paleozoic systems of the Rocky Mountain region. Rocky Mountain Section, Society of Economic Paleontologists and Mineralologists Rocky, Tulsa, Oklahoma, pp 1–28
Surdam RC, Jiao J (2007) The Rock Springs Uplift – an outstanding geological $CO_2$ sequestration site in southwest Wyoming. Wyoming State Geological Survey Challenges in Geologic Resource Development No. 2

Sweeney JJ, Burnham AK (1990) Evaluation of a simple model of vitrinite reflectance based on chemical kinetics. AAPG Bull 74:1559–1570
Teinturier S, Pironon J (2004) Experimental growth of quartz in petroleum environment. Part I: procedures and fluid trapping. Geochim Cosmochim Acta 68(11):2495–2507
Welte DH, Horsfield B, Baker DR (eds) (1997) Petroleum and basin Evolution. Springer-Verlag Germany, 535 p
Westphal H, Eberli GP, Smith LB, Grammer GM, Kislak J (2004) Reservoir characterization of the Mississippian Madison Formation, Wind River Basin, Wyoming. AAPG Bull 88(4):405–432
WOGCC (2013) Wyoming Oil and Gas Conservation Commission http://wogcc.state.wy.us/

# Chapter 7
# Utility of 3-D Seismic Attribute Analysis and VSP for Assessing Potential Carbon Sequestration Targets on the Rock Springs Uplift, Southwest Wyoming

**Yuri Ganshin and Ronald C. Surdam**

**Abstract** One of the most important steps in characterizing a geologic $CO_2$ storage site is the construction of 3-D volumes of seismic attributes. Once these seismic attribute volumes are constructed, key attributes can be correlated to core and well-log observations and analytical measurements. These correlations allow standardizations and extrapolations of a variety of determinative rock/fluid characteristics from the well bore of the stratigraphic test well out into the 3-D seismic survey volume, creating a realistic 3-D model of storage reservoirs and seals. This chapter discusses the technique for performing the tasks required to make the seismic attribute volumes; the correlations between key rock/fluid parameters and seismic attributes; and the crucial extrapolations from 1-D core, log, and VSP observations out into 3-D seismic attribute space. Topics covered include surface seismic specifications, seismic data processing, seismic resolution, vertical seismic profiling (VSP) and data acquisition, comparison of VSP and surface seismic data, comparision of VSP and well data (geologic property modeling), horizon mapping and depth conversion, seismic attributes, seismic interpretation, and qualitative permeability determined from seismic attribute analysis.

## 7.1 Introduction

This study began with a year devoted to seismic data conditioning for reflected compressional wave (P-wave) analysis and seismic attribute computation. A 25-square-mile 3-D seismic dataset was processed through pre-stack time migration (PSTM) at Geokinetics and through further processing at the Carbon Management Institute at the University of Wyoming. Automatic velocity analyses were applied at each

Y. Ganshin (✉) · R. C. Surdam
Carbon Management Institute Laramie, University of Wyoming, Laramie, USA
e-mail: yganshin@uwyo.edu

R. C. Surdam
e-mail: rsurdam@uwyo.edu

R. C. Surdam (ed.), *Geological $CO_2$ Storage Characterization,*
Springer Environmental Science and Engineering, DOI 10.1007/978-1-4614-5788-6_7,
© Springer Science+Business Media New York 2013

common-depth-point (CDP) location and resulted in a high-density interval-velocity volume. This velocity volume served as the basis for 3-D geologic modeling and the time-to-depth transformation of the seismic attributes. We computed multiple morphological and physical seismic attributes for the whole seismic volume: among possible attributes we estimated and analyzed were instantaneous and RMS amplitude, instantaneous and mean frequency, spectrally decomposed amplitudes, coherency and curvature, dip azimuth and dip magnitude, velocity, and acoustic impedance.

Petrophysical analysis of wireline well logs allowed us to identify different lithologic types (e.g., sandstones, shales, dolostones) and the corresponding grain matrix properties (density and P-wave velocity) for pre-Cretaceous strata in the RSU #1 well. On the bases of the strong porosity-velocity correlations established for the major sandstone and carbonate reservoir rocks, we were then able to use seismically derived velocities in building porosity distribution models.

We then turned to the characterization of the Mississippian Madison Limestone and its confining layers. To gain more information on regional heterogeneity, we performed multiresolution spectral decomposition analysis of 3-D seismic data. Several domains with diverse seismically derived properties were identified within the reservoir rocks. These domains possibly reveal different tectonic or sequence stratigraphic features. To date, sparse well control within the study area has precluded geologic verification of these seismically defined domains. There are 34 deep wells in the seismic project area, some with well-log and core data available. However, only one of these wells, the RSU #1, penetrates the targeted deep saline aquifers.

Our specific objective was to apply selected seismic attributes to aid in quantifying the reservoir properties and lateral continuity of $CO_2$ sequestration targets. We systematically tested more than a dozen seismic attributes and found that curvature, interval velocity, acoustic impedance, iso-frequency amplitude, and mean frequency were particularly useful in mapping structural trends, performing seismic facies analysis, and imaging porosity distributions within the target horizons. A one-dimensional geologic-property model was developed for the target interval (10,500–12,700 ft (3,200–3,870 m) below KB (kelly bushing) at the RSU #1 well). The model is based on petrographic core facies determinations and petrophysical relationships, and is consistent with VSP observations through synthetic trace modeling. The geologic property model yields estimates of reservoir thickness, porosity, and permeability.

Depth-converted impedance slices show similarity and consistency that suggest that impedance can be useful as a guide for propagating porosity and permeability throughout the 3-D model. Seismic impedance inversion is an inherently underconstrained problem that does not allow the use of rigorous joint inversion methods. In the absence of a true inverse, a unique and reliable solution can be obtained by defining a set of physical constraints that must be satisfied by the resulting images. In this study we used a method for constructing a “synthetic log” volume that is free of subjectively selected user parameters and utilizes the automatically computed, high-density interval velocity volume that can be directly compared to a recorded sonic log. A comparison of synthetic log sections and horizon maps with

the conventional seismic data from which they were derived clearly demonstrates improved resolution and understanding of the subsurface geology. This allows remapping into porosity units those stratigraphic intervals that are not affected by significant lithologic variation and are characterized by strong velocity-porosity correlation. The resulting porosity maps for the deep saline aquifers are reasonable; however, their accuracy has not been tested, due to sparse well control.

Permeability and porosity are key parameters in reservoir flow simulation. When an impedance-porosity transform is available (as for the Weber Sandstone and Madison Limestone units), porosity can be inferred from acoustic impedance. However, the permeability that necessarily has to be supplied in reservoir modeling seems to be the most elusive of reservoir properties and remains extremely uncertain. In this study, we used a spectral decomposition technique to derive a relative qualitative attribute from seismic data. Based on theoretical predictions for vuggy, dual-porosity carbonate rocks, the normal-incident P-wave reflection should produce low-frequency amplitude resonance for highly permeable reservoir rocks. Correspondingly, we have designed a permeability attribute that is proportional to the difference between the low-frequency spectral amplitude component along the middle Madison reflection horizon and the high-frequency component, and is scaled by the sum of the two components. The resultant permeability attribute maps reveal an extended area of increased permeability south and southwest of the RSU #1 well.

## 7.2 Surface Seismic Specifications

The Jim Bridger 3-D and 3-C is a wide-azimuth seismic data set acquired in Sweetwater County, southwestern Wyoming, using vibroseis as a source and three- component digital sensors covering an area of about 25 $mi^2$. The survey was designed as a baseline study for possible $CO_2$ injection and was acquired by Geokinetics Service Co., Houston, Texas, during November 2010. The cross-spread shooting method used for data acquisition implies multiple perpendicular source and receiver lines (Fig. 7.1). The fold of stack obtainable by this method is relatively high and uniform (averages 30× after CMP binning). However, orthogonal shooting tends to create a non-uniform distribution of offsets, a pattern that is not related to geologic variations and may "leak" into the data, creating an artificial *acquisition footprint*. Regularly oriented gaps in the source and receiver lines due to surface conditions (power plant, ponds, cliffs, roads) (Fig. 7.1) may also introduce acquisition artifacts into the data.

The CMP bin, 110 ft in both the X and Y directions, is less than one-quarter the minimum wavelength ($\lambda_{min}$=500 ft) and ensures that the data is not spatially biased. The final CMP fold map, Fig. 7.2a, shows a maximum fold of 48× at the center of the survey. The middle part of the survey area is characterized by a maximum offset (source-to-farthest-receiver distance) of 19,800 ft, which is adequate for imaging geologic targets in 10,000–15,000 ft depth range. CMP fold coverage and source-to-receiver offset distributions are the most important survey design parameters that affect reflected signal strength and allow lithology/fluid predictions to be made. A rectangular area (3×3 mi)

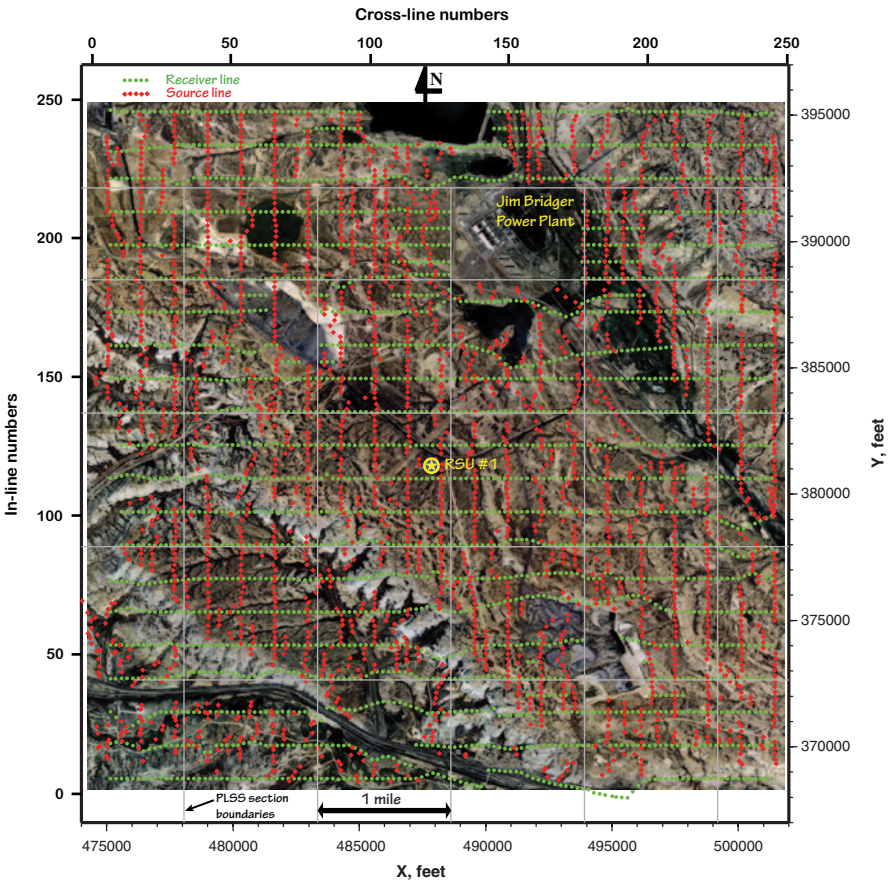


**Fig. 7.1** Jim Bridger 3-D seismic survey. (Source (shotpoint) and receiver layout overlying infrared satellite image)

centered on the RSU #1 well is shown in Fig. 7.2b. This area is characterized by the maximum and most uniform CMP-fold and maximum-offset distributions, enabling the most favorable conditions for seismic imaging of the subsurface geology. The work presented here will concern only compressional (P-wave) data recorded on the vertical component. Table 7.1 summarizes the survey design details.

## 7.3 Seismic Data Preprocessing

Geokinetics did the basic preprocessing of the reflection seismic data. The purpose of data preprocessing was twofold, (1) pre-stack data conditioning for an automated, high-density velocity analyses on CMP gathers and (2) stacked amplitude volume preparation that is suitable for volumetric and horizon attribute analyses. The processing flow used by the Geokinetics processing team is summarized in Table 7.2.

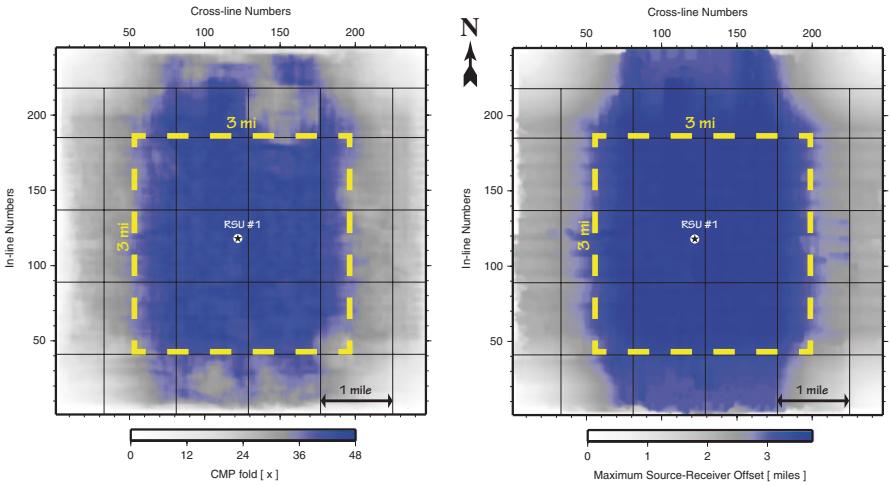


**Fig. 7.2** Jim Bridger 3-D seismic survey. (**a**) CMP fold coverage map and (**b**) maximum source-receiver offset map. The dashed rectangle (3×3 mi) centered around the RSU #1 well, outlines seismic image area where the data is most reliable

The quality of the resultant PSTM stacked amplitude volume is illustrated in Fig. 7.3. Strong and coherent reflections in the time range 1.4–2.2 s correspond to geologic interfaces in the depth range approximately from 7,000 to 13,000 ft below the ground surface at the RSU #1 well location. This means that the structure of the targeted reservoir and sealing stratigraphic units can be imaged with the reflected P-waves. However, an isochrone slice at 2.08 s two-way travel time (horizontal section, Fig. 7.3) clearly demonstrates the acquisition footprint (grid of east-west and north-south stripes) present in the stacked amplitude volume. The theory of Kirchhoff migration assumes that the input data are regularly sampled in X, Y, and offset so that the resulting wavefield can be correctly reconstructed during imaging. If we have a gap in the input, there will be an amplitude anomaly in the output proportional to the gap size. As is seen in Fig. 7.3, the acquisition footprint intensifies northeast from the test well, in the areas with the largest gaps in the shooting scheme (Fig. 7.1). Especially, the seismic data quality deteriorates in the areas corresponding to rough topography and the power plant facilities. Obviously, the footprint removal routine of the Geokinetics processing flow (Step 32) (Table 7.2) didn't do the job completely, thus leaving a potential problem for the subsequent data processing.

## 7.4 Seismic Resolution

Seismic resolution refers to the level of detail that can be seen in seismic data (sections and maps); it is commonly defined as the ability to distinguish separate features. In reflection seismology, the "measuring unit" is the wavelength (λ). Vertical resolution is approximately the one-quarter wavelength λ/4, while lateral resolution is commonly considered to be the larger of the half-wavelength λ/2 or the bin size

**Table 7.1** Survey acquisition details

| | |
|---|---|
| Record length; Sample rate | 6 s, 2 ms |
| Geophone type | SVSM 3-component digital sensor |
| Total geophone stations | 2,514 |
| Total source points | 2,541 |
| Number of live receiver lines | 8 (144 live stations per line) |
| Receiver group and source interval | 220 ft |
| Receiver and source line spacing | 1,320 ft |
| Maximum source to receiver offset | 19,800 ft |
| X, Y coordinate projection | NAD 27, Clarke 1866 |
| X, Y coordinate state plane | Wyoming West Central |
| Survey size | 25.16 $mi^2$ |
| Source type | I/O AVH IV Vibroseis, 4 over flag |
| Sweep parameters | Linear 6–110 Hz |
| Sweep tapers | Linear 300–300 ms |

(110 ft in our survey). In order for two close reflective interfaces to be clearly distinguished, they have to be about one-quarter wavelength apart (Rayleigh Criterion for vertical resolution). Lateral resolution on migrated volumes is difficult to quantify because it depends on many factors, especially the presence of noise. The half-wavelength criterion originates from the sampling theorem that at least two samples per apparent wavelength must be obtained in order to recognize separate features.

Wavelength is obtained from the relationship $\lambda = v/f$, where v is velocity and f is seismic frequency. In the context of our study, the velocity is the compressional wave (P-wave) speed in the vicinity of the target level, which we take as the Weber through Madison interval (2.0–2.2 s on the seismic time sections). As is common in reflection seismology, we use the weighted mean spectral frequency as revealed by continuous Fourier analysis. The dominant seismic frequency in the RSU #1 well vicinity at the target level averages 30 Hz (Fig. 7.4). We take this value as a good representation of the dominant frequency in the entire target area. The average velocity (estimated from smoothed sonic log and detailed seismic interval velocity analysis) of the Weber through Madison section at RSU #1 is about 18,000 ft/s, giving a dominant wavelength of 600 ft. Thus the *vertical resolution* is 150 ft, and the *lateral resolution* is 300 ft. The following assumptions apply to the use of these values: (1) a seismic signal has constant frequency, (2) seismic waves propagate at constant velocity, and (3) the level of background seismic noise is negligible.

## 7.5 Vertical Seismic Profiling (VSP)

A Vertical Seismic Profile is generated by a seismic energy source located at the surface and receivers lowered into a borehole. This type of survey enables calibration of surface seismic data recorded in time-domain to the borehole geology directly, since in VSP we know both *depth* and *time* to seismic reflections. With VSP, geoscientists can rely on accurate, detailed physical measurements rather than on assumptions, predictions, speculations, or synthetic calculations.

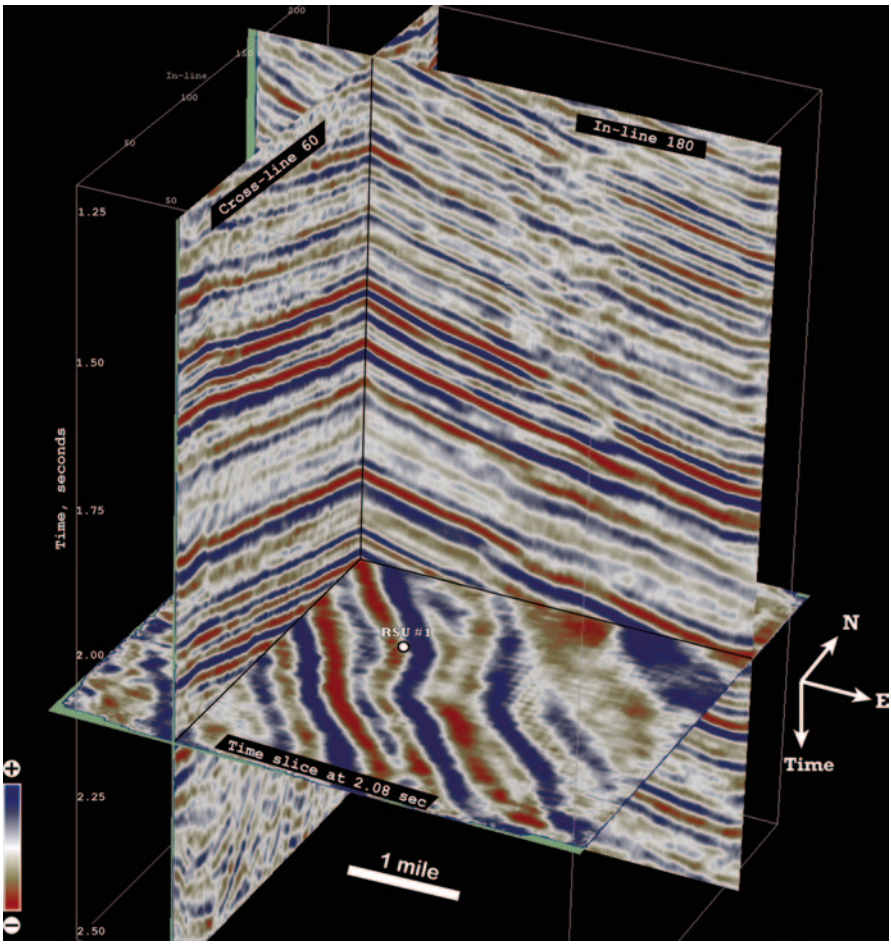


**Fig. 7.3** 3-D seismic amplitude volume displayed in three orthogonal slices. Note an overall northeast dip of reflectors and acquisition footprint pattern in the time slice (regular grid of stripes trending south-north and east-west). Projection of the RSU #1 well location on the time slice is shown approximately

### *7.5.1 VSP Data Acquisition*

Baker Hughes, Inc., Houston, Texas, conducted a zero-offset VSP in the RSU #1 well. The objectives of the VSP Survey were to:

- provide time-depth information and subsurface velocity function.
- generate VSP corridor stack to tie vertical seismic with the 3-D surface seismic.

At the time of the survey, the well was drilled to a depth of 12,810 ft and was cased to 9,750 ft. All measured depths are referenced to the kelly bushing (KB) elevation of 6,860 ft above Mean Sea Level (MSL). The ground elevation at the wellhead is

**Table 7.2** Processing flow (Geokinetics Service Company)

| | |
|---|---|
| 1. | Reformat field records to internal Geokinetics format |
| 2. | Geometry application, trace edits, and 3-D grid application |
| 3. | Convert data to minimum phase |
| 4. | Refraction statics analysis and application |
| 5. | Spherical divergence correction (true amplitude recovery) |
| 6. | Surface consistent gain correction |
| 7. | Noise removal and attenuation (MBNA for deconvolution analysis only) |
| 8. | Surface consistent deconvolution |
| 9. | Noise removal and attenuation (MBNA) |
| 10. | First pass velocity analysis (1×1-mi interval) |
| 11. | Surface consistent residual statics, first pass |
| 12. | Second pass velocity analysis (0.5×0.5-mi interval) |
| 13. | Surface consistent residual statics, second pass |
| 14. | Accelerometer Integration |
| 15. | Noise removal and attenuation (MBNA) |
| 16. | Surface consistent residual statics, third pass |
| 17. | Mute analysis |
| 18. | Post-stack migration |
| 19. | Preparation for PSTM (pre-stack time migration): Common offset bin analysis |
| 20. | Preparation for PSTM: Sort to common offset bins |
| 21. | Preparation for PSTM: Common offset noise attenuation (FXY deconvolution) |
| 22. | Preparation for PSTM: Optimize common offset trace population |
| 23. | PSTM on select target lines for migration velocity analysis |
| 24. | PSTM velocity analysis (0.5×0.5-mi interval) |
| 25. | PSTM on entire 3-D volume using smoothed migration velocity from step 24. Kirchhoff algorithm was used on each common offset gather with the following parameters: 110 ft×110 ft output grid size, 60º migrated dip limit, 30,000-ft migration aperture limit (diameter) |
| 26. | Common offset noise attenuation (FXY deconvolution) |
| 27. | Sort to CMP |
| 28. | Residual velocity analysis (0.5×0.5-mi-interval) |
| 29. | CMP noise removal and attenuation (MBNA) |
| 30. | CMP trim statics |
| 31. | Apply NMO, mute, and stack |
| 32. | Footprint removal |
| 33. | Post stack noise attenuation |
| 34. | Time variant band-pass frequency filter (1500–2500 ms → 6–12–60–70 Hz) |

6,841.2 ft above MSL. The source used for the VSP survey was two LRS-315 seismic vibrators positioned 285 ft from the wellhead at 6,837 ft elevation above MSL. A 12-s, linear upsweep, with 8–80 Hz frequency range was used for seismic wave generation. A two-level, three-component ASR receiver tool was used to record the seismic wavefield. The depth range of recording was 500–12,800 ft below KB. Data was gathered at 76 down-hole receiver stations. There were 360 files recorded during the survey. The time length of the correlated output data was 6 s with a 2 ms sampling rate.

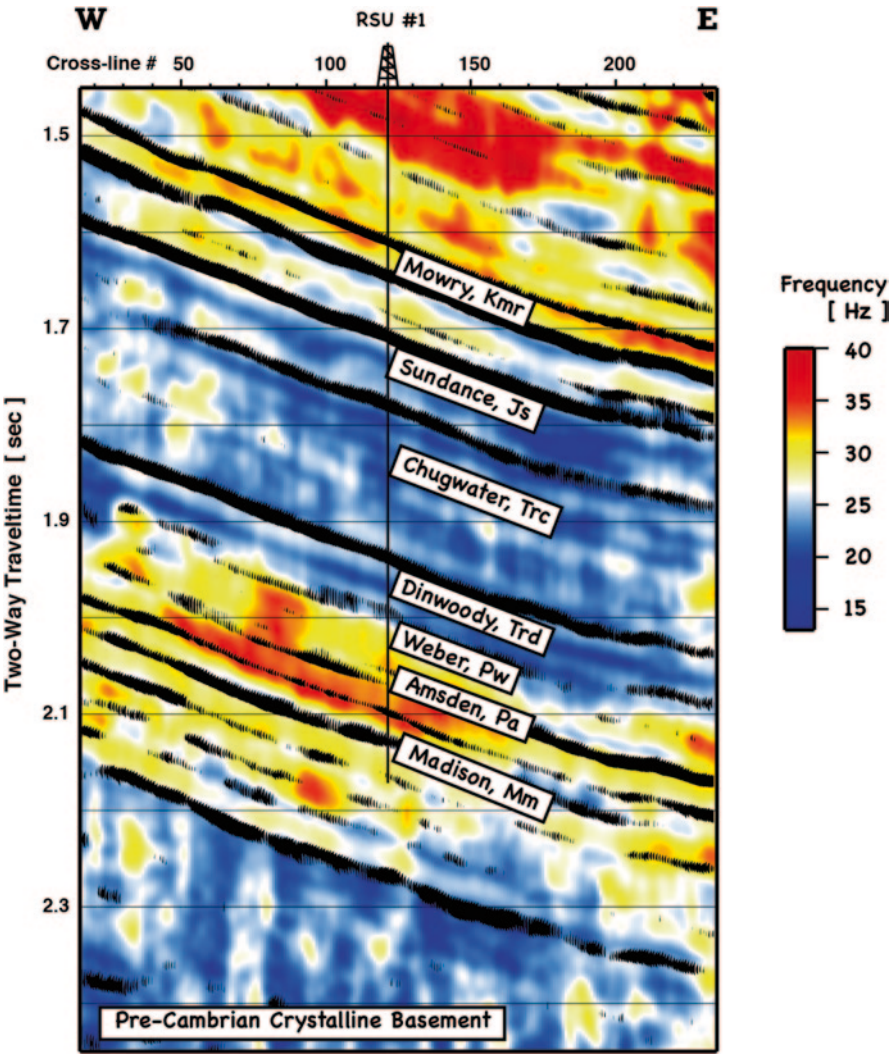


**Fig. 7.4** Interpreted west–east profile through the mean frequency volume at the RSU #1 well location. Seismic frequency image is co-rendered with seismic amplitude section (negative excursions are shown in black)

### *7.5.2 VSP Data Processing*

The Baker Hughes processing team processed the seismic data acquired in the well through the following steps.

**Editing and Stacking** The three-component data was format-converted and referenced to the elevation of the source. The down-hole geophone traces for each depth

level were edited as necessary and then stacked using a median summation technique. The stacked record was arranged according to increasing depth, and the first arrival times were picked. A time/depth curve was computed from the first break times. The accuracy of the depth sensor was checked by comparing the first arrival times during the *down* and *up* runs of the tool.

**Velocity Computations** The observed first arrival times at all depth levels were converted to vertical times, and then referenced to the Seismic Reference Datum (SRD = 7,500 ft above MSL), using a correction velocity of 9,000 ft/sc. These time-depth pairs were then used as input data for final velocity computations, which gave *average, RMS*, and *interval* velocities. [Tabulated and displayed in Electronic Supplementary Material, ESM Plate1]

**Acoustic Log Calibration** The VSP-derived velocity function was calibrated with the acoustic log over the 1,780 ft–12,717-ft measured depth interval below KB. (At each depth level the time difference (drift) between the VSP times and the acoustic times are computed. The drift time is added to all acoustic log values over the calibration interval. This effectively shifts the acoustic log to match the VSP-generated velocity values.)

**Synthetic Seismogram** An acoustic impedance log was computed by multiplying the calibrated acoustic log by the density log. A reflectivity series, showing primaries only (without transmission-loss effects), was derived from the acoustic impedance log. The reflectivity series was then convolved with a seismic wavelet to produce a synthetic seismogram. [The synthetic seismograms, having different frequency content and polarity, are shown in ESM Plate 2]

**Wavefield Separation** VSP wavefields consist of a superposition of the downward and upward traveling (or simply downgoing and upgoing) wavetrains. Both the downgoing and upgoing wavetrains are useful, but need to be separated before they can be studied and utilized. In this study, the wavefields were separated using a median filter. [The downgoing and residual upgoing wavefields are shown, respectively, in panels 2 and 4 of ESM Plate 3] The unwanted wave modes left in the dataset after the wavefield separation were removed by applying a seven-point median filter and zero-phase 10–80-Hz bandpass filter. [The upgoing wavefield at two-way time and the enhanced upwaves are displayed, respectively, in panels 5 and 6 of ESM Plate 3]

**Downwave Deconvolution** The VSP downwave deconvolution shapes the input source wavelet to zero phase and collapses upcoming multiple reflections generated above the depth of the deepest receiver. A 400-ms trace-by-trace deconvolution operator was computed and then applied to the downgoing and upgoing wavefields followed by a zero phase 10–80-Hz bandpass filter. [The deconvolved downgoing and upgoing wavefields are shown respectively in panels 3 and 7 of ESM Plate 3.]

**Corridor Window and Corridor Stack** The basic computed product of the VSP is known as a *corridor stack*, which in appearance resembles a synthetic seismogram. In reality it is a vastly superior well correlation tool, because it contains actual

seismic reflections comparable with the surface seismic data. In this study, a narrow time window was designed to include only primary events with similar reflection character on enhanced deconvolved upwaves. The data that lies outside the stacking corridor was muted [panel 9 of ESM Plate 3]. The resultant muted traces were then stacked to one trace, called a *VSP corridor stack trace*. This stacked trace is repeated eight times for visual clarity and represents the seismic response at the RSU #1 wellbore. [The 10–80-Hz filtered corridor stack, with normal and reverse polarity, is shown, respectively, in panels 10 and 11 of ESM Plate 3]

**L-Plot Correlation Display** An L-Plot correlation display ties together the depth domain and time domain properties of the VSP with well-log data and synthetic seismograms. The VSP deconvolved upwaves are displayed with linear depth-of-trace spacing. Well-log data displayed in the depth domain are plotted above the upwaves panel using the same depth scale. In this way, the reflection events can be directly correlated in the depth domain with the well-log data [ESM Plate 4]. In addition to the depth-domain data, time-domain synthetic seismograms and well logs converted to time domain are also displayed using the same time scale as that of the deconvolved upwaves. This allows time domain event correlation between the well-generated data and VSP data [ESM Plate 4].

**Interpolated Time-Depth Table** The most basic information that we want from the VSP is a seismic time-to-depth relationship. This information was acquired by just picking the first-breaking energy of the direct arrivals. [The time-interpolated results (with 2-ms sample rate) are presented in tabular form in ESM Plate 5 for the two depth-reference points—the seismic reference datum and the kelly bushing of the RSU #1 well.]

## 7.6 Comparison of VSP and Surface Seismic (CMP) Data

The deconvolved and enhanced upgoing events show that the VSP wavefield separation and processing has been fairly successful. The seismic reflections corresponding to the major stratigraphic intervals are continuous across all traces (panel 8, ESM Plate 3). One can easily determine the time of the geologic interface that created the upgoing event by following the characteristic feature of this event up to its intersection with the time axis.

One of the main reasons for acquiring VSP data is to improve the analysis of CMP reflection data. In order to accomplish this objective there should be reasonable correlation between the two data sets. Figure 7.5 illustrates the surface P-wave reflection seismic data with the VSP inserted at the tie point (RSU #1 well location). The overall reflectivity trends of the surface reflection data and VSP data match well. The reflectivity is moderate within the interlayered sand and shale Cretaceous and Jurassic strata and very low within the shale-rich strata of the underlying Triassic formations (Fig. 7.5). The top and base of the major sealing horizon is obvious on the CMP data and the VSP; the relative amplitudes are also comparable

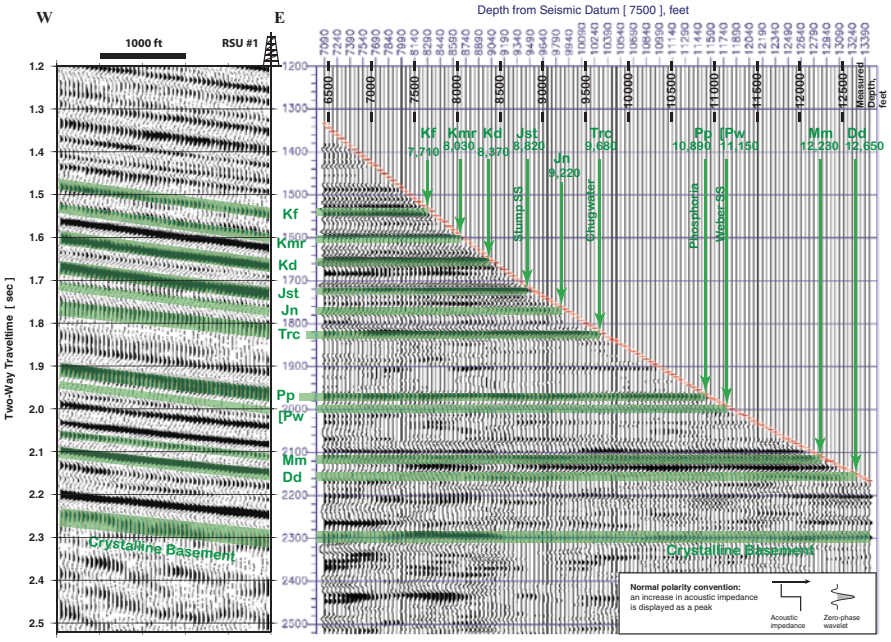


**Fig. 7.5** (**a**) Interpreted west–east profile (*left* panel) through the PSTM seismic volume with the RSU #1 well located on the east side. (**b**) upgoing (reflected) VSP wavefield displayed at the same time (*vertical*) scale as the surface seismic. *Green* highlights the interpreted seismic reflections

(1.83–1.97 s time interval in the VSP panel on Fig. 7.5). Going down in time, the reflectivity increases considerably within the carbonate-rich units of the Paleozoic Phosphoria, Weber, and Madison formations. At the RSU #1 well location, the top of the Weber Sandstone corresponds to a seismic trough at 2.0-s two-way traveltime (TWTT). The Madison Limestone is imaged with a reflection just below 2.1-s TWTT (Fig. 7.5). The seismic trough at a TWTT of 2.13 s at the well location corresponds to the low-impedance middle Madison unit.

The higher frequency content of the VSP data is evident. The prestack VSP traces (VSP panel on Fig. 7.5) show a series of distinct reflections just above and below the Triassic shales, whereas the same reflections on CMP data are overlapping and complex. This difference in frequency content allows for laterally continuous features to be better resolved in CMP data than in VSP data.

## 7.7 Comparison of VSP and Well Data (Geologic Property Modeling)

Forward modeling was used to gain insights into the geometrical and physical relationships between seismic reflection amplitude and rock/reservoir properties derived from the well logs and core. The modeling was limited to the one-dimensional

case along the test well-bore axis within a depth interval that includes the major deep saline aquifers (10,500–12,700 ft below KB). The density and velocity values used in the modeling are based loosely on physical properties of the major target reservoir rocks (the Weber and Madison Formations) and confining units. The perturbed geologic models were convolved with seismic wavelet (10–80-Hz band pass) to produce simple, zero-offset acoustic models of the expected seismic response. These acoustic responses were further compared with the VSP stacked trace using a basic cross-correlation technique. Pearson's cross correlation coefficient was used as a criterion to validate the match between the modeled and observed data. The modeling iteration was stopped after obtaining a fairly strong $(r = 0.86)$ correlation coefficient between the synthetic response and VSP trace. For comparison, the starting model values (original velocity/density logs) produce a synthetic trace that correlates moderately with the observed VSP trace $(r = 0.69)$. The resultant geologic property model contains estimates of reservoir thickness, porosity, and permeability. [The tabulated property model and the corresponding synthetic trace, as well as the wireline log data and the VSP trace, are displayed in ESM Plate 6]

## 7.8 Horizon Mapping and Depth Conversion

This section reports results of using 3-D seismic (P-wave) data and RSU #1 well control to map Lower Cretaceous and pre-Cretaceous formations in the study area. The primary storage candidates on the Rock Springs Uplift are deep saline aquifers in the Pennsylvanian Weber and Mississippian Madison Formations. Hence, we focus on these formations as well as the overlying shaly horizons in the Triassic Chugwater and Dinwoody Formations and Cretaceous Mowry Shale (Fig. 7.6). In general, deep saline aquifers are excellent potential $CO_2$ storage candidates, but significant pre-storage characterization is required to determine their suitability.

Due to low seismic vertical resolution (~150 ft at target depth), reservoir and seal properties away from the well were characterized largely along seismic horizons rather than vertically. Any kind of seismic vertical profile interpretation will inevitably face the upscaling problem of fine-scale lithologies. This means that, for example, the velocity anomaly associated with high-porosity, thin sandstone bed will be smoothed (upscaled) and reduced through velocity averaging with the surrounding lithologies. On the contrary, horizon-based attribute variations are less dependent on lithologic change and can be more readily related to variations in physical rock properties and fluid content.

Figure 7.7 shows our deep structure mapping workflow. Structure mapping is a process of tracking identical wavelet features that correspond to a specific geologic formation (bedding plane) throughout the seismic volume. Formation tops were first tied to the 3-D seismic volume on the basis of our calibration of seismic data with VSP observations (Fig. 7.5). We then created synthetic seismograms of various polarity and bandpass combinations using sonic and density logs from the RSU #1 well. The results of the VSP-seismic calibration were further verified with these synthetic seismograms; this assured the fidelity of the seismic horizon interpretation completed for the well.

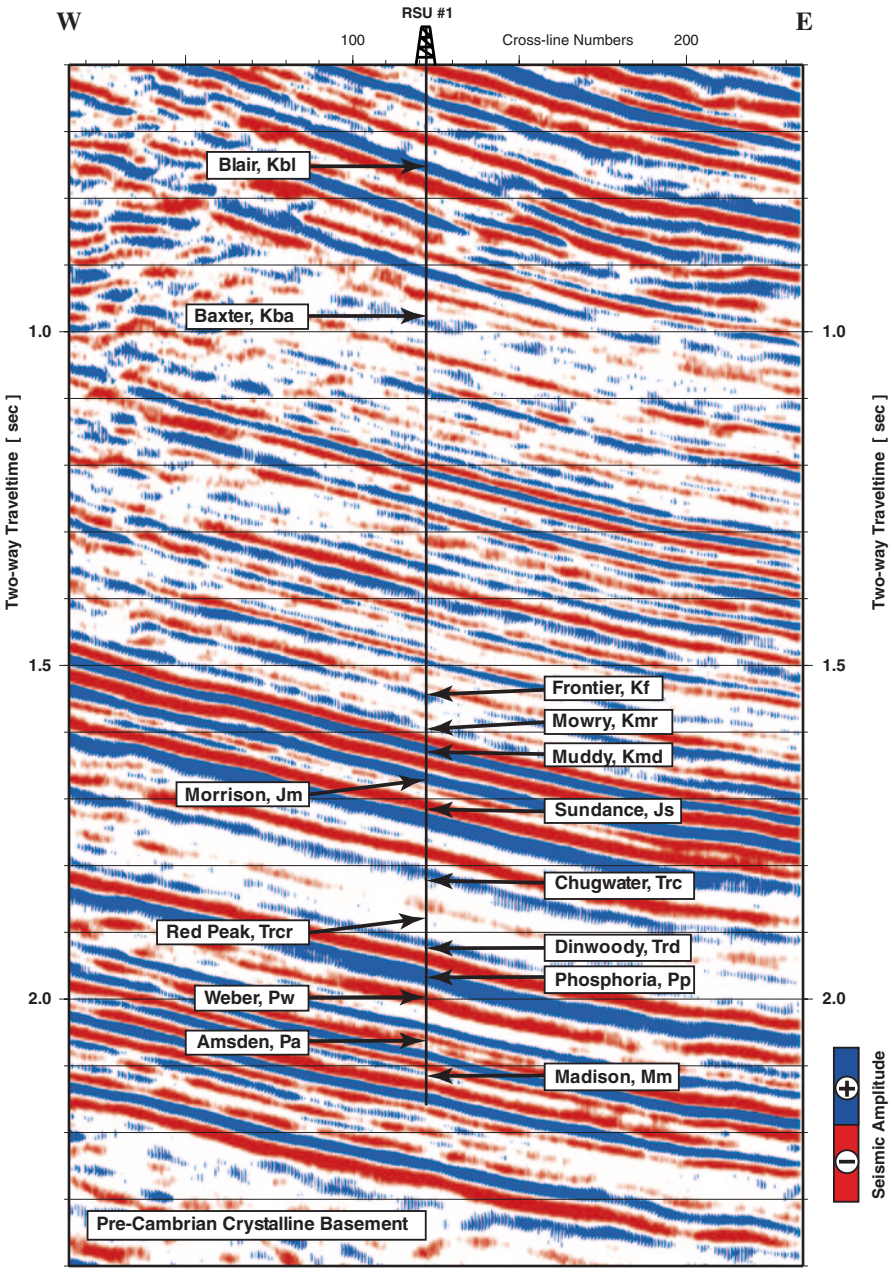


**Fig. 7.6** West–east vertical section through the seismic amplitude volume at the RSU #1 well location. Geologic interpretation (formation tops with symbols) was based on integrated analysis of the logs, VSP, and surface seismic data

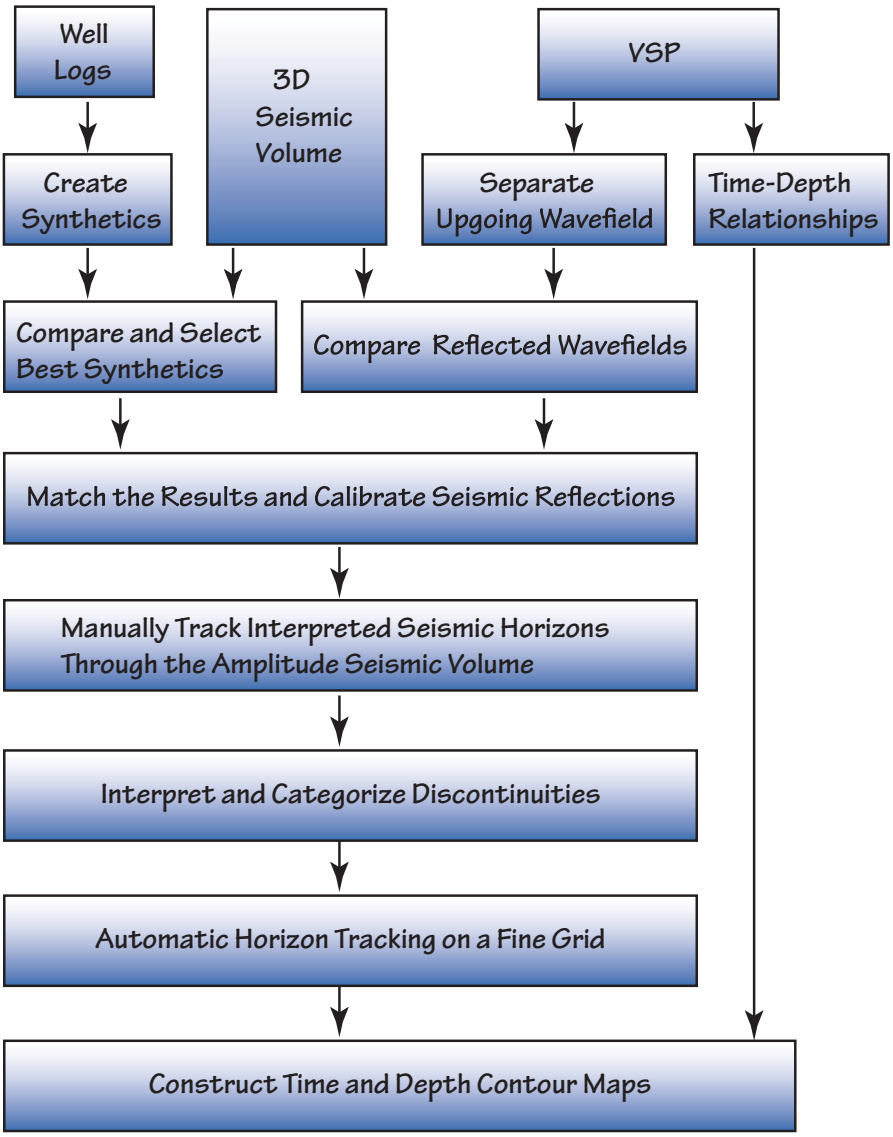


**Fig. 7.7** Block-diagram for structural mapping workflow

Depth structure maps were generated using the time-depth conversion table derived from VSP observations at the RSU #1 well. To achieve uniform depth gridding, the results of the transformation were interpolated using a cubic spline algorithm. To match with well observations, the depth-transformed horizon picks were corrected to the KB datum.

Most interpreted horizons appear to be laterally continuous throughout most of the survey area, but this continuity ceases in the Jim Bridger Power Plant area in

the northeast and the I-80 interstate in the southwest parts of the area (Fig. 7.1). Acquisition footprints due to irregular coverage compromise the seismic images beneath these areas: any subsurface mapping and interpretation of discontinuities in these areas is doubtful with respect to possible $CO_2$ migration pathways. Both time structure and depth structure maps of the Frontier through Madison Formations (youngest to oldest in Fig. 7.6) were produced and interpreted. For reservoir characterization purposes, it is useful to extract seismic attributes not coincident with the tracked horizon but conformal to it and shifted by a chosen number of milliseconds. These horizons, usually called the *phantom horizons*, were also used in this study.

## 7.9 Seismic Attributes

In this study, seismic attributes are recognized as measures of seismic data that lead to better understanding of the subsurface and thus reduce uncertainty in geologic interpretations. Seismic attribute analysis can play a significant role in reservoir property prediction by revealing information that may not be evident in the standard amplitude data. A suite of properties of a seismic trace (such as amplitude, phase, and frequency) can be crossploted with the corresponding well logs to show the relation between the two types of data. The attributes selected on the basis of close correlation with petrophysical properties can be effective in estimating reservoir properties away from the well.

Seismic attributes can be divided into two broad categories, those that help quantify the *geometrical* component of seismic data and those that help quantify the *physical* component of seismic data. The geometrical (morphological) attributes help extract information on reflector dip, azimuth, and terminations, which can be related to faults, karst, and fractures. The physical attributes (seismic event magnitude, frequency and waveform characteristics, propagation velocity) can be related to lithology, porosity, reservoir thickness, or pore-fluid content.

In this study, both stacked amplitude volume and prestack CMP gathers were used to perform the basic seismic measurements necessary to derive attributes. The basic parameters that were measured are travel-time, amplitude, waveform, and frequency. From this information it was possible to compute:

- Velocity—from measurements of delay times and amplitudes along seismic reflections
- Time and depth maps of important horizons—from travel-times (and velocity information)
- Contrast in physical rock properties (velocity and density)—from measurements of reflection amplitude
- Locations of faults and intense fracturing—from discontinuities in seismic reflectivity patterns
- Dip magnitude and azimuth of beddings—from travel-time differences along a reflecting surface
- Stratigraphic changes—from instantaneous frequency measurements

The goal of this seismic attribute computation was to provide quantitative information interpretable in terms of porosity and permeability necessary for fluid flow simulation within these target reservoirs. Locating impermeable barriers to flow as well as assessing the integrity of confining layers was also within the scope of our research. The attempt was made to not overwhelm the study by calculating seismic attributes that lack geologic significance or have no clear physical meaning. Thus, our foremost criterion for selecting attributes was a physical basis for correlation between properties measured in the well bore and the core. For example, interval velocity has a physical correlation with porosity: as velocity increases, porosity typically decreases. Therefore, the scope of this study comprised only the few attributes discussed below.

### *7.9.1 Definition and Computation of Basic Attributes Used in This Study*

**Reflection Strength** Reflection strength is one of the basic outputs of the complex seismic-trace analysis first described by Tanner et al. (1979). The complex trace $C(t)$ is defined as:

$$C(t) = S(t) + \mathrm{i}Q(t), \tag{7.1}$$

where *S(t)* is the seismic trace, $i = \sqrt{-1}$, and *Q(t)* is the quadrature of the seismic trace (Hilbert-transformed component of *S(t)*, or 90° phase shifted *S(t)*).

The reflection strength is the modulus of the complex function:

$$R(t) = \sqrt{S^2(t) + Q^2(t)}, \tag{7.2}$$

where $R(t)$ represents the envelope of the seismic trace signal that is related directly to the acoustic impedance contrast. It may depict an individual interface contrast or, more likely, the combined response of several interfaces. Reflection strength is a physical attribute that can be used to discriminate major changes in lithology and deposition environment, sequence boundaries, pore-fluid content, unconformities, and lateral changes due to porosity variations and faulting.

**RMS Amplitude** RMS amplitude is another measure of seismic trace reflectivity that is measured within a time window. Specifically, it is the square root of the sum of the squares of the amplitudes within the window interval and is independent of amplitude sign. It is conventionally used as a direct hydrocarbon indicator in the search for “bright spots” or “dim spots.” The attribute indicates anomalous amplitude zones and may serve as a lithology and porosity indicator. In this study, we used a 50-ms window for the RMS amplitude calculation, which is equivalent to a 20-Hz signal.

**Mean Frequency** The mean frequency, actually the weighted mean frequency, is derived from a spectrally decomposed seismic trace (generated through a Fourier Transform in this study). The weighted mean is similar to the arithmetic mean, and

is used in situations where instead of each sample frequency contributing equally to the final average, some frequencies contribute more than others. The degree of contribution (weight) is defined by the spectral amplitude value. In the digital signal processing literature the weighted mean frequency is often termed the spectral centroid frequency (or simply the centroid frequency) because it indicates the location of the "center of mass" of the spectrum. Formally, the weighted mean frequency $F$ of a set of frequencies $\{f_1, f_2,\ldots,f_n\}$ with weights $\{a_1, a_2,\ldots, a_n\}$ is the quantity:

$$F = \frac{\sum_1^n a_i f_i}{\sum_1^n a_i}. \tag{7.3}$$

**Bandwidth Attribute** The bandwidth attribute is estimated as the variance with respect to the centroid frequency (standard deviation) that indicates the width of the amplitude spectral distribution $\{a_1, a_2,\ldots, a_n\}$ over a band of frequencies $\{f_1,f_2,\ldots,f_n\}$. Both the bandwidth and the mean frequency are statistical measures of seismic wavelets and relate to various physical conditions of energy transmission, such as bed thickness variation, change in seismic facies, relative absorption characteristics, and variable pore fluid content. The final seismic frequency content is a comprehensive result of many factors prominent among which are the source wavelet, the lithologic properties of the strata, and the application of seismic data processing.

**Spectral Decomposition** The spectral decomposition algorithm, used in this study for several attribute computations, is based on a Short Time Fourier Transform (STFT). The general Fourier Transform relates a waveform (a function of time) to its spectrum (a function of frequency). If the time band of the waveform is multiplied by a constant, then the bandwidth of the spectrum is divided by the same constant. This property is an expression of the Heisenberg uncertainty principle with respect to seismic processing. Simply speaking, if one wants to gain better resolution in time, he must pay for it with resolution reduction in the frequency domain. The spectral decomposition software used in this study implements STFT by choosing frequency-domain windows as opposed to time-domain windows. STFT can be seen as the filtering of a signal through a set of fixed bandwidth band-pass filters whose center frequencies are distributed uniformly along the frequency axis. To bypass the Heisenberg uncertainty principle, we implemented a sort of multiresolution STFT by combining (or averaging) individual spectrograms with different time-frequency resolutions. The *spectral amplitude attribute* that is often referred to in this study is the iso-frequency magnitude resulting from spectral decomposition. This attribute is always computed normalized to the maximum magnitude value.

**Velocity Attribute** The velocity attribute was derived from stacking-velocity analysis applied to prestack CMP gathers. High-density, high-resolution interval velocity volume was calculated using an automated routine that performed velocity analysis at every time sample and at every CMP location. For the homogeneous earth with planar interface, the travel-time curve of the reflections for various offsets between source and receiver is conventionally calculated using:

$$t^2 = t_0^2 + \frac{x^2}{v_{stack}^2}. \tag{7.4}$$

At every CMP gather (with source-receiver offsets $x$) and every time sample $t_0$, a velocity spectrum is calculated for a set of trial stacking velocities $v_{stack}$ using semblance as a coherency measure. The semblance value reflects how well the model path corresponding to the trial velocity $v_{stack}$ fits the actual trajectory of reflected signals in the data. The semblance $S$, as defined by Neidell and Taner (1971), is given by the equation:

$$S = \frac{\sum\left[\sum a(t,x)\right]^2}{N\sum\sum a(t,x)^2} \tag{7.5}$$

The inner sums in this equation are over $N$ traces having various offsets $x$, while the outer sums correspond to time smoothing with the operator centered at time index $t$. Semblance is maximized when the values $a(t, x)$ do not vary with index $x$. Time smoothing is necessary to increase semblance stability for coherent events located close to zero-crossings. Within the computer code, the velocity spectrum is estimated with relatively few trial velocities (25 in this study) and is fitted to a Gaussian curve:

$$f(x) = b + pe^{(-0.5(x-c)/w)^2}, \tag{7.6}$$

where $b$, $p$, $c$, and $w$ represent the *base* (semblance shift), *peak* (peak semblance value), *central point* (central or mean velocity value), and *width* (velocity standard deviation) of the Gaussian distribution, respectively. A velocity distribution fitted with the Gaussian formula enables precise and unambiguous estimation of the peak semblance value and the corresponding stacking velocity. When computation over the trace samples ($t_{0i}$) is complete, the resultant stacking velocity function is smoothed with an operator whose size is proportional to the time $t_0$ and velocity standard deviation (parameter $w$ in the Gaussian curve equation) at that time. The smoothed stacking velocity function is further processed using Dix's formula (1955) to produce interval velocities that can be readily interpreted in terms of lithology, pore-fluid or porosity variations.

**Acoustic Impedance (AI)** Acoustic impedance (the product of the rock density and velocity) is a basic physical property of rocks that is commonly calculated from corresponding density and sonic well logs. AI has the benefit over seismic reflectivity data in that it is a layer property that can be directly related to lithology and to changes due to fluid production/injection. A problem arises when the well-log data is not adequate to image the targeted subsurface. Additionally, reservoir heterogeneity may require more control than from existing well locations alone: in this case (including our study), an acoustic impedance volume can be created through inversion of the P-wave seismic volume.

Our inversion scheme followed an approach known as *synthetic sonic log* section (volume) generation, described first by Lindseth (1979). In outline, the inversion operations included (1) computation of an approximate reflection coefficient

sequence using post-stack seismic amplitude volume, (2) inversion of the reflection coefficients to band-limited, high-frequency velocity coefficients, and (3) use of (2) to modulate low-frequency velocity components, obtained from high-density reflection velocity analysis, to produce synthetic sonic logs. If the subsurface density distribution is known (or estimated), it can be incorporated in this scheme to produce synthetic acoustic impedance logs. In our study, we verified the accuracy of the inverted synthetic volumes by comparing them with the corresponding logs from the RSU #1 well. The P-wave *synthetic sonic log attribute* obtained in this study combines the features of stacked amplitude and interval velocity volumes. Namely, it derives its volumetric property (rather than an interface property) from the interval velocity field, and it derives better resolution from the amplitude volume. Inverted data, a layer property, is a more intuitive tool that allows one to tie lithology and fluid presence to seismic data.

**Seismic Coherency** Seismic coherency is a measure of the consistency of seismic reflections. In other words, it quantifies the similarity in appearance and shape of seismic waveforms from trace to trace. Where events are similar, coherency is high. Low-coherent, discontinuous reflections may be caused by variation in structure, stratigraphy, lithology, porosity, and pore fluids. The semblance-based coherence attribute estimation in this study was performed on post-stack amplitude data. The basic algorithm of coherency estimation can be summarized as follows: for each point in a 3-D seismic volume, compare the waveform of adjacent traces over a short vertical window. At the same time, uniformly tilted strata should not affect the coherency computation.

This was accomplished in the following steps. First, for each volume sample, a small reflection surface ($3\times3$ horizontal samples) is identified around the central sample. The surface coordinates at trace intersections are calculated by finding the maximum cross-correlation value over a vertical analysis window between the central trace and each surrounding trace. A parabolic fitting technique is used for precise time shift (tilt) identification that corresponds to the maximum value of the cross-correlation between the discrete trace samples. The inter-trace tilt effect is removed and the semblance value is calculated using Eq. 7.5 for the spline-interpolated trace samples. For the coherence attribute calculation, the inner sums in the semblance equation (Eq. 7.5) are over $N$ tilt-corrected traces $x$, while the outer sums correspond to time smoothing with the operator centered at time index $t$. As with semblance-based velocity analysis, time smoothing is necessary to increase semblance stability for coherent events located close to zero-crossings.

**Curvature Attribute** In a general sense the seismic curvature attribute is a measure of how deformed a reflecting surface is at a particular location. The more deformed the surface, the larger its curvature. With respect to geometry, curvature is defined as the reciprocal of the radius of curvature, and correspondingly, belongs to the geometrical category of attributes. The suite of curvature attributes utilized in this study, comprises dip magnitude, dip azimuth, maximum and minimum, and strike and dip curvatures. Analysis of these attributes can help remove the effects of regional dip and emphasizes small-scale features such as tight folds, faults, karst, and fractures.

The estimation of volumetric curvature attributes is performed in three stages. First, for each volume sample, a small reflection surface (3 x 3 horizontal samples) is identified around the central sample. The surface Z-positions are calculated by finding the maximum cross-correlation value over a vertical analysis window between the central trace and each surrounding trace. A parabolic fitting technique is used for precise time shift (tilt) identification that corresponds to the maximum value of the cross-correlation between the discrete trace samples. Next, a least-squares quadratic surface Z (X, Y) is fitted to the data within the analysis range. Finally, the set of curvature attributes is computed from the coefficients of the quadratic surface using traditional differential geometry (Roberts 2001). At any point of the surface, the curvature (positive or negative) can be measured at any azimuth. One of these azimuths will yield the largest curvature. This curvature is named the *maximum curvature* and the curvature at the orthogonal azimuth is named the *minimum curvature*. The *maximum* and *minimum curvature* attributes are very effective at delimiting faults and fault geometries, with maximum curvature corresponding to the up-thrown (positive) side of a fault. The curvature attribute extracted in the direction of maximum dip is named the *dip curvature*, while the one extracted in the orthogonal direction (along strike) gives us the *strike curvature*. The last two attributes can be especially useful in examining the local surface morphology and interconnectivity that can help explain buoyancy-driven processes and fluid migration pathways. The curvature attributes described above are lateral second-order derivatives of structural relief components of the seismic time- (or depth)-of-reflection events. This is what makes them so sensitive to subtle structural variations. In contrast, the *dip magnitude* and *dip azimuth* are derived using first-order derivatives, which allows using them as regional structural trend indicators.

## 7.10 Seismic Interpretation

The 3-D seismic data and vertical seismic profiling (VSP) constituted information essential for delineation of structural trends and stratigraphic correlation. Of the available geophysical logs from the RSU #1 well, the $\gamma$-ray, photoelectric factor, resistivity, and neutron porosity logs were primarily useful for general rock/fluid identification and petrophysical analysis. The sonic and density logs were used for porosity and permeability estimation.

### *7.10.1 Method of Interpretation*

A collection of seismic attributes, as described in Sect. 7.9.1, was used for predicting the distribution of physical properties (e.g., porosity, fracture density) of the strata being imaged seismically. It must be understood, though, that most of the links between reservoir properties and seismic attributes are not well established, and that these correlation results may thus be tenuous, questionable, or difficult to explain. Even today, there is a lack of systematic effort by scientists to establish the physical

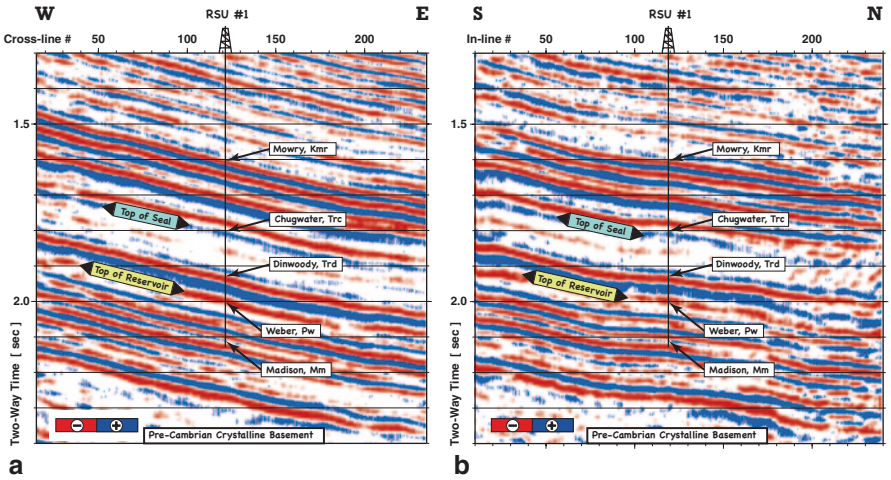


**Fig. 7.8** Interpreted (**a**) west–east and (**b**) south-north vertical sections through the seismic amplitude volume at the RSU #1 well location. Note northeast-dipping reflections on both sections

basis for such relationships, and this is especially true for the Rocky Mountain region. The method used in this study is more qualitative than quantitative. No attempt was made at rigorous numerical modeling; rather, the effort focused on identifying of geobodies (or seismic facies) that share similar attribute properties or a similar set of attribute properties within a seismically imaged volume. These geobodies were calibrated (or tested) with geologic studies and log-derived physical properties.

Attributes-based interpretation takes advantage of the wealth of seismic information available and offers a more efficient way of representing data than conventional methods. Attribute interpretation supplements conventional structural interpretation because the discriminating properties of the attributes may be critically checked for their relevance for a particular structural feature. Therefore, most of the figures presented in this study were produced using blended techniques: for the 2-D vertical sections, derived color-coded attributes are combined (co-rendered) with seismic reflected-amplitude data; and for the map (plan) views, color-coded attribute values are combined with horizon contours. Below, we use vertical sections as the first step toward 3-D interpretation, followed by horizon slices (Sect. 7.10.3).

## *7.10.2 Interpretation—the Use of Vertical Sections*

The study site lies on the east flank of the Rock Springs Uplift, and correspondingly, seismic reflections image the area as a northeast-dipping monocline (Figs. 7.3 and 7.8). Assuming our estimated average P-wave velocity of the target formations to be 18,000 ft/s, the dip ranges from 2 to 8º within the imaged subsurface. The overall strong reflectivity of the subsurface is caused by significant variations in physical rock properties of sediments overlying the crystalline basement (Fig. 7.8). The RSU #1 well was used to identify the main horizons in the interpretation. With

an accuracy of about 20 ms, we were able to track through the seismic time volume the tops of the following units, from top to bottom: the Frontier Formation (*Kf*), Mowry Shale (Kmr), Muddy Sandstone (*Kmd*), Morrison Formation (*Jm*), Sundance Formation (*Js*), Chugwater Formation (*Trc*), Red Peak Member (*Trc*), Dinwoody Formation (*Trd*), Phosphoria Formation (*Pp*), Weber Sandstone (*Pw*), Amsden Formation (*Pa*), and Madison Limestone (*Mm*).

The west-east vertical section with the interpreted formation tops is presented in Fig. 7.6. As is indicated in Fig. 7.8, the top of the major sealing interval coincides with the top of the Chugwater Formation. In the study area, the Chugwater Formation (labeled "Top of Seal" in Fig. 7.8) is composed mostly of seismically transparent, massive rock layers marked by low reflectivity. The seismic reflections intensify as they approach the "Top of Reservoir" interval corresponding to the Weber Sandstone (Fig. 7.8). It is the strong velocity/density contrast between the low-porosity reservoir rocks and the confining layers that increases the intensity of the corresponding reflections.

The RMS amplitude attribute provides better insight into lithologic variations within the strata drilled by the RSU #1 well. Zones of intense reflectivity in Fig. 7.9 are color-coded red and correspond to the following lithologies, from top to the bottom: the Rock Springs coal beds, Mowry Shale and Dakota sandstones, and carbonate rocks interlayered with shales. Blue intervals in Fig. 7.9 correlate with the massive (more uniform and homogeneous) shales, mudstones, and crystalline basement rocks that are almost transparent to the passing seismic energy. For the purposes of our project, it is important to note that an extensive blanket of thick and uniform Chugwater shales overlies the target reservoir rocks (the Weber Sandstone and Madison Limestone).

Seismic interval velocity provides an important clue in lithology identification, porosity distribution, and discrimination of pore fluid properties in subsurface rock/fluid systems. Hence, much effort was put into pre-stack data conditioning for velocity analysis and parameter tuning for an automated velocity computation routine. The resultant interval velocity volume shows great velocity variability in both vertical and lateral slices. Importantly, these seismic velocity variations correlate with lithological units, and do tie with sonic and VSP measurements. Figure 7.10 shows an interpreted west-east profile through the interval velocity volume at the RSU #1 well location. The upper part of Fig. 7.10 (0.4 to ~1.7 s two-way traveltime) images the Cretaceous strata that is characterized by significant velocity fluctuations around the mean value of about 14,000 ft/s. The velocity begins a rapid increase at the base of the Cretaceous rocks and reaches values of 20,000–22,000 ft/s at the top of the Precambrian crystalline basement. The seismically derived vertical velocity distribution agrees well with the trend seen in sonic P-wave velocity (Fig. 7.10).

A pronounced decrease in interval velocity is clearly observed at the base of the Cretaceous-age rocks (blue interval below ~1.6 s two-way traveltime in Fig. 7.10). This reduction in seismic (and also sonic) interval velocity highlights an interval that extends from the top of the Frontier Formation down into the Morrison Formation. The ~1,000 ft of interlayered shales, siltstones, and sandstones shown in Fig. 7.11 contains multiple intervals in which velocity drops below 12,000 ft/s. We interpret this anomalous velocity zone to be related to the generation of hydrocarbons,

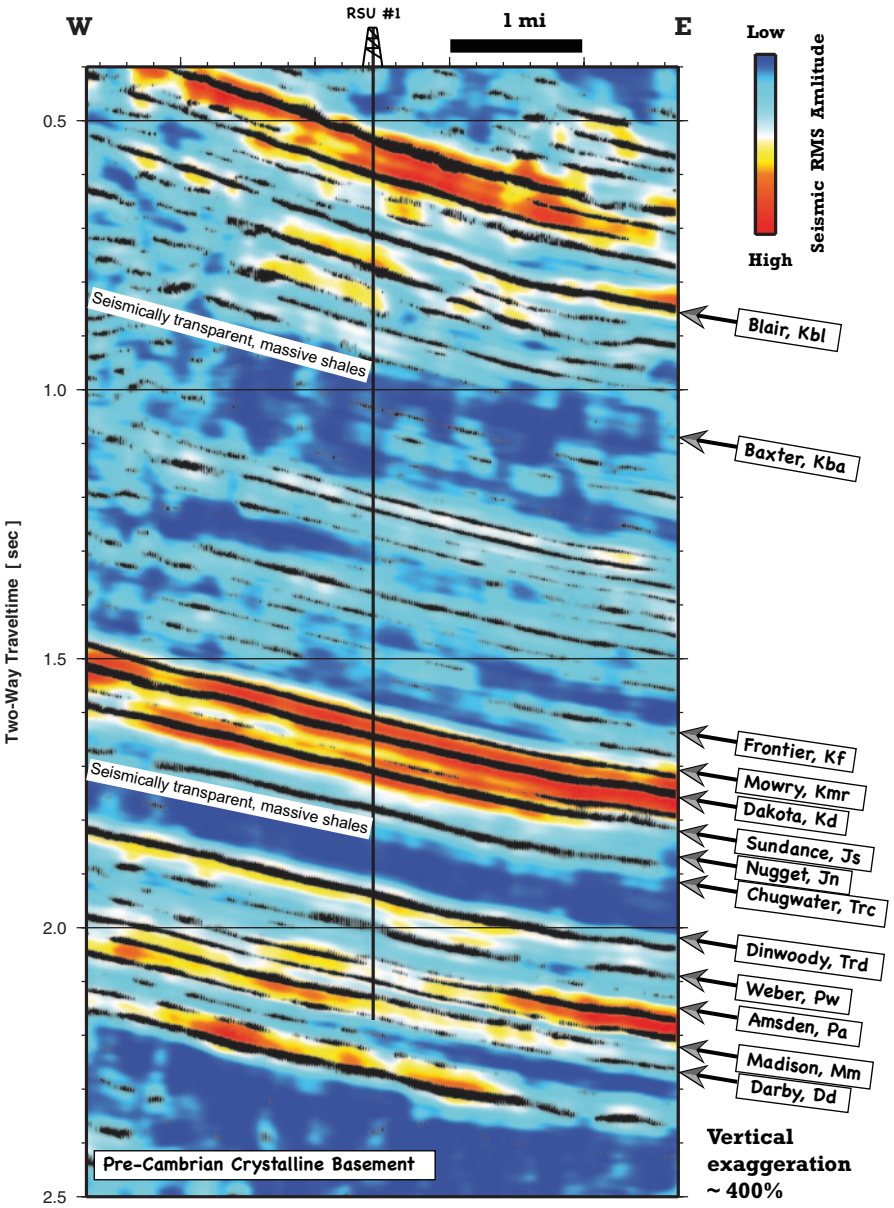


**Fig. 7.9** Interpreted west–east profile through the RMS amplitude volume at the RSU #1 well location. The color-coded RMS-amplitude image is co-rendered with conventional amplitude section (negative excursions are shown in black)

particularly gas, at the time of maximum depth of burial of the source rocks. The Rocky Mountain foreland basins, including the Greater Green River Basin, have undergone a complex geologic history starting with a principal subsidence phase,

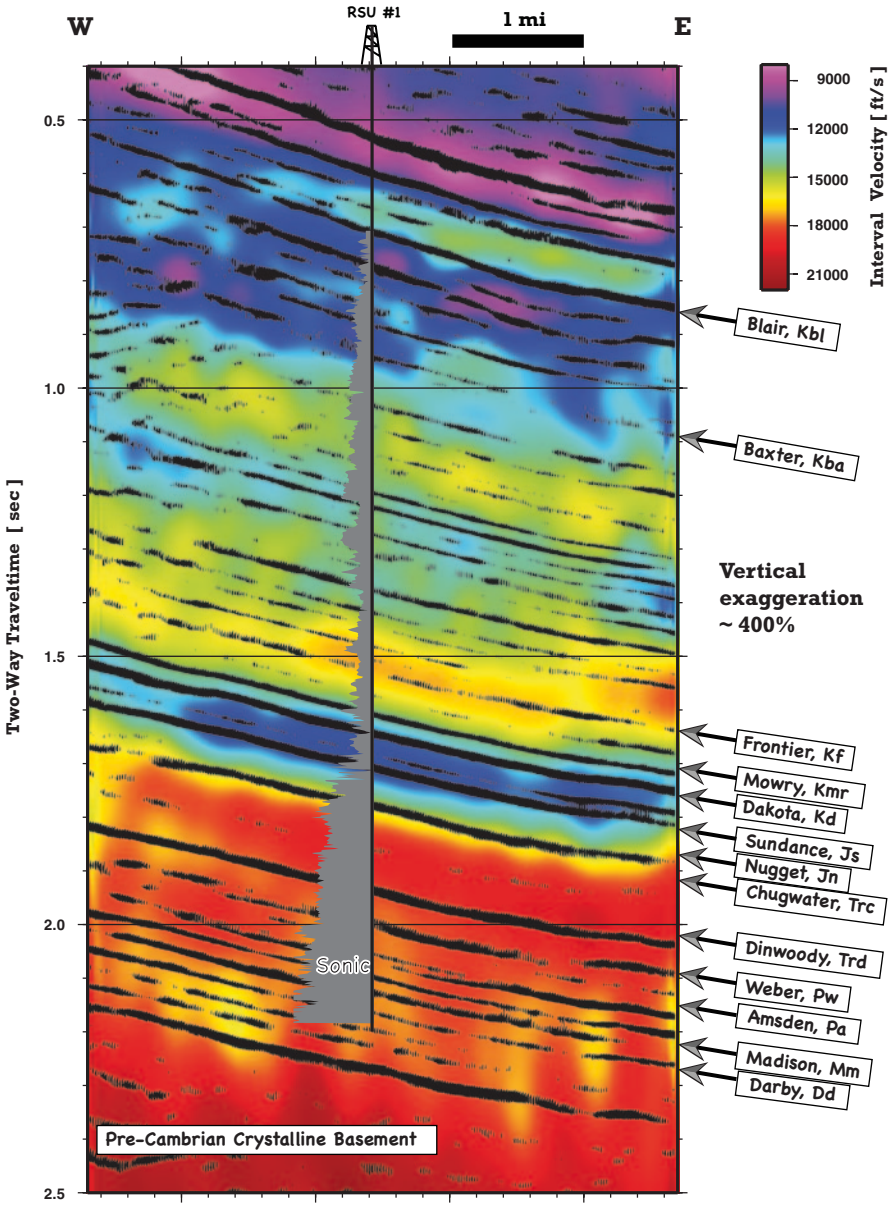


**Fig. 7.10** Interpreted west–east profile through the interval velocity volume at the RSU #1 well location. The color-coded velocity image is co-rendered with seismic amplitude sections. Time-transformed sonic log image (*gray*) is overlaid for velocity comparison

during which most of the basin-filling sediment was deposited, followed by one or more periods of uplift during which substantial amounts of sediment were eroded (Cluff and Cluff 2004). We speculate that gas was generated in the study area within

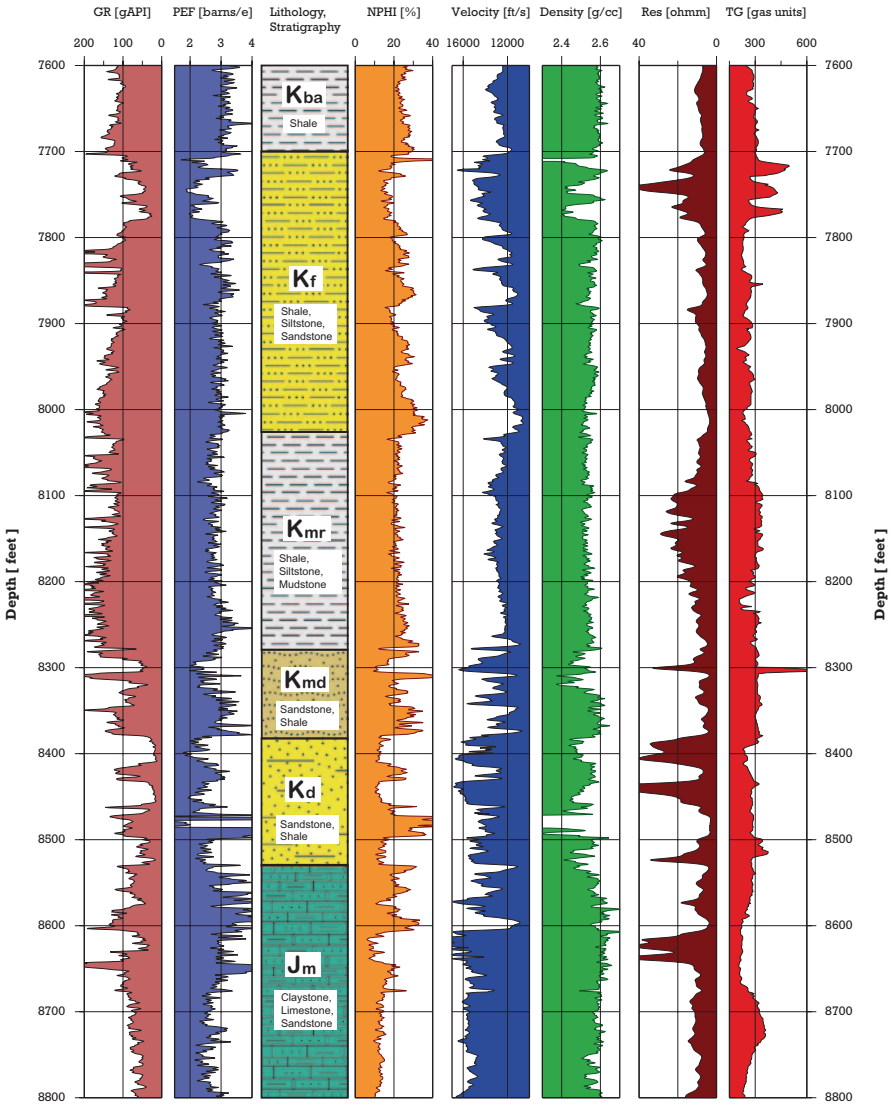


**Fig. 7.11** Interpreted wireline logs from the RSU #1 well over the depth interval with gas shows. From *left* to *right* the panels are: gamma-ray (*GR*), photoelectric factor (*PEF*), lithology and stratigraphy, neutron porosity (*NPHI*), P-wave velocity, deep resistivity (*Res*), and total gas (*TG*) from mud log

the Cretaceous shales at the time of their maximum burial. Constrained by the low permeability of fine-grained shales and siltstones, the gas could not migrate freely, which caused pressure to increase to the point where microfractures were induced, creating migration pathways. The process of gas generation, pressure increase, fracture opening, and migration continued until the gas had migrated into the more accessible units within the interval that extends from the Morrison Formation upward

into the top of the Frontier Formation. The high pressures that were attained during gas generation at maximum burial likely decreased with uplift and erosion in the Late Cretaceous–Early Tertiary, leaving a record of modest present-day pressures that are far less than the paleo-overpressures. We think that sonic and resistivity logs through the Lower Cretaceous section (Fig. 7.11) retain a strong signature of reduced velocity and reduced resistivity directly related to microfractures opened during gas generation. Rock fabric affected by gas generation and associated microfracturing remained unchanged as the section was uplifted. Thus, the sonic and resistivity anomalies, unlike pressure conditions, are irreversible and reveal a signature of the former overpressure (Cluff and Cluff 2004). Geophysical well logs from the RSU #1 well support the proposed correlation between velocity/resistivity anomalies and aligned (parallel to bedding) microfractures in the Lower Cretaceous strata. Note that sonic velocity decreases as resistivity decreases (Fig. 7.11), which agrees with the velocity measurements in the direction perpendicular to bedding (sonic-log tool) and resistivity measurements in the horizontal direction parallel to bedding (induction-log tool). Although multiple gas-show records (total gas (TG) panel Fig. 7.11), no commercial gas inflow was reported while drilling the RSU #1 well. However, several wells in the seismic study area currently produce natural gas from the Frontier Formation.

Seismic inversion for acoustic impedance enhances the vertical resolution of the corresponding interval-velocity volume. This allows for more confident identification of beds having thickness comparable with the theoretical seismic resolution (one-quarter wavelength $\lambda/4$). A west-east vertical section through the acoustic impedance volume with the interpreted formation tops is shown in Fig. 7.12. Unlike the corresponding reflectivity section (Fig. 7.6), acoustic impedance is more readily related to lithology. For example, the Rock Springs coal beds are easily identifiable at early times by their extremely low values (Fig. 7.12). The Late Jurassic–Early Cretaceous source rocks that are responsible for gas generation are also characterized by low impedance values and show better discrimination. The Weber Sandstone and Madison Limestone also show noticeable contrast with the confining layers in Fig. 12. The acoustic impedance contrast for these units is due to enhanced porosity in these reservoir rocks. The impedance-porosity dependence is clearly observed on the crossplots presented in Fig. 7.13. Unlike the major reservoir rocks, the confining shale interval within the Chugwater and Dinwoody Formations is characterized by increased impedance values and a more homogeneous appearance (Fig. 7.12). This allows us to interpret these shales as low-porosity, thick, and laterally continuous.

Figure 7.14 shows three west-east coherence sections one mile apart. Geologicly, highly coherent seismic waveforms indicate laterally continuous lithology, while abrupt changes in waveforms can indicate faults and fractures in sediments. There are several sub-vertical, low-coherency zones that we interpret as potential faults (between red arrowheads in Fig. 7.14). The more prominent of these faults are within Upper Cretaceous strata (above 1.5 s in Fig. 7.14). The time interval with reflections from the target reservoir rocks appears to be laterally more continuous, with possible faulting down-dip of the RSU #1 well (northeast of the well—red arrows).

The basement-involved faulting northeast of the RSU #1 well is more obvious in the color-coded mean-frequency images (Fig. 7.15). The mean frequency of seis-

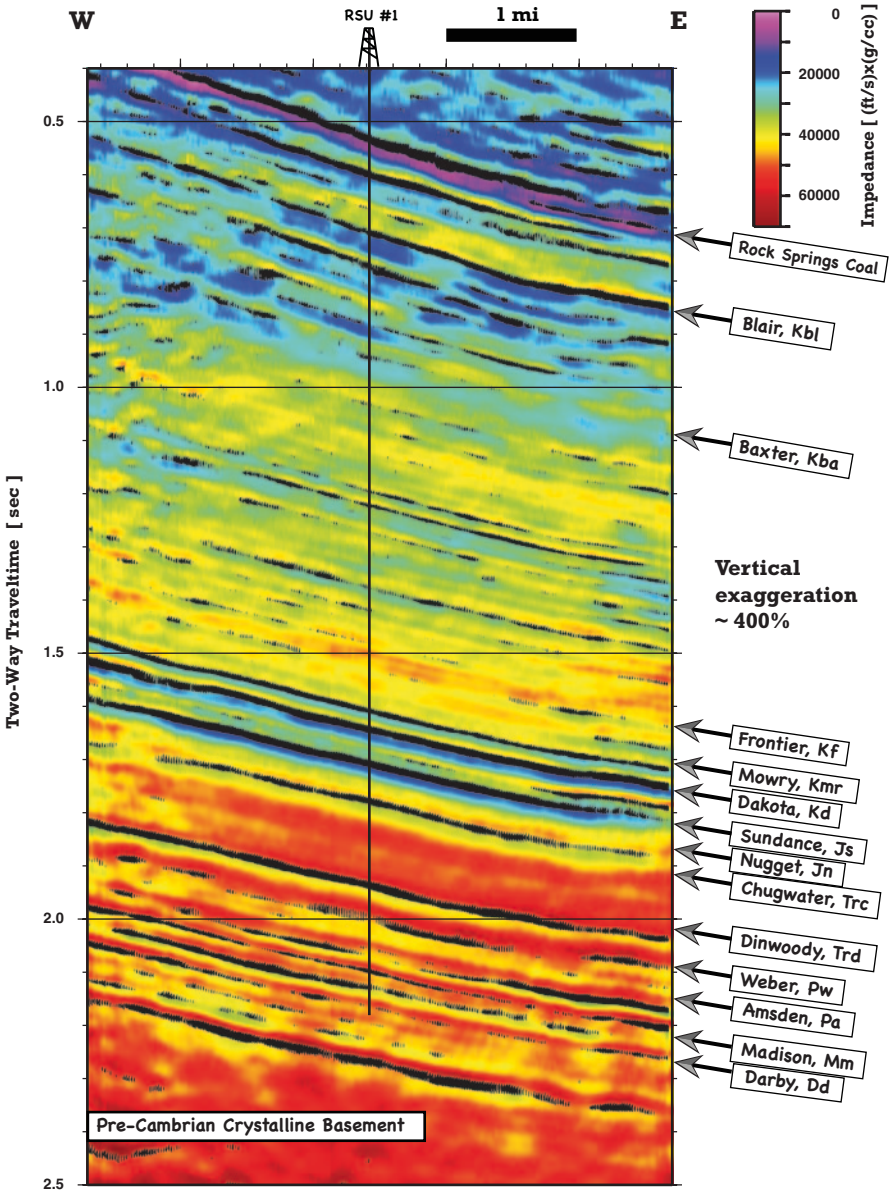


**Fig. 7.12** Interpreted west–east profile through the acoustic impedance volume at the RSU #1 well location. The color-coded impedance image is co-rendered with seismic amplitude section

mic wavelets is related to absorption characteristics in the subsurface, with higher frequencies more attenuated than lower frequencies over a fault zone. Hence, the steeply dipping, sub-parallel structures northeast of the well in Fig. 7.15 are interpreted as potential faults. Frequency can also be used to delineate geologic forma-

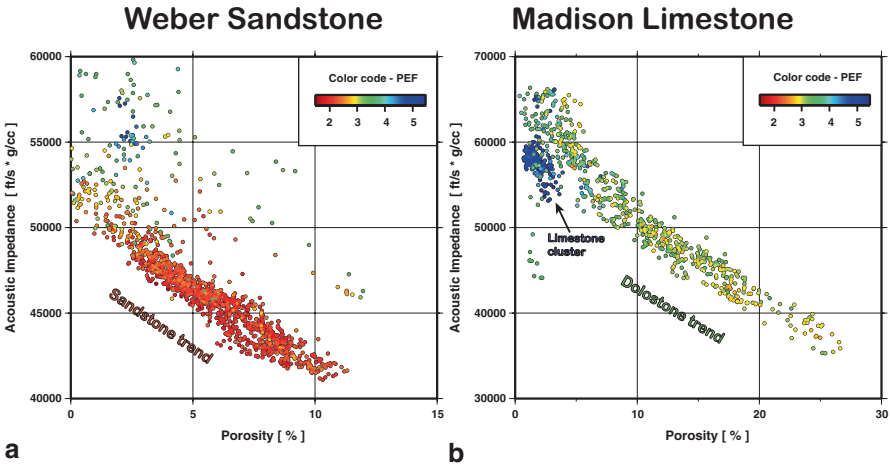


**Fig. 7.13** Acoustic impedance versus density porosity crossplots color-coded with the photoelectric factor (*PEF*). The measurements are from the RSU #1 well within the depth intervals: (**a**) 11,150–11,810 ft (Weber Sandstone), and (**b**) 12,230–12,650 ft (Madison Limestone). Note a pronounced inverse trend in both distributions, that is, acoustic impedance decrease with increasing porosity of the major reservoir rocks

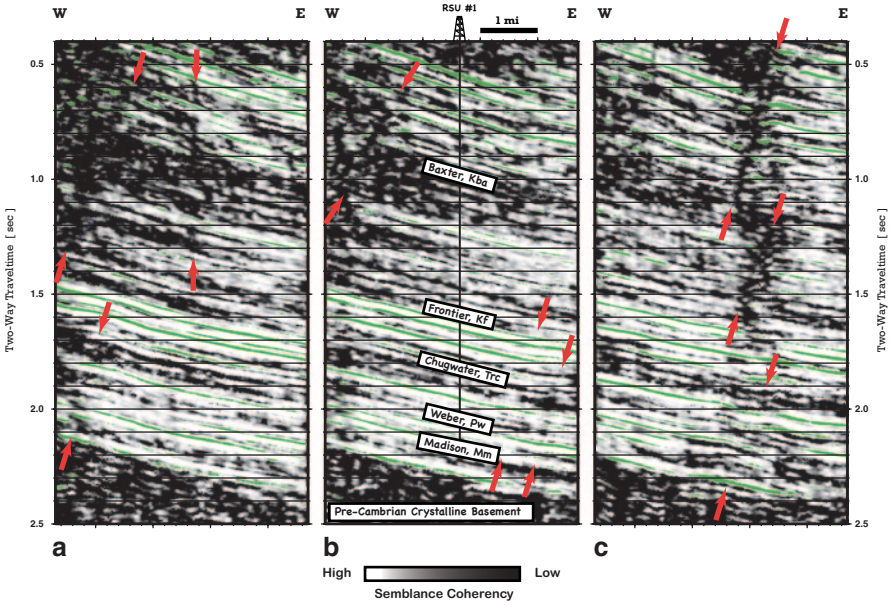


**Fig. 7.14** West–east profiles through the coherency volume: (**a**) one mile south of the RSU #1 well location, (**b**) at the RSU #1 well location, and (**c**) one mile north of the RSU #1 well location. The *gray*-scaled coherency image is co-rendered with seismic amplitude section (*green* reflectors). Low-coherency zones (dark color) with sub vertical orientation are interpreted as potential faults (*red arrowheads*)

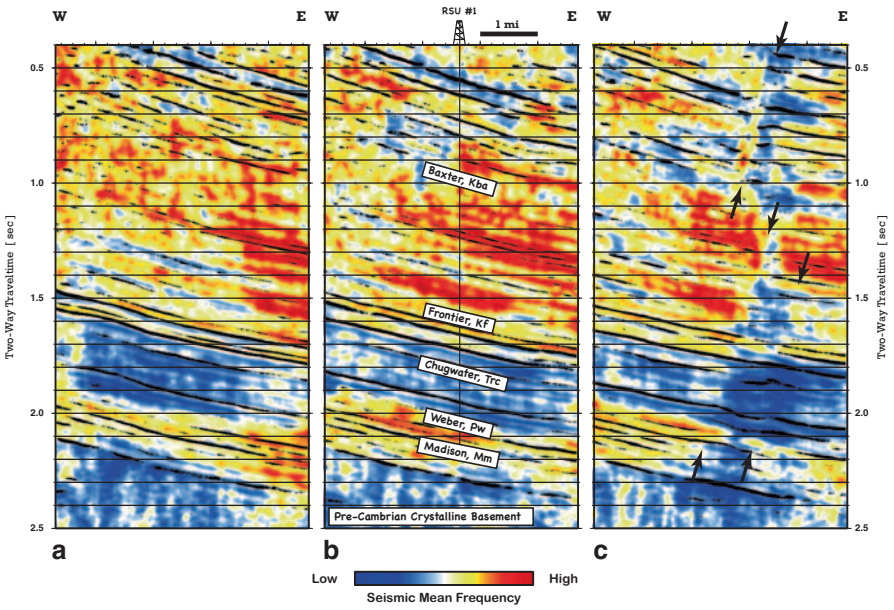


**Fig. 7.15** West–east profiles through the frequency volume: (**a**) one mile south of the RSU #1 test well location, (**b**) at the RSU #1 well location, and (**c**) one mile north of the RSU #1 well location. The color-coded frequency image is co-rendered with seismic amplitude section (*black* reflectors). The steeply dipping structures separated with low-frequency zones (*blue*) are interpreted as potential faults (*black arrowheads* in panel c)

tions, likely as a result of wave interference in different lithologies. The Chugwater Formation, a Triassic red bed, has a distinctly low mean seismic frequency with respect to the underlying targeted reservoirs (Weber and Madison Formations) and overlying Jurassic and Cretaceous units. The characteristic low seismic frequency of the Chugwater Formation was used to help define the lateral continuity of this sealing unit across the study site.

### *7.10.3 Interpretation—The Use of Horizon Slices*

The attribute anomalies discussed in Sect. 7.10.2 are most readily apparent when presented along the interpreted seismic horizons (Fig. 7.6) in the form of attribute *horizon slices*. Attributes examined in this section are the reflection strength, mean frequency, coherence, curvature, dip azimuth and magnitude, spectral amplitude, and synthetic sonic log attributes. Permeability modeling based on petrophysical and attribute analysis is discussed in Sect. 7.11. Here, we present only those figures that demonstrate well-developed trends in attributes or are related to targeted reservoir/seal characterization.

The *structural configuration* mapped from 3-D seismic data clearly depicts a northeast-dipping monocline at all stratigraphic levels examined (Figs. 7.3 and 7.16). The strata are almost flat in the northeastern part of the study area, but their

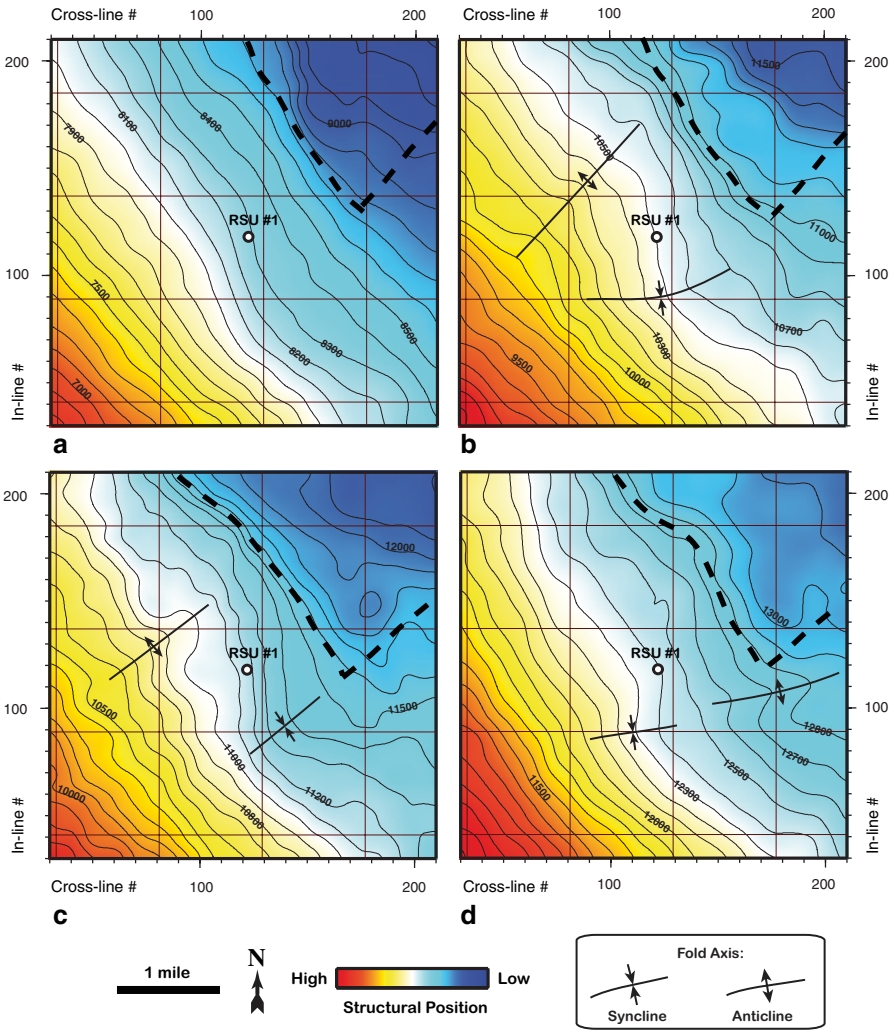


**Fig. 7.16** Color-coded structure maps of the interpreted seismic horizons: (**a**) Muddy, (**b**) Dinwoody, (**c**) Weber, and (**d**) Madison. Contour interval is 100 ft for all maps. The depth reference point is Kelly bushing (*KB*) at the RSU #1 well. *Dashed lines* show interpreted faults

dip steepens to about 8º in the southwest part (Fig. 7.16). The monocline is complicated by minor folding, with the fold axes plunging generally northeast. Due to this secondary bending, the implied general dip changes from roughly northeast to east-northeast in the vicinity of the RSU #1 well (Fig. 7.16). Potential faults identified in vertical sections (Figs. 7.14 and 7.15) appear to correlate with the zone of rapid dip steepening about 1 mi northeast of the well (Fig. 7.16). Based on the contour-line configuration, it is possible to assume that the northwest-striking fault is terminated within the study area by a smaller fault that is roughly orthogonal to the first one.

The principal interpretation objective of this study was to construct a tectonic structural framework that would enable the identification of the faults and fracture

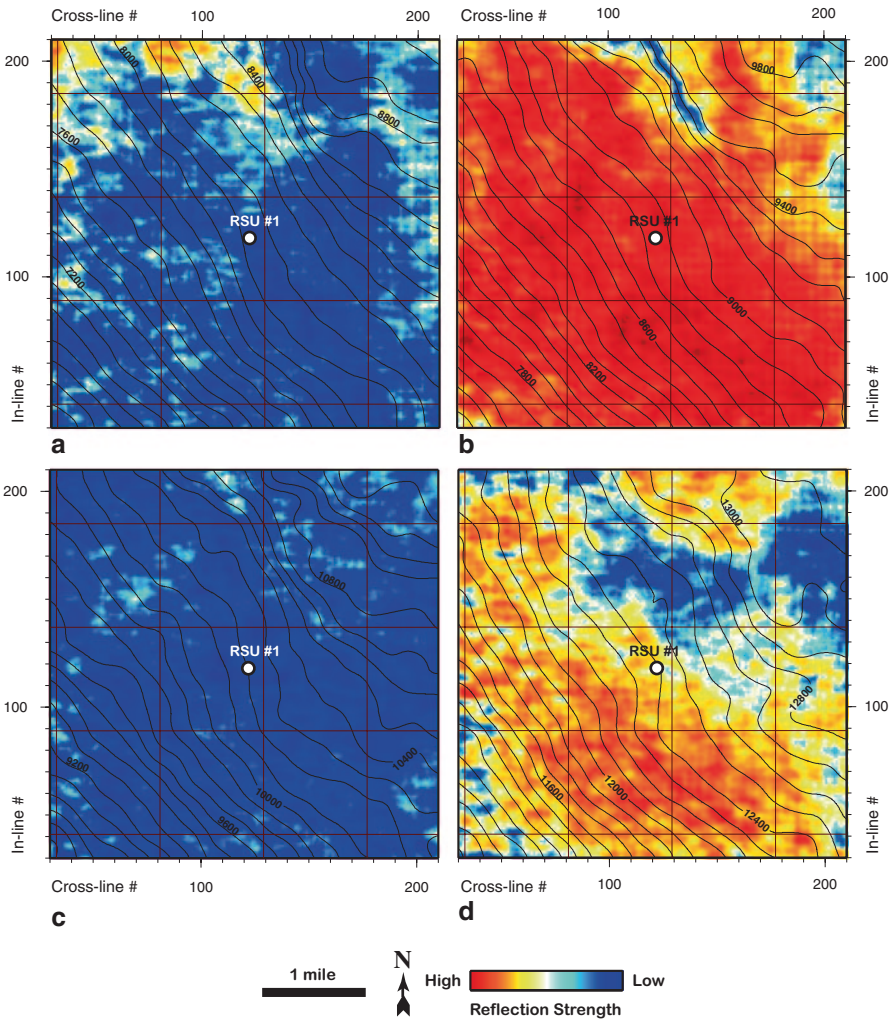


**Fig. 7.17** Reflection strength attribute on top of the following stratigraphic units: (**a**) Mowry, (**b**) Sundance, (**c**) Red Peak, and (**d**) Middle Madison. Reflection strength changes from high (*red*) on interfaces with contrasting physical properties to negligible (*blue*) with seismically transparent, monolithic shale units

network—possible fluid migration pathways. The challenge was to construct this structural picture from a 3-D seismic image that alone could not provide a clear, unambiguous picture of the fault system. Moreover, the seismic data used for structural analysis showed evidence of contamination by an acquisition footprint and processing artifacts arising from irregularities (gaps) in the seismic survey layout, as described in Sects. 7.2 and 7.3 (Figs. 7.1 and 7.3).

Figure 7.17, the reflection strength display, is a phase-independent view of the seismic amplitudes. High reflection strength is commonly associated with major lithologic change (for example, across an unconformity or depositional change),

while low reflectivity indicates consistent lithological environment that is more seismically transparent. Observing how reflection strength changes gives us a good idea of how much the lithology is actually changing in three dimensions. For example, relatively low reflectivity can be observed at the top of stratigraphic intervals corresponding to the Mowry Shale and the Red Peak Formation (Fig. 7.17a, c). We interpret these intervals as relatively monolithic and laterally continuous shale units. This is especially true of the Triassic Red Peak Formation, which shows extremely low reflectivity (consistent blue color in Fig. 7.17c). On the contrary, the top of the Sundance Formation is characterized by extremely strong reflectivity, largely due to the Jurassic-Cretaceous disconformity and also to significant impedance contrast between the alternating shales and sandstones composing this stratigraphic interval (Fig. 7.17b). The top of the middle Madison unit shows high reflectivity (Fig. 7.17d) due to the impedance contrast between the high-density limestone unit and underlying porous dolostones. This contrast vanishes northeast (down-dip) of the RSU #1 well but remains laterally consistent to the southwest and west, the up-dip direction (Fig. 7.17d).

The potential faults discussed previously in this section are more readily apparent where the coherence is mapped over the interpreted horizons (Fig. 7.18). Two orthogonal trends were identified in the coherence data. Most of the NW-SE lineations are subparallel to the strike of bedding. The NW-SE lineations seem to terminate at an orthogonal structure in the northeastern corner of the study area (Fig. 7.18). The tracking of these lineations through the coherence volume presented a significant challenge. The difficulty of imaging fault surfaces arises from the local fracture density associated with fault growth (or slip along a fault surface) that produced broad damage zones around the fault planes. Besides, there are plentiful artificial N-S-and E-W-trending lineations associated with the source and receiver layout (acquisition footprint) that intensify the low-reflective horizons. The grid of these artificial (not related to subsurface geology) lineations is especially harmful for the Mowry Shale and the Red Peak Formation images (Fig. 7.18a, c). For the horizons with relatively high reflection strength (Fig. 7.18b, d), the area southwest of the RSU #1 well (the up-dip direction) seems to be laterally continuous and does not contain traceable fault planes.

Other geometrical attributes were analyzed to get a better idea of the geomorphology of the interpreted horizons and also to gain confidence in our fault interpretation. Figure 7.19 shows a set of these attributes extracted at the top of the Sundance stratigraphic interval. Again, the general structure of the region is monoclinal. However, the dip magnitude map (Fig. 7.19a) shows that the attitude of the bedding is not uniform throughout the area. The area northeast of the RSU #1 well is relatively flat (dip 2–6˚), but the bedding steepens to dip 6–10˚ southwest of the well. The RSU #1 well penetrates the Sundance horizon near the northwest-striking bending zone (Fig. 7.19a). Another axis of bed bending can be identified on the dip azimuth map: the regional northeast dip changes to an almost north dip just south of the well (Fig. 7.19b). It looks like the northeast-striking axis of bending changes to a fault axis in the northeastern corner of the survey area. The two orthogonal fault systems become more readily apparent in the two curvature maps (Fig. 7.19c, d).

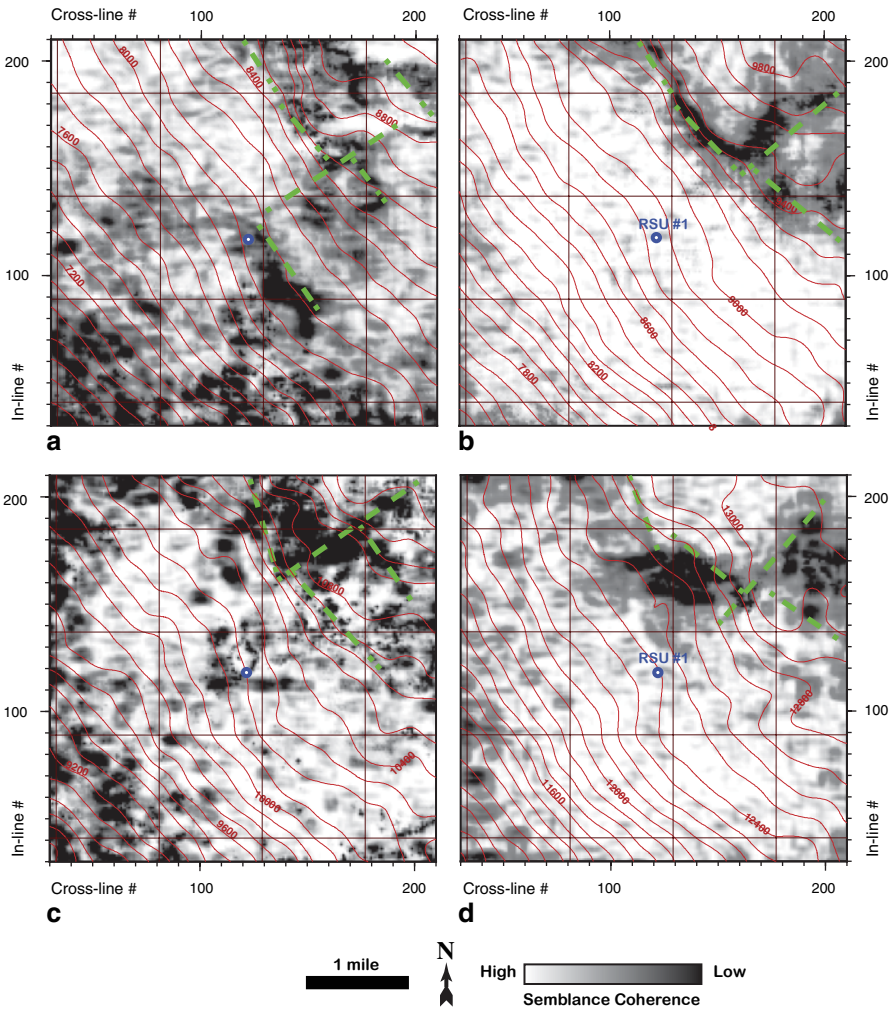


**Fig. 7.18** Interpreted coherence map on top of the following stratigraphic units: (**a**) Mowry, (**b**) Sundance, (**c**) *Red* Peak, and (**d**) Middle Madison. Coherence changes from high (*light color*) in areas with continuous reflections to low (*dark color*) in areas of intense faulting, fracturing, or otherwise poor reflectivity. Interpreted fault axes are shown with *green dashed lines*

The minimum curvature attribute provides better contrast, and the strike curvature allows better resolution of the two faults cutting the strata down-dip (northeast) of the RSU #1 well projection (Fig. 7.19).

The same set of geometric attributes was extracted at the top of the middle Madison stratigraphic interval (Fig. 7.20). The dip magnitude map shows a northwest-striking zone of bending comparable to that interpreted for the Sundance horizon. Although noisier than that of the Sundance horizon, the dip azimuth map of the Madison horizon allows identification of beds bending around an axis that passes

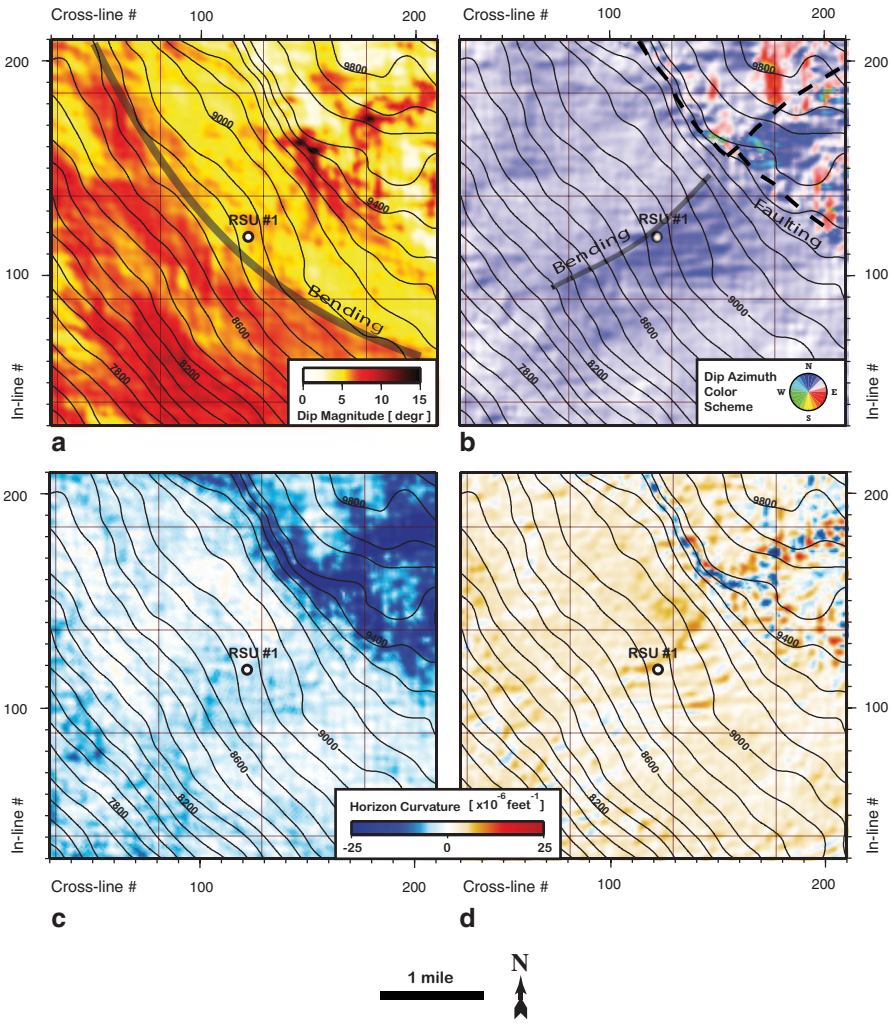


**Fig. 7.19** Geometrical (morphological) attributes on top of the Sundance stratigraphic interval: (**a**) dip magnitude, (**b**) dip azimuth, (**c**) minimum curvature, and (**d**) strike curvature

through the well location (Fig. 7.20b). The northwest-trending fault image, although generally traceable, appears to be more smeared than that on the corresponding Sundance maps. The orthogonal, northeast-trending fault is imaged best in the maximum curvature and dip curvature maps (Fig. 7.20c, d). Compared with those of the Sundance Formation, the northwest-trending structures appear to be shifted up-dip (southwest) on the Madison horizon. This allows us to conclude that both the bending plane and the fault plane dip southwest, which is consistent with our previous interpretation of the vertical coherency sections (Fig. 7.14). The truncated, northeast-trending fault does not greatly change its relative location on the two hori-

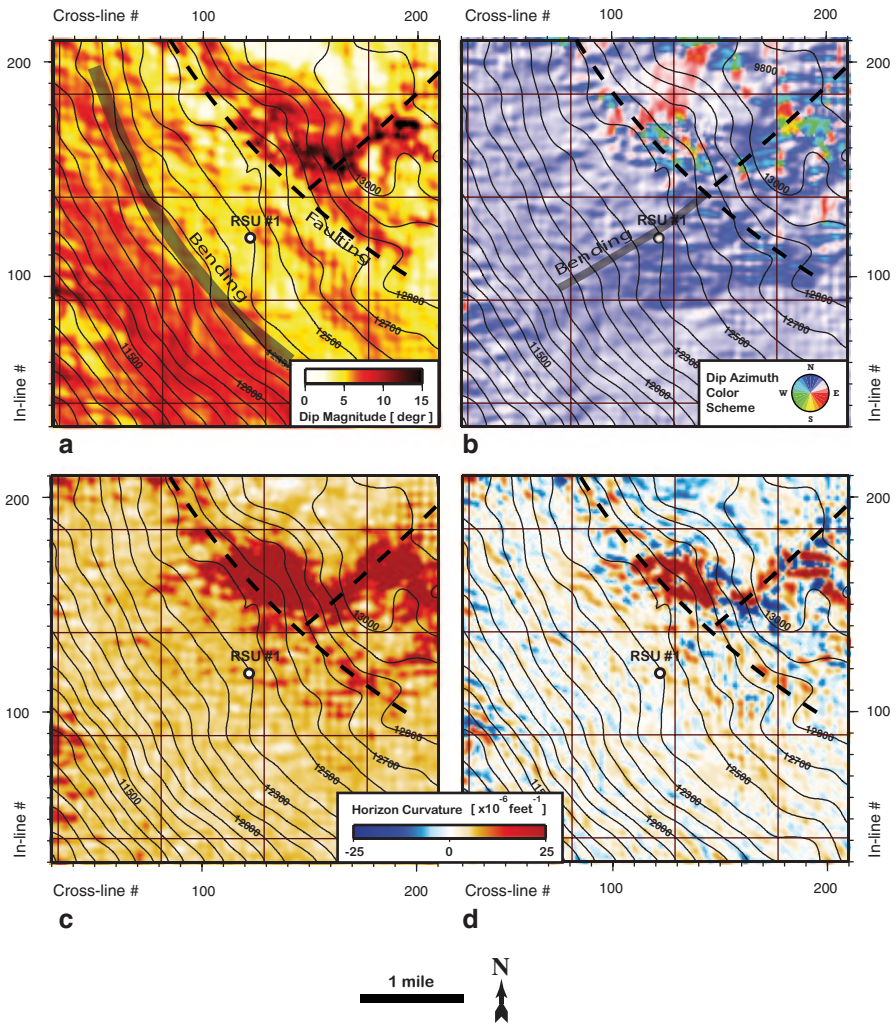


**Fig. 7.20** Geometrical (morphological) attributes along the Madison stratigraphic interval: (**a**) dip magnitude, (**b**) dip azimuth, (**c**) maximum curvature, and (**d**) dip curvature

zons (Figs. 7.19 and 7.20). Hence, at this depth level, the fault plane is sub-vertical. No significant structural complications along the Madison horizon can be observed up-dip of the RSU #1 well; this indicates that the corresponding depth interval is favorable for underground $CO_2$ sequestration.

We used another attribute, mean frequency, to deal with reservoir continuity, compartmentalization, and thickness. We find this attribute to be sensitive to both wave propagation effects and depositional characteristics. Its uses within the study area included:

- Fault/fracture zone indication. Fractures may appear as lower-frequency zones.

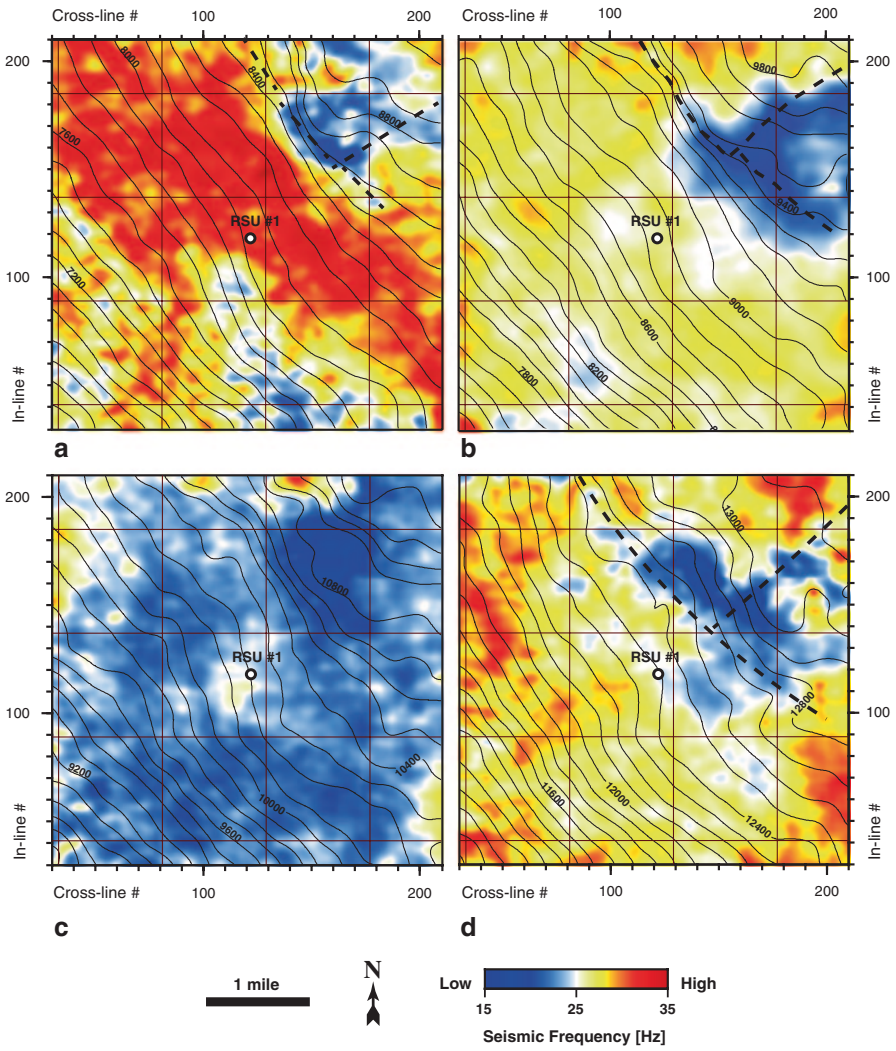


**Fig. 7.21** Mean frequency attribute on top of the following stratigraphic units: (**a**) Mowry, (**b**) Sundance, (**c**) *Red* Peak, and (**d**) Middle Madison. Frequency varies from high (*red*) to low (*blue*)

- Bedding characterization. Higher frequencies indicate the presence of sharp interfaces such as exhibited by thinly laminated shales or complex depositional systems composed of alternating lithologies. Lower frequencies are indicative of relatively monolithic units (e.g. sandstones) with more massive bedding geometries.
- Bed thickness mapping. A reflection from a thin bed has a characteristic expression in the frequency domain that is indicative of the temporal bed thickness. A "thin bed" is indicated where the two reflected waveforms from the top and base of the layer interfere.

**Table 7.3** Seismic modeling parameters

| Modeling unit | Density (g/cc) | P-wave velocity (ft/s) |
|---|---|---|
| Reservoir rocks | 2.52 | 18,000 |
| Encasing rocks | 2.72 | 21,000 |

Figure 7.21 shows mean frequency maps on top of several representative horizons. The Mowry Shale interval, composed of thinly laminated and fractured lithologies, is imaged with high frequencies (red in Fig. 7.21a). The Sundance Formation also appears to be composed of alternating lithologic units with contrasting physical properties, but shales of the Red Peak Formation are mapped as uniform monolithic strata (Fig. 7.21b, c). The broad zone of intense fracturing northeast of the RSU #1 well is consistently imaged with low frequencies. A noticeable acoustic impedance contrast characterizes the middle Madison reservoir unit enclosed within massive carbonate rocks. That is why the frequency distribution map over this stratigraphic interval is mostly composed of high frequencies (red and yellow in Fig. 7.21d).

Forward modeling was performed to examine the physical basis for links between the varying thickness of the middle Madison unit and several seismic attribute responses. We modeled the seismic response to varying thickness on a wedge that mimics the middle Madison unit (Fig. 7.22a). The density and velocity values used in the modeling are loosely based on physical properties of the middle Madison reservoir rocks encased in acoustically dissimilar carbonates (Table 7.3).

To represent the petrophysical profile of the Rock Springs Uplift, we assumed that the porous dolostone wedge is lower in acoustic impedance than the surrounding material. Correspondingly, the top and bottom of the wedge show opposite reflection polarities, which is a realistic and common situation in most stratigraphic profiles with reservoir rocks (Fig. 7.22a). The wedge thickens in value from zero on the left to 600 ft on the right, which corresponds to one dominant wavelength ($\lambda$) at the reservoir depth. The geologic model was convolved with the zero-phase Ormsby wavelet (limited by 4-, 8-, 48-, and 80-Hz cutoff frequencies) to produce a simple, zero-offset acoustic model of the seismic response of the wedge. Based on the vertical resolution limit ($\lambda/4$), the model covers a thickness range from seismically thin beds ($<\lambda/4$) through intermediate beds ($\lambda/4$–$3\lambda/4$) to seismically thick beds ($>3\lambda/4$). From the well-log measurements, the middle Madison reservoir thickness at the RSU #1 well site is 140 ft, which is close to $\lambda/4$. Figure 7.22a shows rows of antisymmetric waveforms that correspond to the top and bottom of a porous dolostone reservoir of varying thickness. For seismically thin and intermediate beds, reflection amplitudes are composite seismic responses resulting from the interference of the top and bottom reflections.

The corresponding amplitude and frequency values measured from the seismic response are shown in Fig. 7.22b, c. The amplitude curve is characterized by a maximum value (called *tuning*) at approximately $\lambda/5$, which is the tuning thickness in our case. As the wedge thins to less than $\lambda/5$, the amplitude begins a sharp decrease to zero. Although such nonlinear changes in seismic amplitude are well-established effects of thin-bed tuning, the corresponding changes in seismic signal frequency are much less

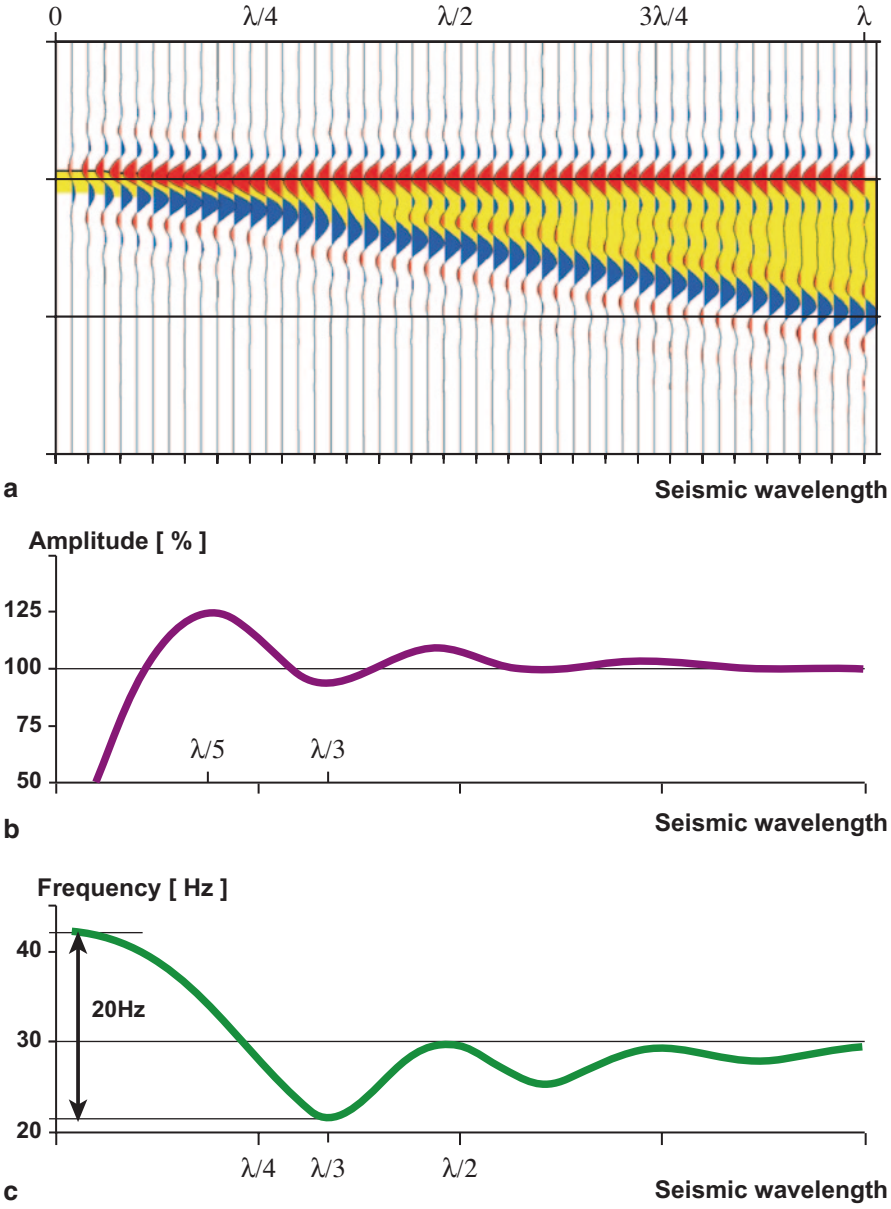


**Fig. 7.22** (**a**) Low-impedance wedge model (*yellow*) and its seismic response generated using zero-phase Ormsby wavelet with frequency passband 8–48 Hz. (**b**) Amplitude and (**c**) mean frequency variations estimated on top of the wedge

well documented. In this study we attempted to fill the gap by calculating the mean frequency of the spectrally decomposed reflection that corresponds to the top of the wedge. The frequency-tuning curve (Fig. 7.22c) demonstrates generally oscillating

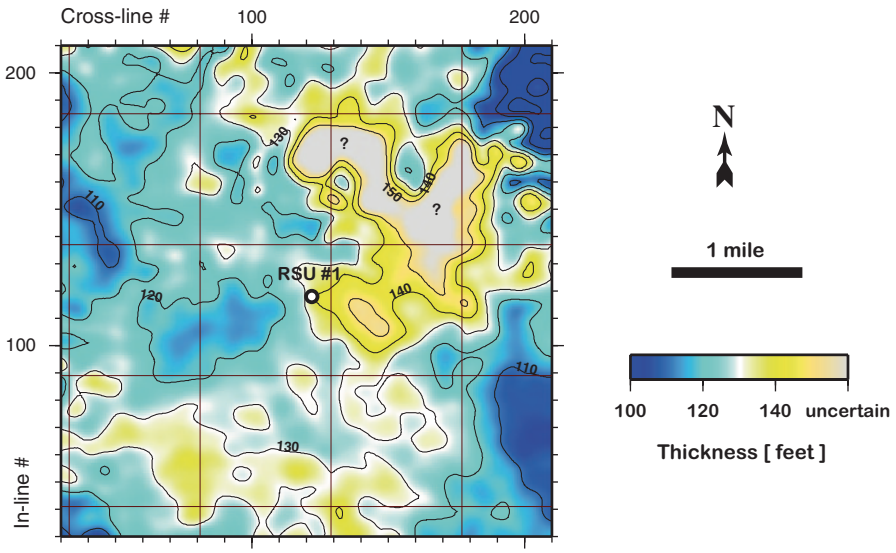


**Fig. 7.23** Color-coded isopach map of the middle Madison reservoir. The reservoir thickness varies from ~110 ft (*blue*) to ~140 ft (*yellow*). Areas with increased uncertainty (possible faulting) are grayed-out

behavior around an average wavelet frequency of 30 Hz. The most important changes in frequency occur from zero to $\lambda/3$ (approximately 200 ft for the model parameters) where the wedge thickens. This interval is characterized by a corresponding decrease in frequency (of approximately 20 Hz). The inversely proportional behavior of the frequency-tuning curve for beds with thickness below $\lambda/3$ is utilized in this study.

The inversely proportional dependence of seismic frequency on thickness for beds thinner than one-third dominant seismic wavelength is not a result of specific modeling parameters. The authors tested wedge models of the embedded layer with both positive and negative impedance contrasts. The authors also analyzed the frequency response of the wedge model produced by 90°-phase wavelets with different average frequencies. The modeling results indicate that, in all cases, the lowest measured frequency corresponds to the wedge thickness equivalent to $\lambda/3$.

To check the applicability of the mean frequency attribute as bed-thickness discriminator, we routinely computed the middle Madison reservoir thickness by measuring the corresponding peak-trough separations within the seismic volume. The resultant isopach map is shown as Fig. 7.23. Within the study area the reservoir thickness varies from about 110 ft to about 140 ft. Except in areas affected by faulting or acquisition footprints or both, the middle Madison isopach map (Fig. 7.23) shows a strong correlation with the frequency distribution over the corresponding reflection horizon (compare Fig. 7.23 with Fig. 7.21d).

Areas where the reservoir thins to less than 120 ft (Fig. 7.23) correspond to high-frequency build-ups in the mean frequency attribute map on top of the middle Madison reservoir (Fig. 7.21d). On the contrary, an increase in reservoir thickness (e.g. southeast of the well, Fig. 7.23) manifests lowering frequency content. Thus, two

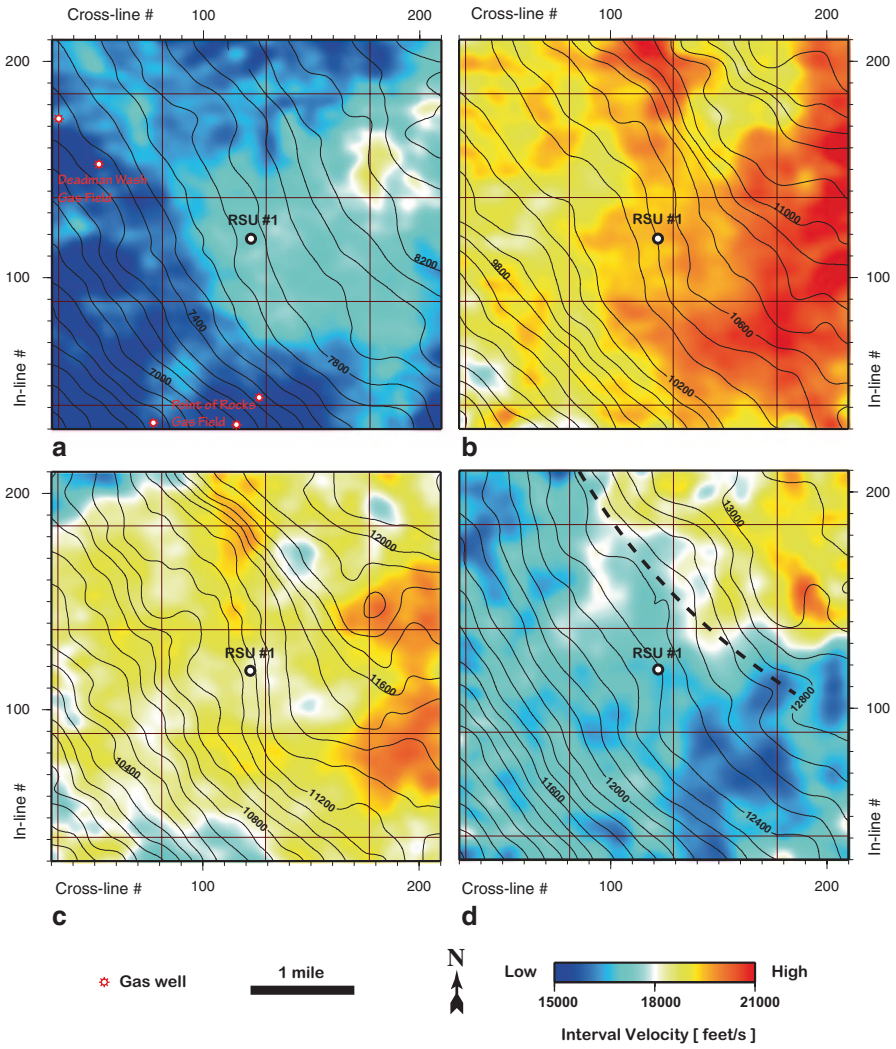


**Fig. 7.24** Velocity attribute on top of the following stratigraphic units: (**a**) Frontier, (**b**) Dinwoody, (**c**) Weber, and (**d**) middle Madison. Velocity varies from high (*red*) to low (*blue*)

different approaches used for reservoir thickness characterization appear to produce comparable results. This gives us greater confidence in the isopach map, Fig. 7.23.

The velocity attribute map*s* shown in Fig. 7.24 actually represent interval velocity models obtained from reflection seismic data. These interval velocities were measured using a standard semblance method and the well-known Dix formulation (Dix 1955). As in any modeling, our degree of confidence in identified features and their associated interpretation depends on the density of the modeled data set. In this study, our semblance measurements are sampled densely, 110 ft×110 ft×2 ms, and that makes our velocity models more precise (and probably more accurate) than those models

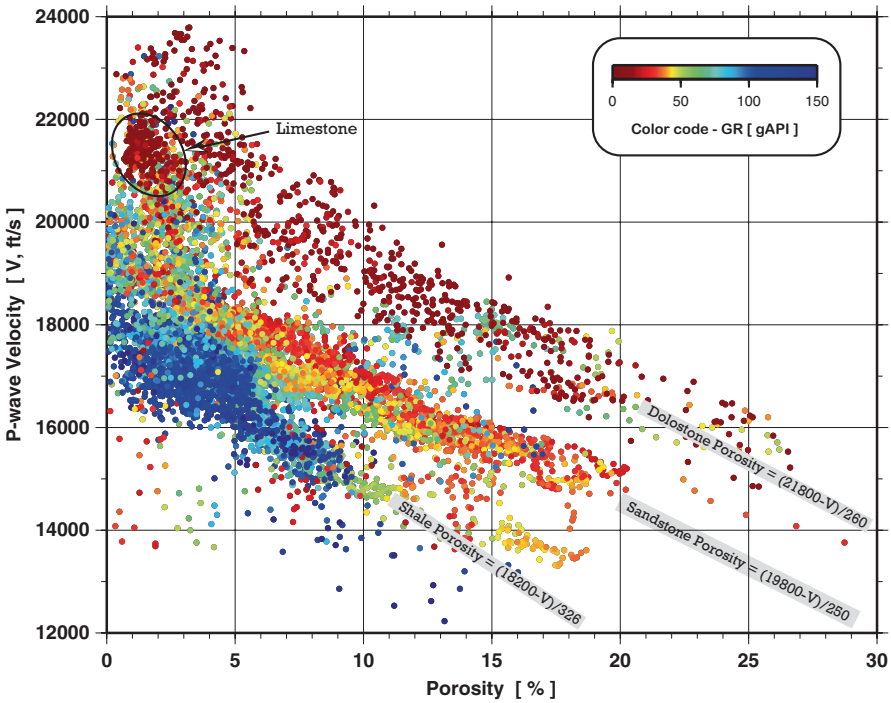


**Fig. 7.25** Sonic P-wave velocity versus density porosity crossplot color-coded with the gamma ray log data. The measured depth interval is from 8,600 to 12,700 ft (pre-Cretaceous strata). Interpreted lithologies and the corresponding linear regression models are shown within the *gray* bars

produced for conventional stacking purposes. In standard templates, semblances are commonly sampled coarsely and then smoothed, resulting in a loss of valid information and resolution. Consequently, the information illustrated on the horizon velocity distribution maps (Fig. 7.24) is commonly unavailable to the interpreter.

Unlike velocity-time profiles, such as that shown in Fig. 7.10, velocity distribution maps (Fig. 7.24) do not exhibit abrupt changes, and the range of lateral velocity variation for most interpreted horizons does not exceed 4,000 ft/s. Since velocity variations are known to commonly correlate well with lithology that remains constant along a seismic horizon, these results are what we would expect. Heterogeneous lithologic characteristics of subsurface formations are manifested mostly by vertical variations in velocity, while lateral velocity variations can be attributed to variable porosity, fracturing, and fluid content. Therefore, we interpret velocity trends observed in lateral subsurface images mostly in terms of porosity and hydrocarbon accumulation.

The first velocity distribution map over the Frontier horizon (Fig. 7.24a) illustrates this interpretation: seismic interval velocities can be used to detect the extent of gas-saturated formations. Low velocity zones are associated with the two prolific gas fields (Fig. 7.24a). The hydrocarbon bearing zones west (Deadman Wash gas field) and south (Point of Rocks gas field) of the RSU #1 well correlate with intense low-velocity anomalies.

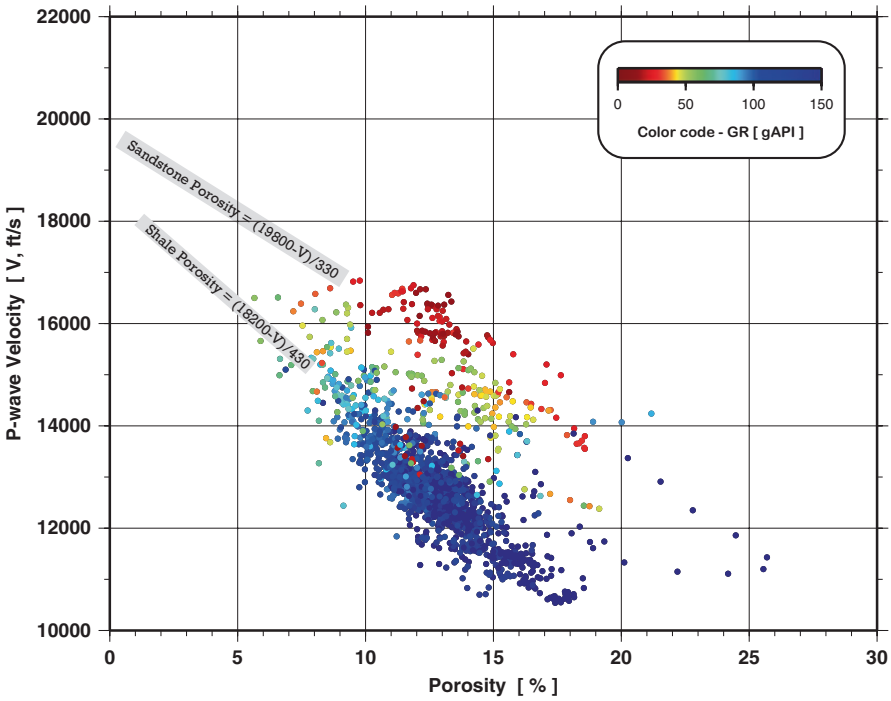


**Fig. 7.26** Sonic P-wave velocity versus density porosity crossplot color-coded with the gamma ray log data. The measured depth interval is from 7,700 to 8,500 ft (Cretaceous Dakota through Frontier Formations). Interpreted lithologies and the corresponding linear regression models are shown within the *gray* bars

Stratigraphically lower horizons, the Dinwoody and the Weber, are characterized by relatively uniform velocity distribution and a higher range of values, 18,500 ft/s to about 20,500 ft/s. There is only a weak trend of velocity decrease west of the test well location on these two horizons (Fig. 7.24b, c). The middle Madison unit (Fig. 7.24d), the deepest interpreted stratigraphic horizon, is distinguished by low overall velocity values (16,000–19,000 ft/s) and strong lateral velocity variations, which may be associated with complex overburden structures.

We used geophysical logs from the RSU #1 well [ESM plate 6] to gain insight into velocity variations along these four horizons (Fig. 7.24). The gamma ray, sonic, density, and neutron porosity log characteristics were used in the correlation analysis. Density porosities were derived assuming a multi-component mineral mixture with variable matrix densities that were interpreted from the neutron/density crossplot. The resultant velocity-porosity relationships were estimated from regression methods that fit linear trends for the intervals identified in Figs. 7.25 and 7.26. On the basis of these petrophysical relationships, and considering negligible lithological variation along the interpreted seismic horizons, we predicted the porosity distribution along the four horizons shown in Fig. 7.27. As expected, the gas fields producing from the Frontier Formation are located over the high-porosity areas (Fig. 7.27a). The Weber Sandstone can be characterized as a tight reservoir,

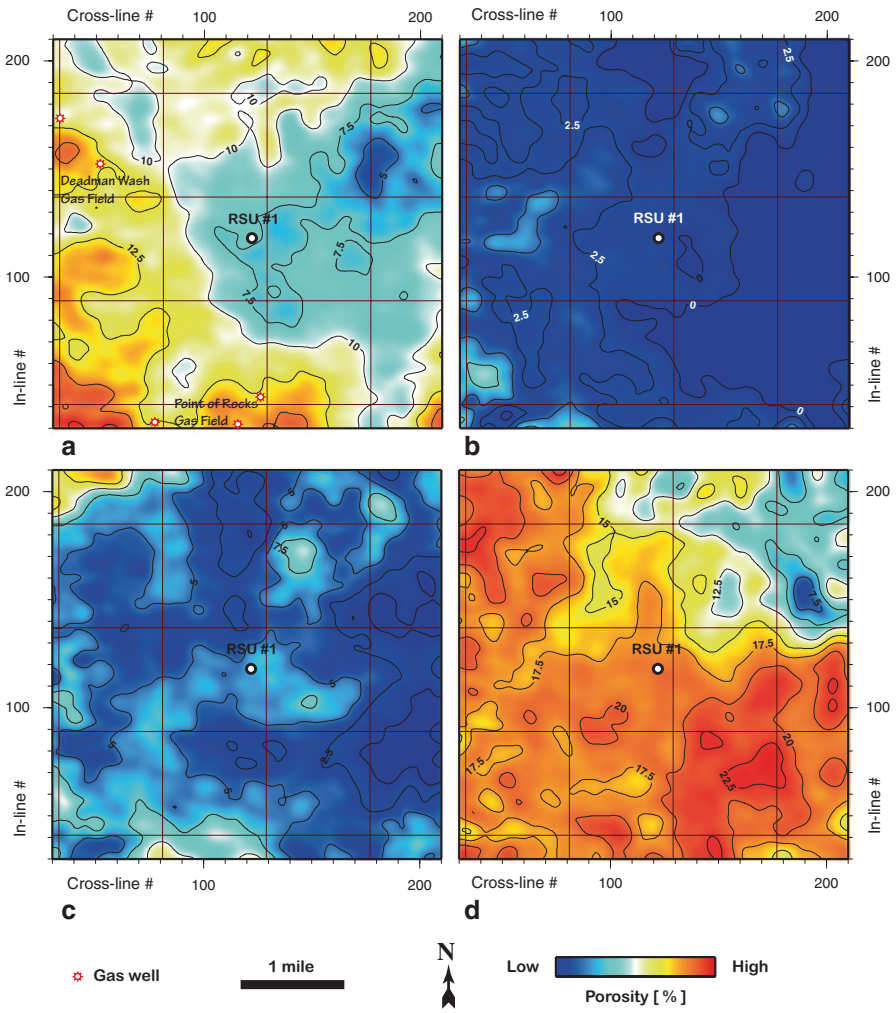


**Fig. 7.27** Porosity maps on top of the following stratigraphic units: (**a**) Frontier, (**b**) Dinwoody, (**c**) Weber, and (**d**) middle Madison. Porosity varies from high (*red* color) to low (*blue* color). Contour lines indicate porosity with contour interval = 2.5 %

with porosities ranging from 5 to 10 %. The middle Madison unit (Fig. 7.27d) looks very promising for $CO_2$ sequestration on the basis of consistently high (greater than 15 %) porosities in the up-dip direction. The integrity of the sealing horizon is verified by extremely low (less than 5 %) porosities on the top of the Dinwoody Formation (Fig. 7.27b), which overlies the targeted reservoir formations.

## 7.11 Qualitative Permeability from Seismic Attribute Analysis

### *7.11.1 Modeling the Seismic Signature of Permeable Layers*

Permeability and porosity are key inputs into reservoir flow simulation. If an impedance-porosity transform is available, porosity can be inferred from acoustic impedance. Such transforms can be derived from sonic, density, and porosity data from well logs. Typically, a theoretical rock physics model is found to explain these data and then used to expand the impedance-porosity interpretation away from the well by the means of inverted seismic data. However, permeability, which is necessary for reliable reservoir modeling, seems to be the most elusive of reservoir properties and remains extremely uncertain.

In this section, we examine the detection of permeable conduits that are important in fluid migration through the fractured, dual-porosity carbonates. *Dual-porosity* rocks are rocks that have both matrix porosity (primary porosity) and fractures (secondary porosity). In dual-porosity rocks, the bulk permeability is provided by fractures or vugs connected with each other and with high-aspect-ratio intergranular pores.

Natural rock reservoirs, including carbonates, are fluid-saturated, porous materials whose elastic properties can be described by Biot's (1962) poroelastic theory. Biot's theory predicts pore-fluid motion relative to the solid rock matrix during the passage of seismic waves through rocks. The corresponding energy loss arising from relative fluid motion is also evaluated. Importantly, Biot's theory gives an opportunity to estimate fluid and rock transport properties by measuring seismic amplitude. Recent studies (Pride et al. 2003; Goloshubin et al. 2008; Kozlov 2007; Ren et al. 2009) found that permeability can affect seismic reflection amplitudes significantly, especially for reservoirs built of layered porous material with heterogeneous permeability distribution.

In general, reflection-coefficient equations for dispersive media are very complicated. However, they can be simplified for normal incidence. For example, Goloshubin and Silin (2006) provide simple expressions for reflection and transmission coefficients for a planar P-wave from a permeable boundary in a fractured reservoir. Goloshubin et al. (2008) derive the reflection coefficient equation for the case of an inhomogeneous reservoir consisting of $N$ permeable lenses. The important feature of this equation is that it accounts for the dependence of the reflected signal on the frequency. This provides the basis for the spectral decomposition technique to be a powerful tool in estimating reservoir transport properties.

Since the middle 90s, various seismic attributes have been proposed for mapping permeability by using detailed analysis of the reflected-waveform amplitude spectra. These attributes are calculated by using a sort of spectral decomposition technique first introduced for seismic interpretation by Morlet et al. (1982) and substantially developed by Partyka et al. (1999). According to Castagna and Sun (2006), spectral decomposition in seismic exploration is a method that produces a continuous time-

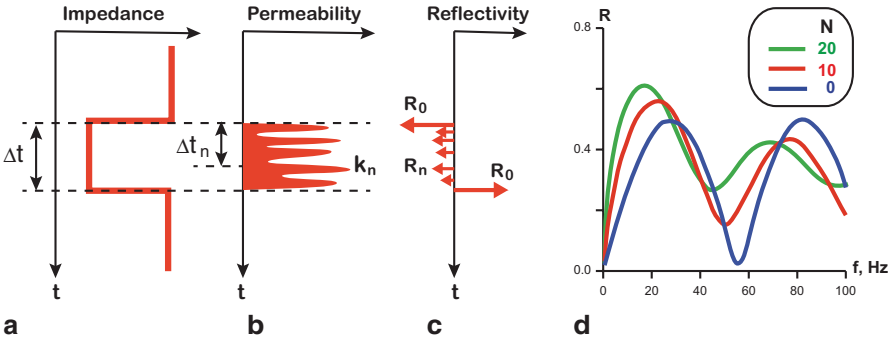


**Fig. 7.28** Reservoir model of a low-impedance layer (**a**) with high-permeability lenses (**b**) and the model response on incident P-wave (**c**): $R_0$ are reflection responses from reservoir's top and base, $R_n$ are responses from the lens n, $\Delta t$ is time thickness of the reservoir, and $\Delta t_n$ is time delay of the seismic response from lens n. Reflection coefficient R from the modeled reservoir as a function of number of lenses N and seismic frequency f (**d**). (All figures modified from Goloshubin et al. (2008))

frequency expression of a seismic trace. Applying instantaneous time-frequency analysis to seismic data makes it possible to compute various permeability-dependent attributes. For example, one group of attributes maps the ratio of the high-frequency part of the amplitude spectrum of a seismic trace to the low-frequency part. Other attributes make use of the slope characteristics of the low- and high-frequency parts. Some permeability attributes demonstrate a relative increase in high-frequency content with increased permeability; other attributes show the opposite. Kozlov (2007) found that for dual-porosity reservoirs consisting of thin, alternating permeable and impermeable layers, the permeability attributes become ambiguous because the frequency dependence of the reflectivity function is strongly affected by layering. Even for a single permeable layer encased within impermeable rock, the permeability attributes can be either directly or inversely proportional to frequency, depending on the layer thickness expressed in the dominant seismic wavelength (Kozlov 2007). Hence, it is important to consider the geometry of a heterogeneous reservoir (thickness and layering) in modeling its comparative permeability.

As derived by Goloshubin et al. (2008), in the case of a normal-incident P-wave reflected from an inhomogeneous reservoir with $N$ permeable lenses (see Fig. 7.28a, b, c for the model delineation), the reflection coefficient $\boldsymbol{R}(\omega)$ approximates to:

$$\boldsymbol{R}(\omega) \approx \boldsymbol{R}_0 - \left(1 - \boldsymbol{R}_0^2\right)\boldsymbol{R}_0 e^{-i\omega\Delta t - a(\omega)} + \sum_{n=1}^{N} \boldsymbol{R}_n \sqrt{\left(\frac{i\omega\rho_f k_n}{\eta}\right)} e^{-i\omega\Delta t_n - a_n(\omega)}, \qquad (7.7)$$

where $\omega = 2\pi f$ is the angular frequency, $R_0$ is the reflection coefficient from the top of the reservoir, $i = \sqrt{-1}$, $\Delta t$ is the two-way travel-time thickness of the reservoir, $\alpha(\omega)$ describes transmission and absorption energy losses from a P-wave reflected from the base of the reservoir, $R_n$ is the reflection coefficient from the n$^{th}$ lens, $\rho_f$ and $\eta$ are the pore-fluid density and viscosity, $k_n$ is the rock permeability of the n$^{th}$ lens, and $\Delta t_n$ and $\alpha_n(\omega)$ are time delay and transmission-absorption losses for the seismic response from lens $n$.

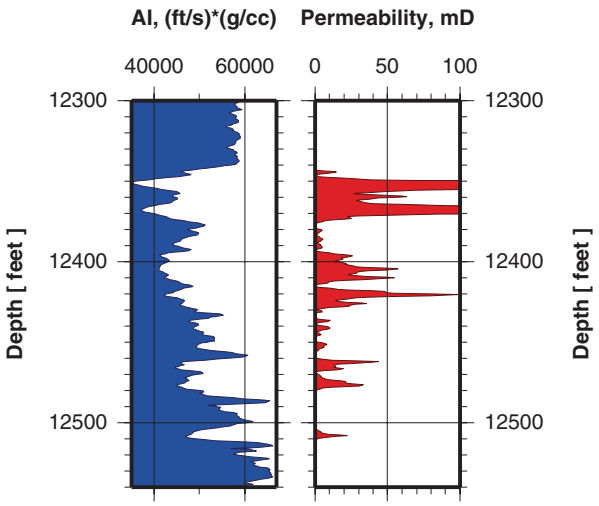


**Fig. 7.29** Acoustic impedance (*AI*) and permeability data derived from the Madison Formation logs in the RSU #1 well. The Middle Madison rocks (from 12,340 to 12.510 ft depth) are dual porosity carbonates characterized with interlayered zones of increased fracturing and permeability (vuggy dolostones) and zones of prevailing microporosity having high impedance and low permeability

Figure 7.28d shows the behavior of the fluid-saturated reservoir reflectivity as a function of seismic frequency $f$ and the number of reservoir layers $N$ having variable permeability $K_n$. There is a significant shift of the first reflected amplitude peak toward lower frequencies. The effect of increased reflectivity at lower frequencies progressively smoothens as the number of high-permeability lenses is increased. However, even with the number of layers $N = 20$, the low-frequency ($f = 20$ Hz) reflectivity is twice as great as the high-frequency ($f = 40$ Hz) reflectivity (Fig. 7.28d). This suggests that spectral analysis of a seismic reflected signal can be used to discriminate reservoirs with dual-porosity—having intense fracturing or vuggy porosity development with associated zones of high fluid mobility—from low-permeability reservoirs with intergranular porosity only. Provided the reservoir modeled in Fig. 7.28 does not have significant thickness variations, we can expect a strong amplitude resonance effect resulting from high-permeability lens development but a uniform distribution of reflectivity with frequency resulting from a low-permeability reservoir.

### *7.11.2 Qualitative Permeability of the Middle Madison Reservoir*

Acoustic impedance and permeability data derived from the Madison Limestone logs in the RSU #1 well demonstrate close resemblance of the Madison to the dual-porosity reservoir modeled in Fig. 7.28. At the RSU #1 well site, impermeable carbonates enclose the dual-porosity, low-impedance, vuggy dolostones of the middle Madison unit between depths of 12,340 and 12,510 ft (3,761 and 3,813 m) (Fig. 7.29). The middle Madison rocks show a high degree of vertical heterogeneity, with permeability variations of several orders of magnitude. About a dozen highly permeable zones within the middle Madison have permeability of more than 10 mD (Fig. 7.29). The alternating permeable and impermeable layers within the middle Madison reservoir match conditions of low-frequency resonance in seismic reflectivity (Fig. 7.28). This leads us to propose that spectral decomposition of reflection seismic data is an effec-

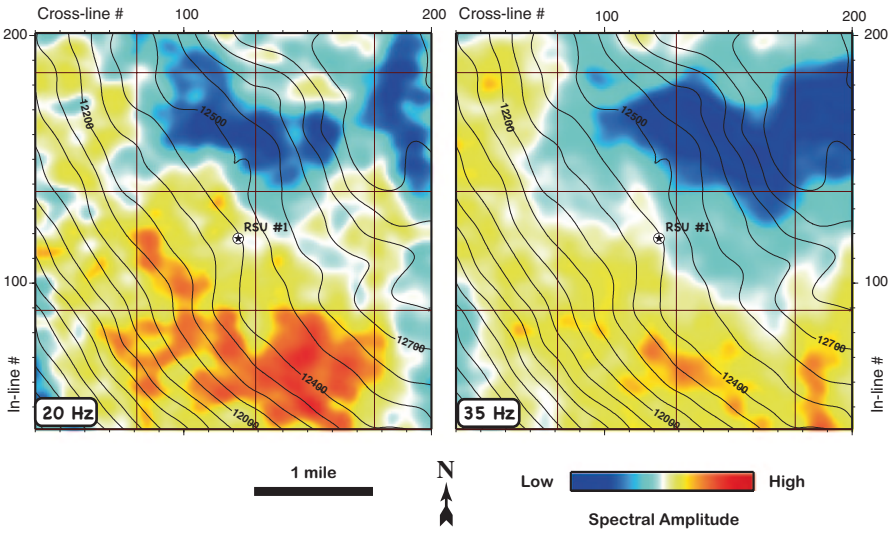


**Fig. 7.30** Middle Madison amplitude slices extracted from the spectrally decomposed volumes: 20-Hz isofrequency amplitude (*left* panel), 35-Hz isofrequency amplitude (*right* panel). Labeled structure contour lines represent depth (ft) below KB at the RSU #1 well

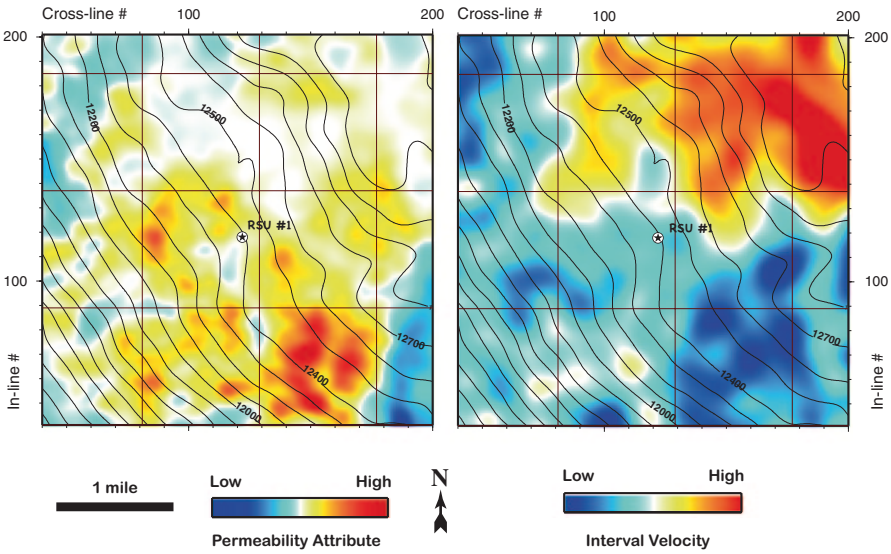


**Fig. 7.31** Color-coded permeability attribute (*left* panel) and interval velocity (*right* panel) maps calculated on top of the Middle Madison horizon. Note that high-permeability area southeast from the RSU #1 well correlates with low-velocity zone. Labeled structure contour lines represent depth (feet) below KB at the RSU #1 well

tive tool for mapping lateral variations of permeability within the middle Madison rocks. According to Kozlov (2007), a decrease of P-wave velocity is another essential aspect of the seismic signature of permeability increase in the case of dual porosity.

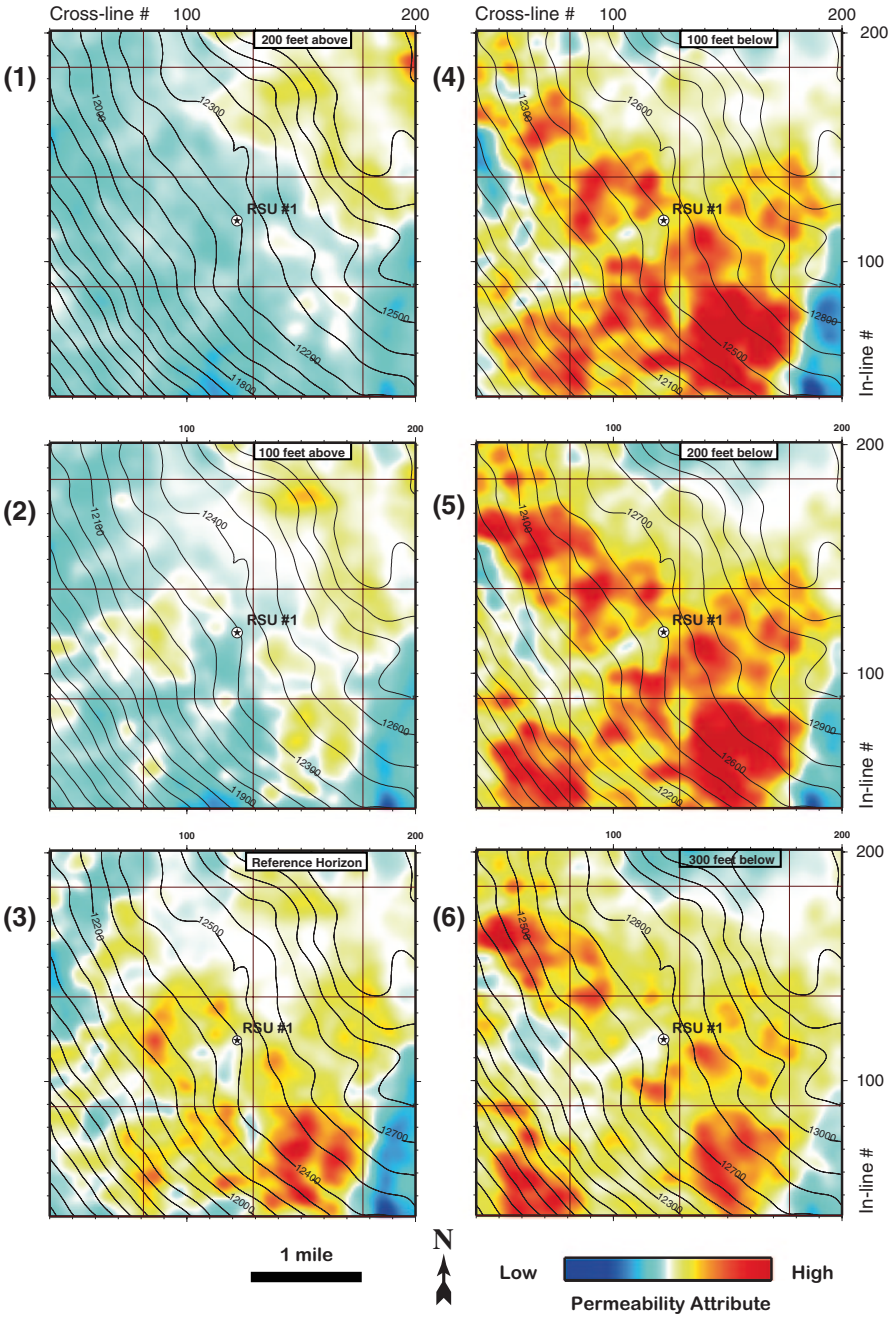


**Fig. 7.32** Color-coded permeability attribute maps calculated along the Middle Madison phantom horizons: (*1*) 200 ft above the reference horizon, (*2*) 100 ft above, (*3*) on top of the Middle Madison, (*4*) 100 ft below the reference, (*5*) 200 ft below the reference, (*6*) 300 ft below the reference horizon. Contour lines represent depth below KB of the corresponding phantom horizons

Figure 7.30 compares two frequency slices corresponding to the middle Madison reflection horizon, extracted from spectrally decomposed volumes; Fig. 30a corresponds to the low-frequency (20 Hz) response, while Fig. 30b shows the reflectivity of the middle Madison horizon at a relatively high frequency (35 Hz). The area northeast of the RSU #1 well is characterized by low reflectivity at both frequencies, while south and west of the well the seismic reflected signal exhibits high amplitudes. This can be explained by increased noise content due to the Jim Bridger power plant located about 1 mi northeast of the RSU #1 well. Considering possible noise originating at the power plant, we designed a *permeability attribute* that is proportional to the difference between the low-frequency spectral amplitude along the middle Madison reflection horizon and the high-frequency spectral amplitude, and is scaled by the sum of the two components. Thus, the areas with high noise content appear to be more attenuated on the permeability attribute maps.

The permeability attribute described above is shown in Fig. 7.31a. Relative variations of this attribute are proportional to the weighted average permeability within the middle Madison reservoir. This statement finds support in Fig. 7.31b, which shows the seismic interval velocity distribution on the top of the middle Madison horizon. There is noticeable correlation between the high-permeability area southeast of the RSU #1 well and the low-velocity anomaly at the same location.

Permeability attribute maps were calculated for several phantom horizons, conformal to the *reference middle Madison horizon*. The maps in Fig. 7.32 allow estimation of the volumetric permeability distribution within the reservoir rocks. The maximum permeability attribute anomaly (corresponding to low-frequency amplitude resonance) is mapped at 100 and 200 ft below the reference horizon (Fig. 7.32d, e) and appears decayed 300 ft below the reference horizon (Fig. 7.32f). On the basis of the seismic data, the middle Madison reservoir is thus at least 100 ft thick. Immediately above the reference horizon, within the upper Madison unit (Fig. 7.32a, b), the permeability attribute appears to have much lower values (corresponding to high-frequency amplitudes resonance) and a much more uniform distribution. At the RSU #1 well location the thickness of the middle Madison unit is 160 ft (Fig. 7.29), which agrees well with the seismically derived permeability attribute distribution. These comparative permeability distribution maps (Fig. 7.32) were computed with the objective of increasing the accuracy of flow simulation for the middle Madison reservoir.

## Glossary of Seismic Terms

**Acquisition** the generation of seismic energy waves within the earth and their distant recording.

**Acquisition footprint** any regularity or pattern in seismic data that is not of geologic origin and can be due to acquisition or processing problems.

**Aliasing** an effect that causes some continuous signals to become indistinguishable when sampled.

**Azimuth** angle measured clockwise from north to a linear direction.

**Bin** an area on the land surface that captures any seismic trace whose midpoint falls into it. All the traces in a bin form a three-dimensional CMP gather.

**Common gather** a collection of seismic traces with a common or fixed characteristic. For example, a common shot gather is all traces generated by the same shot.

**Component** the directional orientation of a source or receiver during acquisition. Conventional surface seismic involves data recording in one vertical component and two horizontal components.

**CMP** (1) literally, common midpoint. The midpoint surface location for a seismic trace that is calculated from source and receiver coordinates. (2) A seismic acquisition and processing technique that yields multiple prestack traces at each midpoint location.

**CMP fold** the number of traces in a CMP gather. Conventional processing involves summation (stacking) of these traces to produce one poststack trace.

**CMP gather** gather of all traces in a seismic survey having the same midpoint number or bin.

**CMP stack** a stack of all prestack traces associated with the same midpoint number or bin.

**Depth structure map** a map in depth units that is generated from a time structure map by means of a time-depth transform function.

**Far offset** the distance from source to farthest receiver.

**Fold** the number of seismic traces within a gather.

**Frequency** the number of wave peaks or cycles per second.

**Gather** see Common gather.

**Horizon slice** a horizontal display or map view of 3-D seismic data showing a particular reflection, as opposed to a time slice that has a constant travel time.

**Interface** a surface in the earth where velocity, density, or other physical parameters change abruptly. Commonly, but not necessarily, coincident with a change in rock type or pore fluid.

**Interpretation** the analysis of geophysical data to generate geologicly reasonable models and predictions about subsurface properties and structures.

**Inversion** (1) a process of estimating subsurface physical parameters (velocity, density, etc.) from seismic data. (2) A situation where a low-velocity layer underlies a high-velocity layer.

**Lateral resolution** the minimum separation of two features in map view before their individual identities are lost.

**Medium** a term designating a specific location (layer or section) within the layered earth model. Plural is media.

**Midpoint** the point on the land surface halfway between source and receiver.

**Migration** the process by which seismic events are geometrically re-located in either space or time to provide a more accurate image of the subsurface.

**Offset** the distance between the source and receiver associated with a trace.

**Phantom horizon** a seismic attribute not coincident with a certain tracked horizon but conformal to it and shifted by a certain number of milliseconds.

**P-wave** the primary or fastest wave traveling away from a seismic energy source. This kind of seismic wave excites particle motion that is parallel to the direction of wave propagation. Currently, this is the main wave type used in reflection seismology.

**Poststack** an object or process related to seismic data after CMP stacking.

**Prestack** an object or process related to seismic data before CMP stacking.

**Processing** a sequence of digital data processing routines followed to enhance reflected seismic signals and to suppress noise.

**Receiver** a device for measuring surface motion due to the passage of seismic or sound waves.

**Reflected wave** the wave that returns back to the surface after reflection from an interface.

**Reflection** (1) the process in which a seismic wave strikes and partially bounces off an interface. (2) An event recorded on the surface as a seismic image (in section or map view) associated with reflection from a particular interface.

**Reflection coefficient** the ratio of the amplitude of a reflected wave to the amplitude of the incident wave.

**Reflection coefficient series** the reflection coefficient as a function of recording time (depth).

**Reflector** the interface associated with a particular reflection event.

**Section** a side-by-side display of many seismic traces.

**Seismic** the reflection seismology method commonly used to provide information about the subsurface structure of rock formations and the physical properties of both the subsurface rocks and the fluids within them.

**Seismic event** any continuous object on a seismic display.

**Seismic trace** a curve representing seismic attribute variation with time or depth at a specific (fixed) location. Usually is plotted with time (depth) increasing downward.

**Seismic wave** are energy wave that travels through the earth's layers. May be of natural (earthquake, volcanic eruption) or artificial origin (explosion, vibrator track).

**Shot** a seismic energy source.

**Signal-to-noise ratio** ratio of peak signal amplitude to average noise amplitude.

**Source** an object or process that generates seismic waves.

**Stack** the single output trace created by summing two or more input traces.

**Synthetic data** numerically created pseudo-seismic data used for testing processing algorithms or validating interpretation details.

**Synthetic seismogram** a simulated seismic trace (at a well location) based on sonic and density logs that is used to associate seismic reflections with geologic horizons.

**3-D seismic** the shooting and processing of seismic data in such a way that a cube of data is produced and interpreted for geologic meaning.

**3-D survey** a dense grid of parallel source lines (cross-line direction in this study) and receiver lines (in-line direction) established for seismic data acquisition and processing.

**Time slice** a horizontal display or view of 3-D seismic data having a certain arrival time.

**Time structure map** a map generated by tracking that displays vertical reflection time to a horizon of interest.

**Trace** a one-dimensional graph of a quantity vs. time or depth.

**Tracking** the interpretation process of following a reflection surface throughout a data volume and extracting the travel time to this surface.

**Velocity** the speed at which a seismic wave travels. Can vary from one location to another in the earth.

**Vertical resolution** the minimum separation of two features on a seismic trace that correspond to the top and base of a geologic unit or bed.

**Vertical seismic profile (VSP)** a seismic acquisition technique in which a surface source shoots into a series of receivers located down a well.

**Wavelength** the distance between successive equivalent points on two wave cycles.

**Zero offset VSP** a VSP that has one source, located at or near the wellhead.

## References

Biot MA (1962) Mechanics of deformation and acoustic propagation in porous media. J Appl Phys 33:1482–1498

Castagna JP, Sun S (2006) Comparison of spectral decomposition methods. First Break 24:75–79

Cluff RM, Cluff SG (2004) The origin of Jonah Field, northern Green River Basin, Wyoming. In: Robinson W, Shanley KW (eds) Jonah Field: case study of a giant tight-gas fluvial reservoir. American Association Petroleum Geologists Studies in Geology, p 127–145 (52, Chap. 8)

Dix CH (1955) Seismic velocities from surface measurements. Geophysics 20:68–86

Goloshubin G, Silin D (2006) Frequency-dependent seismic reflection from a permeable boundary in a fractured reservoir. Society of Exploration Geophysicists 2006 New Orleans annual meeting. Expanded abstracts 1742–1741

Goloshubin G, Silin D, Vingalov V, Takkand J, Latfullin M (2008) Reservoir permeability from seismic attribute analysis. Leading Edge 27:376–381

Kozlov K (2007) Seismic signature of a permeable, dual-porosity layer. Geophysics 72(5):SM281–SM291

Lindseth RO (1979) Synthetic sonic logs—a process for stratigraphic interpretation. Geophysics 44:3–26

Morlet J, Arens G, Fourgeau E, Giard D (1982) Wave propagation and sampling theory, Part II: sampling theory and complex waves. Geophysics 47:222–236

Neidell NS, Taner MT (1971) Semblance and other coherency measures for multichannel data. Geophysics 36:482–497

Partyka GA, Gridley J, Lopez J (1999) Interpretational applications of spectral decomposition in reservoir characterization. Leading Edge 18:353–360

Pride SR, Harris JM, Berryman JG, Yamomoto T, Wu R, Spetzler H, Rector JW, Nowack RL, Nihel KT, Mateeva A, Johnson DL, Fehler M (2003) Permeability dependence of seismic amplitudes. Leading Edge 22:518–525

Ren H, Goloshubin G, Hilterman FJ (2009) Poroelastic analysis of permeability effects in thinly layered porous media. Geophysics 74(6):N49–N54

Roberts A (2001) Curvature attributes and their application to 3-D interpreted horizons. First Break 19:85–99

Taner MT, Koehler F, Sheriff RE (1979) Complex seismic trace analysis. Geophysics 44:1041–1063

# Chapter 8
# Reservoir Fluid Characterization of the Weber Sandstone and Madison Limestone on the Rock Springs Uplift in Southwest Wyoming

**Scott A. Quillinan and J. Fred McLaughlin**

**Abstract** Formation brine characterization provided the data for analytical permitting requirements, evaluating reservoir confinement, and reaction path modeling. The brines of the Weber Sandstone and Madison Limestone of the Rock Springs Uplift are sodium-chloride type with total dissolved solid concentrations in excess of 75,000 mg/L. Due to the high TDS the Wyoming Department of Environmental Quality has classified these as Class VI groundwater.

Solutes of the brines are enriched above the seawater evaporation trend line, indicating that the brines have been heavily influenced by additional mineral dissolution, specifically halite. The composition of dissolved gases were measured and found to be unique to each formation. Dissimilarities in the brine chemistries and associated dissolved gases indicate that the target formations are isolated from each other.

Both the Weber and Madison fluids are supersaturated with respect to dolomite and calcite. With respect to anhydrite, the Weber is saturated or slightly undersaturated and the Madison is undersaturated. Simulations of $CO_2$ injection into the formation brines suggest a decrease in pH and an increase in the partial pressure of $CO_2$, calcite dissolution and anhydrite precipitation. These reactions will likely cause an increase in porosity of 1–3 %.

Hydrogen sulfide concentrations in the reservoir increased between the first and second sampling set (.04 to 127 mg/L in the Weber and from 29 to 87 mg/L in the Madison). Although the cause of this increase is unknown, it is recommended that careful consideration be given to reservoir management during $CO_2$ injection. Additionally, $H_2S$ monitoring should be an element of water production scenarios for CCUS.

S. A. Quillinan (✉) · J. F. McLaughlin
Carbon Management Institute, Laramie, WY, USA
e-mail: scottyq@uwyo.edu

J. F. McLaughlin
e-mail: Derf1@uwyo.edu

R. C. Surdam (ed.), *Geological $CO_2$ Storage Characterization,*
Springer Environmental Science and Engineering, DOI 10.1007/978-1-4614-5788-6_8,
© Springer Science+Business Media New York 2013

## 8.1 Introduction

This section provides detailed geochemical analysis of target formation brines. These analyses provided the baseline data to classify the groundwater, a prerequisite for permitting. In addition, these data were used to evaluate brine evolution and the hydraulic confinement of the reservoirs. Geochemical analyses were then used in creating a geochemical model to further predict fluid–rock interactions in the reservoir.

For this project the Wyoming Department of Environmental Quality issued a Class I UIC (Underground Injection and Control) permit (#12-257) for the University of Wyoming to operate the RSU #1 well for the purpose of completing injectivity testing. In accordance with this permit, the baseline water quality had to be characterized and classified prior to injection. The analytical work required for permitting is described in the Wyoming Water Quality Rules and Regulations (WQRR Chap. 8, Table 1).

Analyte and dissolved gas concentrations of formation fluids and compositions were characterized and evaluated. Conservative analyte analysis was used to characterize the water–rock interaction and as a proxy for long-term storage potential. Comparative analyses of dissolved gases, along with geochemical analysis, was used to determine reservoir confinement and the influence of extraneous fluids.

## 8.2 Methods

CMI collected water samples on August 27th, 2011 from the wellbore using the Baker Atlas RCI (Reservoir Characterization Instrument) and in December, 2012 using a wireline bailer. Samples were analyzed for minor and major elements, radionuclides, organic acids, volatile organics, organic characteristics, and flash gas compositions using the methods described by Brown et al. (1970). The results of these analyses are presented in Table 8.1.

The evolution of solutes within Madison and Weber formation fluids was evaluated by comparing conservative and non-conservative ions (Rittenhouse 1967; Carpenter 1978; McCaffrey et al. 1987; Walter et al. 1990). The concentrations and molarity of Br were compared with those of TDS, Ca, Mg, Cl, K, Na, and Li. Aside from Mg and Ca, all ions were enriched with respect to seawater evaporation trends (Fig. 8.1a–h). There are quantitative differences between the first sample set and the second sample set, as well as differences between the two formations (Fig. 8.1a–h).

Thermodynamic calculations and reaction path models based on the analytical results from the pressurized samples were computed using Geochemists Workbench (Bethke 1996).

**Table 8.1** Analytical results of measured constituents from the RSU #1 well

| Analyses (mg/L unless otherwise indicated) | Weber Formation Energy Labs 08/27/2011 | Weber Formation Core Labs 08/27/2011 | Weber Formation Energy Labs 12/14/12 | Madison Limestone Energy Labs 08/27/2011 | Madison Limestone Core Labs 08/27/2011 | Madison Limestone Energy Labs 12/03/12 |
|---|---|---|---|---|---|---|
| **Microbiological** | | | | | | |
| Heterotrophic (MPN/mL) | <2 | – | 40 | 2 | – | 10 |
| **Major Ions** | | | | | | |
| Alkalinity, Total as $CaCO_3$ | 509 | – | 3030 | 1170 | – | 2620 |
| Carbonate as $CO_3$ | ND | 0 | ND | ND | 0 | ND |
| Bicarbonate as $HCO_3$ | 621 | 720 | 3690 | 1420 | 1610 | 3190 |
| Calcium | 734 | 705 | 539 | 1190 | 1280 | 1630 |
| Chloride | 60,900 | 61,830 | 57,400 | 50,300 | 52,290 | 51,600 |
| Flouride | 11.5 | 8.4 | 6.1 | 3.5 | 13 | 2.8 |
| Magnesium | 37 | 40 | 45 | 158 | 170 | 195 |
| Nitrogen, Ammonia as N | 33.4 | – | 33.1 | 42 | – | 39 |
| Nitrogen, Nitrate + Nitrite as N | 0.1 | ND | ND | ND | ND | 0.1 |
| Nitrogen, Nitrite as N | ND | ND | ND | ND | ND | ND |
| Phosphate | – | ND | – | – | ND | – |
| Potassium | – | 1940 | 1910 | – | 4210 | 3780 |
| Silicon | – | 26 | 45.2 | – | 36 | 59.5 |
| Sodium | 40,700 | 43,250 | 36,500 | 29,000 | 32,820 | 27,900 |
| Strontium | – | 26 | 14 | – | 67 | |
| Sulfate | 11,600 | 10,320 | 6030 | 2800 | 2280 | 1820 |
| **Non-Metals** | | | | | | |
| Dissolved inorganic carbon | 144 | – | 786 | 355 | – | 724 |
| Dissolved organic carbon | 2.9 | – | 4.5 | 1 | – | 4.4 |
| Total organic carbon | 2.7 | – | 4.7 | 1 | – | 4.5 |
| UV Absorbance at 254 nm ($cm^{-1}$) | 0.92 | – | 1.99 | 0.558 | – | 1.28 |
| Total recoverable phenolics | 0.61 | – | 0.16 | 0.05 | – | 0.7 |
| Total cyanide | ND | – | 0.098 | ND | – | 0.339 |
| Sulfide | 0.04 | | 120 | 28 | 0 | 82 |
| Sulfide as hydrogen sulfide | 0.04 | – | 127 | 29 | – | 87 |

**Table 8.1** (continued)

| Analyses (mg/L unless otherwise indicated) | Weber Formation Energy Labs 08/27/2011 | Weber Formation Core Labs 08/27/2011 | Weber Formation Energy Labs 12/14/12 | Madison Limestone Energy Labs 08/27/2011 | Madison Limestone Core Labs 08/27/2011 | Madison Limestone Energy Labs 12/03/12 |
|---|---|---|---|---|---|---|
| **Physical properties** | | | | | | |
| Chemical oxygen demand | 2420 | – | 9120 | 1940 | – | 3050 |
| pH | 7.54 | 7.11 | 6.46 | 7.36 | 6.01 | 6.43 |
| TDS | 89,800 | 119,155 | 109,000 | 75,000 | 95,126 | 89,800 |
| BOD | 56.7 | – | 517 | 50.2 | – | 234 |
| Sodium adsorption ratio | 397 | – | 380 | 209 | – | 174 |
| **Metals** | | | | | | |
| Aluminum | ND | ND | 3.5 | ND | ND | 1.9 |
| Arsenic | 0.095 | – | 0.444 | 1.76 | – | 0.376 |
| Barium | ND | ND | 14.3 | 1 | ND | 4.48 |
| Beryllium | ND | – | 0.007 | ND | – | 0.037 |
| Bismuth | – | – | 0.02 | – | – | 0.02 |
| Boron | 61.1 | – | 71.8 | 95.2 | – | 101 |
| Borate | – | 81 | | – | 120 | – |
| Bromide | – | 94 | 99 | – | 115 | 140 |
| Cadmium | ND | ND | 0.006 | ND | ND | ND |
| Chromium | ND | ND | 0.61 | 0.06 | ND | 0.576 |
| Cobalt | 0.02 | ND | 0.019 | ND | ND | 0.009 |
| Copper | ND | ND | 13.6 | ND | ND | 1.35 |
| Iodide | – | ND | 2 | – | ND | ND |
| Iron | 0.94 | 2.2 | 44.1 | 0.54 | 8.1 | 32.2 |
| Lead | ND | ND | 2.91 | ND | ND | 0.305 |
| Lithium | 92.8 | 100 | 90.5 | 91.9 | 105 | 91.6 |
| Manganese | 0.07 | 0.07 | 0.777 | 0.12 | 0.35 | 7.76 |
| Mercury | ND | – | 0.0006 | ND | – | ND |
| Molybdenum | – | ND | – | – | ND | – |
| Nickel | ND | ND | 0.093 | ND | ND | 0.03 |
| Phosphorus | – | ND | – | – | ND | – |
| Selenium | 0.0004 | – | 0.054 | 0.013 | – | 0.041 |
| Silver | ND | – | ND | ND | – | 0.001 |
| Uranium (μg/L) | – | – | 0.0187 | – | – | 0.0004 |
| Vanadium | ND | – | 0.26 | ND | – | 0.01 |
| Zinc | 0.26 | – | 4.58 | 0.4 | – | 2.1 |
| **Radionuclides (pCi/L)** | | | | | | |
| Gross Alpha | – | – | 400 | – | – | 157 |
| Gross Beta | – | – | 1630 | – | – | 2990 |
| Radium 226 | – | – | 24 | – | – | 39 |
| Radium 228 | – | – | 14 | – | – | 1.2 |
| Cesium 134 | – | – | – | – | – | 0 |

**Table 8.1** (continued)

| Analyses (mg/L unless otherwise indicated) | Weber Formation Energy Labs 08/27/2011 | Weber Formation Core Labs 08/27/2011 | Weber Formation Energy Labs 12/14/12 | Madison Limestone Energy Labs 08/27/2011 | Madison Limestone Core Labs 08/27/2011 | Madison Limestone Energy Labs 12/03/12 |
|---|---|---|---|---|---|---|
| Cesium 137 | – | – | – | – | – | 0 |
| **Data Quality** | | | | | | |
| Anion/Cation Balance (±5) | −3.15% | 0.37% | −5.42% | −3.71% | 2.61% | −4.57% |
| **Organic Acids** | | | | | | |
| Acetate | – | 5.5 | – | – | 0 | – |
| Butyrate | – | 0 | – | – | 0 | – |
| Formate | – | 5.4 | – | – | 1.7 | – |
| Glycolate | – | 0 | – | – | 0 | – |
| Propionate | – | 0 | – | – | 0 | – |
| Valerate | – | 0 | – | – | 0 | – |
| **Volatile organic compounds (µg/L)** | | | | | | |
| 1,1,1,2-Tetrachloroethane | ND | – | ND | ND | – | ND |
| 1,1,1-Trichloroethane | ND | – | ND | ND | – | ND |
| 1,1,2,2-Tetrachloroethane | ND | – | ND | ND | – | ND |
| 1,1,2-Trichloroethane | ND | – | ND | ND | – | ND |
| 1,1-Dichloroethane | ND | – | ND | ND | – | ND |
| 1,1-Dichloroethene | ND | – | ND | ND | – | ND |
| 1,1-Dichloropropene | ND | – | ND | ND | – | ND |
| 1,2,3-Trichlorobenzene | ND | – | ND | ND | – | ND |
| 1,2,3-Trichloropropane | ND | – | ND | ND | – | ND |
| 1,2,4-Trichlorobenzene | ND | – | ND | ND | – | ND |
| 1,2,4-Trimethylbenzene | 210 | – | 190 | 190 | – | 73 |
| 1,2-Dibromo-3-chloropropane | ND | – | ND | ND | – | ND |
| 1,2-Dibromoethane | ND | – | ND | ND | – | ND |
| 1,2-Dichlorobenzene | ND | – | ND | ND | – | ND |
| 1,2-Dichloroethane | ND | – | ND | ND | – | ND |
| 1,2-Dichloropropane | ND | – | ND | ND | – | ND |

**Table 8.1** (continued)

| Analyses (mg/L unless otherwise indicated) | Weber Formation Energy Labs 08/27/2011 | Weber Formation Core Labs 08/27/2011 | Weber Formation Energy Labs 12/14/12 | Madison Limestone Energy Labs 08/27/2011 | Madison Limestone Core Labs 08/27/2011 | Madison Limestone Energy Labs 12/03/12 |
|---|---|---|---|---|---|---|
| 1,3,5-Trimethylbenzene | 30 | – | 62 | 30 | – | 54 |
| 1,3-Dichlorobenzene | ND | – | ND | ND | – | ND |
| 1,3-Dichloropropane | ND | – | ND | ND | – | ND |
| 1,4-Dichlorobenzene | ND | – | ND | ND | – | ND |
| 2,2-Dichloropropane | ND | – | ND | ND | – | ND |
| 2-Chloroethyl vinyl ether | ND | – | ND | ND | – | ND |
| 2-Chlorotoluene | ND | – | ND | ND | – | ND |
| 4-Chlorotoluene | ND | – | ND | ND | – | ND |
| Benzene | ND | – | 230 | ND | – | 13 |
| Bromobenzene | ND | – | ND | ND | – | ND |
| Bromochloromethane | ND | – | ND | ND | – | ND |
| Bromodichloromethane | ND | – | ND | ND | – | ND |
| Bromoform | ND | – | ND | ND | – | ND |
| Bromomethane | ND | – | ND | ND | – | ND |
| Carbon tetrachloride | ND | – | ND | ND | – | ND |
| Chlorobenzene | ND | – | ND | ND | – | ND |
| Chlorodibromomethane | ND | – | ND | ND | – | ND |
| Chloroethane | ND | – | ND | ND | – | ND |
| Chloroform | ND | – | ND | ND | – | ND |
| Chloromethane | ND | – | ND | ND | – | ND |
| *cis*-1,2-Dichloroethene | ND | – | ND | ND | – | ND |
| *cis*-1,3-Dichloropropene | ND | – | ND | ND | – | ND |
| Dibromomethane | ND | – | ND | ND | – | ND |
| Dichlorodifluoromethane | ND | – | ND | ND | – | ND |
| Ethylbenzene | 20 | – | 54 | 20 | – | 26 |
| Hexachlorobutadiene | ND | – | ND | ND | – | ND |
| Isopropylbenzene | 30 | – | 9 | 20 | – | 8.4 |
| *m*+*p*-Xylenes | 55 | – | 280 | 50 | – | 98 |
| Methyl ethyl ketone | ND | – | 280 | ND | – | 88 |
| Methyl tert-butyl ether (MTBE) | ND | – | ND | ND | – | ND |

**Table 8.1** (continued)

| Analyses (mg/L unless otherwise indicated) | Weber Formation Energy Labs 08/27/2011 | Weber Formation Core Labs 08/27/2011 | Weber Formation Energy Labs 12/14/12 | Madison Limestone Energy Labs 08/27/2011 | Madison Limestone Core Labs 08/27/2011 | Madison Limestone Energy Labs 12/03/12 |
|---|---|---|---|---|---|---|
| Methylene chloride | ND | – | ND | ND | – | ND |
| *n*-Butylbenzene | 57 | – | 44 | 40 | – | 53 |
| *n*-Propylbenzene | ND | – | 27 | ND | – | 28 |
| Naphthalene | 190 | – | 74 | 190 | – | 77 |
| *o*-Xylene | ND | – | 110 | ND | – | 66 |
| *p*-Isopropyltoluene | ND | – | 16 | ND | – | 15 |
| *sec*-Butylbenzene | ND | – | 15 | ND | – | 16 |
| Styrene | ND | – | ND | ND | – | ND |
| *tert*-Butylbenzene | ND | – | ND | ND | – | ND |
| Tetrachloroethene | ND | – | ND | ND | – | ND |
| Toluene | ND | – | 490 | ND | – | 86 |
| *trans*-1,2-Dichloroethene | ND | – | ND | ND | – | ND |
| *trans*-1,3-Dichloropropene | ND | – | ND | ND | – | ND |
| Trichloroethene | ND | – | ND | ND | – | ND |
| Trichlorofluoromethane | ND | – | ND | ND | – | ND |
| Vinyl chloride | ND | – | ND | ND | – | ND |
| Xylenes | – | – | 380 | – | – | 160 |
| **Organic Characteristics** | | | | | | |
| Oil and Grease (HEM)[7] mg/L | 270 | – | 1100 | 490 | – | 510 |
| **Compositional Analysis of Flash Gas (Mole %)** | | | | | | |
| Nitrogen | – | 78.888 | – | – | 16.75 | – |
| Carbon Dioxide | – | 14.738 | – | – | 82.892 | – |
| Hydrogen Sulfide | – | 0 | – | – | 0 | – |
| Methane | – | 2.537 | – | – | 0.189 | – |
| Ethane | – | 0.297 | – | – | 0 | – |
| Propane | – | 0.213 | – | – | 0.021 | – |
| *Iso*-Butane | – | 0.043 | – | – | 0.004 | – |
| *N*-Butane | – | 0.071 | – | – | 0.011 | – |
| *Iso*-Pentane | – | 0.397 | – | – | 0.04 | – |
| *N*-Pentane | – | 0.02 | – | – | 0.004 | – |
| Hexanes | – | 2.119 | – | – | 0.006 | – |
| Heptanes | – | 0.244 | – | – | 0.015 | – |
| Octanes | – | 0.116 | – | – | 0.026 | – |
| Nonanes | – | 0.08 | – | – | 0.012 | – |
| Decanes Plus | – | 0.237 | – | – | 0.03 | – |

"ND" Not detected

"–" Not measured

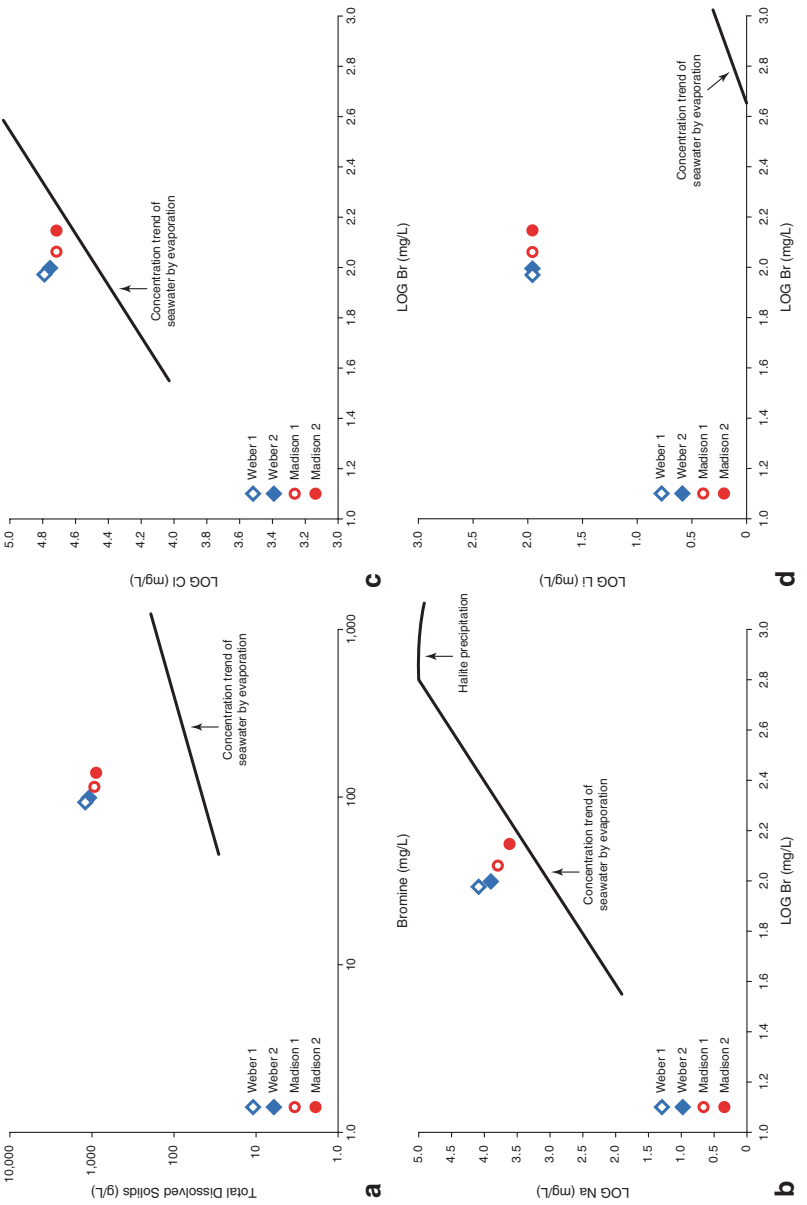


**Fig. 8.1** (**a**) Plot of log TDS versus log bromine relative to the seawater evaporation pathway described by Rittenhouse 1967. (**b**) Plot of log sodium versus log bromine relative to the seawater evaporation pathway described by Rittenhouse (1967). (**c**) Plot of log chlorine versus log bromine relative to the seawater evaporation pathway described by Rittenhouse (1967). (**d**) Plot of log lithium versus log bromine relative to the seawater evaporation pathway described by Rittenhouse (1967).

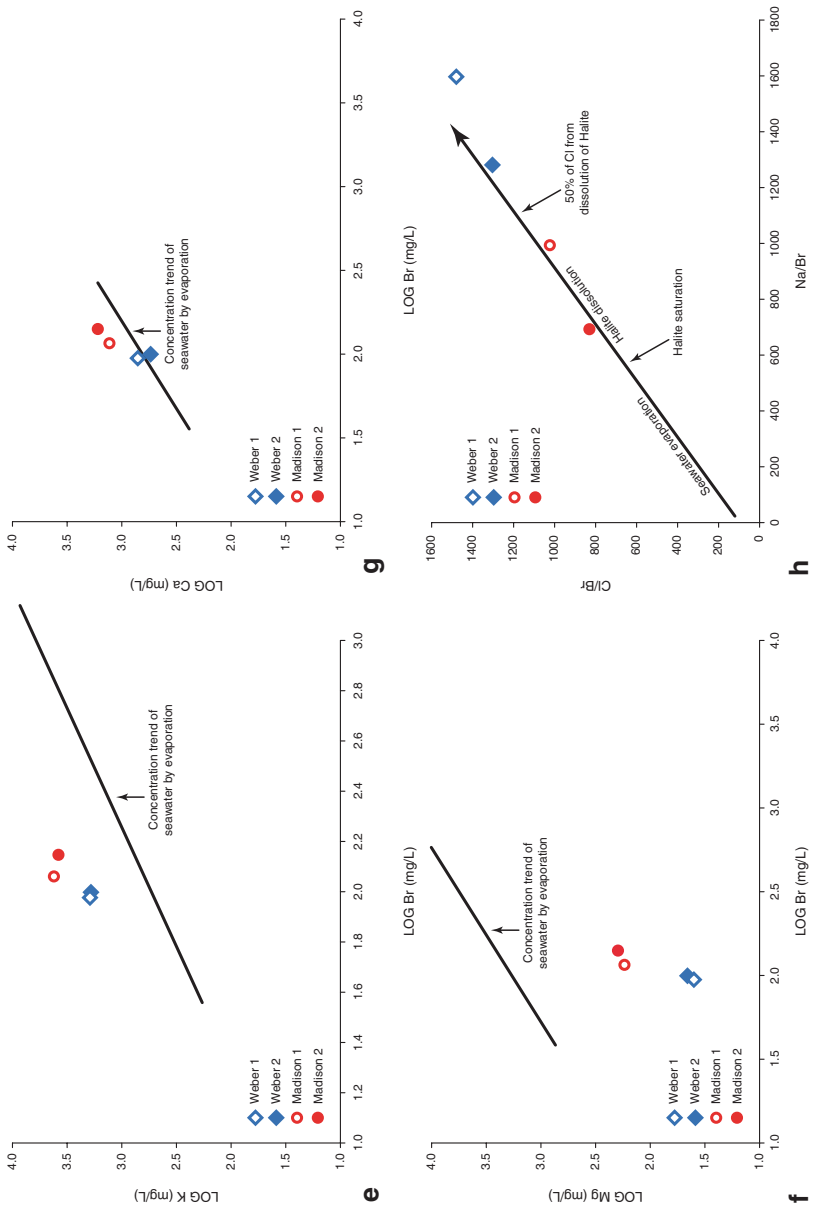


**Fig. 8.1** (continued) (**e**) Plot of log potassium versus log bromine relative to the seawater evaporation pathway described by Rittenhouse (1967). (**f**) Plot of log calcium versus log bromine relative to the seawater evaporation pathway described by Rittenhouse (1967). (**g**) Plot of log magnesium versus log bromine relative to the seawater evaporation pathway described by Rittenhouse (1967). (**h**) Na/Br versus Cl/Br molar ratio plot adapted from Engle and Rowan (2013)

## 8.3 Results

Brines from both formations are sodium-chloride-type with measured TDS concentrations of 89,000–109,000 mg/L in the Weber Sandstone and 75,000–95,000 mg/L in the Madison Limestone. The brine densities are calculated to be 1.06 g/cm$^3$ (Weber) and 1.05 g/cm$^3$ (Madison). Ionic strength ranges from 1.77 molal to 2.03 molal (Weber) and from 1.44 molal to 1.61 molal (Madison). Brine temperatures range from 92 °C (Weber) to 95 °C (Madison), with formation pressures of 4800 psi (Weber) and 5900 psi (Madison).

Comparison of the study-site brines with the USEPA maximum contaminant level (MCL) shows that the formation brines greatly exceed the standards for TDS. In addition, MCLs are exceeded with respect to chloride, fluoride, sulfate, aluminium, barium, iron, lead, manganese, and gross beta.

Formation fluids were analyzed for 63 volatile organic compounds (VOC) (Table 8.1). The first sample set (August, 2011) detected six volatile organic compounds in Weber and Madison brines. VOCs increased to fourteen species in the second round of sampling (December, 2012). With the exception of BTEX (benzene, toluene, ethylbenzene, and xylene) compounds, when a VOC was detected similar concentrations were measured in both reservoirs. This indicates that VOC's were likely introduced during drilling and/or work in the wellbore (see Table 8.1). Benzene, toluene, and xylenes were not detected in the first round of sampling but were measured in the second round; concentrations were highest in the Weber. Ethylbenzene was found in equal concentrations in both formations in the first sample set (20 µg/L), but more than doubled in the Weber in the second sample set (50 µg/L).

Based on these analyses, the Wyoming Department of Environmental Quality classified the groundwater in both reservoirs as Class VI groundwater within 1320 ft of the RSU #1 wellbore in both the Weber and Madison formations. According to the Wyoming Water Quality Rules and Regulations, Class VI groundwater is defined as "unusable, or unsuitable for use," due to high TDS concentrations, excessive contaminates or to excessive depth.

## 8.4 Disscussion

### *8.4.1 Comparative Solute Analysis*

Enrichment of Na and Cl over the seawater evaporation trend line typically is related to halite dissolution (Rittenhouse 1967; Carpenter 1978; McCaffrey et al. 1987; Walter et al. 1990). Both the Weber and the Madison formations contain evaporites, and dissolution of evaporites has enriched the formation waters with respect to Na and Cl (Fig. 8.1b,c,h). Molar ratio analysis of Na:Br and Cl:Br proposed by Walter et al. (1990), highlights the effect of halite dissolution on formation fluids (Fig. 8.1h). Though both formations have Na–Cl concentrations that

are enriched by halite dissolution, it is more pronounced in fluids from the Weber Sandstone (Fig. 8.1h).

Dissolution of minerals is further evidenced by comparison of Li:Br and K:Br systematics, both of which are enriched with respect to seawater evaporation trend lines (Fig. 8.1d,e). The enrichment suggests that post-burial dissolution or alteration of minerals, such as feldspars and clays, has influenced solute concentrations in these formation fluids. Mg is depleted with respect to evaporative seawater, particularly in Weber fluids (Fig. 8.1f). Mg depletion is most likely a byproduct of dolomitization, though the timing of Mg depletion in the fluids (near surface or at depth) is indeterminable from these data. Ca is slightly enriched with respect to evaporative seawater in Madison fluids; Weber fluids straddle the trend line (Fig. 8.1g). The abundance of secondary Ca-minerals, such as calcite and anhydrite, and the reactive nature of these minerals make interpretation of Ca solute concentrations difficult. However, enrichment of Ca in the Madison suggests that dissolution of Ca-minerals has impacted the water chemistry of the formation.

Comparative analysis of solutes in Weber and Madison formation fluids suggests that dissolution of evaporite and other minerals has had a large influence on the composition of the formation fluids. Evaporite dissolution has increased the overall TDS of the formation fluids post-burial, resulting in some of the most saline formation fluids collected in Wyoming (WOGCC 2013). Though potential reaction rates and ionic strengths can vary, the evidence of dissolution and high TDS suggests that the formation fluids and the reservoir rock at the study site have been in contact for a relatively long period. The differences in solute concentrations between formation fluids suggest that the fluids from the Weber and the Madison are in equilibrium with the reservoir rock, and are not likely mixed or mixing. This indicates that both reservoirs are reasonably stable, and both exhibit the ability to hold and retain fluids; these conditions are ideal for CCS, as they indicate a low likelihood of unforeseen migrations or leakage, which reduces the overall risk.

### *8.4.2 Differences Between Sample Sets*

The Na:Br and Cl:Br ratios record a noticeable decrease between the first and the second sample sets (Fig. 8.1h). The differences of solute concentrations between the two sets of samples could be attributable to several factors. The first set of samples was maintained at reservoir pressure by capture cylinders, whereas the second set was collected using a bailer, so pressure was not maintained. The second sampling method could have led to the precipitation of some solutes. However, it is most likely attributed to introduced fluids.

The first set of samples collected had very low concentrations of $H_2S$ (Madison, 29 mg/L; Weber, 0.04 mg/L). The second set of samples measured much higher concentrations of $H_2S$ (Madison 87 mg/L, Weber 127 mg/L). Interestingly, the sulfate concentrations decreased between the first and second sample set

(Table 8.1). This is indicative of reservoir souring. Water circulated during drilling, completion, and work-over of the well may have introduced sulfate reducing bacteria (SRB). SRB ingest sulphate and organic acids and generate $H_2S$. Mixing these drilling waters with highly saline reservoir fluids could sour the reservoir in these mixing zones (e.g. Ligthelm et al. 1991). Though it is uncertain which process or processes directly generated the $H_2S$, if targeted reservoirs and associated fluids are highly sensitive to redox reactions or non-native fluids, fluids injected during CCS must be closely monitored to avoid degrading the reservoir and formation fluids.

It is also advisable to design the downhole data collection program carefully, particularly with regard to alteration of formation fluids or the potential for borehole-adjacent reservoir degradation. While it is foolhardy to omit collection of all downhole data, identifying the most invasive tests and the potential consequences associated with testing should be carefully considered.

### *8.4.3 Dissolved Gas Analysis*

The composition of dissolved gases in Weber and Madison formation fluids are different (Table 8.1 and Fig. 8.2). Though the total abundance of gas in both formations is dominated by three species—nitrogen, carbon dioxide, and alkanes—the mole fractions are markedly different (Table 8.1 and Fig. 8.2). Nitrogen is the dominant gas species (approximately 79 %) in fluids from the Weber Sandstone, followed by carbon dioxide (approximately 15 %) and alkanes, mostly methane and hexane (approximately 6 %). Carbon dioxide is the dominant gas species (approximately 83 %) in fluids from the Madison Limestone, followed by nitrogen (approximately 17 %) and a minor alkane component (< 1 %).

The dissimilarities of gases within formation fluids suggest that the reservoirs are not in hydraulic communication. These data, along with the water chemistry analysis, suggests that the Weber and Madison formation fluids are isolated and injected $CO_2$ is not likely to migrate between reservoirs.

### *8.4.4 Equilibrium Calculations*

CMI calculated species activities and saturation states to characterize thermodynamic controls on the water–rock system. Calculations provide saturation indices for the potentially reactive minerals—dolomite, calcite, and anhydrite. Both the Weber and the Madison are supersaturated with respect to dolomite and calcite. With respect to anhydrite, the Weber is saturated or slightly undersaturated and the Madison is undersaturated (Table 8.2).

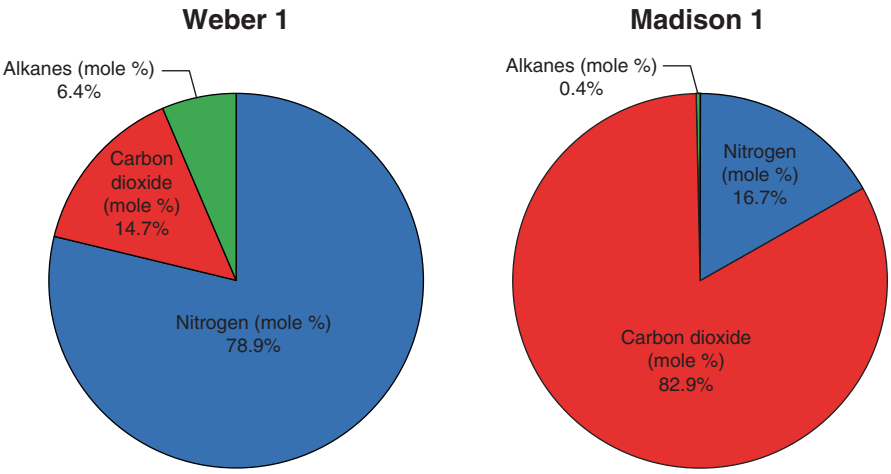


**Fig. 8.2** Percent composition of dissolved gasses in the Weber and Madison Formations

**Table 8.2** Saturation indices calculated at 100 °C. Positive values indicate degree of supersaturation

| | Weber Sandstone | | Madison Limestone | | | |
|---|---|---|---|---|---|---|
| Mineral | Energy Labs 08/27/2011 | Core Labs 08/27/2011 | Energy Labs 12/14/12 | Energy Labs 08/27/2011 | Core Labs 08/27/2011 | Energy Labs 12/03/12 |
| Anhydrite | 0.2025 | −0.1640 | −0.1487 | −0.1224 | −0.1766 | −0.650 |
| Calcite | 1.7160 | 0.5766 | 1.5700 | 1.3190 | 1.1520 | 2.171 |
| Dolomite | 3.8080 | 1.9540 | 3.9010 | 3.0720 | 2.9050 | 5.144 |

### *8.4.5 Reaction Path Modeling*

CMI investigated reaction pathways for the Madison brines in response to injected $CO_2$. Models were focused on the Madison as it is the most likely candidate for injection. The modeling parameters were determined from minerals identified in the petrographic analyses and the measured constituents and physical characteristics of the brine. The simulation evaluates a constant input of aqueous $CO_2$ (hourly) for 365 days. The model simulates a reservoir temperature of 100 °C, and pressure of one atmosphere.

$CO_2$ injection into the Madison is expected to decrease the pH and increase the TDS and the partial pressure of $CO_2$ [$P(CO_2)$] (Figs. 8.3, 8.4, and 8.5). Calcite dissolves as a result of increased $P(CO_2)$, which in turn decreases the pH. The decrease in pH increases the $HCO_3$ in solution and thus further increases $P(CO_2)$. The decrease in $CO_3$ concentration with decreasing pH results in undersaturation of dolomite, leading to dolomite dissolution and in turn increasing the Mg concentration in the brine. Increased Ca concentration from calcite dissolution prompts the precipitation of anhydrite (Fig. 8.6).

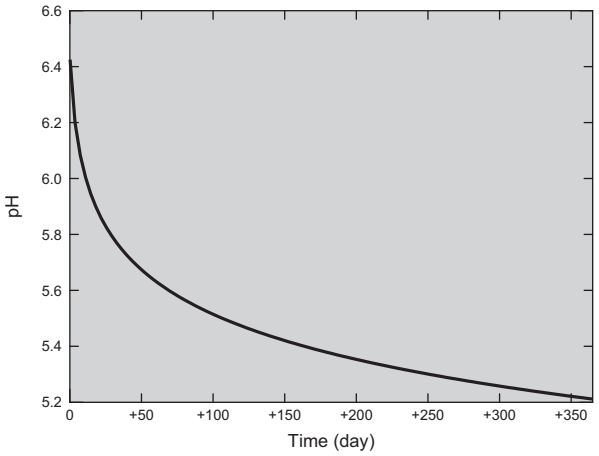


**Fig. 8.3** Modeled decrease in pH for the Madison

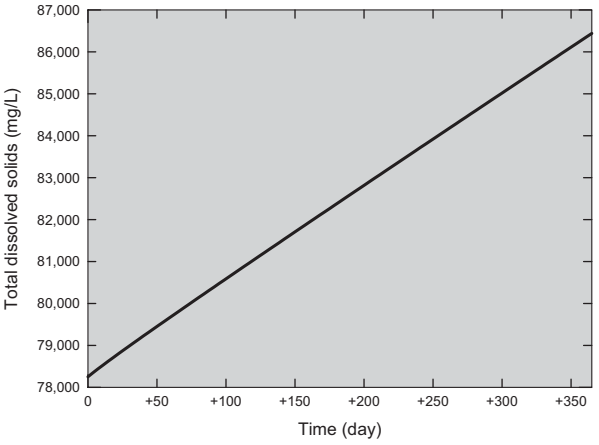


**Fig. 8.4** Modeled increase in total dissolved solids for the Madison

The volume of calcite dissolved slightly exceeds the volume of anhydrite precipitated. Thus the porosity in the reservoir is estimated to increase by 1–3 %. Additional experimental work is needed to determine the petrostatic location and nature of the anhydrite precipitation.

These reactions take place proximal to the well bore. Because these reactions are mostly driven by the increased P ($CO_2$), mobilization of these ions will likely reprecipitate on the periphery of the $CO_2$ plume. As the plume expands outward it could force many generations of calcite growth and dissolution. Anhydrite remains supersaturated once additional $CO_2$ is introduced to the reservoir and therefore captures excess calcium from the fluid. The calcium captured by the anhydrite precipitation may eventually limit calcite reprecipitation.

These calculations are consistent with observations in natural carbonate $CO_2$ fields and fields undergoing $CO_2$ EOR operations and with previous geochemical models (Mazzullo and Harris 1992; Worden and Smith 2004; Kazuba et al. 2011).

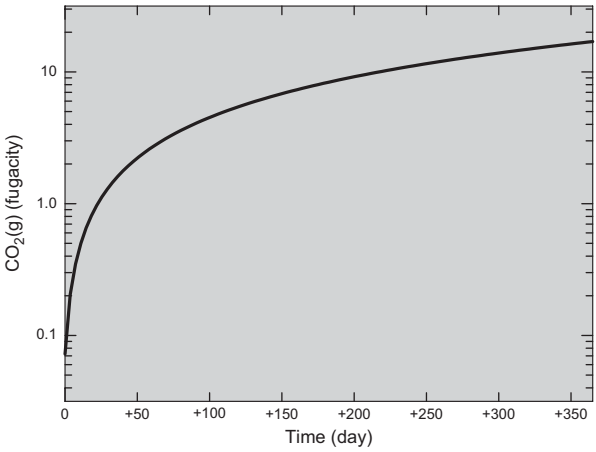


**Fig. 8.5** Modeling results for the Madison show increases in P ($CO_2$) from $CO_2$ injection and calcite dissolution

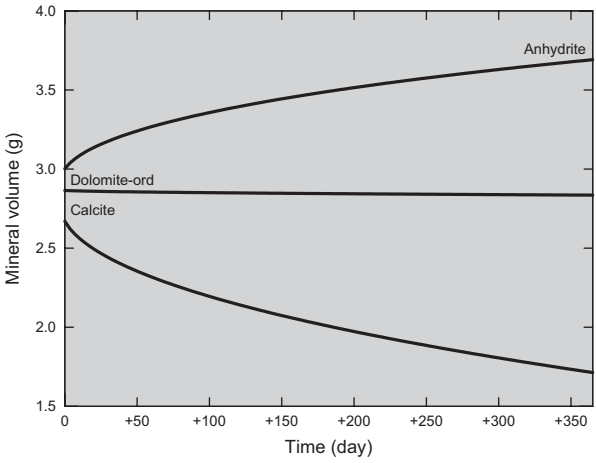


**Fig. 8.6** Modeling results in the Madison show calcite dissolution and anhydrite precipitation in response to $CO_2$ injection. Dolomite shows only slight dissolution

## *8.4.6 Response of Water Quality to Modeled $CO_2$ Injection*

Potential water treatment and metal recovery scenarios are covered in detail in Chap. 11. However, it is important to mention how water quality parameters used to design the water treatment scenario might change in response to injected $CO_2$. Examination of the modeling results and water quality analyses suggest three areas of concern with regard to water treatment scenarios: increasing TDS concentration, increased magnesium concentration, and the measured increase in $H_2S$.

**TDS** Water treatment technologies are sensitive to increases in salinity (Sherwood et al. 1967), in that the salinity of the water determines the percentage of the water that can be recovered (Bourcier et al. 2011; Baker 2004). As described by our geochemical modeling, TDS proximal to the injection well bore is expected to continu-

ally increase as $CO_2$ is injected into the reservoir (Fig. 8.4). More work is required to determine when and how much the TDS will increase at distances away from the wellbore, particularly at water production wells. TDS increases measured in the water production wells may act as an early warning for $CO_2$ break-through.

**Mg** Mg concentration in the brine will increase as dolomite dissolves. It is of interest to mention that the increased magnesium concentrations make lithium extraction more difficult (see Chap. 11.4). Arguably the biggest challenge to date of extracting Li from brines has been the separation of Mg and Li (Daniel et al. 2006; Hamzaoui et al. 2008; Jerome 2003; Konigsberger and Harris 2008; Wen et al. 2006; Zeng et al. 2007; Zhong and Yin 2003). Although the Mg concentration in the brine will increase from dolomite dissolution, this reaction occurs proximal to the wellbore and should not have an effect on the Li: Mg ratio of the brines near the water production wells.

**$H_2S$** Although the cause of the increased $H_2S$ is unknown, if $H_2S$ increases consistently then management will be required in water treatment facilities. Additionally, increased $H_2S$ would cause further increases in TDS concentrations.

These data show that reservoir souring is a concern and should be monitored during water production.

## 8.5 Conclusion

Analysis of the target formation brines has generated a geochemical and water quality baseline at the study site. As a result of these analyses the WYDEQ has classified the brines of the Madison and Weber as class VI (unsuitable for use). In addition, the water quality analyses recorded elevated concentrations of some metals.

The sodium and chloride of the brines are enriched beyond simple evaporation of seawater. This suggests increased water–rock interaction and dissolution of minerals adding to the salinity.

Dissimilarities in the water chemistry and dissolved gas analyses suggest that the Madison reservoir is confined from the Weber reservoir.

Simple geochemical modeling indicates some changes to brine chemistry in response to injected $CO_2$. These changes are summarized as carbonate dissolution and anhydrite precipitation proximal to the well bore. These reactions associated with $CO_2$ injection are expected to decrease the pH (6.4 to 5.2), increase the TDS (> 10,000 mg/L), $HCO_3$, and Mg, and decrease the $SO_4$ concentrations in the brine. These changes should only minimally affect the design of water-treatment facilities.

Hydrogen sulfide concentrations in the reservoir increased between the first and second sampling series. Although the cause of this increase is unknown, it is recommended that careful consideration be given to reservoir management during $CO_2$ injection. Additionally, $H_2S$ monitoring should be an element of water production strategies.

## References

Baker RW (2004) Membrane Technology and Applications 2nd ed. Wiley, Chichester

Bethke CM (1996) Geochemical Reaction Modeling: Concepts and Applications. Oxford University Press

Bourcier WL, Wolery TJ, Wolfe T, Haussmann, Buscheck TA, Aines RD (2011) A preliminary cost and engineering estimate for desalinating produced formation water associated with carbon dioxide capture and storage. Int J Greenhouse Gas Control 5:1319–1328

Brown EM, Skuogstad W, Fishman MJ (1970) Methods for collection and analysis of water samples for dissolved minerals and gases, laboratory analysis. US Geological Survey Technical Water Resource Investigation 5(C1)

Carpenter AB (1978) Origin and chemical evolution of brines in sedimentary basins. Oklahoma Geological Survey 79:60–77

Daniel AB, Teresita FK, Anthony MT (2006) Production of lithium compounds directly from lithium containing brines. US2006115410

Engle MA, Rowan EL (2013) Interprestation of Na–Cl–Br systematics in sedimentary basin brines: comparison of concentration, element ration, and isometric log-ration approaches. Math Geosci 45(1):87–101

Hamzaoui AH, Jamoussi B, M'nif A (2008) Lithium recovery from highly concentrated solutions: response surface methodology (RSM) process parameters optimization. Hydrometallurgy 90:1–7

Jerome, L., 2003. Process for Obtaining Monohydrated Lithium Sulfate from Natural Brines. (US09435606)

Kazuba JP, Navarre-Sitchler A, Thyne G, Chopping C, Meuzlaar T, Hanzaoui (2011) Supercritical carbon dioxide and sulfur in the Madison Limestone: a natural analog in southwest Wyoming for geologic carbon–sulfur co-sequestration. Earth Planet Sci Lett 309:131–140

Konigsberger E, Harris B (2008) Properties of electrolyte solutions relevant to high concentration chloride leaching I. Mixed aqueous solutions of hydrochloric acid and magnesium chloride. Hydrometallurgy 90:177–191

Ligthelm RB, de Boer RB, Brint JF (1991) Reservoir souring: sn analytical model for $H_2S$ generations and transportations in an oil reservoir owing to bacterial activity. Society of Petroleum Engineers SPE23141, pp 369–378

Mazzullo, S. J., and P. M. Harris, 1992, Mesogenetic dissolution: Its role in porosity development in carbonate reservoirs: AAPG Bulletin 76:607–620

McCaffrey MA, Lazar B, Holland HD (1987) The evaporation path of seawater and the coprecipitation of $Br^-$ and $K^+$ with halite. J Sediment Res 57:928–937

Rittenhouse G (1967) Bromine in oil-field waters and its use in determining possibilities of origin of these waters. Am Assoc Petrol Geol Bull 51:2430–2440

Sherwood, T.K., Brian, P.L.T., Fischer R.E., Desalination by reverse osmosis, Ind. Eng. Chem. Fund., 6 (1967), pp. 1–12

Walter LM, Stueber AM, Huston TJ (1990) Br–Cl–Na systematics in Illinois Basin fluids: constraints on fluid origin and evolution. Geology 18:315–318

Wen XM, Ma PH, Zhu CL, He Q, Deng XC (2006) Preliminary study on recovering lithium chloride from lithium-containing waters by nanofiltration. Sep Purif Technol 49:230–236

WOGCC (2013) Wyoming Oil and Gas Conservation Commission, Casper. http://wogcc.state.wy.us/. Accessed continually 2009–2013 (Sect. 5.2) and Feb. 2013

Worden R, Smith L (2004) Geological sequestration of $CO_2$ in the subsurface: lessons from $CO_2$ injection enhanced oil recovery projects in oil fields. Geol Soc Lond Special Publ 233:211–224

Zeng DW, Liu HX, Chen QY (2007) Simulation and prediction of solubility phase diagram for the separation of $MgC_{l2}$ from LiCl brine using HCl as a salting-out agent. Hydrometallurgy 89:21–31

Zhong, H., Yin, H.A., 2003. Study on the properties of the surface and absorpt of Li ion-exchanger of $H_2TiO_3$ type. Ion Exch. Adsorpt. 19 (1), 55–60 (in Chinese with English abstract)

# Chapter 9
# Predicting Permeability in the Target Reservoirs on the Rock Springs Uplift, Southwest Wyoming

**Yuri Ganshin**

**Abstract** Estimates of permeability in carbonate rocks from porosity alone are highly uncertain but can be improved when pore geometry information is incorporated. We developed a permeability model for a 400-ft-thick carbonate reservoir on the Rock Springs Uplift, Wyoming, with the objective of increasing the accuracy of flow simulation during $CO_2$ sequestration. Core data was used to identify hydraulic flow units within the reservoir and to further distinguish them through lithofacies analysis of thin sections. We used both the *Flow Zone Indicator* (FZI) and *Winland's* $R_{35}$ method to identify the flow units. FZI and pore throat radius values were obtained from the log-of-permeability-versus-porosity crossplot of the core sample measurements. For the rock types composing the Madison Limestone on the Rock Springs Uplift, both the FZI and $R_{35}$ methods proved to be effective techniques for rock-type classification. We found that acoustically derived porosity estimates within the Madison Limestone stratigraphic interval correlate well with those derived from the FZI. Sonic velocity in carbonates is a function not only of total porosity but also of the predominant pore type that determines the permeability of the rock. Hence our permeability estimation used both the density porosity and calibrated sonic porosity from conventional wireline logs. In the Madison Limestone, vug development within dolomitized sparitic carbonates has resulted in layered structures of super-permeable zones sandwiched between non-vuggy, less permeable micritic dolostones. Among the various vuggy zones of the Madison stratigraphic interval, permeability was found to vary by two to three orders of magnitude.

We also estimated the permeability in a 670-ft-thick sandstone unit within the Weber Sandstone on the Rock Springs Uplift with the objective of increasing the accuracy of our $CO_2$ flow simulation program. We used core data to identify the porosity-permeability relationship for the cored depth interval. On the basis of this relationship and well log data, we constructed a continuous vertical permeability profile. Seismically derived porosity values along the Weber horizon were used to model spatial permeability variations away from the RSU #1 well. The resulting

Y. Ganshin (✉)
Carbon Management Institute Laramie, University of Wyoming, Laramie, USA
e-mail: yganshin@uwyo.edu

R. C. Surdam (ed.), *Geological $CO_2$ Storage Characterization,*
Springer Environmental Science and Engineering, DOI 10.1007/978-1-4614-5788-6_9,
© Springer Science+Business Media New York 2013

statistical estimators of the permeability distribution led us to classify the Weber Sandstone as highly heterogeneous and variably permeable strata.

## 9.1 The Madison Limestone Reservoir

### *9.1.1 Methodology*

Reliable knowledge of permeability can only be derived from laboratory analysis of core samples. However, that procedure becomes impractical for thick reservoir sections or poorly cored wells. Instead, permeability is commonly estimated in uncored sections or poorly cored wells from the following permeability-versus-porosity relationship—which has no apparent theoretical basis.

$$\log(k) = a\varphi + b \tag{9.1}$$

In Eq. 9.1, permeability $(k)$ is plotted as a log function merely because it is assumed to be log-normally distributed with respect to porosity $(\varphi)$.

Estimates of permeability derived from porosity alone are very ineffective. The uncertainty arises because porosity is a volumetric parameter: it is the ratio of pore volume to bulk volume. Permeability, on the other hand, is a measure of the flow properties of a fluid through the pores, which depends not only on the volumetric proportion of the pore space but also on its geometric distribution and connectivity. Combining these non-volumetric parameters with porosity significantly improves estimates of permeability. Further significant improvement can be obtained by grouping core data on the porosity/permeability plots by rock type.

Rock typing can be understood as a process of classifying reservoir rocks into distinct units, each of which was deposited under similar geologic conditions and has undergone similar diagenetic alteration. When properly classified, a given rock type is characterized by a unique mineralogy (type, abundance, morphology), texture (grain size, grain shape, sorting, packing), pore geometry, and porosity/permeability relationship. Hence, rock typing narrows the search domain of realistic permeability solutions in uncored intervals and in uncored wells.

Of the various quantitative rock-typing techniques presented in the literature (Gunter et al. 1997; Hartmann and Farina 2004; Amaefule et al. 1993; Porras and Campos 2001; Jennings and Lucia 2001; Guo et al. 2007), two techniques—the FZI (Amaefule et al. 1993) and Winland's $R_{35}$ (Gunter et al. 1997)—appear to be more widely used than the others for siliciclastic and carbonate reservoirs.

**The FZI Technique** Amaefule et al. (1993) found that core data provides information on various depositional and diagenetic controls on pore geometry, and that variations in pore geometry attributes lead to the definition of separated zones (hydraulic flow units) with similar flow properties. They proposed a method based

mainly on the Kozeny-Carmen equation (Carmen, 1937) and the concept of the mean hydraulic unit radius (Bird et al. 1960).

The verification of hydraulic-unit zonation on the log-of-permeability-versus-porosity crossplot is necessarily the first step in their proposed method. Next, the Flow Zone Indicator (FZI) is computed for each data point on the crossplot:

$$FZI[\mu] = RQI / \varphi_Z \tag{9.2}$$

using the Reservoir Quality Index (RQI),

$$RQI[\mu] = 0.0314\sqrt{(k / \varphi)}$$

where $\mu$ indicates that FZI and RQI are computed in micrometers, $k$ is permeability measured in millidarcy [mD] and $\varphi$ is porosity [decimal fraction]—and the pore-volume-to-grain-volume ratio ( $\varphi_Z$ ),

$$\varphi_Z = \varphi/(1-\varphi)$$

Then, Eq. 9.2 is rearranged for the estimation of permeability $k$ from porosity $\varphi$ and FZI (i.e., rock type):

$$k(mD) = 1014\varphi^3 (FZI / (1-\varphi))^2 \tag{9.3}$$

**Winland's $R_{35}$ Technique** Winland developed an empirical relationship among porosity, air permeability, and the pore aperture corresponding to a mercury non-wetting phase of 35 % ($R_{35}$) for a mixed suite of sandstones and carbonates. Through multiple regression analysis, Winland came up with an equation published by Kolodzie (1980),

$$\log(R_{35}) = 0.732 + 0.588\log(k_a) - 0.864\log(\varphi) \tag{9.4}$$

where $R_{35}$ is the pore aperture radius (μ, micrometers), $k_a$ is the uncorrected air permeability (mD), and $\varphi$ is porosity (decimal fraction).

Core samples of a given rock type have similar $R_{35}$ values that can be used to define major flow units in reservoirs (Gunter et al. 1997). Similarly to the FZI method, the $R_{35}$ radius (and corresponding rock type) can be estimated on the crossplot of the log of permeability versus porosity built from the cores. Data from laboratory measurements can be further used to develop the hydraulic unit (rock type) tracks and regression models from wireline logs. Permeability for uncored well intervals can then be predicted using the same Winland's $R_{35}$ equation (Eq. 9.4). Both techniques (FZI and $R_{35}$) have been applied successfully to both clastic-type and carbonate-type reservoirs (Amaefule et al. 1993; Gunter et al. 1997).

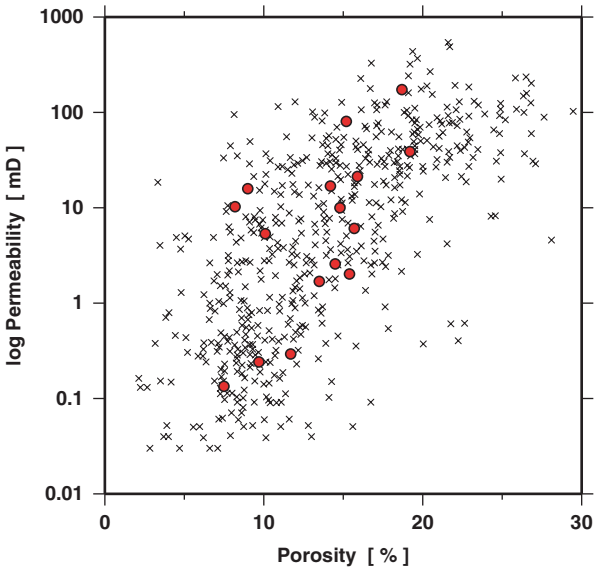


**Fig. 9.1** Simple semilog plot of permeability vs. porosity for dolostones of the Madison Formation. Crosses mainly represent outcrop samples from Ehrenberg et al. (2006). Red dots—core samples from the RSU #1 well, Rock Springs Uplift, Wyoming. Pearson's correlation coefficient for the RSU dataset $\mathbf{R} = 0.50$, coefficient of determination $\mathbf{R^2} = 0.25$

## *9.1.2 Permeability Modeling*

The porosity-permeability relationship varies considerably in different facies of the Madison Limestone. It is more difficult to predict permeability in carbonate rocks than in sandstones because carbonate pore geometry can be very complex. Fig. 9.1 shows a typical porosity-permeability relationship for dolostones of the Madison Limestone with a coefficient of determination $\boldsymbol{R^2}$ of 0.24. Even for core samples taken throughout the RSU #1 well, the spread of permeability measurements reaches three orders of magnitude (red dots in Fig. 9.1) with low correlation ($\boldsymbol{R^2} = 0.25$). It is immediately apparent from Fig. 9.1 that there is no clear correlation between porosity and permeability, which makes it difficult to predict permeability even in cases with a redundant amount of core and laboratory measurements. Therefore, a practical method or workflow to partition the pore types and distinguish rock facies by means of wireline logs is essential for permeability estimation.

In this study, we first test the concept of grouping porosity and permeability data according to their FZI/$R_{35}$ values. Next, we note that different log responses correlate differently with these numbers, and we find that acoustically measured porosity shows the strongest correlation. Finally, using this correlation, we construct a permeability profile for the whole Madison stratigraphic interval.

The laboratory data used in this study are from RSU #1 core plug samples measured at Intertek Westport Technology Center, Houston, Texas. The data include porosity and Klinkenberg-corrected permeability values obtained at reservoir conditions. Fig. 9.2 shows a plot of the porosity/permeability variations in this dataset. The dots represent measured data (red dots in Fig. 9.1); the curves indicate porosity/permeability models calculated from Eq. 9.3 (Fig. 9.2a) and from Eq. 9.4

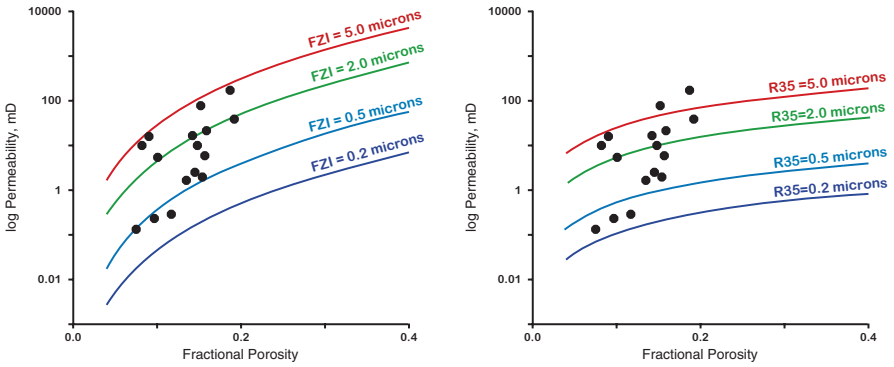


**Fig. 9.2** Semilog plot of permeability vs. porosity for the Middle Madison dolostone, RSU #1 well, Rock Springs Uplift, Wyoming. Dots are core samples from the RSU #1 well (red dots in Fig. 9.1). The colored curves indicate constant hydraulic units (rock types) defined through the *FZI* value (*left*) and the $R_{35}$ value in microns (*right*)

(Fig. 9.2b). The corresponding FZI and $R_{35}$ values used for modeling are labeled over the curves in Fig. 9.2. For both types of models, porosity and permeability correlate very well along an interval with constant FZI or $R_{35}$ value. At the same porosity, samples with higher FZI or $R_{35}$ values have higher permeability. Thus, the FZI and $R_{35}$ values can be understood to denote pore connectivity (hydraulic zones); given the same volumetric pore space, higher connectivity would produce greater permeability along with higher FZI and $R_{35}$. Both the FZI and $R_{35}$ curves tend to ascend with increasing porosity, and both modeled parameters have approximately the same range (0.2–5.0 μ) corresponding to the set of measured porosity/permeability values (Fig. 9.2). The correlation coefficient between the FZI and $R_{35}$ models for the Madison set of measurements is 0.860. Despite on the overall similarity, there is a systematic difference between the two models: the FZI curves are steeper than the $R_{35}$ curves.

Selecting the wireline data for the derivation of the transform equation was the next step in our modeling study. The following wireline logs were used for statistical analysis: gamma ray (GR), photo electric section (PE), density (DEN), P-wave velocity (VEL), neutron porosity (NPHI), focused conductivity—DOI 60 inch (COND), resistivity—DOI 60 inch (RES), density porosity (DPHI), and vuggy porosity (VPHI). The vuggy porosity log was calculated as the difference between density porosity and sonic porosity. The log values were extracted at exactly the same depths as the core plugs. Table 9.1 shows a matrix of the logs together with the calculated FZI and $R_{35}$ values at all the core depths of the Madison Limestone stratigraphic interval. A statistical evaluation of the correlation strength between wireline data and modeled attributes (FZI and $R_{35}$ values) was performed for each log. The cross correlation coefficients for the FZI and $R_{35}$ prediction models are shown at the bottom of each column in Table 9.1.

Positive correlation coefficients designate direct correlation, in which large values of one variable are associated with large values of the other, and small with

**Table 9.1** Modeling and log data for regression analysis

| Depth | FZI | R35 | GR | PE | DEN | VEL | NPHI | COND | RES | DPHI | VPHI |
|---|---|---|---|---|---|---|---|---|---|---|---|
| *12344.0* | 3.921 | 3.432 | 8.98 | 2.830 | 2.555 | 17979 | 20.23 | 299.4 | 3.340 | 16.84 | 6.72 |
| *12349.5* | 1.772 | 4.060 | 10.89 | 3.028 | 2.419 | 15327 | 28.02 | 1163.8 | 0.859 | 24.12 | 7.79 |
| *12352.0* | 4.220 | 4.111 | 12.53 | 2.922 | 2.356 | 15221 | 32.78 | 1214.9 | 0.823 | 27.49 | 11.47 |
| *12354.0* | 4.021 | 6.764 | 14.47 | 3.186 | 2.400 | 16449 | 30.09 | 945.0 | 1.058 | 25.13 | 12.30 |
| *12356.0* | 1.879 | 3.610 | 15.64 | 3.174 | 2.493 | 17592 | 24.49 | 675.8 | 1.480 | 20.16 | 9.69 |
| *12357.5* | 1.561 | 2.693 | 20.18 | 2.906 | 2.544 | 17939 | 22.83 | 584.3 | 1.711 | 17.43 | 8.16 |
| *12362.5* | 0.623 | 0.766 | 16.15 | 3.230 | 2.522 | 17485 | 23.10 | 704.7 | 1.419 | 18.61 | 7.95 |
| *12366.5* | 1.102 | 2.196 | 15.37 | 2.969 | 2.429 | 15674 | 29.54 | 1141.3 | 0.876 | 23.58 | 9.10 |
| *12371.0* | 1.191 | 2.112 | 12.40 | 3.082 | 2.473 | 16661 | 24.62 | 844.0 | 1.185 | 21.23 | 8.20 |
| *12373.0* | 2.064 | 2.864 | 11.74 | 3.195 | 2.516 | 17256 | 22.40 | 526.2 | 1.900 | 18.93 | 7.30 |
| *12375.0* | 1.361 | 1.933 | 13.23 | 2.957 | 2.590 | 18379 | 17.55 | 292.9 | 3.412 | 14.97 | 5.26 |
| *12382.0* | 1.122 | 1.095 | 13.09 | 3.162 | 2.624 | 18978 | 16.22 | 229.7 | 4.353 | 13.16 | 4.80 |
| *12383.5* | 0.461 | 0.328 | 19.86 | 3.554 | 2.633 | 18682 | 15.46 | 231.7 | 4.316 | 12.67 | 3.60 |
| *12385.0* | 0.918 | 0.897 | 14.80 | 3.242 | 2.594 | 18042 | 17.93 | 244.6 | 4.088 | 14.76 | 4.63 |
| *12394.0* | 0.930 | 1.147 | 11.24 | 3.189 | 2.577 | 17359 | 19.31 | 288.3 | 3.468 | 15.67 | 4.29 |
| *12399.5* | 0.374 | 0.312 | 11.72 | 2.960 | 2.534 | 17100 | 21.46 | 353.5 | 2.829 | 17.97 | 5.97 |
| *12400.5* | 0.794 | 0.847 | 13.04 | 3.174 | 2.519 | 16922 | 22.38 | 347.7 | 2.876 | 18.77 | 6.42 |
| *12404.0* | 1.342 | 1.568 | 11.63 | 2.864 | 2.483 | 16552 | 25.86 | 312.5 | 3.200 | 20.70 | 8.16 |
| *12406.5* | 0.782 | 0.937 | 11.21 | 2.827 | 2.503 | 16741 | 23.90 | 283.7 | 3.524 | 19.63 | 7.15 |
| *12407.0* | 1.418 | 2.404 | 10.93 | 2.727 | 2.515 | 16866 | 24.15 | 279.7 | 3.574 | 18.98 | 7.20 |
| *12408.0* | 0.533 | 0.569 | 12.91 | 2.612 | 2.544 | 16957 | 24.77 | 276.2 | 3.620 | 17.43 | 6.82 |
| *12410.0* | 2.192 | 3.264 | 14.06 | 2.835 | 2.486 | 17001 | 25.15 | 261.7 | 3.822 | 20.53 | 8.85 |
| *12414.0* | 1.415 | 2.322 | 11.86 | 3.537 | 2.603 | 17940 | 17.56 | 141.7 | 7.056 | 14.28 | 3.97 |
| *12414.5* | 1.481 | 2.029 | 13.30 | 3.555 | 2.640 | 18116 | 16.23 | 138.3 | 7.213 | 12.30 | 2.64 |
| *12415.0* | 1.048 | 1.442 | 14.73 | 3.548 | 2.671 | 18173 | 16.27 | 140.0 | 7.123 | 10.64 | 1.91 |
| *12421.0* | 4.152 | 8.894 | 17.20 | 3.002 | 2.455 | 17250 | 24.40 | 232.5 | 4.301 | 22.19 | 10.06 |
| *12422.0* | 2.766 | 5.902 | 16.82 | 2.877 | 2.505 | 17538 | 22.90 | 215.7 | 4.635 | 19.52 | 8.49 |
| *12429.0* | 1.213 | 2.144 | 15.45 | 2.894 | 2.627 | 18517 | 18.41 | 74.5 | 13.424 | 12.99 | 4.87 |
| *12432.5* | 0.543 | 0.352 | 10.88 | 4.497 | 2.767 | 19757 | 12.73 | 33.3 | 29.926 | 5.51 | 0.56 |
| *12434.5* | 0.870 | 1.423 | 27.61 | 3.193 | 2.688 | 19548 | 15.47 | 40.1 | 24.901 | 9.73 | 3.69 |
| *12437.5* | 1.513 | 1.052 | 14.19 | 2.986 | 2.614 | 18443 | 18.45 | 65.6 | 15.245 | 13.69 | 5.12 |
| *12447.0* | 0.710 | 0.754 | 9.96 | 2.789 | 2.695 | 19820 | 14.88 | 42.5 | 23.536 | 9.36 | 3.68 |
| *12448.0* | 0.679 | 0.705 | 8.87 | 2.952 | 2.724 | 19555 | 13.75 | 41.4 | 24.139 | 7.81 | 1.86 |
| *12454.0* | 0.800 | 0.998 | 13.78 | 3.392 | 2.651 | 18889 | 18.79 | 44.6 | 22.418 | 11.71 | 5.10 |
| *12459.0* | 0.710 | 0.772 | 8.70 | 2.930 | 2.768 | 21510 | 12.35 | 43.3 | 23.059 | 5.45 | 3.16 |
| *12461.5* | 3.263 | 4.571 | 15.68 | 3.196 | 2.580 | 18920 | 23.28 | 102.8 | 9.724 | 15.51 | 9.27 |
| *12462.5* | 3.522 | 5.452 | 17.73 | 3.247 | 2.550 | 18027 | 24.89 | 137.5 | 7.273 | 17.11 | 9.08 |
| *12466.5* | 3.609 | 3.576 | 19.87 | 3.101 | 2.561 | 17627 | 23.24 | 163.8 | 6.107 | 16.52 | 7.16 |
| *12476.5* | 3.664 | 7.773 | 7.77 | 3.140 | 2.541 | 17749 | 24.17 | 84.1 | 11.890 | 17.59 | 8.44 |
| *12478.5* | 2.032 | 1.959 | 7.74 | 3.075 | 2.604 | 17790 | 20.48 | 67.2 | 14.890 | 14.22 | 5.00 |
| *12492.0* | 0.526 | 0.421 | 10.35 | 4.094 | 2.744 | 19740 | 12.99 | 5.2 | 190.95 | 6.74 | 1.27 |
| *12505.0* | 2.725 | 1.351 | 14.42 | 2.599 | 2.625 | 18748 | 17.23 | 179.3 | 5.578 | 13.10 | 4.82 |
| *12512.5* | 1.927 | 2.994 | 13.68 | 4.090 | 2.770 | 22725 | 9.05 | 42.4 | 23.497 | 5.35 | 3.09 |
| *12513.0* | 2.428 | 5.032 | 13.71 | 4.060 | 2.774 | 23370 | 9.02 | 30.5 | 32.655 | 5.13 | 3.80 |
| *12514.0* | 2.068 | 2.373 | 11.15 | 4.645 | 2.778 | 23777 | 8.97 | 15.3 | 65.327 | 4.92 | 4.17 |
| $R_{FZI}$ = | 1.00 | 0.860 | 0.078 | −.115 | −.393 | −.139 | 0.401 | 0.183 | −.194 | 0.393 | 0.612 |
| $R_{R35}$ = | 0.860 | 1.00 | 0.122 | −.057 | −.411 | −.138 | 0.403 | 0.195 | −.187 | 0.411 | 0.633 |

small. Negative coefficients indicate the opposite. Analysis of the data shown in Table 9.1 demonstrates that the strongest positive correlation exists between the modeled attributes and the vuggy porosity. In both cases, the correlation coefficient ***R*** is greater than 0.6, which means that vuggy porosity is an attribute that directly correlates with the pore connectivity and can be used to estimate permeability. After substituting the vuggy porosity and corresponding regression coefficients for the unavailable variable FZI in Eq. 9.3, we obtain—after some algebraic rearrangement—the following formula to estimate permeability in the Madison Limestone:

$$k = 63\varphi^3\left(VPHI/\left(1-\varphi\right)\right)^2, \tag{9.5}$$

where *VPHI* is vuggy porosity (computed as the difference between density porosity and sonic porosity). We used fractional density porosity values as parameter $\varphi$. By use of Eq. 9.5, a synthetic permeability log was generated for the whole Madison stratigraphic interval (Fig. 9.3). Using a similar approach for the $R_{35}$ attribute and Eq. 9.4, we also modeled permeability for the same interval:

$$\log(k) = 1.7\left[\log\left(0.502\ VPHI - 1.089\right) + 0.864\ \log\left(\phi\right) - 0.732\right]$$

Both specific formulas that we used for permeability modeling are of local applicability only; however, the described methodology is of general applicability, and can be used at different locations and with different rock types.

We used laboratory measurements on the Madison cores to test the validity of our multivariate permeability models (Eqs. 9.4 and 9.5) and to compare them with a univariate linear regression model based on Eq. 9.1. The measured data and permeability estimates for the three models are shown in Table 9.2. A better match between calculated and measured data is demonstrated by the higher correlation coefficients where the models with two independent variables (total porosity and vuggy porosity) were used for permeability estimation than where the conventional, univariate porosity-permeability model was used. This means that porosity and permeability correlate well within an established hydraulic unit or, in other words, for a given pore type. At the same total porosity, carbonate rocks with higher values of vuggy porosity have higher permeability. In this study, both bivariate models demonstrate equally moderate correlation with the laboratory measurements. We believe that the slightly higher correlation coefficient for the $R_{35}$ model than that for the FZI model (Eq. 9.4 vs. Eq. 9.5) is not statistically significant.

**Permeability Distribution** A histogram and cumulative histogram of the permeability distribution and associated statistical estimators of average permeability for the middle Madison reservoir are shown as Fig. 9.11 in Sect. 9.2.2. Following a description of the various average estimators for a statistical distribution as applied to the Weber Sandstone, a discussion in Sect. 9.2.2.2 compares the estimated average permeability of the middle Madison with that of the Weber Sandstone.

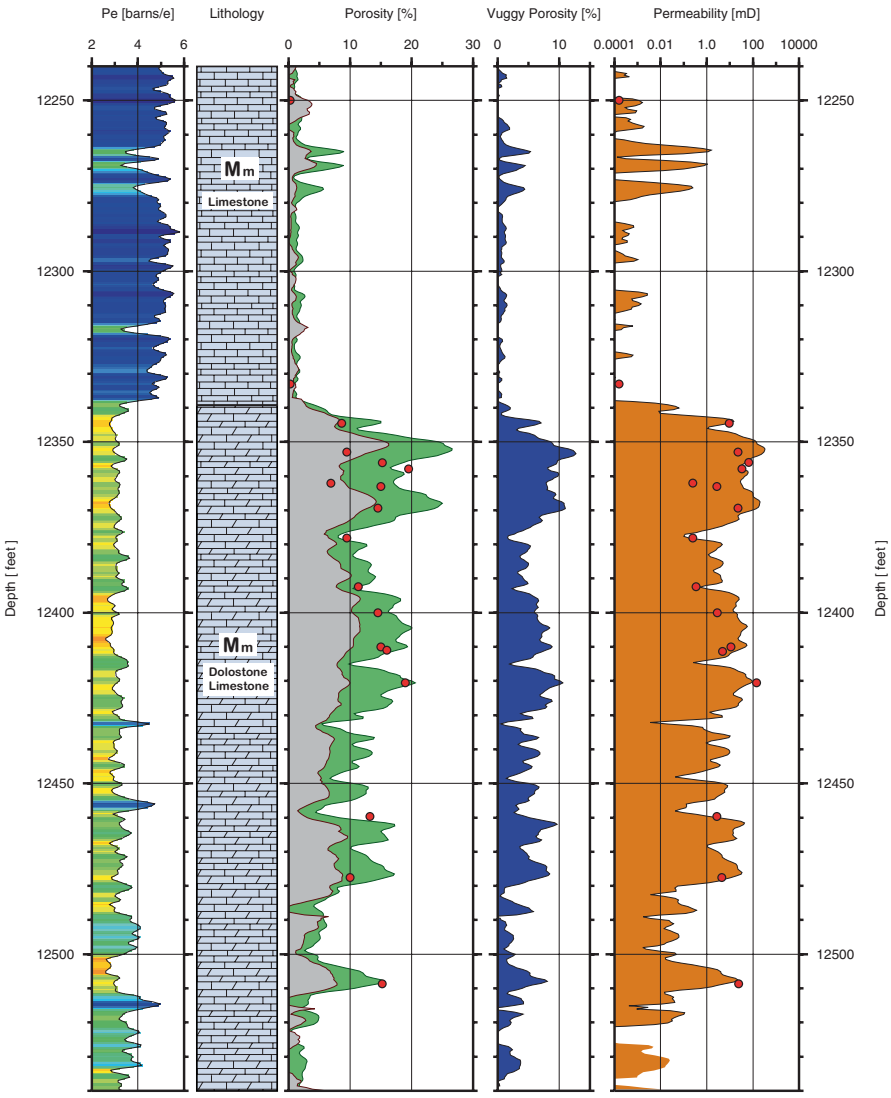


**Fig. 9.3** Open-hole logs and core data in the Madison Formation in the RSU #1 well. Tracks from left to right are (1) photo electric section, (2) lithology, (3) density (*green*) and sonic (*gray*) porosity with total porosities from core (*red dots*), (4) sonic-vug porosity index (difference between density and sonic porosities), (5) permeability from logs (*orange*) overlaid with core measurements (*red dots*)

### *9.1.3 Discussion*

To understand the good correlation between vuggy porosity and permeability reported in Table 9.1 for the Madison cores, we first examine the FZI attribute.

**Table 9.2** Measurements and Modeling Results

| Lab-measured porosity, % | Log-measured vug porosity, VPHI, % | Lab-measured permeability, mD | Modeled (Eq. 1) permeability, mD | Modeled (Eq. 5) permeability, mD | Modeled (Eq. 4) permeability, mD |
|---|---|---|---|---|---|
| 8.20 | 6.72 | 10.20 | 1.25 | 1.86 | 5.11 |
| 22.40 | 7.79 | 59.44 | 68.69 | 71.39 | 32.01 |
| 9.00 | 11.47 | 15.90 | 1.57 | 7.30 | 19.74 |
| 15.20 | 12.30 | 80.10 | 9.02 | 46.55 | 49.28 |
| 19.20 | 9.69 | 38.80 | 27.87 | 64.14 | 41.86 |
| 18.00 | 8.16 | 21.44 | 19.87 | 36.37 | 25.85 |
| 15.40 | 7.95 | 2.01 | 9.57 | 20.32 | 19.35 |
| 21.40 | 9.10 | 19.55 | 51.81 | 82.70 | 42.69 |
| 19.20 | 8.20 | 15.59 | 27.86 | 45.88 | 28.72 |
| 14.20 | 7.30 | 16.80 | 6.80 | 13.06 | 14.03 |
| 15.50 | 5.26 | 9.80 | 9.82 | 9.08 | 6.73 |
| 11.30 | 4.80 | 2.34 | 3.00 | 2.67 | 3.23 |
| 9.70 | 3.60 | 0.24 | 1.91 | 0.91 | 0.92 |
| 11.70 | 4.63 | 1.76 | 3.36 | 2.77 | 3.02 |
| 14.50 | 4.29 | 3.65 | 7.41 | 4.83 | 3.22 |
| 11.70 | 5.97 | 0.29 | 3.36 | 4.61 | 6.33 |
| 13.00 | 6.42 | 1.86 | 4.85 | 7.53 | 8.94 |
| 13.00 | 8.16 | 5.30 | 4.85 | 12.17 | 16.03 |
| 14.50 | 7.15 | 2.59 | 7.41 | 13.43 | 13.76 |
| 18.00 | 7.20 | 17.68 | 19.87 | 28.33 | 19.22 |
| 13.90 | 6.82 | 1.04 | 6.25 | 10.61 | 11.49 |
| 15.00 | 8.85 | 22.75 | 8.53 | 23.04 | 23.81 |
| 17.50 | 3.97 | 15.99 | 17.25 | 7.82 | 3.22 |
| 14.80 | 2.64 | 9.94 | 8.06 | 1.96 | 0.26 |
| 15.70 | 1.91 | 6.06 | 10.39 | 1.25 | 0.06 |
| 18.70 | 10.06 | 173.00 | 24.20 | 63.08 | 43.69 |
| 19.80 | 8.49 | 93.67 | 33.00 | 54.84 | 32.61 |
| 19.10 | 4.87 | 15.88 | 27.09 | 15.93 | 7.30 |
| 8.60 | 0.56 | 0.23 | 1.40 | 0.02 | 0.03 |
| 18.80 | 3.69 | 7.73 | 24.89 | 8.63 | 2.67 |
| 7.70 | 5.12 | 1.24 | 1.09 | 0.88 | 2.23 |
| 13.20 | 3.68 | 1.56 | 5.13 | 2.61 | 1.58 |
| 13.00 | 1.86 | 1.36 | 4.85 | 0.63 | 0.05 |
| 15.00 | 5.10 | 3.03 | 8.53 | 7.65 | 5.87 |
| 13.50 | 3.16 | 1.68 | 5.59 | 2.06 | 0.79 |
| 13.30 | 9.27 | 33.81 | 5.28 | 16.95 | 22.15 |
| 14.40 | 9.08 | 51.26 | 7.20 | 21.18 | 23.77 |
| 9.40 | 7.17 | 13.37 | 1.76 | 3.27 | 7.31 |
| 18.90 | 8.44 | 139.74 | 25.61 | 46.08 | 30.03 |
| 10.10 | 5.00 | 5.34 | 2.14 | 2.01 | 3.10 |
| 10.60 | 1.27 | 0.42 | 2.47 | 0.15 | 0.04 |
| 4.90 | 4.82 | 0.98 | 0.49 | 0.19 | 0.96 |
| 15.90 | 3.09 | 21.40 | 10.99 | 3.42 | 0.89 |
| 19.70 | 3.80 | 70.88 | 32.08 | 10.79 | 3.24 |
| 11.90 | 4.17 | 9.42 | 3.56 | 2.38 | 2.18 |
| *Correlation* | *Coefficient* | *R = 1.0* | *R = 0.473* | *R = 0.649* | *R = 0.664* |

According to Amaefule et al. (1993), the FZI is inversely related to a product of pore parameters (shape factor, tortuosity, and surface-area-to-grain-volume ratio) and reflects connectivity between pores (greater FZI implies greater connectivity). This is a unique and useful attribute that allows us to quantify the flow character of a reservoir and lets us average the rock properties at a small scale, such as core plugs, and compare them with larger-scale variations at, for example, well-bore scale. We consider that FZI and $R_{35}$ are the most reliable quantitative attributes for geometrical pore structure characterization in carbonates, and that these attributes can be directly related to sonic and density readings on wireline logs.

A characteristic of carbonate reservoirs is significant variability in petrophysical properties, especially permeability, because carbonates are subject to rapid and pervasive diagenetic alteration. Such alteration, particularly cementation and dissolution processes, continuously modifies the pore structure to create or destroy porosity, and in extreme cases can mean a complete change in mineralogy from calcite to dolomite. All such modifications alter the elastic properties of the rock, particularly density and sonic velocity. The result is a wide range of density and velocity within carbonates, as observed in the Madison stratigraphic interval where compressional-wave velocity ranges from 15,000 to 24,000 ft/s (4,600–7,300 m/s), and density from 2.35 to 2.85 g/cc (Fig. 9.4).

Porosity is the main controlling factor in determining sonic velocity in rocks; this fact established acoustic logging as an essential borehole measurement. However, in carbonates the pore type is nearly as important in elastic behavior and the resultant sonic velocity. For example, at equal total porosities, moldic or intrafossil pore types allow significantly higher velocities than those allowed by pore types that are embedded in a rigid rock framework, such as interparticle porosity or microporosity (Anselmetti and Eberly 1999).

Sonic and density logs are common measurements in carbonate drill holes. Converting the sonic log to sonic porosity by applying the Wyllie time-average equation (Wyllie et al. 1956) is a widely used method for producing sonic porosity (Schlumberger 1974; Rider and Kennedy 2011). In holes where both tools are run, comparing the two porosity values yields a difference that is commonly termed *secondary porosity* and is quantified with the secondary porosity index, SPI (Schlumberger 1974). The SPI reflects to the presence of vugs and fractures (Schlumberger 1974; Lucia 1999; Doveton 1994) that are not detected by the sonic signal but are detected by the density and neutron-porosity logs.

Mavko and Mukerji (1995), among others, provided the theoretical explanation of this acoustic velocity behavior. High-aspect-ratio pores, such as molds and vugs, provide more grain-to-grain contact than do interparticle and intercrystalline pores. Thus, at equal total porosity, moldic and vuggy types of porosity decrease the pore compressibility and provide more stiffness to the rock, making acoustic velocity higher than in a formation with predominantly intercrystalline porosity.

Many scientists have attempted to estimate quantitatively the influence of vuggy porosity on acoustic logs. Some of them proposed empirical equations, while others just documented a broad range of scatter in velocities at a given porosity. Following Xu et al. (2006) we use the terms “vug” and “vuggy” to refer to voids that are either visually identifiable in thin section images or recognizable through specific

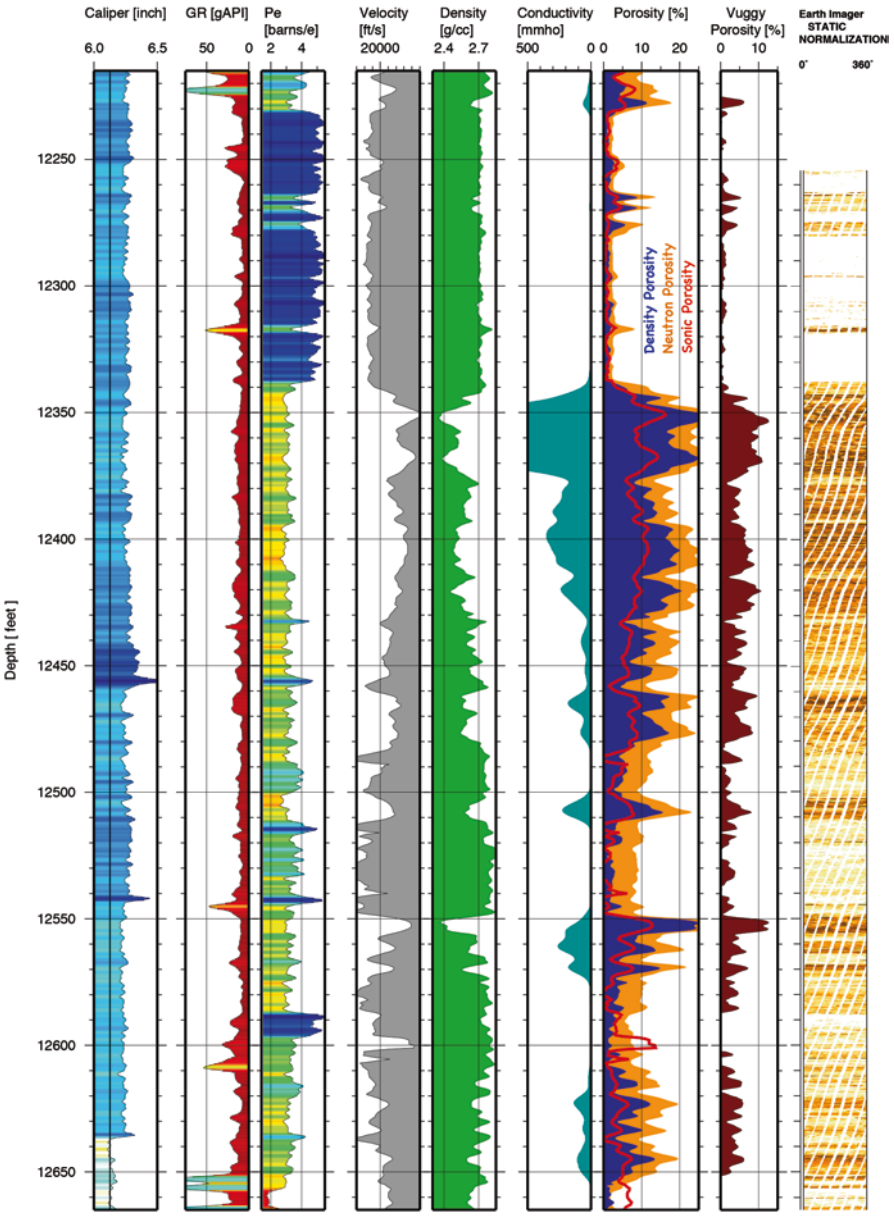


**Fig. 9.4** Open-hole wireline logs from the RSU #1 well for the Madison stratigraphic interval. Porosity panel shows neutron porosity log (*orange bar-graph*) overlaid with the neutron-density crossplot porosity (*blue bar-graph*). The red plot in the Porosity panel represents calculated sonic-log porosity. The Vuggy Porosity panel represents the difference between density and sonic porosity. The rightmost panel shows the Baker Hughes micro-resistivity image log with darker colors representing more conductive rock textures

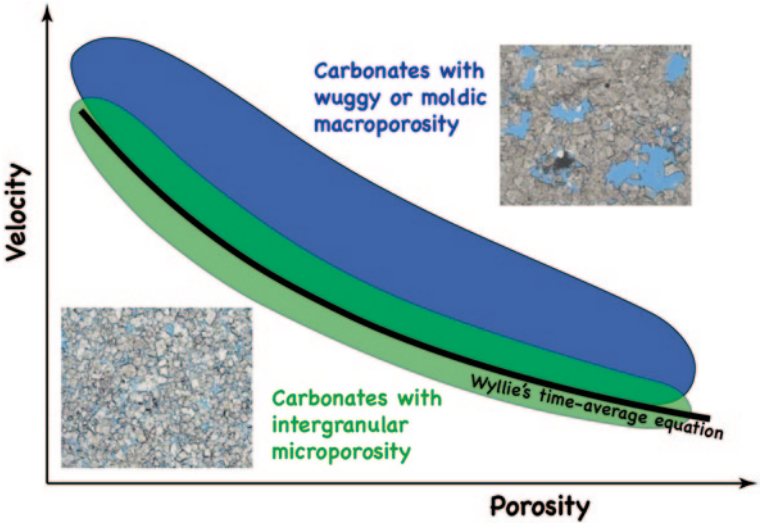


**Fig. 9.5** Cartoon showing the velocity-porosity relationship in carbonate rocks. A first-order inverse relation between velocity and porosity follows the Wyllie's time-average equation regardless of the pore structure. Differences in the pore structure produce a second-order variation on velocity at a given porosity: samples with vuggy or moldic porosity tend to fall into the high-velocity area, whereas samples dominated by microporosity tend to cluster around the time-average trend line. The corresponding thin-section images illustrating the difference in the pore structure are actual Madison Formation samples from the RSU #1 well

well-log signatures such as micro-resistivity images (rightmost panel in Fig. 9.4). In this study we use *primary porosity* to refer to the microporosity homogeneously represented in the cores, and *secondary porosity* to refer to the heterogeneously distributed porosity, which commonly correlates with vuggy or moldic porosity.

Weger et al. (2009) analyzed the velocity-porosity relationship of water-saturated carbonate samples and noticed that samples with vuggy or moldic porosity tend to fall into the high-velocity area, while samples with great amounts of microporosity tend to cluster around the Wyllie time-average equation in the lower part of the velocity-porosity data cloud (Fig. 9.5). Although most samples contain more than one pore type, at any given porosity a trend of increasing velocity with decreasing microporosity is observed (Weger et al. 2009). This observation allows us to conclude that vugs, especially spherical vugs in carbonates, have little effect on compressional sonic waves and cause the sonic (Wyllie's) porosity to read too low. Therefore, the difference between the density and sonic porosities can be regarded as a measure of vuggy porosity.

Data from the Madison Limestone on the Rock Springs Uplift support this statement. For example, the difference between the total porosity (derived from the density log) and the sonic porosity—referred to here as vuggy porosity—correlates well with the secondary or vuggy porosity visible on the micro-resistivity image log from the RSU #1 well (Fig. 9.4). The methodology described in this study uses

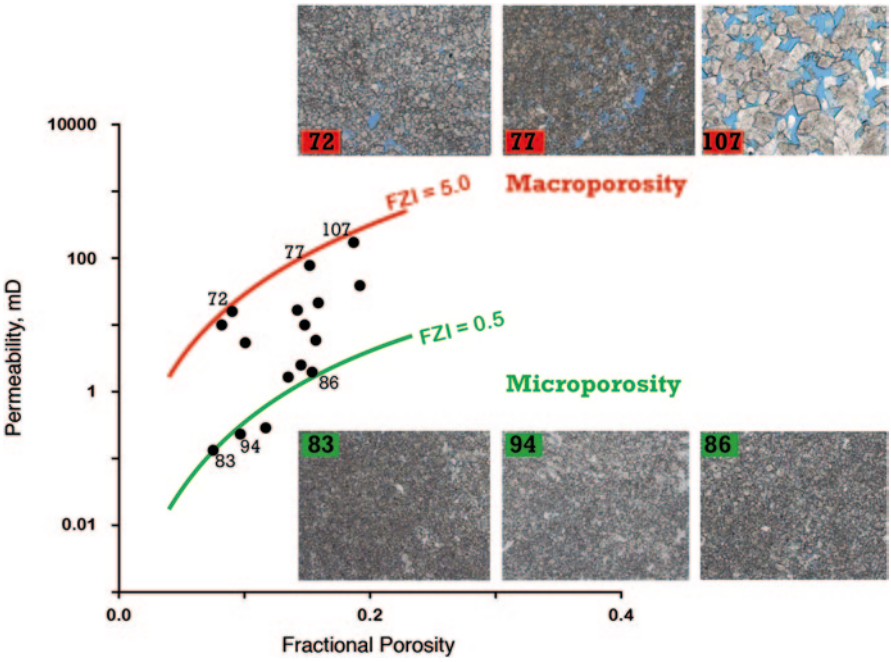


**Fig. 9.6** Semilog plot of permeability vs. porosity for the Madison Limestone samples, RSU #1 well, Rock Springs Uplift, Wyoming. The colored curves indicate constant hydraulic units defined by the *FZI* value. Thin section images (labeled with the sample ID numbers) demonstrate that permeability of the corresponding dolostone sample is a function of the total porosity and the pore structure. Dolostones dominated by large vuggy pore types (*top*) show greater permeability than fine-grained dolostones dominated by intergranular microporosity (*bottom*)

attributes (FZI and $R_{35}$) that quantify the relationship between porosity, permeability, and pore geometry. Carbonate rocks characterized by secondary porosity (large vuggy and moldic pores) in addition to the primary porosity within the matrix have both macroporosity and microporosity. In our methodology, macropores are defined by pores that display the bright colors of the blue epoxy filling the pores in thin section. Samples with great amounts of intergranular microporosity cluster along the low-value FZI curves; they are related to low-permeability dolostones facies in our dataset (Fig. 9.6). In contrast, samples containing moldic and vuggy porosity reveal the highest measured permeability and corresponding FZI values.

The fairly strong correlation between FZI/$R_{35}$ attributes and macroporosity illustrates the importance of considering geometrical pore typing for permeability modeling. Following Amaefule et al. (1993), we define a hydraulic unit as a geologic zone that has a distinct expression in the FZI domain and that controls the permeability of a formation.

### 9.1.4 Conclusion

Modeling permeability in heterogeneous carbonate reservoirs can be challenging due to significant spatial variations in pore geometry. In this study, we have shown that the log-derived vuggy porosity in carbonates correlates well with the Flow Zone Index and Winland's $R_{35}$ radius, methods often used to define major flow units in reservoirs. We used both methods to model facies and permeability across the whole Madison Limestone stratigraphic interval (~ 400 ft thick) using relatively sparse data from laboratory measurements and wireline logs. A fairly high correlation coefficient observed in the estimated-versus-measured core permeability was achieved—an important objective of this study. Our results indicate that capturing complex variations in pore geometry within a rock is the key to successful permeability modeling. We have demonstrated that vuggy and moldic macroporosity must not be ignored in modeling, and that a carbonate interval should be approached as a dual-porosity system. The challenge in predicting permeability is constructing a model that effectively incorporates both types of porosity—homogeneous microporosity and heterogeneous vuggy porosity—without becoming too complex. We have shown that the subdivision of a carbonate reservoir into hydraulic units based on the vuggy porosity index can be routinely performed in most situations, and that this greatly enhances permeability prediction in heterogeneous reservoirs.

## 9.2 The Weber Sandstone Reservoir

### 9.2.1 Permeablity Estimation

The most obvious control on permeability is porosity. However, permeability also depends upon the interconnectivity of the pores, and that in turn depends on the size and shape of grains, the grain size distribution, and such other factors as wetting properties of the rock and diagenetic history. For the Weber Sandstone reservoir, some generalizations can be made:

- The smaller the grains, the smaller the pores and pore throats, and the lower the permeability.
- Secondary porosity is negligible; thus, the bulk permeability is controlled solely by matrix (primary) porosity.

Under these assumptions and based on empirical knowledge (e.g., Archie 1950; Nelson 1994; Nelson 2004), permeability can be estimated from the relationship

$$\log(k) = a\varphi + b \tag{9.6}$$

Almost invariably for a consolidated sandstone, a plot of permeability ($k$) on a logarithmic scale against porosity ($\varphi$) results in a clear trend with a degree of scatter

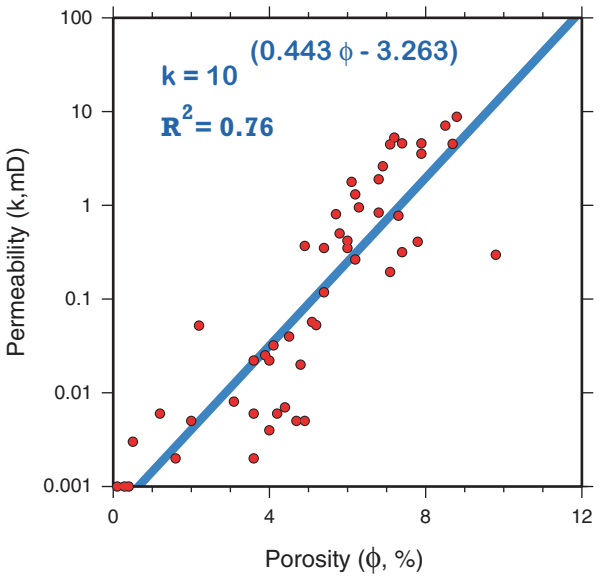


**Fig. 9.7** Semilog plot of permeability vs. porosity for the core samples from the Weber Formation, RSU #1 well, Rock Springs Uplift, Wyoming (*red dots*). The corresponding semi-logarithmic regression for permeability $k$ (the line, equation, and coefficient of determination) is shown in blue

associated with the other influences determining the permeability. Fig. 9.7 shows a log ($k$)-vs.-$\varphi$ plot for the core samples from the Weber Sandstone. There is a strong linear correlation ($R^2 = 0.76$) between log ($k$) and $\varphi$ with a relatively steep trend that is characteristic of "tight gas sands" (Nelson 1994). Clearly, permeability can be predicted from porosity in such an environment.

With insertion of the regression coefficients into Eq. 9.6, the corresponding power-law equation for the Weber Sandstone permeability will be:

$$k = 10^{(0.443\varphi - 3.263)} \tag{9.7}$$

Equation 9.7 was then used to calculate a continuous permeability profile for the Weber Sandstone unit penetrated by the RSU #1 well: porosity estimated from density-log values was used to predict permeability.

The result of modeling is shown in Fig. 9.8. Figure 9.8 also shows other well logs for visual comparison, as well as the core measurements. Although the measured and calculated data sets in Fig. 9.8 do not match perfectly, there is definitely visual correlation between them. For the Weber Sandstone unit, both density-derived and sonic-derived porosities can be used interchangeably for permeability prediction, since strong correlation exists between the density and velocity logs. The permeability profile shown in Fig. 9.8 is characterized by significant variability and a high proportion of low-permeability intervals (with values below 1.0 mD). Overall, the Weber Sandstone in the study area can be classified as a variably permeable, tight formation. The lack of mud cake, as indicated by the caliper log (Fig. 9.8), supports this conclusion.

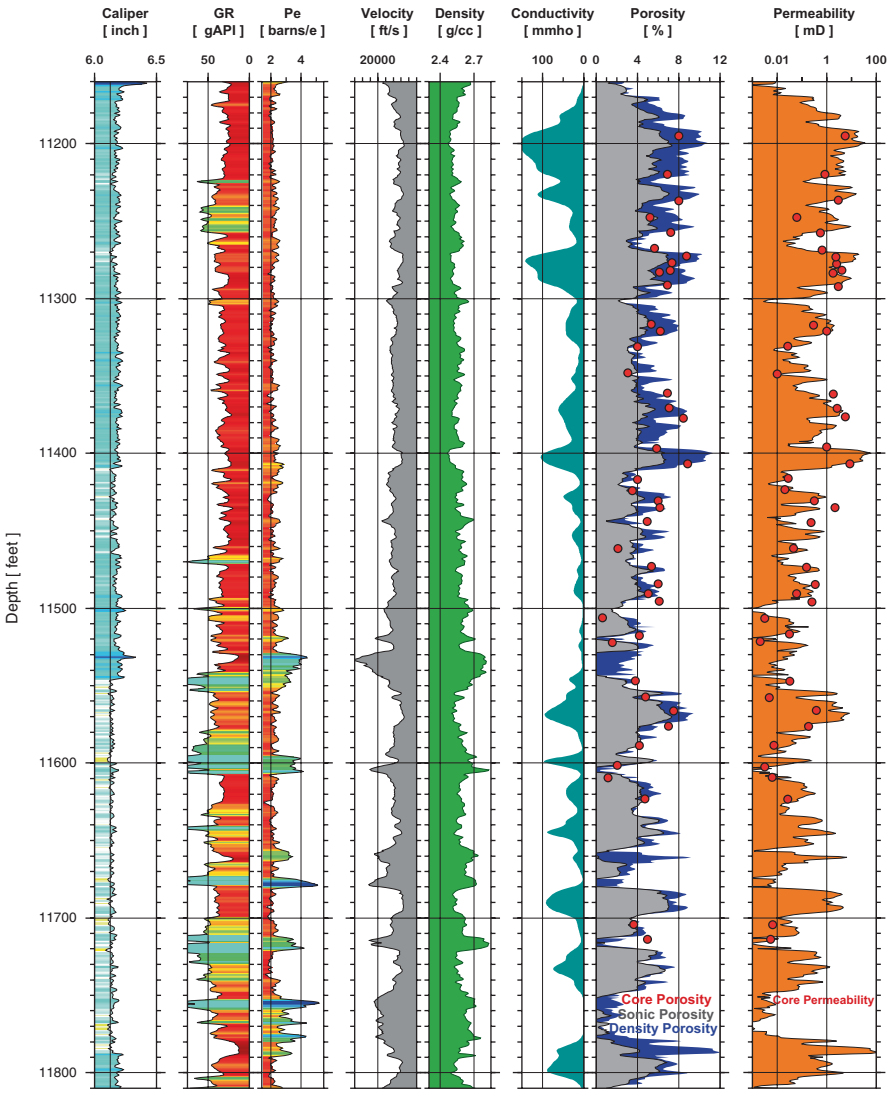


**Fig. 9.8** Open-hole logs and core data in the Weber Formation in the RSU #1 well. Tracks from left to right are (1) caliper, (2) gamma-ray, (3) photo electric section, (4) P-wave velocity, (5) density, (6) conductivity, (7) density (*blue*) and sonic (*gray*) porosity with total porosities from core (*red dots*), (8) modeled permeability (*orange*) overlaid with core measurements (*red dots*)

A similar technique of permeability estimation (Eq. 9.7) can be applied to the lateral distribution of porosity values derived from surface seismic (see Chap. 7). The result of permeability modeling for the Weber Sandstone away from the RSU #1 well is shown in Fig. 9.9. Most of the area on the permeability map is blue and yellow, which correspond to permeability values below 1.0 mD (Fig. 9.9b). We note

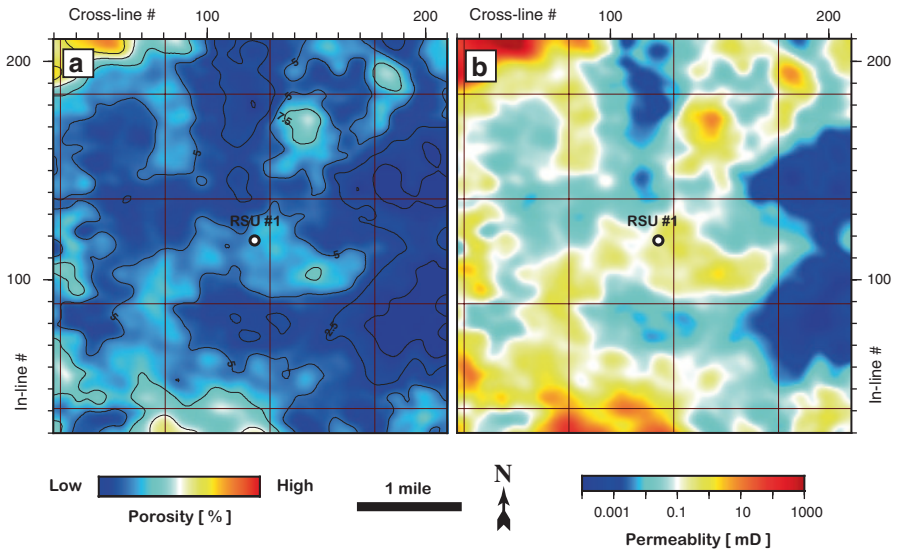


**Fig. 9.9** (**a**) Porosity and (**b**) permeability maps on top of the Weber Sandstone stratigraphic unit. For both plots, increases in value correspond to transition from blue to red. Note that peripheral areas are less reliable in attribute estimation due to decreased seismic coverage

that uncertainty in the seismically derived permeability map, due to the absence of control wells, increases away from the RSU #1 well toward the periphery of the seismic study area.

## *9.2.2 Permeablity Distribution*

### 9.2.2.1 The Weber Sandstone

Plots of petrophysical data vs. depth, e.g, those in Fig. 9.8, can be used to distinguish and separate geologic units. However, many modern flow simulation routines require a general quantitative reservoir descriptor obtained from data samples that are treated as random variables and are not attributed to a specific location. Both the probability and cumulative distribution functions (histograms) are common statistical tools that can be used to derive such a generalized descriptor of a formation. Fig. 9.10 shows histograms of the permeability distribution within the Weber Sandstone, based on estimates per Sect. 9.2.1. We used 1,341 data samples to produce the distributions that correspond to the 670-ft-thick interval, from 11,155 to 11,825 ft in depth.

On a logarithmic scale, the Weber Sandstone is characterized by a multi-peak, slightly right-skewed permeability distribution (Fig. 9.10a). Unlike a normal distribution, the asymmetric one can be described with several averaging estimators:

the arithmetic mean, geometric mean, median, and mode. For a normal distribution all four estimators produce the same number; all four numbers for the Weber Sandstone permeability distribution are different. Our estimators differ greatly, ranging from 0.06 mD for the mode to 1.94 mD for the arithmetic mean. Now, how well do these estimators represent the permeability population?

For the Weber Sandstone permeability, the arithmetic mean is 1.94 mD, which is much greater than the median distribution value, 0.12 mD. According to Jensen et al. (2000), the geometric mean should produce a better estimate for a log-normal distribution. The Weber Sandstone permeability distribution has close to a log-normal shape (only slightly asymmetric); therefore, we might use the geometric mean (0.13 mD) as a statistical permeability estimate for the whole stratigraphic unit. Since the permeability distribution (Fig. 9.9a) is multi-peak, the mode (0.06 mD) is not a useful indicator. The median (0.12 mD) is very close to the geometric mean; hence, we conclude that 0.125 mD (here, the average of the geometric mean and the median) would be the best permeability descriptor for the whole Weber Sandstone section.

The cumulative histogram (Fig. 9.10b) can be used to determine the number of permeability values within a given range that have occurred (interval probabilities). As can be seen in Fig. 9.10b, 50% of the data (samples) have a permeability value ($k_{0.50}$) of about 0.1 mD or less; that is the median value. Only 20% of the data within the depth interval 11,155–11,825 ft (Fig. 9.10) have a permeability value greater than 1.0 mD.

The Dykstra-Parsons coefficient ($V_{DP}$) is commonly used in the petroleum industry as a measure of permeability variation or reservoir heterogeneity (Jensen et al. 2000). It is defined as

$$V_{DP} = \frac{k_{0.50} - k_{0.16}}{k_{0.50}}, \tag{9.8}$$

where $k_{0.50}$ is the median permeability and $k_{0.16}$ is the permeability one standard deviation below the median on a log-probability plot. $V_{DP}$ ranges between zero (0.00) for absolutely homogeneous reservoirs and one (1.00) for "infinitely" heterogeneous reservoirs. With a $V_{DP}$ of 0.91, the Weber Sandstone can be considered a highly heterogeneous reservoir rock.

#### 9.2.2.2 The Madison Limestone Reservoir

The corresponding statistical permeability estimates for the middle Madison unit are listed in Fig. 9.11. This carbonate reservoir is characterized by a wide, multi-peak, left-skewed permeability distribution. The asymmetry of the distribution is much more pronounced than that of the Weber Sandstone unit. The difference between the mode and the geometric mean of the Madison permeability distribution exceeds 20 mD (Fig. 9.11a). We chose the median permeability value of *3.25 mD* as the most appropriate average permeability estimate. However, even the lowest

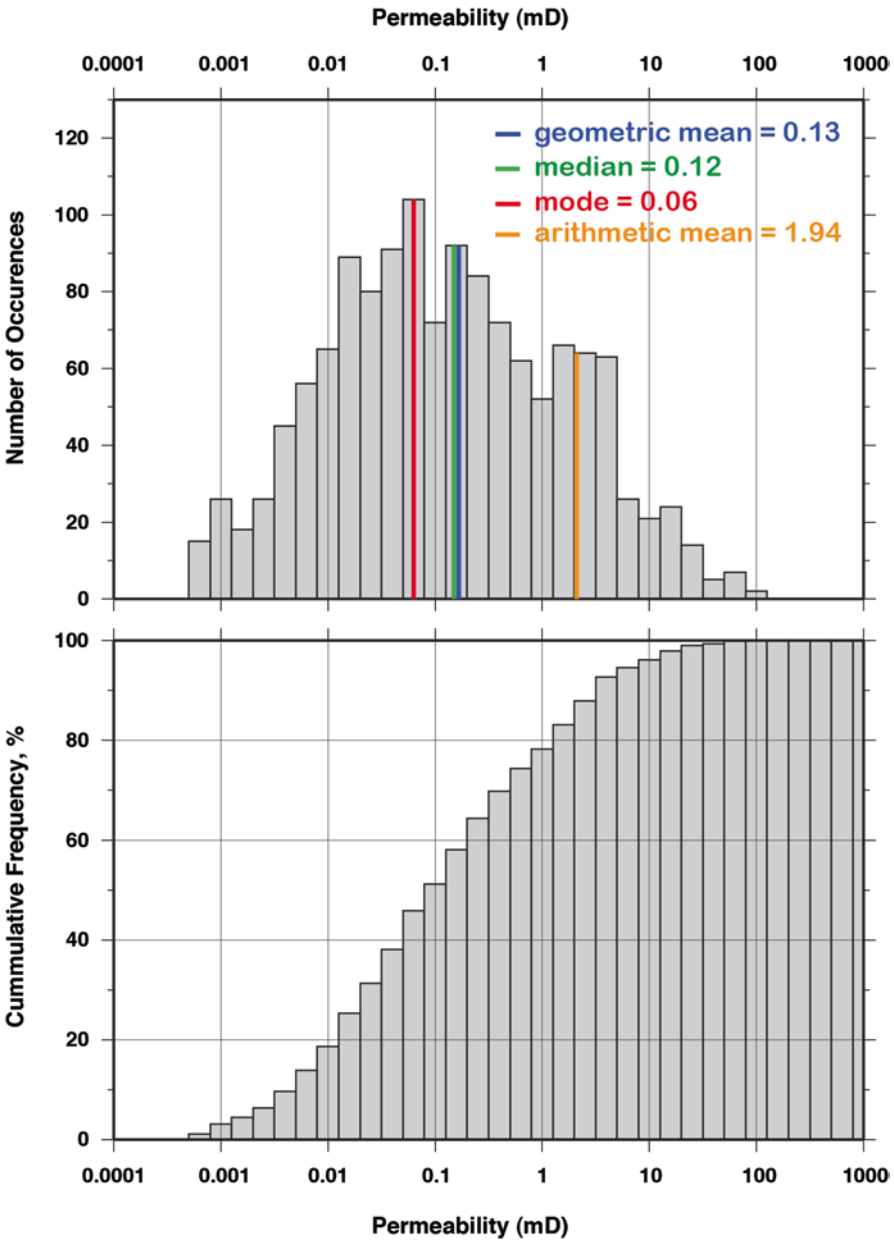


**Fig. 9.10** Permeability distribution within the Weber Sandstone unit (11,155–11,825 ft depth interval; 1,341 data samples). Ordinary histogram (*top*); cumulative histogram (*bottom*)

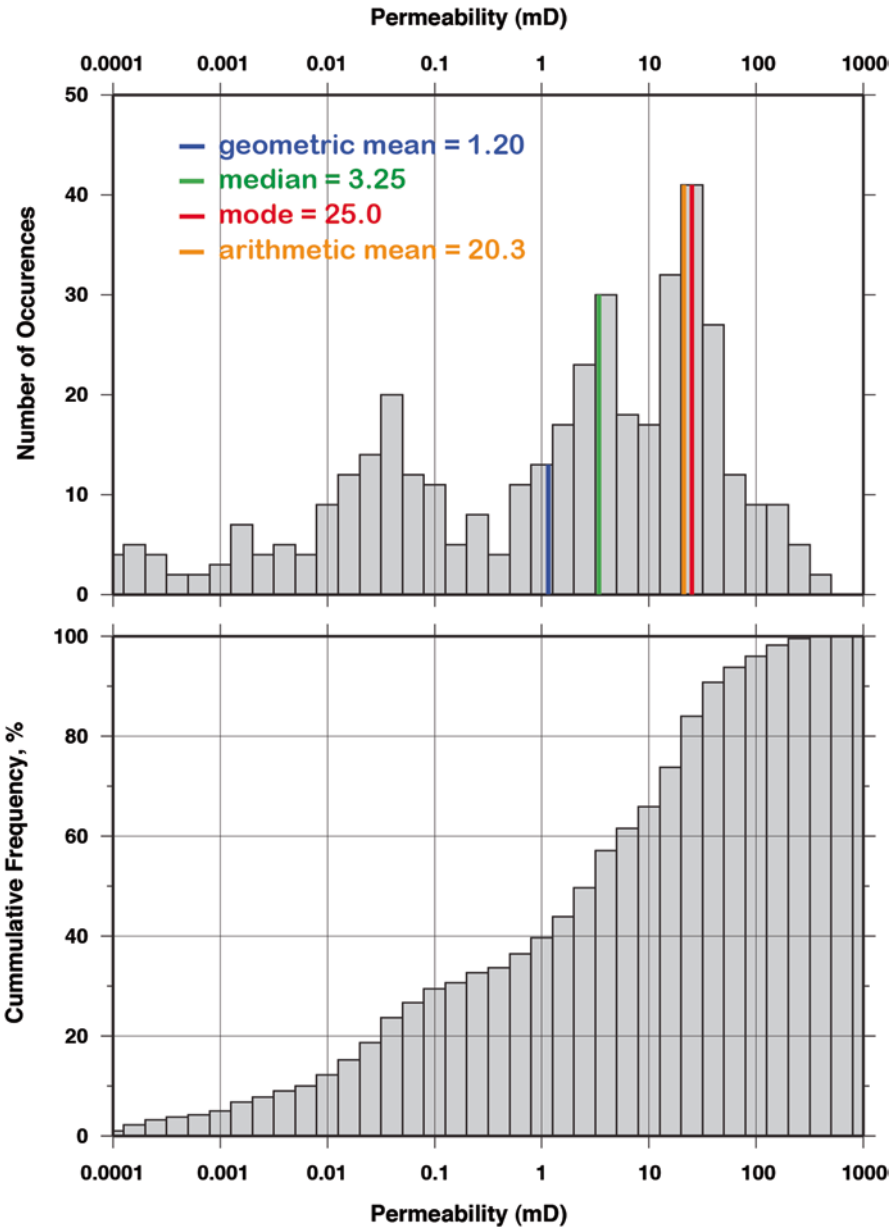


**Fig. 9.11** Permeability distribution within the middle Madison unit (12,340–12,540 ft depth interval; 401 data samples). Ordinary histogram (*top*); cumulative histogram (*bottom*)

descriptor for the middle Madison reservoir—the geometric mean (1.2 mD)—is an order of magnitude higher than the Weber Sandstone permeability estimate. The cumulative histogram indicates that 60 % of the data within the depth interval 12,340–12,540 ft ( ) have permeability values greater than 1.0 mD. On the basis of permeability statistics, we conclude that the middle Madison unit has much better reservoir properties than does the Weber Sandstone. The estimated Dykstra-Parsons heterogeneity index ($V_{DP}$) for the middle Madison depth interval (12,340–12,540 ft) is 0.99, which characterizes this reservoir as extremely heterogeneous.

## References

Amaefule JO, Altunbay M, Taib D, Kersey DG, Keelan DK (1993) Enhanced reservoir description: using core and log data to identify hydraulic (flow) units and predict permeability in uncored intervals/wells. Paper SPE 26436, presented at the SPE 68th annual technical conference and exhibition, Houston. 3–6 October, Texas 1993

Anselmetti FS, Eberli GP (1999) The velocity-deviation log: a tool to predict pore type and permeability trends in carbonate drill holes from sonic and porosity or density logs. AAPG Bull 83(3):450–466

Archie GE (1950) Introduction to petrophysics of reservoir rocks. AAPG Bull 34(5):943–961

Bird RB, Steware WE, Lightfoot EN (1960) Transport phenomena**.** Wiley, New York

Carmen PC (1937) Fluid flow through granular beds. Inst Chem Eng Trans 15:150–166

Doveton JH (1994) Geologic log interpretation—reading the rocks from wireline logs. Soc Econ Paleontol Miner Short Course 29

Ehrenberg SN, Eberli GP, Keramati M, Moallemi SA (2006) Porosity-permeability relationships in interlayered limestone-dolostone reservoirs. AAPG Bull 90(1):91–114

Gunter GW, Finneran JM, Hartmann DJ, Miller JD (1997) Early determination of reservoir flow units using an integrated petrophysical method. Paper SPE 38679, presented at the 1997 SPE annual technical conference and exhibition, San Antonio, Texas, 5–8 October

Guo G, Diaz MA, Paz F, Smalley J, Waninger EA (2007) Rock typing as an effective tool for permeability and water-saturation modeling: a case study in a clastic reservoir in the Oriente Basin. SPE Reserv Eval Eng 10(6):730–739

Hartmann DJ, Farina J (2004) Integrated reservoir analysis: Predicting reservoir performance through collaboration. Occidental Oil & Gas Corporation, Houston, Texas, course workbook

Jennings JW Jr, Lucia FJ (2001) Predicting permeability from well logs in carbonates with a link to geology for interwell permeability mapping. Paper SPE 71336, presented at the SPE annual technical conference and exhibition, New Orleans, 30 September–3 October. DOI: 10.2118/71336-MS

Jensen JL, Lake LW, Corbett PWM, Goggin DJ (2000) Statistics for petroleum engineers and geoscientists, 2nd edn. Handbook of petroleum exploration and production, 2. Elsevier, Amsterdam

Kolodzie S Jr (1980) Analysis of pore throat size and use of the Waxman-Smits equation to determine OOIP in Spindle Field, Colorado. Paper SPE 9382

Lucia FJ (1999) Carbonate reservoir characterization. Springer-Verlag, New York

Mavko G, Mukerji T (1995) Seismic pore space compressibility and Gassmann's relation. Geophysics 60:1743–1749

Nelson PH (1994) Permeability-porosity data sets for sandstones. Lead. Edge (23):1143–1144

Nelson PH (2004) Permeability-porosity relationships in sedimentary rocks. Log Anal.(May–June):38–62

Porras JC, Campos O (2006) Rock typing: a key for petrophysical characterization and definition of flow units, Santa Barbara field, eastern Venezuela Basin. Paper SPE 69458, presented at the 2001 SPE Latin American and Caribbean petroleum engineering conference, Buenos Aires, 25–28 March 2001. DOI: 10.2118/69458-MS

Prasad M (2003) Velocity-permeability relations within hydraulic units. Geophysics 68(1):108–117
Rider MH, Kennedy M (2011) The geologic interpretation of well logs, 3rd edn. Rider-French Consulting Ltd., Scotland
Schlumberger (1974) Log interpretation—applications, vol. 2. Schlumberger Limited, New York
Weger RJ, Eberli GP, Baechle GT, Massaferro JL, Yue-Feng S (2009) Quantification of pore structure and its effect on sonic velocity and permeability in carbonates. AAPG Bull 93(10):1297–1317
Wyllie MR, Gregory AR, Gardner GHF (1956) Elastic wave velocities in heterogeneous and porous media. Geophysics 21(1):41–70
Xu C, Russell D, Gournay J, Richter P (2006) Porosity partitioning and permeability quantification in vuggy carbonates using wireline logs, Permian Basin, West Texas. Petrophysics 47(1):13–22;

# Chapter 10
# Advances in Estimating the Geologic $CO_2$ Storage Capacity of the Madison Limestone and Weber Sandstone on the Rock Springs Uplift by Utilizing Detailed 3-D Reservoir Characterization and Geologic Uncertainty Reduction

**Zunsheng Jiao and Ronald C. Surdam**

**Abstract** In order to implement $CO_2$ storage in deep saline aquifers a diverse set of geologic, geophysical, and geochemical parameters must be characterized in both the targeted reservoir intervals and at the storage site.

All observational, experimental and theoretical information and laboratory measurements are integrated into a comprehensive geologic model in order to obtain an accurate characterization of a specific set of potential storage reservoirs and a targeted storage site. The integration is achieved through a series of performance assessments for a diverse set of storage scenarios utilizing numerical simulation techniques. Two of the important fluid-flow parameters that are investigated with the numerical simulations are $CO_2$ storage capacity and $CO_2$ injectivity. Reliable estimates of these two parameters are essential to both governments making energy policies and environmental regulations, and to industry trying to make quality business decisions.

Three analytical techniques are utilized to evaluate $CO_2$ storage capacity in both the Madison Limestone and Weber Sandstone on the Rock Springs Uplift: (1) a static volumetric approach, (2) a dynamic fluid-flow simulation approach using a homogenous reservoir model, and (3) a dynamic fluid-flow simulation approach using a more realistic 3-D heterogeneous reservoir model. The results from these three approaches demonstrate how as the descriptive characterization of the spatial distribution of the determinative reservoir parameters become more realistic, the uncertainties of the $CO_2$ storage performance assessments are substantially reduced.

Using comprehensive regional geologic, structural, geochemical, log suite, core, and seismic data, we present field-scale heterogeneous reservoir models for the Madison Limestone and Weber Sandstone on the Rock Springs Uplift (RSU). These

Z. Jiao (✉) · R. C. Surdam
Carbon Management Institute Laramie, University of Wyoming, Laramie, USA
e-mail: JJiao@uwyo.edu

R. C. Surdam
e-mail: rsurdam@uwyo.edu

R. C. Surdam (ed.), *Geological $CO_2$ Storage Characterization,*
Springer Environmental Science and Engineering, DOI 10.1007/978-1-4614-5788-6_10,
© Springer Science+Business Media New York 2013

models were used to evaluate uncertainty in critical geologic carbon storage (GCS) performance metrics: storage capacity and well injectivity. The geologic setting of the RSU is presented first and is followed by a description of the techniques used to determine porosity and permeability heterogeneity based on analytic results from log suites, cores, and 3-D seismic data. Random realizations of permeability and porosity (i.e., extrapolations of reservoir properties away from the stratigraphic well into the 3-D seismic volume) are then generated for each of the geologic units including the storage targets (the Weber Sandstone and the Madison Limestone) and sealing formations (the Amsden, Dinwoody, and Chugwater, among others). These heterogeneous property fields then are used to simulate non-isothermal $CO_2$ injection over a 50-year period.

## 10.1 Introduction

Since the beginning of the industrial revolution the amount of anthropogenic $CO_2$ emitted into the atmosphere has risen dramatically as the utilization of fossil fuels has continually increased. Presently the atmospheric $CO_2$ concentration has reached 400 ppm, whereas in 1,850 it was 280 ppm—$CO_2$ is being pumped into the atmosphere at ever-increasing rates. Although several $CO_2$ mitigation schemes have been proposed, such as $CO_2$ storage in deep ocean settings, coal beds, depleted oil/gas reservoirs, and deep saline aquifers, the storage of anthropogenic $CO_2$ in deep saline aquifers is favored by a global scientific consensus. In order to implement $CO_2$ storage in deep saline aquifers, a diverse set of geologic, geophysical, and geochemical parameters must be characterized both in the targeted reservoir intervals and at the overall targeted storage site.

The objective of this chapter is to integrate all available observational, experimental, and theoretical information and laboratory measurements in order to accurately characterize a specific set of potential storage reservoirs and a storage site. The integration is achieved through a series of performance assessments for a diverse set of storage scenarios utilizing numerical simulations. Two important fluid-flow parameters that are investigated with the numerical simulations are $CO_2$ storage capacity and $CO_2$ injection rate. Reliable estimates of these two parameters are essential both to governments drafting energy policies and environmental regulations and to industries making business decisions.

Three simulation approaches are utilized to evaluate $CO_2$ storage capacity in the Madison Limestone and Weber Sandstone on the Rock Springs Uplift (RSU): (1) a static volumetric approach, (2) a dynamic fluid-flow simulation approach using a homogenous reservoir model, and (3) a dynamic fluid-flow simulation approach using a more realistic 3-D heterogeneous reservoir model. The results from these three approaches demonstrate that as the descriptive characterizations of the spatial distribution of the determinative reservoir parameters become more realistic, the uncertainty implicit in the $CO_2$ storage performance assessments is substantially reduced.

In this chapter, using comprehensive regional geologic, structural, geochemical, log suite, core, and seismic data, we develop a field-scale heterogeneous reservoir model for the Madison Limestone and Weber Sandstone on the Rock Springs Uplift. This model is used to evaluate uncertainty in critical geologic carbon storage (GCS) performance metrics: storage capacity and well injectivity. A brief account of the geologic setting of the RSU is followed by a description of the techniques used to determine porosity and permeability heterogeneity based on analytic results from log suites, cores, and 3-D seismic data. Realistic determinations of permeability and porosity (extrapolations of reservoir properties away from the stratigraphic well and into the 3-D seismic volume) are then generated for each geologic unit, especially the storage targets within the Weber Sandstone and Madison Limestone and the primary sealing units—the Amsden, Dinwoody/Red Peak, and Chugwater Formations. These heterogeneous property fields are then used to simulate non-isothermal $CO_2$ injection over 50 years.

## 10.2 Geologic Setting of the Rock Springs Uplift, Wyoming

The Rock Springs Uplift (RSU) has been identified as a large potential geologic $CO_2$ storage site in southwestern Wyoming, with initial estimates of storage capacity for the Weber Sandstone and Madison Limestone on the order of 18 billion tonnes (Gt) and 8 Gt of $CO_2$, respectively, using the Futuregen Protocol (Fig. 10.1a) (Surdam and Jiao 2007). The 2.3-GW Jim Bridger Power Plant located on the RSU has the largest carbon footprint in Wyoming and generates approximately 15 Mt/yr of $CO_2$.

The RSU is an asymmetric, doubly plunging anticline/dome with more than 3,000 m of closed structural relief (Surdam and Jiao 2007) that lies on Rocky Mountain foreland basement. This large, north–south trending, complex uplift separates the Greater Green River Basin into two parts: to the west are the Green River and Bridger Basins; to the east are the Washakie and Great Divide Basins. The size of RSU is 80 km long, south to north and 50 km wide, west to east. The western flank of the RSU dips more steeply than its eastern flank (Fig. 10.1b). There are numerous east- and northeast-trending faults cutting the RSU on the surface, and a major westward-oriented thrust fault on the western flank occurs at depth below the surface (Fig. 10.1); it is thought to be a sealed fault (Surdam and Jiao 2007).

The oldest rocks composing the RSU are the Precambrian metamorphic basement, above which are Paleozoic, Mesozoic and Cenozoic formations (Fig. 10.1c), (Surdam et al. 2009). The oldest rocks exposed on the RSU are Cretaceous marine shales and sandstones, for the Laramide tectonic event that formed the RSU during Late Cretaceous and early Tertiary times did not raise the RSU high enough to expose the Precambrian core.

The targeted saline $CO_2$ storage aquifers are the Weber Sandstone, 200 m thick, and Madison limestone, 130 m thick at CMI's RSU #1 well site on the eastern flank of the RSU. The Pennsylvanian Weber Sandstone is composed of fine- to medium-

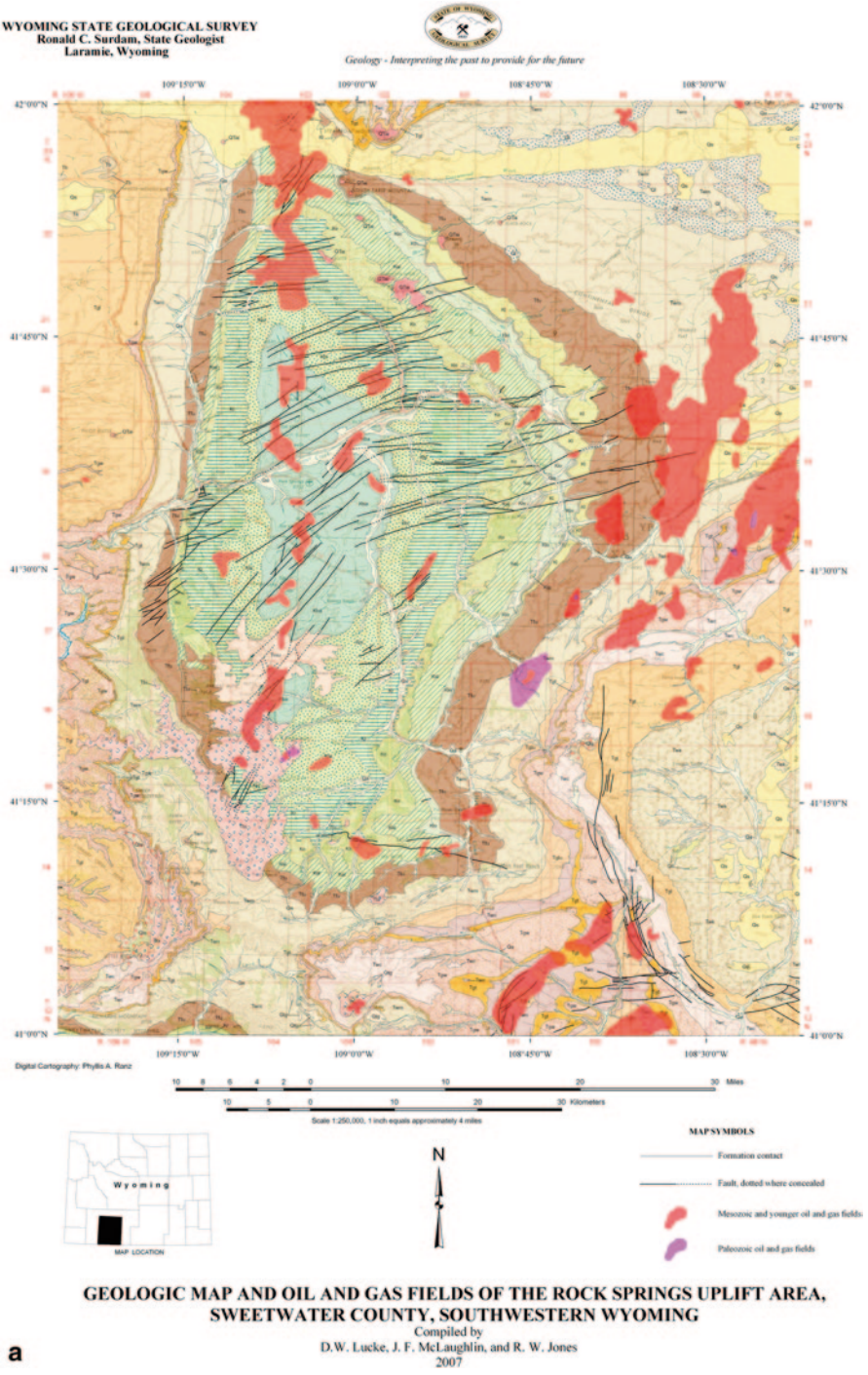


**Fig. 10.1** (**a**) Geologic map of the Rock Springs Uplift, southwest Wyoming. (**b**) East-west structural cross section through the RSU. (**c**) General stratigraphic chart for the Green River Basin where the RSU is located. (Modified from Love et al. (1993))

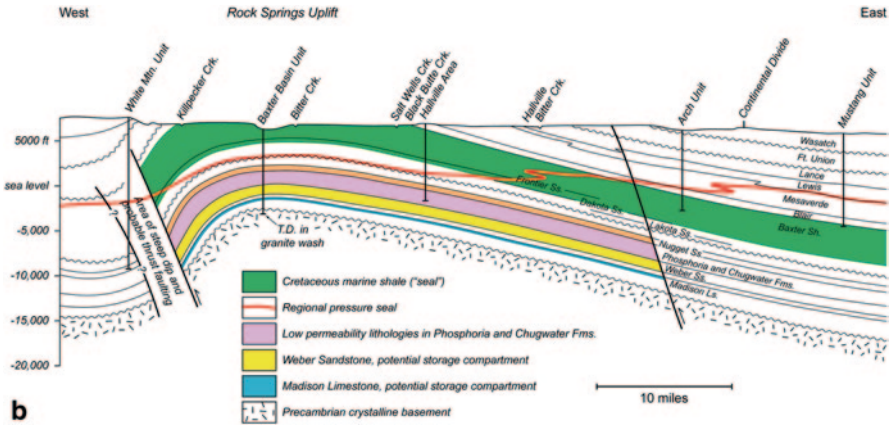


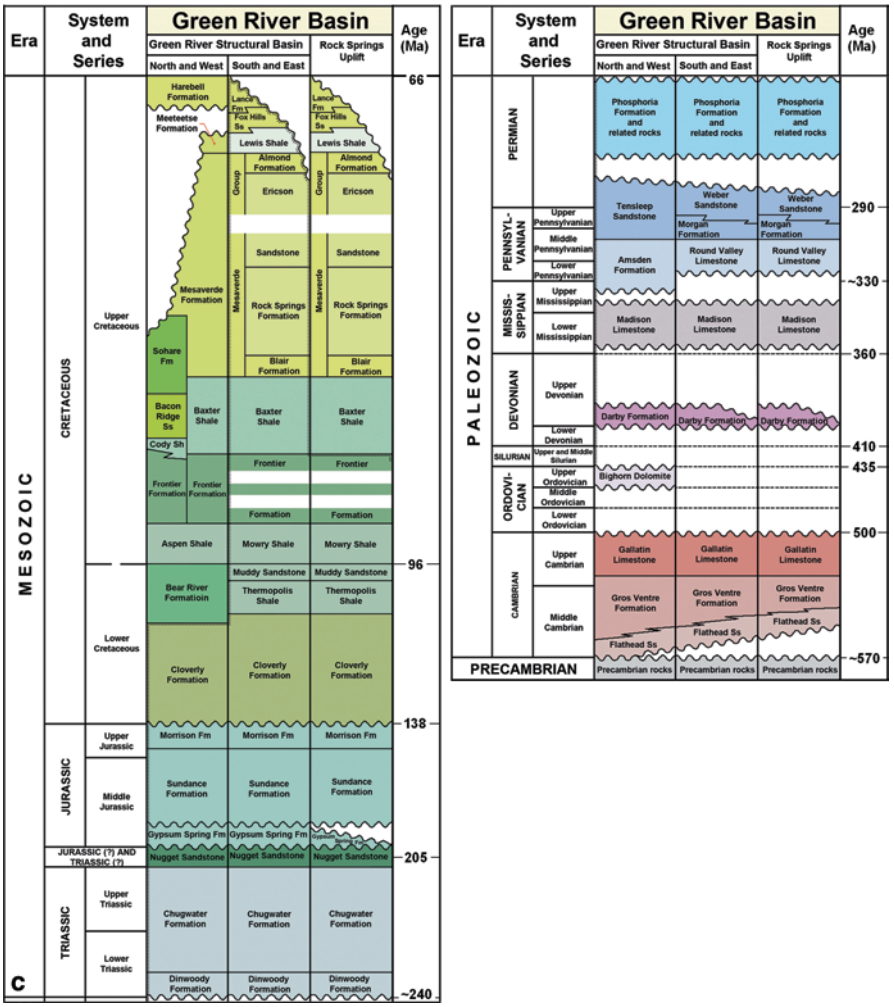


**Fig. 10.1** (continued)

grained, cross-bedded sandstone and siltstone primarily deposited as sand dunes and interdunes for the upper portion, and shallow marine for the lower portion. The Mississippian Madison Limestone consists of massive limestone and dolostone deposited in a shallow marine environment. At the crest of the RSU the Weber Sandstone and Madison Limestone are 1,860 m and 2,250 m below the land surface, respectively. At the RSU #1 well site the Weber and Madison tops are 3,300 m and 3,726 m deep.

The primary caprock for the Weber Sandstone and Madison Limestone is the Triassic Dinwoody and Chugwater siltstone and shale, a thick, low-permeability stratigraphic unit (300–400 m thick) that consists of interbedded red siltstone, shale, and fine-grained sandstone (Clarey and Thompson 2010; Surdam et al. 2009). Above the primary sealing lithologies of the Dinwoody and Chugwater Formations are more than 1,500 m of Cretaceous marine shale that serve as secondary cap-rock sealing units (Surdam and Jiao 2007).

The Permian Phosphoria Formation lies between the targeted $CO_2$ storage reservoir within the Weber Sandstone and the Dinwoody Formation primary seal, and varies in lithology from shaly siltstone to limestone interbedded with dolomite/siltstone. The Phosphoria on the RSU represents a lithofacies transition from organic, chert- and phosphorite-rich black shale west of the RSU to carbonate east of the RSU (Hein et al. 2004; Piper and Link 2002). Therefore, the Phosphoria Formation can serve as source rock, storage reservoir, or cap rock depending on its local lithology.

The total dissolved solids (TDS) in the Weber Sandstone water ranges from 70,000 mg/l to 100,000 mg/l, and in Madison water the TDS ranges 90,000–110,000 mg/l on the RSU. There are no outcrops of the Weber Sandstone and the Madison Limestone near the RSU, and groundwater recharge areas are at least 50–100 mi (80–160 km) away from the RSU, based on nearest outcrops (Surdam et al. 2009). The relatively high TDS in these saline aquifers indicates that the targeted $CO_2$ storage reservoirs are compartmentalized and are not connected directly to shallow meteoric recharge. The oil and gas produced from the Cretaceous Mesaverde and Frontier Formations and the Jurassic Nugget Formations predicts the integrity of the sealing stratigraphic intervals on the RSU.

The advantages of the RSU as a site for CCS are the thickness of the storage formations, burial depth, multiple cap-rock sealing units, huge structural closure, and proximity to substantial $CO_2$ emission sources (Surdam and Jiao 2007).

## 10.3 Storage Capacity Based on the Volumetric Approach

In order to assess the pore volumes of the targeted Weber and Madison reservoirs, the Carbon Management Institute (CMI) constructed a 3-D geologic model of the RSU based on geophysical logs from oil and gas wells, 2-D seismic profiles, and regional geologic data assembled by the Wyoming State Geologic Survey and CMI. The model covers a 90-km × 122-km area that includes all or parts of Townships 12–24 north and Ranges 95–106 west; it is 7.56 km in depth (Fig. 10.1a). The model

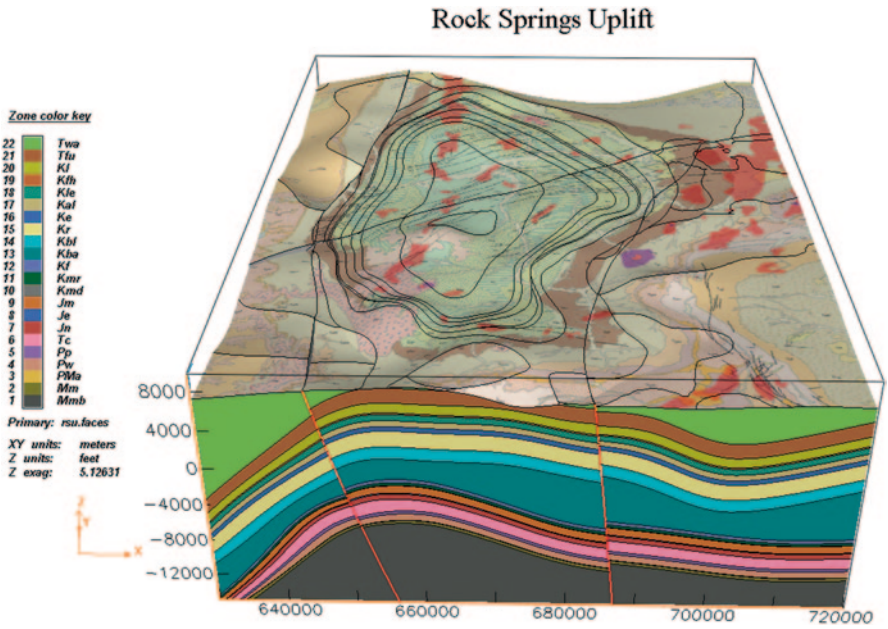


**Fig. 10.2** Geologic structural model of the Rock Springs Uplift area

was built using EarthVison®, a commercial 3-D geospatial modeling software package. Most well total depths (TDs) are in Cretaceous-age formations (e.g., 736 in the Frontier Formation); just 55 wells penetrate the Weber Sandstone, and 14 wells penetrate the Madison Limestone, in the 11,000-km$^2$ (4,200 mi$^2$) model area. The formation tops below the Cretaceous are mainly extrapolated from interpreted 2-D seismic reflections and from well logs from the deep wells that penetrate the targeted formations. Based on regional geologic maps and cross sections, three major faults are included in this geologic structural model. The gridding on the X, Y, and Z axes (width, length, and depth) is $41 \times 41 \times 41$, giving $40 \times 40 \times 40$ cells (64,000 cells). The cell size is 2,250 m wide, 3,050 m long, and 189 m deep. The model was constructed using 2-D and 3-D minimum tension gridding. Figure 10.2 is a northbound oblique view of the geologic structural model of the Rock Springs Uplift area.

Burress et al. (2009) provide a formula for assessing $CO_2$ storage capacity based on the total known volume (TKV). The TKV is the total volume of pore space within a reservoir. The formula for the $S_{TKV}$, the $CO_2$ storage capacity in tonnes, based on the KTV is:

$$S_{TKV} = T_a \times T_i \times N_{tp} \times \Phi \times C_e \times C_f \times \rho_{co_2}, \tag{10.1}$$

where $S_{TKV}$ is the storage resource of the assessed reservoir [t]; $T_a$ is the trap area [m$^2$]; $T_i$ is the interval thickness of the storage formation [m]; $N_{tp}$ is the fraction of $T_i$ occupied by the reservoir interval(s) [decimal fraction]; $\phi$ is the porosity [decimal

fraction]; $C_e$ is the storage efficiency factor (the fraction of the pore space that can be occupied by $CO_2$) [decimal fraction]; $C_f$ is a units conversion factor (here, $C_f = 1$); and $\rho_{CO_2}$ is the density of $CO_2$ [t/m$^3$].

In order to use Eq. 10.1 to calculate the $CO_2$ storage capacity of the Weber Sandstone and Madison Limestone, the trap area ($T_a$)—and thickness of the targeted formations ($T_i$) must first be defined. In other words, we must determine the upper depth limit and the lower depth limit of the targeted reservoir. The pressure and temperature required for $CO_2$ to be a supercritical fluid (31 °C and 7.4 MPa) are typically met at depths greater than 800 m (2,600 ft) under a normal hydrostatic pressure gradient. To reduce the chance that $CO_2$ may migrate to pressure regime and temperature conditions where it could convert from the supercritical state to liquid and vapor, a minimum storage depth of 1,000 m (3,280 ft) was chosen in the study. The minimum storage depth sets the upper depth limit of a potential $CO_2$ reservoir. The Weber Sandstone at the crest of the RSU is buried at a depth of 5,200 ft (1,600 m), so both the Weber and Madison reservoirs meet the minimum pressure and temperature requirements for keeping the stored $CO_2$ in the supercritical condition. The lower depth limit for $CO_2$ storage is more arbitrary than the upper depth limit. If the $CO_2$ pressure at the wellhead is 18 MPa (2,610 psi), and $CO_2$ density is 0.65 g/cm$^3$, the $CO_2$ pressure will be 50.5 MPa (7,322 psi) at the bottom of a 5,000-m-deep (16,400 ft) well. Therefore, $CO_2$ injected at the depth 5,000 m will displace normally pressured formation water (50 MPa or 7,200 psi) without additional compression. ExxonMobil Petroleum Company has injected 1.2 Mt of mixed gas ($CO_2$ and $H_2S$) annually into two Madison Limestone wells at depth of 17,500 ft (5,330 m) since 2004 at Shute Creek, northwest of RSU. Taking these two wells as an analogous case, 5 km (16,400 ft) was chosen for the maximum storage depth.

Assuming that 100 % of the formation thickness is available for $CO_2$ storage ($N_{tp} = 1$), then a 412-km$^3$ total volume of rock and pore space available for the $CO_2$ storage ($T_a \times T_i \times N_{tp}$) is determined from the EarthVision® geologic structural model for the Weber Sandstone on the RSU. For the Madison Limestone, the total volume of rock and pore space is 179 km$^3$.

The porosities $\phi$ of the Weber Sandstone and Madison Limestone were determined from apparent density porosities and neutron porosities derived from available logs. For the Weber Sandstone, a lognormal porosity distribution with maximum 0.12, minimum 0.01, mean 0.05, standard deviation 0.02, and skewness 0.13 was determined from all available measured data (Fig. 10.3a). For the Madison Limestone, the lognormal porosity distribution with maximum 0.18, minimum 0.01, mean 0.09, standard deviation 0.04, and skewness 0.1 was determined from all available measured data (Fig. 10.3b).

For a saline aquifer, the upper limit on the storage efficiency factor $C_e$ is related to the irreducible water saturation of the trap in the presence of $CO_2$. Values for irreducible water saturation in petroleum reservoirs are not well known, but they probably range from a minimum of about 0.2 in gas reservoirs to about 0.6 in oil reservoirs. The results of the $CO_2$ injection simulation, using FEHM software, presented in Sect. 10.4 show that most $CO_2$ saturation ranges between 0.1 and 0.8. The storage efficiency in this study was chosen between 0.1 and 0.8, with distribu-

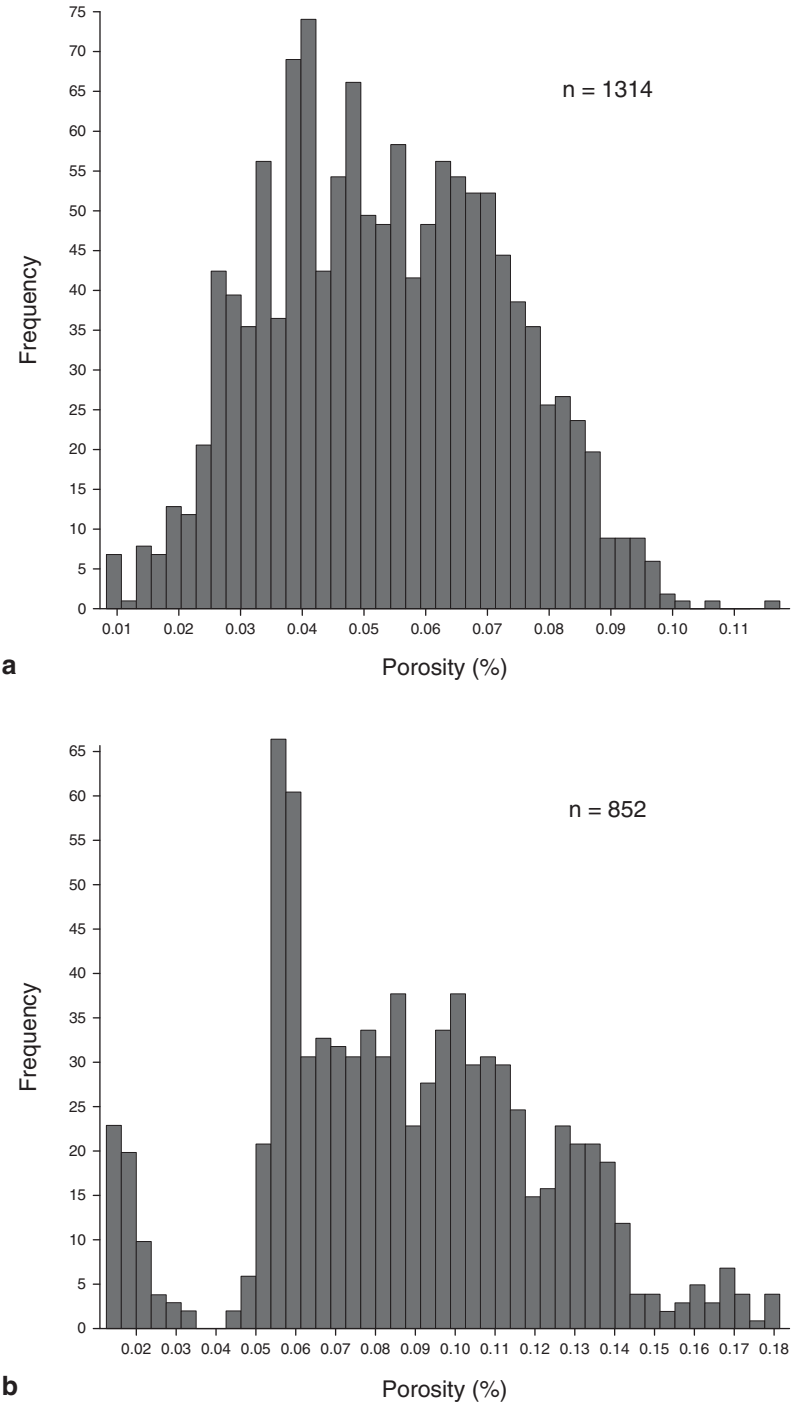


**Fig. 10.3** Histograms of the density-neutron porosity of (**a**) the Weber Sandstone and (**b**) the Madison Limestone, Rock Springs Uplift

tion mean 0.66. Using these parameters, a Monte Carlo simulator from Goldsim software with 5,000 realizations was set up for the Weber Sandstone and Madison Limestone between depths of 1,000 m (elevation 1,070 m) and 5,000 m (elevation –2,930 m) on the RSU. Figure 10.4a shows the probability density of the $CO_2$ storage capacity of the Weber Sandstone on the RSU: the Weber $CO_2$ storage capacity ranges from 2.4 to 20 Gt, with a mean of 9 Gt. For the Madison Limestone, the probability density of the $CO_2$ storage capacity ranges from 1.6 to 14 Gt, with a mean of 6.5 Gt (Fig. 10.4b).

Therefore, on the basis of the volumetric approach the Weber Sandstone and Madison Limestone have sufficient storage capacity to accommodate decades of industrial $CO_2$ emissions in the Greater Green River Basin.

## 10.4 Storage Capacity Assessments Based on the Numerical Simulation Utilizing a Homogeneous Reservoir Model

Although the storage capacity estimates based on the volumetric approach in Sect. 10.3 are acceptable for rough screening calculations, they cannot capture the complexities of three-dimensional flow and transport involving reservoir properties, seal integrity, $CO_2$ dissolution, inclined geologic units, and variable pressures and temperatures leading to changes in density and viscosity of both the brine and $CO_2$. In this and the following sections, the focus is on a 3-D numerical model (volume simulation) congruent with the Jim Bridger 3-D 8 km × 8 km seismic survey. Focusing on this volume with a stratigraphic test well in the center of the domain allows clear illustration of how results from numerical simulations lead to better understanding of injection feasibility, storage capacity, seal integrity, and possible flow and transport issues surrounding the injection of $CO_2$ into the Weber Sandstone and Madison Limestone on the RSU.

### *10.4.1 Generation of the 3-D Computational Hydrostratigraphic Model*

The focused geologic structural model is located one mile south of the Jim Bridger power plant, and consists of a block 8 km × 8 km in map view, with elevation extending from sea-level to 2420 m below sea-level (Fig. 10.5a). Following the logic and methodology outlined by Miller et al. (2007), a computational hydrostratigraphic model that maintains sharp material interfaces between the units of interest was generated from the geologic structural model. In this model, the Voronoi volume elements are aligned to follow the curvature of the unit interfaces and do not stair-step in the manner of a traditional finite element grid (see Miller et al. 2007). This allows more accurate calculation of $CO_2$ moving along the caprock in the up-dip

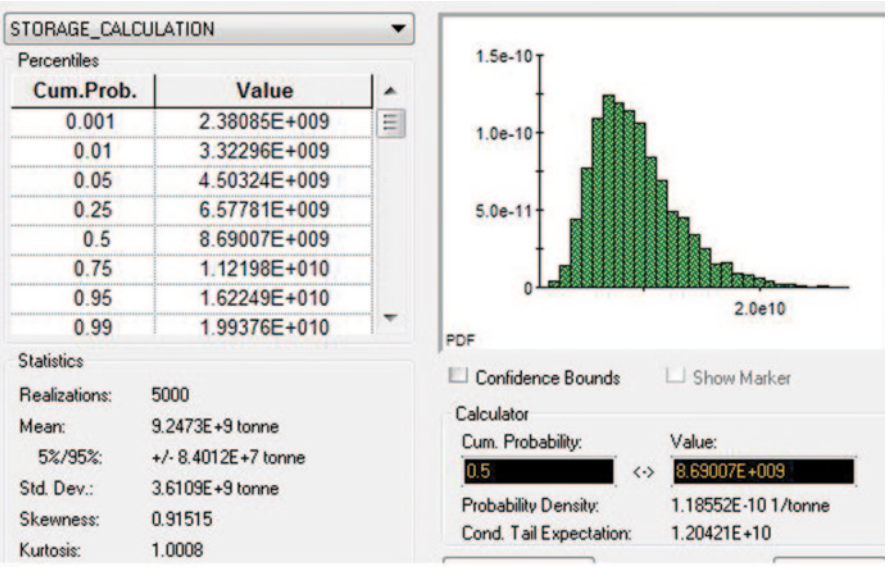


**a**

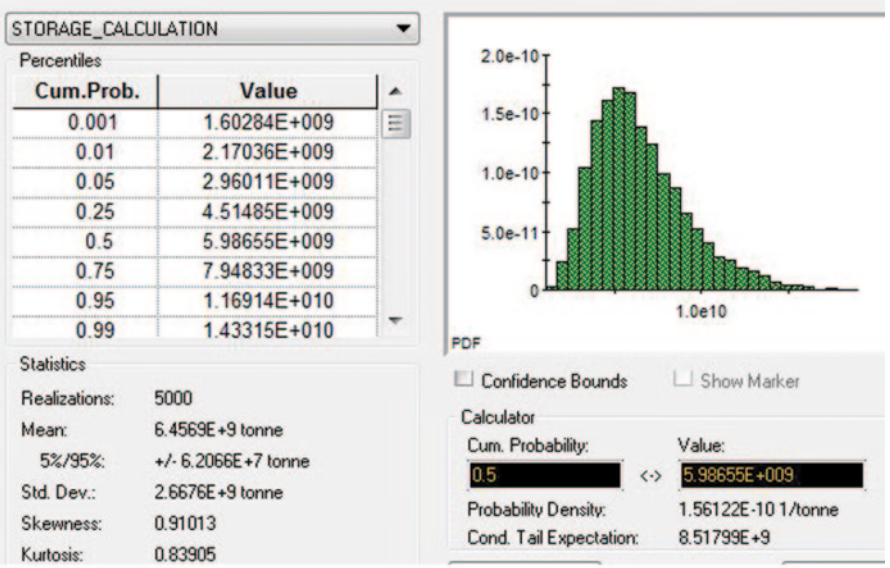


**b**

**Fig. 10.4** (**a**) Probability density of the $CO_2$ storage capacity of the Weber Sandstone in the RSU. A cumulative probability of 25 % yields a value of 6.6 Gt. This indicates that for this particular distribution, we have a 25 % chance of storing 6.6 Gt of $CO_2$ or less. Put another way, this indicates that we have a 75 % chance of storing at least 6.6 Gt $CO_2$ in the Weber Sandstone on the RSU. (**b**) Probability density of the $CO_2$ storage capacity of the Madison Limestone on the RSU. A cumulative probability of 25 % yields a value of 4.5 Gt. This indicates that we have a 75 % chance of storing at least 4.5 Gt $CO_2$ in the Madison Limestone on the RSU

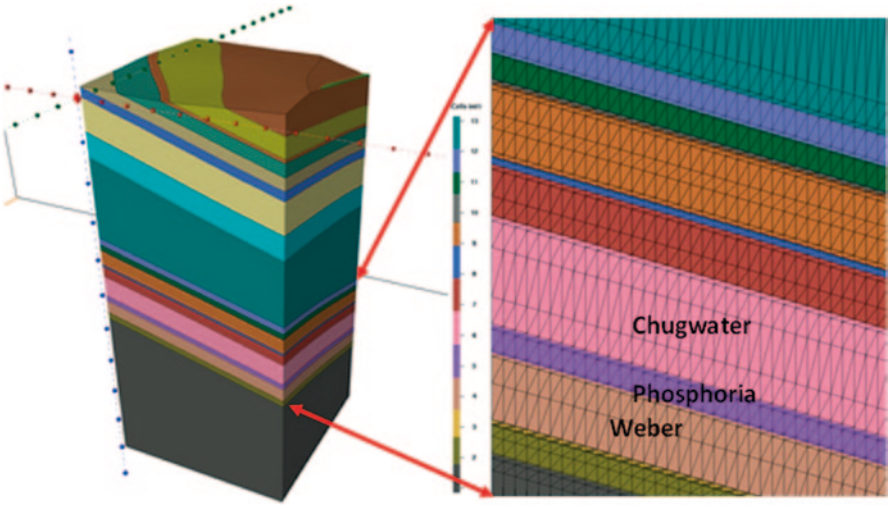


**Fig. 10.5** Cross section of the hydrostratigraphic model showing the map view location of the Jim Bridger Power Plant and enlarged view of the numerical mesh in the region of interest for injection into the Weber sandstone. Horizontal grid spacing is 200 m

direction. Grid spacing is 200 m in the X and Y directions and variable in the vertical Z direction (the average vertical spacing within the targeted reservoir Weber Sandstone and Madison Limestone is 7.5 m), with 255,879 nodes and 1.6 million volume elements (Fig. 10.5b).

### *10.4.2 Carbon Dioxide Injection Simulation*

The numerical simulations of $CO_2$ injection in this study were run on the Los Alamos National Laboratory multiphase porous flow simulator (finite element heat and mass transfer code, or FEHM) (Zyvoloski et al. 1988). FEHM has been used successfully for many multiphase applications including isotopic fractionation in the vadose zone, methane hydrate dissolution and transport, geothermal energy analysis, and simulations of $CO_2$ injection into saline aquifers (Stauffer et al. 2009a, b). The $CO_2$ equations of state are built into a lookup table that can capture the transition from supercritical fluid to liquid/gas across the region of discontinuous derivatives. The solubility of $CO_2$ in brine is determined using the model of Duan et al. (2006) and Stauffer et al. (2009a, b).

Although the Los Alamos FEHM research simulation software is used in this study other available numerical simulation software produces similar results. For example, Zhang and Qin (internal report, University of Wyoming Petroleum Engineering Department) compared the results from the FEHM simulator with those from Schlumberger's Eclipse® software for a potential $CO_2$ storage project involv-

ing the Madison Limestone on the Moxa Arch in Western Wyoming. The results from this study are quite similar, with no significant disparities.

Initial conditions for the targeted domain included a geothermal gradient of 26 °C/km with a bottom temperature of 123 °C and a top temperature of 60 °C, and a hydrostatic pressure gradient ranging from 21.6 MPa (3,130 psi) at the top of the domain (sea-level, depth 2,160 m) to 45.8 MPa (6,640 psi) at the bottom (depth 4,580 m). Further simplifying assumptions for the 3-D injection calculations were that the thermal conductivity of the rocks is constant at 0.5 W/mK, rock density is constant at 2,650 kg/m$^3$, porosities in the Weber Sandstone and Madison Limestone are both assigned at 10 %, and heat capacity is constant at 1,000 J/kgK. A $CO_2$ permeability of 1 mD was assigned to targeted reservoirs, the Weber Sandstone and Madison Limestone. Permeability values used in the simulations for confining formations were assigned at 0.01 mD. A residual saturation of 10 % was assigned to both brine and $CO_2$, using a linear relationship. Capillary pressure effects were ignored. Brine TDS is constant at 90,000 ppm for all formations, and water viscosity is calculated independently of brine content or dissolved $CO_2$. The initial dissolved $CO_2$ concentration was set at zero, as a bounding condition (The formation test report data from the region suggests that the in-situ concentration of dissolved $CO_2$ in the Weber and Madison brines may be greater than zero.) During $CO_2$ injection, the simulator allows for the possibility of $CO_2$ dissolution in water. For all simulations, the down-dip sides (north and east sides) of the domain were closed, whereas the up-dip sides (south and west sides) were open for the reservoir fluids to flow freely out of the simulation area. The open up-dip boundaries are an essential condition for creating accommodation space and preventing the reservoir pressure from elevating to the fracture pressure of the sealing formations. The model includes production of formation brines at the land surface at a distance up-dip from the injection well to manage pressure and to reduce fluid migration out of the study area.

### *10.4.3 $CO_2$ Injection into the Weber Sandstone*

A model injection well was located in section 16, Township 20 North, Range 101 West (sec. 16, T20N, R101W). The thickness of the Weber Sandstone at this location was set at 700 ft (213 m) (657 ft measured in the RSU #1 well). Of the 27 nodes within the Weber Sandstone in the model well, 16 nodes were used for $CO_2$ injection. The reservoir petrophysical properties were held constant. The porosity of the Weber Sandstone was set homogeneous at 10 %, and the permeability was set homogeneous at 1 mD. The confining layers of the Amsden below and the Dinwoody, Chugwater above the Weber were assigned a permeability of 0.01 mD.

Serial injection simulations into the Weber Sandstone were performed, at injection rates of 0.5 Mt/yr, 1.0 Mt/yr, and 1.5 Mt/yr. In the simulation at 1.0 Mt/yr, 10 % porosity, and 1 mD permeability the reservoir pressure elevated quickly when injection began, remained below the hydro-fracture pressure throughout the 50 years of injection and, when injection ceased it returned to near the original reservoir

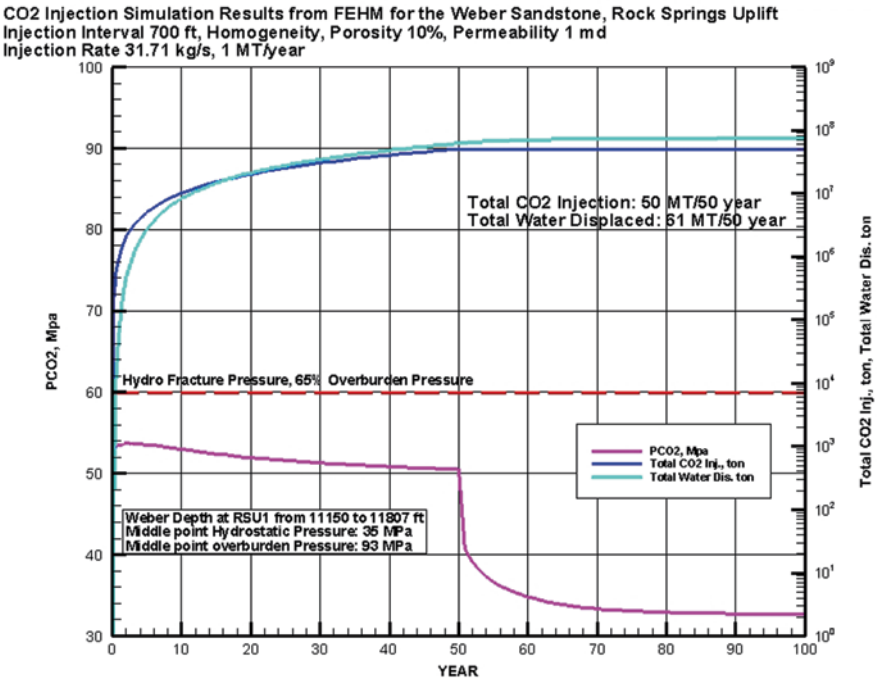


**Fig. 10.6** FEHM $CO_2$ injection simulation results for the Weber Sandston, RSU. The simulation was set up for homogenous reservoir petrophysical conditions with 10% porosity and 1 mD relative permeability. The injection rate of 31.71 kg/s was constant for 50 years; then injection ceased, and the simulation ran for another 50 years without $CO_2$ injection. The reservoir pressure elevated quickly when injection began but was below the hydro-fracture pressure throughout injection. After injection ceased, the reservoir pressure fell back to near the original reservoir pressure within 10 years

pressure within 10 years (Fig. 10.6). When injection ceased at the beginning of the 51st year, 66 Mt of pore fluids had been displaced over the 50-year injection period to maintain the reservoir pressure below the hydro-fracture pressure. At an injection rate of 1.5 Mt/yr the reservoir pressure increased to the fracture pressure, and the simulation was terminated.

The plume of 1 Mt of $CO_2$ after 50 years of a single well injection is nearly circular, with a radius of 1,600 m, covering an area of 8 $km^2$ (Fig. 10.7a). Figure 10.7b is an oblique view of the injected $CO_2$ plume for the targeted Weber Sandstone after 50 years of injection at 1 Mt/year. The $CO_2$ plume has moved across the formation boundary of the Weber Sandstone into the Phosphoria Formation above and the Amsden Formation and just into the Madison Limestone below (Fig. 10.7c). The $CO_2$ plume with saturations from 0.05 to 0.9% and occupied a volume of 1.2 $km^3$. The total volume of the Weber Sandstone above a depth of 5,000 m within the RSU is 412 $km^3$. Therefore, if all the Weber Sandstone on the RSU were used for the storage, its storage capacity could be 17 Gt of $CO_2$.

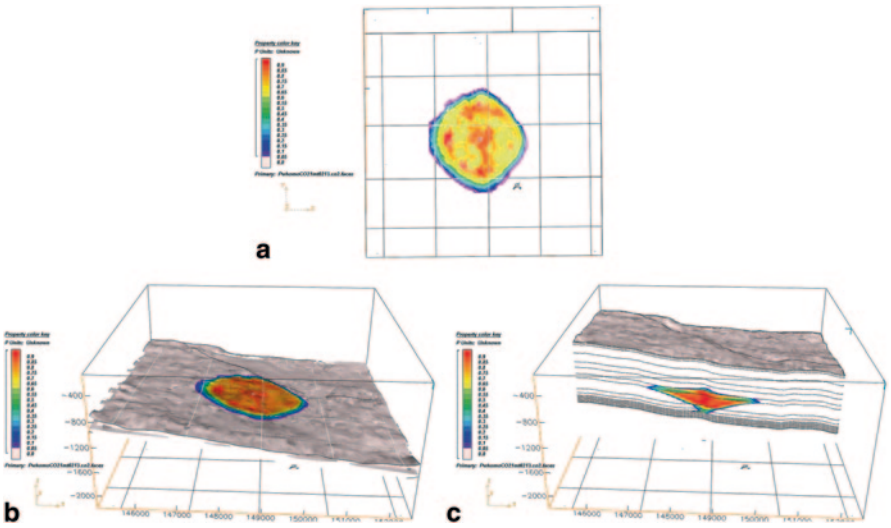


**Fig. 10.7** $CO_2$ plume distribution in the Weber Sandstone after 50 years of injection within the Jim Bridger 3-D seismic survey area, Rock Springs Uplift. The simulation used an injection interval of 700 ft, homogenous porosity (10%) and relative permeability (1 mD), and an injection rate of 1 Mt/yr in a single injection well. The up-dip boundary is open to allow fluid displacement. After 50 years of $CO_2$ injection at a constant injection rate of 31.7 kg/s, the simulation continued for 50 years to let reservoir pressure dissipate and to monitor $CO_2$ migration. **(a)** Map view of the $CO_2$ plume distribution on the top of the Weber Sandstone: the plume is circular with a radius of 1,600 m. The white five-pointed star is the location of the injection well. **(b)** Oblique view. **(c)** East-west cross section

### *10.4.4 $CO_2$ Injection into the Madison Limestone*

The same model injection well located in sec. 16, T20N, R101W was used for the $CO_2$ injection simulation into the Madison Limestone. Of the 16 nodes within the Madison Limestone interval in this well, 12 nodes were used for $CO_2$ injection. The thickness of the Madison Limestone at this location was set at 400 ft (122 m) (426 ft measured in the RSU #1 well). The reservoir petrophysical properties were held constant. The porosity of the Madison Limestone was set homogeneous at 10%, and the permeability was set homogeneous at 1 mD. The confining layers of the Amsden and Dinwoody-Chugwater above and the Darby below the Madison were assigned a permeability of 0.01 mD.

As with the Weber Sandstone simulations, serial injection simulations into the Madison Limestone were performed at injection rates of 0.5 Mt/yr, 1.0 Mt/yr, and 1.5 Mt/yr. For the simulation at 1.0 Mt/yr, 10% porosity, and 1 mD of permeability the reservoir pressure remained below hydro-fracture pressure (65% of the overburden pressure). The reservoir pressure increased quickly when injection started, then leveled off until injection ceased. At the ending of the 50th year 59 Mt of pore fluids had been displaced over the 50-year injection period to maintain the reservoir

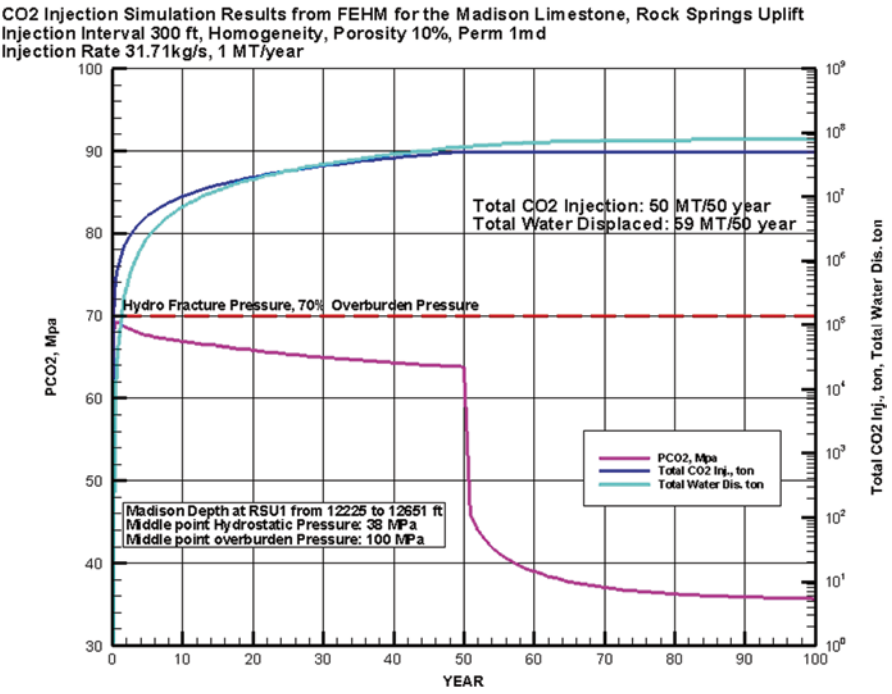


**Fig. 10.8** FEHM $CO_2$ injection simulation results for the Madison Limestone, RSU. The simulation was set up for homogenous reservoir petrophysical conditions with 10% porosity and 1 mD relative permeability. The injection rate of 31.71 kg/s was constant for 50 years; then injection ceased, and the simulation ran for another 50 years without $CO_2$ injection. The reservoir pressure elevated quickly when injection began but was below the hydro-fracture pressure throughout injection. After injection ceased, the reservoir pressure fell back to near the original reservoir pressure within 10 years

pressure below the hydro-fracture pressure. After injection ceased, the reservoir pressure fell back to near the original pressure within 10 years (Fig. 10.8). The injection rate of 1.5 Mt/yr resulted in the reservoir pressure increasing to the fracture pressure, and the simulation was terminated.

The plume of 1.0 Mt $CO_2$ after 50 years at a single injection well is nearly circular with a radius of 1,950 m, covering an area of 12 $km^2$ (Fig. 10.9a). Figure 10.9b, c shows oblique and sectional views of the injected $CO_2$ plume for the targeted Madison Limestone after 50 years of injection at 1 Mt/yr. After 50 years of injection, the $CO_2$ plume has moved upward across the formation boundary of the Madison Limestone into the lower Amsden Formation. The $CO_2$ plume after 50 years of a single well injection with saturations from 0.05 to 0.9% occupied a volume of 1.23 $km^3$ within the Madison Limestone. The total volume of the Madison above a depth of 5,000 m within the RSU is 179 $km^3$. Therefore, if all the Madison Limestone on the RSU were used for storage, its storage capacity could be 7 Gt of $CO_2$.

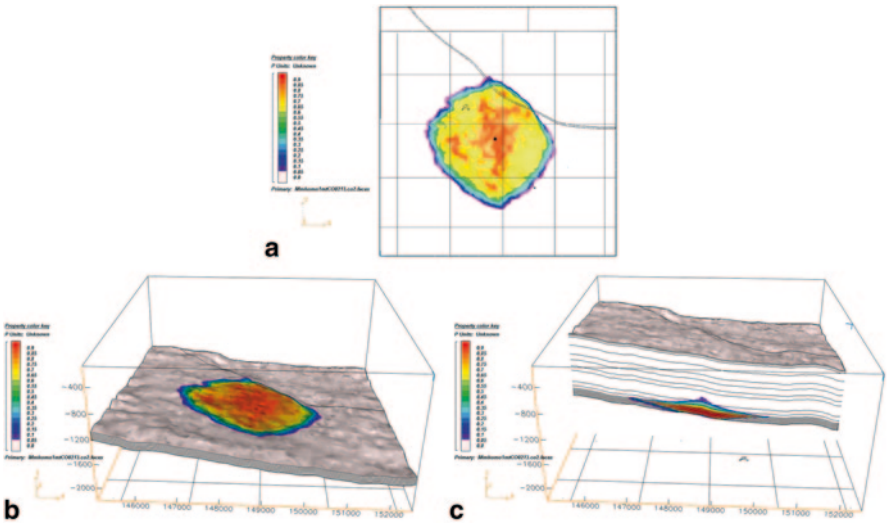


**Fig. 10.9** $CO_2$ plume distribution in the Madison Limestone after 50 years of injection within the Jim Bridger 3-D seismic survey area, Rock Springs Uplift. The simulation used an injection interval of 400 ft, homogenous porosity (10 %) and relative permeability (1 mD), and an injection rate of 1 Mt/yr in a single injection well. The up-dip boundary is open to allow displaced fluid migration. (**a**) Map view of the $CO_2$ plume distribution on the top of the Madison: the plume is circular with a radius of 1,950 m. The black five-pointed star is the location of the injection well. (**b**) Oblique view. (**c**) east-west cross section

## 10.5 Storage Capacity Assessments Based on the Numerical Simulations Utilizing a Heterogeneous Reservoir Model

The regional geologic $CO_2$ storage capacity assessments and numerical $CO_2$ injection simulations discussed in Sects. 10.3 and 10.4 reveal that the greatest uncertainty in the quantitative assessments of the storage capacity of a selected storage site lies in characterizing geologic heterogeneity in three dimensions. Heterogeneities in the porosity and permeability of geologic $CO_2$ storage reservoirs and surrounding strata are the two most important factors influencing storage capacity estimates, injection feasibility, $CO_2$ plume migration pathway determination, sealing strata integrity, reservoir pressure and displacement fluid management, and risk assessment. To reduce the uncertainties relative to the reservoir and confirming strata properties at the RSU geologic $CO_2$ storage site, a stratigraphic test well was drilled, a 3-D seismic survey was acquired, and a log suite and 279 m (916 ft) of core (from the Weber Sandstone and Madison Limestone reservoir units and the Dinwoody Formation and Amsden Formation sealing units) were collected from the newly drilled stratigraphic test well. Three-dimensional data suites derived from core sedimentary facies descriptions, petrographyic observations, laboratory measurements, log analyses, and seismic attribute interpretations reduce uncertainty significantly and improve the accuracy of the numerical simulations.

### 10.5.1 Multi-scale Heterogeneity Characterization

This chapter takes an integrated approach to characterizing the heterogeneities of the porosity and permeability in targeted storage reservoirs and containment formations. The high-vertical-resolution core measurement data and log data were used to generate a reservoir heterogeneity property model based on the seismic attribute analysis results from the newly acquired Jim Bridger 3-D seismic survey (see Chap. 9). First the lithofacies were determined for each formation on the basis of the detailed core descriptions and petrographic observations (see Chap. 6). Second, selected core samples from each lithofacies were measured for porosity and permeability under in-situ conditions. Third, the log porosities were calibrated against the laboratory measured core porosities. Fourth, the relationship between the porosity and acoustic velocity was derived from all available logs for each of the formations. Fifth, the 3-D porosity distribution of the RSU $CO_2$ storage site was populated using the velocity volume of the Jim Bridger 3-D seismic survey (modeling domain) and the function relating the porosity and acoustic velocity derived from the well logs. Sixth, once spatial distributions of porosity in the modeling domain had been acquired, permeability spatial distributions based on empirical correlations between porosity and permeability were obtained. Seventh, 3-D numerical simulations of injection of $CO_2$ into the Weber Sandstone and Madison Limestone using the heterogeneous reservoir properties were conducted with a finite element multiphase flow simulator, FEHM (Zyvoloski et al. 1997).

### 10.5.2 Core Measured Porosity

Routine core analyses were conducted on 128 core plug samples from reservoir strata within Weber Sandstone and Madison Limestone, and containment strata Dinwoody Formation and Amsden Formation from the RSU #1Well. All tests were conducted by Intertek Westport Technology Center. Pore volume and permeability measurements were made with the samples mounted in a rubber-sleeved, hydrostatically loaded overburden cell. The samples were tested at 800 psi (55 MPa) and at a calculated reservoir net confining stress (NCS). Boyle's Law, using helium as the gas medium, was employed to determine pore volume. Unsteady-state Klinkenberg permeability was measured after each pore volume measurement. Permeability to air was calculated using the unsteady-state flow data.

The porosity shows significant variation within the targeted reservoirs of the Weber Sandstone and Madison Limestone (Fig. 10.10a). In the Weber Sandstone samples, porosities range from 0.7 to 8.2% under the reservoir NCS, and densities range from 2.63 to 2.7 g/cm$^3$. The variation of the porosity distribution in the Weber Sandstone is clearly affected by its depositional and diagenetic environments. The Middle-Late Pennsylvanian Weber Sandstone is composed of both clastic and carbonate deposits (Love et al. 1993) that can be divided into an upper eolian facies and lower shallow, warm epicontinental marine facies. The micritic limestone and

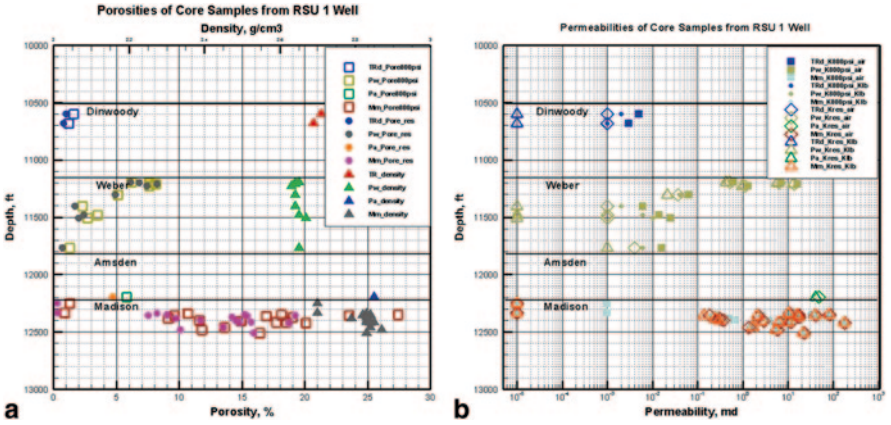


**Fig. 10.10** (**a**) Plot of porosity and density versus depth for the Weber Sandstone and Madison Limestone targeted reservoirs and Dinwoody Formation and Amsden Formation containment units. Both the porosities measured under 800 psi NCS and reservoir NCS are shown. (**b**) Air and Klinkenberg permeability variations in targeted reservoirs and containment formations under 800 psi NCS and reservoir NCS

quartz sandstone in the lower marine facies are very tight; their porosity is less than 5%. The massive quartz sandstone in the upper eolian facies has relatively higher porosity, up to 10%. In the Mississippian Madison Limestone samples, porosities range from 0.3 to 19% under the reservoir NCS, and densities range from 2.7 to 2.87 g/cm$^3$. The porosity and permeability of the Madison Limestone is mainly controlled by the following factors: (1) dissolution associated with karst development on a regional unconformity, (2) large-scale fracturing, (3) dissolution of foram shells in the limestone and dolostone, and (4) dolomitization (see Chap. 6). The greatest variance in the porosity and permeability of the Madison limestone results primarily from the heterogeneous distribution of karstification and dolomitization.

The porosities measured in the containment strata within the Dinwoody formation are less than 1%, and their average density is 2.7 g/cm$^3$ (Fig. 10.10a). The porosity differences between the 800 psi NCS and reservoir NCS are less than 1% in the Weber Sandstone and Dinwoody Formation, but are significant in the Madison Limestone. The porosity difference of the Madison Limestone samples is greater than 5% (e.g., from 14 to 19% under the reservoir NCS). The significant porosity difference of the Madison Limestone under the 800 psi (5.5 MPa) NCS and reservoir NCS (>5,000 psi, 34.5 MPa) may result from two factors, higher porosity and carbonate mineralogy. The porosities measured from several samples from the Madisone Limestone are greater than 20%. These larger porosities are mostly secondary porosity.

Figure 10.10b shows the air and Klinkenberg permeability variations in both targeted reservoirs and containment formations under 800 psi (5.5 MPa) NCS and reservoir NCS. The Klinkenberg permeability in the Weber Sandstone under reservoir NCS (5,000 psi, 34.5 MPa) ranges from 0 to 12.9 mD. The higher permeability

(>1 mD) mainly shows in the upper eolian facies of the Weber Sandstone. In the Madison Limestone, the Klinkenberg permeability under reservoir NCS (5,500 psi) ranges from 0 to 16.8 mD. Several higher permeabilities (up to 183 mD) measured in the Madison Limestone are within the karst or vuggy section. The effect of net confining stress shows mainly on the lower-permeability samples. The Klinkenberg permeability under reservoir NCS can be two orders of magnitude lower than that under the 800 psi NCS in low-permeability samples.

### *10.5.3 Log Porosity and Core Porosity*

To establish confidence in log evaluations, the porosity calculated from logs should agree with those from the core derived measurements. The porosity of a rock is a measure of its capacity to contain or store fluids, and is expressed as the pore volume of the rock divided by its bulk volume. Porosity is classified as total porosity and effective porosity. *Total porosity* is defined as all the pore space containing fluids (water, oil or gas), whether or not they are mobile. This pore space includes any hydrocarbon fluids, mobile water, capillary bound water and clay-bound water**.** *Effective porosity* is the total porosity less the fraction of the pore space occupied by cements such as silica, carbonate, or irreducible water. Because it is not possible to measure effective porosities in a reliable and repeatable manner, calibration with core analyses is best achieved by estimating total porosities from logs and comparing these with measured total porosities in core plugs.

The best way to calculate total porosity is to use the density log, correcting for lithology (using grain density) and fluid density (using invaded-zone resistivity or neutron logs). Formation bulk density is a function of matrix density, porosity, and the density of the fluid in the pores. To determine the density porosity from the bulk density log, the matrix density and density of the fluid in the pores must be known. Based on the results of laboratory core measurements from RSU #1 well, densities of 2.7 g/cm$^3$ for the Dinwoody Formation, 2.64 g/cm$^3$ for the Weber Sandstone, 2.70 g/cm$^3$ for limestone in the Madison Limestone, and 2.84 g/cm$^3$ for dolostone in the Madison Limestone g/cm$^3$ were chosen for the porosity estimates from the bulk density log in this study. Cross plots of the laboratory-measured porosities under reservoir conditions vs. log derived porosity show that neutron porosity overestimates the porosity of the carbonate rocks and carbonaceous shale, whereas density porosity underestimates the porosity of the carbonate rocks (Fig. 10.11a, b). As indicated by Asquith and Gibson (1982), true porosity can be calculated from neutron porosity and density porosity using a root mean square formula (gas-bearing formations) or mathematical mean formula (oil-and-water bearing formations). The heavy magenta line on Fig. 10.12 represents the total porosity estimated from the neutron and density porosity logs from the RSU #1 well. These neutron-density porosities correlate roughly with the core measured porosity (Fig. 10.11c). The neutron-density porosity still overestimates the carbonaceous shale and a few limestone samples. These effects may be caused by the high clay content in the shale and vugs

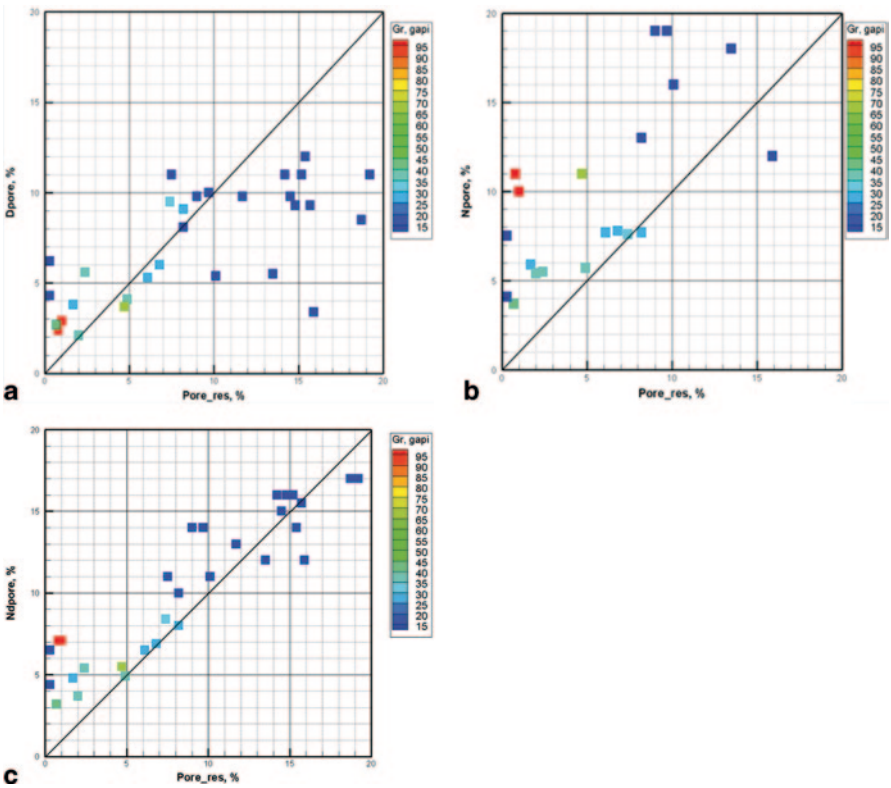


**Fig. 10.11** Crossplot of the laboratory measured porosity at reservoir conditions vs. the log-derived (**a**) bulk density porosity and (**b**) neutron porosity. (**c**) Crossplot of the laboratory measured porosity at reservoir conditions vs. the log derived neutron-density porosity

in the limestone, where the porosity could be shown on the well logs but could not be measured in the laboratory.

### *10.5.4 Sonic Velocity and Neutron-Density Porosity*

Because of the vertical extent of the borehole data used here, the vertical heterogeneity distributions are captured more fully than the horizontal ones. In order to characterize the spatial distributions of the heterogeneity properties of the targeted reservoirs and containment strata, seismic attributes must be correlated with the core and log derived petrophysical properties. Using the log suite from RSU #1 well, the relationships of the neutron-density porosity and sonic velocity were established for the Cretaceous Mowry Shale and Muddy Sandstone; the Jurassic Morrison Formation, Entrada Sandstone Member (Sundance Formation), Gypsum Spring Formation, and Nugget Sandstone; the Triassic Chugwater Formation, Red Peak Member

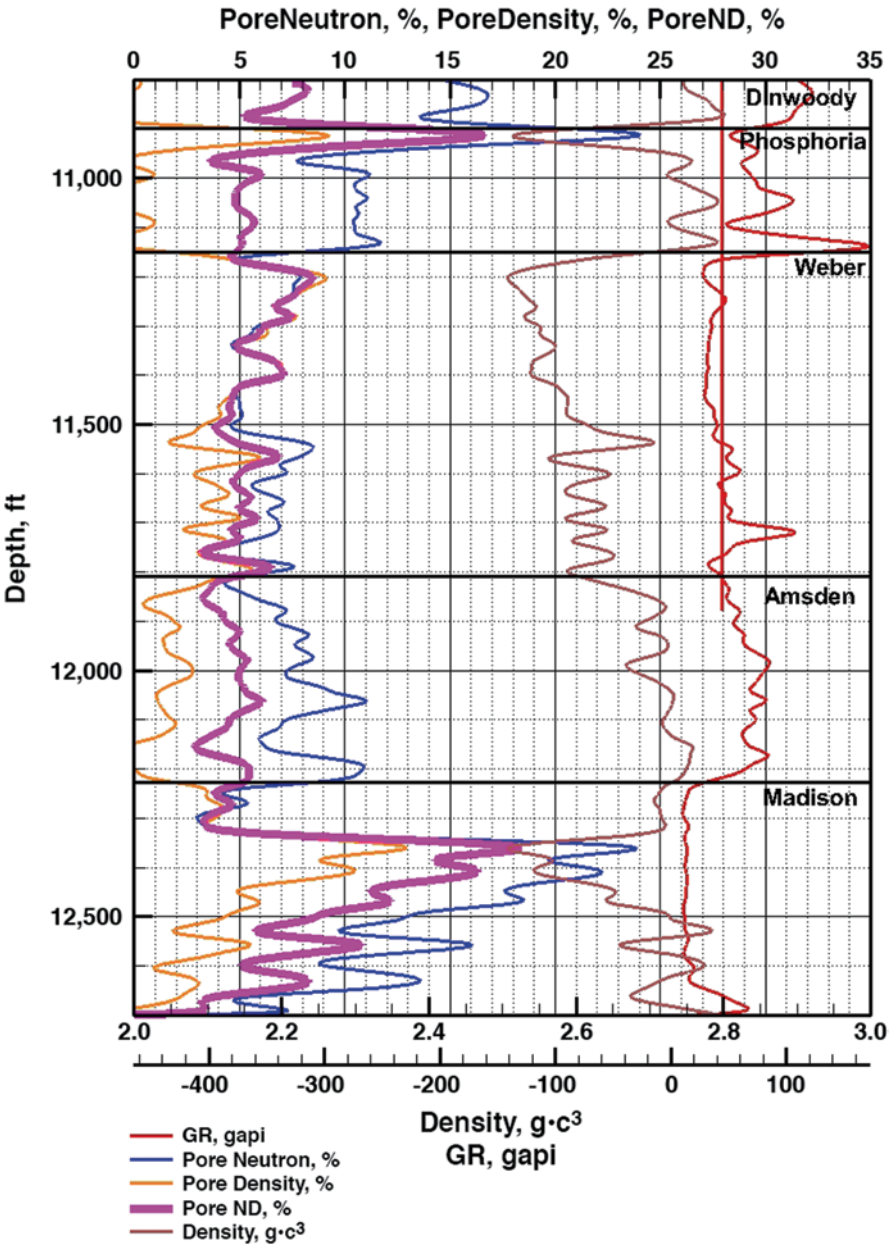


**Fig. 10.12** Plots of the gamma ray, bulk density, neutron porosity, and density porosity for the Dinwoody Formation, Phosphoria Formation, Weber Sandstone, Amsden Formation and Madison Limestone from RSU #1 well logs. The heavy magenta plot is neutron-density porosity calculated from neutron and density porosity and is used to establish the function between the porosity and the sonic velocity

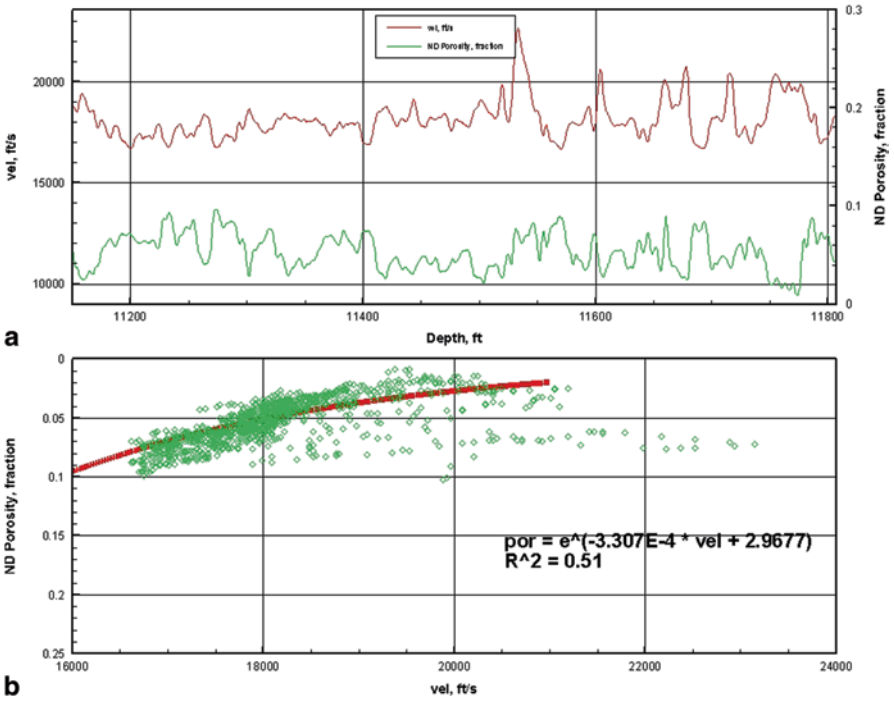


**Fig. 10.13** (**a**) Smoothed sonic velocity and neutron-density porosity logs through the Weber Sandstone in the RSU #1 well. (**b**) Crossplot of the relationship between sonic velocity and neutron-density porosity in the Weber Sandstone

(Chugwater Formation), and Dinwoody Formation; the Permian Phosphoria Formation, the Pennsylvanian Weber Sandstone and Amsden Formation; the Mississppian Madison Limestone; and the Devonian Darby Formation.

The depositional environment of the Weber Sandstone was a near-shore eolian environment, and facies changes (sand dune and inter-dune) within the Weber Sandstone caused significant variations in rock porosity. Figure 10.13a shows the sonic velocity and neutron-density porosity variations of the Weber Sandstone in the RSU #1 well. The relationship between the sonic velocity and neutron-density porosity for the Weber Sandstone is shown on Fig. 10.13b. The higher porosities that plot off (below) the correlation function line are secondary, probably the result of micro fractures. The neutron-density porosities of Weber Sandstone in RSU #1 well range from 2 to 13%, with a mean of 5% (Fig. 10.14a). Applying the function shown on Fig. 10.13b, porosities derived from the sonic velocities range from 1 to 8% with a mean of 5% (Fig. 10.14b). The normal distribution of the sonic velocity (Fig. 10.14c) is comparable with the sonic-derived porosity distribution (Fig. 10.14b).

Figure 10.15a shows the sonic velocity and neutron-density porosity variations of the Madison Limestone in the RSU #1 well. The relationship between the son-

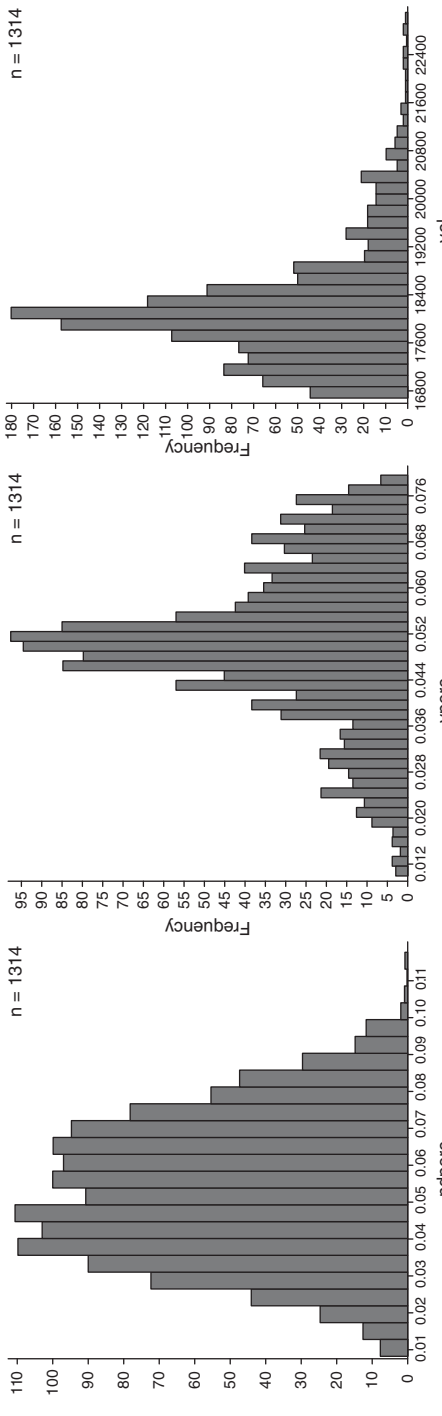


**Fig. 10.14** Histograms of the neutron-density porosity of the Weber Sandstone from the RSU #1 well logs, the porosity derived from sonic velocity, and the sonic velocity from the RSU #1 well

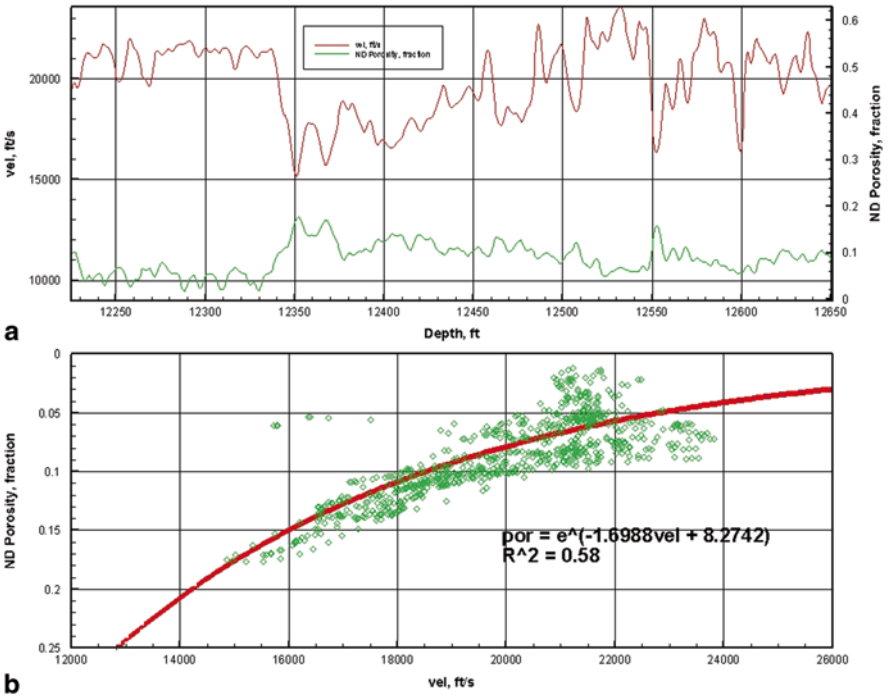


**Fig. 10.15** (**a**) Smoothed sonic velocity and neutron-density porosity logs through the Madison Limestone in the RSU #1 well. (**b**) Crossplot of the relation of sonic velocity and neutron-density porosity in the Madison Limestone

ic velocity and neutron-density porosity for the Madison Limestone is shown on Fig. 10.15b. The neutron-density porosities from well logs of Madison Limestone in RSU1 well range from 1 to 18 %, with a mean of 7 % (Fig. 10.16a). Applying the function shown on Fig. 10.15b, porosities derived from the sonic velocities range from 4 to 18 %, with a mean of 8 % (Fig. 10.16b).

The research group at CMI has developed an innovative technology to construct a more accurate seismic interval velocity model from pre-stack, CMP sorted seismic gather data. This statistical approach is used to generate a more reliable 3-D interval velocity model for the Jim Bridger seismic survey (see Chap. 7). Using the sonic velocity and neutron-density porosity functions established for each formation of interest, the 3-D porosity volume for the $CO_2$ injection simulation domain was generated from the Jim Bridger 3-D interval velocity volume. The distributions of porosities derived from seismic interval velocities for the Weber Sandstone and Madison Limestone targeted reservoirs are shown on Figs. 10.17 and 10.18. The porosities derived from seismic interval velocities for the Weber Sandstone range from 2 to 13 % with a mean of 5 % within the Jim Bridger simulation domain (Fig. 10.17a). The porosities derived from seismic interval velocities for the Madison Limestone range from 7 to 18 % with a mean of 11 % within the Jim Bridger

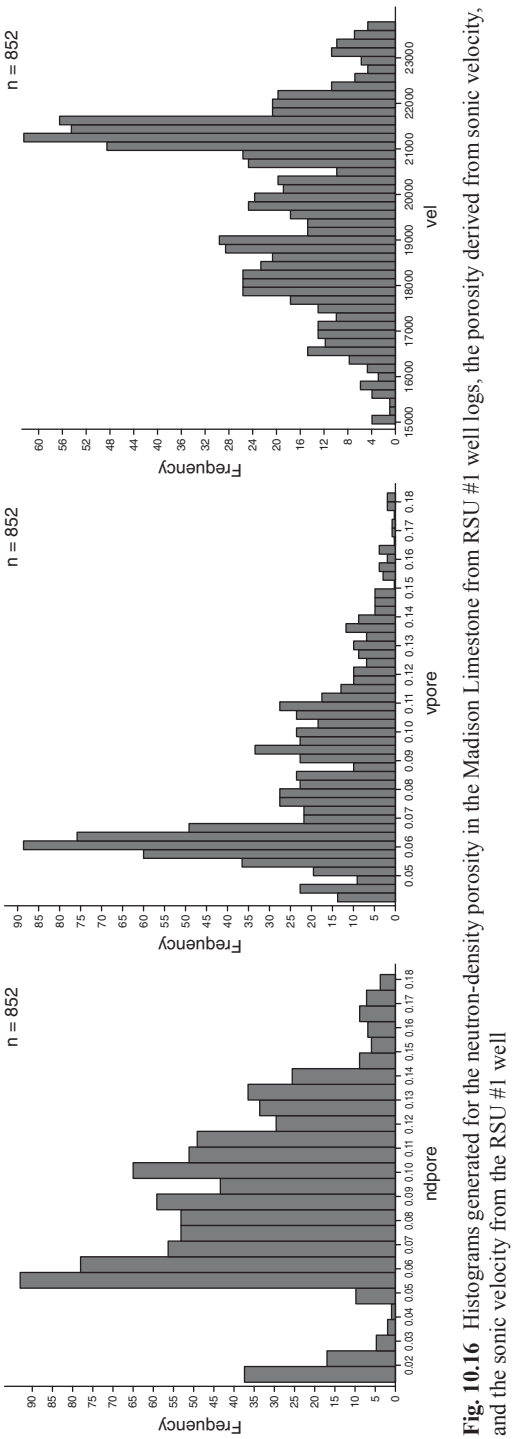


**Fig. 10.16** Histograms generated for the neutron-density porosity in the Madison Limestone from RSU #1 well logs, the porosity derived from sonic velocity, and the sonic velocity from the RSU #1 well

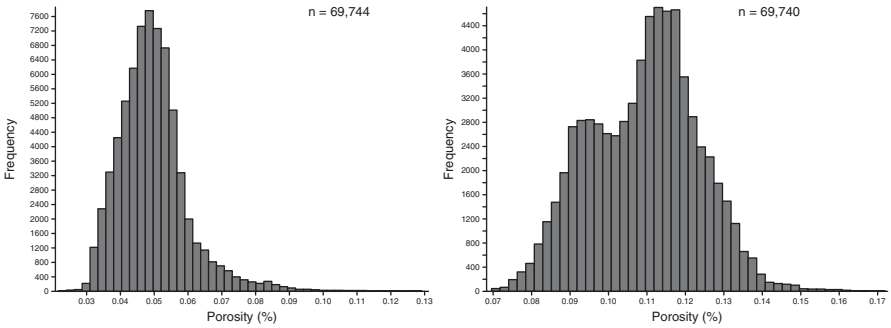


**Fig. 10.17** Histograms of the porosity distributions of the Weber Sandstone (*left*) and Madison Limestone (*right*) within the Jim Bridger 3-D simulation domain

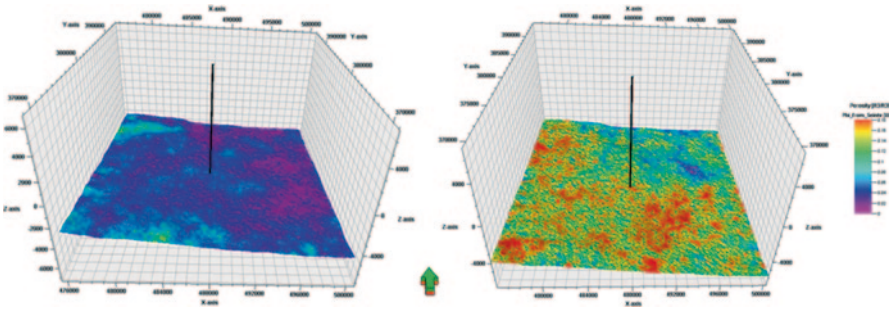

**Fig. 10.18** The porosities derived from the seismic interval velocities for the Weber Sandstone (*left*) and the Madison Limestone (*right*) show significant heterogeneous characteristics in the geologic $CO_2$ storage simulation domain

simulation domain (Fig. 10.17b). The porosities of both the Weber Sandstone and Madison Limestone show significant heterogeneity. The Madison porosities derived from seismic interval velocities show a clear bi-modal distribution. This porosity volume is used in generating a 3-D permeability volume for the Jim Bridger geologic $CO_2$ storage simulation domain.

### *10.5.5 Permeability and Porosity*

The permeability parameters are mapped from porosity through empirical correlations between porosity and permeability. The qualitative permeabilities determined in Chapter 9 were used to check porosity-permeabilities discussed below. Basically using the porosity/permeability cross plots discussed herein it was possible to quantify the high and low qualitative values determined in Chap. 9.

Three sets of porosity/permeability data for the Weber/Tensleep Sandstone collected from the region were utilized in this study (Fox et al. 1975; Bowker and

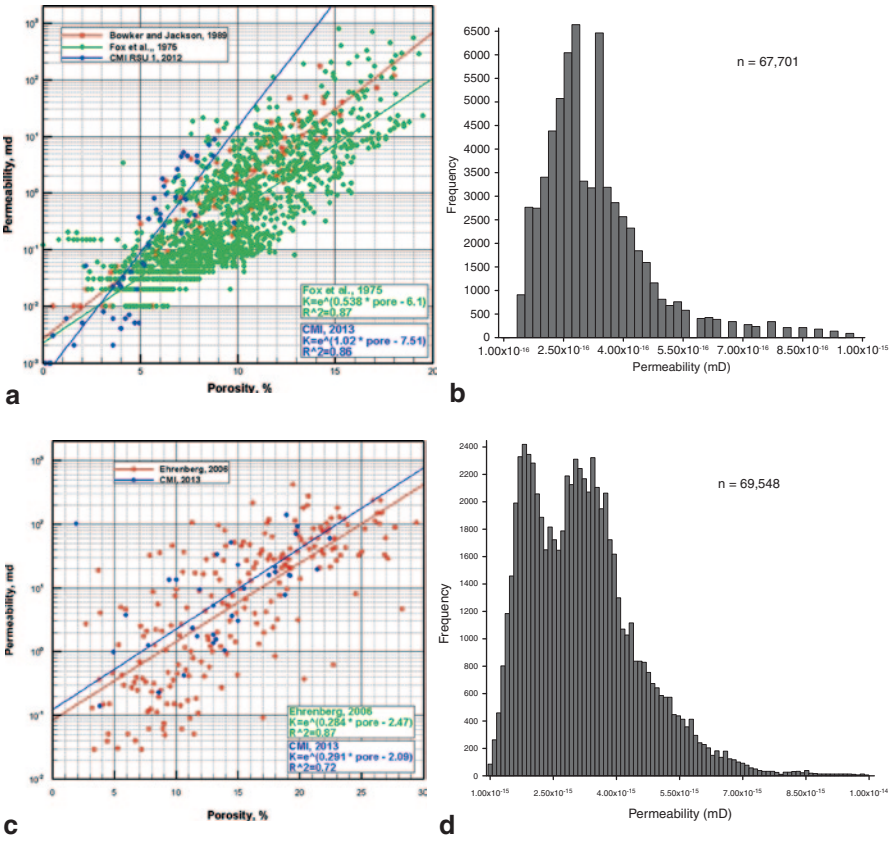


**Fig. 10.19** (**a**) Plot of permeability vs. porosity in the Weber Sandstone, RSU and vicinity. All porosity and permeability data are laboratory measurements on core samples. (**b**) Permeability distribution of the Weber Sandstone in the Jim Bridger modeling domain. (**c**) Plot of permeability vs. porosity in the Madison Limestone, RSU and vicinity. (**d**) Permeability distribution of the Madison Limestone in the Jim Bridger modeling domain. The Madison permeability distribution is bimodal

Jackson 1989, and CMI 2013). The cross plot of porosity and permeability data for the Weber/Tensleep Sandstone samples is shown on Fig. 10.19a. The permeabilities measured in the RSU #1 core sample range from 0 to 10 mD. With a mean porosity of 5%, the permeabilities derived from the three sets of porosity data are fairly close, but in samples with the highest porosity the permeabilities can vary by an order of magnitude among the different data sets. For example, with the same porosity of 10%, the derived permeability is 0.6 mD from the Fox et al. (1975) dataset and 1.05 mD from a CMI research dataset. The Weber Sandstone on the RSU has higher permeabilities than those in the Weber/Tensleep Sandstone in the Wind River Basin and other areas of the Greater Green River Basin. The exponential function relating permeability k to porosity $\phi$ in the Weber Sandstone, derived by applying least-squares curve fitting to the CMI (2013) core-measured porosity/permeability dataset, is:

$$k = e^{1.02\Phi - 7.51}. \tag{10.2}$$

The other two empirical correlations for the Weber/Tensleep Sandstone of Fox et al. (1975) and Bowker and Jackson (1989) are shown on Fig. 10.19a for comparison. The CMI regression has a correlation coefficient $R^2 = 0.86$. The permeability volume of the Jim Bridger modeling domain was derived from the Jim Bridger porosity volume through Eq. 10.2. Figure 10.19b shows the distribution of the derived permeabities from 0 to 1 mD, which accounts for the permeabilities of 98 % of the simulation cells (67,615 of 69,147 cells) in the Weber Sandstone in the Jim Bridger modeling domain. The permeabilities in the Jim Bridger modeling domain range from 0.01 to 20 mD with a mean of 0.3 mD.

For the Madison Limestone, two sets of porosity/permeability datasets, from measurements on core samples from the RSU #1 well and the region, were available to this study (Ehrenberg 2006 and CMI 2013). The cross plot of porosity and permeability for the Madison Limestone samples is shown on Fig. 10.19c. The two datasets show similar trends for the relationship between the porosity and permeability. The permeabilities in the RSU #1 core samples range from 0.001 to 200 mD. An exponential function relating permeability k to porosity ϕ in the Madison was derived by applying least-squares curve fitting to the CMI (2013) core-measured porosity/permeability dataset:

$$k = e^{0.291\Phi - 2.09} \tag{10.3}$$

The Ehrenberg et al. (2006) empirical correlation for the Madison Limestone is shown on Fig. 10.19c for comparison. The CMI regression has a correlation coefficient of $R^2 = 0.72$. The permeability volume of the Jim Bridger modeling domain was derived from the Jim Bridger porosity volume by applying Eq. 10.3. Figure 10.19d shows distribution of the derived permeabilities in the Madison Limestone in the Jim Bridger modeling domain. These permeabilities range from 0.01 to 20 mD with a mean of 3 mD. The peameability of the Madison Limestone in the RSU has a bimodal distribution. The higher porosities and permeabilities are the result of the karst leaching, diagenesis, and microfracture development.

The primary containment formations for geologic $CO_2$ storage on the RSU are the Amsden Formation, Dinwoody Formation, and Red Peak Member of the Chugwater Formation. However the Cretaceous shale in the upper half of the stratigraphic section is more than 1,500 m thick and provides a multitude of secondary sealing sequences. The lithology of these Cretaceous containment formations is shale, mudstone, and carbonaceous shale. The permeability of the shale and clay-rich sandstone is a complex function of porosity, clay content, effective stress, and diagenesis (Yang and Aplin 2010). Because of the difficulty in making laboratory measurements on these lithologies, high-quality data on porosity and permeability in shale and mudstone is relatively rare (Neuzil 1994). In clay-rich lithologies, a simple linear regression relationship cannot capture a realistic relationship between porosity and permeability. In light of this complexity, this study used the empirical

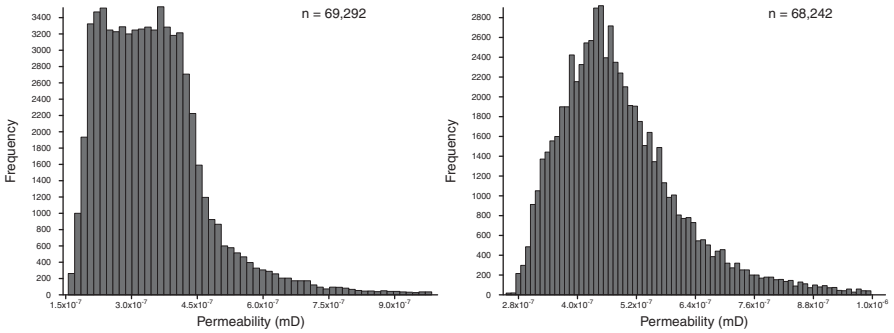


**Fig. 10.20** Histograms showing the permeability distributions in the Dinwoody (*left*) and Chugwater (*right*) containment formations in the RSU geologic $CO_2$ storage simulation domain

correlation of Yang and Aplin (2010) to compute the permeability k of the sealing rocks with an assumed clay content C of 25 %:

$$\begin{aligned} \ln \quad k = & -69.59 - 26.79C + 44.07C^{0.5} \\ & + \left(-53.61 - 80.03C + 132.78C^{0.5}\right)e \\ & + \left(86.61 + 91.91C - 163.61C^{0.5}\right)e^{0.5}, \end{aligned} \tag{10.4}$$

where k is the vertical permeability [$m^2$] ($m^2 \approx 10^{15}$ mD), C is the clay content [decimal fraction, here 0.25], $e = \phi/(1-\phi)$ is the void ratio [decimal fraction], and $\phi$ is the porosity [decimal fraction].

Figure 10.20 shows the permeability of the Dinwoody Formation and Chugwater Formation derived from the Jim Bridge 3-D porosity volume that was used in the RSU $CO_2$ storage simulations.

Modeled permeabilities are assumed to be isotropic for all facies and all rocks except the sealing rock, the Dinwoody and Chugwater formations, to which an anisotropic ratio of 10 was assigned (horizontal permeability is one order of magnitude greater than vertical permeability). The density of all rocks was fixed at 2,650 kg/$m^3$. The Joule-Thomson effect (Han et al. 2010) is included through conservation of enthalpy (Stauffer et al. 2003); however, the dry-out effect (Pruess and Muller 2009), geomechanical effects due to fluid pressure buildup, and geochemical reactions are not considered in the $CO_2$ injection simulations.

On the basis of the vertical extent of the borehole data acquired, the vertical heterogeneities are more fully captured than the horizontal ones. Yet, by combining geologic characterization and detailed 3-D seismic attribute analysis, the spatial (vertical and horizontal) heterogeneities in the simulations described herein are, we believe, as realisitic as is technically possible with the available dataset. The next step is to incorporate the spatial heterogeneities of porosity and permeability into the Jim Bridger 3-D seismic domain to simulate supercritical $CO_2$/brine multiphase fluid flow during $CO_2$ injection for 50 years with observation for 50 years post-injection, using the FEHM simulator.

**Table 10.1** Parameters used for $CO_2$ injection simulations in the Weber Sandstone and Madison Limestone

| Parameter | Symbol | Unit | Value | |
|---|---|---|---|---|
| | | | Weber | Madison |
| Saline aquifer effective permeability | k | $m^2$ | Hetero | Hetero |
| Saline aquifer effective porosity | ϕ | % | Hetero | Hetero |
| Saline aquifer thickness | b | m | 200 | 130 |
| Saline aquifer salinity | s | % | 11 | 8 |
| Saline aquifer thermal conductivity | $\lambda_m$ | W/Km | 3.3 | 3.3 |
| Saline aquifer initial fluid pressure | $P_{inf}$ | MPa | 31–40 | 34–43 |
| Maximum temperature difference | T | °C | 22 | 22 |
| Brine viscosity | $\mu_w$ | Pa s | $1.33\times10^{-4}$ | $1.33\times10^{-4}$ |
| Brine density | $\rho_w$ | $kg/m^3$ | 1,100 | 1,100 |
| $CO_2$ fluid viscosity | $\mu_{CO_2}$ | Pa s | $5.8\times10^{-5}$ | $5.8x10^{-5}$ |
| $CO_2$ fluid density | $\rho_{CO_2}$ | $kg/m^3$ | 700 | 700 |
| Brine compressibility | $c_w$ | $Pa^{-1}$ | $3.5\times10^{-10}$ | $3.5\times10^{-10}$ |
| $CO_2$ fluid compressibility | $c_{CO_2}$ | $Pa^{-1}$ | $1.0\times10^{-9}$ | $1.0\times10^{-9}$ |
| Pore compressibility | cp | $Pa^{-1}$ | $4.5\times10^{-10}$ | $4.5\times10^{-10}$ |
| Injection time | t | year | 50 | 50 |
| Specific storage | $S_s$ | – | $5\times10^{-6}$ | $5\times10^{-6}$ |
| Injection rate | Q | kg/s | constant | constant |
| Gravitational acceleration | g | $m/s^2$ | 9.8 | 9.8 |
| Residual water saturation | $S_{wr}$ | % | 10 | 10 |
| Maximum water saturation | $S_{ws}$ | % | 90 | 90 |
| Residual $CO_2$ saturation | $S_{CO_2r}$ | % | 10 | 10 |
| Maximum $CO_2$ saturation | $S_{CO_2s}$ | % | 90 | 90 |
| Brine thermal expansion | λf | K − 1 | 0.001 | 0.001 |
| Brine specific heat capacity | $C_{pf}$ | J/kg K | $4.2\times10^3$ | $4.2\times10^3$ |

## *10.5.6 Numerical Simulations of $CO_2$ Injection with Heterogenetic Reservoir and Containment Strata*

### 10.5.6.1 Numerical Model Setup

The simulation domain is 8 km × 8 km × 3.6 km in the X, Y, and Z directions (width, length, and depth) and is discretized into 291,954 tetrahedral nodes with horizontal spacing of 150 m generally and 37.5 m near the injection well. The variable vertical resolution is reduced to 10 m in order to capture relatively small vertical correlation lengths in the Chugwater and Dinwoody, Phosphoria, Weber, Amsden, Madison, and Darby formations. The modeled formations dip is 5º northeast and the strike is 130º. Injection of $CO_2$ into the Weber Sandstone and Madison Limestone is assumed to be at a constant temperature (45 °C) and a constant injection pressure of 18.5 MPa (2,680 psi) at the well head. The injection pressure at the penetrated reservoirs is below 65 % lithostatic and is comparable to the maximum sustainable injection pressure estimated by Rutqvist et al. (2007), who analyzed coupled fluid flow and geomechanical fault-slip under conditions of hypothetical compression and extension stress. Important parameters of the CMI simulations are listed in Table 10.1.

The bottom of the simulation domain is a no-flow boundary. The top and up-dip (western and southern) boundaries of the simulation domain are open to flow in and out. The down-dip (northern and eastern) boundaries are closed. Constant temperatures are held at the top (55 °C) and bottom (147 °C) of the domain, which matches a geothermal gradient of 25.6 °C/km. The fixed side boundaries are used to allow an estimate of the amount of water that must be produced to ensure that the injection site does not impact surrounding parcels of land (i.e., land outside the 5 × 5-mi storage domain). Hydrostatic pressure and temperature fields are used as initial conditions for all simulations. The initial $CO_2$ fraction in injection well nodes is set at zero. These simulations incorporate a $CO_2$ density model (Duan et al. 2008) and a solubility model of $CO_2$ in brine (Duan et al. 2006) into their $CO_2$ transport modeling. Combined with thermodynamic updating, the density, viscosity, and solubility of $CO_2$ in the brine are simulated as temperature and pressure change.

#### 10.5.6.2 $CO_2$ Injection into the Weber Sandstone (Heterogeneous Reservoir Model)

The results presented in this section are based on simulations that span 50 years of injection into one well completed in the Weber Sandstone using a realistic model of the Weber's heterogeneous reservoir properties. Fifty years of injection was chosen to simulate $CO_2$ storage because it corresponds to the typical lifetime of a coal-fired power plant in North America (Stauffer et al. 2009b). Porosity and permeability have a significant affect on injection feasibility. Injection rates of 1 Mt/yr, 0.75 Mt/yr, 0.5 Mt/yr, and 0.3 Mt/yr were simulated using the same heterogeneous reservoir model described above in Sect. 10.5, but only the rate of 0.3 Mt/yr of injection was feasible without inducing $CO_2$ migration across set lateral boundaries. The other, higher injection rates caused the simulations to terminate before the end of the 50-year period because of serious convergence errors or unacceptably high formation pressure. At 0.3 Mt/yr, 15 Mt $CO_2$ could be stored within the Weber Sandstone with a single injection well over a 50-year period. In order to keep the reservoir pressure below the hydro-fracture pressure, 19 Mt of formation water would have to be removed over the 50 year period (Fig. 10.21a). In the heterogeneous model the pressure changes are not uniformly distributed as in the homogeneity model, but instead occur mainly around the injection well, in the down-dip directions where the boundaries are closed. No unacceptable pressure elevations occur in the up-dip directions, where the boundaries are open to fluid migration (Fig. 10.21b).

Figure 10.21c is an oblique view and Fig. 10.21d a cross section of the injected $CO_2$ plume in the modeled Weber Sandstone after 50 years of injection at a rate of 0.3 Mt/yr. After 50 years of injection, the $CO_2$ plume remains within the Weber Sandstone reservoir and is irregularly shaped, covering an area of 10 $km^2$ (Fig. 10.21c). Unlike the $CO_2$ plume distributions in the homogeneous model, the $CO_2$ plume distributions in the heterogeneous model show a patchy pattern.

The storage capacity of the Weber Standstone for the entire RSU is estimated by assuming that the 3-D simulation domain is a representative element. Therefore,

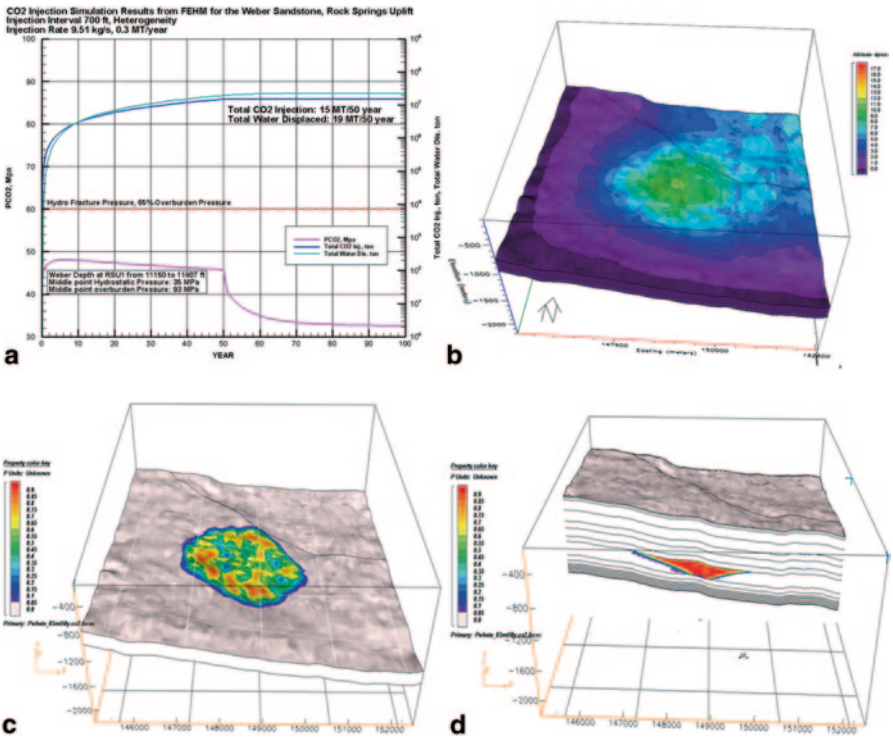


**Fig. 10.21** (**a**) FEHM $CO_2$ injection simulation results for the Weber Sandstone, RSU. The simulation was set up for hetegogeneous reservoir conditions. The injection rate of 9.51 kg/s was constant for 50 years; then injection ceased, and the simulation ran for another 50 years without $CO_2$ injection. (**b**) The pressure regime of the Weber storage reservoir at the end of $CO_2$ injection. Depicted are the differences between the simulated reservoir hydrostatic pressure and the simulated reservoir pressure at the end of 50 years of $CO_2$ injection. (**c**) Oblique view and (**d**) cross section of the $CO_2$ plume in the Weber Sandstone representing the 15 Mt of $CO_2$ injected into the reservoir by the end of 50 years of $CO_2$ injection

once the volume $V_{plume}$ of the $CO_2$ plume in the simulation domain and the volume $V_{RSU}$ of the Weber Sandstone in the whole RSU are known, a simple approximation of the storage capacity C can be calculated by Eq. 10.5:

$$C = \left( \frac{V_{RSU}}{V_{plume}} \right) \times M_{CO_2} \tag{10.5}$$

where $M_{CO_2}$ is the total mass of $CO_2$ injected into the saline aquifer in the simulation domain over 50 years. The $CO_2$ plume with saturations from 0.05 to 0.9% fills a volume of 0.65 $km^3$ with 15 Mt of $CO_2$. The total volume of the Weber Sandstone above depth of 5,000 m within the RSU is 412 $km^3$. Therefore, if all the Weber Sandstone on the RSU were used for the storage, the storage capacity of the Weber on the RSU could be as great as 9.5 Gt of $CO_2$.

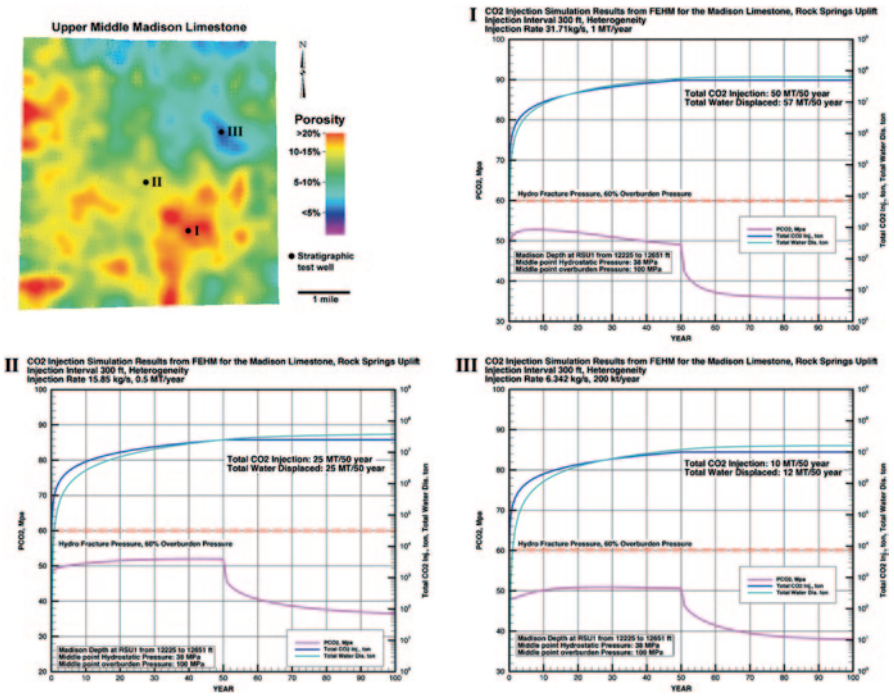


**Fig. 10.22** FEHM $CO_2$ injection simulation results for the Madison Limestone, RSU. The simulations were set up for heterogeneous reservoir conditions. The injection rates of 31.71, 15.85 and 6.34 kg/s were constant for 50 years for wells in the high (**I**), medium (**II**), and low (**III**) reservoir-quality areas, respectively. The injections continued for 50 years, then ceased, and the simulations ran for another 50 years without $CO_2$ injection. The reservoir pressure elevated quickly when injection started, but was below the hydro-fracture pressure throughout injection. After injection ceased, the reservoir pressure fell back to near the original pressure within 10 years

### 10.5.6.3 $CO_2$ Injection into the Madison Limestone

The main reservoir-property heterogeneities in the Madison Limestone on the RSU are in porosity and permeability. The porosities within the modeling domain range from less than 1% to more than 20%, and permeabilities range from 0.001 mD to more than 100 mD. The numerical simulations used an injection interval of 76 m (250 ft) in the middle Madison Limestone. Three wells located in the high, medium, and low reservoir-quality areas in the storage domain were chosen to evaluate the injectivity and storage capacity of the Madison Limestone on the RSU (Fig. 10.22a**).**

After simulated injection started, the fluid pressure increased immediately at the injection well to 50% of overburden pressure. In the higher reservoir-quality case (well I), the fluid pressure field reached a quasi-steady state about four years after injection began, then decreased gradually (Fig. 10.22b). However, in the medium and low reservoir-quality cases (wells II and III) the pressure evolved gradually over the 50-year injection period (Fig. 10.22c, d). The fluid pressure increased mainly

in the injection zone, with an increase in pressure of between 1 MPa (145 psi) and 17 MPa (2,470 psi) in the middle Madison.

Concurrently with the pressure increase at the start of injection, the $CO_2$ plumes began to grow and migrate. At the end of 50 years of injection the supercritical $CO_2$ plumes had expanded away from the injection wells, with preferential flow toward the up-dip open boundaries (Fig. 10.23b, e, h). The $CO_2$ plumes did not grow uniformly in either the horizontal or the vertical direction, because of heterogeneity, pressure interference, and the dip of the formation. In all three simulations the $CO_2$ plume migrated away from the injection well in the up-dip direction and developed a long, narrow front at the top of the Madison Limestone (Fig. 10.23d, g, j). In all three locations, formation water had to be displaced to create accommodation space for the injected $CO_2$ and to keep the reservoir pressure below the hydro-fracture pressure. Also for the three injection scenarios, the reservoir pressure increased rapidly at the start of injection, but quickly decreased to near the reservoir hydrostatic pressure within 10 years after the injection ceased (Fig. 10.22b, c, d).

The injectivity and storage capacities are significantly different among high, medium, and low reservoir-quality areas. In a high reservoir-quality reservoir 50 Mt $CO_2$ could be injected and safely stored in the Madison Limestone over a 50 year period, with an injection rate of 31.71 kg/s and 57 Mt of formation fluid displaced (Fig. 10.22b, well I). In a medium reservoir-quality reservoir, to keep the reservoir pressure below the fracture pressure, only 25 Mt $CO_2$ could be injected and safely stored in the Madison over a 50-year period, with an injection rate of 15.85 kg/s and 25 Mt of formation fluid displaced (Fig. 10.22c, well II). In a low reservoir-quality reservoir, just 10 Mt $CO_2$ could be injected and safely stored in the Madison Limestone over a 50 year period, with an injection rate of 6.34 kg/s and 12 Mt formation water displaced (Fig. 10.22d, well III). In all cases, the amount of displaced fluid was of the same order of magnitude as the amount of $CO_2$ injected into the reservoirs.

The plumes of injected $CO_2$ differ among the high, medium, and low reservoir-quality areas where the injection wells were located (Fig. 10.23a). The results differ from those in the homogeneous reservoir case a common in the heterogeneous case a $CO_2$ plume at the top of the Madison Limestone exhibits an irregular shape and spreads to the left (up-dip direction), through relatively higher porosity and permeability zones toward the open boundary (Fig. 10.23b, e, h). As expected, all $CO_2$ plumes show the expansion at the plume top because of buoyancy-driven spreading along the base of the lower-permeability unit above the Madison (the Amsden Formation) (Fig. 10.23d, g, j). None of the simulated supercritical $CO_2$ plumes have not crossed the domain boundary in 50 years of injection (64 $km^2$).

The differences in the amount of $CO_2$ stored in the high, medium, and low reservoir-quality zones after 50 years of injection reflects significant differences in the porosity and permeability distribution within the middle Madison Limestone (Fig. 10.23a). Because no $CO_2$ has leaked into the overlying Amsden Formation in these simulations, the storage capacity of the Madison is defined on the basis of the amount of $CO_2$ injected over 50 years *separately for each simulation*. Using Eq. 10.5, the storage capacity of the Madison Limestone for the entire RSU is esti-

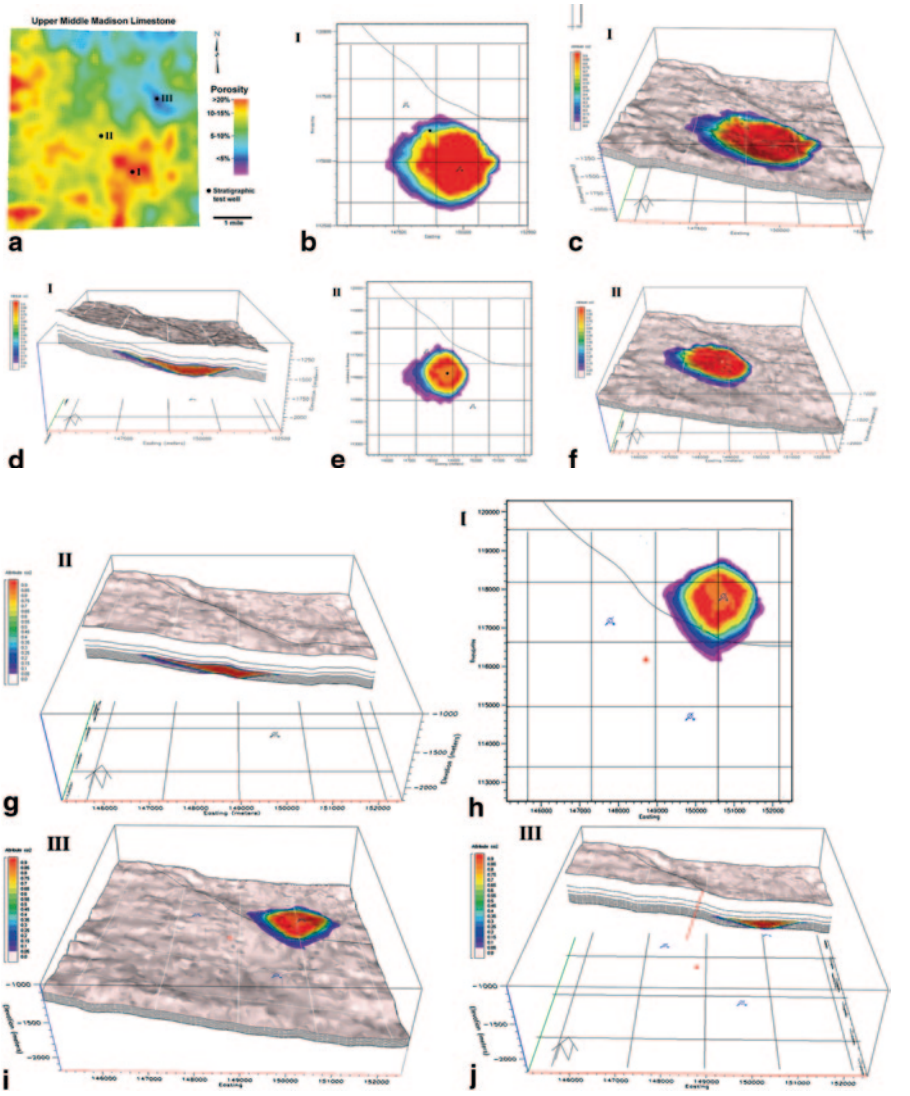


**Fig. 10.23** (**a**) Heterogeneous porosity distrubion in the Madison Limestone within the RSU modeling domain and locations of the high (*I*), medium (*II*) and low (*III*) reservoir-quality areas chosen for simulation. These simulations used an injection interval of 400 ft (122 m). The grids represent section boundaries. (**b**) Map, (**c**) oblique, and (**d**) sectional views of the $CO_2$ plume in the Madison Limestone after 50 years of $CO_2$ injection into a high reservoir-quality area at a rate of 1.0 Mtyr. (**e**) Map, (**f**) oblique, and (**g**) sectional views of the $CO_2$ plume in the Madison after 50 years of $CO_2$ injection into the medium reservoir-quality area at a rate of 0.5 Mtyr. (**h**) Map, (i) oblique, and (j) sectional views of the $CO_2$ plume in the Madison after 50 years of $CO_2$ injection into the low reservoir-quality area at a rate of 0.2 Mt/yr

mated by assuming that the 3-D simulation domain (5 mi × 5 mi, 8 km × 8 km) is a representative element of the RSU (35 mi × 50 mi, 56 km × 80 km). The $CO_2$ plume volumes are 1.1 $km^3$ in the high reservoir-quality case (Fig. 10.23c, d), 0.642 $km^3$ in the medium reservoir quality-case (Fig. 10.23f, g), and 0.337 $km^3$ in the low reservoir-quality case (Fig. 10.23i, j). A volume 179 $km^3$ for the Madison Limestone above a depth of 5,000 m on the whole RSU is derived from the RSU geologic structural model constructed using EarthVision® geospacial modeling software (Fig. 10.2). For the high reservoir-quality case, the Madison Limestone on the RSU can store 8 Gt of $CO_2$; for the medium reservoir-quality case, 7 Gt of $CO_2$; and for the low reservoir-quality case, 5 Gt of $CO_2$. Thus under this set of simuations that account for porosity and permeability heterogeneity, the storage capacity of the Madison Limestone on the RSU is between 5 Gt and 8 Gt, the weighted average value depending on the volumetric proportions of the high, medium, and low reservoir-quality zones.

## 10.6 Comparison of Methods to Assess $CO_2$ Storage Capacity

The work presented in this chapter affords the opportunity to discuss the strengths and weaknesses of each of the three analytical methods: the static volumetric model, dynamic homogenous reservoir model, and dynamic heterogeneous reservoir model. The volumetric model is based on regional data for the average values of key parameters such as thickness, porosity, and permeability. The dynamic reservoir model is based on the measured thickness of reservoir intervals (site-specific well logs), average values of porosity and permeability derived from the laboratory measurements, and injectivity and other fluid-flow measurements from the well bore of the site-specific stratigraphic test well. The dynamic heterogeneous reservoir model is based on the well-bore measured thickness of each lithofacies in each of the reservoir intervals; detailed diagenetic, fluid chemistry, and geochemical studies of specific depositional facies in each of the reservoir intervals; injectivities measured in the well-bore; and, most importantly, laboratory-measured porosities and permeabilities correlated with seismic attributes in order to construct a 3-D model of reservoir petrophysical heterogeneity at and away from the well bore.

In this progression of evaluation methodology there is an inherent decrease in geologic uncertainty. Figure 10.24 compares the three methods for estimating $CO_2$ storage capacity as applied to the Weber Sandstone and Madison Limestone in the 5-mi × 5-mi (8-km × 8-km) storage domain on the RSU. The volumetric method suggests that 793 Mt of $CO_2$ can be stored in the Weber and Madison reservoir interval in the storage domain, whereas the dynamic homogeneous reservoir model suggests that this same reservoir interval can store 655 Mt of $CO_2$. In marked contrast, the numerical simulations for the same storage domain and reservoir interval using the dynamic heterogeneous reservoir model suggests that the Weber Sandstone and Madison Limestone can store 303 Mt of $CO_2$. If the dynamic model that

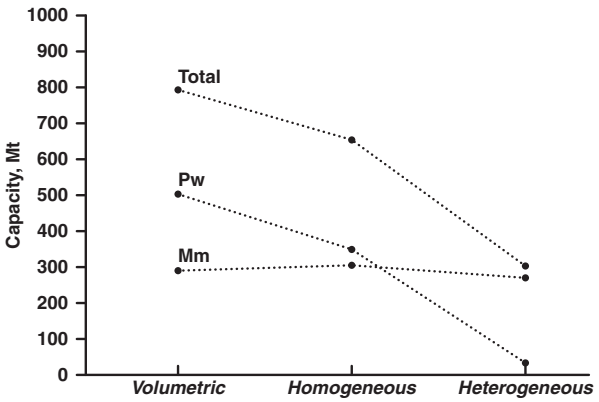


**Fig. 10.24** Comparisons of $CO_2$ storage capacity in the Weber Sandstone (Pw) and Madison Limestone (Mm), and their total capacity, as estimated using a static volumetric model, a dynamic reservoir model , and a dynamic heterogeneous reservoir model

considers the 3-D reservoir heterogeneity is the most realistic configuration of the reservoir interval, then it follows that the volumetric approach overestimates the reservoir storage capacity by a factor of 2.5. Comparing the numerical simulations of the two dynamic reservoir models, the homogeneous model overestimates $CO_2$ storage capacity by a factor of 2.2. Of course, the volumetric approach requires less time and effort, and dynamic simulations with the heterogeneous reservoir model require the most effort and the most data.

For reliable, low-risk evaluations of potential $CO_2$ storage sites, it is imperative to use 3-D reservoir models that include the heterogeneity of petrophysical, diagenetic, and geochemical distributions away from the boreholes within the storage domain. To achieve estimates of $CO_2$ storage capacity for targeted reservoir intervals, data from at least one stratigraphic test well and a 3-D seismic survey over the storage domain are probably essential. Without this site-specific data, risk and performance assessments of $CO_2$ storage scenarios remain plagued by unacceptable uncertainty.

## 10.7 Conclusions

- Reducing geologic uncertainty in evaluations of geologic $CO_2$ storage site scenarios requires a robust database that allows an accurate reconstruction of the targeted storage rock/fluid volume, especially with respect to spatial petrophysical heterogeneities. Results that rely on a generalized regional database to populate a homogenous rock/fluid volume based on average reservoir properties yields general insights into injection/storage characteristics but lacks specificity, resulting in performance assessments plagued by substantial uncertainty. To move from idealistic, highly generalized assessments to realistic, low-risk assessments of the Rock Springs Uplift, it was necessary to acquire high-resolution data specific to the storage site of interest.
- The integration of the 3-D seismic and well log data—along with visual observations from the core—has substantially reduced the uncertainty attached to per-

formance assessments and risk analysis for the RSU storage site characterization project (WY-CUSP). As the new data from laboratory analyses, experimental determinations, and test evaluations become available and are integrated into the RSU property models, uncertainty, particularly with respect to reservoir property heterogeneity was further reduced. This study establishes an exemplary strategy for dealing with $CO_2$ storage projects in relatively deep saline aquifers in the Rocky Mountain region and elswhere.

- Reservoir heterogeneity has a significant affect on the geologic $CO_2$ injection rates and storage capacity of the targeted saline aquifers. Applying the diagnostic protocol for the $CO_2$ sequestration suggested by Department of Energy for the FutureGen project, the $CO_2$ storage capacity of the Weber Sandstone in the RSU was estimated to be 18 Gt (Surdam and Jiao 1997). Appling the volumetric approach proposed by the U. S. Geologic Survey, the $CO_2$ storage capacity of the Weber Sandstone was estimated to be 9 GT with the probability density ranging from 2.4 to 20 Gt. Using the FEHM multi- flow numerical simulator, the $CO_2$ storage capacity of the Weber Sandstone was estimated to be 17 Gt based on the homogeneous reservoir property model (porosity 10%, permeability 1 mD), and 9.5 Gt based on the heterogeneous reservoir property model. The 2.1-GW Jim Bridger Power Plant located a mile from the simulation injection well emits 15 Mt of $CO_2$ annually. Therefore, the Weber Sandstone reservoir in the RSU is capable of storing the $CO_2$ emitted from Jim Bridger Power Plant for 600 years.
- For the Madison Limestone reservoir in the RSU, the geologic $CO_2$ storage capacity was estimated to be 8 Gt using the protocol of the FutureGen project suggested by the Department Energy. Using the USGS volumetric approach, the probability density of the $CO_2$ storage capacity of the Madison Limestone ranges from 1.6 to 14 Gt, with a mean of 6.5 Gt. Using the FEHM multi flow numerical simulator, the $CO_2$ storage capacity of the Madison Limestone was estimated to be 7 Gt for the homogeneous reservoir property model (porosity 10%, permeability 1 mD). Based on the heterogeneous reservoir property model, the $CO_2$ storage capacity of the middle Madison Limestone in the RSU area was estimated to be 8 Gt for the high reservoir-quality domain, 7 Gt for the medium reservoir-quality domain, and 5 Gt for the low reservoir-quality domain. Using results from the $CO_2$ injection simulation for the medium reservoir-quality case, the Madison Limestone could store the $CO_2$ emissions from the Jim Bridger Power Plant for 460 years.
- Well injection rate is highly dependent on the local permeability distribution in the storage formation. The areas and interval with the higher quality reservoir domains are critical for a successful commercial-scale geologic $CO_2$ storage project. The higher-quality reservoir domains substantially reduce the project cost and significantly increase the $CO_2$ injectivity and storage capacity. For the middle Madison Limestone and selected intervals in the Weber Sandstone with higher-quality reservoir domains, the injection rate can be as high as 1 Mt per year, while in the lower-quality reservoir domains, the injection rate can be as low as 0.2 Mt per year.

- Formation brine is displaced by $CO_2$ in the injection simulations in order to keep formation pressure below the hydro-fracture pressure, reduce associated leakage, decrease seismic risk, and create the accommodation space to enhance storage capacity for $CO_2$. It is proposed that brine displacement be allowed and controlled by production at the land surface through production wells on the perimeter of the storage site. The average ratio of the amount (tonnage) of displaced brine to injected $CO_2$ is 1.14. This ratio indicates that for an industrial-scale $CO_2$ injection project with minimal impact on neighboring pore space a little more brine must be displaced than $CO_2$ injected.
- $CO_2$ leakage from the storage formations into the overlying rocks is related to the connectivity of high-permeability layers. Leakage from the Madison limestone into the overlaying Amsden Formation is minimal owing to the lower permeability characteristics of the Amsden. However, migration from the Weber into the Phosphoria is significant. This result implies that the Phosphoria should be considered a secondary storage unit, not a cap-rock, on the RSU. In strong contrast, no $CO_2$ injected into either the Weber or Madison migrated into the primary cap rocks of the overlying Dinwoody Formation. The sealing capacity of the Dinwoody Formation can be as great as a 2,000-ft gas column.

## References

Bowker KA, Jackson WD (1989) The Weber Sandstone at Rangely Field, Colorado. In: Coalson EB et al. (eds) Petrogenesis and petrophysics of selected sandstone reservoirs of the Rocky Mountain region. Rocky Mountain Association of Geologists, p 65–80

Burruss RC, Brennan ST, Freeman PA, Merrill MD, Ruppert LF, Becker MF, Herkelrath WN, Kharaka YK, Neuzil CE, Swanson SM, Cook TA, Klett TR, Nelson PH, and Schenk CJ (2009) Development of a probabilistic assessment methodology for evaluation of carbon dioxide storage. U.S. Geologic Survey Open File Report 2009–1035

Clarey K, Thompson M (2010) Chapter 2, study area. In: Copeland D, Ewald M (eds) Available groundwater determination technical memorandum [Greater Green River Basin]. Report prepared for the Wyoming Water Development Commission by the Wyoming State Geologic Survey et al. Wyoming State Geologic Survey, Laramie, p 2-1–2–25

Duan Z, Sun R, Zhu C, Zhou IM (2006) An improved model for the calculation of $CO_2$ solubility in aqueous solution containing $Na^+$, $K^+$, $Ca^{2+}$, $Mg^{2+}$, $Cl^-$, and $SO_4^{2-}$. Mar Chem 98:131–139

Duan Z, Hu J, Li D, Mao S (2008) Densities of the $CO_2$-$H_2O$ and $CO_2$-$H_2O$-NaCl systems up to 647 K and 100 MPa. Energy Fuels 22:1666–1674

Ehrenberg SN, Eberli GP, Keramati M, Moallemi SA (2006) Porosity-permeability relationships in interlayered limestone-dolostone reservoirs. AAPG Bull 90:91–114

Fox JE, Lambert PW, Mast RF, Nuss NW, Rein RD (1975) Porosity variation in the Tensleep and its equivalent, the Weber Sandstone, western Wyoming: a log and petrographic analysis. Rocky Mt Assoc Geol 12:185–215

Han WS, Stillman GA, Lu M, Lu C, McPherson BJ, Park E (2010) Evaluation of potential nonisothermal processes and heat transport during $CO_2$ sequestration. J Geophys Res 115:B07209. http://dx.doi.org/10.1029/2009JB006745

Hein JR, Perkins RB, McIntye BR (2004) Evolution of thought concerning the origin of the Phosphoria Formation, western US phosphorate field. In: Hein JR (ed) Life cycle of the Phosphoria Formation: from deposition to post-mining environment. Elsevier, p 19–42

Love JD, Christiansen AC, Ver Ploeg AJ (1993) Stratigraphic chart showing Phanerozoic nomenclature for the state of Wyoming. Wyo State Geol Surv Map Ser 41:(MS–41)

Miller TA, Vessilinov VV, Stauffer PH, Birdsell KH, and Gable CW (2007) Integreation of geologic frameworks in meshing and setup of computational hydrogeologic models, Pajarito Plateau, New Mexico. New Mexico Geologic Society Guide Book, 58th Field Conference, Geology of the Jemez Mountains Region III

Neuzil CE (1994) How permeable are clays and shales? Water Resour Res 30:145–150

Piper DZ, Link PK (2002) An upwelling model for the Phophoria sea: a Permian, ocean-margin sea in the northwest United States. AAPG Bull 86(7):1217–1235

Pruess K, Muller N (2009) Formation dry-out from $CO_2$ injection into saline aquifers: 1. Effects of solid precipitation and their mitigation. Water Resour Res 45:W03402. http://dx.doi.org/10.1029/2008WR007101

Stauffer PH, Stein JS, Travis BJ (2003) The correct form of the energy balance for fully coupled thermodynamics in water. Los Alamos National Laboratory Report, LA-UR-03-1555, p 9

Stauffer PH, Surdam RC, Jiao Z, Miller TA, Bentley RD (2009a) Combining geologic data and numerical modeling to improve estimates of the $CO_2$ sequestration potential of the Rock Springs Uplift, Wyoming. Energy Procedia 1:2717–2724

Stauffer PH, Viswanathan HS, Pawar RJ, Guthrie GD (2009b) A system model for geologic sequestration of carbon dioxide. Environ Sci Technol 43:565–570

Surdam RC, Jiao Z (2007) The Rock Springs uplift: an outstanding geologic $CO_2$ sequestration site in southwest Wyoming. Wyoming State Geologic Survey Challenges in Geologic Resource Development No. 2

Surdam RC, Jiao Z, Stauffer PH, Miller T (2009) An integrated strategy for carbon management combing geologic $CO_2$ sequestration, displaced fluid production, and water treatment. Wyoming State Geologic Survey Challenges in Geologic Resource Development No. 8

Yang Y, Aplin AC (2010) A permeability-porosity relationship for mudstone. Mar Petrol Geol 27:1692–1697

Zyvoloski GA, Dash ZV, Kelkar S (1988) FEHM: finite element heat and mass transfer code. Los Alamos National Laboratory Report LA-11224-MS. NNA.19900918.0013

Zyvoloski GA, Robinson BA, Dash ZV, Trease LL (1997) Summary of the models and methods for the FEHM application—a finite element heat-and mass-transfer code. Los Alamos National Laboratory Report LA-13307–MS

# Chapter 11
# Displaced Fluid Management—the Key to Commercial-Scale Geologic $CO_2$ Storage

**Ronald C. Surdam, Scott A. Quillinan and Zunsheng Jiao**

**Abstract** The most critical problem with commercial scale geological $CO_2$ sequestration is management of displaced fluids. All of the high quality numerical simulations of carbon capture, utilization, and storage (CCUS) on the Rock Springs Uplift (RSU), utilizing realistic 3-D reservoir models, demonstrate that commercial-scale geological $CO_2$ storage will require the removal of formation brines in approximately 1:1 ratio of injected $CO_2$ to displaced fluid. Without the production of formation brines the simulations suggest that very quickly injected $CO_2$ will cause pressures in the storage domain to exceed fracture pressures. To solve this problem, Carbon Management Institute (CMI) proposed a strategy that includes integration of fluid production/treatment with injection of $CO_2$. The treatment of the brines involved three important steps: (1) use of the temperature of the produced brines (~100 °C) to produce electricity via a heat exchanger to power the treatment facility, (2) to separate fresh water from the brines via nanofiltration and reverse osmosis, and (3) to recover metals, notably lithium, from the residual brines after partial evaporation. The impact of this approach; production of electricity, fresh water, and metals such as lithium from produced brines transform an anticipated carbon storage penalty into a revenue center.

## 11.1 Introduction

As described in Chap. 2, the University of Wyoming Carbon Management Institute and Wyoming State Geological Survey completed a thorough inventory and prioritization of all Wyoming stratigraphic units and geologic sites capable of se-

R. C. Surdam (✉) · S. A. Quillinan · Z. Jiao
Carbon Management Institute Laramie, University of Wyoming, Laramie, USA
e-mail: rsurdam@uwyo.edu

S. A. Quillinan
e-mail: scottyq@uwyo.edu

Z. Jiao
e-mail: JJiao@uwyo.edu

R. C. Surdam (ed.), *Geological $CO_2$ Storage Characterization,*
Springer Environmental Science and Engineering, DOI 10.1007/978-1-4614-5788-6_11,
© Springer Science+Business Media New York 2013

questering commercial quantities of $CO_2$ (5–15 Mt $CO_2$/yr) (Surdam and Jiao 2007; Surdam 2011). These studies identified the Paleozoic Weber/Tensleep Sandstone and Madison Limestone (and stratigraphic equivalent units) as the leading clastic and carbonate reservoir candidates for commercial-scale geological $CO_2$ sequestration in Wyoming. This conclusion was based on unit thickness, overlying low-permeability lithofacies, reservoir storage and continuity properties, regional distribution patterns, formation fluid chemistry characteristics, and preliminary fluid-flow modeling. This inventory also identified the Rock Springs Uplift in southwestern Wyoming as the most promising geological $CO_2$ sequestration site in Wyoming and probably in any Rocky Mountain basin. This ranking of the Rock Springs Uplift was based on the following attributes (Surdam and Jiao 2007):

- A thick saline aquifer sequence (700 ft of Weber Sandstone and 400 ft of Madison Limestone) overlain by a think sequence of stacked sealing lithologies
- A double-plunging anticline with more than 12,000 ft of closed structural relief
- A huge structural element (50 × 35 mi)
- Targeted reservoir units (Weber Sandstone and Madison Limestone) with characteristics required for $CO_2$ sequestration, including fluid chemistry, porosity, fluid-flow attributes, and burial history (relatively recent basin inversion resulting in reservoir rock/fluid systems formerly buried more than 20,000 ft deep now lying at depths between 6000 ft and 10,000 ft)

The results of the geological sequestration inventory led CMI to collect available geologic, petrophysical, geochemical, and geophysical data for the Rock Springs Uplift and to build a regional 3-D geologic framework model of the uplift. From the results of these tasks and using the FutureGen protocol, they showed that on the Rock Springs Uplift, the Madison Limestone has sufficient pore space to sequester 8 Gt of $CO_2$ and the Weber Sandstone has the capacity to store an additional 18.4 Gt of $CO_2$ (Surdam and Jiao 2007).

In cooperation with the Los Alamos National Laboratory (LANL), the CMI team combined these geologic databases with numerical models to improve estimates of the $CO_2$ sequestration potential of the Rock Springs Uplift. The 3-D geologic model was constructed using EarthVision® software and was gridded using LaGrit software. Shallow and deep sequestration sites on the Rock Springs Uplift were evaluated using the LANL-PENS software (Stauffer et al. 2009).

The results of this research are significant in the global effort to accomplish substantial commercial-scale $CO_2$ sequestration. For example, one evaluated scenario was the sequestration of 15 million tons (Mt) of $CO_2$ per year for 50 years into the Weber Sandstone in a nine-point injector pattern within a 16 × 16-km (10-mi × 10-mi) area on the Rock Spring Uplift (Fig. 11.1). These parameters were chosen because the Jim Bridger power plant (2200 MW) is located on the uplift and emits 15 Mt/yr of $CO_2$. The modeled nine-point injection pattern was located near the power plant on the east flank of the RSU. The nine simulated injection wells, each injecting 1.7 Mt/yr of $CO_2$ were spaced approximately 1 mi apart. For the commercial-scale sequestration scenario, no fluid flow was allowed down-dip and the initial pressure up-dip was specified at below fracture pressure. After 50 years of injection, the $CO_2$ plumes around the injection wells barely impinged on one another. All the

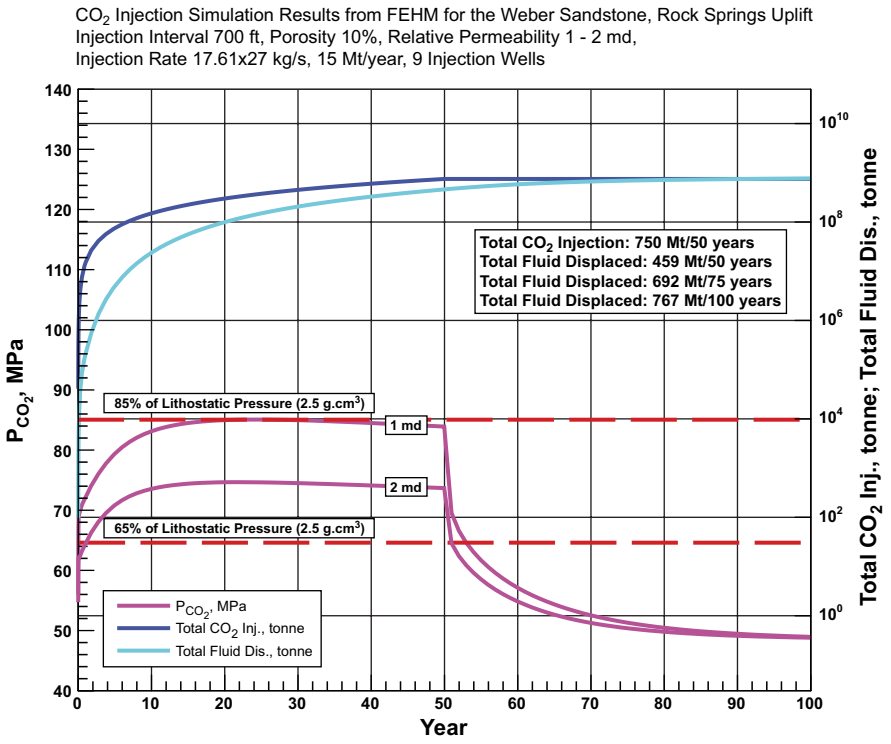


**Fig. 11.1** $CO_2$ injection simulation results utilizing Los Alamos National Laboratory's FEHM simulators for the Weber Sandstone, Rock Springs Uplift, Wyoming. (Modified from Surdam et al. 2009)

$CO_2$ (750 Mt was contained within the 16 × 16-km storage area (area of review). Moreover, the preliminary modeling in this scenario demonstrates that once injection stops, the pressure buildup in the individual injection wells decreases to near initial pressure in 25 years (Surdam and Jiao 2007; Surdam et al. 2009, 2011).

The most critical problem in this geological $CO_2$ sequestration simulation is the relationship between the volume of injection $CO_2$ and the displaced fluid that must leave the storage area (Fig. 11.2). In the example cited above, 750 Mt of $CO_2$ is sequestered in the storage domain and 1 $km^3$ of fluid must leave the domain over a 75-year period (50 years of $CO_2$ injection and 25 years post-injection). The key questions are as follows: Can the accommodation space be found within the geologic site to accept this huge volume of fluid that must leave the storage domain? If so, given the heterogeneity of most geological settings (fluid-flow compartmentalization), can fluid migration pathways be maintained so that the displaced fluid can migrate from the storage domain to some external accommodation space without disrupting the confining units and destroying the integrity of the rock/fluid system?

These difficult questions plague not only the RSU project but many other CCS projects as well. Much of the uncertainty raised by these questions can be avoided with proper management of displaced fluids in a CCS project. To manage the

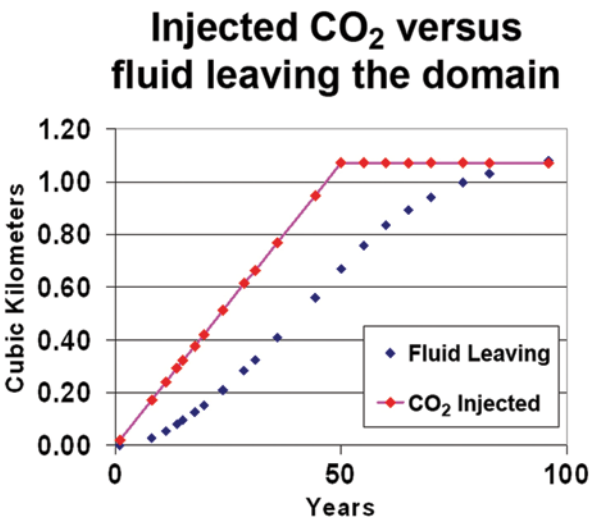


**Fig. 11.2** $CO_2$ injection simulator results reveal that 750 Mt of $CO_2$ is sequestered in the storage domain and 1 $km^3$ of fluid must leave the storage domain (migrate out or be produced) to manage the reservoir pressure under the fracture pressure of the Weber Sandstone at the injection site. (Modified from Stauffer et al. 2009 and Surdam et al. 2009)

displaced fluids in the RSU $CO_2$ storage project, the CMI/WSGS team proposed a strategy that includes integration of fluid production/water treatment with $CO_2$ injection (Surdam et al. 2009). If the ratio of produced fluids to injected $CO_2$ remains near 1:1, this strategy greatly reduces the probability of creating damaging pressure effects and unsuspected $CO_2$ migration beyond the defined storage area. Most importantly, a major objective in designing a successful carbon storage project on the RSU is minimization of the domain outside of the $CO_2$ storage area that is affected by potential fluid plume migration. Without displaced fluid management, carbon storage on the RSU would be highly problematic.

Using this strategy in the RSU project, it will be possible to inject 750 Mt of $CO_2$ into the Paleozoic Weber and Madison formations and to sequester the $CO_2$ in a 16 × 16-km storage domain over a 50-year period (Fig. 11.1). It is noteworthy that the injection of the 750 Mt of $CO_2$ will displace 1 $km^3$ of fluid over a 75-year period (Fig. 11.2).

If 15 million tonnes of $CO_2$ is injected annually into the $CO_2$ storage reservoirs, approximately 80 million barrels of fluid will be displaced each year for 75 years (a total of 6 billion barrels). Lindner-Lunsford et al. (1989) showed that the salinity concentrations (TDS) in groundwater in the targeted Paleozoic aquifers in southwestern Wyoming generally exceed 30,000 mg/L, so any produced fluids must be treated. Aines et al. (2010) showed that at an osmotic pressure limit of 1200 psi, a Tensleep/Weber brine (Na–Cl–$SO_4$; 25,000 mg/L) can be treated via reverse osmosis (RO) at 50 °C, achieving up to 80% $H_2O$ removal. Also, they showed that osmotic pressure, not mineral scaling, is the most important constraint on RO treatment of brines (Aines et al. 2010).

Numerical simulations, using real rock/fluid system characteristics, demonstrate that it is feasible to inject 15 Mt of $CO_2$ per year for 50 years into the Weber/Madison formations on the Rock Springs Uplift (a total of 750 Mt of $CO_2$) in relatively small areas of the RSU. This volume of $CO_2$ can be contained beneath a 16 × 16-km

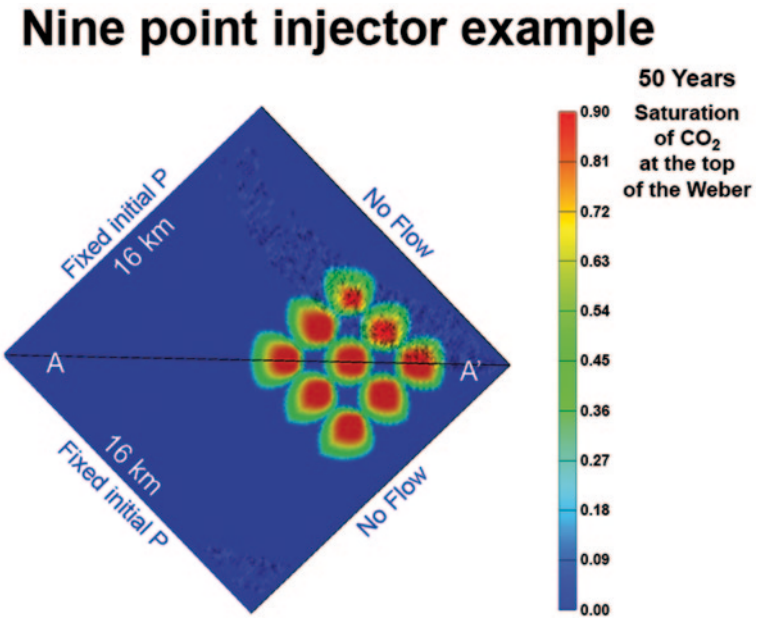


**Fig. 11.3** The 750 Mt $CO_2$ injection over a period of 50 years at the Rock Springs Uplift (see Fig. 11.1 and 11.2) is contained within the Weber Sandstone beneath a 16 × 16-km area. (Modified from Stauffer et al. 2009)

area (the storage domain; Fig. 11.3). Over a 75-year period, this volume of $CO_2$ will displace one cubic kilometer of fluid. Without management, this huge volume of displaced fluid will further cause unwanted fractures within the storage domains, or will migrate out of the storage domain, probably up-dip toward the crest of the structure, 30 km to the west. Numerical simulations for the RSU 50-year storage scenario (with *unmanaged* displaced fluids) suggests that pressure effects will occur 30–40 km up-dip from the site of $CO_2$ injection, necessitating a huge area of review (1200 $km^2$) under proposed regulations. Under new EPA regulations and Wyoming state statutes governing $CO_2$ sequestration, commercial-scale storage of $CO_2$ on the RSU (10 Mt $CO_2$ or greater) will definitely require displaced fluid-management. At present, the fluid management strategy of choice is fluid production, RO treatment, with the water and metal recovery driven by reservoir temperature and pressure.

## 11.2 Fluid Treatment Strategy

This section highlights a proposed produced fluid management study. Recent site-specific fluid analysis from RSU #1 measured TDS concentrations ranging from 80,000 mg/L to 100,000 mg/L. Research has shown that the lower range of these waters could be treated with standard RO with low recovery, ~10 % (Aines et al. 2010). By combining multistage RO or adding nanofiltration membranes at the

front end of RO treatment, makes the treatment of these waters probable (Aines et al. 2010; Bourcier et al. 2011).

In conventional applications (i.e., treatment of sea water), much of the cost of the procedure is the energy required to pressurize the treatment system. Pressures of 700–1200 psi are needed to create the reverse osmosatic pressure gradient between the saline and fresh water (Fritzmann et al. 2007). Reverse osmosis is limited by the maximum pressure difference that the membrane spacers can withstand without collapsing and causing the membrane to become impermeable (Matsuura 2001). The current limit for commercially available membrane spacers is 1200 psi (Bourcier 2011); presently the membrane itself can withstand higher pressures. Higher-pressure membranes have been developed for osmatic pressures of 1500 psi (Baker 2004) but have not been demonstrated commercially. This is likely due to the large amount of energy required to pressurize seawater to above 1200 psi; thus, seawater treatment is not economical at 1500 psi.

However, in treating displaced fluids, pressure is an asset rather than a problem because the fluid arrives at the membrane pressurized (the in situ formation fluids in the Weber/Madison formations on the Rock Springs Uplift come in at 4800–5900 psi). The energy needed to drive the RO process would be harvested directly from the pressure of the formation. Consequently, treating these produced fluids would cost half as much as treating sea water with RO (Aines at al. 2010). Estimated recovery for the RSU brines are approximately 10 % using osmotic pressures of 1200 psi, but could exceed 20 % by incorporating nanofiltration and increasing osmatic pressure to 1500 psi (Aines et al. 2010; Bourcier et al. 2011).

Nanofiltration membranes resemble RO membranes but discriminate against larger-molecular-weight ions and divalent ions due to larger pore sizes and a surface charge on the membrane. Hilal et al. (2004) suggest that nanofiltration membranes reject >90 % of the divalent ions while letting monovalent ions pass. Nanofiltration is used to partially lower the salinity of the brine in order to increase the efficiency of the RO process and is especially attractive in fluids that have a hardness of >10,000 mg/L. Though RSU brines are relatively soft (2000–5000 mg/L), the nanofiltration phase could be utilized as a pressure-reduction step, decreasing scaling potential in the RO process by removing Ca, Mg, and $SO_4$, and lastly to begin the separation process for potential mineral recovery (Sect. 11.4).

The temperature of the brines provides another means for further energy/cost reduction benefit when compared to seawater treatment. The brines of the RSU have a measured temperature of 92–100 °C. Modern binary power generating units have demonstrated success with temperatures as low as 73 °C (Green and Nix 2006). Geothermal heat recovered from produced brine could generate enough electricity to defray the cost of water treatment, and perhaps, to sell an excess. Aines et al. (2010) report that the lifetime of RO membranes is greatest when fluid temperatures range between 40 °C and 50 °C. Thus RSU brines would need to undergo a cooling phase prior to treatment; it simply makes sense to harvest that heat via a heat exchanger for electricity generation.

Figure 11.4 illustrates a potential course of operations for the water treatment of RSU brines. First, the water is produced from the formation, arriving to the surface at about 100 °C, 5000 psi, and 80,000 mg/L TDS, a strongly sodium-chloride

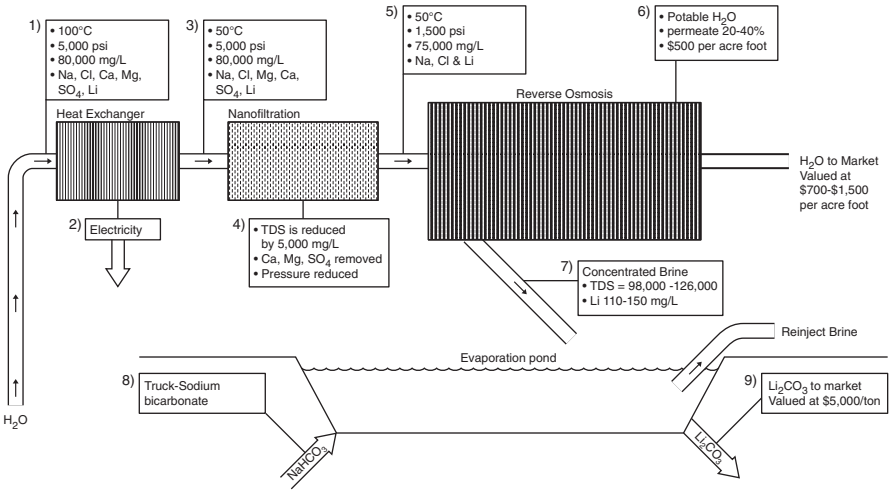


**Fig. 11.4** Water treatment schematic

brine, with lesser amounts of Ca, Mg, and $SO_4$. The first step in the operation is a geothermal heat exchanger: this step not only harvests thermal energy for electricity generation, but decreases the temperature of the brine to optimize the RO treatment. Next, the brine is passed through a nanofiltration membrane, and as a result the overall TDS is reduced to about 75,000 mg/L, pressure is reduced to 1500 psi, and more than 90% of the calcium, magnesium, and sulfate are removed. Removing the divalent ions greatly reduces the risk of mineral scale during RO treatment, also effectively lowering the lithium-to-magnesium ration. The feed is now ready for RO treatment. The permeate from the RO process is estimated to be 20–40% of the original feed stream while 60–80% is further concentrated in the brine. The permeate water is ready to be sold to market. The TDS concentration of the residual brine is expected to increase from 75,000 mg/L to 98,000 mg/L–126,000 mg/L (Fig. 11.5). By concentrating the brine the lithium concentration is also increased from 95 mg/L to 110 mg/L–150 mg/L (Fig. 11.6). The residual brine is then moved to evaporation ponds for mineral recovery. The last step is to dispose of any remaining brine back into the subsurface.

## 11.3 Value Added Products

A treatment scenario as described above produces value-added products: fresh water, electricity, and metals. In arid Wyoming, the need and demand for potable water is very high: local coal-to-power and coal-to-chemical plants, agriculture operations, hydraulic fracturing water, residential users, and downstream users in the Colorado River drainage, among others, all require increasing amounts of water. Bourcier et al. (2011) suggest that treatment cost for reservoir pressure driven RO

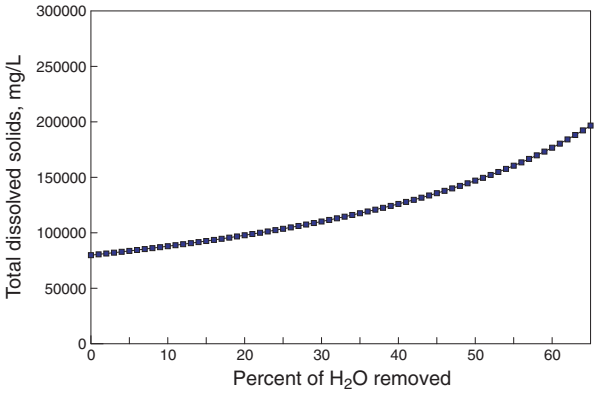


**Fig. 11.5** TDS concentration in the brine as fresh water is removed during treatment

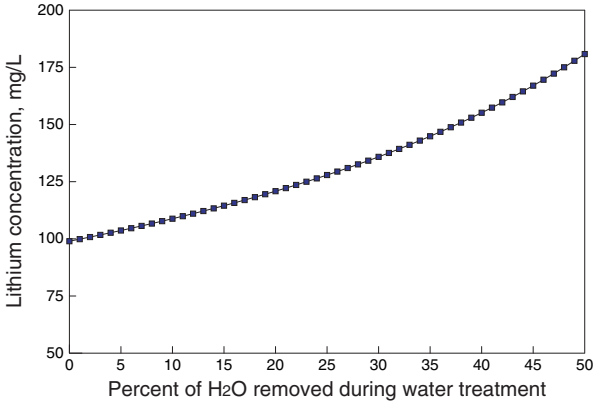


**Fig. 11.6** Lithium concentration in the brine as fresh water is removed during treatment

with 20% recovery might range between US $450 to US $600 per acre-ft of permeate. Agriculture users in some areas of the Colorado River drainage pay more than US $700 per acre-ft. Therefore it is conceivable that the sale of fresh water to market could in fact cover the cost of treating the produced fluid.

Treating these formation fluids at a reverse osmosis treatment plant, or other desalination facility, would yield approximately 10,000 acre-ft of portable water per year, which could be used by an adjacent power plant; by the community of Rock Springs, Wyoming; as replacement water in the Upper Colorado river drainage; or perhaps by communities along the Colorado Front Range. The heat associated with the produced brines (100–130 °C) could be used to generate power for the power plant or the water treatment plant or both.

The feasibility of such a large-scale desalination endeavor is demonstrated by desalination projects in Israel, where desalination plants produce 2 million barrels of potable water per day −13% of the country's annual water consumption (water-technology.net 2012).

Geological $CO_2$ sequestration on the scale required by a large power plant—on the Rock Springs Uplift or elsewhere in the Rocky Mountain region—will require displaced fluid management. Work at the Wyoming State Geological and CMI suggests an integrated $CO_2$ sequestration/fluid production/fluid treatment strategy to accomplish $CO_2$ sequestration on the Rock Spring Uplift: carbon is sequestered on a commercial scale at depth while displaced fluids are produced and treated at the surface. The volume of treated water produced as a result of this strategy represents a valuable commodity in arid southwestern Wyoming. The metals recoverable form the concentrated brine also represent value: recent discoveries at CMI suggest that treatment of displaced brine at a carbon storage facility would result in a substantial economic asset. In fact, recovery of metals from the residual brine may not only pay for the displaced-fluid treatment, but may create a significant profit center. (For the profitable recovery of lithium, for example, see Sect. 11.4). Finally, even the heat contained in the produced brine (92–100 °C) is valuable, as process heat or as a heat exchange source for steam generation.

The proposed integrated strategy may be expensive, but there is presently no viable alternative in Rocky Mountain basins. Finally, it is important to realize that this proposed strategy will be a test of the whole idea of $CO_2$ sequestration: if commercial-scale geological $CO_2$ sequestration cannot be accomplished on the Rock Springs Uplift, it probably cannot be accomplished anywhere in the Rocky Mountain region.

## 11.4 Changing Markets with a New US Lithium Resource—Transitioning from a Significant Lithium Importer to an Independent Lithium Producer

In the global transition to greener economies, demand and competition for lithium resources has significantly intensified. A reliable, abundant, available supply of lithium (Li) is key to accelerating this transition in the United States, particularly with respect to batteries required for energy storage and electronic devices ranging from ordinary cell phones to high-tech military applications. The University of Wyoming Carbon Management Institute (CMI) discovered a vast new lithium resource during its $CO_2$ storage site characterization project, WY-CUSP—a resource that could transform the United States from a net lithium importer to an independent Lithium producer during the next 25 years.

In evaluating formation fluids retrieved from its RSU #1 well on the Rock Springs Uplift, CMI noted that formation fluids from the Weber and Madison formations contain relatively high concentrations of lithium. The lithium concentrations in two sets of samples from both formations, collected in August 2011 and December 2012, ranged from 90 mg/L to 100 mg/L. In sufficient volume, fluids with these lithium concentrations could support a successful lithium recovery industry. The huge volume of Weber/Madison formation fluids available on the Rock Springs Uplift potentially provides the United States with an abundant new source of lithium.

Integrated deployment of carbon capture, utilization, and storage (CCUS) technology together with recovery of a huge new domestic lithium resource would (1) substantially reduce US dependence on foreign lithium imports within 25 years (we currently import up to 80% of our lithium); (2) lay the foundation for entirely new integrated energy development industries and create a new US lithium market; (3) enable continued use of domestic fossil fuels by storing $CO_2$ (emission reduction) and providing $CO_2$ to enhanced oil recovery projects; (4) create a new source of potable water; and (5) keep the United States at the forefront of emerging advanced lithium and CCUS technologies.

The lithium resource discovered by CMI is a significant component of the formation brines within Wyoming's premier $CO_2$ storage reservoirs (the Mississippian Madison Limestone and Pennsylvanian Weber/Tensleep Sandstone) at the state's highest-priority $CO_2$ storage site (the Rock Springs Uplift (RSU) in southeastern Wyoming). The lithium concentration in these formation brines is 90–100 mg/L. CMI proposes to facilitate development of this lithium resource by designing water treatment and lithium production facilities, along with other infrastructure necessary to integrate lithium recovery into a CCUS framework; the CMI strategy would transform an enormous lithium resource into a substantial proven domestic lithium reserve. On the Rock Springs Uplift the potential $CO_2$ storage reservoirs lie at depths of 7000–12,000 ft (2000–3500 m). Due to the depth of the lithium-rich brines, the economic viability of lithium recovery depends on implementation of CCUS at the site. Though CCUS technology and methods for extracting lithium from brines exist and are currently in use, these technologies have never been integrated, and lithium has never been produced on a commercial scale from such deep brines: consequently, the proposed integration of these two technologies is currently a new and untried process.

Numerical simulations and performance assessments of $CO_2$ storage scenarios for RSU site indicate that, concurrent with $CO_2$ injection, pressure management via brine production and surface treatment will be required (1:1 ratio, brine:$CO_2$). Injection of $CO_2$ into the brines could increase the lithium concentration in the brines through dissolution of $Li_2CO_3$ in the rock matrix. The brine treatment, designed around reverse osmosis, will increase the lithium concentration of residual brines by 120% (Fig. 11.4). Presently, the lithium concentration of the brines at Silver Peak, Nevada—the main existing lithium-producing site in the nation—is approximately 230 mg/L.

With injection and storage of 1 million tonnes of $CO_2$ annually and a recovery rate of 65%, 312 tonnes of $Li_2CO_3$ would be recovered per year on the RSU from produced brines. Stationary sources in southwestern Wyoming currently emit 29 Mt of $CO_2$ annually, the injection of which could yield enough lithium to replace annual US imports and cut the state's annual $CO_2$ emissions by 50%. Consider the following:

- Recovery of lithium from produced brines transforms the economic penalty normally associated with pressure management in carbon storage applications into a source of profit.
- The lithium resource within the Madison Limestone underlying just the 25-$mi^2$ (65-$km^2$) study area is estimated at 76,000 tonnes (assuming 10% porosity), ap-

proximately three years of global lithium production (averaging roughly 25,000 tonnes per year). The RSU and Madison Limestone cover nearly 2000 $mi^2$ (5000 $km^2$), so the lithium resource in the Madison on the RSU is truly unique, huge, and capable of changing the world market.

- The lithium resource in the Weber Sandstone is even larger: the lithium resource in the Weber Sandstone underlying just the 25-$mi^2$ (65-$km^2$) study area is estimated at 152,000 tonnes (assuming 10% porosity), approximately six years of global lithium production. The Weber Sandstone on the RSU covers nearly 2000 $mi^2$ (5000 $km^2$): the lithium resource in the Weber Sandstone is also unique, huge, and capable of changing world markets.
- Combined, the formation fluids in the Madison Limestone and Weber Sandstone within a 100 $mi^2$ area contain 900,000 tonnes of lithium, equivalent to 36 years of present global lithium production. Should these concentrated brines in the Madison and Weber formations be present throughout the RSU (2000 $mi^2$, 5000 $km^2$), these units, with four-way closure and 10,000 ft (3000 m) of structural relief, could contain as much as 18 Mt of lithium.
- The lithium reserves at Silver Peak, Nevada, the largest producer of lithium in the United States, are 118,000 tonnes from a 20 $mi^2$ (52 $km^2$) area.
- Before lithium can be precipitated from brine, magnesium salts must be removed; low Mg concentrations are desirable. The magnesium concentrations in brines derived from the Madison Limestone and Weber Sandstone are relatively low, about 150 mg/L and 40 mg/L, respectively. The Mg: Li ratio for the Madison and Weber brines on the RSU is less than 2:1, whereas the Mg:Li ratio in the brines of the "lithium triangle" in South America (home to 70% of the world's economic lithium deposits) is 6:1.
- Southwestern Wyoming hosts the world's largest soda ash industry. Production of 1 tonne of $Li_2CO_3$ from brine (LiCl) requires 1.8 tonnes of soda ash. The RSU is located just 20–30 mi (30–50 km) by railroad or interstate highway from this soda ash source.
- The scientific tools, experience, and expertise necessary to understand recovery of lithium on the RSU have been gathered by CMI during extensive research into $CO_2$ injection to inform CMI's CCUS characterization project. This research includes a 5 × 5-mi (8 × 8-km) 3-D seismic survey; a 12,812-ft-deep (3900 m) stratigraphic test well; 916 ft (278 m) of high-quality core; specialized electric log suites; formation fluid samples; continuous visual documentation of core; core flooding tests; continuous permeability scans; and a wide variety of core measurements. Most importantly, CMI now has the ability to accurately simulate $CO_2$ injection and brine production scenarios.
- The potential impact of the recovery of the RSU lithium resources on the global market is huge: it could transform the US from a significant lithium importer to an independent lithium producer.
- Risks associated with the project are not technical, but rather hinge on federal greenhouse-gas emissions policy. For instance, recent new USEPA regulations mandating CCUS technologies for new coal-fired power plants should provide additional incentive to create regional CCUS complexes.

CMI's lithium discovery will create new industries (domestic lithium production), reduce US dependence on foreign lithium and fossil fuel imports, overcome a major hurdle for CCUS by making pressure management profitable, reduce GHG emissions, create an additional market for soda ash, sustain Wyoming's coal extraction industry by implementing CCUS, and provide $CO_2$ for enhanced oil recovery projects (the 4–8 billion barrels of stranded oil in Wyoming will require 1.8–3.3 billion tonnes of $CO_2$ for tertiary recovery). Importantly, active development of this resource will ensure US technological leadership in developing and deploying advanced lithium and CCUS technologies. For Wyoming, important results will be new industries, increased direct and indirect employment, new or expanded markets, and sustained or expanded traditional economies.

## References

Aines R, Wolery T, Bourcier W (2010) Fresh water generation from aquifer-pressured carbon storage. Ninth annual conference on carbon capture and sequestration. Pittsburgh, Pennsylvania

Baker RW (2004) Membrane technology and applications (2nd ed). Wiley, Chichester

Bourcier WL, Wolery TJ, Wolfe T, Haussmann, Buscheck TA, Aines RD (2011) A preliminary cost and engineering estimate for desalinating produced formation water associated with carbon dioxide capture and storage. Int J Greenhouse Gas Control 5:1319–1328

C. Fritzmann, J. Löwenberg, T. Wintgens, T. Melin, State-of-the-art of reverse osmosis desalination, Desalination, Volume 216, Issues 1–3, 5 October 2007, Pages 1-76, ISSN 0011-9164, http://dx.doi.org/10.1016/j.desal.2006.12.009

Green B, Nix RG (2006) Geothermal – the energy under our feet, geothermal resource estimates for the United States: National Renewable Energy Laboratory Technical Report NREL/TP-840–40665

Hilal N, Al-Zoubi H, Darwish NA, Mohammed AW, Arabi MA (2004) A comprehensive review of nanofiltration membranes: treatment, pretreatment, modeling, and atomic force microscopy. Desalination 170:281–308

Lindner-Lunsford, JB, Kimball BA, Chafin DT, Bryant CG (1989) Hydrogeology of aquifers of Paleozoic age, upper Colorado River basin – excluding the San Juan Basin-in Colorado, Utah, Wyoming, and Arizona. U.S. Geological Survey Hydrologic Investigations Atlas HA-702, scale 1:2,500,000 and 1:6,000,000

Matsuura T (2001) Progress in membrane science and technology for seawater desalination – a review. Desalination 134:47–54

Stauffer PH, Surdam RC, Jiao ZS, Miller T (2009) Combining geological data and numerical modeling to improve estimates of the $CO_2$ sequestration potential of the Rock Springs Uplift, Wyoming. In: Proceedings of the 9th greenhouse gas technology conference. Energy Procedia 1(1):2714–2724. Elsevier

Surdam RC, Jiao ZS (2007) The Rock Springs Uplift – an outstanding geological $CO_2$ sequestration site in the southwest Wyoming. Wyoming State Geological Survey Challenges in Geologic Resource Development No. 2

Surdam RC, Jiao ZS, Stauffer P, Miller T (2009) An integrated strategy for carbon management combining geological $CO_2$ sequestration, displaced fluid production and water treatment. Wyoming State Geological Survey Challenges in Geological Resource Development No. 8

Surdam RC, Jiao ZS, Stauffer P, Miller T (2011) The key to commercial-scale $CO_2$ sequestration: displaced fluid management. Energy Procedia 4, pp 4246–4251

water-technology.net (2012) Ashkelon, Israel. Net Resources International. www.water-technology.net/projects/israel. Accessed January, 2013

# Chapter 12
# The Carbon Management Institute's Integrated $CO_2$ Storage/EOR Strategy: the Advantages of Deploying Innovative, Multiple-Resource Development Strategies Designed to Foster Sustainability of Energy and Environmental Resources

**Ronald C. Surdam, Ramsey D. Bentley and Zunsheng Jiao**

**Abstract** The Powder River Basin (PRB) offers an opportunity to illustrate the advantages to Wyoming of deploying an innovative, multiple-resource development strategy designed to foster the sustainability of the state's energy and environmental resources. Such a multiple resource development plan is based on viewing the PRB's particular assemblage of energy/environmental resources as a synergistic system rather than a collection of disparate parts. This approach relies on synergistic relationships among resource elements in order to increase the efficiency of development, minimize environmental degradation, sustain long-term resource use, and maximize revenue to the state.

The key resource elements of an integrated development strategy for the PRB are:

- Coal resources and mines (vast coal reserves)
- A significant source of water (groundwater produced during coalbed methane development)
- Coal-to-chemicals plants capable of capturing $CO_2$ (located at mine-mouth sites)
- Nearby $CO_2$ storage sites (depleted, Cretaceous compartmentalized gas fields)
- Depleted oil fields suitable for enhanced oil recovery (significant amounts of stranded oil)
- $CO_2$ storage in these depleted oil fields (doubling the geologic $CO_2$ storage capacity)

By developing this suite of resource elements as a system, it would be possible to optimize the benefits to the energy industry while maximizing the sustainability of

R. C. Surdam (✉) · R. D. Bentley · Z. Jiao
Carbon Management Institute Laramie, University of Wyoming, Laramie, USA
e-mail: rsurdam@uwyo.edu

R. D. Bentley
e-mail: rbentley@uwyo.edu

Z. Jiao
e-mail: jjiao@uwyo.edu

R. C. Surdam (ed.), *Geological $CO_2$ Storage Characterization,*
Springer Environmental Science and Engineering, DOI 10.1007/978-1-4614-5788-6_12,
© Springer Science+Business Media New York 2013

energy resource development, and maximizing state revenues for future generations. In addition, the strategy described here would reverse the regional trend of coal- and energy-related job loss. Most importantly, all of this resource development can be accomplished within the existing regulatory framework and without significantly increasing the industrial footprint. It is vital to our future that Wyoming seek new, more effective, efficient, and sustainable approaches to energy development.

## 12.1 Introduction

The resource-rich Powder River Basin (PRB) of northeastern Wyoming offers an ideal opportunity to design and implement a new and different approach to future energy development in the state. This chapter explores formulation of an integrated energy development platform for the PRB that emphasizes synergistic relationships in order to optimize the effective and efficient exploitation of the state's energy resources while minimizing environmental damage. The basic tenet underlying this approach is that it is more effective and efficient to develop a set of resources together/concurrently rather than separately.

## 12.2 Resource Elements

We first identify the resource elements associated with the area of interest. The key resource elements that illustrate the power of an integrated developmental strategy for the Powder River Basin are:

- Coal resources and mines (with large reserves)
- Significant source of water (groundwater produced during coal bed methane development)
- Coal-to-chemical plants capable of capturing $CO_2$ (mine-mouth location)
- Nearby $CO_2$ storage sites (depleted, compartmentalized gas fields)
- Depleted oil fields suitable for enhanced oil recovery (significant amounts of stranded oil)
- Additional $CO_2$ storage in depleted oil fields

Using these six key resource elements, it is possible to neatly explain and illustrate the effectiveness of this new approach to energy resource development in Wyoming, and how this approach can be used to minimize environmental degradation.

### *12.2.1 Coal Resources*

Wyoming has 65 billion tons (65 Bt) of coal reserves – 46 billion tons (42 Bt) of which are recoverable using current mining technology – and additional vast coal resources that will become reserves with the advent of new mining techniques. At

**Fig. 12.1** Active coal mine in Wyoming's Powder River Basin. Wyoming's coal industry contributes US $ 1.2 billion annually to state revenues. (Meg Ewald photo)

current rates of extraction, the state's coal reserves will last well into the next century. Most importantly, the PRB has a huge coal asset (the basin produces 40 % of the nation's coal) that is currently exported via rail (approximately 450 million tons (410 Mt per year) to support coal-fired power generation at 135 facilities in 39 states, including Wyoming (Jones et al. 2009) (Fig. 12.1). Presently, Wyoming coal (Table 12.1) supplies the nation with approximately 8 quadrillion Btus of energy per year, or 8 % of the total annual U.S. energy budget (Surdam 2008). Additionally, on a cost-per-Btu basis, Wyoming coal is the nation's cheapest large-scale source of energy (Fig. 12.2). Moreover, Wyoming coal has remained an extraordinarily reliable energy source with dependable long-term delivery schedules and an absence of unpredictable price spikes.

A paradox facing Wyoming's coal industry is a very uncertain future in supplying the nation's dwindling fleet of coal-fired power plants, but a very bright future with respect to a new coal-to-chemicals industry (Fig. 12.3). The technology to support such a value-added industry is available, but has not yet been deployed in the US. In contrast, China currently uses coal as feedstock to produce commercial quantities of methanol, ethanol, acetate, olefins, ammonia, diesel, and gasoline, among other products. Inherent in these coal-to-chemical technologies is the ability to capture $CO_2$. Therefore, the critical question for these types of industrial facilities is this: *Can the captured $CO_2$ be stored successfully in geologic storage sites?*

In a future carbon-constrained world, the EPA will regulate $CO_2$ and other greenhouse gas (GHG) emissions in the U.S. under the Clean Air Act (Massachusetts v. EPA Supreme Court ruling, 2007). The EPA has declared that GHGs pose a danger

**Table 12.1** Top ten exporters of energy to the United Sates in 2006

| | | Crude Oil | | Natural Gas | | Coal | | |
|---|---|---|---|---|---|---|---|---|
| Rank | Country or state | MM bbls/yr | Quadrillion Btus | Tcf | Quadrillion Btus | MT/yr | Quadrillion Btus | Total (Quadrillion Btus) |
| 1 | Wyoming | 52.93 | 0.28 | 1.75 | 1.77 | 446.74 | 7.96 | 10.01 |
| 2 | Canada | 648.97 | 3.41 | 3.59 | 3.63 | 1.49 | 0.04 | 7.08 |
| 3 | West Virginia | 1.83 | 0.01 | 0.22 | 0.22 | 152.37 | 3.91 | 4.14 |
| 4 | Mexico | 575.61 | 3.02 | 0.01 | 0.01 | 0 | 0 | 3.04 |
| 5 | Saudi Arabia | 519.40 | 2.73 | 0 | 0 | 0 | 0 | 2.73 |
| 6 | Venezuela | 416.83 | 2.19 | 0 | 0 | 3.07 | 0.08 | 2.27 |
| 7 | Nigeria | 378.51 | 1.99 | 0.06 | 0.06 | 0 | 0 | 2.05 |
| 8 | Alaska | 270.47 | 1.42 | 0.42 | 0.43 | 0 | 0 | 1.85 |
| 9 | Iraq | 201.85 | 1.06 | 0 | 0 | 0 | 0 | 1.06 |
| 10 | Angola | 187.25 | 0.98 | 0 | 0 | 0 | 0 | 0.98 |
| | *Total* | *3,253.61* | *17.08* | *6.05* | *6.12* | *603.67* | *11.99* | *35.19* |

Note: total may not equal sum of components because of independent rounding. Coal imports include coal to Puerto Rico and the U.S. Virgin Islands.
Sources: Bureau of the Census, U.S. Department of Commerce, Monthly Report IM 145
EIA, U.S. Natural Gas Imports by Country
EIA, U.S. Crude Oil Net Imports by Country
EIA, Gross Heat Content of Coal Production, Most Recent Annual Estimates, 1980–2006

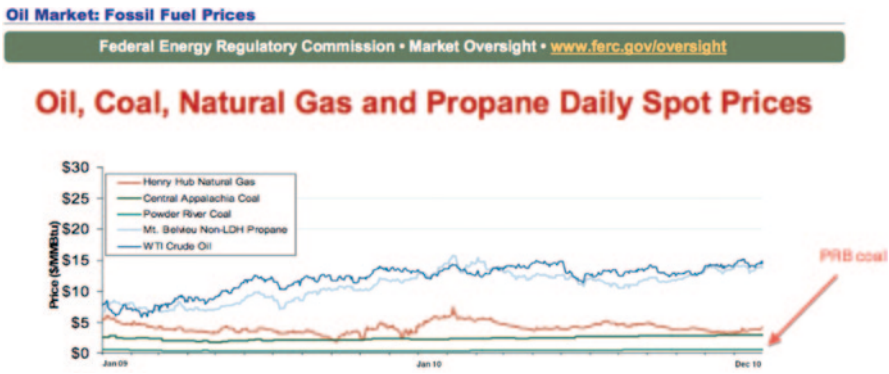


**Fig. 12.2** Two-year price trends contrasting Powder River Basin coal with other energy sources. Note low price and lack of price spikes with respect to PRB coal

to public health and welfare, and the agency will regulate them as pollutants under the act. Indeed, the agency began to do so early in 2012 when it released new emissions standards for new construction or modification of coal- and natural-gas-fired power plants. As a result, carbon capture and storage must succeed if any new or modified coal-based industrial facilities are to be constructed in Wyoming, or elsewhere in the nation. In any discussion of energy issues, particularly with respect to Wyoming, it is important to remember that coal is our nation's most abundant, readily available, and cheapest form of energy ($ 0.50 per million Btus, vs. natural

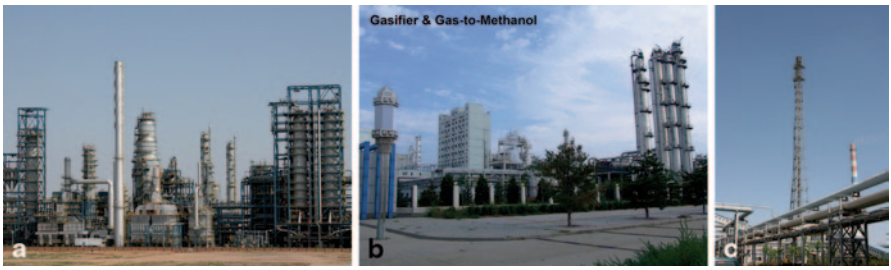


**Fig. 12.3** (**a**) Coal-to-diesel plant and (**b**) coal-to-methanol plant, Shaanxi and Inner Mongolia provinces, China. By 2015, China will produce 280 million barrels of methanol, 14 million barrels of diesel, 100 million barrels of acetate, and 1.2 trillion cubic feet of syngas from coal ($ 34 billion worth of products) annually. Coal conversion technology already exists and has been proven on a commercial scale, and Wyoming has all of the resource elements necessary for successful development of a coal conversion industry in the state. (**c**) Coal-to-methanol facility in Shaanxi Province. The tall structure in the center of the photo is the $CO_2$ emission stack. Conveyor belts used to transport coal from the mine to the facility can be seen at the bottom right and bottom left edges of the photo. (John Jiao photos)

gas at about $ 3 per million Btus). Without proven, effective carbon storage, any future regulation of carbon emissions will jeopardize access to and use of Wyoming's huge coal resource. An example of the intense pressure facing the nation's aging coal-fired power generating fleet is the April 14, 2011 announcement of a legal settlement over air quality concerns that led the Tennessee Valley Authority to agree to close 18 coal-fired units at three facilities (i.e., 16% of TVA's power generating capacity) over the following five years. This agreement includes substantial fines, $ 350 million for environmental projects, a loss of 2700 MW of power and 300 TVA to 400 TVA jobs, and a decreased demand for Wyoming coal on the order of 1 million tons (0.9 Mt) per year.

In this chapter, the Carbon Management Institute outlines a strategy that prevents the damage to Wyoming's economy that would result from any significant bypassing of Wyoming's coal resources. Enhancing the value of PRB coal by encouraging the growth of value-added coal products that can be produced with minimal environmental damage is a key element in any future PRB energy development scenario.

### *12.2.2 Water*

The most readily available water resource in the PRB is the groundwater produced by the coal bed methane (CBM) industry. Production experience gives a typical fluid/gas production scenario for a CBM well as follows (Fig. 12.4a):

- The well produces substantial amounts of water in the first year or two of operation as hydrostatic pressure decreases.
- Gas production peaks at the end of year one or during year two.
- Production of water/gas declines steeply over the next three to five years.
- The productive life of a typical CBM well is usually five to ten years.

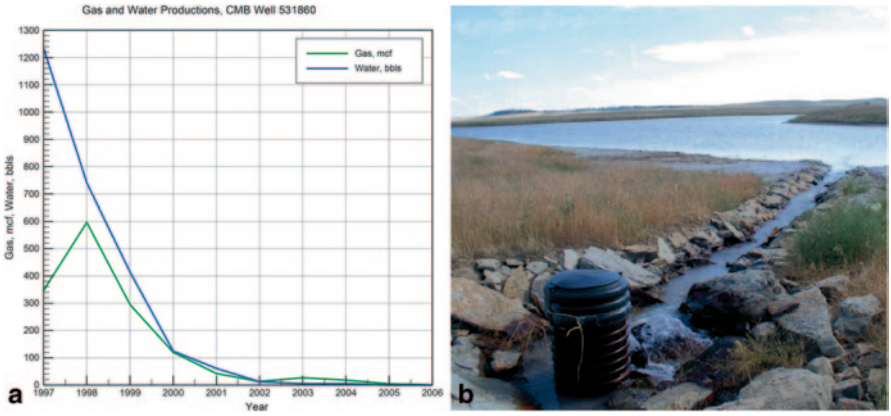


**Fig. 12.4** (**a**) Annual gas and water production curves of CBM well Thielen 20-41. Note that this typical well produces substantial amounts of water in the first two years, and that gas production peaks in the second year. (Reprinted from Surdam et al. 2007). (**b**) Groundwater produced during coal bed methane development flows into a containment pond in Wyoming's Powder River Basin: this is a typical water discharge scenario in the basin. (John Jiao photo)

This scenario represents the typical production behavior of an average CBM well in the PRB, but this average encompasses a wide range of production values (some CBM wells have produced only gas, and others have yielded only water over a five-year period).

Water production has proved the most controversial aspect of CBM development in the PRB. The problem stems from the fact that the CBM produced water in the basin is typically sodic, with sodium adsorption ratios (SAR) of 2–6 milliequivalents per liter or more. The water has salinity values of 500 mg/L–3500 mg/L, but in a region with sodic soils (such as the PRB), the water's high sodic content renders it unsuitable for agricultural use without treatment. Therefore, beneficial use of CBM produced water is problematic. Excluding Anadarko's use of CBM water in its water-flooding operation at the Salt Creek oil field and a small amount of treated water, the produced water is not put to beneficial use once it reaches the surface, but is instead discharged into nearby streams and ponds (Fig. 12.4b). Consequently, a very contentious atmosphere has emerged concerning what some perceive as "wasted" CBM produced water, particularly with respect to handling and disposal. The recent non-degradation ruling regarding waters entering Montana from Wyoming will exacerbate the combative discussions of CBM produced water issues. The relevant question for our purposes is this: *How large is the water resource associated with CBM activity in the PRB, and how long will it be available?*

To answer these questions, the Wyoming State Geologic Survey (WSGS) studied CBM production records extensively, using the Wyoming Oil and Gas Conservation Commission (WOGCC) database to evaluate gas and water production histories of 22,211 CBM wells over nearly a decade (1997–2006; see Surdam et al. 2007). Using the results of this study and estimating the number of CBM wells slated for development in the PRB, the WSGS predicted CBM water production over the next

decade (through 2020). Estimates of future drilling activity for CBM production in the PRB were based on approved and pending environmental documents, BLM permitting activity, WOGCC records, and estimates from the Wyoming Department of Environmental Quality and the Wyoming State Engineer's Office (Surdam et al. 2007; Fig. 12.5a).

In summary, the water/gas production histories of 22,211 CBM wells two years old or older in the PRB (as of 2007) showed that these wells typically produced approximately 2.3 trillion cubic feet (TCF) of gas, and approximately 4.2 billion barrels of water (1 barrel = 42 gallons; Surdam et al., 2007). The average water/gas ratio for the wells studied is 1.83 barrels of water per thousand cubic feet (MCF) of produced gas. Although it is difficult to predict future production trends based on CBM well production histories in the PRB, if it is assumed that CBM wells have a five-year lifespan and the estimated number of CBM wells that will be drilled over the next decade are used in the analysis, calculations suggest that on average, CBM activities in the PRB will produce one billion barrels of water annually. (These estimates of produced and available CBM water exclude the water currently used by Anadarko in its Salt Creek enhanced oil recovery project.) For the next 10–20 years, approximately one billion barrels of CBM produced water will be available annually in the PRB for beneficial use in industrial endeavors.

If a coal-to-chemical industry requires additional water resources, deep basin brines could meet this demand. At depths greater than 10,000 ft present-day depth in the center of the PRB, the Paleozoic Madison and Tensleep formations contain fluids with salinities (TDS) greater than 10,000 ppm (Fig. 12.5b). Therefore, the deep Tensleep and Madison formations do not contain drinking water as defined by the Safe Drinking Water Act (TDS < 10,000 ppm). Consequently, the Madison/Tensleep fluids could either be used at in-situ composition, or could be produced and treated to a composition compatible with industrial processes. Aines et al. (2010) showed that, using an osmotic pressure limit of 1200 psi, a Tensleep brine (Na-Cl-$SO_4$; TDS of 25,000 ppm) can be treated via reverse osmosis (RO) at 50 °C to achieve up to 80 % water removal. In conventional desalination applications (i.e., treatment of seawater), much of the cost of the procedure stems from the energy required to pressurize the treatment system. However, in treating the produced brine, pressure is an asset rather than a problem because the fluid arrives already pressurized (in-situ formation fluids in the Madison/Tensleep formations in the PRB at 10,000 feet present-day depth have pressures of 4500 + psi). As a result, treating produced fluids, excluding the drilling and production expense, costs half as much as treating seawater with RO (Aines et al., 2010). Reverse osmosis yields a product (fresher water) that would meet industrial specifications, and any residual brine could subsequently be re-injected into the deep formations. The first choice of water for a coal-to-chemical industry remains CBM produced water, but treated deep formation fluids would serve as an alternate source if additional water is required. Importantly, the deep formation fluids could be produced with no effect on shallower subsurface potable water resources. The use of deep formation fluids would not compete with domestic or agricultural interests, nor would it degrade surface or subsurface water resources.

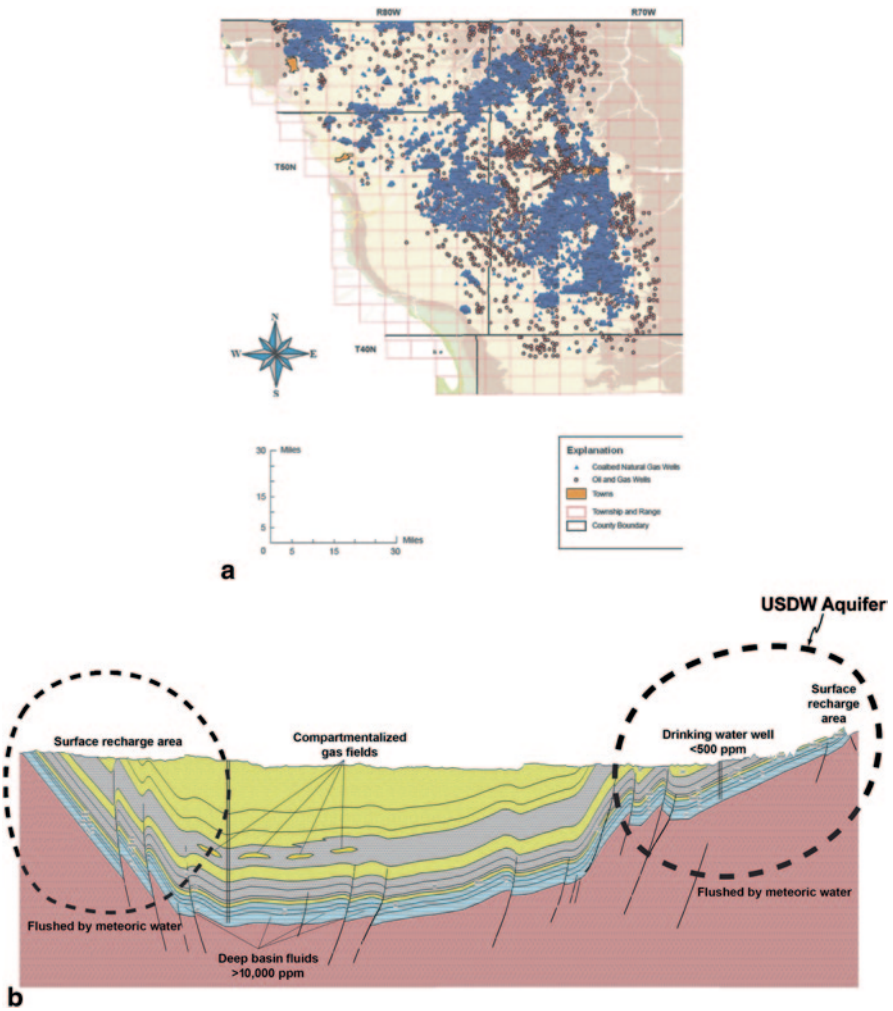


**Fig. 12.5** (**a**) Map showing the distribution of coal bed methane wells – along with oil and conventional natural gas wells – in Wyoming's Powder River Basin. (Reprinted from Copeland and Ewald 2008) (**b**) Cross section showing aquifers and water recharge zones in relation to depleted gas fields and deep basin brines in Wyoming's Powder River Basin

### *12.2.3 Coal-to-Chemical Applications*

Though coal-to-chemical technology has not yet been deployed in the U.S., China has developed and used this technology to spawn a huge chemical industry. At present, China generates commercial quantities of methanol, ethanol, olefins, ammonia, acetate, diesel, and gasoline, among other chemicals. For example, in Shaanxi Province, six coal-to-methanol plants each produce 0.5–0.7 Mt of methanol annually.

Over the next five years, the province plans to double the current number of coal-to-methanol plants; when that occurs, Shaanxi Province will produce almost all the methanol required by the Chinese fabric industry. As an aside: synthetic fibers and blends of natural and synthetic fibers produced in China are derived from coal. So, if you are wearing garments made in China, you are most likely wearing Chinese coal.

The following aspects of the coal-to-methanol plants in Shaanxi Province are pertinent:

- Plants are located at coal mine mouths (Fig. 12.3c).
- The methanol plants use coal gasifiers (Fig. 12.3b; the building in the center of the photo houses a GE gasifier).
- The $CO_2$ emitted by these plants is captured (95+% pure $CO_2$) and vented (Fig. 12.3c). In the near future, the $CO_2$ captured at these plants will be used in tertiary recovery projects in nearby depleted oil fields or stored for future use.
- A typical coal-to-methanol plant uses 1.8 Mt to 2.0 Mt of coal annually, emits 4 Mt of $CO_2$, and uses approximately 6 Mt of water.

Also relevant to the present discussion is the emergence of a coal-to-diesel industry in China. Annually, each coal-to-diesel plant produces 7–14 million barrels of diesel, uses 3.5 Mt to 7 Mt of coal, captures 2 Mt to 4 Mt of $CO_2$, has an 8:1 water to diesel ratio, is 60% efficient (using sub-bituminous coal), and requires a crude oil price of $ 50/barrel to break even. The coal-to-diesel plant shown in Fig. 12.3a uses a hydrolysis/catalysis process developed in China. It is a mine-mouth industrial plant capable of producing commercial quantities of a coal-derived, value-added product: diesel fuel. A variety of coal-to-chemical technologies are being employed profitably overseas, especially in China, and the deployment of these technologies in the U.S. is only a matter of time. The coal-to-chemical technologies embraced by China have two great advantages: all the production plants have the inherent ability to capture $CO_2$, and all the plants generate products that substantially increase the value of coal (see Fig. 12.6 for an example illustrating this point).

Although a robust coal-to-chemical/syngas industry has not developed in Wyoming, it is simply a matter of having the creative will to try something new that provides the resource sustainability inherent in that industry. Thankfully for future generations in Wyoming, economics will eventually force the issue and accelerate the transition to a better, more responsible use of the state's coal resources. To illustrate this point, consider Fig. 12.6, which shows the value-added potential of Btu conversion technologies to coal reserves (Childress 2011): if sold as coal (coal is mined and transported to customers via rail), Peabody Energy's coal reserves are worth US $ 288 billion, but if sold as motor fuel (coal is gasified and converted to gasoline/diesel), the same reserves are worth US $ 3.6 trillion. Using gasification, the coal-to-liquids/syngas technologies inherently capture and provide storage-ready $CO_2$, and most importantly, increase the value of the resource by an order of magnitude.

In summary, the Wyoming PRB has all the resources, including human resources, necessary to support the deployment of a robust industry based on converting

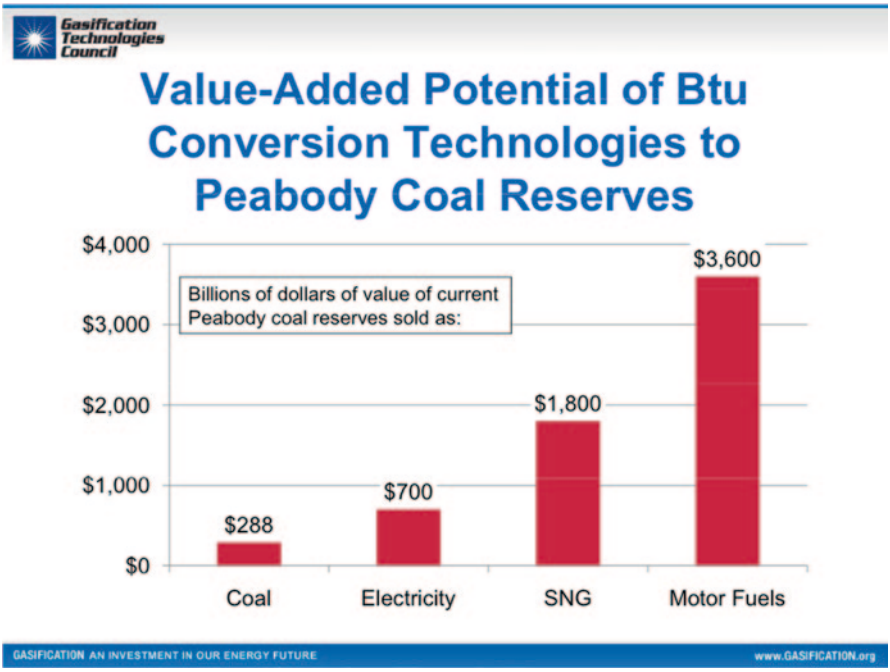


**Fig. 12.6** Value of Peabody Energy Co.'s coal reserves sold in different forms. Technologies that inherently capture $CO_2$ (coal converted via gasification to gas/liquid fuels) add significant value and provide storage-ready $CO_2$. (From Childress 2011)

coal to added-value products. Development of such an industry in Wyoming could be accomplished in a decade or less. In Shaanxi Province, China, six plants were constructed in five years, and an additional six or more facilities are slated for construction over the next five years. The technology has existed since before World War II, and is presently being modified, improved, and deployed in China on a huge scale.

### *12.2.4 $CO_2$ Storage*

In other Laramide basins in Wyoming, the Pennsylvanian Tensleep/Weber sandstones and Mississippian limestones are potential targets for $CO_2$ storage. For example, in the Greater Green River Basin, the Weber Sandstone and Madison Limestone have great potential as $CO_2$ storage reservoirs, especially on the Rock Springs Uplift and Moxa Arch (Surdam and Jiao 2007; Surdam et al. 2009). At both sites, the Weber and Madison formation fluids consist of brines (salinity > 70,000 ppm). In the Greater Green River Basin, these two Paleozoic units – because of a relatively recent basin inversion and a lack of meteoric water recharge – produce saline waters; in the PRB, however, these units produce copious quantities of potable water at relatively shallow depth (< 5000 ft), particularly at the eastern basin margin owing

to meteoric water recharge and fresh water flushing (Fig. 12.5b). Regulations being promulgated by the U.S. Environmental Protection Agency will prohibit $CO_2$ injection (Class VI wells) into Underground Source of Drinking Water (USDW) aquifers; as a result, $CO_2$ storage in the Pennsylvanian/Mississippian stratigraphic section in the Greater Green River Basin will be possible, but storage in these units in the PRB will prove more problematic. Therefore, alternate $CO_2$ storage reservoirs must be identified in the PRB.

The prime candidates are depleted and originally abnormally pressured gas fields. In the PRB, the Cretaceous stratigraphic section is dominated by relatively low-permeability lithologies (shales and siltstones), and contains relatively thin, discontinuous valley-fill and shore-face sandstones (Muddy Sandstone), offshore marine bars (Shannon Sandstone), and beach sandstones (Frontier Formation). Where this collection of Cretaceous shales and sandstones ocuur at a present-day depth of 8000 ft or more, the section is typically overpressured (Fig. 12.7a) (Surdam et al. 2005). The various discontinuous sandstones within the overpressured shales are gas-charged: most of these Cretaceous anomalously pressured sandstones have produced gas since the 1960s and presently host highly depleted gas fields (Fig. 12.7b, c, d). Typically, the shales are gas-charged and anomalously pressured from approximately 8000 ft present-day depth down to the lowest organic carbon-rich shale in the Cretaceous stratigraphic section (Surdam et al. 2005). The top, bottom, and lateral extent of the anomalously pressured section can be mapped successfully by examining the sonic and seismic interval velocity distributions for specific lithologies (Fig. 12.7a); the velocity of a specific lithology slows substantially within the low-permeability volume when it is gas-charged and anomalously pressured. Above the anomalously pressured section, many of the marine sandstones have been flushed with meteoric water, but within the anomalously pressured volume, the sandstones contain fluids similar in composition to fluids in the rocks as originally deposited (sea water) (Fig. 12.8). This suggests that the sandstones within the anomalously pressured volume have been and remain isolated from meteoric water recharge (potable water). Thus, $CO_2$ stored in depleted gas fields within the anomalously pressured Cretaceous rock volume would have no interaction with or deleterious effects on potable water in the PRB.

Each of the significant Cretaceous depleted gas fields in the PRB were evaluated for $CO_2$ storage potential (Table 12.2). The screening process began with a compilation of production histories of all oil and gas fields in the PRB, for it was assumed that depleted fields with the highest cumulative production would have the greatest storage capacity. All oil and gas fields in the basin were listed according to cumulative production, from highest production to lowest. Next, the list of potential fields was reduced to include only Cretaceous compartmentalized fields: criteria for this decision included type of reservoir drive mechanism, reservoir depth, producing formation, and initial reservoir pressure. Lack of a water drive and initial overpressuring were preferred because data indicated that after depletion, pore space would be available in the reservoir and would not have been refilled with formation fluid after the removal of hydrocarbons. Anomalous pressure (overpressure) indicates a closed rock/fluid system (compartmentalization) isolated from meteoric water recharge.

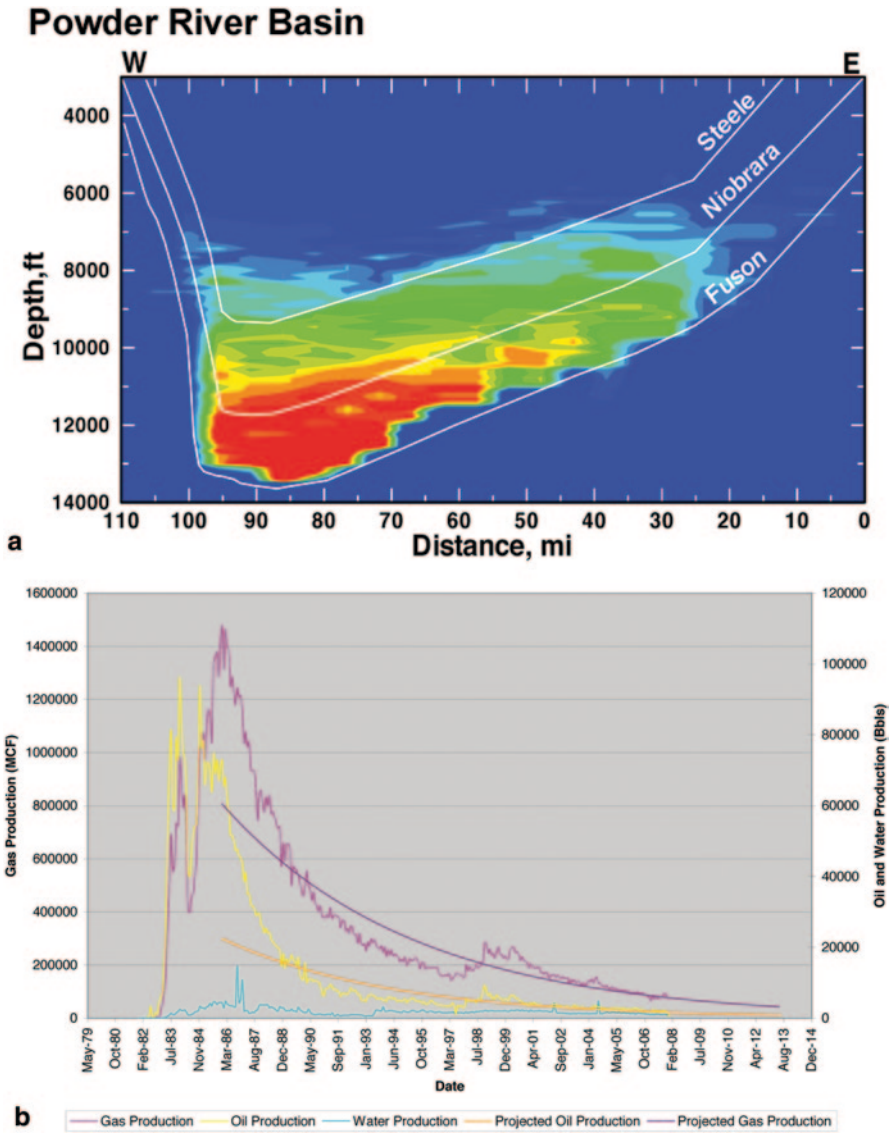


**Fig. 12.7** (**a**) Anomalous velocity profile for the Powder River Basin. The transition from normal pressures to anomalous pressures (velocity surface inversion) typically occurs at present-day depths of 8000–9000 ft. The blue area represents a normally pressured, water-dominated, single-phase fluid-flow system, whereas red and green areas indicate anomalously pressured, multiphase fluid-flow systems (i.e., gas-charged). (Modified from Surdam et al. 2005). Oil, gas, and water production decline curves for (**b**) the Amos Draw Complex and (**c**) Kitty Field. The west–east cross section (**d**) through the Amos Draw and Kitty fields displays the pressure regimes within the Muddy Sandstone. The Mowry Shale acts as the primary seal above the Muddy Sandstone, and the Skull Creek Shale seals from below. The Muddy Sandstone is laterally sealed and internally separated into flow compartments by the Roset unconformity. (Reprinted from Bentley and Lusk 2008)

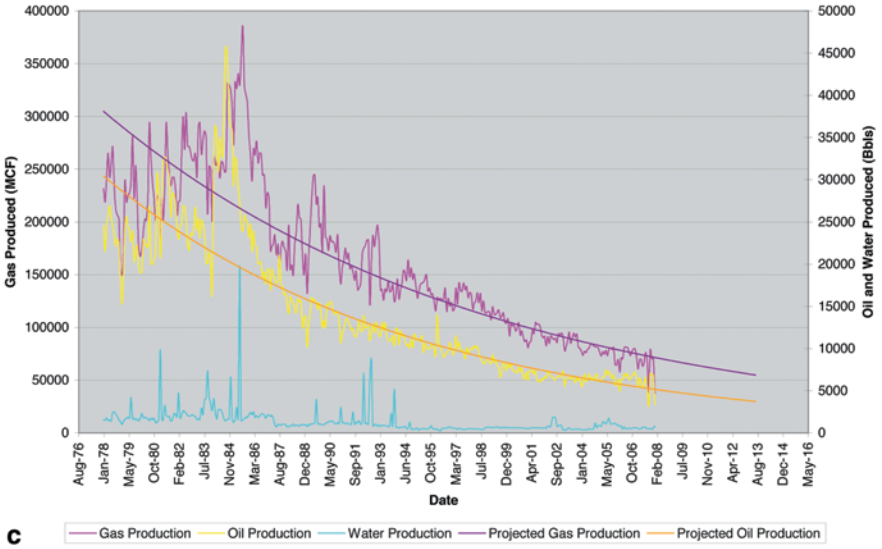


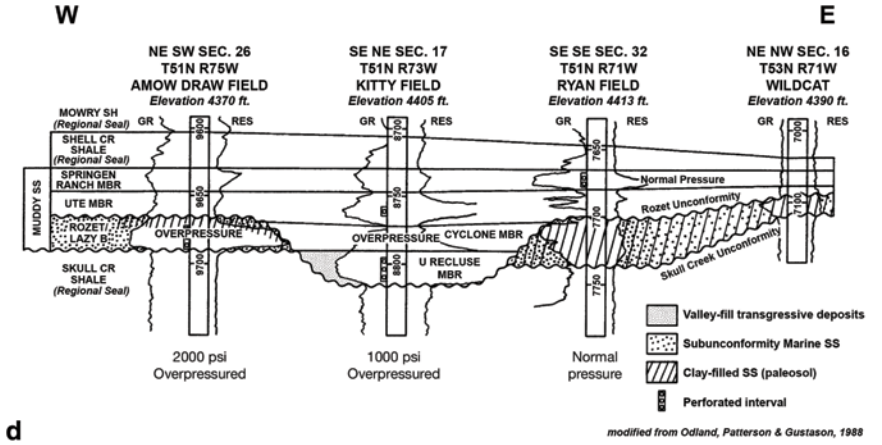


**Fig. 12.7** (continued)

Table 12.2 shows preliminary $CO_2$ storage calculations for the highest-priority potential storage sites (depleted oil/gas fields). The top ten candidate fields have an estimated combined storage capacity of 181.5 Mt $CO_2$. The numbers shown in Table 12.2 were calculated using USGS methodology (Burruss et al. 2009). The volumetric calculations shown in the table are based on field production numbers and specific reservoir conditions. They probably should be considered conservative estimates of $CO_2$ storage capacity. Data for the screening process came from the Wyoming Oil and Gas Conservation Commission website, a subscription to IHS

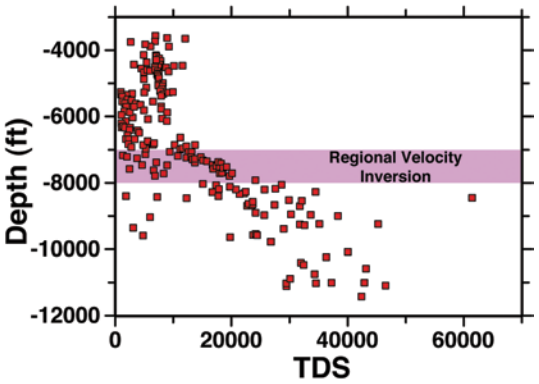


**Fig. 12.8** Total dissolved solids (TDS) in formation water from the Muddy Sandstone vs. depth in Wyoming's Powder River Basin. The approximate position of the regional velocity inversion surface is shown. Above this surface, the marine connate waters in the Muddy Sandstone have been diluted; below the surface, there is significantly less, and in most samples, no dilution of the original formation water. (Reprinted from Surdam et al. 2003)

Energy Online, Wyoming Geologic Association Oil and Gas Symposium publications, the National Institute of Standards, and in-house well field data at the Wyoming State Geologic Survey. The top ten depleted fields are distributed over the central basin, with the Amos Draw, Kitty, Horse Creek, and Hilight fields located near open-pit coal mines (Fig. 12.9).

### *12.2.5 Potential Enhanced Oil Recovery Targets*

Enhanced oil recovery (EOR) techniques, particularly $CO_2$ flooding, are becoming increasingly important to oil production in Wyoming. Since the 1970s, with the exception of a brief period during the mid-1980s, oil production in Wyoming has declined steadily (Fig. 12.10). In 2005, this decline stabilized and oil production leveled off at nearly 60 million barrels per year. So far in the 21$^{st}$ century, enhanced oil recovery (tertiary recovery) and condensate production in the giant Jonah, Pinedale, and Wamsutter gas fields of western Wyoming have offset the still-declining production in the state's older, conventional oil fields. The UW Enhanced Oil Recovery Institute (EORI) estimates that 4.0–8.0 billion barrels of recoverable oil remain in production zones and residual oil zones within Wyoming's depleted oil fields.

Prime EOR targets in the Powder River Basin are the Minnelusa fields in the northeastern part of the basin (Bentley and Lusk 2008). The EORI has determined that the basin hosts approximately 150 of these candidate Minnelusa oil fields, many of which have gone through the secondary water flood stage and appear ideal for tertiary $CO_2$ miscible flooding. These 150 EOR candidate fields together contained 1.2 billion barrels of original oil in place (OOIP). Use of $CO_2$ flooding in these fields should recover at least 15 % of the OOIP, or 180 million barrels of oil: at

**Table 12.2** Ten depleted fields proposed for potential geologic $CO_2$ storage, in order of preliminary estimated volumetric capacity

| | | Reservoir | | | $CO_2$ Density | | Formation Production | | | Fm. injection | | $CO_2$ Capacity |
|---|---|---|---|---|---|---|---|---|---|---|---|---|
| Field | Formation | Pressure (psi) | Temp (°F) | Depth (ft) | Kg/m3 | Tonnes/ m3 | Oil (bbls) | Gas (bbls) | Water (bbls) | Water (bbls) | NCV1 (bbls) | tonnes |
| Hilight | Muddy | 4,895 | 165 | 9,575 | 802.57 | 0.803 | 76,239,459 | 296,896,150 | 267,206,535 | 240,485,881 | 399,856,881 | 51,025,262 |
| Powell | Frontier | 8,037 | 266 | 12,530 | 768.60 | 0.769 | 20,586,727 | 261,251,707 | 742,263 | 864,192 | 281,716,505 | 34,427,842 |
| Hartzog Draw | Shannon | 5,000 | 190 | 9,183 | 755.68 | 0.756 | 114,363,356 | 40,640,606 | 29,346,447 | – | 184,350,409 | 22,150,277 |
| Kitty Buck | Muddy | 4,397 | 184 | 9,210 | 730.30 | 0.730 | 22,274,983 | 124,759,023 | 497,472 | 288,312 | 147,243,1660 | 17,097,538 |
| Draw North | Dakota | 8,100 | 280 | 12,315 | 752.10 | 0.752 | 24,506,580 | 92,412,871 | 1,668,288 | 9,756,6790 | 108,830,988 | 13,014,434 |
| Amos Draw (complex) | Muddy | 5,590 | 260 | 10,052 | 659.30 | 0.659 | 4,760,159 | 114,477,981 | 581,463 | 0 | 119,819,603 | 12,560,533 |
| Sand Dunes | Muddy | 6,300 | 240 | 12,470 | 733.25 | 0.733 | 18,250,679 | 78,533,694 | 76,880 | 1,043,080 | 95,818,173 | 11,171,129 |
| House Creek | Sussex | 3,241 | 179 | 8,257 | 633.76 | 0.634 | 32,614,208 | 15,600,673 | 41,489,283 | – | 89,704,163 | 9,039,295 |
| Spearhead Ranch | Frontier | 7,000 | 270 | 12,575 | 720.12 | 0.720 | 5,285,024 | 49,122,089 | 88,119 | 0 | 54,495,232 | 6,239,654 |
| Scott | Parkman | 3,051 | 184 | 8,550 | 590.72 | 0.591 | 17,675,931 | 26,476,239 | 8,339,425 | 2,164,236 | 50,327,359 | 4,726,971 |
| | | | | | | | | | | | *Total* | *181.5* |

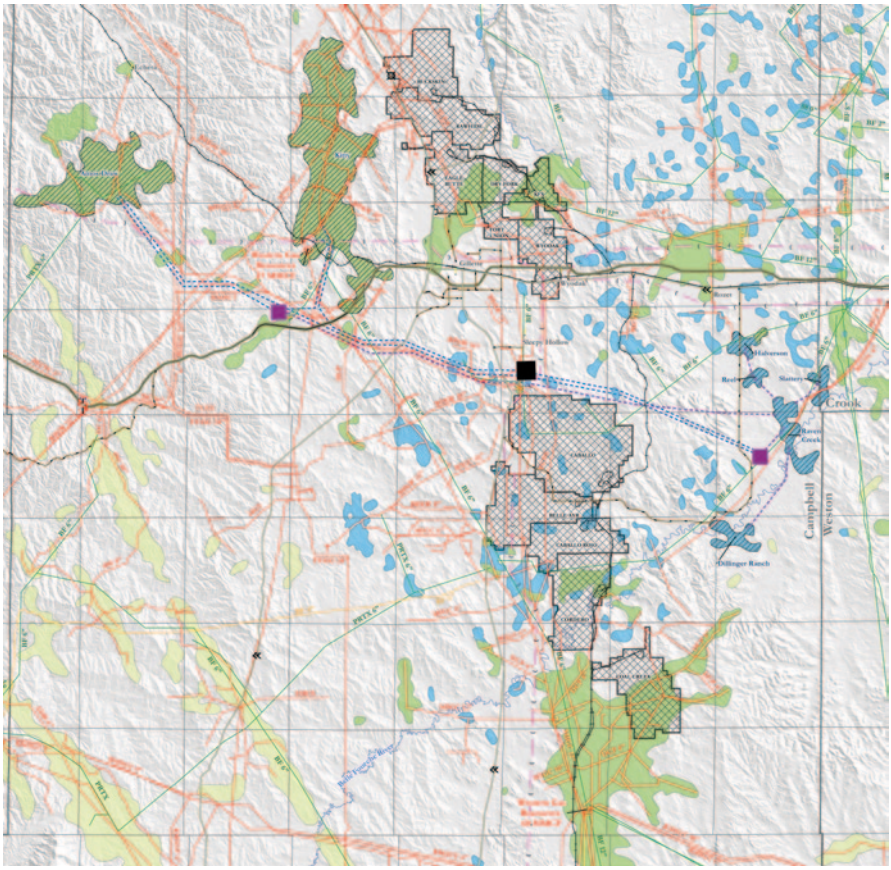


**Fig. 12.9** Map of area surrounding Gillette, Wyoming. Cross-hatched areas represent open-pit coal mines, blue areas are depleted Minnelusa oil fields, green areas show depleted anomalously pressured gas fields, and the black dot denotes a potential site for a coal conversion facility. Blue dashed lines are necessary $CO_2$ pipelines, and red lines are existing hydrocarbon pipelines. Violet squares indicate locations of proposed compressor stations. (Modified from Bentley and Lusk 2008)

US $ 80/barrel, this new EOR production would be worth US $ 14.4 billion. At the required 10 mcf of $CO_2$ per barrel of recovered oil, it will take 1.8 trillion cubic feet (Tcf) of $CO_2$ to recover the 180 million barrels of oil. At the very least, the total $CO_2$ cost (assuming a price of $ 2.00 per Mcf of $CO_2$) would be $ 3.6 billion. $CO_2$ cost could be substantially higher for Minnelusa flooding, the final cost depending on supply and demand and the state of delivery infrastructure at the time of purchase.

Two additional aspects of the Minnelusa oil fields in the PRB should be noted. First, the fields (Figs. 12.7b, c and 12.9) are in advanced decline. Second, the potential recoverable tertiary oil reserves in the 150 candidate fields are currently not large enough to support construction of long-range trans-basin pipelines. Therefore, two choices for EOR in the PRB Minnelusa fields remain: (1) acquire a local source of $CO_2$, or (2) wait for the development of a statewide $CO_2$ pipeline infrastructure (network) and regional anthropogenic $CO_2$ storage facilities.

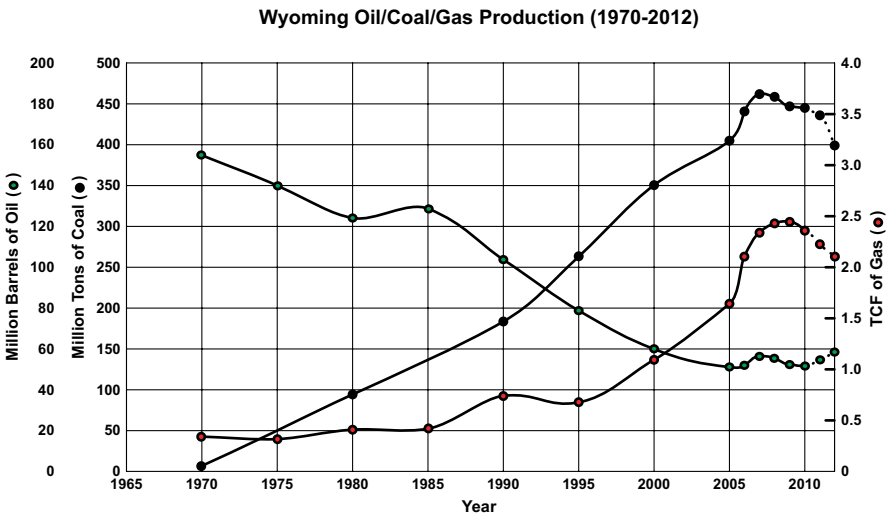


**Fig. 12.10** Wyoming coal, natural gas, and oil production from 1970 to 2010. (Modified from Surdam 2007)

### *12.2.6 Additional PRB $CO_2$ Storage Capacity*

Once the tertiary treatment is complete and the residual oil is recovered from the Minnelusa fields, the fields can then store $CO_2$. This additional storage capacity will more than double the 181 Mt of estimated storage capacity available in the ten depleted, anomalously pressured gas fields described above (Table 12.2).

## 12.3 Integrated Energy/Environmental Development Strategy

Five of the six key elements of a future integrated energy/environmental development strategy for the PRB are not only in place, but lie in close spatial proximity to one another (Fig. 12.9). The close proximity of the resource elements is critical to the proposed new development plan, and will minimize development cost, optimize operational efficiency, and effectively reduce the industrial footprint.

The value of the simultaneous multiple-resource approach to energy development in the PRB will be illustrated by describing a potential development scenario that merges all six key elements while reducing environmental degradation and restoring ecological resources. The illustrative scenario that follows is not unique, but flexible and easily modified. Therefore, the detail and general focus in the following discussion should be on the multitude of benefits to Wyoming such an approach delivers.

First, open-pit coal mining would continue using existing extractive technology or newly developed, improved technology as it becomes available. In the future, the coal mined to support the new proposed coal-to-chemical facilities hopefully will offset any decline in coal production caused by the retirement of the oldest and most inefficient conventional coal-fired power plants, followed gradually by the rest of the coal-fired power plant fleet, probably after 2050. Clearly, the retired coal-fired power plants are currently not being replaced by similar new plants, but instead will be replaced by natural gas-fired power plants, some form of integrated combined cycle plant (technologies still under development), renewable energy, nuclear reactors, or some combination of these. One of the aims of the scenario being developed for the PRB is to sustain a strong extractive coal industry in the future. Maintenance of the US $ 1.2 billion contributed annually to the Wyoming economy by the extractive coal industry (Fig. 12.1) is an important aspect of any future PRB energy development plan. The significant increase in product value created by the coal-to-chemical/synfuel industry (Fig. 12.6) will result in far greater state revenues.

Second, the new coal-to-chemical facilities should be located as close to the mines as possible. In Shaanxi Province, China, the coal-to-chemical plants and associated coal mines are sited in the same location – either over underground coal mines or next to open-pit coal mines. Ideally, in Wyoming the mined coal would be transported from the open-pit coal mines to the coal-to-chemical facilities via conveyor belt. This type of transportation eliminates the need for additional rail or truck traffic, both of which contribute to habitat fragmentation and air quality degradation.

Next, the coal-to-chemical/syngas facilities will need access to water resources. As previously described, CBM produced water would best support these coal conversion facilities. The volume of water required to supply the plants will vary depending on facility specifications. In China, the coal-to-methanol plants are designed for a 6:1 ratio of water to product (barrels).

Preliminary calculations suggest that over the next 20 years, the CBM industry will produce one billion barrels of water annually (Surdam et al., 2007). This volume of water, if used at coal-to-chemical plants similar to those in China, would support an annual yield of about 160 million barrels of product. As this new industry grows or the CBM industry slows, the required water resources could be supplemented or replaced by produced and treated water from deep saline aquifers in the basin center (Fig. 12.5b). However, one billion barrels of water would support approximately 40 methanol plants (each producing 700,000 tonnes of methanol annually), or 24 diesel plants similar to those in commercial operation in China (Fig. 12.2). It follows that it would take many decades before a Wyoming coal conversion industry's demand for water would exceed the available CBM water supply.

The problem with the CBM water lies not in the volume available, but in transporting it. The CBM water is scattered and must be collected and then transported to the coal mines. The ideal transport conduit for the water is the Belle Fourche River that runs from the "Big George" CBM area northeast to Keyhole Reservoir (approximately 35 miles east of Gillette; Bentley and Lusk 2008). Keyhole

Reservoir would provide an outstanding storage site for the CBM water prior to use in coal conversion facilities. The obstacle to this route for water transport is a 1943 water compact between Wyoming and South Dakota pertaining to the Belle Fourche River Basin: the compact ensures that almost all unappropriated river water belongs to South Dakota. If this proposed scenario were to include storing water in Keyhole Reservoir, Wyoming would have to negotiate an agreement with South Dakota to establish ownership of CBM water transferred via the Belle Fourche River drainage and stored in Keyhole Reservoir.

An alternative water transportation plan entails building a collection pipeline from Dead Horse (the "Big George" CBM area) to the vicinity of the existing coal mines. Small storage ponds would have to be constructed at each of the coal-to-chemical facilities. More information regarding pipelines that could potentially transport CBM water is available (Surdam et al. 2006).

At this point in the scenario, the resources to support an industrial coal-to-chemical/syngas facility are assembled in the vicinity of an open-pit coal mine, with the plant site as close to the mine as is practical. Thus far, no new mines are required, water resources currently wasted are put to beneficial use, and existing coal conversion technology is deployed. No new environmental impacts will result from any part of the plan, except perhaps from the construction of underground pipelines – and in this case, the disruption would be temporary and mitigated rapidly.

Consider the significance to Wyoming and the U.S. of deploying coal conversion technology. The CBM water produced annually in the PRB could support production of 10% of the diesel fuel consumed in the nation. Using the Chinese coal-to-diesel technology as a model, 10–20 coal-to-diesel plants in the PRB could produce approximately 150 million barrels of diesel annually (6.3 billion gallons), or 10% of the nation's yearly diesel consumption. At this rate, a coal-to-diesel industry in the PRB, constrained by available CBM water, could replace 12 days worth of the nation's crude oil imports (currently, the US imports approximately 12 million barrels of crude oil per day).

### *12.3.1 Carbon Emission Storage*

In the following discussion, the typical $CO_2$ emissions from commercial coal-to-methanol and coal-to-diesel facilities in China are used to derive estimates of $CO_2$ emissions from a Wyoming coal conversion industry. (Chap. 13 details the coal-to-chemical industry in China's coal-rich Ordos Basin.) A Chinese methanol plant annually uses 2.0 Mt of coal and 6.0 Mt of water, emits 4.0 Mt of $CO_2$, and generates 0.7 Mt of methanol. A diesel plant annually uses 3.5 Mt of coal and approximately 10 Mt of water, emits 2 Mt of $CO_2$, and generates 7 million barrels (0.9 Mt) of diesel.

Let us assume that two methanol plants and two diesel plants are built in the initial phase of the establishment of a coal conversion industry in the Powder River Basin (5–10 year timeframe). These plants would generate 1.5 Mt of methanol and 14 million barrels of diesel annually, and would emit 12 Mt of $CO_2$. In the second

phase of coal conversion development (another 5–10 years later), the number of plants could double: four methanol and four diesel plants together emitting 24 Mt of $CO_2$ annually. The question is this: *how and where can these emissions be stored?* Fortunately, areas of depleted and compartmentalized Cretaceous gas fields (Table 12.2, Fig. 12.9) lie adjacent to the coal mines and proposed mine-mouth coal conversion facilities. The Hilight, Kitty, and Amos Draw depleted gas fields are ideal locations for (1) storage sites for $CO_2$ emitted by coal conversion facilities on the eastern margin of the PRB, and (2) sources of $CO_2$ for EOR projects in adjacent depleted Minnelusa oil fields (Fig. 12.9). The total available $CO_2$ storage capacity of these three fields is approximately 80 Mt (Table 12.2). Potential storage sites for EOR projects in other parts of the basin also exist. These depleted gas fields would initially be used as $CO_2$ surge tanks to support EOR activities. When the stranded oil in the Minnelusa is recovered, the depleted gas fields could be used for more permanent storage. Using the initial storage site as a surge tank would allow adjacent EOR projects in the Minnelusa fields to have optimal flexibility in designing variable injection rates and in alternating water and $CO_2$ injection strategies.

### *12.3.2 $CO_2$ Utilization*

As shown in Fig. 12.9, more than 150 depleted Minnelusa oil fields in the PRB with EOR potential (Bentley and Lusk, 2008) are located near the resource confluence, and are eligible for tertiary recovery via $CO_2$ flooding. Many have gone through secondary recovery (water flood) and appear ideal for $CO_2$ miscible flooding. These 150 Minnelusa fields together contained 1.2 billion barrels of original oil in place (OOIP). Typically, $CO_2$ flooding recovers at least 15 % additional production, or from the Minnelusa fields, 180 million barrels of oil. At the current oil price of approximately $ 80/barrel, the Minnelusa stranded oil would be worth US $ 14.4 billion.

Recovering the stranded oil via $CO_2$ flooding would require 1.8 trillion cubic feet of $CO_2$ (10 Mcf per barrel of oil), or 93 Mt of $CO_2$ (19.3 Mcf/t of $CO_2$) for the duration of Minnelusa activities. If the EOR project lasted 20 years, the four coal conversion facilities envisioned in phase one of the industrialization (12 Mt of $CO_2$ emitted annually) would more than adequately support the Minnelusa EOR activities. Importantly, the $CO_2$ used for the EOR projects would acquire monetary value. A very conservative estimate suggests that, at $ 2/Mcf, about US $ 4 billion worth of $CO_2$ would be required to recover the 180 million barrels of stranded oil in the Minnelusa. Therefore, a resource typically regarded as a problem with respect to disposal and sequestration would be worth approximately US $ 4 billion in this scenario. Moreover, the Minnelusa fields from which the stranded oil is recovered would be converted to permanent storage sites for $CO_2$, doubling the 180 Mt of $CO_2$ storage capacity in the depleted Cretaceous gas fields listed in Table 12.2: at the end of EOR operations, there would be 360 million tonnes of $CO_2$ storage capacity available to coal conversion facilities.

### *12.3.3 Benefits of the Integrated Development Approach*

Integrated development supports the extractive coal mining industry in the PRB (conventional open-pit technology), and gives monetary value to water produced during CBM development by using it to support a new coal conversion industry in the basin. The proposed scenario involves deployment of mine-mouth coal conversion technology to derive a variety of added-value products from coal. This technology exists and has been tested and improved in China at commercial scale. In China, this coal conversion technology produces methanol, ethanol, acetate, diesel, gasoline, syngas, plastics, and fertilizer.

All coal conversion facilities, unlike conventional coal-fired power plants, inherently capture $CO_2$. The captured $CO_2$ can be pressurized at the conversion plant and then transported via pipeline locally as a supercritical fluid. Pipeline transport distances between the coal conversion facilities and storage sites would average 3 km to 8 km (2–5 mi). The $CO_2$ would be stored in the depleted gas fields and retrieved at variable rates for EOR activities in adjacent Minnelusa oil fields. Enhanced oil recovery projects using $CO_2$ flooding are characterized by variable demand for $CO_2$: high rates of $CO_2$ injection initially, followed by variable demand rates. Commonly, EOR proceeds by alternating water flooding and $CO_2$ flooding. Also, with 150 eligible Minnelusa fields – some small and some large – numerous $CO_2$ floods would proceed simultaneously. The depleted gas fields are ideal because the stored $CO_2$ could be produced at variable rates, pressurized, and transported by a single pipeline to a compressor station in the middle of a Minnelusa oil field swarm. Each individual field and operator would then take delivery of the supercritical $CO_2$ at the compressor station and arrange for transport through small, temporary pipelines.

At this point, the $CO_2$ originally generated at the coal conversion facilities is monetized and available for injection/flooding in the depleted Minnelusa oil fields. In the example cited (EOR in the Minnelusa oil fields of the PRB), the $CO_2$ flooding will recover at least 180 million barrels of stranded oil that would not otherwise be recovered. Once the stranded oil is recovered, the oil fields can provide additional $CO_2$ storage, doubling the $CO_2$ storage capacity in the region (depleted gas fields plus depleted oil fields).

The University of Wyoming Enhanced Oil Recovery Institute and the Wyoming State Geologic Survey estimate that Wyoming has 4–8 billion barrels of stranded oil, mostly in the Powder River and Bighorn basins. The strategy outlined in this chapter can serve as a model for the use of anthropogenic $CO_2$ to recover stranded oil by using the confluence of regional resources to effectively and efficiently sustain resource development with minimal environmental impact.

#### 12.3.3.1 Economic Benefits

The resource development plan outlined in this report would provide many diverse benefits to the state of Wyoming and the energy industry. For example, it would expedite the recovery of stranded oil by providing an anthropogenic source of $CO_2$. In

the case of the depleted Minnelusa fields, that oil at today's price ($ 80/bbl) would be worth US $ 14.4 billion. It would also provide a mechanism to monetize $CO_2$, a byproduct of the coal conversion industry: in this case, the $CO_2$ would be worth approximately US $ 4 billion. The anthropogenic $CO_2$ in the model presented here would not represent a regulated disposal problem, but rather a much sought-after and valuable commodity. The deployment of a coal conversion industry – even at the relatively modest scale described here – would generate US $ 14 billion worth of diesel and methanol in the first five to ten years. If the number of coal conversion facilities doubled in the second 5–10-year period, the products generated would be worth US $ 28 billion. Also important, CBM water in this scenario would no longer be wasted, but would serve instead as a valuable resource put to beneficial use. In brief, the plan includes the deployment of a new resource industry that yields both added-value products and a new and greatly needed source of $CO_2$. This new source of $CO_2$ would constitute a valuable commodity rather than an environmental problem: it would be used to recover stranded oil that otherwise might never be recovered. The plan would deploy a new industry, recover bypassed energy resources, minimize environmental impacts, and convert a wasted resource into a valuable commodity. Most importantly, it would sustain resource development opportunities for future Wyoming generations and extend state revenue derived from energy resource industries.

#### 12.3.3.2 Job Creation

The Ordos Basin in Shaanxi Province, China, has many structural and energy resource similarities to the Powder River Basin of northeastern Wyoming. Consider that the Ordos Basin is part of a cratonic platform that developed into a stable basin during the Paleozoic with subsequent tectonic activity dominated by both regional subsidence and uplift. In Shaanxi Province, with the exception of uplifts and depressions that developed at the margins, the Ordos Basin is characterized by a huge monoclinal structure (110,000 $km^2$) with a 1–2 ° dip to the west (the Shaanbei Slope).

More than 40 oil fields have been discovered in the Ordos Basin, including the largest oil field discovered in China in the past decade. Four of China's five largest gas fields, with reserves in excess of 100 $Bm^3$ of gas, are located in the Ordos Basin. The basin also contains 367 Bt of coal reserves, and produces more coal than any other area of China.

The greatest difference between the Powder River Basin and the Ordos Basin is the existence of coal conversion facilities: the Ordos Basin hosts 22 coal-to-methanol plants and one coal-to-diesel plant (with one additional plant approved but not yet constructed), while the PRB has no significant coal conversion facilities, but a multitude of large open-pit coal mines. In the Ordos Basin, the 22 coal-to-methanol plants produce more than 10 million tons of methanol, use 30–40 million tons of coal, require 110 Mt of water, and emit 42 Mt of $CO_2$ annually. These numbers do not include the coal and water necessary to generate the electricity required by the

coal conversion plants (typically from coal-fired power generation), or the amount of $CO_2$ emitted by the power-generating facilities.

Most importantly, each of the coal conversion plants employs approximately 400 workers, so the 22 plants in the Ordos Basin provide approximately 9,000 jobs. During the construction phase, the number of jobs provided would be much higher. In summary, a network of coal conversion plants in the Powder River Basin would substantially aid in reversing the current trend of coal-related job loss in northeastern Wyoming, while providing value-added domestic products derived from coal.

### *12.3.4 Environmental Impacts*

The proposed integrated energy development strategy will not only benefit Wyoming economically, but will do so without causing any new significant negative environmental impacts. In fact, one could argue that the scenario's implementation would have several positive environmental effects, including a reduction in $CO_2$ emissions and an end to the current waste of CBM produced groundwater and its associated negative effects on streams and pastureland. Most significantly, the proposed strategy will occur entirely on existing developed lands already subject to habitat destruction and fragmentation (coal mines, oil and gas fields): the strategy will have no new negative developmental or ecological consequences, will not expand the footprint of energy development in the state, will not exploit or degrade lands and habitat currently untouched by energy development, and will not exacerbate the impact of existing energy development in the basin. This is particularly important given the potential listing of the sage grouse (*Centrocercus urophasianus*) under the Endangered Species Act. Extensive sage grouse habitat spans the PRB, and Wyoming is seeking ways to facilitate energy development while avoiding further declines in grouse populations that could trigger listing of the species and cripple the state's energy industry. The integrated strategy outlined here would dovetail nicely with the state's efforts. Relatively minor environmental impacts caused by the construction of small pipelines will be temporary and mitigated to the greatest extent possible (pipelines installed underground and routed along existing transportation corridors such as county roads, etc.). In addition, existing facilities and infrastructure would be upgraded and streamlined to further minimize environmental impacts.

## 12.4 Conclusions

The energy development plan presented in this chapter focuses on the future synchronous development of resources in the Powder River Basin. The example used to illustrate the benefits of such an approach is based on the confluence of a set of natural resources in the Powder River Basin, but the approach itself is flexible and could be tailored to fit other Wyoming and many Rocky Mountain basins. This

approach emphasizes synergistic relationships among resource elements in order to optimize the effective and efficient exploitation of the state's energy resources while minimizing environmental degradation. The fundamental idea is that it is more effective and efficient to develop a set of resource elements together systematically rather than separately.

In the systematic approach, a contentious problem associated with the development of one resource becomes part of a useful solution in the development of another. Until now, resource development in Wyoming has often tended to focus on one particular resource at the expense of others, an approach designed to maximize short-term economic benefits rather than ensure long-term economic sustainability. The state has the opportunity today to try something new: the approach described in this chapter will foster open resource management discussions and compromises, improve education and long-term planning, and build positive, collaborative relationships among different resource industries rather than perpetuate a single-resource mindset. Most importantly for future generations, the innovative resource development strategy outlined in this report will help achieve long-term sustainable use of Wyoming's energy and environmental resources while maintaining state revenues derived from natural resources.

## References

Aines R, Wolery T, Bourcier W, Wolfe T, Haussmann C (2010) Fresh water generation from aquifer-pressured carbon storage. Lawrence Livermore National Laboratory Report LLNL-PROC-424230. Presented at the Ninth annual conference on carbon capture and sequestration, Pittsburgh, Pa., May 10–13, 2010

Bentley R, Lusk A (2008) Clean coal technology, carbon capture and sequestration, and enhanced oil recovery in Wyoming's Powder River Basin: an integrated approach. Wyoming State Geologic Survey Challenges in Geologic Resource Development No. 7

Burruss RC, Brennan ST, Freeman PA, Merrill MD, Ruppert LF, Becker MF, Herkelrath WN, Kharaka YK, Neuzil CE, Swanson SM, Cook TA, Klett TR, Nelson PH, Schenk CJ (2009) Development of a probabilistic assessment methodology for evaluation of carbon dioxide storage. U.S. Geologic Survey Open-File Report 2009–1035

Childress R (2011) World gasification industry—status, trends, and drivers. Gasification Technologies Council. Gasification technologies workshop, Tampa, FL, April 6, 2011

Copeland DA, Ewald ML (eds) (2008) Water associated with coal beds in Wyoming's Powder River Basin—geology, hydrology, and water quality. Wyoming State Geologic Survey Exploration Memoir No. 2

Fan M, Heller P (2012) Reservoir characterization of the Muddy Formation in the Powder River Basin, NE Wyoming. Internal report to the Clean Coal Technologies Program, University of Wyoming School of Energy Resources, p. 23

Jones N, Quillinan S, McClurg J (2009) Wyoming Coal. Wyoming State Geologic Survey Public Information Circular No. 44

Surdam RC (2008) Wyoming's energy development in the context of the global energy economy. Wyoming State Geologic Survey Challenges in Geologic Resource Development No. 6

Surdam RC, Jiao Z (2007) The Rock Springs Uplift: an outstanding geologic $CO_2$ sequestration site in southwest Wyoming. Wyoming State Geologic Survey Challenges in Geologic Resource Development No. 2

Surdam RC, Jiao Z, Ganshin Y (2005) A new approach to exploring for anomalously pressured gas accumulations—the key to unlocking huge, unconventional gas resources. Wyoming State Geologic Survey Exploration Memoir No. 1

Surdam RC, Clarey KE, Bentley RD, Stafford JE, Jiao Z (2006) Powder River Basin desalination project feasibility. Wyoming State Geologic Survey Challenges in Geologic Resource Development No. 1

Surdam RC, Jiao Z, Clarey K, DeBruin RH, Bentley R, Stafford J, Deiss A, Ewald M (2007) An evaluation of coalbed methane production trends in Wyoming's Powder River Basin: a tool for resource management. Wyoming State Geologic Survey Challenges in Geologic Resource Development No. 3

Surdam RC, Jiao Z, Stauffer P, Miller T (2009) An integrated strategy for carbon management combining geologic $CO_2$ sequestration, displaced fluid production, and water treatment. Wyoming State Geologic Survey Challenges in Geologic Resource Development No. 8

# Chapter 13
# A Feasibility Study of the Integration of Geologic $CO_2$ Storage with Enhanced Oil Recovery ($CO_2$ Flooding) in the Ordos Basin, China

**Zunsheng Jiao, Ronald C. Surdam, Lifa Zhou and Yajun Wang**

**Abstract** Rich in energy resources, China's Ordos Basin shares many similarities with Wyoming's Greater Green River Basin and Powder River Basin. As a result, the energy development strategy employed in Wyoming basins should be applicable to the Ordos Basin. The Ordos Basin's coal, coalbed methane, and natural gas reserves are ranked first in China, and its oil reserves are ranked fourth. The coal deposits in the Ordos Basin account for 39% (3.98 Tt) of Chinese coal resources, and six of the thirteen largest coal mines in China are in the basin. China's large energy base and the facilities essential to its fast-growing coal-to-chemicals industry are located in the Ordos Basin. The concurrent development of relatively new coal conversion industries with existing oil and gas industries in the Ordos Basin (Northern Shaanxi Province) provides the opportunity to apply the systematic approach to energy production developed in Wyoming: the integration of geologic $CO_2$ storage and enhanced oil recovery (EOR) using $CO_2$ flooding ($CO_2$-EOR). The coal conversion industry (coal-to-methanol, coal-to-olefins, etc.) provides affordable, capture-ready $CO_2$ sources for developing large-scale $CO_2$-EOR and carbon storage projects in the Ordos Basin. Compared with other CCUS projects, the ability to use $CO_2$ from the coal-conversion industry for $CO_2$-EOR and geologic $CO_2$ storage will make these projects in the Ordos Basin more cost-effective and technologically efficient while reducing $CO_2$ emissions to the atmosphere.

Z. Jiao (✉) · R. C. Surdam
Carbon Management Institute Laramie, University of Wyoming, Laramie, USA
e-mail: JJiao@uwyo.edu

R. C. Surdam
e-mail: rsurdam@uwyo.edu

L. Zhou · Y. Wang
Shaanxi Provincial Institute of Energy Resources and Chemical Engineering Xian, Shaanxi, P. R. China
e-mail: zhoulf@nwu.edu.cn

Y. Wang
e-mail: yajunwang@139.com

R. C. Surdam (ed.), *Geological $CO_2$ Storage Characterization,*
Springer Environmental Science and Engineering, DOI 10.1007/978-1-4614-5788-6_13,
© Springer Science+Business Media New York 2013

The Shaanbei Slope of the Ordos Basin is a huge monoclinal structure with a high-priority potential $CO_2$ storage reservoir (Majiagou Formation) that lies beneath a sequence of Mesozoic rocks more than 2000 m thick containing a multitude of low-permeability lithologies. The targeted Ordovician Majiagou Formation in the area of interest is more than 700 m thick. This carbonate reservoir is located at depths where the pressure and temperatures are well above the supercritical point of $CO_2$. The targeted reservoir contains high-salinity brines (20,000–50,000 ppm TDS) that have little or no economic value. Preliminary simulation results show that the Ordovician Majiagou Formation in the Ordos Basin has excellent potential for geologic $CO_2$ sequestration and could store the $CO_2$ currently emitted by coal-to-chemicals facilities in Shaanxi Province for hundreds of years.

The extremely low porosity, low permeability, low oil saturation, anomalously low reservoir pressure, and high reservoir heterogeneity of the targeted $CO_2$-EOR formations in the Ordos Basin make using $CO_2$ for enhanced oil recovery much more challenging here than in the U.S. These reservoir characteristics together constitute a major reason that $CO_2$-EOR is not widely employed in the Ordos Basin at present, even though highly concentrated $CO_2$ from coal conversion plants has been available for years. Comparisons of reservoir and crude oil properties in the Ordos Basin with the current US $CO_2$-EOR screening guidelines reveal that the gravity, viscosity, crude oil composition, and formation type of the Ordos reservoirs all are favorable for $CO_2$ miscible flooding. The major challenges come from anomalously low reservoir pressure, low porosity, and higher reservoir heterogeneity.

## 13.1 Introduction

Rich in energy resources, China's Ordos Basin shares many similarities with Wyoming's Greater Green River and Powder River Basins. As a result, many elements of the energy development strategy developed for the Wyoming basins should prove directly applicable to the Ordos Basin. The Ordos Basin's coal, coalbed methane, and natural gas reserves rank first in China, and its oil reserves rank fourth. The coal deposits in the Ordos Basin account for 39 % (3.98 Tt) of total Chinese coal resources, and six of the thirteen largest coal mines in China are in the basin. China's largest energy base and the facilities essential to its fast-growing coal-to-chemicals industry are in the Ordos Basin. The coal conversion industry (coal-to-methanol, coal-to-olefins, etc.) will provide affordable, capture-ready $CO_2$ for large-scale $CO_2$-EOR and carbon storage projects in the Ordos Basin. The use of $CO_2$ from the coal-conversion industry for $CO_2$-EOR and geologic $CO_2$ storage in the Ordos Basin will make these EOR projects cost-effective and technologically efficient while reducing $CO_2$ emissions to the atmosphere.

Successful implementation of geologic $CO_2$ sequestration to manage carbon and mitigate climate change requires subsurface storage space for huge volumes of supercritical $CO_2$. A chosen storage formation must be capable of retaining the stored $CO_2$ for hundreds to thousands of years. A superior geologic storage site must pos-

sess three essential characteristics: adequate pore space, well connected pores, and a high-quality trapping mechanism. The Carbon Management Institute (CMI) at the University of Wyoming and the Shaanxi Provincial Institute of Energy Resources and Chemical Engineering (SPIERCE) have proposed that the Ordovician Majiagou Formation in the Ordos Basin is a superior potential geologic storage reservoir.

Furthermore, the concurrent development of relatively new coal conversion industries and existing oil and gas industries in the Ordos Basin has created a unique opportunity to apply the synergistic approach developed in Wyoming: the integration of geologic $CO_2$ storage and enhanced oil recovery using $CO_2$ flooding ($CO_2$-EOR). $CO_2$-EOR is a widely accepted and effective tertiary recovery technique that the oil industry has used for decades. In the United States, $CO_2$-EOR projects in Wyoming and Texas have demonstrated that $CO_2$-EOR can routinely increase oil recovery by 5–20%, depending on reservoir conditions and the applied technologies. With stranded oil recovery in a reservoir, about one-third of the injected $CO_2$ remains in the subsurface during the $CO_2$-EOR process, while about two-thirds is recycled and recompressed for injection back into the reservoir. By completion of production, the EOR project has created the significant potential for permanent $CO_2$ storage in the depleted reservoir. The integration of geologic $CO_2$ storage and enhanced oil recovery will increase oil and gas production, reduce $CO_2$ storage net expense and will improve environmental quality.

Applying experience gained from $CO_2$-EOR and CCS projects in Wyoming, researchers at the CMI are working closely with scientists from Northwest University, the Shaanxi Provincial Institute of Energy Resources and Chemical Engineering (SPIERCE), and the Yanchang Petroleum Company to expedite $CO_2$-EOR and geologic $CO_2$ storage projects in the Ordos Basin. At present, many CCS projects focus on $CO_2$ emitted by coal-fired power plants. High energy consumption penalties and the high cost of $CO_2$ capture from coal-fired power plants have become serious technical and financial obstacles for commercial-scale CCS and $CO_2$-EOR projects. In Northern Shaanxi Province, the coal conversion industies (coal-to-methanol, coal-to-olefins, etc.) provide affordable, capture-ready $CO_2$. Compared with other CCS projects, the use of $CO_2$ from the coal conversion industry for $CO_2$-EOR and geologic $CO_2$ storage will make these projects in the Ordos Basin more cost-effective and technologically efficient.

The geologic $CO_2$ storage capacity of the Majiagou Formation in the Ordos Basin has been assessed using high-resolution numerical simulation, as well as a volumetric approach. Presently, the mature oil fields in the Ordos Basin are being screened and prioritized on the basis of $CO_2$-EOR criteria and proximity to $CO_2$ sources (the coal conversion plants). Targeted high-priority candidates will be investigated further. Compared with the $CO_2$-EOR projects in the Texas and New Mexico Permian Basin and Wyoming Green River, Powder River, and Wind River Basins, the biggest challenge for $CO_2$-EOR projects in Northern Shaanxi Province is the development of advanced technology to deal with anomalously low-pressured reservoirs characterized by very low porosity and permeability and high reservoir heterogeneity. Three-dimensional reservoir characterization, $CO_2$-EOR potential screening, geologic storage reservoir modeling and injection numerical simulation,

systematic performance assessment, and economic evaluation will be used to select sites for a $CO_2$-EOR storage demonstration project in the Ordos Basin.

## 13.2 Geologic Setting

### *13.2.1 Geology*

With an area of 370,000 km$^2$, the Ordos Basin (Fig. 13.1a) is the second largest sedimentary basin in China. The basin covers parts of Shaanxi, Shanxi, and Gansu provinces and the Ningxia and Inner Mongolia autonomous regions. Tectonically, the basin lies in the western North China Block and is bordered by the Luliang Mountains to the east, Qinling Mountains to the south, Liupan Mountains and Helan Mountains to the west, and Lang Mountains and Yin Mountains to the north. Separated by the Great Wall are the Maowusu and Kubuqi deserts to the north and the Loess Plateau to the south.

The Yellow River borders the Ordos Basin on the west, north, and east: all the water systems in the basin are part of the Yellow River drainage. Most watercourses in the desert and plain areas are intermittent streams that typically flow into desert lakes or salt marshes. Though its surface streams have small permanent flow and poor water quality, often drying out in summer, the Ordos Basin is rich in groundwater.

The Ordos Basin is a typical cratonic basin that developed into a large stable basin during the Paleozoic. The Shaanbei Slope with the exception of thrust fault features and depressions at the margins, the basin is a huge (110,000 km$^2$) monoclinal structure with a 1–2° west dip (Fig. 13.1b). The Shaanbei Slope is a relatively stable tectonic environment with rare regional faults, and is considered a favorable structural unit for geologic $CO_2$ storage.

The basement in the Ordos Basin consists of metamorphic Archean and Lower Proterozoic rocks. The basin has experienced five tectonic stages: (1) Middle to Late Proterozoic aulacogen, (2) Early Paleozoic shallow foreshore platform, (3) Late Paleozoic coastal plain, (4) Mesozoic inland basin, and (5) Cenozoic faulting depressions surrounding the basin. The Ordos Basin can be subdivided into six structural units: the Yimeng Uplift, Weibei Uplift, Jinxi Fault-Fold Belt, Shaanbei Slope, Tianhuan Depression, and Western Edge Fault Belt (Fig. 13.1a).

Sedimentary strata of the Proterozoic, Paleozoic, Mesozoic, and Cenozoic are extant in the Ordos Basin. The thickness of Paleozoic and Mesozoic sedimentary strata ranges from 2,559 to 7,847 m (Fig. 13.1c). From the Cambrian to the Early Ordovician, the Ordos Basin region was a shallow marine carbonate platform, and 300 to 600 m of carbonate rocks were deposited in the main part of the Ordos Basin. During the later Early Ordovician to Middle Ordovician, the North China Block (including the Ordos Basin) experienced a large-scale marine transgression that deposited 100–900 m of the Majiagou Formation, which consists of dolomite, lime-

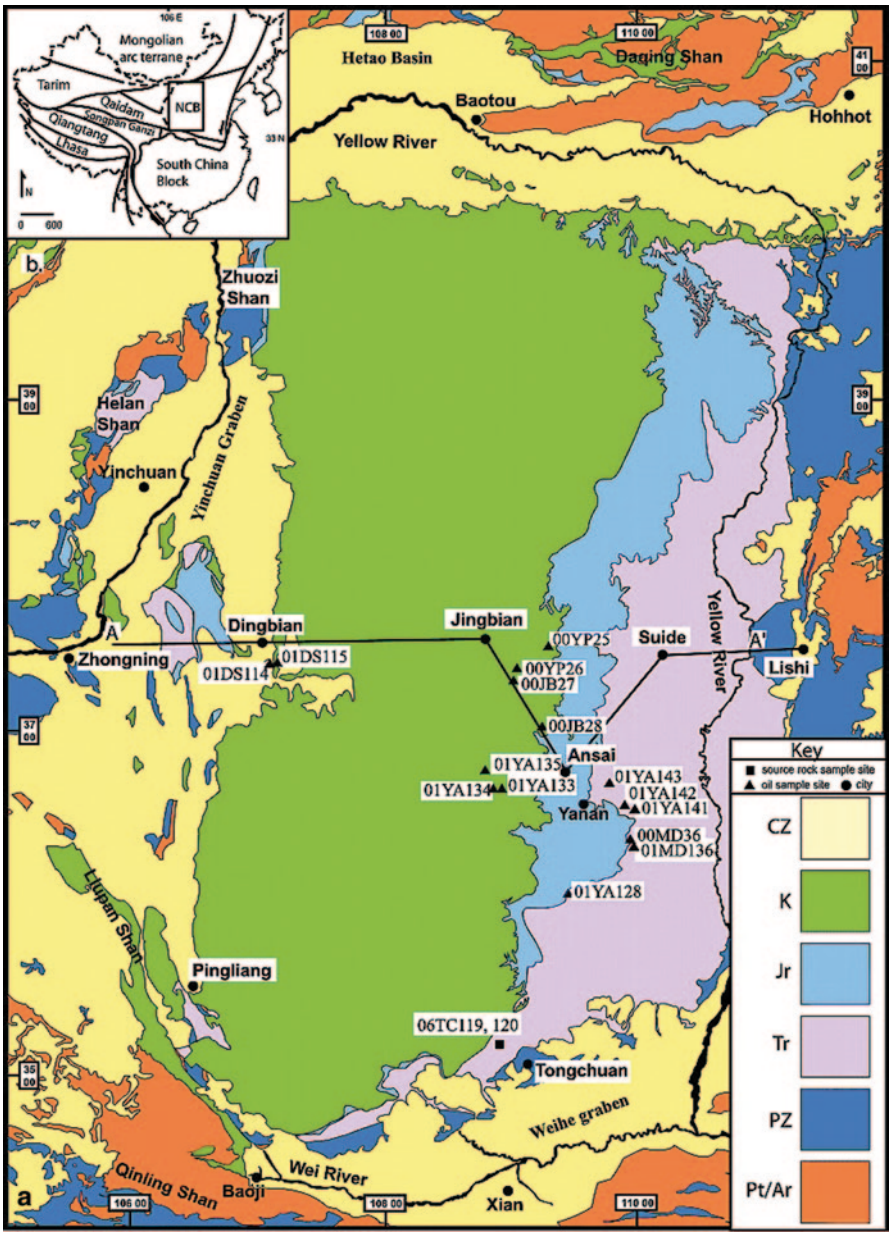


**Fig. 13.1** (**a**) Geologic map of the Ordos Basin, China. (**b**) East-west geologic cross section of the Ordos Basin. (Modified from Li et al. 1989). (**c**) Stratigraphic column showing formation thickness, depositional environments, and reservoir and trap rocks in the Ordos Basin. (Modified from Yang et al. 2005)

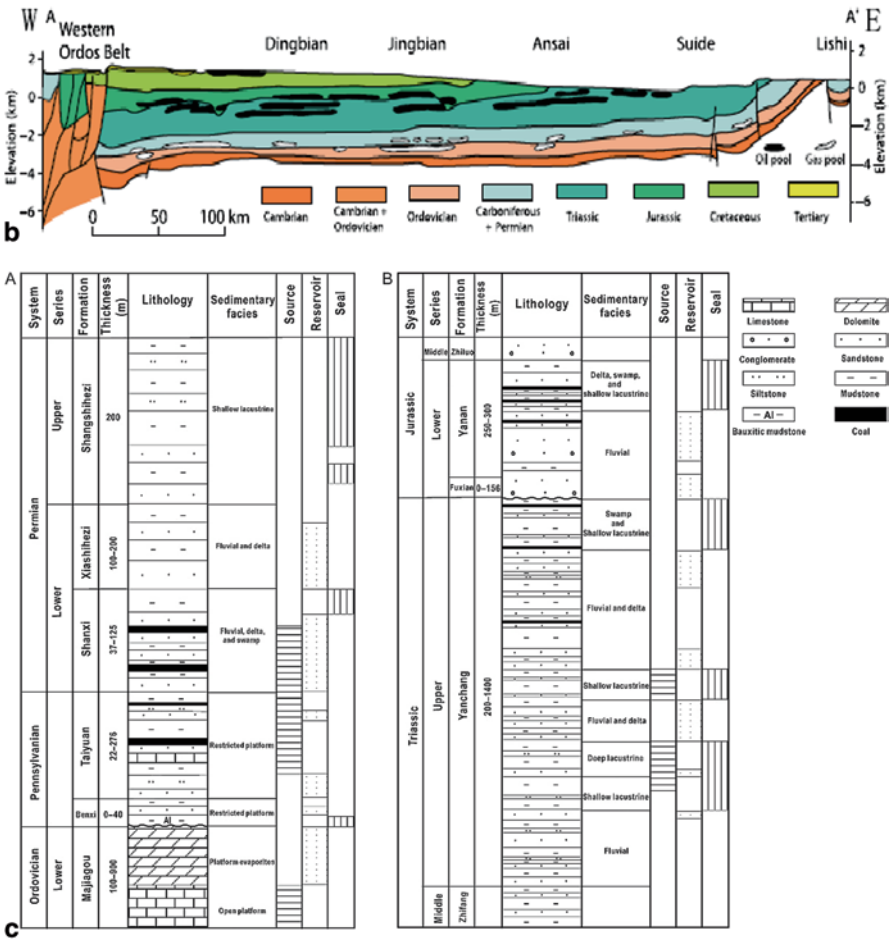


**Fig. 13.1** (continued)

stone, and evaporitic rocks in the interior of the basin. Upper Ordovician, Silurian, Devonian, and Mississippian strata do not occur within the basin, and their absence is marked by a major regional unconformity between the Middle Ordovician and Pennsylvanian strata. During a 150 m.y. hiatus from the Middle Ordovician to the Mississippian, intense karstification of the Ordovician dolomites resulted in a wide distribution of karst strata along the regional unconformity forming the reservoir rocks of the Jingbian gas field. The average thickness of the upper Paleozoic sedimentary rocks ranges from 800 to 1000 m, mainly including the gas-bearing intervals of the Pennsylvanian Benxi Formation and the Permian Taiyuan, Shanxi, Shihezi, and Shiqianfeng formations. During the Triassic and Jurassic, a thick terrestrial stratigraphic section consisting of lacustrine, fluvial, wetland, and deltaic strata accumulated—comprising shales, mudstones, coal, and sandstones with a thickness

of 2300–5700 m. The Triassic Yanchang Formation is a major oil-rich unit in the Ordos Basin. During the Early Cretaceous, 100–1200 m of eolian sediments (eolian sandstones) were deposited in the Ordos Basin. In the Cenozoic, climate change brought drought to the Ordos Basin, and accompanied by uplift, the basin accumulated more than 200 m of wind-blown loess sediments.

The potential geologic $CO_2$ storage reservoirs in the Majiagou Formation lie beneath a 2000+ m thick sequence of Mesozoic rocks containing a multitude of low-permeability sealing lithologies. The Majiagou carbonate reservoir in the location of interest is more than 700 m thick and is located at depths where the pressure and temperature are well above the supercritical point of $CO_2$ (31 °C and 7.4 MPa). The targeted reservoir contains high-salinity brines (20,000–50,000 ppm) with no economic value at present. The Majiagou reservoir is continuous, as inferred from well logs and cores showing that porosity ranges from 1 to 15 % with average measured porosity of 8 % and that permeability ranges from 1 to 35 mD.

### *13.2.2 Oil, Gas, and Coal Resources*

A major national energy and chemical industry development center, the Ordos Basin is the largest energy supplier in China, accounting for nearly 6, 13, and 39 % of national natural gas, coalbed methane, and coal reserves, respectively. The basin's crude oil reserves rank fourth in China. Oil, natural gas, coal, coalbed methane, and sandstone-type uranium are found in various tectonic structures and various sequences of Paleozoic to Mesozoic strata. While the oil reservoirs occur mainly in Triassic and Jurassic units in the southern basin, gas reservoirs occur predominantly in the northern basin in the Ordovician Majiagou Formation and Permian Shanxi and Shihezi formations (Figs. 13.1c and 13.2a). Coal resources are widely distributed in the Carboniferous, Permian, Jurassic, and Triassic stratigraphic section. The sandstone-type uranium deposits and coalbed methane are distributed mainly along the basin margins.

More than 40 oil fields have been discovered in the basin, including Xifeng field, the largest oil field found in the past 10 years, with reserves of 400 Mt of crude oil. Four of China's five largest gas fields, each with reserves of at least 100 $Gm^3$, are located in the Ordos Basin (Sulige, Jianbian, Wushenqi, and Yulin gas fields; Fig. 13.2a). The Ordos Basin contains more than 8 Gt of equivalent petroleum resources and about 11 $Tm^3$ of natural gas. In 2012, oil production from Petro China Changqing was 22.3 Mt and production from the Yanchang Group was 12.55 Mt: production from these two companies together is close to the total oil production of the Ordos Basin. Natural gas production in the Ordos Basin was 28.9 $Gm^3$, accounting for 25 % of China's 2012 gas production.

The Ordos Basin contains more than 39 % of China's coal resources, with resources of 3.98 Tt; of these resources, 2.41 Tt occur less than 1500 m deep. Coal production in the Ordos Basin was about 1.1 Gt in 2011; six of the thirteen major national coal mines are located in the Ordos Basin. The reserves of coalbed methane in the Ordos Basin are estimated to be at 7.8–11.3 $Tm^3$.

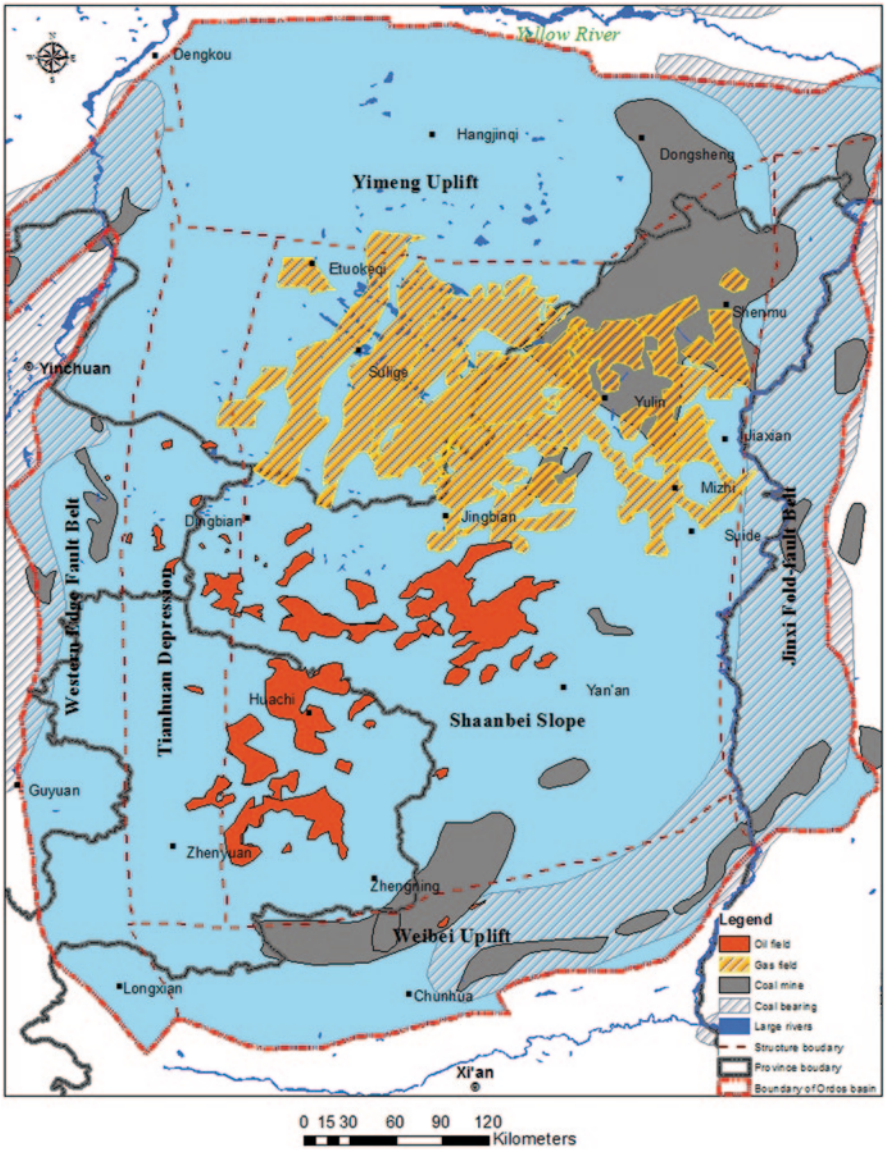


**Fig. 13.2** (**a**) Map showing oil, gas, and coal fields in the Ordos Basin, and (**b**) map of large stationary $CO_2$ point sources designated by type and annual emissions in the Ordos Basin

### *13.2.3 Sources of Anthropogenic $CO_2$ in the Ordos Basin*

Along with being China's number-one energy producer, the Ordos Basin also hosts the nation's largest coal-to-chemicals industry base. As more and more coal-fired power plants and coal-to-chemicals plants have been built near the coal mines in the Ordos Basin, anthropogenic $CO_2$ emissions have increased correspondingly and enormously.

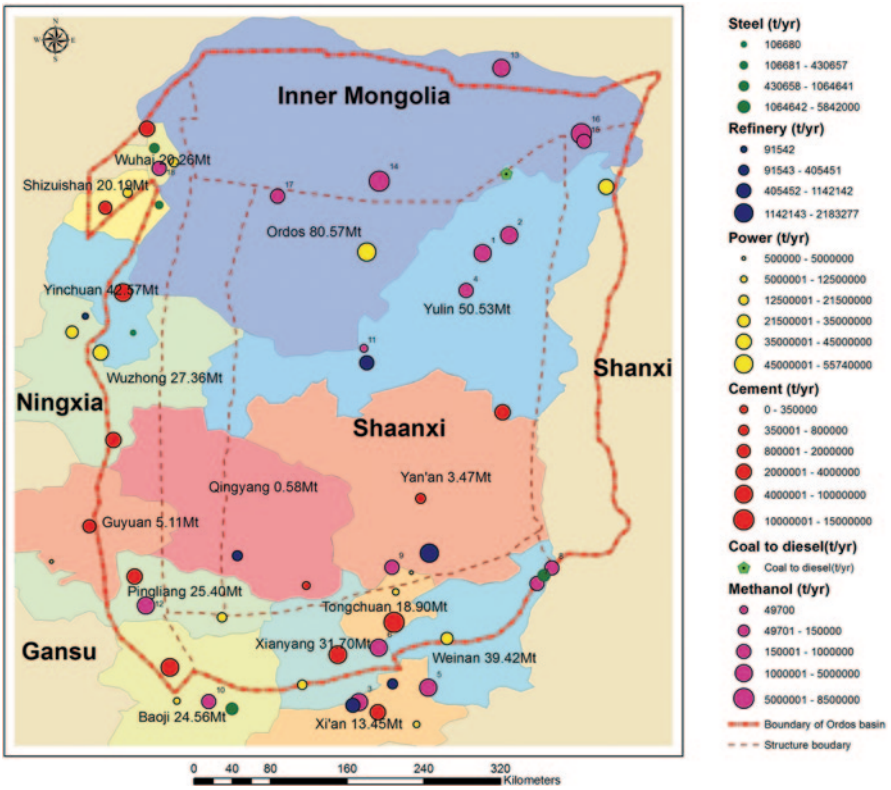


**Fig. 13.2** (continued)

Industrial sectors examined within the scope of this study include coal-fired power plants, coal conversion plants (methanol, acetic acid, diesel, ethylene oxide), cement plants, iron and steel plants, petroleum refining facilities, and ammonia plants. The $CO_2$ emissions calculation methodology presented here is based on IPCC Guidelines for national greenhouse gas inventory and is based on available plant capacity and reported productivity. Total major anthropogenic $CO_2$ emissions ECO2 is given by:

$$ECO_2 = \sum_{j}^{n} \sum_{i}^{m} ECO_{2ji}, \tag{13.1}$$

where for recorded production

$$ECO_{2ji} = EF_{ji} \times P_{1ji},$$

and for production capacity

$$ECO_{2ji} = EF_{ji} \times P_{2ji} \times A_{ji} \times T_{ji},$$

**Table 13.1** Estimated emission factors *EFji* for $CO_2$ emission sources (*i*) characterizing various industry sectors (*j*), in Kt of $CO_2$ per Kt of product, Kt of $CO_2$ per GWn for powerplants

| Sector | $CO_2$ emission factor | | | |
|---|---|---|---|---|
| Cement(kt/kt) | 0882[a] | 0.867[b] | 1.111[c] | 1.102[d] |
| Power(kt/GWh) | 1.000 | | | |
| Iron & Steel(kt/kt) | 1.270 | | | |
| Refinery(kt/kt) | 0.219 | | | |
| Methanol(kt/kt) | 5.67 ± 0.5 | | | |
| Coal to diesel(kt/kt) | 8.800 | | | |

[a] Dry process1; [b] Dry process2; [c] wet process1; [d] wet, process2

where $ECO_{2ji}$ is the estimated annual $CO_2$ emissions from the *i*th emission source within the *j*th industry sector; $EF_{ji}$ is the emission factor of the *i*th $CO_2$ emission source within the *j*th industry sector; $P1_{ji}$ is the production yield of the *i*th $CO_2$ emission source within the *j*th industry sector; $P2_{ji}$ is the production capacity of the *i*th $CO_2$ emission source within the *j*th industry sector; $T_{ji}$ is the production rate, full load time (hours); *n* is the number of industry sectors *j*; and *m* is the number of emission sources *i* within sector *j*.

$CO_2$ emissions calculated for cement plants, refineries, iron and steel facilities, and ammonia plants are based on reported production, while production capacity was used for power plants and a mixture of production and production capacity for ethylene oxide and ethylene plants. Table 13.1 shows $CO_2$ emission factors for these sectors.

Figure 13.2b shows the stationary $CO_2$ sources in the Ordos Basin that emit at least 0.1 Mt of $CO_2$ per year. These sources comprise coal-to-chemicals plants, coal-fired power plants, refineries, cement plants, and ammonia and other chemical plants. Thus, this analysis does not consider all anthropogenic $CO_2$ emissions, and specifically does not include those from small industrial $CO_2$ point sources, transportation, direct energy use in commercial and residential buildings, land use, or agriculture.

More than 67 large stationary point sources in the Ordos Basin emit more than 0.1 M/year of $CO_2$. Annual $CO_2$ emissions from these sources total an estimated 409 Mt/year. Among these emissions are 44.02 Mt from methanol plants and 6.86 Mt from coal-to-diesel plants, giving 50.88 Mt of $CO_2$ per year emitted in high concentration (>95%), ready for capture, and ready for use for $CO_2$ flooding in the Ordos Basin.

## 13.3 Geologic Structural Modeling

We constructed a regional 3-D geologic structural model of the Ordos Basin utilizing well logs, isopach maps, and geologic data assembled from the literature. The model covers a major portion of the major Shaanbei Slope Block (420 × 750 km), and was built using the EarthVison® software, a 3-D geospatial modeling package. No faults are included in this geologic structural model. The model was generated around a 340×490×7-km 3-D grid matrix: the gridding on the X, Y, and Z axes

(width, length, and depth), 69×99×71, resulted in cells 5000 m wide, 5000 m long, and 100 m deep, respectively; 2-D and 3-D minimum-tension gridding was used. The 3-D geologic structural model was used to calculate the $CO_2$ storage capacity of the Majagou Formation using a volumetric approach.

A smaller 3-D geologic model, for a 50×50-km area centered near Hengshan city, was extracted from the regional geologic structural model. This smaller-scale model was used to generate a 3-D computational mesh for the Majiagou $CO_2$ injection simulation.

### *13.3.1 Generation of the 3-D Computational Mesh*

Following the logic and methodology outlined by Miller et al. (2007), a 3-D computational hydrostratigraphic mesh was created from the smaller 50-km×50-km geologic structural model. In this computational mesh, the simulation cells or nodes were aligned to follow the curvature of the unit interfaces and do not stair-step in the manner of a traditional finite element grid. This allows more accurate calculation of $CO_2$ moving along the base of the caprock in the up-dip direction. This numerical mesh consists of a block 50-km×50-km in map view within the 340×490 km regional geologic structure model of the Shaanbei Slope Block, with elevation extending from 200 m above sea level to 3200 m below sea level. The grid spacing is 250 m in the X and Y directions at the injection area and increases logarithmically away from the injection area. The grid spacing in the Z (vertical) direction is 50 m in the injection interval and 100 m both above and below the injection interval. The total mesh comprises 320,000 nodes with 1.92 million volume elements (six volume elements per node).

### *13.3.2 $CO_2$ Injection Simulation Setups*

Simulations of $CO_2$ injection were run on the Los Alamos National Laboratory Finite Element Heat and Mass Transfer (FEHM) multiphase porous flow simulator.

Initial conditions set for the model domain included a geothermal gradient of 26 °C/km with a domain bottom temperature of 135 °C and a domain top temperature of 47 °C, and a hydrostatic pressure ranging from 13 MPa at the top of the model domain 200 m above sea level to 44 MPa at the bottom of the modeling domain 3200 m below sea level. Further simplifying assumptions for the 3-D injection calculations were:

| | |
|---|---|
| Rock thermal conductivity | 0.5 W/mK |
| Rock density | 2650 kg/m$^3$ |
| Heat capacity | 1000 J/kgK |

Relative permeability for all rocks was assigned with a residual saturation of 10% for both brine and $CO_2$ using a linear relationship. Capillary pressure effects were ignored; brine TDS was assumed constant at 20,000 ppm for all formations, and water viscosity was calculated independently of brine content or dissolved $CO_2$. The initial dissolved $CO_2$ concentration was set to zero. During $CO_2$ injection simulation, the simulator accounted for $CO_2$ dissolution in water. For all simulations, the down-dip sides (west and south sides of the domain) were closed, whereas the up-dip sides (north and east sides) are open to reservoir fluid flow.

#### 13.3.2.1 Majiagou Formation Simulations and Results

An important consideration in the $CO_2$ injection simulation scenarios is pressure buildup during injection. A limiting value of 75% of overburden pressure was selected for all simulations in order to ensure that the Majiagou Formation and overlaying sealing formations were not fractured during injection.

In order to evaluate the impacts of injection rate, porosity, and permeability on storage capacity, reservoir pressure evolution, and $CO_2$ plume migration trends, a series of $CO_2$ injection simulations was conducted with various combinations of injection rates and with various porosities and permeabilities for the targeted Majiagou Formation:

| | |
|---|---|
| Injection rate | 0.5, 1.0, 2.0 Mt/yr |
| Porosity | 5, 10% |
| Permeability | 1, 5 mD |

All simulations used a formation thickness of 500 m (the actual thickness of the Majiagou Formation at the site is more than 700 m) within the 50×50×3.4-km numerical mesh block.

Three Majiagou simulations (with nine injection wells) with injection rates of 0.5, 1.0, and 2.0 Mt/year per well at a porosity of 10% and a permeability of 5 mD resulted in the storage of 4.5, 9, and 18 Mt/yr, respectively. These simulations were run for 100 years with $CO_2$ injection ending after the first 50 years (Fig. 13.3a). With an increase in the injection rate in the nine injection wells from 4.5 to 18 Mt/year, the maximum reservoir pressure increased from 40 to 55 MPa but remained below 60 MPa, 75% of the fracture pressure (80 MPa) of the Majiagou Formation in the study area. With greater $CO_2$ injection, the amount of fluid displaced also increased.

Figure 13.3b shows the results of three simulations with injection rates of 0.5, 1.0, and 2.0 Mt/year at a constant porosity of 5% and a permeability of 1 mD. Compared with the 10% porosity, 5 mD injection simulations (Fig. 13a), both the reservoir pressure and the volume of displaced fluid were greater with greater injection rate, but the magnitude of increase was much larger. With 1 mD permeability and at an injection rate of 18 Mt/year, (9 wells×2.0 Mt/year/well), the reservoir pressure reached 75% of the fracture pressure of the Majiagou Formation after 10 years of

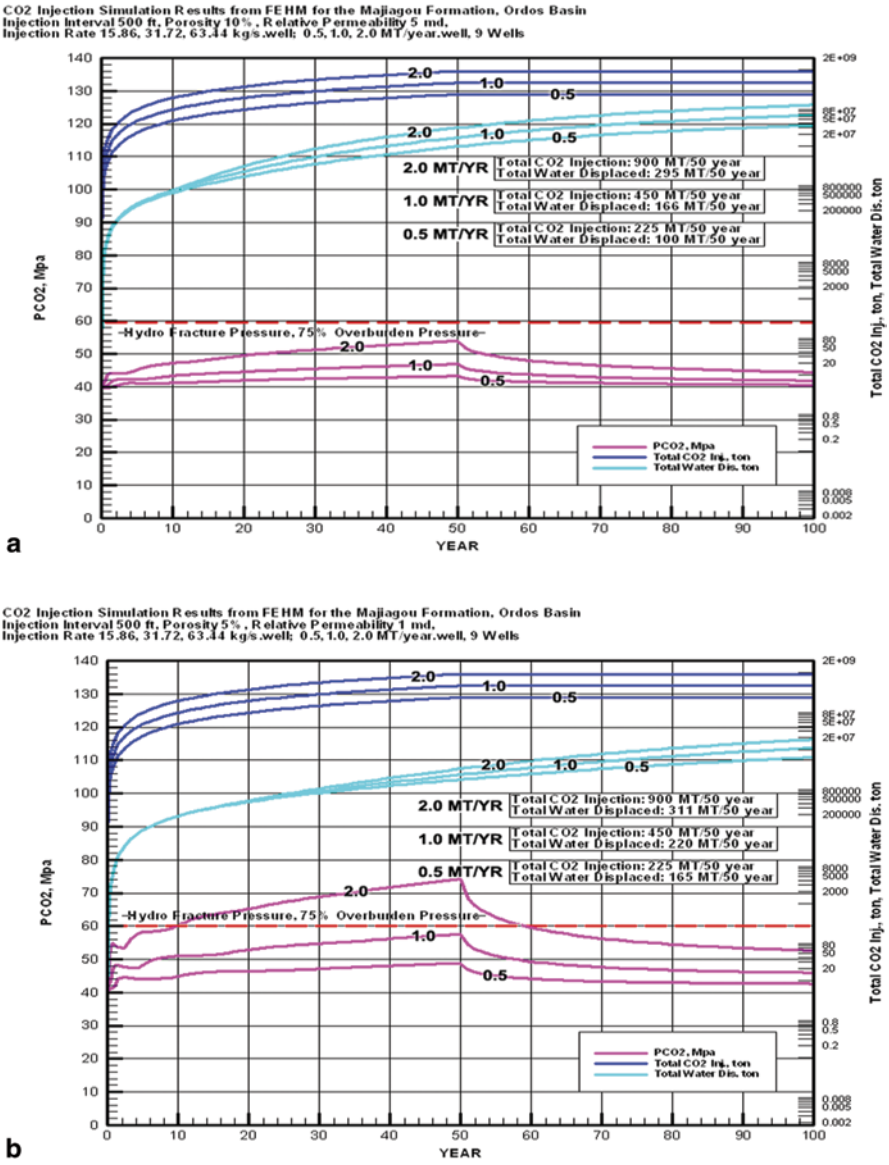


**Fig. 13.3** FEHM simulation results for various porosities, permeabilities, and $CO_2$ injection rates. (From Jiao et al. 2011)

injection and kept increasing to near the lithostatic pressure. In all cases, the reservoir pressure dropped sharply when $CO_2$ injection stopped (Fig. 13.3a, b).

On the basis of all available measured data, an average porosity of 10% and a relative permeability of 5 mD for the Majiagou Formation were considered the most likely values for preliminary simulation. The input parameters for the most

reasonable simulation were a 1.0 Mt/year per well injection rate, 10 % porosity, and 5 mD permeability. With this set of parameters, results from the 50-year injection simulation show a total 450 Mt of $CO_2$ injected into the targeted reservoir and a total 166 Mt of original pore fluid displaced by the $CO_2$. Furthermore, the reservoir pressure remains well below the 75 %-of-fracture-pressure limit (Fig. 13.3a).

Simulation results suggest that saturation in the $CO_2$ plumes ranges from 0.1 to 0.9. The modeling results from this simulation showed that the $CO_2$ plume produced from a 1.0 Mt/year injection rate was relatively small after a total 450 million tonnes of $CO_2$ had been injected. The $CO_2$ plume remained within the 16 km × 15 km injection area after 50 years of $CO_2$ injection and stayed within an area of 17.7 km × 16 km after 100 years, 50 years post injection.

### *13.3.3 Storage Capacity Based on the Volumetric Approach*

Burrus et al. (2009) present a method for estimating $CO_2$ storage capacity, the total known volume (TKV), based on the volume of pore space in a reservoir. The storage capacity in tonnes $S_{TKV}$ [t] of a reservoir is given by:

$$S_{TKV} = T_a \times T_i \times N_{tp} \times \emptyset \times C_e \times C_f \times \rho_{CO_2}, \tag{13.2}$$

where $T_a$ is the trap area [$m^2$]; $T_i$ is the interval thickness of the storage formation [m]; $N_{tp}$ is the fraction of $T_i$ occupied by the reservoir interval [decimal fraction]; $\emptyset$ is the porosity [decimal fraction]; $C_e$ is the storage efficiency factor (the fraction of the pore space that can be occupied by $CO_2$) [decimal fraction]; $C_f$ is a unit conversion factor (here, $C_f = 1$); and $\rho_{CO_2}$ is the density of $CO_2$ [$t/m^3$].

In order to use Eq. 13.2 to calculate the $CO_2$ storage capacity of the Majiagou Formation, the trap area ($T_a$) must first be defined. In other words, we must determine the upper and the lower depth limit of the targeted reservoir. The pressure and temperature required for $CO_2$ to be a stable supercritical fluid (31 °C and 7.4 MPa) are typically met at depths greater than 800 m (2600 ft) under a normal hydrostatic pressure gradient. To reduce the chance that the $CO_2$ would migrate to pressure and temperature conditions where it would change from the supercritical phase to liquid and vapor, a minimum storage depth of 1000 m (3,280 ft) was chosen for these estimates. The minimum storage depth sets the upper depth limit of a potential $CO_2$ reservoir. The choice of the lower depth limit for $CO_2$ storage is more arbitrary than that of the upper depth limit. It is based on the conclusion that if the $CO_2$ pressure at the wellhead is 15 MPa (2,175 psi) and $CO_2$ supercritical density is 0.65 $g/cm^3$, the $CO_2$ pressure will be 41 MPa (6000 psi) at the bottom of a 4000-m-deep (13,120 ft) well. Therefore, $CO_2$ injected at this depth will displace normally pressured formation water without additional compression. In the present study, 4 km (13,120 ft) is chosen for the maximum storage depth. On the assumption that 25 % of the formation thickness is available for storage the total volume of rock for $CO_2$ storage

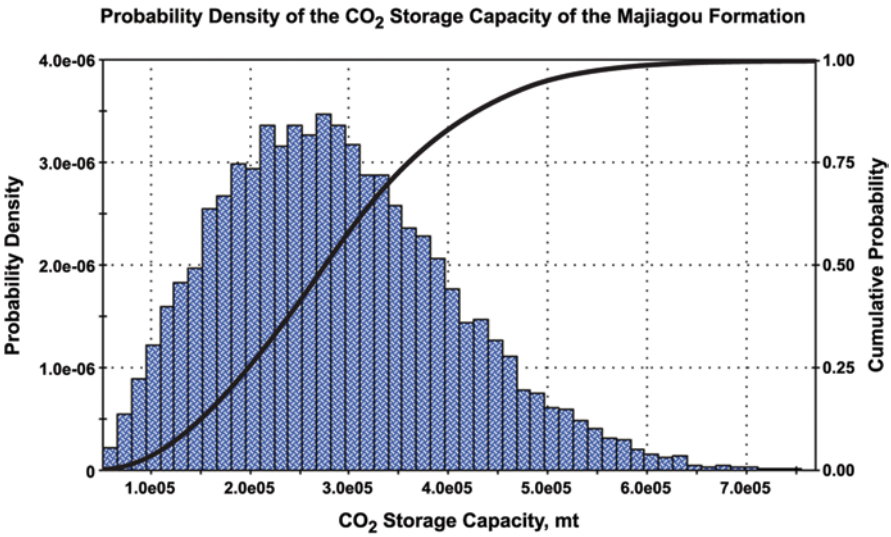


**Fig. 13.4** Probability density of the $CO_2$ storage capacity in the Majiagou Formation, Ordos Basin. A cumulative probability of 25% yields a value of 200 Gt; this indicates that for this particular distribution, we have a 25% chance of storing 200 Gt of $CO_2$ or less. Put another way, this indicates that we have a 75% chance of storing at least 200 Gt $CO_2$ in the Majiagou Formation in the Ordos Basin

($T_a \times T_i \times N_{tp}$) was determined from the EarthVision® geologic structure model of the Majiagou Formation in the Ordos Basin to be 14,500 $km^3$.

A lognormal porosity distribution with a mean of 0.085, standard deviation 0.02, and skewness 0.44 was determined from all available Majiagou porosity measured data. For a saline aquifer, the upper limit on the storage efficiency factor *Ce* is related to the irreducible water saturation of the trap with $CO_2$ present. Values for irreducible water saturation in petroleum reservoirs are not well known, but probably range from a minimum of about 0.2 in gas reservoirs to about 0.6 in oil reservoirs. The results of the $CO_2$ injection simulation using FEHM show that most $CO_2$ saturation values range between 0.1 and 0.6. We chose a storage efficiency factor *Ce* for these simulations of 0.1 and 0.6.

A Monte Carlo simulation from Goldsim software with 10,000 realizations using the volume, porosity, and storage parameters described above was set up for the Majiagou Formation between depths of 1000 and 4000 m in the Shaanbei Slope of the Ordos Basin. Figure 13.4 shows the probability density of the $CO_2$ storage capacity of the Majiagou Formation in the Ordos Basin: ranges from 60 to 700 Gt, with a mean of 287 Gt (Fig. 13.4). Thus, the Majiagou Formation has sufficient storage capacity to accommodate decades of $CO_2$ emissions generated by the coal industry in the Ordos Basin.

## 13.4 Lessons Learned From Current U.S. $CO_2$-EOR Projects

Over the past 40 years, $CO_2$ flooding has become an established technology capable of effectively enhancing oil recovery in mature and mostly-depleted oil reservoirs. Particularly, $CO_2$ flooding improves the efficiency of oil recovery significantly compared with primary (pressure depletion) and secondary (water flooding) recovery methods (Oil and Gas Journal 2012, Manrique et al. 2010).

Production from 120 individual U.S. $CO_2$-EOR projects during 2012 averaged 352,221 barrels of oil per day (BOPD) (Oil and Gas Journal 2012), approximately 6% of the total U.S. crude oil production of about 6 million BOPD. Of the $CO_2$-EOR production, 308,564 BOPD was from $CO_2$ miscible flooding and 43,657 BOPD was from $CO_2$ immiscible flooding. $CO_2$ flooding technology has surpassed thermal technology (steam, in-situ combustion, and hot water) as the most commonly used method of tertiary enhanced oil recovery.

Miscible $CO_2$ flooding has achieved widespread use in the southwestern U.S., mainly in the Permian Basin, Rocky Mountains, and Mid-Continent region. There is additional EOR production in Alaska partly related to $CO_2$ injection. The oil and gas industry generally handles $CO_2$ in its supercritical phase, which is stable above the critical point, 6.9 MPa (1,087 psi) and 31 °C (88 °F). In its supercritical phase, injected $CO_2$ in the reservoir behaves like a liquid with respect to density and like a gas with respect to viscosity. Under suitable reservoir pressure and oil composition conditions, injected $CO_2$ mixes thoroughly with the crude oil within the reservoir, resulting in oil volume increase through oil swelling and a subsequent reduction of oil viscosity, eliminating interfacial tension between the oil and $CO_2$, and reducing the capillary forces that inhibit oil flow through the pores of the reservoir (Brock et al. 1989; Shtepani 2007; Manrique et al. 2012) Theoretically, all contacted oil could be recovered under $CO_2$ miscible flooding (Shtepani 2007), although in U.S. $CO_2$ flooding experience, recovery is usually limited to about 5–22% of the original oil in place. $CO_2$ flooding efficiency is affected by such parameters as reservoir residual pressure, residual oil saturation, oil composition and viscosity, reservoir porosity and permeability, sedimentary architecture, and especially reservoir heterogeneity and natural fractures.

On the basis of years of experience in the laboratory, field pilot and demonstration tests, and full-scale commercial operations, numerous miscible $CO_2$ enhanced oil recovery screening criteria have been suggested (Brashear and Kuuskraa 1978; Goodlett et al. 1986; Taber et al. 1997a, b; Klins 1984; Taber and Martin 1983; DOE 2010; Eduardo et al. 2008; Brock et al. 1989; Manrique et al. 2012). $CO_2$ flooding has been applied successfully in both sandstone and carbonate reservoirs. Homogenous, well connected, thin beds are preferred. For an optimal miscible $CO_2$ project, the crude oil specific gravity should be greater than 22° API; that of current projects ranges between 27° and 44° API. The recommended viscosity is less than 10 cp; that of current projects ranges from 0.3 to 6 cp. The residual oil saturation recommended is greater than 40%; the oil saturation of current projects range from 15 to 70%. A high percentage of intermediate composition in the crude oil (C5 to C12) is favorable for miscible $CO_2$ flooding. Residual reservoir pressure is a critical

parameter for a $CO_2$ flooding project. Many projects inject water to establish reservoir pressure before $CO_2$ flooding. The residual reservoir pressure must be greater than the minimum miscible pressure, which is generally determined by reservoir depth; the depth of existing projects ranges from 2500 ft to more than 11,250 ft (Peterson et al. 2012). Reservoir temperature is not a critical screening criterion, but higher temperatures increase the expandability of the crude oil. Porosity values vary widely among different depositional systems, but generally range between 6 and 30% (Beike and Holtz 1996). The type of porosity, as well as the amount, is important to EOR projects. Well-connected pores approaching uniform size are best for $CO_2$-EOR miscibility projects. Permeability determines the fluid dynamics of the reservoir. High permeability will allow large volumes of $CO_2$ to be injected into a single well, thus reducing cost. Homogenous high permeability will also allow $CO_2$ to move more quickly into a reservoir, increasing sweep efficiency.

Reservoir heterogeneity and natural fractures can contribute to an unsuccessful $CO_2$ flooding project, especially in a depositional system having high vertical and horizontal variability in permeability. Highly permeable strata can promote unstable flow (viscous fingering), resulting in early break-through of $CO_2$ and reduction of oil sweep efficiency. To prevent the occurrences of unstable flow and to reduce the amount of $CO_2$ consumed, $CO_2$ is typically injected into the reservoir alternately with water (WAG), because water sweeps through the reservoir more uniformly. WAG injection can significantly reduce viscous fingering and allow $CO_2$ flow through the reservoir after full miscibility is achieved.

## 13.5 An Integrated Energy/CCUS Development Strategy

The Carbon Management Institute at the University of Wyoming has created an integrated energy/CCUS development strategy to systematically and concurrently develop the coal mining and coal conversion industries, coalbed methane (CBM) production, $CO_2$ enhanced oil recovery, and $CO_2$ storage in the Powder River Basin, Wyoming. Chapter 12 is a full account of that integrated strategy.

The Ordos Basin geologic setting and energy resources profile are similar to those of the Powder River Basin. The concurrent development of new coal conversion industries and oil-and-gas industries in northern Shaanxi Province offers the opportunity for applying the integrated strategy developed in Wyoming: the integration of geologic $CO_2$ storage, and $CO_2$-EOR. The coal conversion industries (coal to methanol, coal to olefins, etc.) provide affordable, capture-ready $CO_2$ sources for large-scale $CO_2$-EOR and storage projects in the Ordos Basin. The ability to use $CO_2$ emitted by the coal-conversion industries for $CO_2$-EOR and geologic $CO_2$ storage will make these projects in the Ordos Basin cost-effective and technologically efficient.

An integrated energy development strategy has been developed for the Shaanbei National Energy Base. This integrated energy development strategy aims to synchronously, synergistically develop coal mining, the coal conversion industry,

coalbed methane production (CBM), $CO_2$ enhanced oil recovery, and $CO_2$ storage in the Shaanbei National Energy Base.

First, coal mining would continue using existing extractive technology or improved technology. Second, the new coal-to-chemicals facilities would be located as close to the coal mines as possible. In the Ordos Basin, recently constructed coal-to-chemicals plants are sited over underground coal mines (Shenmu Jinjie Industry Park and Yanchang Jinbian Industry Park). Third, coalbed-methane produced water would best support these coal conversion facilities. The volume of water required to supply the plants will vary. In the Ordos Basin, coal-to-methanol plant design is based on a 6:1 ratio of water to product. A 0.6-Mt methanol plant in the Ordos Basin annually uses 1.8 Mt of coal and 6.0 Mt of water, and emits 4.0 Mt of $CO_2$. A 7-million-barrels-per-year diesel plant annually uses 3.5 Mt of coal and approximately 56 Mt of water, and emits 2 Mt of $CO_2$. At present, the coal conversion industry in the Ordos Basin would generate 9.24 Mt of methanol and 0.78 Mt of diesel annually, and would emit 50.88 Mt of $CO_2$ in total. This readily captured, highly concentrated $CO_2$ would be stored in the adjacent depleted oil and gas fields or saline aquifers, such as Majiagou reservoirs, which have a tremendous $CO_2$ storage capacity. Furthermore, Liao et al. (2012) have assessed the $CO_2$ storage capacities of 14 depleted oil fields in the Ordos Basin at 100 Mt. These depleted oil fields are ideal (1) for storage of $CO_2$ emitted by coal conversion facilities and (2) as sources of $CO_2$ for EOR projects in adjacent depleted Yanchang reservoirs.

As shown in Fig. 13.2, more than 40 mature Yanchang oil fields with EOR potential are located near coal mining/conversion resource confluences, and are eligible for tertiary recovery via $CO_2$ flooding. Many have gone through the secondary recovery water flooding stage and appear ideal for $CO_2$ miscible flooding. These Yanchang oil fields together contained 2 Gt of original oil in place (OOIP) (Wang et al. 2007). Typically, $CO_2$ flooding could recover at least 10% additional production in the the Yanchang oil fields, 200 Mt of oil. Recovering the stranded oil via $CO_2$ flooding would require 700 Mt of $CO_2$ (3.5 t per tonne of incremental oil recovered). For a 30-year EOR project, about 23 Mt of $CO_2$ would be required annually. The current coal conversion facilities envisioned (50.88 Mt of $CO_2$ emitted annually) could more than adequately support theses EOR activities. A conservative estimate suggests that the $CO_2$ would be worth $40/t, or US$28 billion. Therefore, the $CO_2$ typically regarded as a problem with respect to sequestration would be worth approximately US$28 billion in this scenario. Moreover, the Yanchang reservoirs from which the stranded oil is recovered could be converted to permanent storage sites for $CO_2$, doubling the $CO_2$ storage capacity available to the coal conversion facilities.

## 13.6 $CO_2$ EOR Potential and Challenge in the Ordos asin

Most oil production in the Ordos Basin is from the Triassic Yanchang Formation (Fig. 13.1c). The interbedded lenticular sandstone, siltstone, mudstone, and shale accumulated in fluvial, delta, and lacustrine depositional environments. The Tri-

assic Yanchang reservoirs have extremely low porosity, low permeability, low oil saturation, anomalously low reservoir pressure, and great heterogeneity. These characteristics have directly resulted in very low primary and secondary recovery, less than 15% in most oil fields in the basin. Table 13.2 shows reservoir and crude oil properties for selected Yanchang reservoirs.

The depth of Yanchang reservoirs in the Ordos Basin ranges from 150 to 2200 m. The individual sandstone beds range in thickness from 7 to 15 m. The porosities range from 8 to 17%. Permeabilities range from 0.5 to 38 mD, and many are less than 1 mD. The formation water type is calcium chloride with total dissolved solid from 10,000 to 70,000 ppm. The reservoir is regionally underpressured, even at the beginning of field development. The crude oil is light or intermediate, with specific gravity ranging from 0.72 to 0.84 or 35 to 62° API. Most of the reservoirs have oil saturations from 40 to 60%. Because all reservoir sandstones were deposited in fluvial and lacustrine environments, very low continuity and high heterogeneity is common in most reservoirs. Multi-age natural fractures are found in most cores from the Yanchang reservoirs.

A typical distribution of the Yanchang pay zones in an Ordos Basin reservoir shows compartmentalized, disconnected, lenticular sandstone and siltstone pay zones separated by mudstones and shales. Multiple fracture systems compound the reservoir heterogeneity.

Low porosity, low permeability, low oil saturation, anomalously low pressure, and high reservoir heterogeneity make using $CO_2$ enhanced oil recovery more challengeing than any $CO_2$ EOR project in the United States. This is a major reason that $CO_2$ EOR has not been widely developed in the Ordos Basin, even though $CO_2$ sources have been available for years. Table 13.2 lists reservoir and crude oil properties for selected oil reservoirs in the Ordos Basin. The depth of the reservoirs ranges from 200 to 2200 m. The individual bed thickness in the pay zone ranges from 5 to 18 m. The crude oil is light oil or intermediate oil with specific gravity ranging from 0.73 to 0.86 (33 to 62° API) and viscosity ranging from 1.3 to 9 mPas. All Yanchang reservoirs are anomalously underpressured, with a pressure coefficient of 0.9 (0.39 psi/ft). Therefore, the residual pressure in most candidate reservoirs is below the minimum miscible pressure. Most reservoirs are characterized by low porosity and permeability. The porosity for selected reservoirs ranges from 8 to 17%, and permeability from 0.5 to 38 mD.

Table 13.3 compares Ordos reservoir and crude oil properties with current U.S. $CO_2$-EOR screening guidelines and practice (Taber et al. 1997; Shtepani 2007; Lake et al. 2008). In this comparison gravity, viscosity, crude oil composition, oil saturation, and formation type of the Ordos reservoirs are favorable for $CO_2$ miscible flooding. The major challenge results from the anomalously low reservoir pressure, low porosity, and greater reservoir heterogeneity. The low permeability may help to increase $CO_2$-oil multiple contact chances but may hinder attainment of sufficient flow rates.

Even though a $CO_2$-EOR project in the Ordos Basin faces challenges, Ordos has many favorable characteristics for developing $CO_2$-EOR technology. Besides available local $CO_2$ sources, the thin beds and compartmentalized reservoirs are

**Table 13.2** Reservoir and crude oil properties for selected oil reservois in the Ordos Basin, China

| Oil field | Depth meter | Reservoir | Bed Thinck. (m) | Specific Gravity | API | Viscosity (mPa.s) | Pressure (Mpa) | Temp. (°C) | Porosity (%) | Perm. (md) | Oil Satura (%) | TDS (mg/l) | MMP[1](Mpa) |
|---|---|---|---|---|---|---|---|---|---|---|---|---|---|
| YC | 200–250 | Chang 6 | 13 | 0.84 | 37 | 4.9 | 1.8 | 19 | 9.9 | 0.55 | | 10,000 | |
| YP | 400–450 | Chang 2 | 7.6 | 0.85 | 35 | 5.5 | 3.6 | 23 | 13 | 6.5 | | 46,000 | |
| ZC | 400–450 | Chang 6 | 7.6 | 0.84 | 37 | 5.5 | 3.6 | 23 | 11.2 | 1.65 | 53.6 | 42,400–87,600 | |
| QH | 400–450 | Chang 2 | 8.7 | 0.84 | 37 | 6.3 | 3.6 | 23 | 14 | 15 | | | |
| YD | 350–550 | Chang 6 | 15.7 | 0.84 | 37 | 6.3 | 4 | 24 | 9.4 | 0.5 | 51 | | |
| GG | 150–350 | Chang 6 | 16 | 0.83 | 39 | 3.9 | 2 | 20 | 9.5 | 0.54 | 50.3 | 10,000 | |
| ZY | 150–350 | Chang 6 | 14.5 | 0.85 | 35 | 3.5 | 2 | 20 | 9.2 | 0.3 | 56 | | |
| ZL | 600–800 | Chang 2 | 5–18 | 0.85 | 35 | 8.9 | 7 | 32 | 17 | 7.3 | 42 | 50,000–70,000 | |
| TJ | 600 | Chang 2 | 14.8 | 0.84 | 37 | 4.6 | | 29 | 17.6 | 38.2 | | | |
| PQ | 1,000 | Chang 2, 4+5, 6 | 9.9 | 0.86 | 33 | 4.45–7.83 | 9 | 41 | 11 | 2.8 | 55 | | |
| QY | 1,000 | Chang 6 | 12 | 0.84 | 37 | 3.92 | 9 | 41 | 13.5 | 1.6 | 55.6 | | |
| HS | 1,100 | Chang 6 | 9.8 | 0.845 | 36 | 5.42 | 10 | 44 | 13.7 | 2.5 | 56 | | |
| XH | 1,200 | Chang 6 | 6.7 | 0.85 | 35 | 5 | 11 | 47 | 12 | 2.5 | | | |
| HU | 1,800 | | 12 | 0.77 | 52 | 1.64 | 18 | 71.6 | 10 | 0.5 | | | 19.5 |
| MU | 2,200 | | 14 | 0.73 | 62 | 1.35 | 22 | 76 | 8 | 0.5 | | | 19.8 |
| DB | 2,000 | 12 Chang 6 | 0.78 | 50 | 2 | 12 | 44 | 8 | 1 | 40 | 70,000 | 15.7 | |

All crude oil is light/intermediate type. All watert is $CaCl_2$

[1] Minimum miscibility pressure

**Table 13.3** Comparison of Ordos reservoir/crude oil properties with the US $CO_2$ EOR screening Guidline

| | US Recommended | US Current Projects Rang | Ordos |
|---|---|---|---|
| Gravity | <0.92 (>22 API) | 0.81–0.89 (27–44 API) | 0.73–0.86 (33–62 API) |
| Viscosity | <10 cp | 0.3–6 | 1.3–9 cp |
| Composition | High C5 to C12 percent light -intermediates | | Light-intermediates |
| Oil Saturation | >40% | 15–70% | 40–56 |
| Formation | Thin beds | Sandstone/carbonate | Thin sandstone beds |
| Porosity | >8% | 4–18% | 5–17% |
| Per me ability | Not critical | 3–31 md | 0.1–7 md |
| Depth | >800 m (2,600 ft) | | 200–2500 m (650–8200 ft) |

favorable for creating a stable flow (reducing $CO_2$ flow fingering) and increasing sweep efficiency. Reservoir pressure is one of the most important factors of $CO_2$ miscibility in oil. According to Klins and Bardon (1991) and Shtepani et al. (2007), it is possible to achieve a different level of miscibilities, ranging from immiscible (low-pressure reservoirs) through intermediate- to high-pressure applications (miscible displacement). The minimum miscibility pressure has a wide range of values depending on depth, temperature, and crude oil composition. A minimum of 8 MPa (1,160 psi) is generally regarded as a target reservoir pressure at which to conduct a successful $CO_2$ flood. This condition imposes an important restriction related to the current level of reservoir pressure for miscible $CO_2$ flooding. A significant number of reservoirs in the Ordos Basin fall below this level (Fig. 13.5).

Figure 13.5 shows oil fields superimposed on a map of the burial depth of the Yanchang Formation, the main oil and gas producing formation in the Ordos Basin. The heavy black line is the 800 m contour of the burial depth of the top of Yanchang Formation. The depths of oil fields that fall inside the heavy black line are below 800 m depth. Because the oil and gas reservoirs in the Ordos Basin typically have a very low content of movable formation water, water flooding is not efficient for secondary oil recovery. Injecting $CO_2$ into a reservoir before oil production could be an efficient way to establish reservoir pressures that meet the minimum miscible pressure requirement.

A pre-$CO_2$ injection simulation for building reservoir pressure was generated for a different scenario. For the test reservoir, the average depth of the targeted reservoir is 1500 m, porosity is 10%, and permeability is 1 mD. The injection rate of supercritical $CO_2$ is 23 kg/min. The depleted reservoir is anomalously underpressured at 11.5 MPa. The simulation results from the Los Alamos National Laboratory FEHM simulator shows that minimum miscible pressure could be established for this reservoir after 100 days of supercritical $CO_2$ injection (Fig. 13.6).

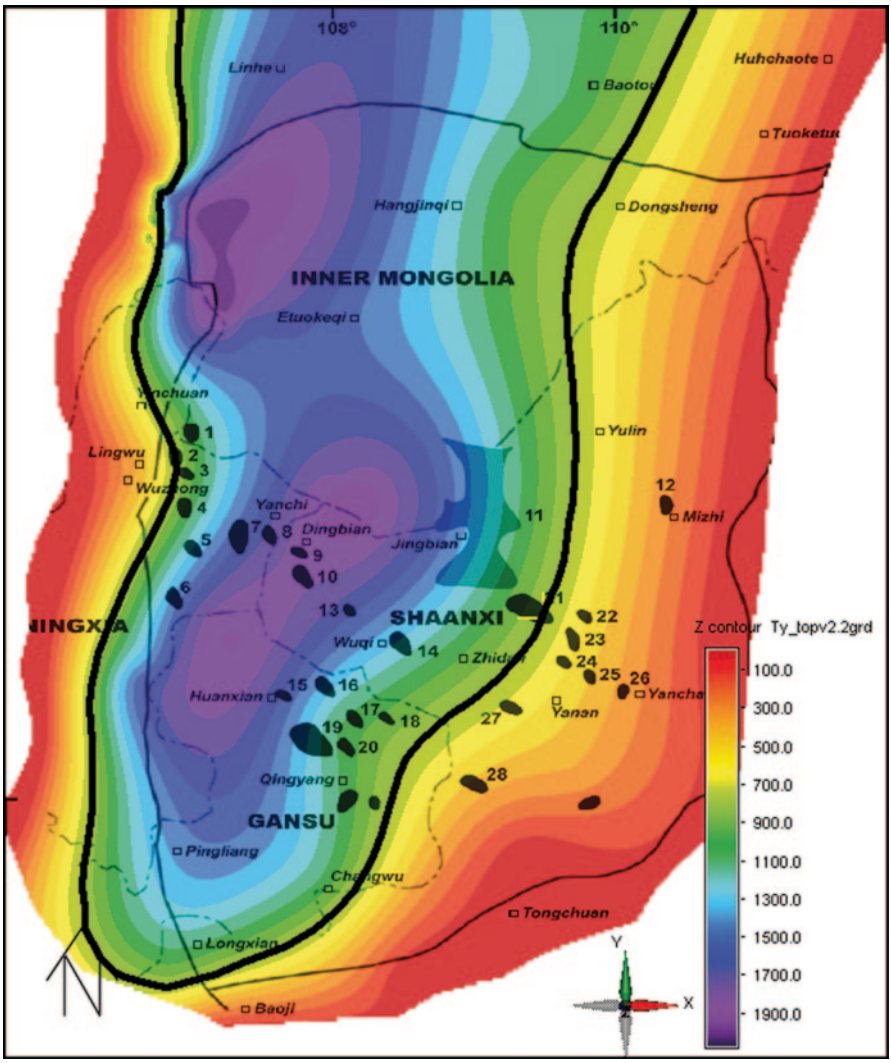


**Fig. 13.5** Yanchang Formation oil fields superimposed on a map of the burial depth of the Yanchang Formation top

## References

Brashear JP, Kuuskraa VA (1978) The potential and economics of enhanced oil Recovery. J Petrol Technol. SPE paper 6350

Brock W, Bryan L (1989) Summery results of $CO_2$ EOR field tests, 1972–1987. SPE paper 18977

Goodlett G (1986) Lab evaluation requires appropriate techniques. Oil Gas J June:23

Jiao Z, Surdam RC, Zhou L, Stauffer P (2011) A feasibility study of geological $CO_2$ sequestration in the Ordos Basin. Energy Procedia 4:5982–5989

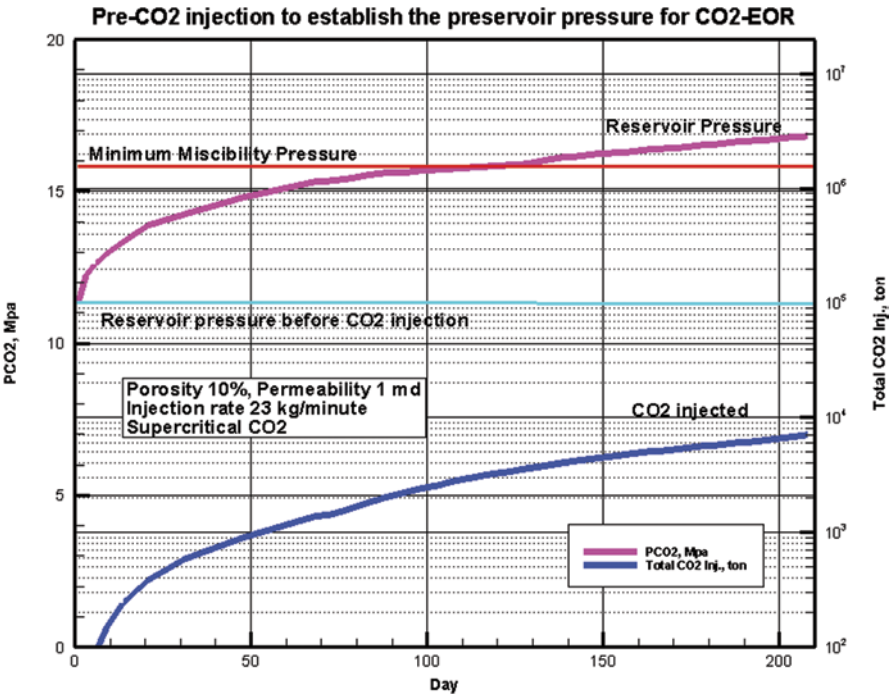


**Fig. 13.6** Plot of the results of the $CO_2$ injection simulation from the LANL FEHM simulator showing injection rate and time needed to establish the minimum miscible pressure for a miscible $CO_2$ flooding project

Klins MA (1984) Carbon dioxide flooding, basic mechanisms and project design. International Human Resources Development Corporation, Boston

Klins MA, Bardon CP (1991) Carbon dioxide flooding. Institut Francais du Pétrole

Koottungal L (2012) 2012 worldwide EOR survey. Oil Gas J April:2

Kuuskraa V, Ferguson R (2008) Storage $CO_2$ with enhanced oil recovery. DOE/NETL 402/1312/02-07-08

Lake L, Walsh M (2008) Enhanced oil recovery (EOR) field data, literature search. University of Texas at Austin

Marique E, Izadi CM, Lantz M, Alvarado V (2008) Effective EOR decision strategies with limited data: field cases demonstration. SPE paper 113269

Marique E, Thomas C, Ravikiran R, Izadi M, Lantz M, Romero J, and Alvarado V (2010) EOR: current status and opportumities. SPE paper 130113

Meyer J (2008) Summary of carbon dioxide enhanced oil recovery ($CO_2$-EOR) injection well technology. American Petroleum Institute

National Energy Technology Laboratory (NRTL) (DOE) (2010) Carbon dioxide enhanced oil recovery. www.netl.doe.gov

Peterson C, Pearson E, Chodur V, Periera C (2012) Beaver Creek Madison $CO_2$ enhanced oil recovery project case study, Riverton, Wyoming. SPE paper 152862

Shtepani E (2007) Experimental and modeling requirements for compositional simulation of miscible $CO_2$-EOR processes. SPE paper 111290

Surdam R, Jiao Z, Bentley R, Ganshin Y, Heller P, Fan M, DeBruin R, Rodgers J (2011) $CO_2$ sequestration in depleted compartmentalized gas fields—the key to deploying clean coal technology in the Powder River Basin, Wyoming. University of Wyoming School of Energy Resources, Laramie

Taber JJ, Martin FD (1983) Technical screening guides for the enhanced recovery of oil. SPE paper 12069

Taber JJ, Martin FD, Seright RS (1997a) EOR Screening criteria revisited—Part 1: Introduction to screening criteria and enhanced recovery field projects. SPE paper 35385

Taber JJ, Martin FD, Seright RS (1997b) EOR screening criteria revisited—Part 2: Application and impact on oil prices. SPERE Aug:199–205

Yang Y, Li W, Ma L (2005) Tectonic and stratigraphic controls of hydrocarbon systems in the Ordos Basin: a multicycle cratonic basin in the central China, AAPG Bull 89(2):255–269

# Chapter 14
# Summary of the WY-CUSP Characterization Program

**Ronald C. Surdam**

**Abstract** The goals of the WY-CUSP program were to improve estimates of geological $CO_2$ reservoir storage capacity, to evaluate the long-term integrity and permanence of confining layers, and to manage injection pressure and produced brine at the Rock Springs Uplift $CO_2$ storage site. In the process of achieving these goals, a new and substantially more effective strategy and technology has been developed to achieve the most accurate performance assessments and resultant risk reductions for detailed geologic $CO_2$ storage site characterization. The strategies and technologies used to perform the tasks resulting in achieving the project goals are the subject of this work—optimizing $CO_2$ storage efficiency at the Rock Springs Uplift study site and elsewhere. The ultimate mission of the WY-CUSP program, managed by the University of Wyoming Carbon Management Institute—delivery of a certified commercial $CO_2$ storage site in Wyoming that could be used as a surge tank for $CO_2$ utilization—has been accomplished.

## 14.1 The Rationale for $CO_2$ Storage in Wyoming

The Wyoming Carbon Underground Storage Project (WY-CUSP) is critical to the optimization of energy resource development in Wyoming. Both the Wyoming Geological Survey (WSGS) and the University of Wyoming's Enhanced Oil Recovery Institute estimate that, in Wyoming, 4–8 billion barrels (0.6–1.2 $Gm^3$) of stranded oil could be recovered by $CO_2$ flooding. Even if the number of gas processing plants in Wyoming was doubled and all the $CO_2$ produced stayed in Wyoming, it would still take more than 100 years to recover the state's stranded oil. Enhanced oil recovery operations in Wyoming desperately need an additional, substantial source of $CO_2$—anthropogenic $CO_2$.

R. C. Surdam (✉)
Carbon Management Institute Laramie, University of Wyoming, Laramie, USA
e-mail: rsurdam@uwyo.edu

R. C. Surdam (ed.), *Geological $CO_2$ Storage Characterization,*
Springer Environmental Science and Engineering, DOI 10.1007/978-1-4614-5788-6_14,
© Springer Science+Business Media New York 2013

Another industry that could flourish in Wyoming is coal-to-chemicals production. The technologies that convert coal to chemicals via gasification inherently capture $CO_2$ and can therefore provide storage-ready $CO_2$. All the coal-to-chemical processes produce substantial quantities of $CO_2$. However, unlike conventional coal-fired power plants, coal-to-chemical facilities produce $CO_2$ that can be effectively and efficiently captured. For these technologies and associated industries to be deployed in Wyoming, the state will have to document the availability of commercial-scale $CO_2$ storage capacity.

Everything learned from the WY-CUSP program with respect to the Weber/Tensleep and Madison formations is applicable to natural gas storage. Natural gas has been plagued in the past by demand fluctuations, supply disruptions, and hedge price variations. With the power-generating sector demanding more natural gas, we will see a premium on peak load demand as opposed to base load demand. Peak load demand will require gas storage sites capable of providing high deliverability of gas for short periods of time. At present, 44% of natural gas storage occurs in four states (Michigan, Illinois, Pennsylvania, and Texas); Wyoming only accounts for 1.1% of the nation's natural gas storage capacity. For Wyoming to excel as a future national gas supplier, the state will require substantial additional gas storage capacity.

The storage of $CO_2$ in a geologic structure such as the Rock Springs Uplift would displace enormous quantities of formation fluid (brines). The fluid management plan proposed by the Carbon Management Institute (CMI) involves producing this fluid and treating it at the surface to USEPA Underground Sources of Drinking Water (USDW) standards, then reinjecting the residual brine. Aines et al. (2010) along with their colleagues at Lawrence Livermore National Laboratory have shown that these subsurface brines can be treated effectively and efficiently, and at approximately half the cost of desalinating seawater. Storage of 15 Mt of $CO_2$ annually could result in 6600 acre-ft of treated potable water annually; over a 75 year period, storage of $CO_2$ at 15 Mt/yr will provide nearly 500,000 acre-ft of potable water (valued at US $100 million to US $600 million). In addition, it was recognized that formation brines are enriched in several economic metals. The recovery of these metals, such as lithium, from produced brines transforms the economic penalty associated with pressure management in carbon storage operations into a source of revenue. The recovery of metals and potable water during $CO_2$ sequestration on the RSU would substantially offset $CO_2$ storage costs.

Carbon storage is vital to protecting the coal extraction industry in Wyoming, particularly as it relates to allowing the coal-fired power generating sector of our economy to meet pending and future regulations. However, to view $CO_2$ storage and the WY-CUSP program solely in the context of that benefit misses the very broad context in which $CO_2$ storage would function: essentially, $CO_2$ storage could be the keystone of Wyoming's energy and water development in the twenty-first century. To sequester $CO_2$ from the atmosphere, to carry out the efficient recovery of stranded oil, to capture $CO_2$ emissions from a major coal-to-chemicals industry, to efficiently accommodate widely fluctuating natural gas demand, to supply increased potable water and lithium needs: all revolve around the sequestration and

storage of $CO_2$. Consequently the CMI suggests that our most productive strategy rests on adopting a proactive approach to $CO_2$ storage and working to create a certified commercial $CO_2$ storage site in Wyoming.

## 14.2 The WY-CUSP Site Characterization Strategy

The goal of the Wyoming Carbon Underground Storage Project (WY-CUSP) is to demonstrate that successful, commercial-scale $CO_2$ storage can be achieved in Wyoming. The characterization portion of the WY-CUSP program focused on reservoirs (the Pennslyvanian Weber/Tensleep Sandstone and Mississippian Madison Limestone) and overlaying confining intervals at a potential $CO_2$ storage site on the northeastern limb of the Rock Springs Uplift, southwestern Wyoming.

Preliminary, regionalized geologic characterization work on the Rock Springs Uplift (RSU) documented four-way closure; 10,000 ft (3000 m) of structural relief; multiple stacked confining layers, and a 1000-ft-thick (300 m) section of potential storage reservoirs at depths and pressures where $CO_2$ will be supercritical (Surdam et al. 2009). Initial results from the application of both the FutureGen and USGS diagnostic protocols for evaluating $CO_2$ storage capacity suggest that the Weber Sandstone and Madison Limestone on the Rock Springs Uplift could store all Wyoming's stationary, anthropogenic $CO_2$ emissions (approximately 55 Mt of $CO_2$/yr) for 500–700 years.

All available surface and subsurface information pertaining to the storage reservoirs, confining layers, and structural setting was collected by CMI in the course of the project. On the RSU, a 20,000-mi$^2$ (50,000-km$^2$) area, only 19 wells penetrate the targeted Paleozoic stratigraphic storage interval. Using existing data, preliminary numerical simulations of a wide variety of injection/storage scenarios document that the Rock Springs Uplift and Weber/Madison reservoirs are able to support (1) numerous commercial $CO_2$ storage facilities with enough storage capacity for all the $CO_2$ emitted by two large coal-fired power plants (Jim Bridger—2300 MW, 18 Mt $CO_2$/yr; Naughton—700 MW, 9 Mt $CO_2$/yr), (2) the world's largest concentration of trona processing plants, and (3) any future coal-to-chemicals plants or enhanced oil recovery projects constructed in Wyoming.

Initial modeling of injection and storage in reservoirs on the RSU identified two crucial problems; pressure-related, reservoir management of displaced fluids, and uncertainty in numerical simulations and performance assessments due to lack of realistic documentation of the 3-D heterogeneity of geological and petrophysical parameters. The WY-CUSP program has demonstrated how these previously insurmountable problems can be overcome: the integration of a robust geologic database with seismic attribute volumes.

To address the issues regarding reservoir pressure management, CMI worked with Roger Aines and Tom Wolery at Lawrence Livermore National Laboratory (LLNL) to design a customized water treatment strategy for produced brines. Water samples retrieved from the Weber and Madison formations in the Rock Springs

Uplift #1 stratigraphic test well (RSU #1) have accelerated this work. The WY-CUSP team has delivered designs for a reverse-osmosis water treatment plant capable of handling large quantities of pressurized fluids produced from the Weber/Madison reservoirs. In arid southwestern Wyoming, the need and demand for potable water is high; residential users, agricultural operations, coal-fired power plants, coal-to-chemical facilities, and downstream users in the Colorado River drainage, among others, will require ever-increasing amounts of water in the future. In the process of characterizing the formation fluids in the Madison Limestone and Weber Sandstone, the CMI team discovered that the fluids contain significant quantities of lithium. This observation allowed the CMI team to substantially expand and improve the water treatment plan for the displaced fluids. The expanded design includes the following key elements:

- Utilization of heat energy from the deep brine to generate electricity to operate the treatment facility.
- Use of nannofilters and reverse osmosis to separate potable water from the produced, pressurized brines.
- Separation of lithium and other metals from the residual brines after partial evaporation.
- Reinjection of residual brines down-dip from the $CO_2$ injection site and storage domain.

This water treatment design transforms a potentially prohibitive expense (cost of formation fluid production and treatment) into a real revenue-generating center (generation of electricity, sale of fresh water and metals).

To obtain the information essential to our characterization strategy, the WY-CUSP program drilled a stratigraphic test well and acquired a 3-D seismic survey for a nominated site. The drilling was outstandingly successful: 916 ft (279 m) of core was retrieved, along with a complete log suite (including wellbore and a photoelectric (Pe) log for mineral composition, spectral logs, borehole images, fluid samples, core samples, and a VSP survey). Drilling was successful thanks to the excellent performance of our drilling operator, Baker Hughes and the drill rig and crew provided by True Drilling of Casper, Wyoming. In addition, PetroArc International completed continuous visual documentation of the core, including grain size, mineralogy, facies distribution, and porosity. PENCOR and Energy Laboratories provided the chemical analyses of the fluid samples. All the data interpretation and integration was completed by the WY-CUSP team (CMI, UW students and faculty, colleagues at the Wyoming State Geological Survey, and Wyoming contractors).

Before the well is completely abandoned, a string of geophones will be run through the well to create a baseline of natural micro-seismicity at the study site. This information will probably be required for future permitting of commercial-scale $CO_2$ injection/storage projects on the RSU and elsewhere.

WY-CUSP researchers integrated 3-D seismic data with petrophysical data, core observations, and in-situ well tests to construct porosity, permeability, lithofacies, and fracture distribution volumes for the Weber and Madison reservoirs beneath a 25-$mi^2$ (64-$km^2$) area centered on the RSU #1 stratigraphic test well. Within these property volumes, it is now possible to isolate individual reservoir

horizons and construct maps of the distribution of seismic attributes and associated petrophysical properties, most importantly porosity and permeability. A 5-mi × 5-mi (8-km × 8-km) 3-D seismic survey, 916 ft (279 m) of core, a complete wireline well log suite retrieved from the 12,810-ft-deep (3904 m) RSU #1 well, and geological descriptions of the study area and the Greater Green River Basin were used in refining seismic interpretations. The three-dimensional configuration of heterogeneity in petrophysical properties of the storage reservoir intervals is derived from the seismic/log/core/geology integration, and substantially reduces the geologic uncertainties of numerical simulation of $CO_2$ injection scenarios (i.e. improved performance assessments and lower risk).

After having drilled and logged the RSU #1 test well in the fall of 2011, the CMI team realized the need for additional downhole information, and the well was re-entered during November 2012 to acquire that information. The most important analysis was measurement of injectivity in the storage intervals in the Madison Limestone and Weber Sandstone. A series of small-scale $CO_2$ injectivity tests (less than 5000 tonnes of $CO_2$ spread over six or more reservoir intervals in the Weber and Madison formations) would have been ideal. However, the CMI team could not meet financial and political barriers associated with using $CO_2$, so they instead used water as a surrogate in the injectivity tests (into four intervals in the Weber Sandstone and three intervals in the Madison Limestone). Using $CO_2$ would have required an Underground Injection Control (UIC) Class VI permit, whereas the water injectivity tests were accomplished under CMI's existing UIC Class I permit. The cost of food-grade $CO_2$ to be used for well testing also was prohibitive. Lastly, there was political resistance to using $CO_2$ for well testing because there exists a critical shortage of $CO_2$ for EOR projects in Wyoming. A significant amount of additional testing was accomplished by re-entering the well in November 2012. Among the information retrieved were temperature and pressure logs, well casing integrity tests, cement bond logs, step-rate injection tests, DSTs, fracture gradient tests, hydraulic head, fluid samples (bailed and pressurized), and a variety of Department of Environment Quality required tests.

CMI's results from this project have significant utility in reducing risk in $CO_2$ storage/hydrocarbon (EOR)/water production projects in the Rocky Mountain region and elsewhere. This work, for the first time, establishes a strategy for dealing accurately with projects relating to *deep* (> 10,000 ft, > 3000 m) injection/storage and production of $CO_2$/water in saline aquifers—reservoirs generally considered too deep and too tight for effective injection and storage.

## 14.3 Overview of Essential data for the Successful, Detailed Geologic Characterization of Potential CCUS Sites; Lessons from the WY-CUSP Project

Though there are numerous variables, and site-specific heterogeneity that will ultimately impact the long-term success of a potential CCUS site, CMI geoscientists have identified five essential components that were necessary for the detailed geo-

logic characterization of this study site. The collection, evaluation, and integration of the five key components can be accomplished at any selected site, allowing researchers to define geologic heterogeneity, storage capacity, confining permanence, geochemical responses, reservoir management scenarios, and most importantly the minimization of geologic unknowns associated with $CO_2$ injection. It is important to note that the five components can be collected after the site selection process, a task that is no less important to the long-term success and implementation of CCUS. These five components include:

1. 3-D seismic data across the study site
2. Petrophysical data (a robust well-log suite)
3. In-situ, downhole reservoir tests
4. Core and wellbore cuttings
5. Formation fluid samples

These five data components allowed CMI researchers to thoroughly identify, define, and address geologic uncertainties within the study site, and produce a robust geologic model. The CMI team is confident that the collection, evaluation and integration of these five datasets will substantially improve the characterization efforts at any potential geological storage site.

Clearly, these data were not the singular source of the project's success. Effective interpretation and integration of these data was largely due to the diverse expertise of geoscientists at CMI and the University of Wyoming. It is suggested that similar efforts are best served by a team of researchers and geoscientists representing diversity of expertise and depth of experience.

## 14.4 WY-CUSP Deliverables

In this book we have developed a strategy to evaluate a potential commercial-scale geological $CO_2$ storage site. Our strategy includes developing databases, gathering pertinent data and associated analytical results, integrating core observations with seismic and petrophysical data, developing seismic attribute volumes with modern techniques, correlating seismic attributes with petrophysical parameters, inputting 3-D volumes of petrophysical characteristics of both reservoirs and confining layers into numerical simulators for accurate performance assessments, and ultimately achieving credible risk evaluations. In the process of implementing this strategy, the CMI team has compiled all the information needed for permitting either a small-scale $CO_2$ injection/storage demonstration, or a full-scale commercial geological $CO_2$ storage project. Most importantly, the team has tried to describe the methods used in approaching and solving the obstacles faced in achieving a detailed, geologic characterization of a potential geological $CO_2$ storage site. There is an old adage that "a smart person learns from experience, but a wise person learns from the experience of others." We offer the WY-CUSP experience for the benefit of all others and hope it helps their efforts to characterize potential geological $CO_2$ storage sites.

## References

Aines R, Wolery T, Bourcier W, Wolfe T, Haussmann C (2010) Fresh water generation from aquifer-pressured carbon storage. Lawrence Livermore National Laboratory Report LLNL-PROC-424230. Presented at the Ninth annual conference on carbon capture and sequestration, Pittsburgh, PA, May 10–13, 2010

Surdam RC, Jiao Z, Stauffer P, Miller T (2009) An integrated strategy for carbon management combining geological $CO_2$ sequestration, displaced fluid production, and water treatment: Wyoming State Geological Survey. Challenges in Geologic Resource Development No. 8, p 25